



SPECTRAL-LUMINESCENT PROPERTIES OF ORTHORHOMBIC AND MONOCLINIC TUNGSTATE AND MOLYBDATE CRYSTALS DOPED WITH EUROPIUM, TERBIUM, THULIUM, AND YTTERBIUM IONS

Anna Volokitina

ADVERTIMENT. L'accés als continguts d'aquesta tesi doctoral i la seva utilització ha de respectar els drets de la persona autora. Pot ser utilitzada per a consulta o estudi personal, així com en activitats o materials d'investigació i docència en els termes establerts a l'art. 32 del Text Refós de la Llei de Propietat Intel·lectual (RDL 1/1996). Per altres utilitzacions es requereix l'autorització prèvia i expressa de la persona autora. En qualsevol cas, en la utilització dels seus continguts caldrà indicar de forma clara el nom i cognoms de la persona autora i el títol de la tesi doctoral. No s'autoritza la seva reproducció o altres formes d'explotació efectuades amb finalitats de lucre ni la seva comunicació pública des d'un lloc aliè al servei TDX. Tampoc s'autoritza la presentació del seu contingut en una finestra o marc aliè a TDX (framing). Aquesta reserva de drets afecta tant als continguts de la tesi com als seus resums i índexs.

ADVERTENCIA. El acceso a los contenidos de esta tesis doctoral y su utilización debe respetar los derechos de la persona autora. Puede ser utilizada para consulta o estudio personal, así como en actividades o materiales de investigación y docencia en los términos establecidos en el art. 32 del Texto Refundido de la Ley de Propiedad Intelectual (RDL 1/1996). Para otros usos se requiere la autorización previa y expresa de la persona autora. En cualquier caso, en la utilización de sus contenidos se deberá indicar de forma clara el nombre y apellidos de la persona autora y el título de la tesis doctoral. No se autoriza su reproducción u otras formas de explotación efectuadas con fines lucrativos ni su comunicación pública desde un sitio ajeno al servicio TDR. Tampoco se autoriza la presentación de su contenido en una ventana o marco ajeno a TDR (framing). Esta reserva de derechos afecta tanto al contenido de la tesis como a sus resúmenes e índices.

WARNING. Access to the contents of this doctoral thesis and its use must respect the rights of the author. It can be used for reference or private study, as well as research and learning activities or materials in the terms established by the 32nd article of the Spanish Consolidated Copyright Act (RDL 1/1996). Express and previous authorization of the author is required for any other uses. In any case, when using its content, full name of the author and title of the thesis must be clearly indicated. Reproduction or other forms of for profit use or public communication from outside TDX service is not allowed. Presentation of its content in a window or frame external to TDX (framing) is not authorized either. These rights affect both the content of the thesis and its abstracts and indexes.



UNIVERSITAT
ROVIRA I VIRGILI



ITMO UNIVERSITY

Spectral-luminescent properties of orthorhombic and monoclinic tungstate and molybdate crystals doped with europium, terbium, thulium and ytterbium ions

VOLOKITINA ANNA



DOCTORAL THESIS
2021

UNIVERSITAT ROVIRA I VIRGILI
SPECTRAL-LUMINESCENT PROPERTIES OF ORTHORHOMBIC AND MONOCLINIC TUNGSTATE AND MOLYBDATE CRYSTALS DOPED
WITH EUROPIUM, TERBIUM, THULIUM, AND YTTERBIUM IONS
Anna Voloikitina

Anna Volokitina

SPECTRAL-LUMINESCENT PROPERTIES
OF ORTHORHOMBIC AND MONOCLINIC
TUNGSTATE AND MOLYBDATE CRYSTALS
DOPED WITH EUROPIUM, TERBIUM,
THULIUM AND YTTERBIUM IONS

DOCTORAL THESIS

Supervised by Dr. Xavier Mateos Ferré
Department of Physical and Inorganic Chemistry

Supervised by Dr. Alexander Baranov
Faculty of Photonics



UNIVERSITAT ROVIRA i VIRGILI

Tarragona
2021



**Национальный исследовательский университет ИТМО
(Университет ИТМО)**

На правах рукописи

Волокитина Анна Андреевна

**Спектрально-люминесцентные свойства
ромбических и моноклинных кристаллов
вольфраматов и молибдатов, активированных
ионами европия, тербия, тулия и иттербия**

Специальность 1.3.6

«Оптика (физико-математические науки)»

**Диссертация на соискание учёной
степени кандидата физико-математических наук**

Научный руководитель:

доктор физико-математических наук
Баранов Александр Васильевич

Доктор химических наук
Хавьер Матеос Ферре

Санкт-Петербург 2021



UNIVERSITAT
ROVIRA I VIRGILI

DEPARTAMENT DE QUÍMICA FÍSICA
I INORGÀNICA

Campus Sescelades
Marcel·lí Domingo, s/n
43007 Tarragona
Tel. +34 977 55 81 37
Fax +34 977 55 95 63
www.quimica.urv.es

FAIG CONSTAR que aquest treball, titulat "Spectral-luminescent properties of orthorhombic and monoclinic tungstate and molybdate crystals doped with europium, terbium, thulium and ytterbium ions", que presenta Anna Volokitina per a l'obtenció del títol de Doctor, ha estat realitzat sota la meua direcció al Departament de Química Física i Inorgànica d'aquesta universitat.

HAGO CONSTAR que el presente trabajo, titulado "Spectral-luminescent properties of orthorhombic and monoclinic tungstate and molybdate crystals doped with europium, terbium, thulium and ytterbium ions", que presenta Anna Volokitina para la obtención del título de Doctor, ha sido realizado bajo mi dirección en el Departamento De Química Física e Inorgánica de esta universidad.

I STATE that the present study, entitled "Spectral-luminescent properties of orthorhombic and monoclinic tungstate and molybdate crystals doped with europium, terbium, thulium and ytterbium ions", presented by Anna Volokitina for the award of the degree of Doctor, has been carried out under my supervision at the Department of Physical and Inorganic Chemistry of this university.

Tarragona, 03 November 2021

El director de la tesi doctoral
El director de la tesis doctoral
Doctoral Thesis Supervisor

**MATEOS
FERRE,
XAVIER
(FIRMA)**

Firmado digitalmente por MATEOS
FERRE, XAVIER (FIRMA)
Nombre de reconocimiento (DN):
c=ES, serialNumber=39722594F,
sn=MATEOS, givenName=XAVIER,
cn=MATEOS FERRE, XAVIER
(FIRMA)
Fecha: 2021.11.04 13:29:15 +01'00'

Dr. Xavier Mateos Ferré

CONTENTS

Synopsis (in Russian)	8
Synopsis (in English)	36
Introduction	61
CHAPTER 1. Anisotropic tungstate and molybdate crystals as promising laser media (literature review).	64
1.1 Spectroscopy of rare-earth ions.	64
1.1.1 Eu^{3+} and Tb^{3+} ions.	65
1.1.2 Tm^{3+} ions	68
1.1.3 Yb^{3+} ions	68
1.2 Calculation of spectroscopic parameters and transition cross-sections.	69
1.2.1 Judd-Ofelt theory.	69
1.2.2 Determination of absorption, stimulated-emission and gain cross-sections.	72
1.2.3 Determination of luminescence decay times.	73
1.3 Low-symmetry tungstate and molybdate crystals as active media of near-infrared lasers.	74
1.3.1 Molybdate crystals.	75
1.3.2 Tungstate crystals.	75
CHAPTER 2. Materials and methods of experiments.	76
2.1 Objects of study.	76
2.2 Brief description of single-crystal growth methods.	76
2.3 Methods for studying the crystalline structure.	78
2.4 Methods for studying spectral-luminescent properties	79
2.4 Methodology of conducting laser experiments.	81
CHAPTER 3. Anisotropy of spectral-luminescence properties of Eu^{3+} and Tb^{3+} ions in $\text{AM}(\text{XO}_4)_2$ ($\text{A} = \text{K}, \text{Cs}$; $\text{M} = \text{Y}, \text{Gd}$; $\text{X} = \text{W}, \text{Mo}$) crystals.	83
3.1 Crystal structure (XRD analysis).	83

3.2 Raman spectroscopy.	86
3.3 Absorption spectroscopy. Judd-Ofelt theory.	89
3.3.1 Crystals doped with Eu^{3+} ions.	89
3.3.2 Crystals doped with Tb^{3+} ions	94
3.4 Anisotropy of luminescent properties.	100
3.4.1 Crystals doped with Eu^{3+} ions +	100
3.4.2 Crystals doped with Tb^{3+} ions.	106
3.5 Magnetic dipole transition ${}^5\text{D}_0 \rightarrow {}^7\text{F}_1$ of Eu^{3+} ions in $\text{KY}(\text{XO}_4)_2$ ($\text{X} = \text{W},$ Mo) crystals.	110
3.6 Color characteristics of luminescence	112
3.7 Chapter conclusions.	114
CHAPTER 4. Spectral-luminescent and laser properties of the $\text{Tm}^{3+}:\text{KY}(\text{MoO}_4)_2$ crystal.	115
4.1 Crystal structure (XRD analysis).	115
4.2 Raman spectroscopy.	117
4.3 Absorption cross-section.	119
4.4 Stimulated-emission and gain cross-sections. Luminescence decay times.	121
4.5 Lasing in $\text{Tm}^{3+}:\text{KY}(\text{MoO}_4)_2$ crystal plates and thin films produced by cleaving.	123
4.5.1 Microchip-lasers set-up.	123
4.5.2 Laser performance.	125
4.6 Chapter conclusions.	128
CHAPTER 5. Spectral-luminescent and laser properties of the $\text{Yb}^{3+},$ $\text{Li}^+:\text{ZnWO}_4$ and $\text{Yb}^{3+}:\text{KY}(\text{MoO}_4)_2$ crystals	129
5.1 Crystal structure (XRD analysis)	129
5.2 Raman spectroscopy.	131
5.3 Absorption cross-sections	135

5.4 Stimulated-emission cross-sections and gain cross-sections.	
Luminescence decay times	138
5.5 Low-temperature spectroscopy.	144
5.5.1 Stark-splitting of Yb^{3+} multiplets.	144
5.5.2 Applicability of the “barycenter law” for the studied crystals.	148
5.6 Laser experiments	149
5.6.1 Laser set-ups.	149
5.6.2 Output characteristics of the microchip laser based on $\text{Yb}^{3+}:\text{KY}(\text{MoO}_4)_2$ crystal plates	154
5.6.3 Output characteristics of the laser based on the Yb^{3+} , $\text{Li}^+:\text{ZnWO}_4$ crystal	152
5.7 Chapter conclusions	154
Conclusions	155
References	158
Appendix A (mandatory) Texts of articles.	166

Реферат

Актуальность темы

Низкосимметричные кристаллы, к которым относятся ромбические и моноклинные кристаллы вольфраматов и молибдатов [1], в последние годы выступают в качестве перспективных активных сред лазеров. К особенностям таких кристаллов можно отнести наличие значительной анизотропии спектрально-люминесцентных свойств в поляризованном свете. Анализ современного состояния исследований низкосимметричных кристаллов показал, что выбранные в диссертационной работе кристаллы вольфраматов и молибдатов, допированные ионами редкоземельных элементов, перспективны для получения в них эффективной лазерной генерации в видимой и ближней ИК области спектра [2-5]. К преимуществам таких кристаллов относится возможность достижения высоких значений концентраций ионов-активаторов без заметного тушения люминесценции [6], высокие поперечные сечения поглощения и вынужденного испускания в поляризованном свете [7,8], хорошие термооптические свойства [9]. Также такие кристаллы являются КР-активными.

Семейство выбранных для изучения кристаллов очень обширное, многие кристаллы уже достаточно хорошо изучены, при этом спектрально-люминесцентные свойства выбранных в диссертационной работе кристаллов, как и возможность использования их в качестве активной лазерной среды на момент постановки задачи и до сих пор остаются малоизученными и публикаций по данной тематике относительно немного.

Известно, что кристаллы, активированные ионами иттербия (Yb^{3+}) и тулия (Tm^{3+}), позволяют получить лазерную генерацию в ближнем инфракрасном диапазоне (в области длин волн ~ 1 мкм и ~ 2

мкм, соответственно) [10-12]. Лазеры ближнего ИК диапазона имеют достаточно широкую область применений: молекулярная спектроскопия, медицина, дальнометрия, системы связи и контроля и т.д. Излучение ИК диапазона характеризуется малыми потерями при прохождении через атмосферу, а ионы Tm^{3+} люминесцируют в так называемой условно-безопасной для сетчатки глаза области ИК диапазона.

Кристаллы, содержащие ионы европия (Eu^{3+}) [13-18] и тербия (Tb^{3+}) [19-26], люминесцируют в видимой области спектра. Они могут найти применение в качестве люминофоров [13-15, 22-26], а также они представляют большой интерес для использования в качестве активных лазерных сред [16-21], генерирующих в видимом диапазоне.

Следует отметить, что в последние годы одним из немаловажных направлений в разработке современных устройств во всех сферах является уменьшение всех компонентов - миниатюризация. С этой точки зрения большой интерес вызывают компактные лазеры, обладающие микрочип-конфигурацией резонатора. Они обладают достаточно простой конструкцией, однако для эффективной генерации микрочип-лазеров требуется очень тщательный выбор активной среды. Подходящими средами являются среды, которые характеризуются положительной термической линзой, позволяют достигать высоких концентраций ионов-активаторов и обладают большими значениями поперечных сечений поглощения, вынужденного испускания и усиления. Поэтому в настоящее время большой интерес вызывает исследование спектрально-люминесцентных свойств кристаллов двойных молибдатов, слоистая структура которых позволяет создавать эффективные активные среды лазера толщиной до нескольких десятков микрометров [27], а также проведение экспериментов, подтверждающих возможность получения эффективной лазерной

генерации на тонких пластинках и плёнках, изготовленных из таких кристаллов.

Таким образом, комплексное исследование спектрально-люминесцентных свойств новых кристаллов, включающее как изучение анизотропии спектрально-люминесцентных свойств, определение основных спектроскопических характеристик и установление возможности использования таких кристаллов в качестве активной среды лазера, так и проведение экспериментов по получению лазерной генерации на этих кристаллах, в том числе на тонких кристаллических пластинках и плёнках, представляет большой интерес и является актуальной задачей.

Цели и задачи исследования

Целью настоящей диссертационной работы является детальное исследование анизотропии спектрально-люминесцентных свойств низкосимметричных (ромбических и моноклинных) кристаллов молибдатов и вольфраматов с ионами европия (Eu^{3+}), тербия (Tb^{3+}), тулия (Tm^{3+}) и иттербия (Yb^{3+}), а также определение возможности использования таких кристаллов в качестве активных сред лазеров для видимой и ближней ИК области спектра и получение лазерной генерации в этих материалах, в том числе в микрочип-конфигурации резонатора.

В диссертационной работе были поставлены следующие **задачи**:

- изучить анизотропию спектрально-люминесцентных свойств выбранных кристаллов в поляризованном свете;

- исследовать анизотропию магнитно-дипольных переходов ионов Eu^{3+} в кристаллах $\text{KY}(\text{WO}_4)_2$ и $\text{KY}(\text{MoO}_4)_2$;

- рассчитать вероятности переходов, поперечные сечения поглощения, вынужденного испускания и усиления, а также определить времена жизни люминесценции ионов-активаторов;

- изучить анизотропию колебательных свойств кристаллических матриц;

- определить Штарковское расщепление уровней ионов Yb^{3+} в кристаллическом поле;

- получить лазерную генерацию в кристалле $\text{Yb}^{3+}, \text{Li}^+:\text{ZnWO}_4$, а также выяснить возможность получения лазерной генерации на основе тонких плёнок кристаллов двойных молибдатов $\text{Tm}^{3+}:\text{KY}(\text{MoO}_4)_2$ и $\text{Yb}^{3+}:\text{KY}(\text{MoO}_4)_2$ и получить лазерную генерацию в микрочип-конфигурации резонатора.

Объектом исследования являлись моноклинные и ромбические кристаллы вольфраматов и молибдатов: $\text{KY}(\text{WO}_4)_2$, $\text{KLu}(\text{WO}_4)_2$, $\text{KY}(\text{MoO}_4)_2$, $\text{CsGd}(\text{MoO}_4)_2$ и ZnWO_4 , в качестве ионов активаторов выступали ионы европия (Eu^{3+}), тербия (Tb^{3+}), тулия (Tm^{3+}) и иттербия (Yb^{3+}).

Предметом исследования являлись спектрально-люминесцентные свойства ионов в указанных кристаллах, колебательные свойства кристаллических матриц, а также генерационные свойства кристаллов.

Научная новизна работы

1. Исследованы ключевые спектрально-люминесцентные характеристики ионов европия (Eu^{3+}), тербия (Tb^{3+}), тулия (Tm^{3+}) и иттербия (Yb^{3+}) в кристаллах $\text{KY}(\text{WO}_4)_2$, $\text{KLu}(\text{WO}_4)_2$, $\text{KY}(\text{MoO}_4)_2$, $\text{CsGd}(\text{MoO}_4)_2$ и ZnWO_4 ;

2. Впервые определено Штарковское расщепление уровней ионов Yb^{3+} и ширина бесфононной линии этого иона в кристаллах ZnWO_4 и

$KY(MoO_4)_2$. Обнаружено, что механизм гетеровалентной компенсации заряда в кристаллах $ZnWO_4$ приводит к значительному увеличению ширины бесфонной линии и к большой величине Штарковского расщепления нижнего мультиплета ионов иттербия;

3. Впервые сформулированы поляризационные правила отбора для переходов магнито-дипольной природы в оптически двухосных кристаллах. Они были экспериментально подтверждены в кристаллах $Eu^{3+}:KY(WO_4)_2$ и $Eu^{3+}:KY(MoO_4)_2$.

4. Впервые в кристаллах $Tm^{3+}:KY(MoO_4)_2$ и $Yb^{3+}:KY(MoO_4)_2$ была продемонстрирована возможность лазерной генерации в тонких кристаллических плёнках и пластинках, полученных методом механического скола.

Теоретическая и практическая значимость работы

Теоретическая значимость работы заключается в том, что была получена информация об анизотропии спектрально-люминесцентных свойств ионов европия, тербия, тулия и иттербия в кристаллах $KY(WO_4)_2$, $KLu(WO_4)_2$, $KY(MoO_4)_2$, $CsGd(MoO_4)_2$ и $ZnWO_4$. В частности, был исследован магнито-дипольный переход ионов европия в кристаллах $Eu^{3+}:KY(WO_4)_2$ и $Eu^{3+}:KY(MoO_4)_2$ и установлены поляризационные правила отбора для магнито-дипольных переходов в оптически двухосных кристаллах. Была установлена связь между слоистой структурой кристаллов двойных молибдатов $KY(MoO_4)_2$, $CsGd(MoO_4)_2$ и сильной анизотропией их спектральных свойств.

Практическая значимость работы определяется тем, что были определены ключевые спектроскопические характеристики новых кристаллов, были рассчитаны поперечные сечения поглощения, вынужденного испускания и усиления. Для кристаллов с ионами европия и тербия были определены цветовые характеристики

люминесценции. Полученные в диссертационной работе результаты могут в дальнейшем использоваться для разработки новых лазеров, в том числе для создания миниатюрных лазеров с микрочип-конфигурацией резонатора. Было продемонстрировано, что на основе кристаллов двойных молибдатов $KY(MoO_4)_2$, обладающих слоистой структурой, методом механического скалывания можно получать тонкие кристаллические пластинки и плёнки (толщиной до нескольких десятков мкм), пригодные для использования в качестве активных лазерных сред. Была продемонстрирована эффективная генерация микрочип-лазера на основе таких тонких кристаллических пластинок и плёнок изготовленных из кристаллов $KY(MoO_4)_2$ с ионами Tm^{3+} или Yb^{3+} .

Положения, выносимые на защиту

1. Кристаллы двойных молибдатов $KY(MoO_4)_2$ и $CsGd(MoO_4)_2$ характеризуются исключительно сильной анизотропией поперечных сечений поглощения и вынужденного испускания для редкоземельных ионов, что связано с их слоистой структурой и низкой локальной симметрией люминесцентных центров (C_2).

2. Моноклинные кристаллы цинкового вольфрамата $ZnWO_4$, соактивированные ионами Yb^{3+} и Li^+ (обеспечивающими локальную компенсацию заряда), характеризуются большим Штарковским расщеплением нижнего мультиплета ионов иттербия (804 см^{-1}), высокой анизотропией поперечных сечений вынужденного испускания в поляризованном свете и широкими спектрами усиления, что обуславливает их привлекательность для генерации импульсов сверхкороткой длительности.

3. Поляризационные правила отбора для магнитно-дипольных переходов редкоземельных ионов в оптически двухосных кристаллах с

локальной симметрией люминесцентных центров C_2 определяются взаимной ориентацией вектора напряжённости магнитного поля и магнитного диполя относительно оси симметрии второго порядка.

4. Слоистая структура и совершенная спайность кристаллов калий-иттриевого двойного молибдата $KY(MoO_4)_2$, активированных ионами Yb^{3+} и Tm^{3+} , позволяет изготавливать тонкие кристаллические пластинки и плёнки, подверженные упругой деформации, толщиной до нескольких десятков микрометров, для использования в качестве активных элементов эффективных микрочип-лазеров, генерирующих в спектральной области ~ 1 мкм и ~ 2 мкм.

Личный вклад соискателя

Содержание диссертационной работы и научные положения, выносимые на защиту, отражают личный вклад автора в работу. Проведение спектроскопических экспериментов, представленных в диссертационной работе, выполнены диссертантом. Обсуждение полученных результатов и подготовка их к публикации проводилась совместно с соавторами. Совместно с соавторами были проведены лазерные эксперименты. Вклад диссертанта был определяющим.

Апробация результатов диссертации

Основные результаты диссертации докладывались и обсуждались на следующих конференциях:

1. VII Конгресс молодых ученых, Россия, Санкт-Петербург, 2018.
2. VIII Конгресс молодых ученых, Россия, Санкт-Петербург, 2019.
3. “Saint Petersburg OPEN 2017” 4th International School and Conference on Optoelectronics, Photonics, Engineering and Nanostructures, Россия, Санкт-Петербург, 2017.

4. Научная и учебно-методическая конференция Университета ИТМО, Россия, Санкт-Петербург, 2018.
5. 6th International School and Conference Saint-Petersburg OPEN, Россия, Санкт-Петербург, 2019.
6. SPIE Photonics Europe, Франция, online, 2020.
7. 9th Eps-Qeod Europhoton Virtual Conference, Чехия, online, 2020.
8. Международная конференция ФизикА.СПб, Россия, Санкт-Петербург, 2020.
9. 19th International Conference on Laser Optics ICLO 2020, online.
10. CLEO/EUROPE-EQEC 2021, online, 2021.
11. "Saint Petersburg OPEN 2021", Россия, Санкт-Петербург, 2021.

Достоверность научных достижений

Достоверность результатов исследований, научных положений и выводов, представленных в диссертации, подтверждается использованием современных и проверенных методов исследования, воспроизводимостью и ясной трактовкой полученных результатов и подтверждается положительными оценками рецензентов журналов, в которых опубликованы результаты работы. Полученные экспериментальные данные согласуются с результатами теоретических расчётов, а также с экспериментальными и теоретическими данными, полученными другими авторами.

Структура и объем диссертации

Диссертация состоит из введения, пяти глав, заключения и списка литературы из 92 наименований. Материал работы изложен на 272 страницах и содержит 56 рисунков и 10 таблиц.

Основное содержание

Во **введении** и в **первой главе** обосновывается актуальность исследований, проводимых в рамках диссертационной работы. Первая глава посвящена литературному обзору. В ней даётся общее представление об анизотропных кристаллах молибдатов и вольфраматов в качестве перспективных лазерных сред. В первом разделе главы описываются спектроскопические характеристики редкоземельных ионов в кристаллических матрицах. Второй раздел посвящен разбору методов расчёта спектроскопических параметров, поперечных сечений и времён жизни люминесценции. В нём также приводится краткое описание теории Джадда-Офельта. В последнем разделе рассматриваются низкосимметричные кристаллы как активные среды лазеров ИК диапазона. Приводится литературный обзор оптических свойств и генерационных характеристик кристаллов вольфраматов и молибдатов, активированных ионами редких земель.

Во **второй главе** приводится описание объектов исследования, краткое описание методов выращивания монокристаллов, описывается экспериментальная техника и использованные методы исследования структуры и спектрально-люминесцентных свойств, а также приводятся методики проведения лазерных экспериментов.

В **третьей главе** приводятся результаты исследования спектрально-люминесцентных свойств кристаллов, активированных ионами Eu^{3+} и Tb^{3+} . Общая химическая формула кристаллов может

быть записана в виде $AM(XO_4)_2$ ($A = K, Cs$; $M = Y, Lu, Gd$; $X = W, Mo$). Были исследованы кристаллы двойного калий-иттриевого молибдата и двойного цезий-гадолиниевого молибдата с ионами европия $Eu^{3+}:KY(MoO_4)_2$ и $Eu^{3+}:CsGd(MoO_4)_2$, кристалл двойного калий-иттриевого вольфрамата с ионами европия $Eu^{3+}:KY(WO_4)_2$ и кристалл двойного калий-лютециевого вольфрамата с ионами тербия $Tb^{3+}:KLu(WO_4)_2$.

В первом разделе приводятся результаты исследования структуры кристаллов. Методом порошкового рентгенофазового анализа была подтверждена фазовая чистота и структура кристаллов. Были определены пространственные и точечные группы кристаллов, постоянные решеток и объемы элементарных ячеек. По полученным данным и в соответствии с результатами уточнения Ритвельда была схематически построена структура кристалла. На рисунке 1 приведён фрагмент такой структуры, построенной для кристалла $Eu^{3+}:KY(MoO_4)_2$. Было показано, что основной особенностью кристаллов двойных молибдатов является их слоистая структура.

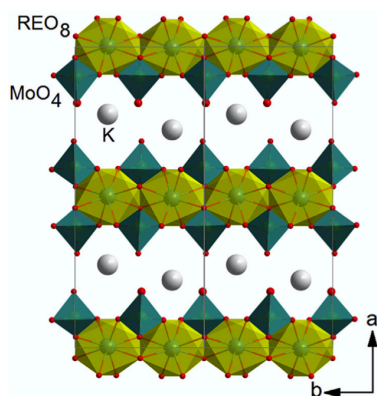


Рисунок 1 – фрагмент структуры кристалла $Eu^{3+}:KY(MoO_4)_2$ в проекции на плоскость $a-b$

Во втором разделе описаны результаты исследования методом спектроскопии комбинационного рассеяния света. Измерения проводились в поляризованном свете для всех возможных геометрий

кристаллов. На рисунке 2 приведены спектры комбинационного рассеяния света, зарегистрированные для кристалла $\text{Eu}^{3+}:\text{KY}(\text{MoO}_4)_2$. Видно, что спектры сильно поляризованы, в них можно выделить три диапазона, различающиеся по интенсивности колебаний. Первый низкочастотный диапазон (до 275 см^{-1}) содержит слабые колебания, связанные с T' -модами К, Y и Mo, R-модами и акустооптическими связанными модами. Во втором диапазоне колебаний ($319\text{-}435 \text{ см}^{-1}$) наблюдаются внутренние моды, связанные с деформационными (δ) колебаниями мостиковых кислородных тетраэдров $[\text{MoO}_4]^{2-}$. Наиболее интенсивный диапазон колебаний содержит сильно поляризованные полосы, относящиеся к валентным колебаниям мостикового кислородного тетраэдра $[\text{MoO}_4]^{2-}$.

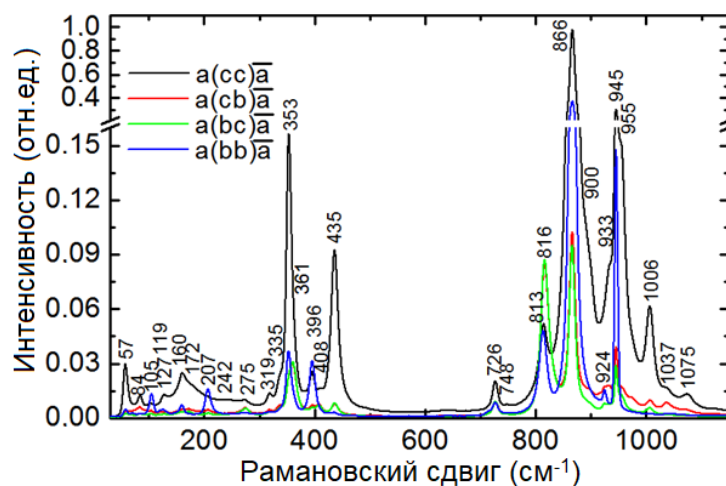


Рисунок 2 – поляризованные спектры комбинационного рассеяния света, измеренные для *a*-среза кристалла $\text{Eu}^{3+}:\text{KY}(\text{MoO}_4)_2$, $\lambda_{\text{возб}} = 488 \text{ нм}$.

В третьем разделе рассматривается исследование поглощения поляризованного света кристаллами и приводятся результаты расчёта спектроскопических параметров в соответствии с теорией Джадда-Офельта в приближении промежуточного конфигурационного взаимодействия (IC1). Во всех кристаллах наблюдалась сильная анизотропия спектров поглощения поляризованного света, это связано

с тем, что кристаллы двойных вольфраматов и молибдатов являются низкосимметричными. Для ионов Tb^{3+} наблюдаемые полосы поглощения при комнатной температуре обусловлены переходами из основного состояния (7F_6) в возбуждённые состояния. Несмотря на сходную структуру энергетических уровней, для ионов Eu^{3+} в спектрах поглощения наблюдаются переходы не только из основного состояния (7F_0), но и из термически заселённых (7F_1) и возбуждённых (7F_2) состояний. В ближней ИК области спектра наблюдаются переходы в низколежащие возбуждённые состояния (состояния ${}^7F_1 - {}^7F_6$ и ${}^7F_5 - {}^7F_0$ для ионов Eu^{3+} и Tb^{3+} соответственно). Такие переходы являются спин-разрешёнными, таким образом, наблюдаемая интенсивность полос поглощения в этой области значительно выше, чем в видимой области спектра.

В четвёртом разделе приводятся результаты исследований анизотропии люминесцентных свойств. Спектры люминесценции были зарегистрированы для трёх главных поляризаций света. Для ионов Eu^{3+} в спектрах наблюдались полосы, относящиеся к энергетическим переходам из метастабильного уровня 5D_0 в нижележащие энергетические состояния 7F_J ($J = 0-6$). Для ионов Tb^{3+} полосы люминесценции соответствуют переходам из состояния 5D_4 в нижележащие энергетические состояния. Все полосы люминесценции сильно поляризованы. На рисунке 3 приведены рассчитанные по зарегистрированным спектрам люминесценции спектры поперечных сечений вынужденного испускания (σ_{SE}) кристаллов $Eu^{3+}:CsGd(MoO_4)_2$ (а), $Eu^{3+}:KY(MoO_4)_2$ (б), $Tb^{3+}:KLu(WO_4)_2$ (в).

В пятом разделе рассматривается магнитно-дипольный переход ${}^5D_0 \rightarrow {}^7F_1$ ионов Eu^{3+} в кристаллах $KY(XO_4)_2$ ($X = W, Mo$). При исследовании люминесценции этого перехода (рисунок 4) было обнаружено, что количество и относительная интенсивность пиков

зависят не только от поляризации света E , но и от направления распространения k .

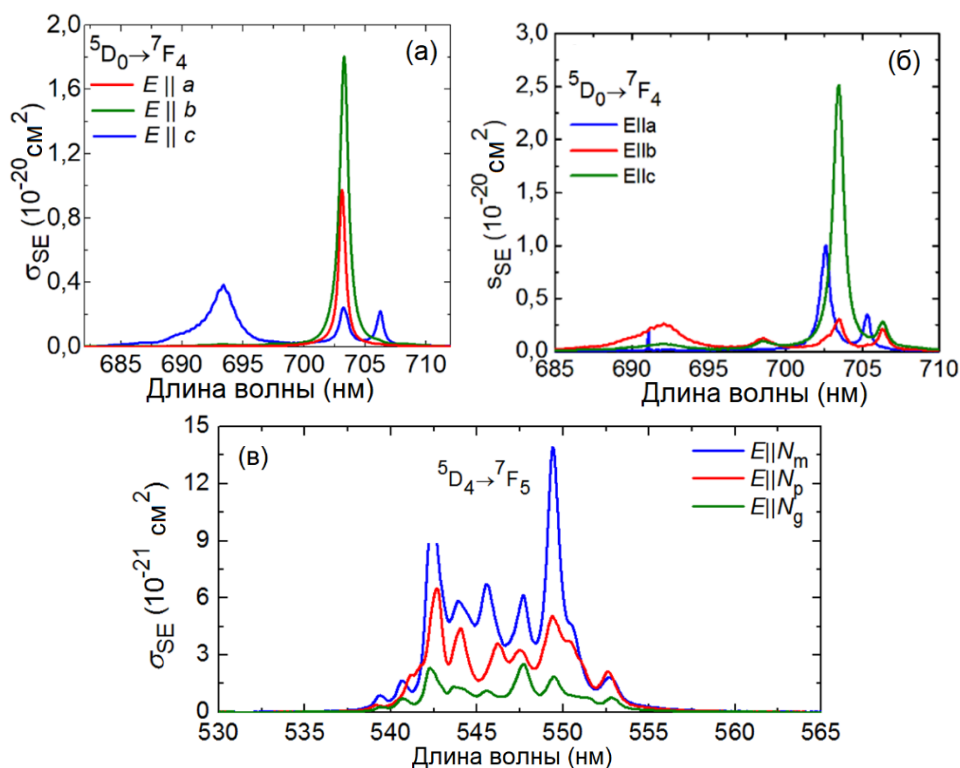


Рисунок 3 – Поперечные сечения поляризованного вынужденного испускания, σ_{SE} , в кристаллах $\text{Eu}^{3+}:\text{CsGd}(\text{MoO}_4)_2$ (а), $\text{Eu}^{3+}:\text{KY}(\text{MoO}_4)_2$ (б), $\text{Tb}^{3+}:\text{KLu}(\text{WO}_4)_2$ (в).

Такой эффект не наблюдается для остальных переходов ${}^5D_0 \rightarrow {}^7F_J$ ($J = 2 - 6$), которые являются чисто электрическими дипольными (ED). Магнитный дипольный переход обусловлен взаимодействием активного иона с компонентом магнитного поля света через магнитный диполь, ориентация которого задаётся вектором M . При этом имеет значение ориентация вектора напряженности магнитного поля H по отношению к M .

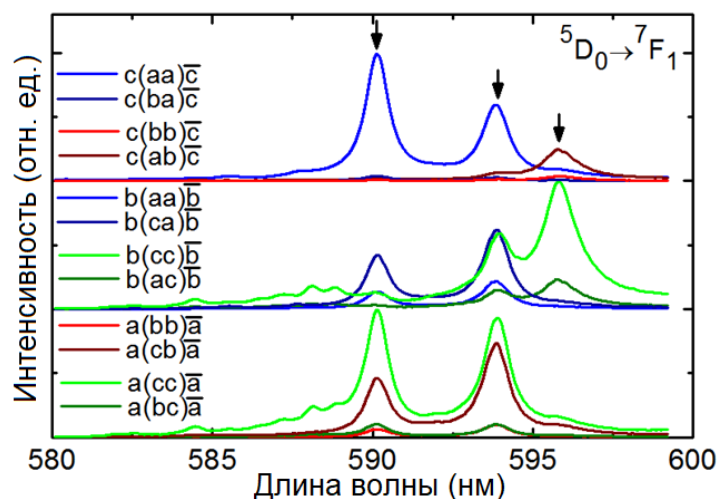


Рисунок 4 – Спектры поляризованной люминесценции для магнитно-дипольного (MD) перехода ${}^5D_0 \rightarrow {}^7F_1$ ионов Eu^{3+} в кристалле Eu:KYMo , $\lambda_{\text{возб}} = 458$ нм. Используются обозначения Порто. Стрелки указывают электронные переходы.

Таким образом были установлены поляризационные правила отбора (см. таблицу 1) для магнитно-дипольных переходов редкоземельных ионов в оптически двухосных кристаллах с локальной симметрией люминесцентных центров C_2 .

Таблица 1 – Поляризационные правила отбора для магнитно-дипольного перехода ${}^5D_0 \rightarrow {}^7F_1$ ионов Eu^{3+} в кристаллах $\text{Eu}^{3+}:\text{KY}(\text{MoO}_4)_2$ и $\text{Eu}^{3+}:\text{KY}(\text{WO}_4)_2$

Направление ориентации вектора M	Разрешенные переходы ${}^5D_0 \rightarrow {}^7F_1$	Благоприятные направления излучения k	Возможные поляризации e_{pk}
$M \parallel C_2 (M \parallel a)$	$\Gamma_1 \rightarrow \Gamma_2$	$\parallel b$	$\parallel c$
$M \parallel C_2 (M \parallel b, c)$	$\Gamma_1 \rightarrow \Gamma_2^{(1)}, \Gamma_2^{(2)}$	$\parallel c$	$\parallel b$
		$\parallel a$	$\parallel b, c$
		$\parallel b$	$\parallel a, c$
		$\parallel c$	$\parallel a, b$

В шестом разделе были определены цветовые характеристики (цветовые координаты, доминантная длина волны и чистота цвета) люминесценции ионов Eu^{3+} и Tb^{3+} (таблица 2) в кристаллах в соответствии с цветовым пространством CIE 1931.

Таблица 2 – Цветовые координаты люминесценции кристаллов $\text{Eu}^{3+}:\text{KY}(\text{MoO}_4)_2$ и $\text{Tb}^{3+}:\text{KLu}(\text{WO}_4)_2$, рассчитанные в соответствии с цветовым пространством CIE 1931

Кристалл	x	y	Чистота цвета	Доминантная длина волны
$\text{Eu}^{3+}:\text{KY}(\text{MoO}_4)_2$	0.665	0.335	>99%.	612 нм, красный
$\text{Tb}:\text{KLuW}$	0.380	0.608	> 97%	561 нм, желтовато-зелёный

Четвёртая глава посвящена исследованиям спектрально-люминесцентных и генерационных свойств кристалла двойного калий-иттриевого молибдата с ионами тулия, $\text{Tm}^{3+}:\text{KY}(\text{MoO}_4)_2$. Для подтверждения структуры и фазовой чистоты кристалла был проведён порошковый рентгенофазовый анализ, описанный в первом разделе главы. Кристалл относится к классу орторомбических кристаллов с пространственной группой $Pbna - D^{14}_{2h}$, No 60. Во втором разделе главы подробно описываются исследования данного кристалла методом комбинационного рассеяния света.

В третьем разделе приводятся результаты исследования абсорбционных свойств кристалла. Полосы поглощения в спектре обусловлены переходами ионов Tm^{3+} из основного энергетического состояния ($^3\text{H}_6$) в вышележащие возбужденные состояния (от $^3\text{F}_4$ до $^1\text{D}_2$). Спектр поглощения сильно поляризован, однако заметная анизотропия поглощения в плоскости (100) не может быть отнесена к слоистой структуре и, скорее всего, связана с низкой симметрией люминесцентных центров C_2 .

Энергетический переход $^3\text{H}_6 \rightarrow ^3\text{H}_4$ ионов Tm^{3+} подходит для накачки, например, мощными промышленными лазерными AlGaAs диодами. Максимальное значение поперечного сечения поглощения σ_{abs} составляет $7.70 \times 10^{-20} \text{ см}^2$ на длине волны 802.8 нм, а соответствующая полуширина полосы поглощения составляет 10.0 нм (для поляризации $\mathbf{E} \parallel \mathbf{b}$).

В четвёртом разделе приводится анализ люминесцентных свойств, спектров поперечных сечений испускания и усиления кристалла $\text{Tm}:\text{KY}(\text{MoO}_4)_2$. Ионы Tm^{3+} люминесцируют в ближней ИК области спектра, в условно-безопасном для глаз спектральном диапазоне, рисунок 5(a). Максимальное значение сечений вынужденного испускания σ_{SE} составляет $2.70 \times 10^{-20} \text{ cm}^2$ на длине волны 1856 нм с полушириной полосы излучения (FWHM) $> 110 \text{ nm}$ (для $E \parallel b$).

Кривая затухания люминесценции Tm^{3+} из состояния $^3\text{F}_4$ носит моноэкспоненциальный характер. Время жизни люминесценции составляет $\tau_{\text{lum}} = 2.29 \text{ ms}$.

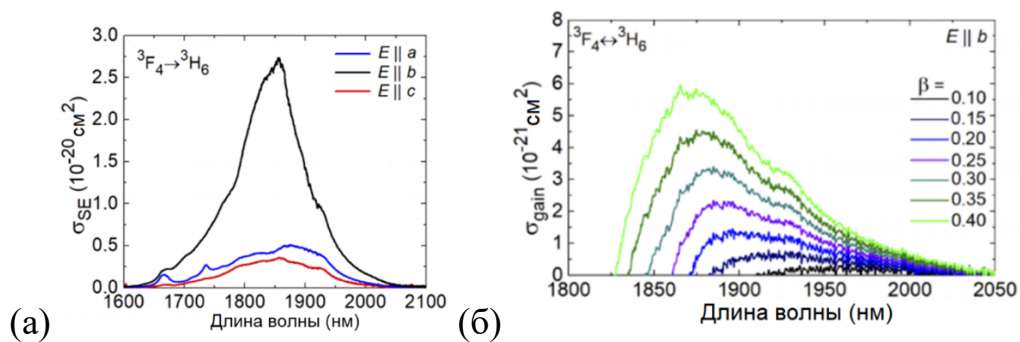


Рисунок 5 – (а) поперечные сечения вынужденного испускания σ_{SE} для $^3\text{F}_4 \rightarrow ^3\text{H}_6$ перехода в кристалле $\text{Tm}^{3+}:\text{KY}(\text{MoO}_4)_2$, поляризации света $E \parallel a, b, c$; (б) Сечения усиления для перехода $^3\text{F}_4 \leftrightarrow ^3\text{H}_6$ ионов Tm^{3+} в кристалле $\text{KY}(\text{MoO}_4)_2$

Чтобы получить возможность определить ожидаемую длину волны излучения лазера на кристалле $\text{Tm}^{3+}:\text{KY}(\text{MoO}_4)_2$, были рассчитаны сечения усиления, σ_{gain} . На рисунке 5 (б) приведены полученные спектры, рассчитанные для поляризации света $E \parallel b$. Спектры относительно широкие и гладкие.

В пятом разделе описываются лазерные эксперименты и приводятся результаты по получению лазерной генерации на кристаллических пластинках и тонких плёнках кристалла $\text{Tm}:\text{KY}(\text{MoO}_4)_2$, полученных методом скалывания без какой-либо

последующей обработки. В разделе подробно описывается экспериментальная лазерная установка (рисунок 6), главной особенностью которой является микрочип-конфигурация резонатора.

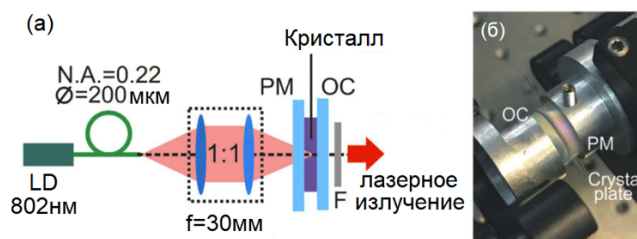


Рисунок 6 – (а) Схема микрочип-лазера с диодной накачкой на кристалле $\text{Tm:KY}(\text{MoO}_4)_2$: LD - лазерный диод, PM – входное зеркало резонатора, OC – выходное зеркало, F - фильтр; (б) фотография лазера на кристаллической пластинке.

Для накачки использовался лазерный диод AlGaAs, излучающий неполяризованное излучение на длине волны 802 нм. Была продемонстрирована эффективная лазерная генерация, рисунок 7.

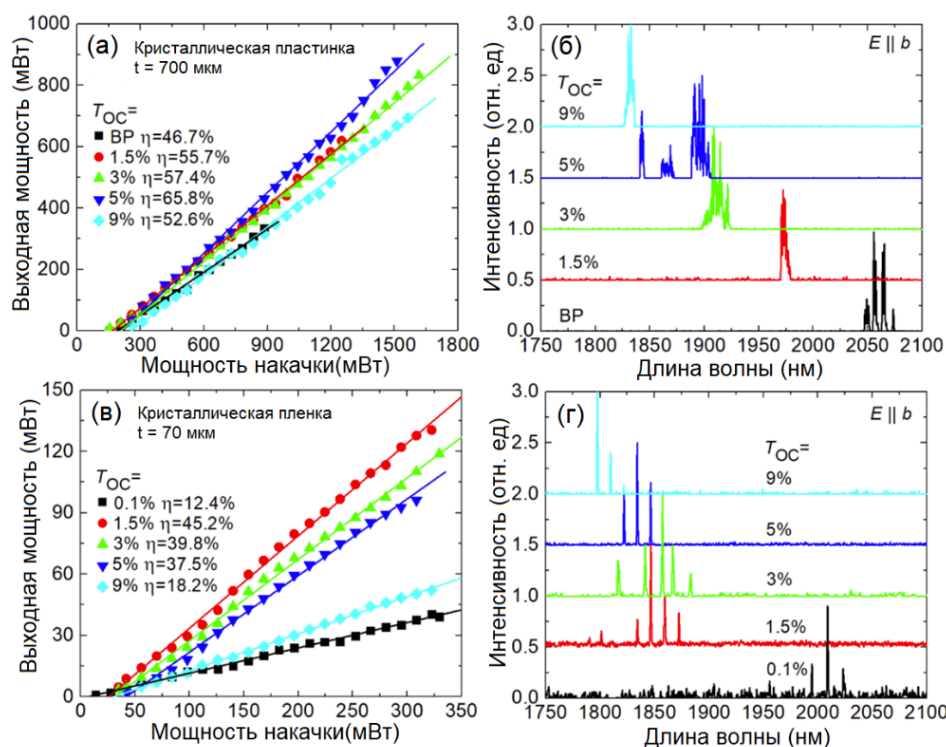


Рисунок 7 – выходные характеристики лазера на кристаллической пластинке ($t = 700$ мкм) (а) и на тонкой кристаллической пленке ($t = 70$ мкм) (в), (б, г) – спектры лазерного излучения, измеренные при максимальных P_{abs} .

Максимальная выходная мощность лазера на кристаллической пластине, имеющей толщину 700 мкм, составила 0,88 Вт на длине волны 1840–1905 нм с дифференциальной эффективностью $\eta = 65,8\%$. Во втором эксперименте на кристаллической плёнке толщиной 70 мкм была достигнута максимальная выходная мощность 131 мВт на длине волны 1801–1872 нм с $\eta = 45,2\%$.

В пятой главе описываются спектрально-люминесцентные и генерационные свойства кристаллов, содержащих ионы иттербия: кристалла калий-иттриевого молибдата $\text{Yb}^{3+}:\text{KY}(\text{MoO}_4)_2$ и кристалла цинкового вольфрамата $\text{Yb}^{3+},\text{Li}^+:\text{ZnWO}_4$.

В первом разделе главы приводятся исследования методом рентгенофазового анализа, подтверждающие структуру и фазовую чистоту кристаллов. Кристалл $\text{Yb}^{3+}:\text{KY}(\text{MoO}_4)_2$ является орторомбическим и обладает слоистой структурой (рисунок 8), кристалл $\text{Yb}^{3+},\text{Li}^+:\text{ZnWO}_4$ – моноклинный.

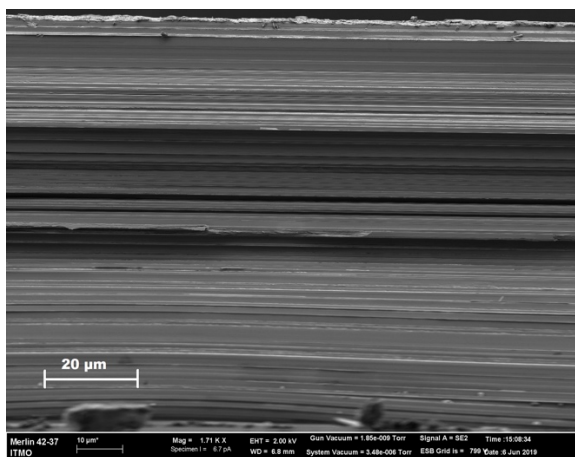


Рисунок 8 – Изображение края сколотого кристалла $\text{Yb}^{3+}:\text{KY}(\text{MoO}_4)_2$, полученное с помощью сканирующего электронного микроскопа. Ось *a* расположена вертикально.

Во втором разделе приводятся детальное описание результатов исследования кристаллов методом комбинационного рассеяния света, проведённого для всех возможных геометрий и поляризаций света.

В третьем разделе рассматривается абсорбционная спектроскопия кристаллов. В спектрах поглощения наблюдается сильная анизотропия поляризованного света. Полоса поглощения на ~ 1 мкм относится к энергетическому переходу ${}^2F_{7/2} \rightarrow {}^2F_{5/2}$ иона Yb^{3+} .

В четвёртом разделе описываются спектры поперечных сечений вынужденного испускания и усиления, а также времена жизни люминесценции. Следует отметить, что кристаллы цинкового вольфрамата ZnWO_4 , соактивированные ионами Yb^{3+} и Li^+ , характеризуются высокой анизотропией поперечных сечений вынужденного испускания в поляризованном свете, рисунок 9 (а), и широкими спектрами усиления, рисунок 9 (б). Это обуславливает их привлекательность в качестве активной среды лазера для генерации импульсов сверхкороткой длительности.

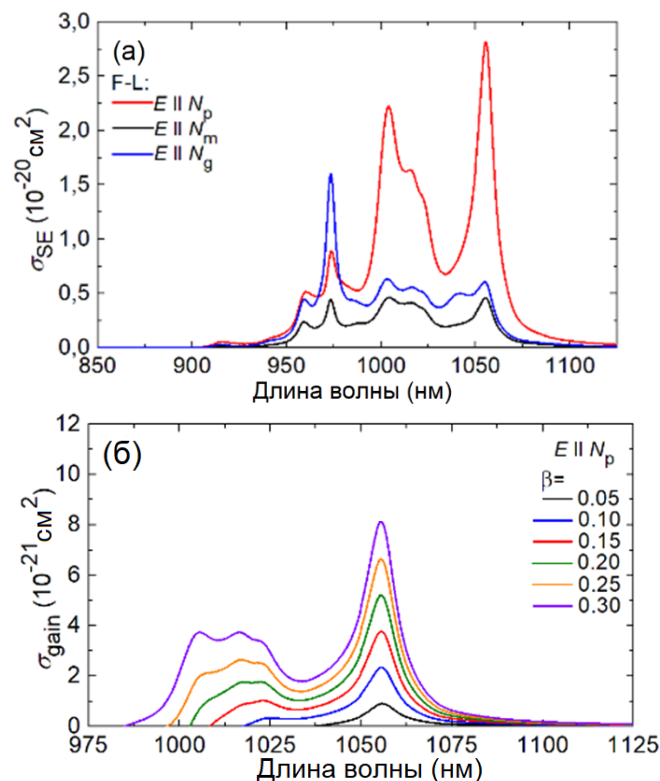


Рисунок 9 – (а) сечения вынужденного испускания, σ_{SE} , для ионов Yb^{3+} в $\text{Yb}^{3+}, \text{Li}^+ : \text{ZnWO}_4$, поляризация света $E \parallel N_p$, комнатная температура, (б) поперечные сечения усиления, σ_{gain} , спектры перехода ${}^2F_{5/2} \leftrightarrow {}^2F_{7/2}$ ионов Yb^{3+} в ZnWO_4 .

В пятом разделе описываются результаты низкотемпературной спектроскопии и Штарковское расщепление мультиплетов ионов Yb^{3+} в кристаллах $\text{KY}(\text{MoO}_4)_2$ и ZnWO_4 . Поляризованные спектры поглощения и люминесценции (рисунок 10) были записаны в интервале температур 6 – 300 К.

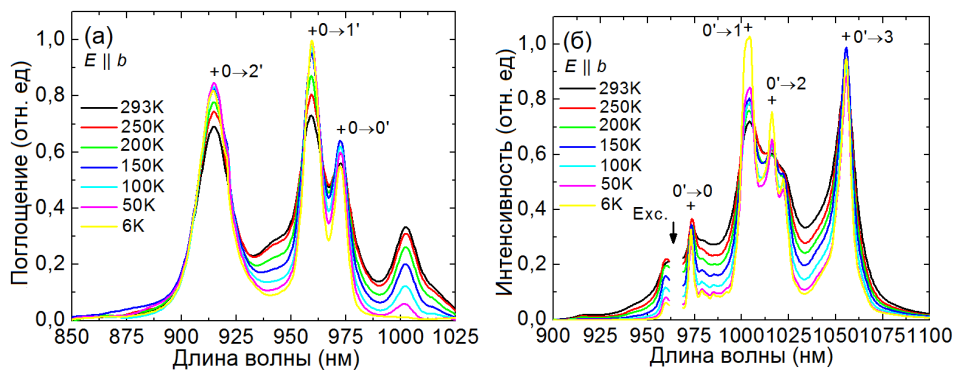


Рисунок 10 – Низкотемпературная (6–293 К) спектроскопия кристалла 1,8 ат.% $\text{Yb}^{3+}, \text{Li}^+:\text{ZnWO}_4$: спектры поглощения (а) и люминесценции (б) для поляризации света $E \parallel b$

При температуре 6 К электрон-фононная связь сильно подавляется, однако для ионов Yb^{3+} в кристалле ZnWO_4 наблюдается большая ширина бесфононной линии $\Delta\lambda_{\text{ZPL}} = 3,0$ нм и большое Штарковское расщепление нижнего мультиплета ионов Yb^{3+} (804 см^{-1}). Оно намного шире, чем в кристалле $\text{KY}(\text{MoO}_4)_2$, в котором величина Штарковского расщепления составляет 601 см^{-1} , см. рисунок 11.

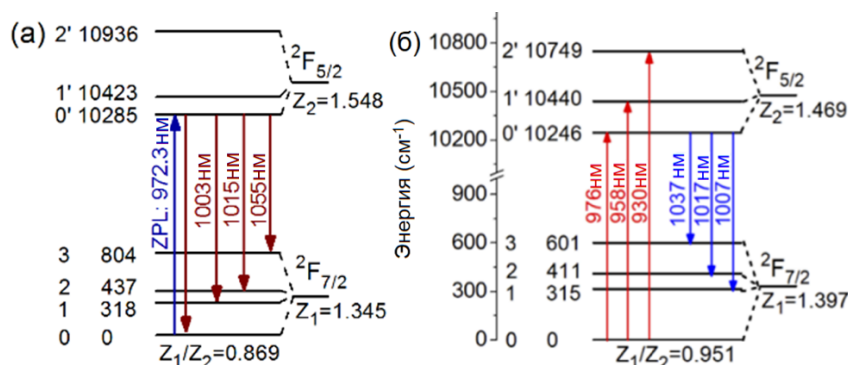


Рисунок 11 – (а) Расщепление энергетических уровней иона Yb^{3+} в кристаллическом поле, определенное для кристалла ZnWO_4 (а) и для кристалла $\text{KY}(\text{MoO}_4)_2$ (б)

Известно, что для всех редкоземельных ионов энергия барицентра любого изолированного мультиплета $2S+1L_J 4f^n$ линейно изменяется с энергией барицентра любого другого мультиплета, рисунок 12. Энергии барицентров $\langle E(^2F_{5/2}) \rangle$ и $\langle E(^2F_{7/2}) \rangle$ для кристаллов $\text{Yb}^{3+}, \text{Li}^+:\text{ZnWO}_4$ и $\text{Yb}^{3+}:\text{KY}(\text{MoO}_4)_2$ хорошо согласуются с линейной аппроксимацией выражения $E(^2F_{5/2}) = 10166.6 + 0.997 \times E(^2F_{7/2})$ [cm^{-1}], описывающего зависимость барицентра возбуждённого уровня редкоземельного иона от основного уровня.

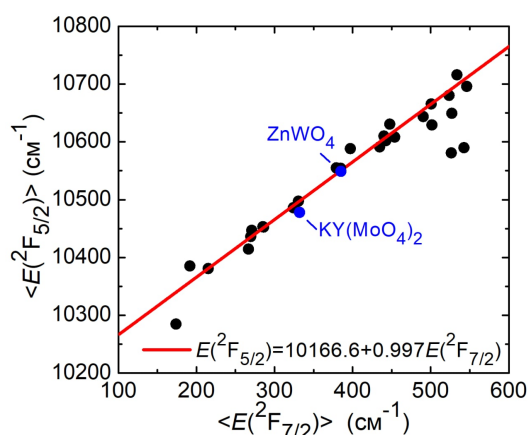


Рисунок 12 – Зависимость барицентра возбуждённого уровня от основного, показывающая положение кристаллов $\text{Yb}^{3+}, \text{Li}^+:\text{ZnWO}_4$ и $\text{Yb}^{3+}:\text{KY}(\text{MoO}_4)_2$ (синие кружки).

В шестом разделе приводятся результаты экспериментов по получению эффективной лазерной генерации. Из кристалла $\text{Yb}^{3+}:\text{KY}(\text{MoO}_4)_2$ методом механического скола без последующей обработки была изготовлена тонкая кристаллическая пластинка толщиной 286 мкм. Пластинка была помещена в компактный резонатор, обладающий микрочип-конфигурацией. В качестве накачки был выбран InGaAs лазерный диод, излучающий на длине волны 968 нм. Результаты лазерных экспериментов приведены на рисунке 13. Максимальная выходная мощность лазера на тонкой пластинке кристалла $\text{Yb}^{3+}:\text{KY}(\text{MoO}_4)_2$ составляла 0,81 Вт на длине волны 1021-1044 нм с высоким дифференциальным КПД = 76,4%.

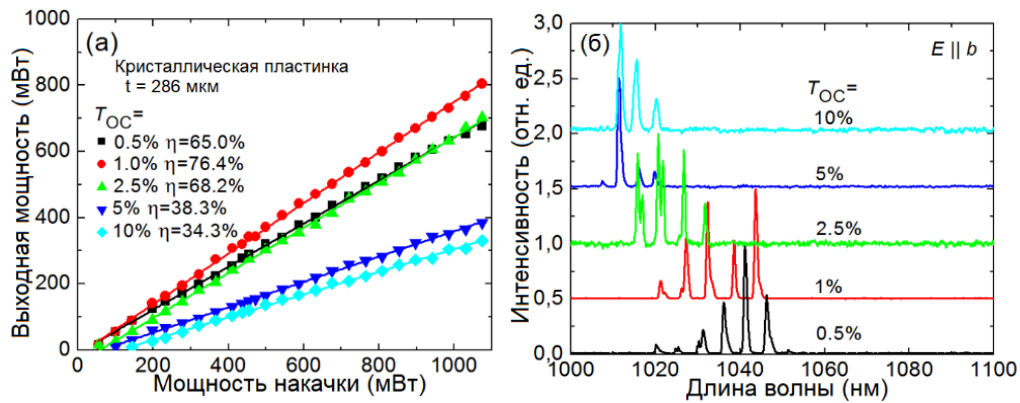


Рисунок 13 – (а) выходные характеристики микрочип-лазера на кристаллической пластинке $\text{Yb}^{3+}:\text{KY}(\text{MoO}_4)_2$ с диодной накачкой, (б) спектры лазерного излучения микрочип-лазера, измеренные при $P_{\text{abs}} = 1,0$ Вт. Поляризация лазера $E \parallel b$.

Во втором эксперименте из кристалла $\text{Yb}^{3+},\text{Li}^{+}:\text{ZnWO}_4$ был подготовлен прямоугольный активный элемент, вырезанный для распространения света по оси a , входная и выходная грани которого были отполированы до лазерного качества. Кристалл был помещён в линейный плоско-вогнутый резонатор. Накачка осуществлялась тем же InGaAs лазерным диодом. Лазер на кристалле $\text{Yb}^{3+},\text{Li}^{3+}:\text{ZnWO}_4$ генерировал максимальную выходную мощность 2,90 Вт на длине волны ~ 1059 нм с дифференциальной эффективностью $\eta = 57.9\%$ (по отношению к поглощенной мощности накачки).

Основные результаты диссертационной работы

В диссертационной работе было проведено комплексное исследование спектрально-люминесцентных свойств новых ромбических и моноклинных кристаллов $\text{KY}(\text{WO}_4)_2$, $\text{KLu}(\text{WO}_4)_2$, $\text{KY}(\text{MoO}_4)_2$, $\text{CsGd}(\text{MoO}_4)_2$ и ZnWO_4 , активированных ионами европия, тербия, тулия и иттербия, а также была продемонстрирована эффективная лазерная генерация в ИК области спектра, в том числе в микрочип-лазере.

Было показано, что кристаллы двойных молибдатов, к которым относятся кристаллы калий-иттриевого двойного молибдата

$KY(MoO_4)_2$ и цезий-гадолиниевого двойного молибдата $CsGd(MoO_4)_2$, характеризуются исключительно сильной для редкоземельных ионов анизотропией поперечных сечений поглощения и вынужденного испускания. Например, для кристалла $Tm^{3+}:KY(MoO_4)_2$ величина поперечного сечения поглощения для поляризации $E \parallel b$ на порядок выше, чем для поляризации $E \parallel c$, и составляет 7.70×10^{-20} см². А величина поперечного сечения вынужденного испускания для этой поляризации в 6-8 раз больше, чем для остальных поляризаций. Такая анизотропия прежде всего связана с низкой локальной симметрией люминесцентных центров (C_2), а также со слоистой структурой кристаллов.

Были сформулированы поляризационные правила отбора для магнитно-дипольных переходов в оптически двухосных кристаллах с локальной симметрией люминесцентных центров C_2 . Они определяются взаимной ориентацией вектора напряжённости магнитного поля и магнитного диполя относительно оси симметрии второго порядка. При детальном исследовании анизотропии люминесценции магнитно-дипольного перехода $^5D_0 \rightarrow ^7F_1$ ионов Eu^{3+} в кристаллах $Eu^{3+}:KY(WO_4)_2$ и $Eu^{3+}:KY(MoO_4)_2$ было обнаружено влияние поляризации возбуждающего света и ориентации кристалла на форму спектра люминесценции. Таким образом, было получено первое экспериментальное подтверждение поляризационных правил отбора.

Впервые было определено Шарковское расщепление уровней ионов Yb^{3+} в кристаллах $ZnWO_4$ и $KY(MoO_4)_2$, было установлено, что в кристалле цинкового вольфрамата $ZnWO_4$, соактивированного ионами Yb^{3+} и Li^+ (обеспечивающими локальную компенсацию заряда), наблюдается большое (804 см⁻¹) Штарковское расщепление нижнего мультиплета ионов иттербия, в то время как для кристалла $KY(MoO_4)_2$ эта величина составляет 601 см⁻¹. Также в кристалле $ZnWO_4$

наблюдается значительное увеличение ширины безфононной линии $\Delta\lambda_{ZPL} = 3.0$ нм, что намного шире, чем в кристалле $\text{Yb:KY}(\text{WO}_4)_2$ ($\Delta\lambda_{ZPL} < 0.1$ нм). Также кристаллу ZnWO_4 свойственна высокая анизотропия поперечных сечений вынужденного испускания в поляризованном свете и широкими спектрами усиления.

Было показано, что слоистая структура и совершенная спайность кристаллов калий-иттриевого двойного молибдата $\text{KY}(\text{MoO}_4)_2$, позволяет изготавливать тонкие кристаллические пластинки и плёнки, подверженные упругой деформации, толщиной до нескольких десятков микрометров. Такие плёнки и пластинки обладают лазерным качеством и пригодны для использования в качестве активных элементов микрочип-лазеров без какой-либо последующей обработки. Впервые была продемонстрирована работа лазера на тонких кристаллических пластинках и плёнках кристаллов $\text{Tm:KY}(\text{MoO}_4)_2$ и $\text{Yb}^{3+}:\text{KY}(\text{MoO}_4)_2$. Максимальная выходная мощность лазера на кристаллической пластинке толщиной 286 мкм изготовленной из $\text{Yb}^{3+}:\text{KY}(\text{MoO}_4)_2$, составила 0,81 Вт на длине волны 1021-1044 нм с высоким дифференциальным КПД = 76,4%. Максимальная выходная мощность лазера на $\text{Tm:KY}(\text{MoO}_4)_2$ кристаллической пластинке толщиной 700 мкм составила 0,88 Вт. Лазер генерировал излучение на длине волны 1840–1905 нм с дифференциальной эффективностью $\eta = 65,8\%$. Лазер на тонкой $\text{Tm:KY}(\text{MoO}_4)_2$ кристаллической плёнке генерировал излучение с максимальной выходной мощностью 131 мВт на длине волны 1801–1872 нм с $\eta = 45,2\%$.

Публикации по теме диссертации

По теме диссертации были сделаны следующие публикации в изданиях, индексируемых в Web of Science и Scopus и входящих в перечень ВАК:

1. Subbotin K., Loiko P., Slimi S., **Volokitina A.**, Titov A., Lis D., Chernova E., Kuznetsov S., Solé R.M., Griebner U., Petrov V., Aguiló M, Díaz F., Camy P., Zharikov E., Mateos X. Monoclinic zinc monotungstate $\text{Yb}^{3+}, \text{Li}^+:\text{ZnWO}_4$: Part I. Czochralski growth, structure refinement and Raman spectra // *Journal of Luminescence* – 2020, Vol. 228 pp. 117601, IF 3.28, JCR – Q2
2. **Volokitina A.**, David S.P., Loiko P., Subbotin K., Titov A., Lis D., Solé R.M., Jambunathan V., Lucianetti A., Mocek T., Camy P., Chengh W., Griebner U., Petrov V., Aguiló M, Díaz F., Mateos X. Monoclinic zinc monotungstate $\text{Yb}^{3+}, \text{Li}^+:\text{ZnWO}_4$: Part II. Polarized spectroscopy and laser operation // *Journal of Luminescence* – 2021, Vol. 231, pp. 117811, IF 3.28, JCR – Q2
3. Loiko P., Mateos X., Dunina E., Kornienko A., **Volokitina A.**, Vilejshikova E., Serres J.M., Baranov A., Yumashev K., Aguiló M., Díaz F. Judd-Ofelt modelling and stimulated-emission cross-sections for Tb^{3+} ions in monoclinic $\text{KYb}(\text{WO}_4)_2$ crystal // *Journal of Luminescence* – 2017, Vol. 190, pp. 37-44, IF 3.28, JCR – Q2
4. Kurilchik S., Loiko P., Yasukevich A., Trifonov V., **Volokitina A.**, Vilejshikova E., Kisel V., Mateos X., Baranov A., Goriev O. Orthorombic $\text{Yb}:\text{Li}_2\text{Zn}_2(\text{MoO}_4)_3$ – a novel potential crystal for broadly tunable lasers // *Laser Physics Letters* – 2017, Vol. 14.8, pp. 085804, IF 2.328, JCR – Q1
5. **Volokitina A.**, Loiko P., Vilejshikova E., Mateos X., Dunina E., Kornienko A., Kuleshov N., Pavlyuk A., $\text{Eu}^{3+}:\text{KY}(\text{MoO}_4)_2$: A novel anisotropic red-emitting material with a layered structure // *Journal of Alloys and Compounds* – 2018, Vol. 762, pp. 786-796, IF 4.65, JCR – Q1
6. Loiko P., **Volokitina A.**, Mateos X., Dunina E., Kornienko A., Vilejshikova E., Aguiló M., Diaz F. Spectroscopy of Tb^{3+} ions in monoclinic $\text{KLu}(\text{WO}_4)_2$ crystal application of an intermediate configuration interaction theory // *Optical Materials* – 2018, Vol. 78, pp. 495-501, IF 2.023, JCR – Q2
7. **Volokitina A.**, Loiko P., Pavlyuk A., Slimi S., Solé R.M., Salem E.B., Kifle E., Serres J.M., Griebner U., Petrov V., Aguiló M, Díaz F., Mateos X. Laser operation of cleaved single-crystal plates and films of $\text{Tm}:\text{KY}(\text{MoO}_4)_2$ // *Optics express* – 2020, Vol. 28.7, pp. 9039-9048, IF 3.669, JCR – Q1
8. **Volokitina A.**, Loiko P., Pavlyuk A., Serres J.M., Slimi S., Salem E.B., Kifle E., Griebner U., Petrov V., Wang L., Solé R.M., Aguiló M., Díaz F., Mateos X. Spectroscopy and efficient laser operation of cleaving

Yb:KY(MoO₄)₂ crystal // Optical Materials Express – 2020, Vol. 10.10, pp. 2356-2369, IF 3.064, JCR – Q1

9. Loiko P.; Vileshnikova E.V., **Volokitina A.A.**, Trifonov V.A., Serres J.M. Mateos X., Kuleshov N.V., Yumashev K.V., Baranov A.V., Pavlyuk A.A. Growth, structure, Raman spectra and luminescence of orthorombic Li₂Mg₂(MoO₄)₃ crystals doped with Eu³⁺ and Ce³⁺ ions // Journal of Luminescence – 2017, Vol. 188, pp. 154-161, IF 3.28, JCR – Q2

10. **Volokitina A.**, Loiko P., Pavlyuk A., Solé R.M., Aguiló M., Díaz F., Mateos X., Novel Molybdate Laser Crystal with a Layered Structure: Orthorombic Er³⁺: KY(MoO₄)₂ // International Conference Laser Optics (ICLO). IEEE - 2020.

11. Loiko P. **Volokitina A.**, Serres J.M., Trifonov V., Pavlyuk A., Slimi S., Salem E.B., Solé R.M., Aguiló M., Díaz F. Laser Operation of Cleaved Single-Crystal Plates and Films of Tm:KY(MoO₄)₂ // Laser Applications Conference - 2019

12. **Volokitina A.**, Loiko P., Serres J.M., Mateos X., Kuleshov N., Trifonov V., Pavlyuk A. Growth and spectroscopy of orthorombic Yb:KY(MoO₄)₂ laser crystal with a layered structure // Journal of Physics: Conference Series – 2019, Vol. 1410, No. 1

13. **Volokitina A.A.**, Subbotin K.A. Loiko P.A., Titov A.I., Lis D.A., Slimi S., Solé R.M., David S.P., Jambunathan V., Lucianetti A., Spectroscopic Study and First Laser Operation of Monoclinic Yb³⁺,Li⁺:ZnWO₄ Crystal // 2020 International Conference Laser Optics (ICLO) IEEE – 2020.

14. **Volokitina A.**, Loiko P., Pavlyuk A., Serres J.M., Slimi S., Salem E.B., Solé R.M., Baranov M., Kifle E., Aguiló M., Díaz F., Griebner U., Petrov V., Mateos X. Efficient laser operation in cleaved single-crystal plates of Yb:KY(MoO₄)₂: A novel molybdate compound // Fiber Lasers and Glass Photonics: Materials through Applications II – 2020, Vol. 11357

Список литературы

1. Klevtsov P. V. et al. Polymorphism of the double molybdates and tungstates of mono- and trivalent metals with the composition M⁺R³⁺(EO₄)₂ // Journal of Structural Chemistry – 1977, Vol 18, №. 3 pp. 339-355.

2. Liu J. et al. Efficient high-power laser operation of Yb:KLu(WO₄)₂ crystals cut along the principal optical axes // Optics letters – 2007, Vol 32, №. 14, pp. 2016-2018
3. Serres J. M. et al. Diode-pumped microchip Tm:KLu(WO₄)₂ laser with more than 3 W of output power // Optics letters – 2014, Vol 39, №. 14, pp. 4247-4250.
4. Loiko P. et al. In-band-pumped Ho:KLu(WO₄)₂ microchip laser with 84% slope efficiency // Optics letters – 2015, Vol 40, №. 3, pp. 344-347.
5. Griebner U. et al. Passively mode-locked Yb:KLu(WO₄)₂ oscillators // Optics Express – 2005, Vol 13, №. 9, pp. 3465-3470.
6. Pujol M. C. et al. Growth, optical characterization, and laser operation of a stoichiometric crystal KYb(WO₄)₂ // Physical Review B – 2002, Vol. 65, №. 16, pp. 165121.
7. Mateos X. et al. Crystal growth, spectroscopic studies and laser operation of Yb³⁺-doped potassium lutetium tungstate // Optical Materials – 2006, Vol. 28, №. 5, pp. 519-523.
8. Lagatsky A. A. et al. Diode-pumped CW lasing of Yb:KYW and Yb:KGW // Optics communications – 1999, Vol. 165, №. 1-3, pp. 71-75.
9. Silvestre Ò. et al. Thermal properties of monoclinic KLu(WO₄)₂ as a promising solid state laser host // Optics express – 2008, Vol. 16, №. 7, pp. 5022-5034.
10. Petrov V. et al. Growth and properties of KLu(WO₄)₂, and novel ytterbium and thulium lasers based on this monoclinic crystalline host // Laser & Photonics Reviews – 2007, Vol. 1, №. 2, pp. 179-212.
11. Cascales C. et al. Structural, spectroscopic, and tunable laser properties of Yb³⁺-doped NaGd(WO₄)₂ // Physical Review B – 2006, Vol. 74, №. 17, pp. 174114.
12. Voron'ko Y. K. et al. Growth and spectroscopic investigations of Yb³⁺-doped NaGd(MoO₄)₂ and NaLa(MoO₄)₂—new promising laser crystals // Optical Materials – 2006, Vol. 29, №. 2-3, pp. 246-252.
13. Wakefield G. et al. Luminescence properties of nanocrystalline Y₂O₃:Eu // Advanced Materials – 2001, Vol. 13, №. 20, pp. 1557-1560.
14. Neeraj S. et al. Novel red phosphors for solid-state lighting: the system NaM(WO₄)_{2-x}(MoO₄)_x:Eu³⁺ (M:Gd,Y,Bi) // Chemical Physics Letters – 2004, Vol 387, №. 1-3, pp. 2-6.

15. Wang Z. et al. Luminescence of $(\text{Li}_{0.333}\text{Na}_{0.334}\text{K}_{0.333})\text{Eu}(\text{MoO}_4)_2$ and its application in near UV InGaN-based light-emitting diode // *Chemical Physics Letters* – 2005, Vol 412, №. 4-6, pp. 313-316.
16. Bagaev S. N. et al. 25% Eu:KGd(WO₄)₂ laser crystal: spectroscopy and lasing on the $^5\text{D}_0 \rightarrow ^7\text{F}_4$ transition // *Quantum Electronics* – 2011, Vol. 41, №3, pp. 189-192.
17. Dashkevich V. I. et al. Red Eu,Yb:KY(WO₄)₂ laser at~ 702 nm // *Laser Physics Letters* – 2015, Vol. 12, №. 8, pp. 085001.
18. Loiko P. A. et al. Spectroscopic characterization and pulsed laser operation of Eu³⁺:KGd(WO₄)₂ crystal // *Laser Physics* – 2013, Vol. 23, №. 10, pp. 105811-1-7.
19. Kränkel C. et al. Out of the blue: semiconductor laser pumped visible rare-earth doped lasers // *Laser & photonics reviews* – 2016, Vol 10, №. 4, pp. 548-568.
20. Metz P. W. et al. Efficient continuous wave laser operation of Tb³⁺-doped fluoride crystals in the green and yellow spectral regions // *Laser & Photonics Reviews* – 2016, Vol 10, №. 2, pp. 335-344
21. Metz P. W. et al. Performance and wavelength tuning of green emitting terbium lasers // *Optics express* – 2017, Vol. 25, №. 5, pp. 5716-5724.
22. Hayakawa T. et al. Visible emission characteristics in Tb³⁺-doped fluorescent glasses under selective excitation // *Journal of luminescence* – 1996, Vol 68, №. 2-4, pp. 179-186.
23. Sun X. et al. Luminescence behavior of Tb³⁺ ions in transparent glass and glass-ceramics containing CaF₂ nanocrystals // *Journal of Luminescence* – 2009, Vol. 129, №. 8, pp. 773-777.
24. Hao Z. et al. Blue-green-emitting phosphor CaSc₂O₄:Tb³⁺: tunable luminescence manipulated by cross-relaxation // *Journal of The Electrochemical Society* – 2009, Vol 156, №. 3, pp. H193-H196.
25. Liao J. et al. Synthesis and luminescence properties of Tb³⁺:NaGd(WO₄)₂ novel green phosphors // *Journal of luminescence* – 2009, Vol. 129, №. 7, pp. 668-671.
26. Ju X. et al. Luminescence properties of ZnMoO₄: Tb³⁺ green phosphor prepared via co-precipitation // *Materials Letters* – 2011, Vol. 65, №. 17-18, pp. 2642-2644.
27. Kaminskii A. A. et al. Ribbon and sheet miniature crystal laser // *Quantum Electronics* – 1994, Vol. 24, №. 12, pp. 1029..

Synopsis

Relevance of the chosen topic

Recently, families of the low-symmetry crystals, including rhombic and monoclinic tungstate and molybdate crystals, are attractive as laser media [1]. The main feature of such crystals is the significant anisotropy of the spectral-luminescent properties in polarized light. An analysis of the current state of research on low-symmetry crystals has showed that tungstates and molybdates crystals doped with rare-earth ions selected for study in the thesis are promising for obtaining efficient lasing in the visible and near-IR spectral regions [2-5]. The advantages of such crystals include the possibility of achieving high concentrations of rare-earth ions without noticeable quenching of luminescence [6], high value of absorption and stimulated emission cross sections in polarized light [7,8], and good thermo-optical properties [9]. Also, such crystals are Raman-active.

The family of crystals selected for the study is very wide, many crystals have already been known and well-studied. However, at the time of establishing the thesis goals, the spectral-luminescent properties of the crystals selected in the thesis, as well as the possibility of using them as active laser media still have been poorly studied and relatively few publications on this topic were made.

Crystals doped with ytterbium (Yb^{3+}) and thulium (Tm^{3+}) ions are known for their lasing in the near infrared range (in the wavelength range of $\sim 1 \mu\text{m}$ and $\sim 2 \mu\text{m}$, respectively) [10-12]. Near-IR lasers have variety of applications: molecular spectroscopy, medicine, ranging, communication, control systems, etc. The IR radiation is characterized by low losses in the atmosphere, and the Tm^{3+} ions luminesce in the so-called eye-safe region.

Crystals containing europium (Eu^{3+}) [13-18] and terbium (Tb^{3+}) [19-26] ions luminesce in the visible region of the spectrum. They can be widely

used as commercial phosphors, and they are also laser-active for the visible range.

It should be noted that in recent years, one of the important directions in the development of modern devices in all areas is the miniaturization of all components. In these terms, compact microchip lasers are of great interest. They have a relatively simple construction of the resonator. Nevertheless, for the efficient lasing, microchip lasers require very careful selection of the active medium. Suitable media have to provide high doping concentrations, high values of absorption, emission and gain cross sections, and a positive thermal lens. Thus, at present, it is of great interest to study the spectral and luminescent properties of double molybdates crystals with layered structure providing the creation of active media for lasers with a thickness of up to several tens of micrometers [27]. The carrying out experiments confirming the possibility of obtaining efficient lasing on thin plates and films made of such crystals is of a great interest as well.

Thus, a comprehensive study of the spectral-luminescent properties of new crystals, including both the study of the anisotropy of the spectral-luminescent properties, the determination of the main spectroscopic characteristics and the establishment of the possibility of using such crystals as an active medium for a laser, and the conduct of laser experiments on thin plates and films of these crystals, is of great interest and is a relevant task.

Research goals and objectives

The main goal of this thesis is a detailed study of the anisotropy of the spectral-luminescent properties of low-symmetry (rhombic and monoclinic) molybdate and tungstate crystals doped with europium (Eu^{3+}), terbium (Tb^{3+}), thulium (Tm^{3+}) and ytterbium (Yb^{3+}) ions, as well as determining the possibility of using such crystals as active laser media for the visible and

near-IR spectral regions and obtaining lasing in these materials, including in the microchip-laser configuration.

In order to achieve the goal in the framework of the thesis, the following **objectives** have been established:

- Study the anisotropy of the spectral-luminescent properties of chosen crystals in polarized light.

- Investigate the anisotropy of magnetic-dipole transitions of Eu^{3+} ions in $\text{KY}(\text{WO}_4)_2$ and $\text{KY}(\text{MoO}_4)_2$ crystals.

- Calculate the probabilities of transitions; absorption, stimulated emission and gain cross sections; as well as to determine the lifetimes of the luminescence of the rare-earth ions.

- Study the anisotropy of the vibronic properties of the crystals.

- Determine the crystal-field splitting of the Yb^{3+} ions in the $\text{KY}(\text{MoO}_4)_2$ and ZnWO_4 crystals;

- Obtain lasing in a $\text{Yb}^{3+}, \text{Li}^+:\text{ZnWO}_4$ crystal, find out the possibility of lasing on the thin films of $\text{Tm}^{3+}:\text{KY}(\text{MoO}_4)_2$ and $\text{Yb}^{3+}:\text{KY}(\text{MoO}_4)_2$ crystals and achieve lasing in the microchip-laser configuration.

The *objects* of the study were monoclinic and rhombic crystals of tungstates and molybdates: $\text{KY}(\text{WO}_4)_2$, $\text{KLu}(\text{WO}_4)_2$, $\text{KY}(\text{MoO}_4)_2$, $\text{CsGd}(\text{MoO}_4)_2$ and ZnWO_4 , doped with europium (Eu^{3+}), terbium (Tb^{3+}), thulium (Tm^{3+}) and ytterbium (Yb^{3+}).

The *subjects* of research were the spectral-luminescent properties of ions in these crystals, the vibronic properties of crystal hosts, as well as the laser operation and lasing properties of crystals.

Scientific novelty of research

1. The main spectral-luminescence characteristics of europium (Eu^{3+}), terbium (Tb^{3+}), thulium (Tm^{3+}) and ytterbium (Yb^{3+}) ions in $\text{KY}(\text{WO}_4)_2$,

$\text{KLu}(\text{WO}_4)_2$, $\text{KY}(\text{MoO}_4)_2$, $\text{CsGd}(\text{MoO}_4)_2$ and ZnWO_4 crystals have been studied.

2. The Stark splitting of multiplets and the width of the zero-phonon line of the Yb^{3+} ions in ZnWO_4 and $\text{KY}(\text{MoO}_4)_2$ crystals have been determined for the first time. It was found that the heterovalent mechanism of substitution in ZnWO_4 crystals leads to a notable broadening of the zero-phonon line and to a high value of the Stark splitting of the Yb^{3+} multiplets.

3. The polarization selection rules for the pure magnetic-dipole transitions in optically biaxial crystals have been established for the first time. They were experimentally confirmed in $\text{Eu}^{3+}:\text{KY}(\text{WO}_4)_2$ and $\text{Eu}^{3+}:\text{KY}(\text{MoO}_4)_2$ crystals.

4. For the first time in $\text{Tm}^{3+}:\text{KY}(\text{MoO}_4)_2$ and $\text{Yb}^{3+}:\text{KY}(\text{MoO}_4)_2$ crystals, efficient lasing was achieved in thin crystal films and plates obtained by the method of mechanical cleavage.

The theoretical and practical significance

The theoretical significance of this work is that the detailed information about the anisotropy of the spectral-luminescent properties of europium, terbium, thulium and ytterbium ions in $\text{KY}(\text{WO}_4)_2$, $\text{KLu}(\text{WO}_4)_2$, $\text{KY}(\text{MoO}_4)_2$, $\text{CsGd}(\text{MoO}_4)_2$ and ZnWO_4 crystals was obtained. In particular, the pure magnetic-dipole transition of europium ions in $\text{Eu}^{3+}:\text{KY}(\text{WO}_4)_2$ and $\text{Eu}^{3+}:\text{KY}(\text{MoO}_4)_2$ crystals was studied, and polarization selection rules for magnetic-dipole transitions in optically biaxial crystals were established. The dependence of strong anisotropy of spectral properties of double molybdates $\text{KY}(\text{MoO}_4)_2$, $\text{CsGd}(\text{MoO}_4)_2$ crystals and their layered structure was described.

The practical significance of the work is determined by the fact that the key spectroscopic characteristics of the new crystals were determined, and the absorption, stimulated emission and gain cross sections were

calculated. For crystals doped with europium and terbium ions, the color characteristics of the luminescence were determined. The results obtained in the thesis can be further used for the development of new lasers, including for the miniaturized microchip-lasers design. It was demonstrated that the method of mechanical cleavage of double molybdate $KY(MoO_4)_2$ crystals with a layered structure can be used to obtain thin crystal plates and films (up to several tens of microns thick) suitable for use as active laser media. Efficient laser operation in cleaved crystal plates and films of $KY(MoO_4)_2$ crystals doped with Tm^{3+} , and Yb^{3+} ions was performed.

Research statements of the thesis to be defended

1. Double molybdate $KY(MoO_4)_2$ and $CsGd(MoO_4)_2$ crystals exhibit extremely strong anisotropy of absorption and stimulated emission cross sections for rare-earth ions, which are associated with their layered structure and low local symmetry of luminescent centers (C_2).

2. Monoclinic zinc tungstate $ZnWO_4$ crystals co-doped with Yb^{3+} and Li^+ ions (providing heterovalent mechanism of substitution), are characterized by a large Stark splitting of the lower multiplet of ytterbium ions (804 cm^{-1}), high anisotropy of stimulated emission cross sections in polarized light, which determine their attractiveness for generating ultrashort pulses.

3. Polarization selection rules for magnetic-dipole transitions of rare-earth ions in optically biaxial crystals with local symmetry of luminescent centers C_2 are determined by the mutual orientation of the magnetic field vector and the magnetic dipole relative to the second-order symmetry axis.

4. The layered structure and perfect cleavage of potassium-yttrium double molybdate $KY(MoO_4)_2$ crystals, doped by Yb^{3+} , and Tm^{3+} ions, provide the possibility to produce thin (up to several tens of micrometers thick) crystal plates and films subject to elastic deformation, suitable for laser

active media for effective microchip-lasers emitting in the spectral range of $\sim 1 \mu\text{m}$ and $\sim 2 \mu\text{m}$.

Personal contribution

The content of the thesis and research statements for the defense reflect the personal contribution of the author to this work. The spectroscopic experiments presented in the thesis were performed by the author. The discussion of the obtained results and their preparation for publication were carried out jointly with co-authors. Laser experiments were carried out jointly with co-authors. The contribution of the candidate was decisive.

Approbation

The main results of the dissertation were reported and discussed at the following conferences:

1. VII Congress of Young Scientists, Russia, St. Petersburg, 2018.
2. VIII Congress of Young Scientists, Russia, St. Petersburg, 2019.
3. “Saint Petersburg OPEN 2017” 4th International School and Conference on Optoelectronics, Photonics, Engineering and Nanostructures, Russia, St. Petersburg, 2017.
4. Scientific and educational conference of ITMO University, Russia, St. Petersburg, 2018.
5. 6th International School and Conference Saint-Petersburg OPEN, Russia, St. Petersburg, 2019.
6. SPIE Photonics Europe, France, online, 2020.
7. 9th Eps-Qeod Europhoton Virtual Conference, Czech Republic, online, 2020.
8. International Conference Physicist A. SPb, Russia, St. Petersburg, 2020.

9. 19th International Conference on Laser Optics ICLO 2020, online, 2020.
10. CLEO/EUROPE-EQEC 2021, online, 2021.
11. "Saint Petersburg OPEN 2021", Russia, Saint Petersburg, 2021.

The reliability

The reliability of the results, research statements and conclusions presented in the thesis is confirmed by using modern and proven research methods, reproducibility and a clear interpretation of the obtained results is confirmed by the positive reviews in the journals in which the results of the work are published. The obtained experimental data agree with the results of theoretical calculations, as well as with experimental and theoretical data obtained by other authors.

The structure and scope of the thesis

The thesis consists of the introduction, five chapters, a conclusion and a list of references with 92 items. The total volume of the thesis is 272 pages, including 56 figures and 10 tables.

Main content

In the **introduction** and in the **first chapter**, the relevance of the research carried out within the framework of the thesis is discussed. The first chapter is devoted to the literature review. It shows a general idea of anisotropic crystals of molybdates and tungstates in terms of promising laser media. The first section of the chapter describes the spectroscopic characteristics of rare-earth ions in crystal hosts. The second section is devoted to the analysis of methods for calculating spectroscopic parameters, absorption, stimulated-emission and gain cross-sections, and luminescence lifetimes. It also provides a brief description of the Judd-Ofelt theory. In the

last section, low-symmetry crystals are considered as active media for IR lasers. A literature review of the optical properties and lasing characteristics of tungstate and molybdate crystals doped with rare-earth ions is presented.

The **second chapter** describes the objects of study, a brief description of the single crystals growth methods, describes the experimental techniques and the methods used to study the structure and spectral-luminescent properties, and also describes the methods of conducting laser experiments.

The **third chapter** presents the results of a study of the spectral-luminescent properties of crystals doped with Eu^{3+} and Tb^{3+} ions. The general chemical formula of crystals can be written as $\text{AM}(\text{XO}_4)_2$ ($\text{A} = \text{K}, \text{Cs}$; $\text{M} = \text{Y}, \text{Lu}, \text{Gd}$; $\text{X} = \text{W}, \text{Mo}$). Double potassium-yttrium molybdate and double cesium-gadolinium molybdate crystals doped with europium ions, $\text{Eu}^{3+}:\text{KY}(\text{MoO}_4)_2$ and $\text{Eu}^{3+}:\text{CsGd}(\text{MoO}_4)_2$, a double potassium-yttrium tungstate crystal doped with europium ions, $\text{Eu}^{3+}:\text{KY}(\text{WO}_4)_2$, and double potassium-lutetium tungstate crystal doped with terbium ions, $\text{Tb}^{3+}:\text{KLu}(\text{WO}_4)_2$ were studied.

In the first section, the results of studying the crystal structure are presented. The phase purity and the crystal structure were confirmed by X-ray powder diffraction. Space groups and point groups of crystals, lattice constants and unit-cell volumes were determined. The structure of the crystal was schematically illustrated according with the Rietveld refinement. Figure 1 shows an example of such structure constructed for the $\text{Eu}^{3+}:\text{KY}(\text{MoO}_4)_2$ crystal. It was shown that the main feature of double molybdate crystals is their layered structure.

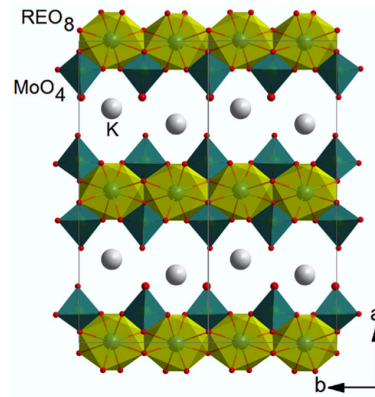


Figure 1 – fragment of the $\text{Eu}^{3+}:\text{KY}(\text{MoO}_4)_2$ crystal structure in projection on the a - b plane.

The second section describes the results of Raman spectroscopy studies. The measurements were carried out in polarized light for all possible crystal geometries. Figure 2 shows the Raman spectra measured for the $\text{Eu}^{3+}:\text{KY}(\text{MoO}_4)_2$ crystal. The spectra are strongly polarized as a result of layered structure; the spectra contain bands located in three ranges with different intensity. The first low-frequency range (up to 275 cm^{-1}) contains weak vibrations associated with T'-modes K, Y and Mo, R-modes and acousto-optic coupled modes. In the second range of vibrations ($319\text{-}435\text{ cm}^{-1}$), there are internal modes associated with bending (δ) vibrations of the oxygen bridged $[\text{MoO}_4]^{2-}$ tetrahedra. The most intense vibration range contains strongly polarized bands related to stretching vibrations (ν) of the oxygen bridged $[\text{MoO}_4]^{2-}$ tetrahedra.

The third section shows the study of the polarized absorption spectroscopy of crystals, and the results of calculating the spectroscopic parameters in accordance with the Judd-Ofelt theory in the approximation of intermediate configuration interaction (ICI) are presented. In all crystals, a strong anisotropy of the absorption spectra of polarized light was observed, this is due to the fact that the crystals of double tungstates and molybdates possess low-symmetry. For Tb^{3+} ions, the observed absorption bands at room temperature are due to transitions from the ground state ($^7\text{F}_6$) to excited

states. Despite the similar structure of energy levels, the absorption spectra of Eu^{3+} ions exhibit transitions not only from the ground state (${}^7\text{F}_0$), but also from thermally populated (${}^7\text{F}_1$) and excited (${}^7\text{F}_2$) states. In the near-IR region of the spectrum, transitions to lower-lying excited states are observed (states ${}^7\text{F}_1 - {}^7\text{F}_6$ and ${}^7\text{F}_5 - {}^7\text{F}_0$ for Eu^{3+} and Tb^{3+} ions, respectively). Such transitions are spin-allowed; thus, the observed intensity of absorption bands in this region is much higher than in the visible.

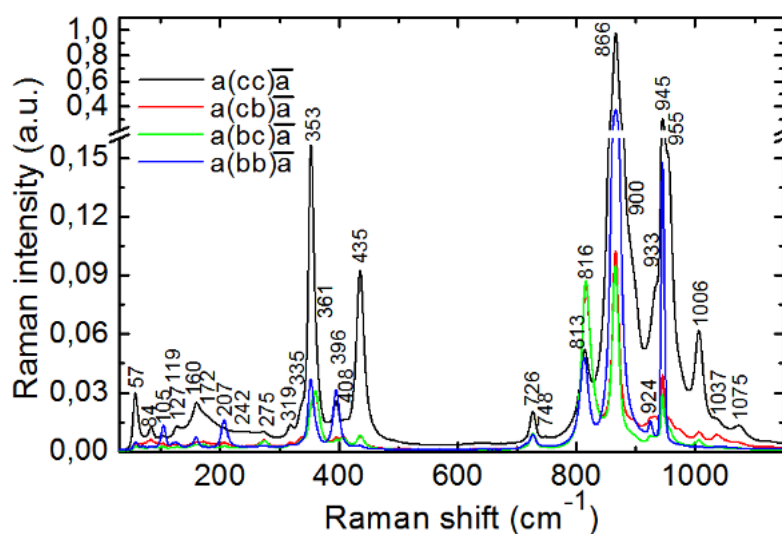


Figure 2 – Polarized Raman spectra of *a*-cut $\text{Eu}^{3+}:\text{KY}(\text{MoO}_4)_2$ crystal, $\lambda_{\text{exc}} = 488 \text{ nm}$.

In the fourth section, the results of studies of the luminescent anisotropy are presented. Luminescence spectra were recorded for three main light polarizations. For Eu^{3+} ions, the spectra exhibit bands related to energy transitions from the metastable ${}^5\text{D}_0$ level to the lower ${}^7\text{F}_J$ energy states ($J = 0-6$). For Tb^{3+} ions, the luminescence bands correspond to transitions from the ${}^5\text{D}_4$ state to the lower energy states. All luminescence bands are strongly polarized. Figure 3 shows the spectra of polarized stimulated-emission cross-section (σ_{SE}) of $\text{Eu}^{3+}:\text{CsGd}(\text{MoO}_4)_2$ (a), $\text{Eu}^{3+}:\text{KY}(\text{MoO}_4)_2$ (b), $\text{Tb}^{3+}:\text{KLu}(\text{WO}_4)_2$ (c) crystals calculated from the recorded luminescence spectra.

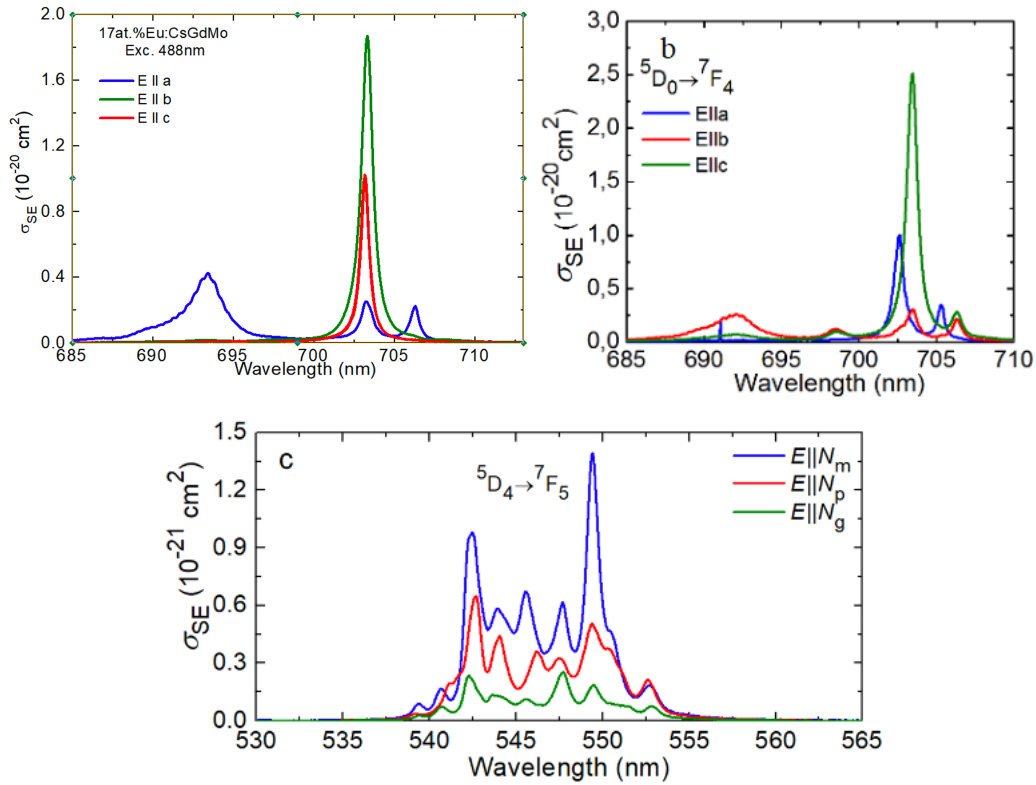


Figure 3 – Polarized stimulated-emission cross-section, σ_{SE} , spectra for $\text{Eu}^{3+}:\text{CsGd}(\text{MoO}_4)_2$ (a), $\text{Eu}^{3+}:\text{KY}(\text{MoO}_4)_2$ (b), and $\text{Tb}^{3+}:\text{KLu}(\text{WO}_4)_2$ (c) crystals.

In the fifth section, the pure magnetic-dipole (MD) transition ${}^5\text{D}_0 \rightarrow {}^7\text{F}_1$ of Eu^{3+} ions in $\text{KY}(\text{XO}_4)_2$ ($\text{X} = \text{W}, \text{Mo}$) crystals is considered. By detailed study of the luminescence of this transition (Figure 4), it was found that the number and relative intensity of the peaks depend not only on the polarization of light \mathbf{E} , but also on the direction of propagation \mathbf{k} .

This effect is not observed for the remaining transitions ${}^5\text{D}_0 \rightarrow {}^7\text{F}_J$ ($J = 2 - 6$), which are purely electric dipole (ED) transitions. The magnetic dipole transition is caused by the interaction of the active ion with the component of the magnetic field of light through the magnetic dipole, the orientation of which is set by the vector \mathbf{M} . In this case, the orientation of the magnetic field vector \mathbf{H} with respect to \mathbf{M} .

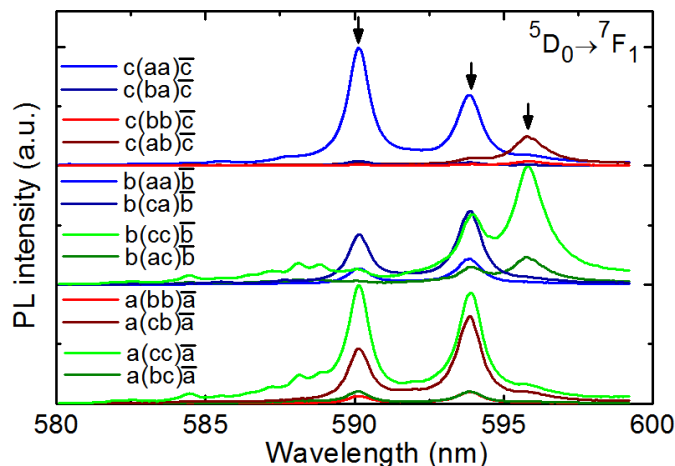


Figure 4 – Polarized luminescence spectra for the purely MD transition ${}^5D_0 \rightarrow {}^7F_1$ of Eu^{3+} ions in the Eu:KYMo crystal, $\lambda_{\text{exc}} = 458 \text{ nm}$. The $k_{\text{exc}}(\mathbf{E}_{\text{exc}}\mathbf{E}_{\text{lum}})k_{\text{lum}}$ notations are used. The *arrows* indicate the Stark-to-Stark transitions.

Thus, polarization selection rules for magnetic-dipole transitions of rare-earth ions in optically biaxial crystals with local symmetry of C_2 luminescent centers were established (see Table 1).

Table 1 – Polarization selection rules for the ${}^5D_0 \rightarrow {}^7F_1$ MD transition of Eu^{3+} ions in KYMo .

\mathbf{M} vector (MD)	${}^5D_0 \rightarrow {}^7F_1$	Preferred \mathbf{k}	Possible $e_{\rho\mathbf{k}}$	No.
$\mathbf{M} \parallel C_2 (\mathbf{M} \parallel \mathbf{a})$	$\Gamma_1 \rightarrow \Gamma_1$	$\parallel \mathbf{b}$	$\parallel \mathbf{c}$	1
		$\parallel \mathbf{c}$	$\parallel \mathbf{b}$	2
$\mathbf{M} \perp C_2 (\mathbf{M} \parallel \mathbf{b}, \mathbf{c})$	$\Gamma_1 \rightarrow \Gamma_2^{(1)}, \Gamma_2^{(2)}$	$\parallel \mathbf{a}$	$\parallel \mathbf{b}, \mathbf{c}$	3, 4
		$\parallel \mathbf{b}$	$\parallel \mathbf{a}, \mathbf{c}$	5, 6
		$\parallel \mathbf{c}$	$\parallel \mathbf{a}, \mathbf{b}$	7, 8

In the sixth section, the color characteristics (color coordinates, dominant wavelength, and color purity) of the luminescence of Eu^{3+} and Tb^{3+} ions (table 2) in crystals were determined in accordance with the CIE 1931 color space.

The **fourth chapter** is devoted to studies of the spectral-luminescent and lasing properties of a double molybdate crystal doped with thulium ions, $\text{Tm}^{3+}:\text{KY}(\text{MoO}_4)_2$. The first section of the chapter describes the crystal structure and phase purity confirmed by powder X-ray diffraction. The

crystal belongs to the class of orthorhombic crystals with the space group $Pbna - D^{14}_{2h}$, No 60. In the second section of the chapter studies of this crystal by the Raman spectroscopy method are described in detail.

Table 2 – Color coordinates of the luminescence of $\text{Eu}^{3+}:\text{KY}(\text{MoO}_4)_2$ and $\text{Tb}^{3+}:\text{KLu}(\text{WO}_4)_2$, crystals, calculated in accordance with the CIE 1931 color space

Crystall	x	y	Color purity	Dominant wavelength
Eu:KY(MoO ₄) ₂	0.665	0.335	>99%.	612 nm, kred
Tb:KLuW	0.380	0.608	> 97%	561 nm, yellowish green

In the third section, the study results of the absorption properties of the crystal are presented. The absorption bands in the spectrum correspond to the transitions of Tm^{3+} ions from the ground energy state ($^3\text{H}_6$) to the excited states (from $^3\text{F}_4$ to $^1\text{D}_2$). The absorption spectrum is strongly polarized; however, the noticeable absorption anisotropy in the (100) plane cannot be attributed to the layered structure and is most likely associated with the low symmetry of the C_2 luminescent centers.

The $^3\text{H}_6 \rightarrow ^3\text{H}_4$ energy transition of Tm^{3+} ions is suitable for pumping by high-power industrial/commercial laser AlGaAs diodes. The maximum absorption cross section σ_{abs} is $7.70 \times 10^{-20} \text{ cm}^2$ at the wavelength of 802.8 nm, and the corresponding full width at the half maximum (FWHM) is 10.0 nm (for polarization $\mathbf{E} \parallel \mathbf{b}$).

In the fourth section, an analysis of the luminescence properties, stimulated-emission, and gain cross-section spectra of the $\text{Tm}:\text{KY}(\text{MoO}_4)_2$ crystal is presented. Tm^{3+} ions emit in the near-IR region of the spectrum, Figure 5 (a). The maximum value of the stimulated-emission cross-sections σ_{SE} is $22.70 \times 10^{-20} \text{ cm}^2$ at the wavelength of 1856 nm with FWHM > 110 nm (for $\mathbf{E} \parallel \mathbf{b}$).

The decay curve of Tm^{3+} luminescence from the $^3\text{F}_4$ state is single-exponential. The luminescence lifetime is $\tau_{\text{lum}} = 2.29 \text{ ms}$.

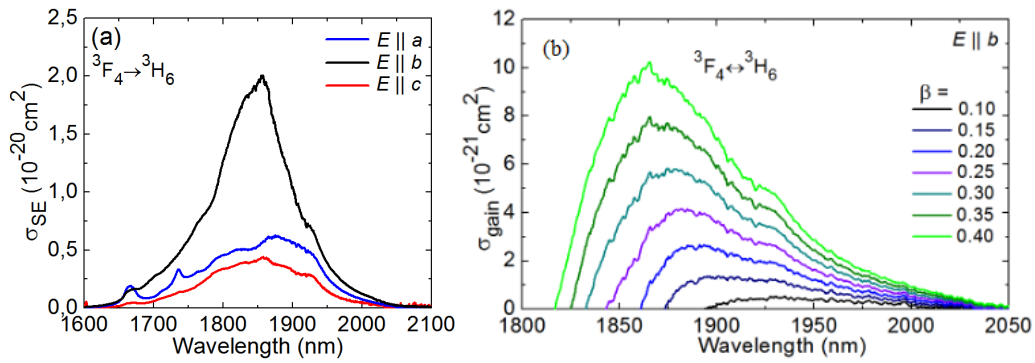


Figure 5 – (a) stimulated-emission (SE) cross-sections, σ_{SE} , for the ${}^3F_4 \rightarrow {}^3H_6$ transition, light polarizations are $E \parallel a, b, c$; (b) Gain cross-sections for the ${}^3F_4 \leftrightarrow {}^3H_6$ transition of Tm^{3+} in $KY(MoO_4)_2$ crystal the light polarization is $E \parallel b$.

The determination of the expected laser emission wavelength on the $Tm^{3+}:KY(MoO_4)_2$ crystal, the gain cross-sections, σ_{gain} , were calculated. Figure 5 (b) shows the obtained spectra calculated for light polarization $E \parallel b$. The spectra are relatively smooth and broad.

In the fifth section, laser experiments and results of achieving lasing on crystal plates and thin films of a $Tm:KY(MoO_4)_2$ crystal obtained by cleaving without any subsequent processing are described. The section describes in detail the experimental laser setup (Figure 6), the main feature is the microchip laser cavity.

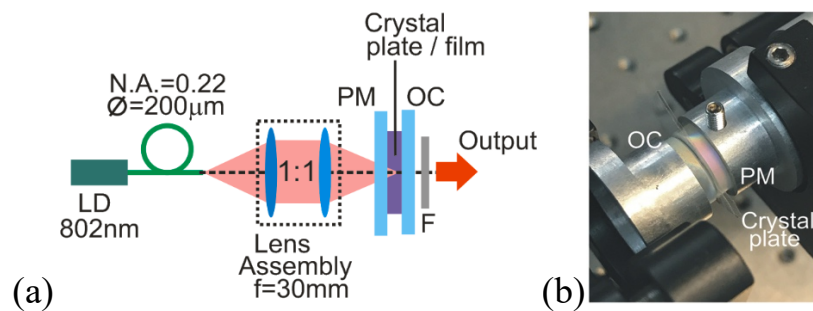


Figure 6 – (a) Scheme of the diode-pumped microchip $Tm:KY(MoO_4)_2$ laser: LD – laser diode, PM – pump mirror, OC – output coupler, F – cut-off filter; (b) photograph of the microchip laser.

The AlGaAs laser diode emitting unpolarized light at the wavelength of 802 nm was used for pumping. Efficient lasing was demonstrated, Figure 7.

The laser on a crystal plate with a thickness of 700 μm generated a maximum output power of 0.88 W at 1840-1905 nm with a slope efficiency $\eta = 65.8\%$. In the second experiment on a crystal film with a thickness of 70 μm , a maximum output power of 131 mW was achieved at 1801–1872 nm with $\eta = 45.2\%$.

The **fifth chapter** describes the spectral-luminescent and lasing properties of crystals doped with ytterbium ions: potassium-yttrium molybdate $\text{Yb}^{3+}:\text{KY}(\text{MoO}_4)_2$ crystal and zinc tungstate $\text{Yb}^{3+},\text{Li}^+:\text{ZnWO}_4$ crystal.

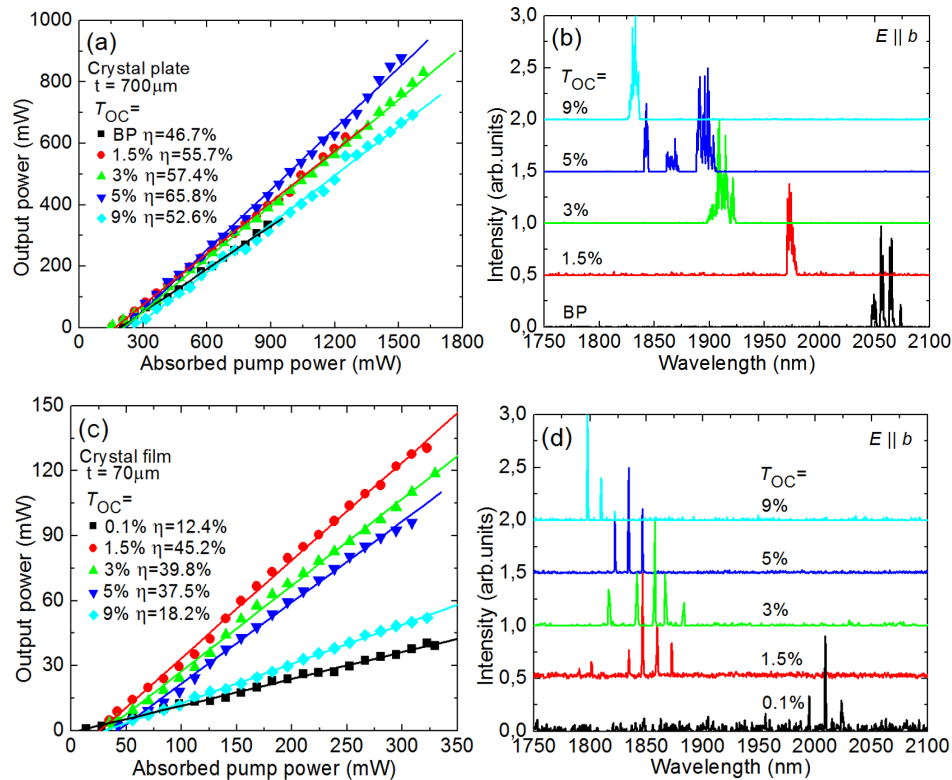


Figure 7 – Input-output dependences of the laser on a crystal plate ($t = 700 \mu\text{m}$) and on a thin crystal film ($t = 70 \mu\text{m}$) (c); (b,d) typical spectra of the laser emission measured at maximum P_{abs} . The laser polarization is $E \parallel b$.

In the first section of the chapter, X-ray powder diffraction studies are presented, the phase purity and crystal structure was confirmed. The $\text{Yb}^{3+}:\text{KY}(\text{MoO}_4)_2$ crystal is orthorhombic and has a layered structure (Figure 8), the $\text{Yb}^{3+},\text{Li}^+:\text{ZnWO}_4$ crystal is monoclinic.

In the second section, a detailed description of the results of studying crystals by Raman spectroscopy method, carried out for all possible geometries and polarizations of light, is given.

The third section shows the results of the absorption spectroscopy. The absorption spectra exhibit strong anisotropy of polarized light. The absorption band at $\sim 1 \mu\text{m}$ corresponds to the $^2\text{F}_{7/2} \rightarrow ^2\text{F}_{5/2}$ energy transition of the Yb^{3+} ion.

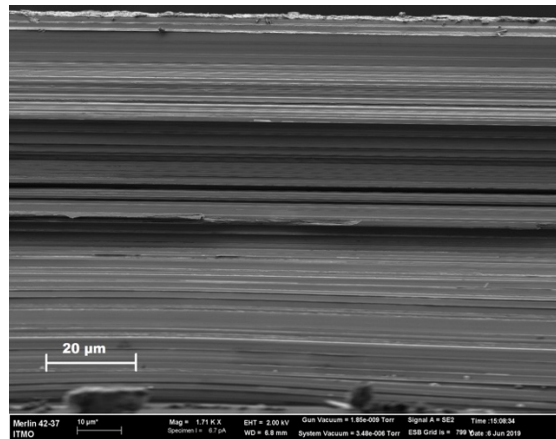


Figure 8 – Image of the edge of a cleaved $\text{Yb}^{3+}:\text{KY}(\text{MoO}_4)_2$ crystal obtained using a scanning electron microscope. The a axis is vertical.

Section four describes the stimulated-emission and gain cross-section spectra, as well as the luminescence lifetimes. It should be noted that crystals of zinc tungstate ZnWO_4 , co-activated with Yb^{3+} and Li^+ ions, exhibit a high anisotropy of the stimulated-emission cross-sections in polarized light, Figure 9 (a), and wide gain cross-sections spectra, Figure 9 (b). This feature makes them attractive as an active laser media for generating ultrashort pulses.

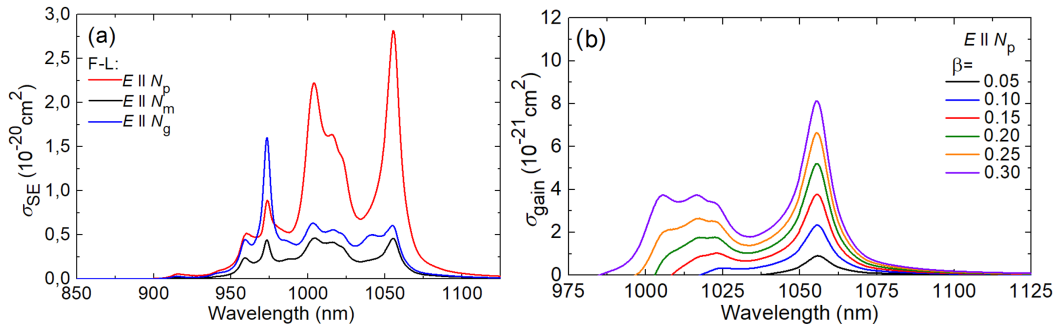


Figure 9 – (a) stimulated-emission cross-section, σ_{SE} , spectra of $\text{Yb}^{3+}, \text{Li}^+:\text{ZnWO}_4$ crystal. The light polarizations is $E \parallel N_p$; (b) gain cross sections spectra of the ${}^2F_{5/2} \leftrightarrow {}^2F_{7/2}$ transition of Yb^{3+} ions in ZnWO_4 .

Section five describes the results of low-temperature spectroscopy and the Stark splitting of Yb^{3+} multiplets in $\text{KY}(\text{MoO}_4)_2$ and ZnWO_4 crystals. Polarized absorption and luminescence spectra (Figure 10) were recorded in the temperature range 6 – 300 K.

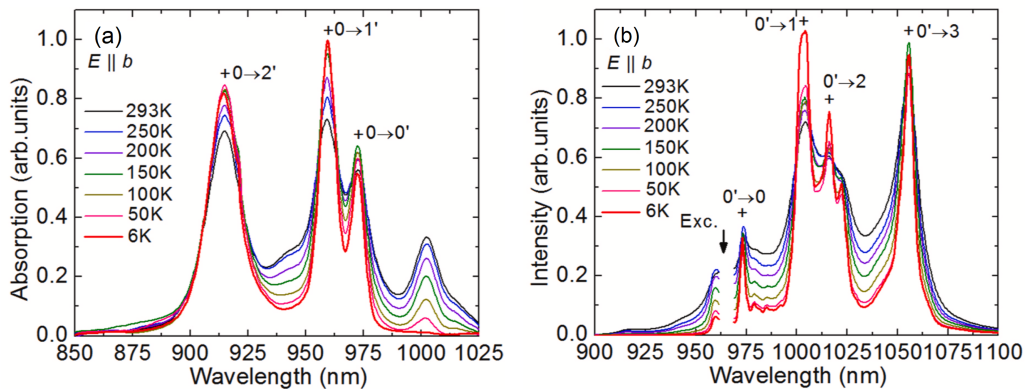


Figure 10 – Low-temperature spectroscopy of $\text{Yb}^{3+}, \text{Li}^+:\text{ZnWO}_4$ crystal: absorption (a) and luminescence (b) spectra for light polarization $E \parallel b$.

At the temperature of 6 K, the electron-phonon coupling is strongly suppressed; however, for Yb^{3+} ions in the ZnWO_4 crystal, a large bandwidth of the zero-phonon line $\Delta\lambda_{ZPL} = 3.0$ nm, and a large Stark splitting of the lower multiplet of Yb^{3+} ions (804 cm^{-1}) are observed. It is much wider than in the $\text{KY}(\text{MoO}_4)_2$ crystal, in which the Stark splitting is 601 cm^{-1} , see Figure 11.

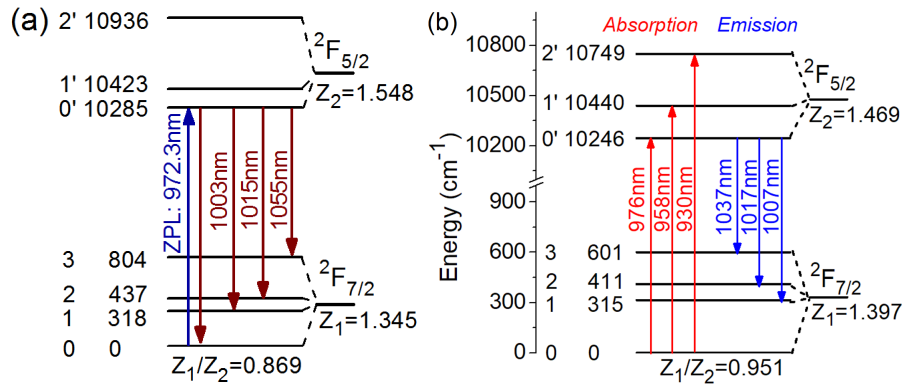


Figure 11 – Crystal-field splitting for Yb^{3+} ions: Scheme of the Stark sub-levels for the ZnWO_4 crystal (a) and for the $\text{KY}(\text{MoO}_4)_2$ crystal (b).

It is known that for all rare-earth ions, the barycenter energy of any isolated $^{2S+1}L_J 4f^m$ multiplet depends on the barycenter energy of any other isolated multiplet in a linear way, Figure 12. The barycenter energies $\langle E(^2F_{5/2}) \rangle$ and $\langle E(^2F_{7/2}) \rangle$ for $\text{Yb}^{3+}, \text{Li}^+ : \text{ZnWO}_4$ and $\text{Yb}^{3+} : \text{KY}(\text{MoO}_4)_2$ are in well agreement with the linear approximation of the equation $E(^2F_{5/2}) = 10166.6 + 0.997 \times E(^2F_{7/2})$ [cm^{-1}], which describes the dependence of the barycenter of the excited level of a rare-earth ion on the ground level. This analysis confirms the correctness of the constructed energy-level scheme.

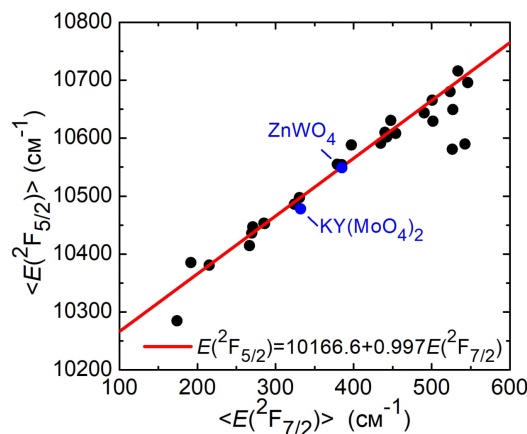


Figure 12 – Barycenter plot for Yb^{3+} ions in $\text{Yb}^{3+}, \text{Li}^+ : \text{ZnWO}_4$ and $\text{Yb} : \text{KY}(\text{MoO}_4)_2$ crystals (blue circle). The red line denotes the linear fit of all the crystals.

In the sixth section, the results of experiments on obtaining efficient lasing are presented. A thin (286 μm) crystal plate was mechanically cleaved

from the large $\text{Yb}^{3+}:\text{KY}(\text{MoO}_4)_2$ crystal. No post-cleavage treatment was applied to both surfaces. The crystal plate was placed in a compact microchip cavity. The InGaAs laser diode emitting at a wavelength of 968 nm was used as a pump source. The results of laser experiments are shown in Figure 13. Laser generated a maximum output power of 0.81 W at the wavelength of 1021-1044 nm with a slope efficiency = 76.4%.

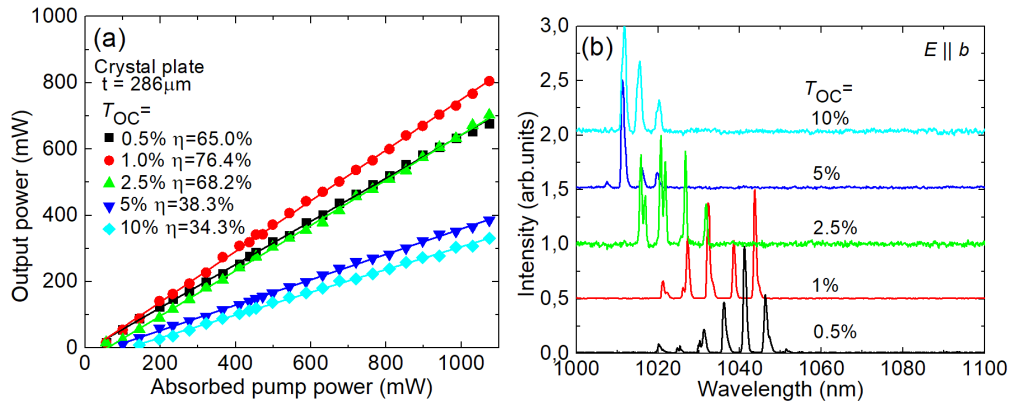


Figure 13 – Diode-pumped $\text{Yb}:\text{KY}(\text{MoO}_4)_2$ crystal-plate microchip laser: (a) input-output dependences, η – slope efficiency; (b) typical laser emission spectra measured at $P_{\text{abs}} = 1.0$ W. The laser polarization is $\mathbf{E} \parallel \mathbf{b}$.

In the second experiment, a rectangular active element was prepared from a $\text{Yb}^{3+},\text{Li}^+:\text{ZnWO}_4$ crystal. It was cut for light propagation along the \mathbf{a} -axis. The input and output facets were polished to laser quality. The crystal was placed in a linear plane-concave cavity. The same InGaAs laser diode was used for pumping. The $\text{Yb}^{3+},\text{Li}^+:\text{ZnWO}_4$ laser generated a maximum output power of 2.90 W at ~ 1059 nm with a slope efficiency $\eta = 57.9\%$ (with respect to the absorbed pump power).

In the **conclusion**, the main results of the research were summarized, and the main findings were presented.

In the dissertation work, a comprehensive study of the spectral-luminescent properties of new orthorhombic and monoclinic $\text{KY}(\text{WO}_4)_2$, $\text{KLu}(\text{WO}_4)_2$, $\text{KY}(\text{MoO}_4)_2$, $\text{CsGd}(\text{MoO}_4)_2$ and ZnWO_4 crystals, doped with

europium, terbium, thulium and ytterbium ions was performed. The efficient lasing in the IR region of the spectrum was demonstrated.

It was shown that double molybdates crystals, which include potassium-yttrium double molybdate $KY(MoO_4)_2$ crystals and cesium-gadolinium double molybdate $CsGd(MoO_4)_2$ crystals, are characterized by a strong anisotropy of absorption and stimulated-emission cross-sections for rare-earth ions. For example, for a $Tm^{3+}:KY(MoO_4)_2$ crystal, the absorption cross-section for polarization $E \parallel b$ is an order of magnitude higher than for polarization $E \parallel c$, and it is $7.70 \times 10^{-20} \text{ cm}^2$. And the value of the stimulated-emission cross-section for this polarization is 6-8 times more than for other polarizations. This anisotropy is primarily associated with the low local symmetry of the luminescent centers (C_2), and with the layered structure of the crystals as well.

Polarization selection rules were formulated for magnetic-dipole transitions in optically biaxial crystals with local symmetry of C_2 luminescent centers. They are determined by the mutual orientation of the magnetic field vector and the magnetic dipole relative to the second-order symmetry axis. A detailed study of the luminescence anisotropy of the magnetic-dipole transition $^5D_0 \rightarrow ^7F_1$ of Eu^{3+} ions in $Eu^{3+}:KY(WO_4)_2$ and $Eu^{3+}:KY(MoO_4)_2$ crystals revealed the influence of the exciting light polarization and crystal orientation on the shape of the luminescence spectrum. Thus, the first experimental confirmation of the polarization selection rules was obtained.

Stark-splitting of the energy levels of Yb^{3+} ions in $ZnWO_4$ and $KY(MoO_4)_2$ crystals was determined for the first time. It was found that a large (804 cm^{-1}) Stark splitting of the lower multiplet of Yb^{3+} ions is observed in the zinc tungstate $ZnWO_4$ crystal co-doped with Yb^{3+} and Li^+ ions (providing heterovalent mechanism of substitution), while for the $KY(MoO_4)_2$ crystal this value is 601 cm^{-1} .

Also, in the ZnWO_4 crystal, a significant increase in the bandwidth of the zero-phonon line $\Delta\lambda_{\text{ZPL}} = 3.0$ nm is observed, which is much wider than in the $\text{Yb:KY}(\text{WO}_4)_2$ crystal ($\Delta\lambda_{\text{ZPL}} < 0.1$ nm). Also, the ZnWO_4 crystal is characterized by high anisotropy of the stimulated-emission cross-sections in polarized light and broad gain cross-sections spectra.

It was shown that the layered structure and perfect cleavage of the potassium-yttrium double molybdate $\text{KY}(\text{MoO}_4)_2$ crystals make it possible to produce thin crystal plates and films subject to elastic deformation up to several tens of micrometers thick. Such films and plates have laser quality and are suitable for active elements in microchip lasers without any post-cleavage processing. The laser operation in thin crystal plates and films of $\text{Tm}^{3+}:\text{KY}(\text{MoO}_4)_2$ and $\text{Yb}^{3+}:\text{KY}(\text{MoO}_4)_2$ crystals was demonstrated for the first time. Laser based on a 286 μm thick $\text{Yb}^{3+}:\text{KY}(\text{MoO}_4)_2$ crystal plate generated a maximum output power of 0.81 W at the wavelength of 1021-1044 nm with a slope efficiency = 76.4%. Laser based on 700- μm -thick crystal plate of the $\text{Tm}:\text{KY}(\text{MoO}_4)_2$ generated a maximum output power of 0.88 W. The laser emitted at the wavelength of 1840-1905 nm with a slope efficiency $\eta = 65.8\%$. A thin-film $\text{Tm}:\text{KY}(\text{MoO}_4)_2$ laser generated a maximum output power of 131 mW at the wavelength of 1801–1872 nm with $\eta = 45.2\%$.

Publications

The main results of the thesis have been presented in publications, which are indexed by Web of Science and Scopus:

1. Subbotin K., Loiko P., Slimi S., **Volokitina A.**, Titov A., Lis D., Chernova E., Kuznetsov S., Solé R.M., Griebner U., Petrov V., Aguiló M, Díaz F., Camy P., Zharikov E., Mateos X. Monoclinic zinc monotungstate $\text{Yb}^{3+},\text{Li}^+:\text{ZnWO}_4$: Part I. Czochralski growth, structure refinement and Raman spectra // Journal of Luminescence – 2020, Vol. 228 pp. 117601, IF 3.28, JCR – Q2

2. **Volokitina A.**, David S.P., Loiko P., Subbotin K., Titov A., Lis D., Solé R.M., Jambunathan V., Lucianetti A., Mocek T., Camy P., Chengh W., Griebner U., Petrov V., Aguiló M, Díaz F., Mateos X. Monoclinic zinc monotungstate $\text{Yb}^{3+}, \text{Li}^{+}:\text{ZnWO}_4$: Part II. Polarized spectroscopy and laser operation // *Journal of Luminescence* – 2021, Vol. 231, pp. 117811, IF 3.28, JCR – Q2

3. Loiko P., Mateos X., Dunina E., Kornienko A., **Volokitina A.**, Vilejshikova E., Serres J.M., Baranov A., Yumashev K., Aguiló M., Díaz F. Judd-Ofelt modelling and stimulated-emission cross-sections for Tb^{3+} ions in monoclinic $\text{KYb}(\text{WO}_4)_2$ crystal // *Journal of Luminescence* – 2017, Vol. 190, pp. 37-44, IF 3.28, JCR – Q2

4. Kurilchik S., Loiko P., Yasukevich A., Trifonov V., **Volokitina A.**, Vilejshikova E., Kisel V., Mateos X., Baranov A., Goriev O. Orthorombic $\text{Yb}:\text{Li}_2\text{Zn}_2(\text{MoO}_4)_3$ – a novel potential crystal for broadly tunable lasers // *Laser Physics Letters* – 2017, Vol. 14.8, pp. 085804, , IF 2.328, JCR – Q1

5. **Volokitina A.**, Loiko P., Vilejshikova E., Mateos X., Dunina E., Kornienko A., Kuleshov N., Pavlyuk A., $\text{Eu}^{3+}:\text{KY}(\text{MoO}_4)_2$: A novel anisotropic red-emitting material with a layered structure // *Journal of Alloys and Compounds* – 2018, Vol. 762, pp. 786-796, IF 4.65, JCR – Q1

6. Loiko P., **Volokitina A.**, Mateos X., Dunina E., Kornienko A., Vilejshikova E., Aguiló M., Díaz F., Spectroscopy of Tb^{3+} ions in monoclinic $\text{KLu}(\text{WO}_4)_2$ crystal application of an intermediate configuration interaction theory // *Optical Materials* – 2018, Vol. 78, pp. 495-501, IF 2.023, JCR – Q2

7. **Volokitina A.**, Loiko P., Pavlyuk A., Slimi S., Solé R.M., Salem E.B., Kifle E., Serres J.M., Griebner U., Petrov V., Aguiló M, Díaz F., Mateos X. Laser operation of cleaved single-crystal plates and films of $\text{Tm}:\text{KY}(\text{MoO}_4)_2$ // *Optics express* – 2020, Vol. 28.7, pp. 9039-9048, IF 3.669, JCR – Q1

8. **Volokitina, A.**, Loiko P., Pavlyuk A., Serres J.M., Slimi S., Salem E.B., Kifle E., Griebner U., Petrov V., Wang L., Solé R.M., Aguiló M., Díaz F., Mateos X. Spectroscopy and efficient laser operation of cleaving $\text{Yb}:\text{KY}(\text{MoO}_4)_2$ crystal // *Optical Materials Express* – 2020, Vol. 10.10, pp. 2356-2369, IF 3.064, JCR – Q1

9. Loiko P.; Vilejshikova E.V., **Volokitina A.A.**, Trifonov V.A., Serres J.M. Mateos X., Kuleshov N.V., Yumashev K.V., Baranov A.V., Pavlyuk A.A. Growth, structure, Raman spectra and luminescence of orthorombic $\text{Li}_2\text{Mg}_2(\text{MoO}_4)_3$ crystals doped with Eu^{3+} and Ce^{3+} ions // *Journal of Luminescence* – 2017, Vol. 188, pp. 154-161, IF 3.28, JCR – Q2

10. **Volokitina A.**, Loiko P., Pavlyuk A., Solé R.M., Aguiló M., Díaz F., Mateos X., Novel Molybdate Laser Crystal with a Layered Structure: Orthorombic Er^{3+} : $\text{KY}(\text{MoO}_4)_2$ // International Conference Laser Optics (ICLO). IEEE - 2020.

11. Loiko P. **Volokitina A.**, Serres J.M., Trifonov V., Pavlyuk A., Slimi S., Salem E.B., Solé R.M., Aguiló M., Díaz F. Laser Operation of Cleaved Single-Crystal Plates and Films of $\text{Tm}:\text{KY}(\text{MoO}_4)_2$ // Laser Applications Conference - 2019

12. **Volokitina A.**, Loiko P., Serres J.M., Mateos X., Kuleshov N., Trifonov V., Pavlyuk A. Growth and spectroscopy of orthorombic $\text{Yb}:\text{KY}(\text{MoO}_4)_2$ laser crystal with a layered structure // Journal of Physics: Conference Series – 2019, Vol. 1410, No. 1

13. **Volokitina A.A.**, Subbotin K.A. Loiko P.A., Titov A.I., Lis D.A., Slimi S., Solé R.M., David S.P., Jambunathan V., Lucianetti A., Spectroscopic Study and First Laser Operation of Monoclinic $\text{Yb}^{3+}, \text{Li}^+:\text{ZnWO}_4$ Crystal // 2020 International Conference Laser Optics (ICLO) IEEE – 2020.

14. **Volokitina A.**, Loiko P., Pavlyuk A., Serres J.M., Slimi S., Salem E.B., Solé R.M., Baranov M., Kifle E., Aguiló M., Díaz F., Griebner U., Petrov V., Mateos X. Efficient laser operation in cleaved single-crystal plates of $\text{Yb}:\text{KY}(\text{MoO}_4)_2$: A novel molybdate compound // Fiber Lasers and Glass Photonics: Materials through Applications II – 2020, Vol. 11357

List of references

1. Klevtsov P. V. et al. Polymorphism of the double molybdates and tungstates of mono- and trivalent metals with the composition $\text{M}^+\text{R}^{3+}(\text{EO}_4)_2$ // Journal of Structural Chemistry – 1977, Vol 18, №. 3 pp. 339-355.

2. Liu J. et al. Efficient high-power laser operation of $\text{Yb}:\text{KLu}(\text{WO}_4)_2$ crystals cut along the principal optical axes // Optics letters – 2007, Vol 32, №. 14, pp. 2016-2018

3. Serres J. M. et al. Diode-pumped microchip $\text{Tm}:\text{KLu}(\text{WO}_4)_2$ laser with more than 3 W of output power // Optics letters – 2014, Vol 39, №. 14, pp. 4247-4250.

4. Loiko P. et al. In-band-pumped $\text{Ho}:\text{KLu}(\text{WO}_4)_2$ microchip laser with 84% slope efficiency // Optics letters – 2015, Vol 40, №. 3, pp. 344-347.

5. Griebner U. et al. Passively mode-locked $\text{Yb}:\text{KLu}(\text{WO}_4)_2$ oscillators // Optics Express – 2005, Vol 13, №. 9, pp. 3465-3470.

6. Pujol M. C. et al. Growth, optical characterization, and laser operation of a stoichiometric crystal $\text{KYb}(\text{WO}_4)_2$ // *Physical Review B* – 2002, Vol. 65, №. 16, pp. 165121.
7. Mateos X. et al. Crystal growth, spectroscopic studies and laser operation of Yb^{3+} -doped potassium lutetium tungstate // *Optical Materials* – 2006, Vol. 28, №. 5, pp. 519-523.
8. Lagatsky A. A. et al. Diode-pumped CW lasing of Yb:KYW and Yb:KGW // *Optics communications* – 1999, Vol. 165, №. 1-3, pp. 71-75.
9. Silvestre Ò. et al. Thermal properties of monoclinic $\text{KLu}(\text{WO}_4)_2$ as a promising solid state laser host // *Optics express* – 2008, Vol. 16, №. 7, pp. 5022-5034.
10. Petrov V. et al. Growth and properties of $\text{KLu}(\text{WO}_4)_2$, and novel ytterbium and thulium lasers based on this monoclinic crystalline host // *Laser & Photonics Reviews* – 2007, Vol. 1, №. 2, pp. 179-212.
11. Cascales C. et al. Structural, spectroscopic, and tunable laser properties of Yb^{3+} -doped $\text{NaGd}(\text{WO}_4)_2$ // *Physical Review B* – 2006, Vol. 74, №. 17, pp. 174114.
12. Voron'ko Y. K. et al. Growth and spectroscopic investigations of Yb^{3+} -doped $\text{NaGd}(\text{MoO}_4)_2$ and $\text{NaLa}(\text{MoO}_4)_2$ —new promising laser crystals // *Optical Materials* – 2006, Vol. 29, №. 2-3, pp. 246-252.
13. Wakefield G. et al. Luminescence properties of nanocrystalline $\text{Y}_2\text{O}_3:\text{Eu}$ // *Advanced Materials* – 2001, Vol. 13, №. 20, pp. 1557-1560.
14. Neeraj S. et al. Novel red phosphors for solid-state lighting: the system $\text{NaM}(\text{WO}_4)_{2-x}(\text{MoO}_4)_x:\text{Eu}^{3+}$ ($\text{M}=\text{Gd}, \text{Y}, \text{Bi}$) // *Chemical Physics Letters* – 2004, Vol 387, №. 1-3, pp. 2-6.
15. Wang Z. et al. Luminescence of $(\text{Li}_{0.333}\text{Na}_{0.334}\text{K}_{0.333})\text{Eu}(\text{MoO}_4)_2$ and its application in near UV InGaN-based light-emitting diode // *Chemical Physics Letters* – 2005, Vol 412, №. 4-6, pp. 313-316.
16. Bagaev S. N. et al. 25% $\text{Eu:KGd}(\text{WO}_4)_2$ laser crystal: spectroscopy and lasing on the $^5\text{D}_0 \rightarrow ^7\text{F}_4$ transition // *Quantum Electronics* – 2011, Vol. 41, №3, pp. 189-192.
17. Dashkevich V. I. et al. Red $\text{Eu, Yb:KY}(\text{WO}_4)_2$ laser at ~ 702 nm // *Laser Physics Letters* – 2015, Vol. 12, №. 8, pp. 085001.
18. Loiko P. A. et al. Spectroscopic characterization and pulsed laser operation of $\text{Eu}^{3+}:\text{KGd}(\text{WO}_4)_2$ crystal // *Laser Physics* – 2013, Vol. 23, №. 10, pp. 105811-1-7.

19. Kränkel C. et al. Out of the blue: semiconductor laser pumped visible rare-earth doped lasers // *Laser & photonics reviews* – 2016, Vol 10, №. 4, pp. 548-568.

20. Metz P. W. et al. Efficient continuous wave laser operation of Tb³⁺-doped fluoride crystals in the green and yellow spectral regions // *Laser & Photonics Reviews* – 2016, Vol 10, №. 2, pp. 335-344

21. Metz P. W. et al. Performance and wavelength tuning of green emitting terbium lasers // *Optics express* – 2017, Vol. 25, №. 5, pp. 5716-5724.

22. Hayakawa T. et al. Visible emission characteristics in Tb³⁺-doped fluorescent glasses under selective excitation // *Journal of luminescence* – 1996, Vol 68, №. 2-4, pp. 179-186.

23. Sun X. et al. Luminescence behavior of Tb³⁺ ions in transparent glass and glass-ceramics containing CaF₂ nanocrystals // *Journal of Luminescence* – 2009, Vol. 129, №. 8, pp. 773-777.

24. Hao Z. et al. Blue-green-emitting phosphor CaSc₂O₄:Tb³⁺: tunable luminescence manipulated by cross-relaxation // *Journal of The Electrochemical Society* – 2009, Vol 156, №. 3, pp. H193-H196.

25. Liao J. et al. Synthesis and luminescence properties of Tb³⁺:NaGd(WO₄)₂ novel green phosphors // *Journal of luminescence* – 2009, Vol. 129, №. 7, pp. 668-671.

26. Ju X. et al. Luminescence properties of ZnMoO₄: Tb³⁺ green phosphor prepared via co-precipitation // *Materials Letters* – 2011, Vol. 65, №. 17-18, pp. 2642-2644.

27. Kaminskii A. A. et al. Ribbon and sheet miniature crystal laser // *Quantum Electronics* – 1994, Vol. 24, №. 12, pp. 1029.

Введение

Низкосимметричные кристаллы, к которым относятся ромбические и моноклинные кристаллы вольфраматов и молибдатов [1], в последние годы выступают в качестве перспективных активных сред лазеров. К особенностям таких кристаллов можно отнести наличие значительной анизотропии спектрально-люминесцентных свойств в поляризованном свете. Анализ современного состояния исследований низкосимметричных кристаллов показал, что выбранные в диссертационной работе кристаллы вольфраматов и молибдатов, допированные ионами редкоземельных элементов, перспективны для получения в них эффективной лазерной генерации в видимой и ближней ИК области спектра [2-5]. К преимуществам таких кристаллов относится возможность достижения высоких значений концентраций ионов-активаторов без заметного тушения люминесценции [6], высокие поперечные сечения поглощения и вынужденного испускания в поляризованном свете [7,8], хорошие термооптические свойства [9]. Также такие кристаллы являются КР-активными.

Семейство выбранных для изучения кристаллов очень обширное, многие кристаллы уже достаточно хорошо изучены, при этом спектрально-люминесцентные свойства выбранных в диссертационной работе кристаллов, как и возможность использования их в качестве активной лазерной среды на момент постановки задачи и до сих пор остаются малоизученными и публикаций по данной тематике относительно немного.

Известно, что кристаллы, активированные ионами иттербия (Yb^{3+}) и тулия (Tm^{3+}), позволяют получить лазерную генерацию в ближнем инфракрасном диапазоне (в области длин волн ~ 1 мкм и ~ 2 мкм, соответственно) [10-12]. Лазеры ближнего ИК диапазона имеют

достаточно широкую область применений: молекулярная спектроскопия, медицина, дальнометрия, системы связи и контроля и т.д. Излучение ИК диапазона характеризуется малыми потерями при прохождении через атмосферу, а ионы Tm^{3+} люминесцируют в так называемой условно-безопасной для сетчатки глаза области ИК диапазона.

Кристаллы, содержащие ионы европия (Eu^{3+}) [13-18] и тербия (Tb^{3+}) [19-26], люминесцируют в видимой области спектра. Они могут найти применение в качестве люминофоров [13-15, 22-26], а также они представляют большой интерес для использования в качестве активных лазерных сред [16-21], генерирующих в видимом диапазоне.

Следует отметить, что в последние годы одним из немаловажных направлений в разработке современных устройств во всех сферах является уменьшение всех компонентов, то есть миниатюризация. С этой точки зрения большой интерес вызывают компактные лазеры, обладающие микрочип-конфигурацией резонатора. Они обладают достаточно простой конструкцией, однако для эффективной генерации микрочип-лазеров требуется очень тщательный выбор активной среды. Подходящими средами являются среды, которые характеризуются положительной термической линзой, позволяют достигать высоких концентраций ионов-активаторов и обладают большими значениями поперечных сечений поглощения, вынужденного испускания и усиления. Поэтому в настоящее время большой интерес вызывает исследование спектрально-люминесцентных свойств кристаллов двойных молибдатов, слоистая структура которых позволяет создавать эффективные активные среды лазера толщиной до нескольких десятков микрометров [27], а также проведение экспериментов, подтверждающих возможность получения эффективной лазерной

генерации на тонких пластинках и плёнках, изготовленных из таких кристаллов.

Таким образом, комплексное исследование спектрально-люминесцентных свойств новых кристаллов, включающее как изучение анизотропии спектрально-люминесцентных свойств, определение основных спектроскопических характеристик и установление возможности использования таких кристаллов в качестве активной среды лазера, так и проведение экспериментов по получению лазерной генерации на этих кристаллах, в том числе на тонких кристаллических пластинках и плёнках, представляет большой интерес и является актуальной задачей.

ГЛАВА 1. Анизотропные кристаллы вольфраматов и молибдатов – перспективные лазерные среды (литературный обзор)

1.1 Спектроскопия ионов редкоземельных элементов

В рамках настоящей работы было проведено комплексное исследование кристаллов ромбических и моноклинных вольфраматов и молибдатов, допированных трёхвалентными ионами редкоземельных элементов (RE^{3+}). Люминесцентные свойства таких кристаллов определяются главным образом люминесцентными характеристиками ионов RE^{3+} . Поэтому для детального анализа спектрально-люминесцентных свойств кристаллов с ионами RE^{3+} , важно понимать спектральные характеристики самих ионов-активаторов.

К редкоземельным элементам относится группа из 17 химических элементов, в которую входят скандий (Sc), иттрий (Y), лантан (La) и лантаноиды (церий (Ce), празеодим (Pr), неодим (Nd), прометий (Pm), самарий (Sm), европий (Eu), гадолиний (Gd), тербий (Tb), диспрозий (Dy), гольмий (Ho), эрбий (Er), тулий (Tm), иттербий (Yb), лютеций (Lu)).

Все эти элементы проявляют сходные химические свойства. Это объясняется практически одинаковым заполнением электронных оболочек атомов, а именно: структура двух внешних электронных оболочек (5s и 5p) не изменяется с увеличением заряда, а электроны заполняют внутреннюю глубоколежащую электронную оболочку 4f-орбиталь. Неспаренные электроны, находящиеся на этой оболочке, не участвуют в образовании химических связей и наделяют редкоземельные ионы люминесцентными и магнитными свойствами. Таким образом спектры люминесценции ионов RE^{3+} обусловлены электронными 4f-4f переходами внутри незаполненной оболочки. На спектральные характеристики ионов RE^{3+} в значительной степени влияет экранирование оптически-активных электронов на 4f оболочках

внешними полностью заполненными электронными оболочками. Электронные переходы в спектрах поглощения и люминесценции обычно состоят из узких линий [28]. При этом 4f-электроны практически не чувствительны к локальному окружению иона, то есть под влиянием кристаллического поля не происходит сильного смещения максимумов полос поглощения или люминесценции при расположении иона в узле кристаллической решётки.

Люминесценция RE^{3+} ионов может наблюдаться в ближней УФ-, видимой, ближней ИК и ИК областях спектра. Она характеризуется высокой чистотой цвета, что делает RE^{3+} ионы привлекательными для использования в лазерных кристаллах [1]. При этом каждый RE^{3+} ион обладает своим характерным спектром поглощения и люминесценции и обладает уникальными свойствами.

В настоящей работе в качестве ионов-активаторов были выбраны ионы европия (Eu^{3+}), тербия (Tb^{3+}), тулия (Tm^{3+}) и иттербия (Yb^{3+}). Ниже будут рассмотрены спектроскопические особенности каждого из этих ионов.

1.1.1 Ионы европия Eu^{3+}

Трёхвалентные ионы европия широко распространены в спектроскопических исследованиях. Они характеризуется интенсивной красной (~610 нм) люминесценцией, связанной с доминирующим в спектре энергетическим переходом ${}^5D_0 \rightarrow {}^4F_2$. Спектр ионов Eu^{3+} относительно легко интерпретировать. Особенностью структуры энергетических уровней ионов Eu^{3+} является наличие метастабильного состояния 5D_0 , отделённого от более низколежащих энергетических состояний ${}^4F_0-{}^4F_6$, где $J = 0 \dots 6$, энергетическим зазором ~12000 cm^{-1} [13, 29]. Такая величина энергетического зазора обуславливает слабую безызлучательную релаксацию. Благодаря этому наблюдается высокая

квантовая эффективность ионов Eu^{3+} . На рисунке 1.1.1 приведена схема энергетических уровней ионов Eu^{3+} , построенная по результатам исследования люминесценции в кристалле калий-иттриевого двойного вольфрамата.

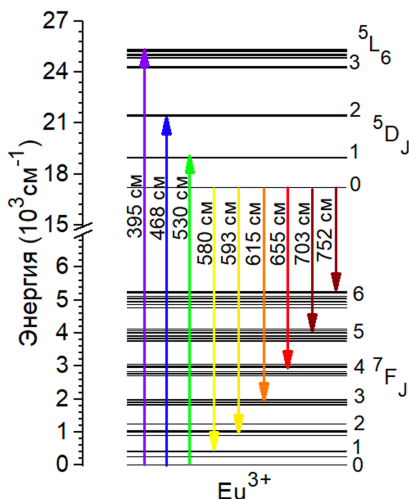


Рисунок 1.1.1 – Схема энергетических уровней ионов европия. Цветными стрелками обозначены поглощательные и излучательные переходы.

Как уже было отмечено, кристаллическое окружение ионов RE^{3+} приводит лишь к небольшому смещению максимума поглощения или люминесценции. Однако, благодаря своим люминесцентным свойствам ионы Eu^{3+} известны в качестве структурных проб [30-33]. Их люминесценция чувствительна к симметрии локального окружения ионов. В частности, электрический дипольный (ED) переход $5D_0 \rightarrow 4F_2$ является очень чувствительным переходом, изменение интенсивности и расщепления этого перехода связаны с изменениями в локальном окружении. Данный переход не наблюдается в средах с центром инверсии или в средах с высокой локальной симметрией, а в средах без центра инверсии этот переход доминирует над магнитным дипольным (MD) переходом $5D_0 \rightarrow 4F_1$.

1.1.2 Ионы тербия Tb³⁺

Схема энергетических уровней ионов тербия Tb³⁺ сходна со схемой энергетических уровней ионов Eu³⁺. Ионы Tb³⁺ также характеризуются высоко лежащим метастабильным состоянием ⁵D₄ (~20500 см⁻¹) и набором низколежащих состояний ⁷F_J (J = 0...6) [29] (рисунок 1.2). Благодаря энергетическим переходам ⁵D₄ → ⁷F_J, в видимой области спектра наблюдается излучение на нескольких длинах волн, попадающих в синий, зеленый, желтый и красный спектральные диапазоны [20], а структура высоко лежащих возбужденных состояний ионов Tb³⁺ позволяет эффективно возбуждать эти ионы УФ излучением. Наиболее интенсивным переходом в спектре люминесценции является переход ⁵D₄ → ⁷F₅ на длине волны излучения ~545 нм, следовательно, при возбуждении УФ излучением можно наблюдать интенсивную зелёную люминесценцию ионов Tb³⁺ [25,26,33].

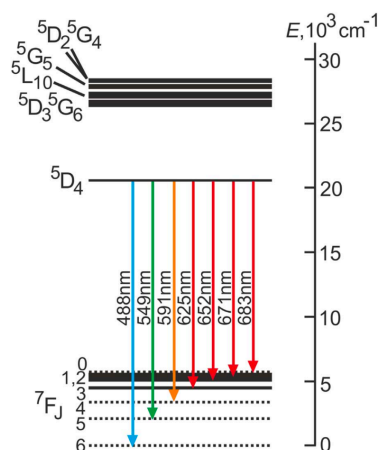


Рисунок 1.1.2 – Схема энергетических уровней ионов тербия. Цветными стрелками обозначены излучательные переходы с уровня ⁵D₄ в кристалле KYW

Уровень ⁵D₄ является долгоживущим (время жизни: от сотен мкс до нескольких мс) [20], и соответствующий квантовый выход

люминесценции также как и для ионов Eu^{3+} может быть высоким из-за слабых безызлучательных процессов.

1.1.3 Ионы тулия Tm^{3+}

Характерной особенностью ионов Tm^{3+} является интенсивная люминесценция в ближней ИК области спектра (~ 2 мкм), возникающая за счёт энергетического перехода ${}^3\text{F}_4 \rightarrow {}^3\text{H}_6$ [10,34-36]. Этот спектральный диапазон относится к условно-безопасному для глаз. Условно-безопасной считается такая спектральная область, в которой роговица и хрусталик глаза обладают высоким коэффициентом поглощения, а значит лишь малая доля лазерного излучения в этом диапазоне достигает сетчатки глаза.

В кристаллических матрицах можно достигнуть высоких уровней концентрации ионов Tm^{3+} . Для верхнего лазерного уровня (${}^3\text{F}_4$) ионов Tm^{3+} характерна слабая безызлучательная релаксация и КР-активность.

1.1.3 Ионы иттербия Yb^{3+}

Ионы Yb^{3+} обладают простой схемой энергетических уровней, исключая нежелательные процессы, такие как ап-конверсионный перенос энергии или поглощение в возбуждённом состоянии. Они люминесцируют в ближней ИК области спектра (~ 1 мкм), которая соответствует энергетическому переходу с уровня ${}^2\text{F}_{5/2}$ на уровень ${}^2\text{F}_{7/2}$. В низкосимметричных и разупорядоченных кристаллах наблюдается уширение полос поглощения и люминесценции, что может являться дополнительным преимуществом ионов Yb^{3+} . Материалы, допированные Yb^{3+} , могут накачиваться мощными лазерными диодами, например InGaAs, излучающими на $\sim 0,98$ мкм.

На сегодняшний день было продемонстрировано достаточно много успешных экспериментов по получению эффективной лазерной

генерации на длине волны ~ 1 мкм на кристаллах, активированных ионами Yb^{3+} [2, 5, 12, 37-41].

1.2 Расчет спектроскопических параметров и поперечных сечений переходов

1.2.1 Теория Джадда-Офельта

Для описания интенсивности $f-f$ электронных переходов в спектрах редкоземельных ионов широко применяется теория Джадда-Офельта. Она была независимо предложена в 1962 году Брайаном Р. Джаддом [42] из Калифорнийского университета в Беркли и докторантом Джорджем С. Офельтом [43] из Университета Джона Хопкинса. Благодаря этой теории были изучены схемы уровней многих редкоземельных ионов, а для ионов RE^{3+} , помещённых в кристаллическую решетку, было объяснено возникающее в спектрах поглощения и люминесценции расщепление уровней.

В соответствии с теорией Джадда-Офельта спектроскопические характеристики редкоземельных ионов, к которым относятся силы осцилляторов, параметры интенсивности, вероятности спонтанных переходов, коэффициенты ветвления люминесценции, а также радиационные времена жизни, взаимосвязаны с составом кристаллической матрицы и определяются структурой окружения ионов RE^{3+} и характером взаимодействия ионов с окружающим полем.

Силы осцилляторов в поглощательных переходах для ионов RE^{3+} рассчитываются измеренных спектров поглощения как [44]:

$$\langle f_{exp}^{\Sigma} \rangle(JJ') = \frac{m_e c^2}{\pi e^2 N_{\text{RE}^{3+}} \langle \lambda \rangle^2} \langle \Gamma(JJ') \rangle, \quad (1)$$

где m_e и e – масса и заряд электрона соответственно, c – скорость света, N_{RE} – концентрация ионов, $\langle \Gamma(JJ') \rangle$ – интегральный коэффициент поглощения, а $\langle \lambda \rangle$ – «центр тяжести» полосы поглощения. В теории J-O

все значения для трёх поляризаций усредняются, например, $\langle f_{\text{exp}}^E \rangle = 1/3(f_p^E + f_m^E + f_g^E)$.

Также силы осциллятора в поглощении можно теоретически рассчитать как [44]:

$$\langle f_{\text{calc}}^{\Sigma} \rangle(JJ') = \frac{8}{3h(2J'+1)\langle \lambda \rangle} \frac{(\langle n \rangle^2 + 2)^2}{9\langle n \rangle} \langle S_{\text{calc}}^{\text{ED}} \rangle(JJ') + \langle f_{\text{calc}}^{\text{MD}} \rangle(JJ'). \quad (2)$$

Здесь h – постоянная Планка, а $\langle n \rangle$ – средний показатель преломления, $\langle S_{\text{calc}}^{\text{ED}} \rangle$ – сила осциллятора ED перехода.

Теория J-O описывает электрические дипольные (ED) переходы. Вклад магнитных дипольных (MD) переходов с $J-J' = 0, \pm 1$ рассчитывается отдельно.

В приближении промежуточного конфигурационного взаимодействия (ICI) силы линии ED переходов приведены в [45,46]:

$$\langle S_{\text{calc}}^{\text{ED}} \rangle(JJ') = \sum_{k=2,4,6} U^{(k)} \tilde{\Omega}_k, \quad (3)$$

где:

$$\tilde{\Omega}_k = \Omega_k [1 + 2R_k (E_J + E_{J'} - 2E_f^0)], \quad (4a)$$

$$U^{(k)} = \langle (4f^n)SLJ || U^k || (4f^n)S'L'J' \rangle^2. \quad (4b)$$

Здесь $U^{(k)}$ – матричные элементы неприводимых тензорных операторов U^k для переходов в поглощении [47], R_k ($k = 2, 4, 6$) – параметры, представляющие конфигурационное взаимодействие. В модели промежуточного конфигурационного взаимодействия обобщенные параметры интенсивности $\tilde{\Omega}_k$ – линейные функции энергий двух мультиплетов (E_J и $E_{J'}$), участвующих в переходе, а E_f^0 – средняя энергия конфигурации $4f_n$. В модели промежуточного конфигурационного взаимодействия имеется 6 свободных параметров, а именно Ω_k и R_k ($k = 2, 4, 6$). Если в конфигурационное взаимодействие входит только возбужденная конфигурация противоположной

четности $4f^{n-1}5d^1$, то $R_2 = R_4 = R_6 = \alpha \approx 1/(2\Delta)$ и уравнение (4a) упрощается до [45]:

$$\tilde{\Omega}_k = \Omega_k [1 + 2\alpha(E_J + E_{J'} - 2E_f^0)]. \quad (5)$$

Уравнение (3) с параметрами интенсивности, заданными уравнением (5), упоминается как модифицированная теория Джадда-Офельта. В этом случае существует 4 свободных параметра, а именно Ω_2 , Ω_4 , Ω_6 и α . Здесь Δ имеет значение энергии возбужденной конфигурации $4f^{n-1}5d^1$. Для случая вышележащей возбужденной конфигурации противоположной четности ($\Delta \rightarrow \infty$):

$$\langle S_{\text{calc}}^{\text{ED}} \rangle(JJ') = \sum_{k=2,4,6} U^{(k)} \Omega_k. \quad (6)$$

Этот случай соответствует теории Джадда-Офельта. В этом случае есть три свободных параметра: Ω_2 , Ω_4 и Ω_6 .

Вероятности спонтанных излучательных переходов вычисляются по силам линии [44]:

$$A_{\Sigma}^{\text{calc}}(JJ') = \frac{64\pi^4 e^2}{3h(2J'+1)\langle \lambda \rangle^3} n \left(\frac{n^2 + 2}{3} \right)^2 S_{\text{ED}}^{\text{calc}}(JJ') + A_{\text{MD}}(JJ'). \quad (7)$$

Средние значения длин волн $\langle \lambda \rangle$ для каждого перехода $J \rightarrow J'$ определяются по барицентрам спектров поглощения и люминесценции. Из значений A для отдельных излучательных переходов $J \rightarrow J'$ вычисляется полная вероятность $A_{\text{tot}}^{\text{calc}}$, радиационные времена жизни возбужденных состояний τ_{rad} и коэффициенты ветвления люминесценции для отдельных излучательных переходов $B(JJ')$:

$$\tau_{\text{rad}} = \frac{1}{A_{\text{tot}}^{\text{calc}}}, \quad \text{где} \quad A_{\text{tot}}^{\text{calc}} = \sum_{J'} A_{\Sigma}^{\text{calc}}(JJ'), \quad (8a)$$

$$B(JJ') = \frac{A_{\Sigma}^{\text{calc}}(JJ')}{\sum_{J'} A_{\Sigma}^{\text{calc}}(JJ')} \quad (8b)$$

1.2.2 Определение поперечных сечений поглощения, вынужденного испускания и усиления

В настоящей работе исследуются оптически двухосные кристаллы, следовательно, они имеют три основных показателя преломления $n_p < n_m < n_g$. Спектроскопические характеристики таких кристаллов могут быть охарактеризованы спектрами, зарегистрированными в поляризованном свете так, чтобы поляризация света была параллельна осям оптической индикатрисы ($\mathbf{E} \parallel N_p$, $\mathbf{E} \parallel N_m$, $\mathbf{E} \parallel N_g$) [10]. В таком случае поперечные сечения поглощения (σ_{abs}) вычисляются следующим образом:

$$\sigma_{\text{abs}} = \alpha / N_{\text{RE}^{3+}} \quad (9)$$

где α – коэффициент поглощения, $N_{\text{RE}^{3+}}$ – концентрация ионов RE^{3+} .

Спектры сечений вынужденного испускания вычисляются по формуле Фюхтбауэра-Ладенбурга (ФЛ) [48], либо по интегральному методу соответствия (Reciprocity Method) [49].

Для расчёта спектров поперечных сечений поляризованного вынужденного испускания (σ_{SE}) по методу Фюхтбауэра-Ладенбурга используется следующая формула [48]:

$$\sigma_{\text{SE}}^i(\lambda) = \frac{\lambda^5}{8\pi n_i^2 \tau_{\text{rad}} c} \frac{1}{3} \frac{W_i(\lambda) B(JJ')}{\sum_{i=p,m,g} \int \lambda W_i(\lambda) d\lambda} \quad (10)$$

Здесь $W_i(\lambda)$ – измеренная спектральная плотность мощности люминесценции для i -й поляризации, $i = p, m, g$, n_i – соответствующий показатель преломления, τ_{rad} – радиационное время жизни возбуждённого состояния, интегрирование выполняется в пределах полосы излучения, соответствующей конкретному переходу.

При использовании формулы Фюхтбауэра-Ладенбурга хорошо использовать тонкие образцы, чтобы минимизировать влияние

перепоглощения излучения, которое может исказить истинный спектр люминесценции.

В длинноволновой области спектра поглощение очень мало и могут возникать ошибки при определении сечений вынужденного испускания. Чтобы минимизировать ошибки можно использовать оптически более плотные образцы, что не всегда бывает возможным.

Для расчёта спектров поперечных сечений поляризованного вынужденного испускания (σ_{SE}) по интегральному методу соответствия используется следующая формула [50,51]:

$$\sigma_{SE}^i(\lambda) = \sigma_{abs}^i(\lambda) \frac{Z_1}{Z_2} \exp\left(-\frac{(hc/\lambda) - E_{ZPL}}{kT}\right), \quad (11)$$

где h – постоянная Планка, (hc/λ) – энергия фотона (в см^{-1}), k – постоянная Больцмана, T – температура кристалла (комнатная температура), E_{ZPL} – энергия бесфононного перехода, а Z_m – статистические суммы нижнего ($m = 1$) и верхнего ($m = 2$) многообразий:

$$Z_m = \sum_k g_k^m \exp(-E_k^m / kT). \quad (12)$$

Здесь $g_k^m = 1$ – это вырождение подуровня с номером k и энергией E_k^m , отсчитываемой от самого нижнего подуровня каждого мультиплета.

Зачастую методы соответствия и метод Фюхтбауэра-Ладенбурга дополняют друг друга и используются вместе для расчёта достоверных спектров поперечных сечений вынужденного испускания.

1.2.3 Определение времени жизни люминесценции

Для регистрации кривых затухания люминесценции использовались тонкие образцы, чтобы избежать перепоглощения люминесценции. Полученные кривые аппроксимировались

моноэкспоненциальным законом $I_{lum}(t) = I_0 \exp(-t/\tau_{lum})$, из которого определялось время затухания τ_{lum} .

Квантовая эффективность люминесценции определялась как отношение времени затухания люминесценции к радиационному времени жизни люминесценции: $\eta_q = \tau_{lum}/\tau_{rad}$ (13).

1.3 Низкосимметричные кристаллы вольфрамов и молибдатов как активные среды лазеров ИК диапазона

Кристаллы двойных молибдатов и двойных вольфрамов представляют большой класс оксидных матриц, подходящих для допирования трёхвалентными ионами редких земель (RE^{3+}). Общая химическая формула таких кристаллов имеет вид $RE^{3+}:A^+Ln(XO_4)_2$, где A = одновалентный катион K, Li, Na, Rb или Cs; Ln – катионы Y^{3+} , Lu^{3+} или Gd^{3+} и т.д., X – Mo или W, а RE^{3+} – ионы-активаторы. Таким образом эти семейства кристаллов представляют большое множество кристаллических систем [1]. Такие кристаллы известны достаточно долгое время, но некоторые из них до сих пор остаются мало изученными, в том числе с точки зрения применения в качестве активных лазерных сред. В последние годы достаточно много исследований было посвящено моноклинным калиевым двойным вольфраматам $KRE(WO_4)_2$ [10], тетрагональным натриевым двойным молибдатам и двойным вольфраматам $NaRE(W/MoO_4)_2$ [52]. Эти кристаллы оказались очень привлекательными для эффективных непрерывных лазеров [2-4] и для лазеров с синхронизацией мод [5], излучающих в ближнем ИК-диапазоне спектра на основе ионов Yb^{3+} , Tm^{3+} или Ho^{3+} .

К малоизученным кристаллам этих семейств относятся выбранные в работе ромбические кристаллы двойных молибдатов и

моноклинные кристаллы двойных вольфраматов и цинковых молибдатов.

1.3.1 Кристаллы молибдатов

В настоящей работе исследуются кристаллы калий-иттриевого двойного молибдата и цезий-гадолиниевого двойного молибдата, с общей химической формулой $RE^{3+}:ALn(MoO_4)_2$, где $A = K$ или Cs ; $Ln - Y^{3+}$, или Gd^{3+} , а RE^{3+} – ионы редких земель. Ранние исследования подобных кристаллов были сосредоточены на структуре [53]. Позднее были проведены исследования спектроскопии [27, 54] и вынужденного лазерного излучения [55,56] ионов Nd в кристалле $KY(MoO_4)_2$.

Было показано, что кристаллы двойных молибдатов обладают слоистой структурой с совершенной спайностью [53]. Благодаря этим структурным особенностям в таких кристаллах наблюдается идеальный скол вдоль одной из кристаллографических осей. С одной стороны, это в некоторой степени ограничивает применение таких кристаллов в качестве активных лазерных сред, однако они оказались привлекательны для изготовления тонкопленочных лазеров [27].

1.3.2 Кристаллы вольфраматов

В настоящее время большой научный интерес также вызывает исследование кристаллов двойных вольфраматов, имеющих общую химическую формулу $RE:KLn(WO_4)_2$, где $Ln - Y^{3+}$, Yb^{3+} или Lu^{3+} , а $RE -$ ионы редких земель. С точки зрения лазерных применений такие кристаллы обладают рядом преимуществ по сравнению с другими оксидными кристаллическими матрицами [10, 17-19, 57]. Они имеют высокие показатели механической прочности, позволяют добиться высоких концентраций активных ионов, в кристаллах наблюдается слабая безызлучательная релаксация из возбуждённых состояний

ионов RE^{3+} , в них достигаются более высокие пиковые значения поперечных сечений поглощения и вынужденного испускания, а также высокая анизотропия спектрально-люминесцентных свойств ионов-активаторов, что необходимо для эффективного возбуждения лазерной генерации [10, 17, 18].

ГЛАВА 2. Материалы и методы эксперимента

2.1 Объекты исследования

В качестве объектов исследования в настоящей диссертационной работе были выбраны монокристаллы вольфраматов и молибдатов, активированные трёхвалентными ионами редких земель. Были исследованы кристаллы двойного калий-иттриевого молибдата и двойного цезий-гадолиниевого молибдата с ионами европия $Eu^{3+}:KY(MoO_4)_2$ и $Eu^{3+}:CsGd(MoO_4)_2$, кристалл двойного калий-иттриевого вольфрамата $Eu^{3+}:KY(WO_4)_2$, кристалл двойного калий-лютециевого вольфрамата с ионами тербия $Tb^{3+}:KLu(WO_4)_2$, кристалл двойного калий-иттриевого молибдата с ионами тулия $Tm^{3+}:KY(WO_4)_2$, кристалл двойного калий-иттриевого молибдата с ионами иттербия $Yb^{3+}:KY(WO_4)_2$ и кристалл цинкового вольфрамата, соактивированный ионами иттербия и лития $Yb^{3+},Li^+:ZnWO_4$.

2.2 Краткое описание методов выращивания монокристаллов

Для исследований спектрально-люминесцентных свойств были использованы кристаллы, предоставленные Институтом неорганической химии имени А.В. Николаева, СО РАН, Россия, Новосибирск, а также в Университетом Ровира и Вирхилий, Испания, Таррагона.

Кристаллы двойных вольфраматов были выращены раствор-расплавным методом с использованием дивольфрамата калия ($K_2W_2O_7$) в качестве растворителя. Данный метод подробно описан в [18, 19]. В качестве исходных материалов были выбраны оксиды K_2CO_3 , Ln_2O_3 ($Ln = Y^{3+}$ или Lu^{3+}), RE_2O_3 и WO_3 чистотой $>99.9\%$. Для начала зарождения и роста кристалла использовалась заготовленная затравка из нелегированного $KLn(WO_4)_2$, которая была ориентирована вдоль кристаллографической оси [010]. Структура выращенных кристаллов подтверждалась методом порошкового рентгенофазового анализа.

Кристаллы семейства двойных молибдатов химически стабильны и обладают относительно низкой температурой плавления (~ 970 C), не проявляя никаких полиморфных превращений ниже точки плавления. Такие кристаллы могут быть выращены методом Чохральского. Подробный процесс роста кристалла описан в статье [92]. В качестве исходных материалов были взяты RE_2O_3 , (чистота: 4N), Y_2O_3 (5N), MoO_3 (4N) и K_2CO_3 (5N), они были тщательно измельчены, перемешаны и помещены в платиновый тигель (объем: 140 см^3 , диаметр: 50 мм). Тримолибдат калия ($K_2Mo_3O_{10}$) добавляли для предотвращения частичной диссоциации расплава и стабилизации процесса роста. Тигель нагревался до 1050°C на воздухе и выдерживался при этой температуре в течение 2–3 ч для гомогенизации расплава. Затем расплав охлаждался до начальной температуры роста кристалла ($\sim 960^\circ\text{C}$). Затравка из нелегированного кристалла $KYMo$ была ориентирована так, чтобы её кристаллографическая ось [001] была перпендикулярна расплаву. Затравка вращалась со скоростью ~ 20 оборотов в минуту; скорость вытягивания составляла 1-2 мм/ч; скорость охлаждения расплава составляла $\sim 2^\circ\text{C}/\text{сут}$. Скорость роста кристалла составляла 5-10 г/сут. После завершения процесса роста кристалл вынимали из расплава и медленно охлаждали до комнатной

температуры. Отжиг после роста кристалла не проводился. Выращенный кристалл имел идеальный скол по плоскости (100).

2.3 Методы исследования структуры кристаллов

2.2.1 Исследование методом рентгенофазового анализа (РФА).

Для записи рентгенограмм образцы кристаллов были тщательно измельчены. Спектры рентгенограмм были записаны в НИТИОМ ВНЦ "ГОИ им. С.И. Вавилова" и использованием дифрактометра Shimadzu XRD-6000 с использованием $\text{CuK}\alpha$ -излучения и Ni фильтра, а также в Университете Rovira i Virgili в Испании с помощью дифрактометра Siemens D-5000 с использованием $\text{CuK}\alpha$ -излучения (1.5406 Å).

2.2.2 Сканирующая электронная микроскопия.

Исследование сколотой поверхности и боковой поверхности кристаллических пластинок проводились методом сканирующей электронной микроскопии (SEM) на микроскопе MERLIN (Carl Zeiss) в университете ИТМО и в университете Rovira i Virgili в Испании. Кристаллические пластины были подготовлены методом простого механического скола, с использованием острого лезвия, расположенного перпендикулярного направлению роста кристалла. Для получения изображений боковой поверхности пластинка была аккуратно разломана вдоль направления роста кристалла.

2.2.2 Исследование методом комбинационного рассеяния света.

Комбинационное рассеяние (КР) света – это неупругое рассеяние света, при котором частота рассеянного излучения изменяется на частоту фононов, то есть на частоту колебательного движения атомов кристаллической решетки. При увеличении частоты КР наблюдается антистоксово рассеяние, при уменьшении – стоксово. Число и положение полос в спектре КР определяется структурой и составом вещества.

Спектры КР исследуемых кристаллов были записаны при комнатной температуре на спектрометре микро-КР InVia Renishaw (Великобритания), позволяющем проводить измерения в геометрии обратного рассеяния света. Данный прибор оборудован 50-кратным объективом фирмы Leica, который одновременно фокусирует лазерное излучение на образце и собирает рассеянное излучение. Для записи спектров КР в среднем проводилось по 30 накоплений сигнала. Спектры КР возбуждались излучением Ar^+ лазера на длинах волн 457, 488, 514 или 633 нм. В зависимости от спектров люминесценции кристалла выбиралась длина волны возбуждающего излучения, с минимальным вкладом люминесценции в спектр КР.

2.4 Методы исследования спектрально-люминесцентных свойств

2.4.1 Поглощение

Спектры поглощения в ультрафиолетовой (УФ), видимой и ближней инфракрасной (ИК) области спектра (0.3 – 2 мкм) были записаны на спектрофотометре Shimadzu в Университете ИТМО или Varian CARY-5000 в университете Rovira i Virgili в Испании. Спектральная ширина щели (SBW) при измерениях составляла 0.01 нм. Для регистрации спектров поглощения в ИК области использовался FTIR спектрофотометр Bruker Tensor 27 со спектральным разрешением 1 см^{-1} . Для записи спектров поглощения в поляризованном свете в спектрофотометр дополнительно устанавливалась поляризационная призма Глана-Тейлора, преобразующая излучение с произвольной поляризацией в линейно-поляризованное [58].

2.4.2 Люминесценция

Спектры люминесценции измерялись на различном оборудовании:

1. На спектрофлуориметре Cary Eclipse (Aligent).

2. На оптических анализаторах спектра (OSA Hamamatsu, AQ6373, OSA Yokogawa, AQ6315-E.). В качестве источника возбуждающего излучения в этом случае был использован настраиваемый непрерывный титан-сапфировый лазер, а также 0.96-0.98 мкм InGaAs лазерные диоды. Спектральное разрешение составляло 0.1 нм. Для регистрации спектров в поляризованном свете дополнительно использовалась призма Глана-Тейлора.

3. Некоторые спектры люминесценции были зарегистрированы на спектрометре микро-КР InVia Renishaw. Возбуждающее излучение спектрометра имеет линейную поляризацию, также спектрометр можно дополнительно оборудовать поляризатором и пластинкой $\lambda/2$, для записи поляризованных спектров люминесценции. Таким образом можно проводить измерения спектров люминесценции, зная поляризацию возбуждающего и излучаемого света. Обозначения такой поляризации были приняты в соответствии с обозначениями Порто для спектроскопии комбинационного рассеяния света. Конфокальный микроскоп оборудован объективом x50 и решеткой 1800 л/мм. Длина волны возбуждения λ_{exc} составляла 458 нм или 488 нм, а полученные спектры при необходимости объединялись для охвата спектрального диапазона 0.48-0.7 мкм. Спектральное разрешение составляло $\sim 1 \text{ см}^{-1}$. Спектры люминесценции были калиброваны на спектральную чувствительность прибора.

2.4.3. Времена жизни люминесценции

Для исследований кинетики затухания люминесценции использовался флуоресцентный спектрометр Cary Eclipse (Aligent). Длина волны возбуждения λ_{exc} определялась из спектров поглощения. Затухание контролировалось из интересующего возбуждённого энергетического состояния, точное значение которого определялось по

спектрам люминесценции. Полученные кривые затухания люминесценции строились в полулогарифмическом масштабе и аппроксимировались моноэкспоненциальным законом $I_{lum}(t) = I_0 \exp(-t/\tau_{lum})$, из которого определялось время затухания τ_{lum} .

2.4.4 Низкотемпературная спектроскопия

Для записи спектров поглощения при низкой температуре в спектрофотометр Varian CARY-5000 дополнительно помещался криостат Oxford Instruments Ltd., работающий на жидком гелии с размещением образца в вакууме. Криостат характеризуется широким диапазоном температур и позволяет понижать температуру от 300 К до 6 К с необходимым шагом.

Указанный криостат использовался так же и для регистрации спектров люминесценции при низких температурах.

2.5 Методика проведения лазерных экспериментов

Процесс подготовки кристаллов вольфрамов к лазерным экспериментам заключался в изготовлении прямоугольного образца и полировке входных и выходных граней кристалла, при необходимости на грани наносилось покрытие.

Образцы тонких кристаллических плёнок и пластинок из кристаллов двойных молибдатов, обладающих слоистой структурой, были получены методом простого механического скола. Такие образцы имели идеальную поверхность скола и не требовали дальнейшей обработки входной и выходной поверхности.

Для исследования генерационных свойств для каждого отдельного кристалла собиралась своя установка. Схематически лазерная установка изображена на рисунке 2.4.1. Исследуемый образец кристалла помещается в компактный оптический резонатор, образованный набором входного (РМ) и выходных (ОС) зеркал. В

качестве входного зеркала резонатора в экспериментах было выбрано плоское зеркало с высоким коэффициентом пропускания на длине волны накачки и с высоким коэффициентом отражения на длине волны лазерной генерации. В качестве выходного зеркала резонатора выбиралось плоское или вогнутое зеркало с коэффициентом пропускания 0.1% – 10% на длине волны генерации лазера. В микрочип-конфигурации резонатора входное и выходное зеркало были плоскими и аккуратно прижимались к лазерному образцу так, что геометрическая длина оптического резонатора была равна толщине образца.

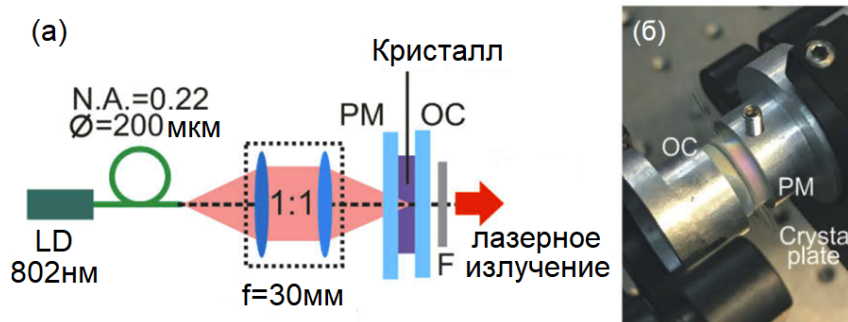


Рисунок 2.4.1 – (а) Схема лазерной установки в микрочип-конфигурации с диодной накачкой: LD – лазерный диод, PM – зеркало накачки, OC – выходное зеркало, F – отсекающий фильтр; (б) фотография резонатора лазера на кристаллической пластинке.

Накачка лазерного элемента осуществлялась с помощью оптоволоконного лазерного диода. Луч накачки коллимировался и фокусировался в лазерный элемент с помощью линзы с фокусным расстоянием $f = 30$ мм. В результате диаметр пятна накачки составлял $2W_p = 200 \pm 10$ мкм. Для отделения остаточного излучения накачки от лазерного излучения использовался фильтр (FEL1000, Thorlabs).

ГЛАВА 3. Анизотропия спектрально-люминесцентных свойств ионов Eu^{3+} и Tb^{3+} в кристаллах $\text{AM}(\text{XO}_4)_2$ ($\text{A} = \text{K}, \text{Cs}$; $\text{M} = \text{Y}, \text{Gd}$; $\text{X} = \text{W}, \text{Mo}$)

В настоящей главе приводятся результаты исследования спектрально-люминесцентных свойств кристаллов, активированных ионами Eu^{3+} и Tb^{3+} . Общая химическая формула кристаллов может быть записана в виде $\text{AM}(\text{XO}_4)_2$ ($\text{A} = \text{K}, \text{Cs}$; $\text{M} = \text{Y}, \text{Lu}, \text{Gd}$; $\text{X} = \text{W}, \text{Mo}$). Были исследованы кристаллы двойного калий-иттриевого молибдата и двойного цезий-гадолиниевого молибдата с ионами европия $\text{Eu}^{3+}:\text{KY}(\text{MoO}_4)_2$ и $\text{Eu}^{3+}:\text{CsGd}(\text{MoO}_4)_2$, кристалл двойного калий-иттриевого вольфрамата с ионами европия $\text{Eu}^{3+}:\text{KY}(\text{WO}_4)_2$ и кристалл двойного калий-лутециевого вольфрамата с ионами тербия $\text{Tb}^{3+}:\text{KLu}(\text{WO}_4)_2$.

3.1 Структура кристаллов (Рентгенофазовый анализ)

Фазовая чистота и структура выращенных кристаллов $\text{Eu}^{3+}:\text{KY}(\text{MoO}_4)_2$ были подтверждены методом порошкового рентгенофазового анализа (XRD), см. рисунок 3.1.1. Кристалл $\text{Eu}^{3+}:\text{KY}(\text{MoO}_4)_2$ ромбический, он относится к пространственной группе $Pbna - D^{14}_{2h}$, № 60, точечная группа mmm). В соответствии с проведённым уточнением Ритвельда [59] были определены постоянные решетки кристалла: $a = 18.1976(6) \text{ \AA}$, $b = 7.9528(7) \text{ \AA}$ и $c = 5.0832(4) \text{ \AA}$, углы $\alpha = \beta = \gamma = 90^\circ$, объём элементарной ячейки V составляет $735.65(9) \text{ \AA}^3$, а расчетная плотность $\rho_{\text{calc}} = 4.083 \text{ г/см}^3$ (количество структурных единиц $Z = 4$), см. рисунок 3.1.1, красная кривая. Приведенное значение хи-квадрат $\chi^2 = (R_{\text{wp}}/R_{\text{exp}})^2$ для этого образца равно 1.291 ($R_{\text{wp}} = 7.00\%$, $R_{\text{exp}} = 6.16\%$).

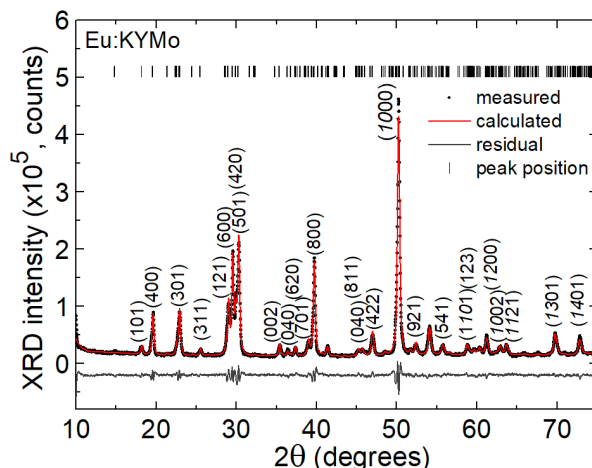


Рисунок 3.1.1 – Рентгенограмма кристалла 6 ат.% Eu:KYMo [59], числа обозначают индексы Миллера (hkl). Символы – экспериментальные данные, красная кривая – результат уточнения Ритвельда, серая кривая – остаточный график, вертикальные штрихи – рассчитанные положения пиков.

С помощью анализа Ритвельда были получены координаты атомов и межатомные расстояния, см. таблицу 3.1.

Таблица 3.1 – Дробные координаты атомов кристалла 6 ат.% Eu: KYMo [59]

Атом	Символ Вайкоффа	Симметрия	x/a	y/b	z/c
K	$4c$	C_2	0.273(2)	1/4	0
Y Eu	$4c$	C_2	0.504(2)	1/4	0
Mo	$8d$	C_1	0.101(5)	0.006(7)	0.025(9)
O1	$8d$	C_1	0.181(5)	0.524(7)	0.114(2)
O2	$8d$	C_1	0.080(8)	0.706(8)	0.198(6)
O3	$8d$	C_1	0.069(8)	0.155(4)	0.205(4)
O4	$8d$	C_1	0.447(4)	0.002(1)	0.275(8)

В соответствии с этими результатами с использованием программного обеспечения ImageJ была схематически построена структура кристалла $\text{Eu}^{3+}:\text{KY}(\text{MoO}_4)_2$, приведённая на рисунке 3.1.2. В структуре кристалла $\text{KY}(\text{MoO}_4)_2$ координационное число (то есть характеристика, показывающая число ближайших ионов в кристаллической решётке) для катионов K^+ , Y^{3+} и Mo^{6+} составляет $6+4$, 8 и $4+1$ соответственно. Координационное число $4+1$ для ионов Mo^{6+} обозначает искажённую тетраэдрическую координацию с четырьмя близко расположенными ионами O^{2-} (межатомные расстояния: 1.48-1.84

Å) и одним дополнительным катионом O^{2-} , расположенным на немного большем расстоянии (2,53 Å). Аналогичный эффект наблюдается для полиэдров $[KO_6]$. Непрерывные пояса искаженных октаэдров $[YO_8]$ с общими ребрами параллельны оси b , рис. 3.1.2 (а). В плоскости $a-b$ они имеют общие углы с тетраэдрами $[MoO_4]$. Таким образом радикал $[Y(MoO_4)_2]^-$ образует пористые слои, параллельные плоскости $b-c$, что хорошо видно на рис. 3.1.2 (б). Связь этих слоев, разделенных $a/2$, обеспечивают только многогранники $[KO_6]$. Этим объясняется идеальный скол по плоскости (100) в этом кристалле.

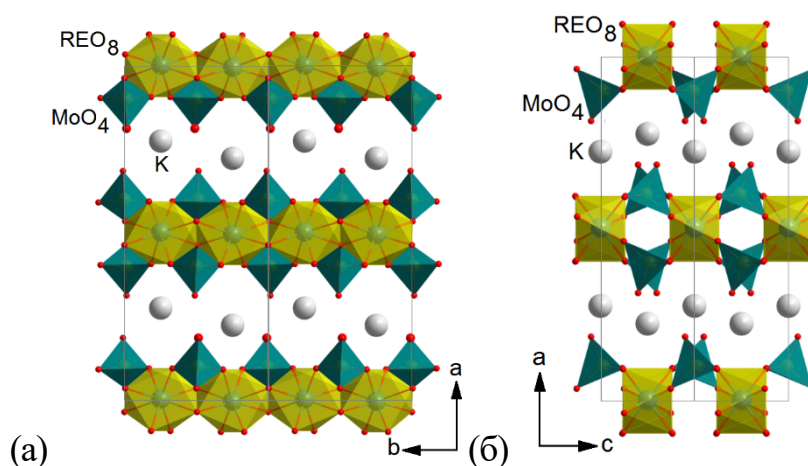


Рисунок 3.1.2 – Структура кристалла $Eu^{3+}:KY(MoO_4)_2$ в проекции на кристаллографические плоскости $a-b$ и $a-c$. Жёлтые и зелёные многогранники обозначают группы $[Y/EuO_8]$ и $[MoO_4]$ соответственно.

Для кристаллов $KY(MoO_4)_2$ межатомные расстояния $Y-O$ в полиэдрах $[YO_8]$ находятся в диапазоне 1.82-2.50 Å, а самое короткое расстояние $Y^{3+}-Y^{3+}$ составляет 3.98 Å, что близко к таковому в моноклинном KYW , 4.06 Å [53]. Наименьшее расстояние $Y^{3+}-Y^{3+}$ наблюдается вдоль оси b для катионов, лежащих в плоскости слоя $b-c$, вдоль оси c это расстояние немного больше – 5.08 Å. Намного большее расстояние $Y^{3+}-Y^{3+}$ наблюдается вдоль оси a (то есть от слоя к слою), а именно 9.49 Å.

Кристаллу $KY(MoO_4)_2$ свойственна низкая локальная симметрия люминесцентных центров C_2 . Ось симметрии C_2 перпендикулярна плоскости спайности (100) (то есть параллельна оси a) [60].

3.2 Спектроскопия комбинационного рассеяния света

Для измерений поляризованных спектров КР кристаллов был использован конфокальный микро-КР микроскоп, длина волны возбуждения составила λ_{exc} составляла 488 нм (ионный лазер Ar^+). Поскольку наличие линий разных колебаний и их интенсивности зависят от направлений распространения (k) и поляризаций (E) возбуждающего и рассеянного излучения, были измерены спектры КР для всех возможных геометрий кристаллов, а для их обозначения использовались обозначения Порто.

Поляризованные спектры КР кристалла $Eu^{3+}:KY(MoO_4)_2$ для геометрий $a(xx)a$, $b(xx)b$ и $c(xx)c$ показаны на рис. 3.2.1. Здесь стандартные обозначения $k_{exc}(E_{exc}|E_{sc})k_{sc}$ имеют вид, где векторы $E_{exc}|E_{sc}$ и $k_{exc}|k_{sc}$ обозначают поляризацию и направление распространения возбуждающего и рассеянного света соответственно. Спектры сильно поляризованы из-за особенности слоистой структуры кристалла. Колебательные свойства недопированного кристалла $KY(MoO_4)_2$ были подробно описаны ранее [60,61]. В настоящей работе приводятся только основные особенности спектров КР для кристалла $Eu^{3+}:KY(MoO_4)_2$.

Как уже было отмечено, основной особенностью кристалла является его слоистая структура, которая безусловно сказывается и на колебательных свойствах кристалла. В спектре комбинационного рассеяния для перпендикулярных слоям волновых векторов на относительно низких частотах появляются дополнительные колебательные полосы. Также при анализе спектров КР важно

учитывать взаимодействия между изолированными тетраэдрами $[\text{MoO}_4]^{2-}$ [60]. Элементарная ячейка ромбического $\text{KY}(\text{MoO}_4)_2$ содержит 48 атомов, соответственно в кристалле существует $48 \times 3 = 144$ фундаментальных колебания. Симметрии этих колебаний можно описать неприводимым представлением в центре зоны Бриллюэна ($\mathbf{k} = 0$) как $\Gamma = 17A_g + 19B_{1g} + 17B_{2g} + 19B_{3g} + 17A_u + 19B_{1u} + 17B_{2u} + 19B_{3u}$. Только 72 четные (g) колебательные моды являются комбинационно-активными, в том числе 17 симметричных колебаний A_g , 72 антисимметричных нечетных (u) моды B_{1u} , B_{2u} и B_{3u} являются ИК-активными, а 17 колебаний симметрии A_u не являются активными ни в КР, ни в ИК спектрах.

Правила отбора допускают колебания симметрии B_{1g} только для геометрий $k_{\text{exc}}(ac)k_{\text{sc}}$ и $k_{\text{exc}}(ca)k_{\text{sc}}$, B_{2g} – для $k_{\text{exc}}(bc)k_{\text{sc}}$ и $k_{\text{exc}}(cb)k_{\text{sc}}$, а B_{3g} – и для $k_{\text{exc}}(ab)k_{\text{sc}}$ и $k_{\text{exc}}(ba)k_{\text{sc}}$. Для симметричных колебаний A_g только диагональные элементы тензора поляризуемости отличны от нуля, что соответствует геометриям $k_{\text{exc}}(aa)k_{\text{sc}}$, $k_{\text{exc}}(bb)k_{\text{sc}}$ и $k_{\text{exc}}(cc)k_{\text{sc}}$. Применяя структурную модель, в которой пары $[\text{MoO}_4]^{2-}$ тетраэдров, связанных кислородными мостиками, рассматриваются как многоатомные ионные группы, фактор-групповой анализ распределяет 72 комбинационно-активных колебания по $n(\Gamma) = 18$ трансляционным модам, $n(R) = 6$ вибрационным и $n(\text{Mo}_2\text{O}_8) = 48$ внутренним модам ионной группы $[\text{Mo}_2\text{O}_8]^{4-}$. Упрощенное рассмотрение в рамках модели, в которой тетраэдры $[\text{MoO}_4]^{2-}$ изолированы, дает только 36 комбинационно-активных внутренних мод $[\text{MoO}_4]^{2-}$, которых недостаточно для интерпретации всех наблюдаемых колебаний.

Поляризованные спектры КР кристалла $\text{Eu}^{3+}:\text{KY}(\text{MoO}_4)_2$ приведены на рисунке 3.2.1. Они содержат полосы, расположенные в трех диапазонах, различающихся по интенсивности.

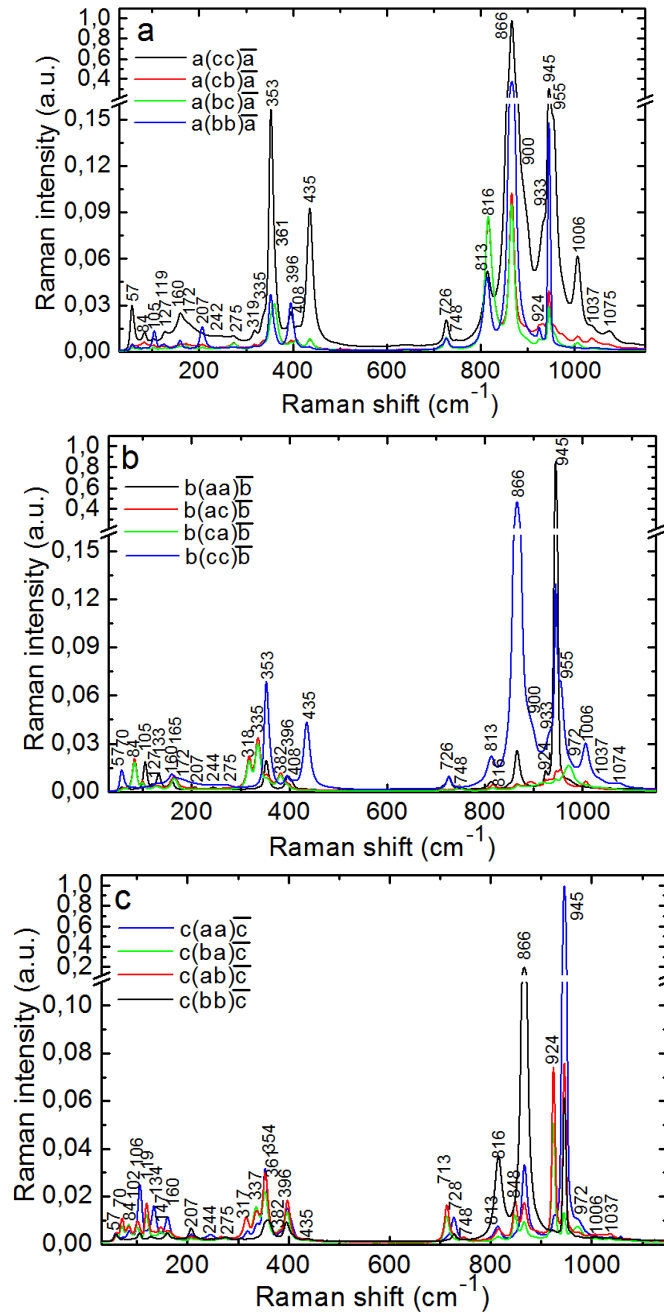


Рисунок 3.2.1 – Поляризованные спектры КР кристалла $\text{Eu}^{3+}:\text{KY}(\text{MoO}_4)_2$ *a*-срез (a), *b*-срез (b) и *c*-срез (c), $\lambda_{\text{возб}} = 488$ нм.

Первый диапазон ($57\text{-}275\text{ см}^{-1}$) содержит слабые колебания, связанные с T' -модами ионов K, Y и Mo, R-модами и акустооптическими связанными модами, лежащими в диапазоне частот менее 80 см^{-1} . Внутренние моды наблюдаются на более высоких частотах $>300\text{ см}^{-1}$. Второй диапазон колебаний ($319\text{-}435\text{ см}^{-1}$) содержит полосы промежуточной интенсивности, связанные с

деформационными (δ) колебаниями кислородных мостиков тетраэдров $[\text{MoO}_4]^{2-}$. Последний диапазон (частоты $726\text{-}1006\text{ см}^{-1}$) содержит очень интенсивные моды из-за валентных (ν) колебаний кислородного мостика $[\text{MoO}_4]^{2-}$. Наиболее интенсивные и сильно поляризованные полосы комбинационного рассеяния появляются на частотах 866 и 945 см^{-1} . Максимальная энергия фононов $\text{Eu}^{3+}:\text{KY}(\text{MoO}_4)_2$ $h\nu_{\text{max}}$ составляет 955 см^{-1} .

Моноклинный кристалл двойного вольфрамата $\text{Eu}^{3+}:\text{KY}(\text{WO}_4)_2$, имеет более низкую максимальную энергию фононов 905 см^{-1} [44]. В частности, в его спектре КР отсутствует щель $450\text{-}700\text{ см}^{-1}$, характерная для кристаллов типа шеелита, например тетрагонального $\text{NaY}(\text{WO}_4)_2$ [63]. Эта щель возникает из-за изолированного характера тетраэдров $[\text{WO}_4]$ в таких кристаллах. Для кристалла $\text{KY}(\text{WO}_4)_2$, напротив, полиэдры $[\text{WO}_6]$ связаны двойным кислородным мостиком (WOOW) [10]. В кристалле $\text{KY}(\text{MoO}_4)_2$ кислородный мостик тетраэдров $[\text{MoO}_4]$ только частично появляется в плоскости ***b-c***.

Таким образом колебательные свойства ромбического кристалла $\text{KY}(\text{MoO}_4)_2$ лежат между колебательными свойствами тетрагонального $\text{NaY}(\text{WO}_4)_2$ и моноклинного $\text{KY}(\text{WO}_4)_2$.

3.3 Абсорбционная спектроскопия. Теория Джадда-Офельта

3.3.1 Кристаллы с ионами европия Eu^{3+}

На рисунке 3.3.1 приведены спектральные зависимости показателя поглощения для кристалла $6\text{ ат.}\% \text{Eu}:\text{KY}(\text{MoO}_4)_2$ в видимой области спектра.

Исследование спектров проводилось в поляризованном свете для для поляризаций света параллельных ***a***, ***b*** и ***c***. Видно, что спектры поглощения сильно поляризованы. Такая анизотропия свойственна

всем кристаллам двойных молибдатов из-за их низкосимметричной и слоистой структуры.

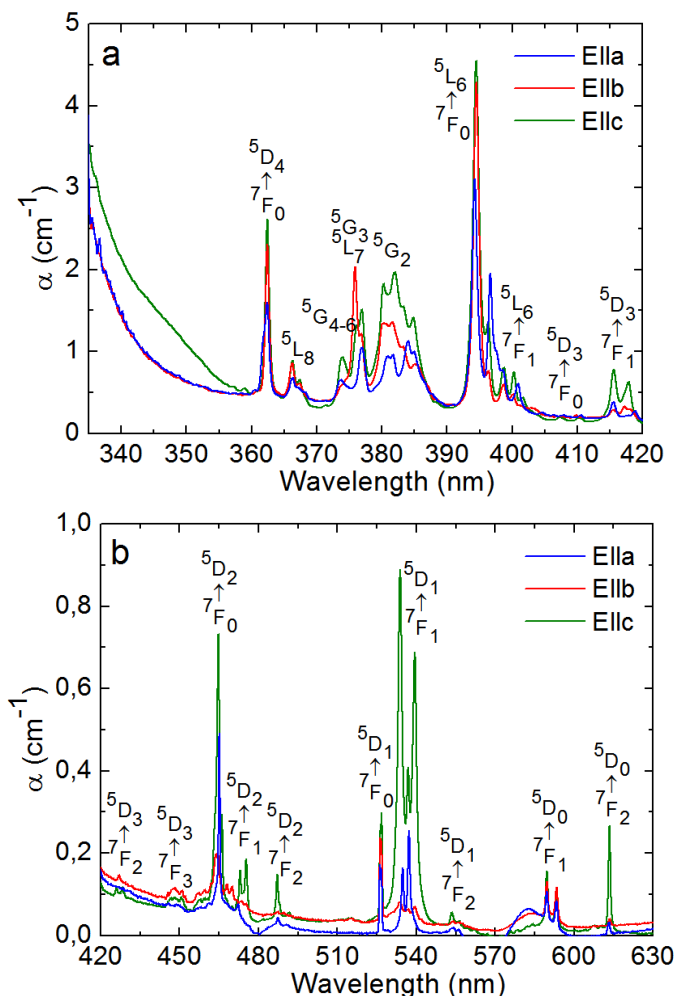


Рисунок 3.3.1 – Спектры поглощения кристалла 6 ат.% Eu:KY(MoO₄)₂ в видимой области спектра: (а, б) поляризованные спектры поглощения для поляризаций света $E \parallel a, b, c$.

Для ионов Eu³⁺ все переходы поглощения в видимой области спектра запрещены по спину, и поэтому их вероятность относительно мала. Стоит отметить, что для ионов Eu³⁺ нижележащие возбужденные состояния ($7F_1$ и $7F_2$) отделены от основного состояния $7F_0$ относительно небольшой по сравнению с kT (~ 203 см⁻¹) (k – постоянная Больцмана, T – температура) энергетической щелью (360 см⁻¹ и 1020 см⁻¹ соответственно [29]). Таким образом, эти состояния являются термически заселёнными даже при комнатной температуре. В спектрах

поглощения кристалла $\text{Eu:KY}(\text{MoO}_4)_2$ чётко наблюдаются переходы не только из основного состояния (${}^7\text{F}_0$), но и из термически заселённых (${}^7\text{F}_1$) и возбуждённых (${}^7\text{F}_2$) состояний, а их относительная интенсивность определяется как правилами отбора, так и тепловой заселённостью, которая составляет 0.33 для ${}^7\text{F}_1$ и 0.02 для ${}^7\text{F}_2$, по сравнению с 0.65 для ${}^7\text{F}_0$ [18].

Рассмотрим переходы в состояние ${}^5\text{D}_0$. Переход $0 \rightarrow 0$ ($J \rightarrow J'$) запрещен для ED и MD. На рисунке 3.3.1 (б) соответствующей линии нв спектре нет, а переходы из состояний ${}^7\text{F}_2$ и ${}^7\text{F}_1$ отчетливо наблюдаются на длинах волн ~ 613 и 589 нм соответственно. Аналогичным образом можно отнести переходы из состояний ${}^7\text{F}_{0-2}$ в вышележащие ${}^5\text{D}_1$ (526-558 нм), ${}^5\text{D}_2$ (464-492 нм), ${}^5\text{D}_3$ (407-450 нм) и ${}^5\text{L}_6$ (394-404 нм). Для моноклинного кристалла Eu:KYW при комнатной температуре в спектрах поглощения регистрировался только переход ${}^7\text{F}_2 \rightarrow {}^5\text{D}_0$ [18]. Полосы поглощения, обусловленные переходами в возбужденные состояния Eu^{3+} выше ${}^5\text{L}_6$ (${}^5\text{G}_2$, ${}^5\text{G}_3+{}^5\text{L}_7$, ${}^5\text{G}_{4-6}$, ${}^5\text{L}_8$), перекрываются, и их точное отнесение затруднено. Интенсивная полоса на длине волны ~ 362 нм связана с переходом ${}^7\text{F}_0 \rightarrow {}^5\text{D}_4$.

Край поглощения кристалла Eu:KYM_2 в УФ области составляет 340 нм ($E_g = 3,64$ эВ). Это значение E_g меньше, чем для моноклинного Eu:KYW (4.24-4.32 эВ) [18].

В спектрах поглощения кристалла Eu:KYM_2 наблюдается сильная поляризационная анизотропия. Как видно из спектров, самое сильное поглощение соответствует поляризации $E \parallel c$. На рисунке 3.3.2 представлен обзор спектра поглощения для этой поляризации с цветной заливкой, соответствующей длинам волн поглощаемого света и указывающей на возможности возбуждения Eu^{3+} . Лазеры на ионах Eu^{3+} в зелёном диапазоне могут накачиваться с помощью удвоенной частоты (2ω) Nd на длине волны 0.53 мкм (${}^7\text{F}_{0,1} \rightarrow {}^5\text{D}_1$) [17]. Подобно

накачке лазеров видимого диапазона (например, Tb^{3+}) полупроводниковыми лазерами с удвоенной частотой [20], ионы Eu^{3+} потенциально могут возбуждаться на длине волны 0.46 мкм (${}^7F_{0,1} \rightarrow {}^5D_2$). Самая сильная полоса поглощения ионов Eu^{3+} в видимой области спектра на 0.40 мкм (${}^7F_{0,1} \rightarrow {}^5L_6$) хорошо согласуется с излучением голубых GaN-диодов.

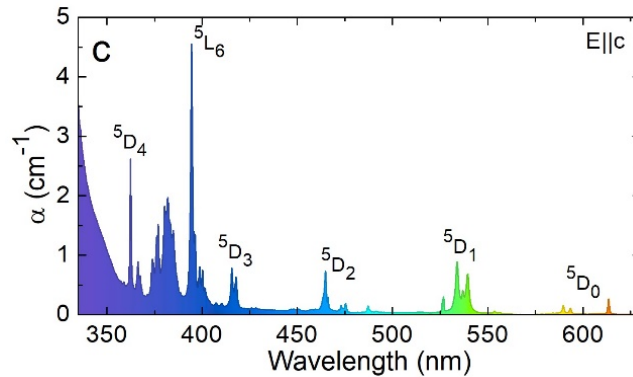


Рисунок 3.3.2 – Обзор спектра поглощения кристалла 6 ат.% $Eu:KY(MoO_4)_2$ в видимой области спектра для $E \parallel c$, цветовая заливка соответствует длине волны поглощаемого света.

Для перехода ${}^7F_{0,1} \rightarrow {}^5D_1$ максимальное сечение поглощения σ_{abs} составляет $0.37 \times 10^{-20} \text{ см}^2$ на 533.9 нм для $E \parallel c$. Полуширина соответствующей полосы поглощения составляет <2 нм. Для того же перехода значения σ_{abs} намного ниже для поляризаций света $E \parallel a$ ($0.11 \times 10^{-20} \text{ см}^2$ на 537.2 нм) и для $E \parallel b$ ($0.03 \times 10^{-20} \text{ см}^2$ на 533.9 нм). Эти значения ниже, чем для моноклинного кристалла $Eu:KYW$, для которого максимум σ_{abs} составляет $1.71 \times 10^{-20} \text{ см}^2$ на длине волны 534,3 нм для поляризации $E \parallel N_m$ [18]. Это можно объяснить более низкой симметрией кристаллической матрицы двойного вольфрамата. Полуширина соответствующей полосы поглощения кристалла $Eu:KYW$ составляет всего 0,5 нм [18].

В ближней ИК области спектра (рисунок 3.3.3) наблюдаются полосы поглощения, относящиеся к переходам из основного состояния ионов Eu^{3+} в низколежащие возбуждённые состояния ${}^7F_1 - {}^7F_6$. Такие

переходы являются спин-разрешёнными, поэтому наблюдаемая интенсивность полос поглощения в этой области значительно выше, чем в видимой области спектра. Для кристалла Eu:КУМо край поглощения в ИК области составляет 5.14 мкм ($\sim 1950 \text{ см}^{-1}$). Таким образом, в спектрах наблюдаются только переходы ${}^7F_{0,1} \rightarrow {}^7F_6, {}^7F_5, {}^7F_4$ и частично 7F_3 .

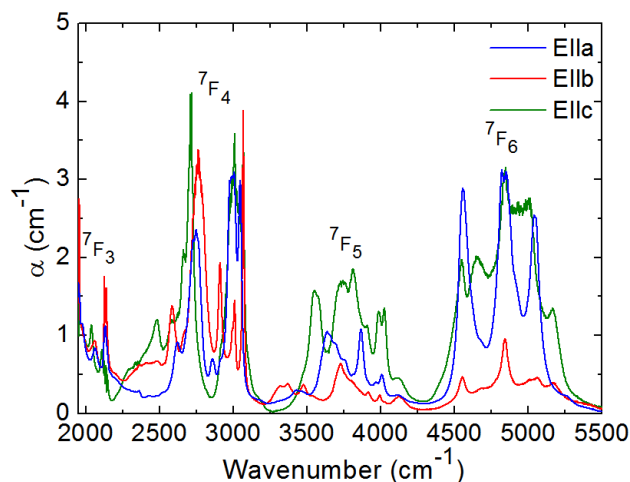


Рисунок 3.3.3 – Поляризованные спектры поглощения кристалла 6 ат.% Eu:КУМо в ближнем ИК диапазоне: поляризации света равны $E \parallel a, b, c$.

Спектр неполяризованного возбуждения кристалла Eu:КУМо для длины волны $\lambda_{\text{люм}} = 612 \text{ нм}$ показан на рис. 3.3.4. Он хорошо согласуется с измеренными спектрами поглощения.

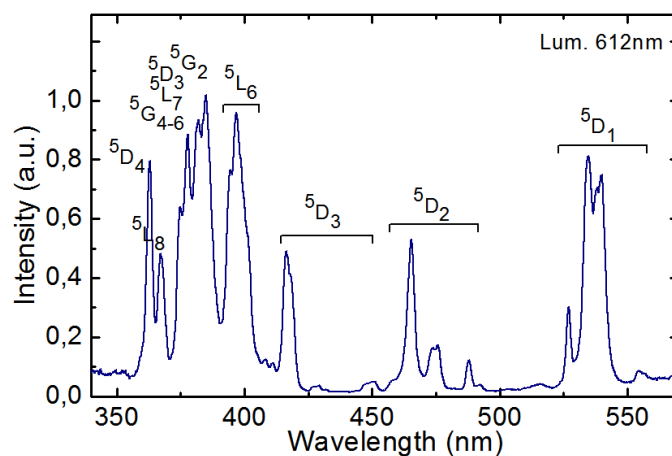


Рисунок 3.3.4 – Спектр неполяризованного возбуждения кристалла 6 ат.% Eu:КУМо, $\lambda_{\text{lum}} = 612 \text{ нм}$.

3.3.2 Кристаллы с ионами европия Tb³⁺

Спектры поглощения ионов Tb³⁺ в кристалле Tb³⁺:KLu(WO₄)₂ в видимой области показаны на рис. 3.3.5. На рис. 3.3.6 приведены спектры поглощения в ближнем ИК диапазоне. Исследование спектров проводилось в поляризованном свете для поляризаций света вдоль $E \parallel N_p$, N_m и N_g .

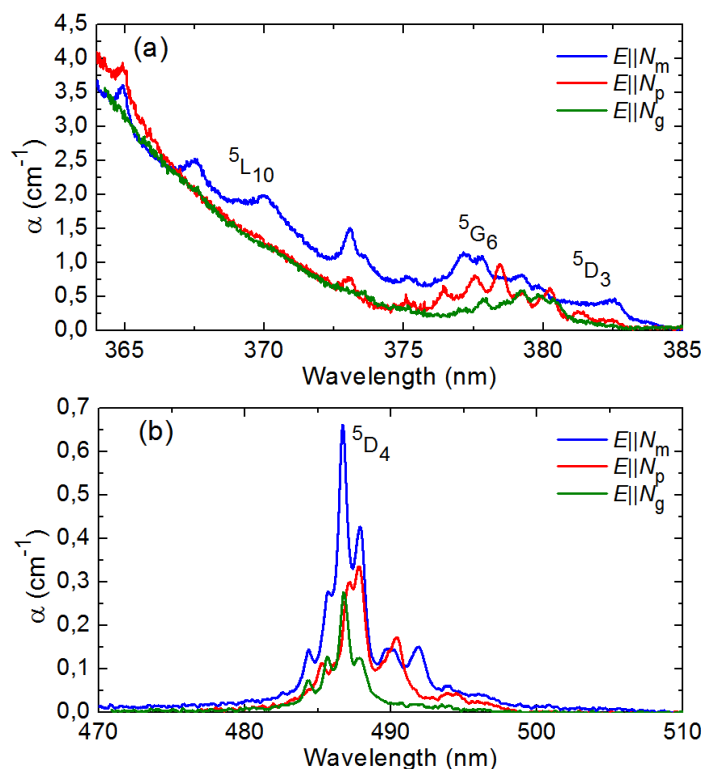


Рисунок 3.3.5 – Спектры поглощения поляризованного света видимого диапазона при КТ кристаллом 3 ат.% Tb³⁺:KLu(WO₄)₂: переходы $^7F_6 \rightarrow ^5D_3$, 5G_6 , $^5L_{10}$ (а) и переход $^7F_6 \rightarrow ^5D_4$ (б).

В кристалле Tb³⁺:KLu(WO₄)₂ наблюдается сильная анизотропия спектров поглощения поляризованного света, такая анизотропия свойственна всем кристаллам двойных вольфраматов, допированных ионами RE³⁺, из-за их низкосимметричной структуры. Как видно из спектров, максимальное поглощение соответствует поляризации света $E \parallel N_m$. Форма спектров для $E \parallel N_m$ и $E \parallel N_g$ достаточно похожа и отличается от формы спектров для поляризации $E \parallel N_p$. Это связано с направлением оси N_p в таких кристаллах, она параллельна оси

симметрии C_2 . Из-за этого правила отбора для 4f-4f-переходов различны для света, поляризованного вдоль оси N_p и вдоль осей N_m и N_g [63].

Для ионов Tb^{3+} все полосы поглощения при комнатной температуре обусловлены переходами только из основного состояния (7F_6) в возбужденные. Такое поведение отличается от поведения ионов Eu^{3+} с очень сходной структурой энергетических уровней [44], для которых в спектрах поглощения появляются переходы, происходящие не только из основного состояния (7F_0), но и из термически населенных 7F_1 и даже 7F_2 возбужденных состояний (см. раздел 3.3.1).

На рисунке 3.3.5 (б) приведена слабая полоса поглощения света кристаллом $Tb^{3+}:KLu(WO_4)_2$ в видимой области (480-500 нм). Она обусловлена спин-запрещенным переходом $^7F_6 \rightarrow ^5D_4$. Максимальное значение поперечного сечения поглощения, σ_{abs} , для поляризации света $E \parallel N_m$, составляет 3.42×10^{-21} см² на длине волны 486.7 нм с полушириной соответствующего полосы поглощения равной 1.0 нм. Значение σ_{abs} примерно в два раза ниже для поляризации света $E \parallel N_p$ (1.73×10^{-21} см² на 487.8 нм) и $E \parallel N_g$ (1.43×10^{-21} см² на 486.7 нм). Многочисленные полосы поглощения в диапазоне 365-385 нм обусловлены спин-запрещенными переходами к высшим возбужденным состояниям 5D_3 , 5G_6 и $^5L_{10}$, рис.3.3.5 (а). Край оптического поглощения кристалла $Tb^{3+}:KLu(WO_4)_2$ в УФ области соответствует длине волны $\lambda_g \sim 360$ нм ($E_g = 3.44$ эВ).

В ближней ИК-области (рис.3.3.6) полосы поглощения ионов Tb^{3+} обусловлены переходами в нижние возбужденные состояния $^7F_5 - ^7F_0$. Поскольку эти переходы являются разрешенными по спину, пиковые значения поперечных сечений поглощения σ_{abs} (около $2 \dots 3 \times 10^{-20}$ см²) на порядок выше, чем для полос поглощения в видимой и УФ области

(1 ... 2×10^{-21} cm^2). В ИК диапазоне кристалл $\text{Tb}^{3+}:\text{KLu}(\text{WO}_4)_2$ прозрачен до ~ 5.3 мкм.

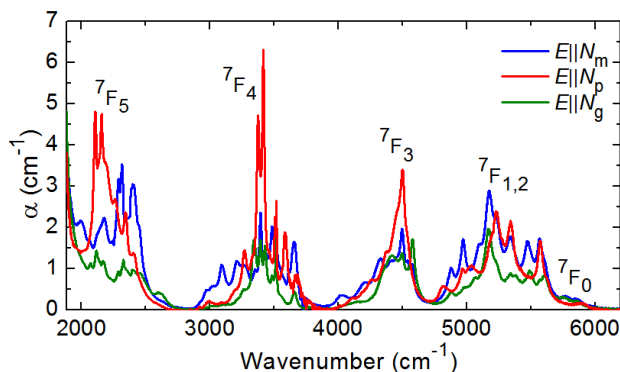


Рисунок 3.3.6 – Спектры поглощения в ближней ИК-области кристалла 3 ат.% Tb:KLuW в поляризованном свете при комнатной температуре.

Для кристалла $\text{Tb}^{3+}:\text{KLu}(\text{WO}_4)_2$ были выполнены расчёты спектроскопических параметров в соответствии с теорией Джадда-Офельта [42, 43] и её модификацией, учитывающей конфигурационное взаимодействие, в приближении промежуточного конфигурационного взаимодействия (ICI). Силы осцилляторов в поглощательных переходах для ионов Tb^{3+} определялись из измеренных спектров поглощения по формуле 1, см. раздел 1.2.1. Теоретические значения сил осцилляторов $\langle f_{\text{calc}} \rangle$ в поглощении были рассчитаны по формуле 2. Полученные значения $\langle f_{\text{calc}} \rangle$ с указанием вклада электрического ED и магнитного диполей MD, а также экспериментальные значения f_{exp}^x силы осцилляторов, усреднение по поляризации: $\langle f_{\text{exp}}^x \rangle = 1/3(f_{\text{p}}^x + f_{\text{m}}^x + f_{\text{g}}^x)$ и *rms dev.* - среднеквадратичное отклонение между $\langle f_{\text{exp}}^x \rangle$ and $\langle f_{\text{calc}}^x \rangle = \langle f_{\text{calc}}^{\text{ED}} \rangle + \langle f_{\text{calc}}^{\text{MD}} \rangle$ приведены в таблице 3.2.

Теория J-O описывает электрические дипольные (ED) переходы. Вклад магнито-дипольных (MD) переходов с $J - J' = 0, \pm 1$ был рассчитан отдельно согласно приближению Рассела-Саундерса для свободного иона. Для рассматриваемого спектра поглощения Tb^{3+} это переходы ${}^7\text{F}_6 \rightarrow {}^7\text{F}_5$ и ${}^7\text{F}_6 \rightarrow {}^5\text{G}_6$.

Силы линии ED переходов в приближении промежуточного конфигурационного взаимодействия (ICI) были рассчитаны по формуле 3. Расчетная сила осциллятора в поглощательных переходах $\langle f_{\text{calc}}^{\text{ED}} \rangle$ для кристалла Tb:KLuW с использованием моделей J-O, mJ-O и ICI приведена в таблице 3.2. Теория промежуточного конфигурационного взаимодействия (ICI) обеспечивает наименьшее среднеквадратичное отклонение (0.295) экспериментальных значений силы осциллятора $\langle f_{\text{exp}}^{\Sigma} \rangle$ от рассчитанных $\langle f_{\text{calc}}^{\Sigma} \rangle = \langle f_{\text{calc}}^{\text{ED}} \rangle + \langle f_{\text{calc}}^{\text{MD}} \rangle$. Для теории Джадда-Офельта (J-O) оно равно 0.477, а для модифицированной теории (mJ-O) – 0.482.

Таблица 3.2 – Экспериментальная и расчетная силы осцилляторов поглощения для кристалла 3 ат.% Tb: KLuW.

Переход	$f_{\text{exp}}^{\Sigma}, 10^{-6}$			$\langle f_{\text{exp}}^{\Sigma} \rangle^*, 10^{-6}$	$\langle f_{\text{calc}}^{\text{ED}} \rangle^*, 10^{-6}$			$\langle f_{\text{calc}}^{\text{MD}} \rangle$
	N_p	N_m	N_g		J-O	mJ-O	ICI	
${}^7F_6 \rightarrow {}^7F_5$	7.20	9.45	4.26	6.97	6.38 ^{ED}	6.27 ^{ED}	6.33 ^{ED}	0.57 ^{MD}
${}^7F_6 \rightarrow {}^7F_4$	4.97	5.04	2.15	4.06	4.32 ^{ED}	4.38 ^{ED}	4.28 ^{ED}	-
${}^7F_6 \rightarrow {}^7F_3$	4.33	3.60	2.97	3.63	3.27 ^{ED}	3.22 ^{ED}	3.32 ^{ED}	-
${}^7F_6 \rightarrow {}^7F_{1,2}$	4.98	6.22	3.24	4.81	4.98 ^{ED}	4.95 ^{ED}	4.89 ^{ED}	-
${}^7F_6 \rightarrow {}^7F_0$	0.96	1.07	0.45	0.83	0.86 ^{ED}	0.85 ^{ED}	0.85 ^{ED}	-
${}^7F_6 \rightarrow {}^5D_4$	0.34	0.59	0.16	0.36	0.20 ^{ED}	0.22 ^{ED}	0.24 ^{ED}	-
${}^7F_6 \rightarrow {}^5D_3 + {}^5G_6$	1.42	2.70	1.25	1.79	0.64 ^{ED}	0.76 ^{ED}	1.55 ^{ED}	0.21 ^{MD}
<i>rms dev.</i>					0.477	0.482	0.295	

Наилучшие параметры всех используемых теорий приведены в таблице 3.3. В частности, для модели ICI $\Omega_2 = 18.170$, $\Omega_4 = 23.394$, $\Omega_6 = 13.459$ [10^{-20} см²] и $R_2 = -0.102$, $R_4 = 0.203$, $R_6 = 0.170$ [10^{-4} см]. Среднеквадратичное отклонение, полученное в настоящей работе для Tb:KLuW намного ниже, чем указано для Tb:KYbW (0.887 для теории J-O и 0.726 для SCI) [47]. В основном это связано с дополнительными измерениями спектров поглощения в ближней ИК-области, выполненными в настоящей работе (рис. 3.3.6), где наблюдаются интенсивные спин-разрешенные переходы ${}^7F_6 \rightarrow {}^7F_J$ поглощения.

Table 3.3 – Параметры теорий Джадда-Офельта (J-O), модифицированной теории Джадда-Офельта (mJ-O) и приближения конфигурационного взаимодействия (ICI), применяемые для расчета сил осцилляторов поглощения для кристалла Tb: KLuW.

Теория	Параметры	Значение
J-O	$\Omega_k [10^{-20} \text{ cm}^2]$	$\Omega_2 = 23.524, \Omega_4 = 8.111, \Omega_6 = 6.918$
mJ-O	$\Omega_k [10^{-20} \text{ cm}^2];$ $\alpha [10^{-4} \text{ cm}]$	$\Omega_2 = 25.496, \Omega_4 = 9.590, \Omega_6 = 7.589;$ $\alpha = 0.033$
ICI	$\Omega_k [10^{-20} \text{ cm}^2];$ $R_k [10^{-4} \text{ cm}]$	$\Omega_2 = 18.170, \Omega_4 = 23.394, \Omega_6 = 13.459;$ $R_2 = -0.102, R_4 = 0.203, R_6 = 0.170$

Вероятности спонтанных излучательных переходов были вычислены по формуле 7. Значения $U^{(k)}$ для переходов в испускании были взяты из [47] для кристалла KYb(WO₄)₂. В клад MD был рассчитан согласно приближению свободного иона. Из барицентров поглощения (рис. 3.3.5 и 3.3.6) и люминесценции ионов Tb³⁺ были определены средние значения длин волн $\langle \lambda \rangle$ для каждого перехода $J \rightarrow J'$. Из значений вероятности спонтанных излучательных переходов $A_{JJ'}$ для каждого отдельного излучательного перехода $J \rightarrow J'$ была вычислена полная вероятность $A^{\text{calc}}_{\text{tot}}$, радиационные времена жизни возбужденных состояний τ_{rad} и коэффициенты ветвления люминесценции для отдельных излучательных переходов $B(JJ')$, см. формулу 8.

Результаты вероятностей излучательных переходов из возбужденных состояний ⁵D₄ и ⁵D₃ (согласно теории промежуточного конфигурационного взаимодействия) приведены в таблице 3.4. Радиационное время жизни метастабильного состояния ⁵D₄ составляет 0.450 мс. В таблице 3.5 сравниваются значения τ_{rad} для состояний ⁵D₄ и ⁵D₃, определенных с помощью теорий J-O, mJ-O и ICI.

Таблица 3.4 – Рассчитанные вероятности излучательных переходов ионов Tb³⁺ в кристалле 3 ат.% Tb:KLuW (для теории промежуточного конфигурационного взаимодействия).

Возбуждённый уровень	Уровень перехода	A_{JL}, c^{-1}	$B_{JL}, \%$	A_{tot}, c^{-1}	$\tau_{rad}, \text{мс}$
⁵ D ₄ →	⁷ F ₆	351.4 ^{ED}	15.8	2221.6	0.450
	⁷ F ₅	1076.6 ^{ED} +90.5 ^{MD}	52.5		
	⁷ F ₄	241.3 ^{ED} +0.4 ^{MD}	10.9		
	⁷ F ₃	139.5 ^{ED} +10.8 ^{MD}	6.8		
	⁷ F ₂	65.5 ^{ED}	2.9		
	⁷ F ₁	148.7 ^{ED}	6.7		
	⁷ F ₀	97.9 ^{ED}	4.4		
⁵ D ₃ →	⁷ F ₆	383.2 ^{ED}	8.5	4535.0	0.221
	⁷ F ₅	1227.5 ^{ED}	27.1		
	⁷ F ₄	916.9 ^{ED} +105.2 ^{MD}	22.5		
	⁷ F ₃	340.2 ^{ED} +1.6 ^{MD}	7.5		
	⁷ F ₂	772.2 ^{ED} +30.4 ^{MD}	17.7		
	⁷ F ₁	413.6 ^{ED}	9.1		
	⁷ F ₀	--	-		
	⁵ D ₄	294.5 ^{ED} +49.7 ^{MD}	7.6		

Для изоструктурного кристалла Tb:KYbW [47] рассчитанное с использованием теории сильного конфигурационного взаимодействия $\tau_{rad}({}^5D_4)$ составило 2.08 мс. Это значение больше, чем определено для кристалла Tb:KLuW. Скорее всего, это также связано более низкой точностью проведенного в [47] анализа, в котором отсутствовало исследование поглощения в ближней ИК-области, проведенное в настоящей работе (рис. 3.3.6). Кристалл Tb:KLuW обладает более коротким радиационным временем жизни состояния ⁵D₄ по сравнению с другими оксидными кристаллами TbAl₃(BO₃)₄ ($\tau_{rad}({}^5D_4) = 2.07$ мс) [64] и TbAlO₄ ($\tau_{rad}({}^5D_4) = 3.5$ мс) [33].

Таблица 3.5 – Рассчитанные радиационные времена жизни возбужденных состояний ⁵D₄ и ⁵D₃ ионов Tb³⁺ в кристалле KLuW (для теорий J-O, mJ-O и ICI).

Возбуждённое состояние	$\tau_{rad}, \text{мс}$		
	J-O	mJ-O	ICI
⁵ D ₄	0.500	0.449	0.450
⁵ D ₃	0.323	0.275	0.221

3.4 Анизотропия люминесцентных свойств

3.4.1 Кристаллы с ионами европия Eu^{3+}

Спектры люминесценции кристалла $\text{Eu}^{3+}:\text{KY}(\text{MoO}_4)_2$, зарегистрированные для трёх главных поляризаций света ($\mathbf{E} \parallel N_p$, $\mathbf{E} \parallel N_m$, $\mathbf{E} \parallel N_g$) приведены на рисунке 3.4.1; на рисунке 3.4.2 – для кристалла $\text{Eu}^{3+}:\text{KY}(\text{WO}_4)_2$; и на рисунке 3.4.3 – для кристалла $\text{Eu}^{3+}:\text{CsGd}(\text{MoO}_4)_2$. Длина волны возбуждающего излучения составляла 488 нм.

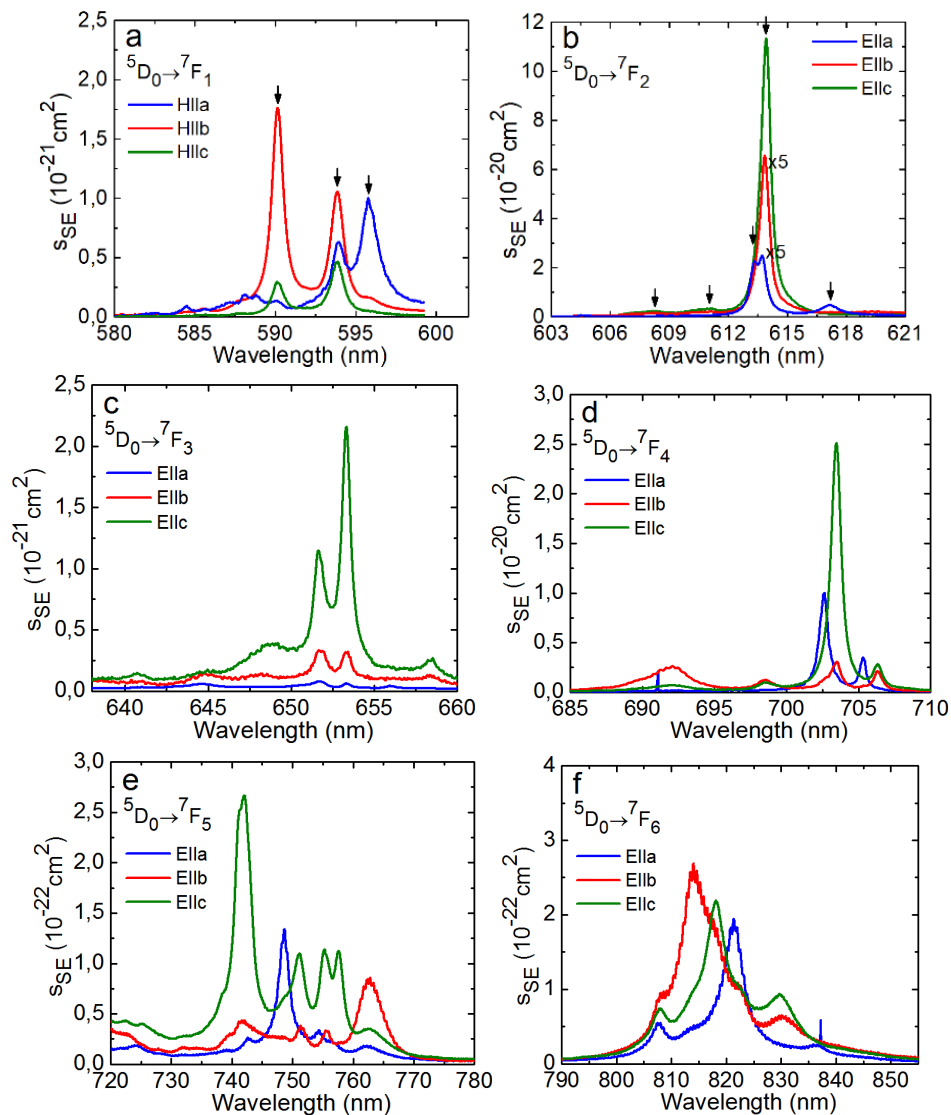


Рисунок 3.4.1 – Поперечные сечения поляризованного вынужденного испускания ионов Eu^{3+} в кристалле $\text{KY}(\text{MoO}_4)_2$.

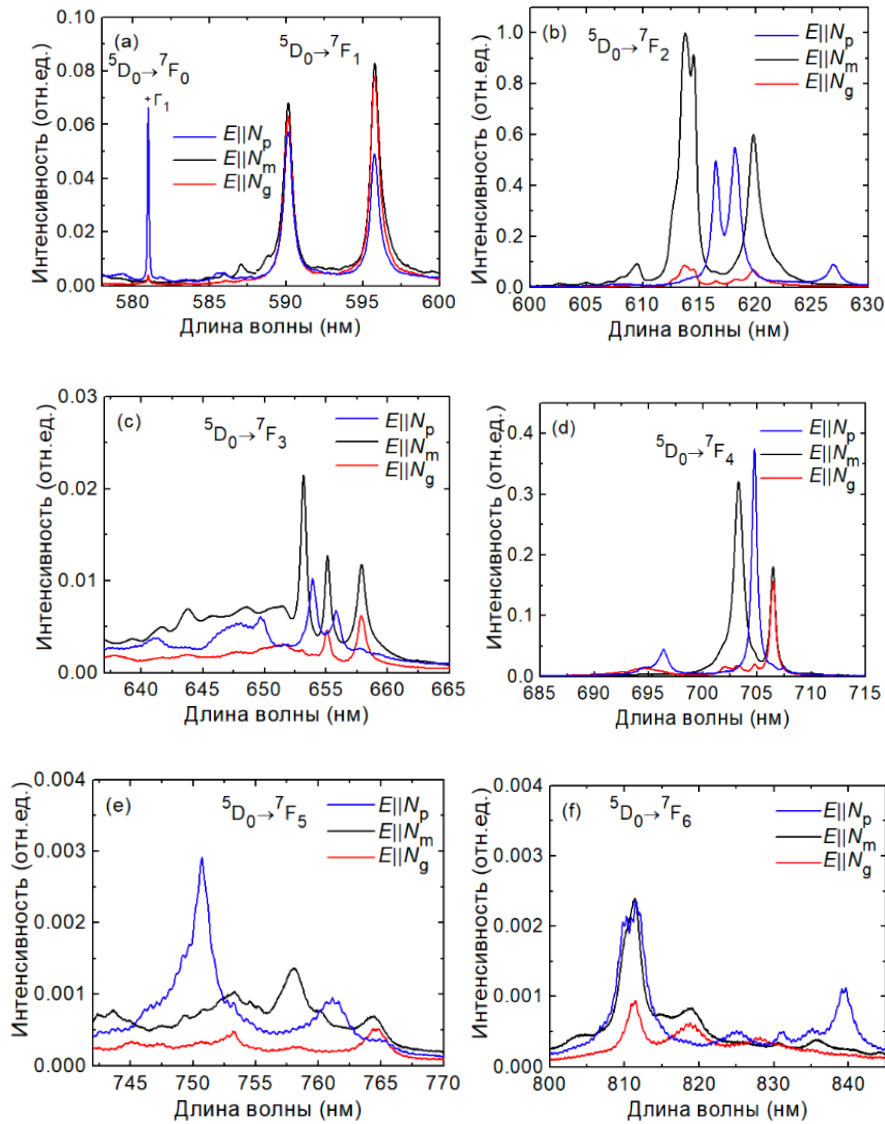


Рисунок 3.4.2 – Спектры люминесценции кристалла $\text{Eu}^{3+}:\text{KY}(\text{WO}_4)_2$ для поляризаций света $E \parallel N_p$, $E \parallel N_m$ и $E \parallel N_g$. Длина волны возбуждающего излучения 488 нм.

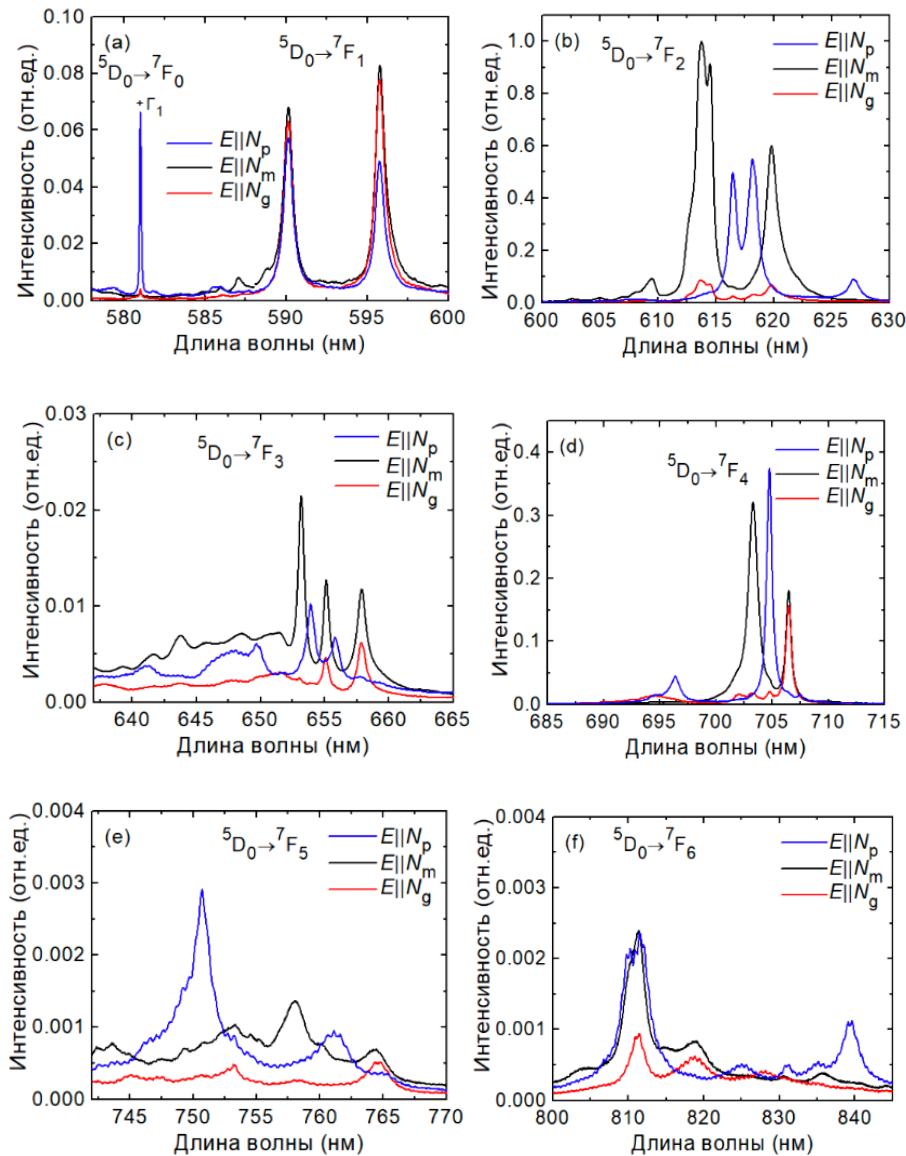


Рисунок 3.4.3 – Спектры люминесценции кристалла $\text{Eu}^{3+}:\text{CsGd}(\text{WO}_4)_2$ для поляризаций света $E \parallel N_p$, $E \parallel N_m$ и $E \parallel N_g$. Длина волны возбуждающего излучения 488 нм.

При возбуждении ионов Eu^{3+} излучением на длине волны 488 нм (что соответствует возбуждению в короткоживущее состояние 5D_2 , из которого ионы попадают в метастабильное состояние 5D_0), в спектре люминесценции наблюдается ряд полос с максимумами на длинах волн 580, 593, 614, 655, 703, 752 и 811 нм. Эти полосы относятся к энергетическим переходам из метастабильного уровня 5D_0 в нижележащие энергетические состояния 7F_J ($J = 0 - 6$), соответственно (7F_0 – основное состояние ионов Eu^{3+}). Интенсивная полоса

люминесценции на длине волны ~ 614 нм, соответствующая переходу ${}^5D_0 \rightarrow {}^7F_2$, доминирует в спектре и обуславливает красно-оранжевый цвет люминесценции кристалла. Все полосы люминесценции сильно поляризованы, что указывает на сильную анизотропию спектрально-люминесцентных свойств кристаллов $\text{Eu}^{3+}:\text{CsGd}(\text{MoO}_4)_2$, $\text{Eu}^{3+}:\text{KY}(\text{MoO}_4)_2$ и $\text{Eu}^{3+}:\text{KY}(\text{WO}_4)_2$. Наиболее интенсивная люминесценция наблюдается для поляризации света $\mathbf{E} \parallel N_m$.

Интерпретация наблюдаемых полос люминесценции в кристалле $\text{Eu}^{3+}:\text{KY}(\text{WO}_4)_2$ приведена на рис.3.4.4 в виде схемы энергетических состояний ионов Eu^{3+} . Стрелками обозначены возможные длины волн для возбуждения люминесценции и полосы люминесценции в видимой области спектра.

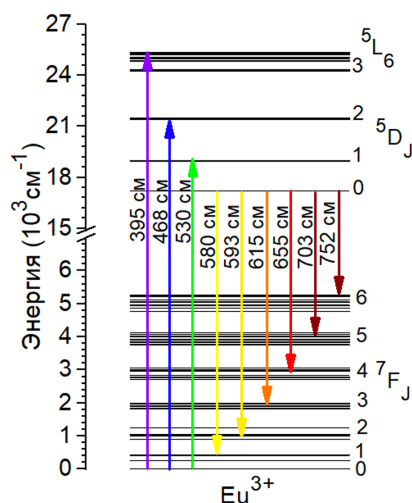


Рисунок 3.4.4 – Схема энергетических уровней ионов Eu^{3+} в кристалле $\text{KY}(\text{WO}_4)_2$. Цветными стрелками обозначены поглощательные и излучательные переходы.

Используя параметры Джадда Офельта, определенные из спектров поглощения кристалла $\text{Eu}^{3+}:\text{KY}(\text{MoO}_4)_2$ (см. таблицу 3.6), были рассчитаны вероятности спонтанных излучательных переходов $A_{J'J''}^{\Sigma}$ из возбужденных состояний 5D_0 и 5D_1 . Вклад MD перехода был взят из работы [65].

Таблица 3.6 Рассчитанные параметры Джадда-Офельта для ионов Eu^{3+} в кристалле КУМо.

Рассчёт по спектрам:	$\Omega_k, 10^{-20} \text{ см}^2$		
	Ω_2	Ω_4	Ω_6
поглощения	13.16	5.86	3.60
люминесценции	13.47	6.61	3.61

На основе A_{JJ}^{Σ} по формулам 7 и 8 были определены полные вероятности радиационного затухания A^{tot} , радиационные времена жизни τ_{rad} и коэффициенты ветвления люминесценции $B(JJ')$, полученные значения приведены в таблице 3.7.

Таблица 3.7. Рассчитанные по спектрам люминесценции в рамках теории Джадда-Офельта вероятности излучения ионов Eu^{3+} в КУМо.

Переход	$\langle \lambda \rangle, \text{ нм}$	$A_{JJ}, \text{ с}^{-1}$	$\langle B_{JJ} \rangle, \%$	$A_{\text{tot}}, \text{ с}^{-1}$	$\tau_{\text{rad}}, \text{ мс}$
${}^5\text{D}_0 \rightarrow {}^7\text{F}_1$	591	127.95 ^{MD}	8.191	1562	0.640
${}^7\text{F}_2$	614	1168.18 ^{ED}	74.787		
${}^7\text{F}_4$	700	255.94 ^{ED}	16.385		
${}^7\text{F}_6$	816	9.938 ^{ED}	0.636		

Радиационное время жизни (τ_{rad}) состояния ${}^5\text{D}_0$ в кристалле $\text{Eu}^{3+}:\text{KY}(\text{MoO}_4)_2$ составляет 0.640 мс. Это время жизни больше, чем у кристалла $\text{Eu}^{3+}:\text{KY}(\text{WO}_4)_2$ (0.464 мс), что можно объяснить особенностями структуры КУМо, состоящего из изолированных слоёв, содержащих полиэдры $[\text{YO}_8]$.

Спектры люминесценции для каждого перехода ${}^5\text{D}_0 \rightarrow {}^7\text{F}_J$ ($J = 1 \dots 6$) измерялись в поляризованном свете. Из этих спектров и значения τ_{rad} для состояния ${}^5\text{D}_0$ по формуле 10 [48] были рассчитаны поперечные сечения вынужденного испускания. Полученные значения для кристалла $\text{Eu}^{3+}:\text{KY}(\text{MoO}_4)_2$ представлены на рисунке 3.4.1.

Для переходов ${}^5\text{D}_0 \rightarrow {}^7\text{F}_2$ и ${}^5\text{D}_0 \rightarrow {}^7\text{F}_4$, которые представляют интерес для лазерной генерации, самые высокие значения σ_{SE} соответствуют поляризации $\mathbf{E} \parallel \mathbf{c}$, а именно $11.4 \times 10^{-20} \text{ см}^2$ на длине волны 613.9 нм и $2.5 \times 10^{-20} \text{ см}^2$ на 703.5 нм, соответственно. Несмотря

на большее радиационное время жизни состояния 5D_0 для ионов Eu^{3+} в кристалле $KY(MoO_4)_2$, пиковые значения σ_{SE} больше, чем для Eu^{3+} в моноклинном $KY(WO_4)_2$ (например, $4.0 \times 10^{-20} \text{ см}^2$ на 613.4 нм) [44]. Это связано с более сильной поляризационной анизотропией люминесцентных свойств $Eu^{3+}:KY(MoO_4)_2$.

Измеренные кривые затухания люминесценции ионов Eu^{3+} в кристалле $Eu^{3+}:KY(MoO_4)_2$, построенные в полулогарифмическом масштабе, показаны на рисунке 3.4.5. Люминесценция ионов Eu^{3+} регистрировалась из состояния 5D_0 (на длине волны 612 нм). Было использовано несколько длин волн возбуждающего излучения, на рисунке приведены $\lambda_{\text{возб}} = 400 \text{ нм}$ и 532 нм . Измеренные кривые затухания люминесценции имеют явно моноэкспоненциальный характер. Время затухания люминесценции τ_{lum} составляет 650-654 мкс. Рассчитанный по формуле 12 квантовый выход люминесценции более 99%. Это согласуется с большим энергетическим зазором между возбуждённым метастабильным состоянием 5D_0 и нижележащим уровнем 7F_6 ($\sim 12200 \text{ см}^{-1}$ [29]). Максимальная фонная частота в кристалле $Eu^{3+}:KY(MoO_4)_2$, $h\nu_{\text{max}} = 955 \text{ см}^{-1}$, см. раздел 3.2, рисунок 3.2.1, а значит вероятность безызлучательных переходов практически нулевая. С этой точки зрения кристалл $Eu^{3+}:KY(MoO_4)_2$ – отличный люминесцентный материал.

На рисунке 3.4.5 можно также увидеть небольшое разгорание люминесценции с характерным временем $\tau_{\text{возг}} = 16 \text{ мс}$ для $\lambda_{\text{возб}} = 400 \text{ нм}$ и $\tau_{\text{возг}} = 11 \text{ мс}$ для $\lambda_{\text{возб}} = 532 \text{ нм}$. Это связано со временем жизни возбужденных состояний выше уровня 5D_0 .

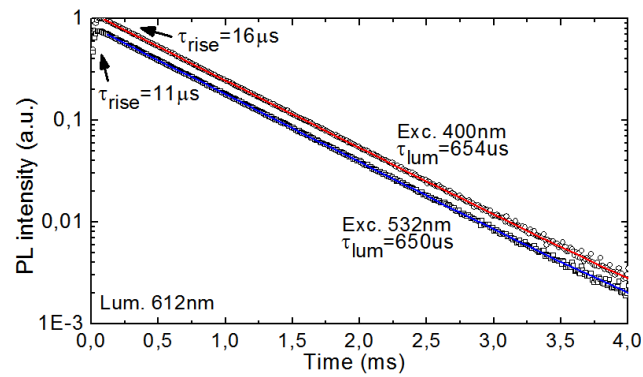


Рисунок 3.4.5 – Кривые затухания люминесценции для кристалла 6 ат.% $\text{Eu}^{3+}:\text{KY}(\text{MoO}_4)_2$, $\lambda_{\text{возб}} = 400$ или 532 нм, $\lambda_{\text{lum}} = 612$ нм, *символы* – экспериментальные данные, *линии* – их одноэкспоненциальные соответствия.

Две выбранные для возбуждения длины волны соответствуют переходам ${}^7\text{F}_1 \rightarrow {}^5\text{L}_6$ и ${}^7\text{F}_1 \rightarrow {}^5\text{D}_1$, соответственно. Ионы Eu^{3+} , возбужденные в состояния ${}^5\text{L}_6$ или ${}^5\text{D}_1$, могут излучать фотоны или испытывать безызлучательную релаксацию в метастабильное состояние ${}^5\text{D}_0$. Второй процесс более вероятен. Это связано с малыми энергетическими зазорами между возбужденными состояниями ${}^5\text{L}_6$ и ${}^5\text{D}_1$ ($<3000 \text{ см}^{-1}$) [29]. Таким образом, время жизни состояния ${}^5\text{D}_1$ составляет около 11 мс, а время жизни более высоких состояний составляет около нескольких мс.

3.4.2 Кристаллы с ионами тербия Tb^{3+}

Спектры люминесценции ионов Tb^{3+} также были измерены для всех трёх основных поляризаций света $\mathbf{E} \parallel N_p$, N_m и N_g . В спектрах наблюдаются переходы ${}^5\text{D}_4 \rightarrow {}^7\text{F}_J$ ($J = 6 \dots 0$): 484-500 нм (синий, $J = 6$), 540-552 нм (зеленый, $J = 5$), 578-593 нм (оранжевый, $J = 4$), 614-627 нм (красный, $J = 3$), 639-665 нм (красный, $J = 2$), 665-685 нм (темно-красный, $J = 1$) и 686-700 нм (темно-красный, $J = 0$). Наиболее интенсивная полоса люминесценции, характерная для материалов, допированных ионами Tb^{3+} , относится к переходу ${}^5\text{D}_4 \rightarrow {}^7\text{F}_5$ [33].

По этим спектрам с помощью уравнения Фюхтбауэра-Ладенбурга (формула 10) были рассчитаны поперечные сечения поляризованного вынужденного испускания (σ_{SE}). Показатель поглощения был взят из [10]. Рассчитанные спектры σ_{SE} кристалла Tb:KLuW показаны на рисунке 3.4.6.

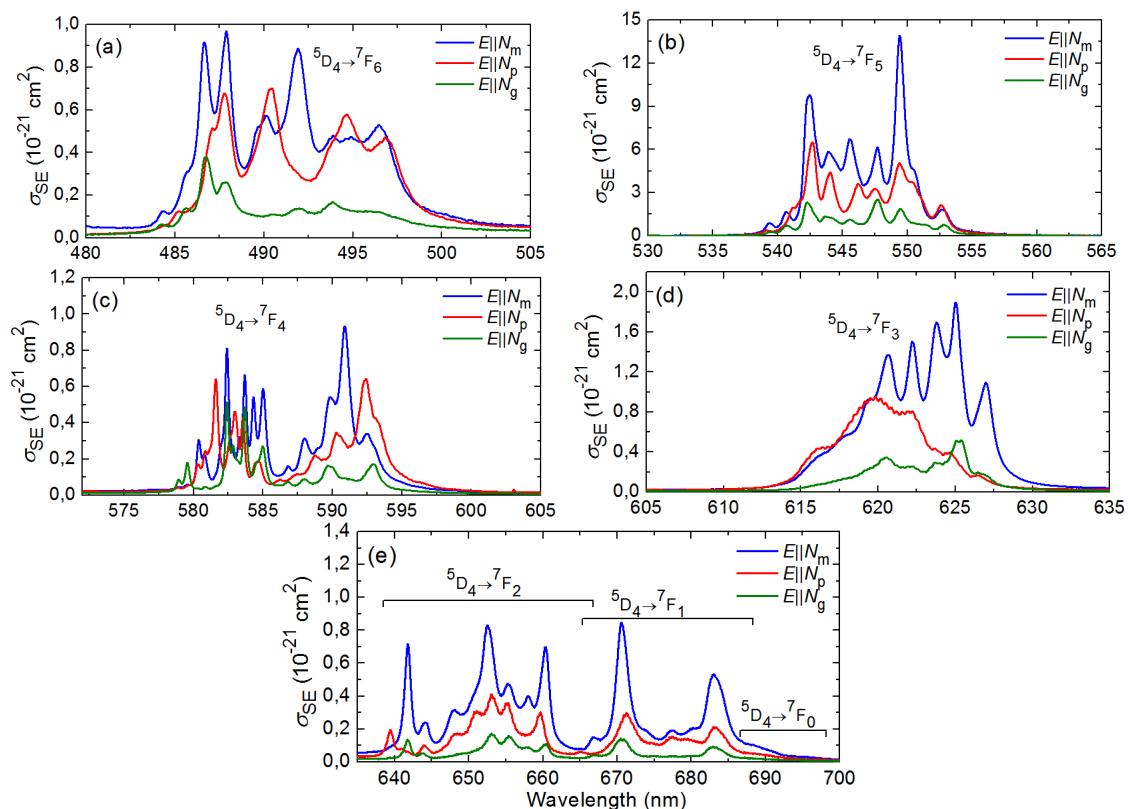


Рисунок 3.4.6 – Поперечные сечения вынужденного испускания, σ_{SE} , для ионов Tb³⁺ в кристалле KLuW при комнатной температуре.

В спектрах люминесценции ионов Tb³⁺ кристалле KLuW наблюдается сильная анизотропия поляризованного света. Максимальные значения σ_{SE} соответствуют поляризации $E \parallel N_m$ (следовательно, именно эта поляризация является наиболее привлекательной для лазерной генерации). Для перехода ${}^5D_4 \rightarrow {}^7F_5$, соответствующего длине волны 549.4, нм оно составляет $11.4 \times 10^{-21} \text{ см}^2$. Самые низкие значения σ_{SE} наблюдаются для света, поляризованного вдоль оси N_g . Пиковые значения σ_{SE} для всех переходов ${}^5D_4 \rightarrow {}^7F_J$ приведены в таблице 8.

Таблица 3.8. Пиковые значения поперечных сечений вынужденного испускания, σ_{SE} , ионов Tb^{3+} в кристалле KLuW для поляризации света $E \parallel N_m$.

Переход	$\sigma_{SE}, 10^{-21} \text{ cm}^2$	$\lambda_{max}, \text{ nm}$	Цвет
$^5D_4 \rightarrow ^7F_6$	1.15	487.9	синий
$^5D_4 \rightarrow ^7F_5$	11.4	549.4	зелёный
$^5D_4 \rightarrow ^7F_4$	2.29	590.9	оранжевый
$^5D_4 \rightarrow ^7F_3$	1.75	625.0	красный
$^5D_4 \rightarrow ^7F_2$	1.84	652.5	красный
$^5D_4 \rightarrow ^7F_1$	1.88	670.6	тёмно-красный
$^5D_4 \rightarrow ^7F_0$	0.23	688.4	тёмно-красный

Схема энергетических уровней ионов Tb^{3+} в кристалле KLuW и наблюдаемые переходы в поглощении и испускании показаны на рис. 3.4.7.

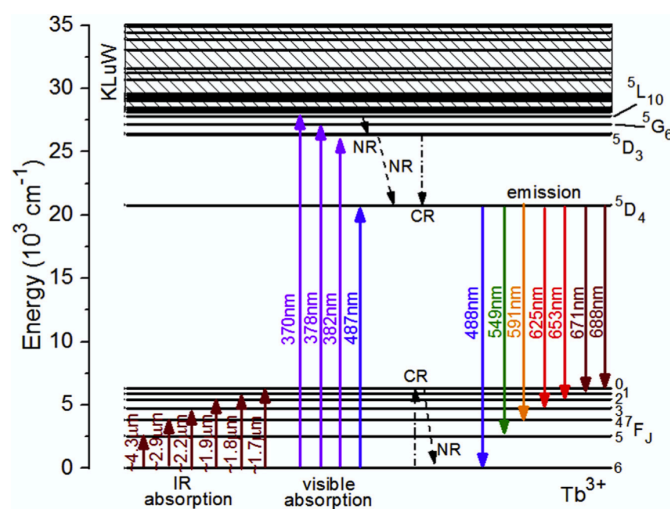


Рисунок 3.4.7 – Схема энергетических уровней ионов Tb^{3+} в кристалле KLuW и наблюдаемые переходы в поглощении и испускании (показаны сплошными стрелками). NR – безызлучательная релаксация, CR – кросс-релаксация. Заштрихованная область – поглощение света кристаллической матрицей KLuW.

Измеренные кривые затухания люминесценции ионов Tb^{3+} в кристалле 3 ат.% $Tb:KLu(WO_4)_2$, построенные в полулогарифмическом масштабе, показаны на рисунке 3.4.8. Люминесценция ионов Tb^{3+} регистрировалась из состояния 5D_4 (на длине волны 545 нм). Было использовано несколько длин волн возбуждающего излучения, а именно 475 нм (прямое возбуждение в излучающее состояние), 380 нм

(до состояния 5D_3) и 365 нм (до более высокоэнергетического состояния $^5L_{10}$). Все измеренные кривые затухания люминесценции имеют явно моноэкспоненциальный характер. Это хорошо согласуется с размещением ионов Tb^{3+} в позициях одного типа (позиция Lu^{3+} с симметрией C_2 и VIII-кратной координацией O^{2-} [10]).

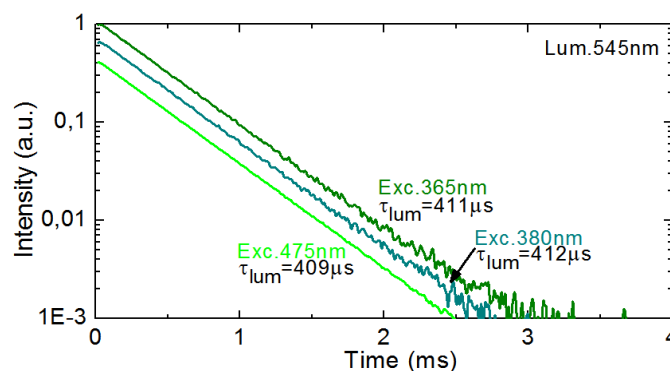


Рисунок 3.4.8 – Кривые затухания люминесценции ионов Tb^{3+} на 545 нм для кристалла 3 at.% $Tb:KLuW$, длина волны возбуждения 365 нм, 380 нм или 475 нм, τ_{lum} – время затухания люминесценции.

Время затухания люминесценции τ_{lum} составляет 411 ± 3 мкс. Рассчитанная квантовая эффективность люминесценции $\eta_q = 91\%$. Такое большое значение квантовой эффективности люминесценции ионов Tb^{3+} можно объяснить наличием большого энергетического зазора между состоянием 5D_4 и нижним возбужденным состоянием (7F_0), величина которого составляет примерно 15000 см^{-1} [29]. Максимальная частота фона $h\nu_{max}$ в кристалле $KLu(WO_4)_2$ составляет 908 см^{-1} [10], таким образом безызлучательная релаксация из состояния 5D_4 не является вероятной. Подобный эффект наблюдался для метастабильного состояния 5D_0 ионов Eu^{3+} в кристалле $KLu(WO_4)_2$ [44], и в кристалле $KY(MoO_4)_2$ (см. раздел 3.4.1).

Для изоструктурных кристаллов 1 at.% $Tb:KYbW$ и 5 at.% $Tb:KYW$ времена затухания люминесценции $\tau_{lum}(^5D_4)$ были определены как 395 мкс и 460 мкс соответственно [47,66], что близко к полученному для кристалла $Tb:KLu(WO_4)_2$ значению.

3.5 Магнитно-дипольный переход ${}^5D_0 \rightarrow {}^7F_1$ ионов Eu^{3+} в кристаллах $\text{KY}(\text{XO}_4)_2$ ($\text{X} = \text{W}, \text{Mo}$)

Для кристаллов калий-иттриевого двойного молибдата и калий-иттриевого двойного вольфрамата $\text{KY}(\text{XO}_4)_2$ ($\text{X} = \text{W}, \text{Mo}$), активированных ионами Eu^{3+} было проведено детальное исследование анизотропии магнитно-дипольного перехода ${}^5D_0 \rightarrow {}^7F_1$ ионов Eu^{3+} , которому соответствует люминесценция на длине волны 590 нм.

На рисунке 3.5.1 приведены спектры люминесценции ионов Eu^{3+} , соответствующие этому переходу в кристалле $\text{Eu:KY}(\text{MoO}_4)_2$ и в кристалле $\text{Eu:KY}(\text{WO}_4)_2$. Спектры были записаны для различных ориентаций вектора напряжённости электрического поля \mathbf{E} для возбуждающего и регистрируемого излучения.

Переход ${}^5D_0 \rightarrow {}^7F_1$ является чисто магнитным дипольным (MD) и при исследовании соответствующей люминесценции в поляризованном свете было обнаружено, что количество и относительная интенсивность пиков зависят не только от поляризации света \mathbf{E} , но и от направления распространения \mathbf{k} [67]. Подобное поведение известно для одноосных кристаллов [68], для которых оптическая ось параллельна оси \mathbf{c} .

Такой эффект не наблюдается для остальных переходов ${}^5D_0 \rightarrow {}^7F_J$ ($J = 2 - 6$), которые являются чисто электрическими дипольными (ED). Магнитный дипольный переход обусловлен взаимодействием активного иона с компонентом магнитного поля света через магнитный диполь, ориентация которого задаётся вектором \mathbf{M} . При этом имеет значение ориентация вектора напряженности магнитного поля \mathbf{H} по отношению к \mathbf{M} .

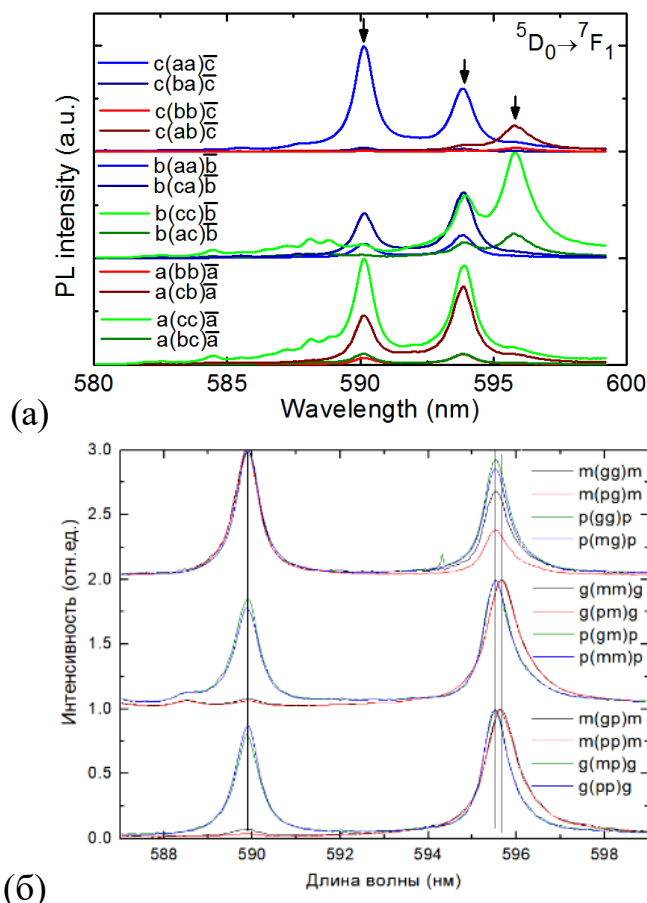


Рисунок 3.5.1 – Анизотропия спектров люминесценции, соответствующей магнитному дипольному (MD) переходу ${}^5D_0 \rightarrow {}^7F_1$ ионов Eu^{3+} в кристалле $\text{KY}(\text{MoO}_4)_2$ (а) и в кристалле $\text{KY}(\text{WO}_4)_2$ (б). Длина волны возбуждающего излучения 488 нм. Вертикальные линии обозначают Штарковские переходы. Используются обозначения $a(bc)a$ (а) или $m(dg)m$ (б), соответствующие методике Порто для описания спектров КР, $k_{\text{exc}}(E_{\text{exc}}E_{\text{lum}})k_{\text{lum}}$.

Вероятность MD межштарковского перехода в излучении равна [69]:

$$dW^{\text{MD}} = \frac{\omega_f^3}{2\pi\hbar c^3} \left| e_{\rho k} \cdot \left[\mathbf{k} \times \langle f | \mathbf{M} | i \rangle \right] \right|^2 d\Omega, \quad (13)$$

На верхней части рисунка 3.5.2 (б) (поляризация люминесценции: $\mathbf{E} \parallel N_g$, т.е. различные геометрии $a(bg)d$ два пика относятся к переходам $\Gamma_1 \rightarrow \Gamma_2^{(1)}$, $\Gamma_2^{(2)}$. На средней части рисунка для спектров $g(mm)g$ и $g(pm)g$ появляется дополнительный по сравнению с верхним рисунком пик, относящийся к переходу $\Gamma_1 \rightarrow \Gamma_1$. На нижней части рисунка также

наблюдается полоса, обусловленная переходом $\Gamma_1 \rightarrow \Gamma_1$, относящаяся к поляризациям $m(gp)m$ и $m(pp)m$.

Таким образом были установлены поляризационные правила отбора (см. таблицу) для магнитно-дипольных переходов редкоземельных ионов в оптически двухосных кристаллах с локальной симметрией люминесцентных центров C_2 .

Таблица 3.9 – Поляризационные правила отбора для магнитно-дипольного перехода ${}^5D_0 \rightarrow {}^7F_1$ ионов Eu^{3+} в кристаллах $KY(MoO_4)_2$ и $KY(WO_4)_2$

Направление ориентации вектора M	Разрешенные переходы ${}^5D_0 \rightarrow {}^7F_1$	Благоприятные направления излучения k	Возможные поляризации e_{pk}
$M \parallel C_2 (M \parallel a)$	$\Gamma_1 \rightarrow \Gamma_1$	$\parallel b$	$\parallel c$
		$\parallel c$	$\parallel b$
$M \perp C_2 (M \parallel b, c)$	$\Gamma_1 \rightarrow \Gamma_2^{(1)}, \Gamma_2^{(2)}$	$\parallel a$	$\parallel b, c$
		$\parallel b$	$\parallel a, c$
		$\parallel c$	$\parallel a, b$

3.6 Цветовые характеристики люминесценции

Спектр люминесценции кристалла $Eu^{3+}:KY(MoO_4)_2$, полученный при возбуждении на длине волны 488 нм, показан на рисунке 3.6.1. Заливка спектра соответствует цвету излучения. Интенсивная узкая полоса на длине волны ~614 нм (${}^5D_0 \rightarrow {}^7F_2$ Eu^{3+} переход) доминирует в спектре и обуславливает красно-оранжевую люминесценцию.

На вставке показана фотография кристалла под светом УФ-лампы. Цветовые координаты излучения были определены по стандарту CIE 1931 (Commission internationale de l'éclairage) с использованием программного обеспечения MathCad. Полученные цветовые координаты $x = 0.665$ и $y = 0.335$, что соответствует красному цвету. Доминантная длины волны λ_d равна 612 нм, а чистота цвета $p > 99\%$.

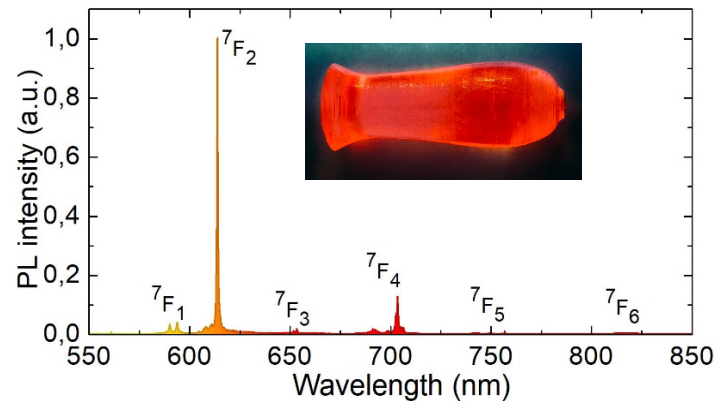


Рисунок 3.6.1 – Спектр люминесценции кристалла 6 ат.% $\text{Eu}^{3+}:\text{KY}(\text{MoO}_4)$, $\lambda_{\text{возб}} = 458 \text{ нм}$, *цветовая заливка* соответствует длине волны излучения. На вставке – фотография кристалла при возбуждении УФ-лампой.

На рисунке 3.6.2 приведён спектр люминесценции кристалла $\text{Tb}:\text{KLuW}$ при возбуждении синим светом длиной волны 488 нм (до возбуждённого состояния $^5\text{D}_4$) для поляризованного света $E \parallel N_m$. Полоса, связанная с переходом $^5\text{D}_4 \rightarrow ^7\text{F}_6$, измерялась отдельно использованием лазера на длине волны 458 нм. Соответствующие цвета излучения указаны на рисунке заливкой цвета. Наиболее интенсивная полоса люминесценции обусловлена переходом $^5\text{D}_4 \rightarrow ^7\text{F}_5$, типичным для материалов с примесью Tb^{3+} [33].

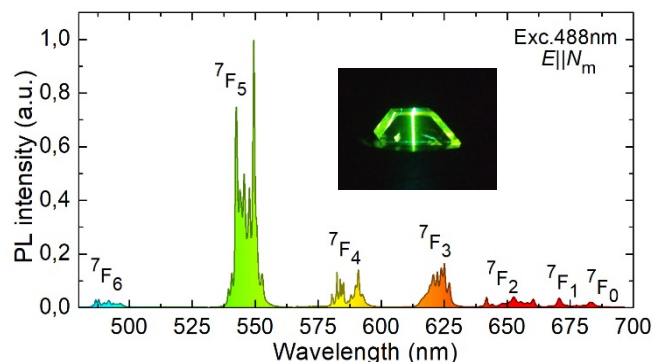


Рисунок 3.6.2 – Спектр люминесценции кристалла 3 ат.% $\text{Tb}:\text{KLuW}$ соответствующий поляризации света $E \parallel N_m$; длина волны возбуждения 488 нм. *Цвет заливки* соответствует длине волны излучения. На вставке приведена фотография кристалла.

На вставке показана фотография люминесценции кристалла. Наблюдаемая люминесценция также была охарактеризована согласно

стандарту CIE 1931. Полученные значения цветовых координат: $x = 0.380$ и $y = 0.608$. Таким образом излучение кристалла попадает в желтовато-зеленую область. Доминантная длина волны $\lambda_d = 561$ нм, параметр чистоты цвета $p > 97\%$ (для наблюдателя на 2 градуса).

3.7 Краткие выводы по главе 3

В данной главе проведено исследование люминесценции и поглощения ионов Eu^{3+} и Tb^{3+} . Все исследованные кристаллы показали высокую анизотропию спектрально-люминесцентных свойств ионов-активаторов. Были рассчитаны основные спектроскопические параметры, вероятности переходов, коэффициенты ветвления люминесценции, радиационные времена жизни люминесценции, поперечные сечения поглощения, вынужденного испускания и усиления, были определены времена затухания люминесценции ионов Eu^{3+} и ионов Tb^{3+} в исследуемых кристаллах. Было проведено детальное исследование анизотропии магнитно-дипольного перехода ${}^5\text{D}_0 \rightarrow {}^7\text{F}_1$ ионов Eu^{3+} в моноклинном кристалле $\text{KY}(\text{WO}_4)_2$ и в ромбическом кристалле $\text{KY}(\text{MoO}_4)_2$. Были установлены поляризационные правила отбора для магнитно-дипольных переходов редкоземельных ионов в оптически двухосных кристаллах. Были определены цветовые характеристики люминесценции исследуемых кристаллов.

ГЛАВА 4. Спектрально-люминесцентные и генерационные свойства кристалла $Tm^{3+}:KY(MoO_4)_2$

Известно, что кристаллы калий-иттриевых молибдатов обладают совершенной спайностью [53, 54, 60, 61]. Кристалл $Tm:KY(MoO_4)_2$ также обладает данным свойством и в нём, как и в других кристаллах этого семейства, наблюдается идеальный естественный скол вдоль одной из кристаллографических плоскостей. Эта особенность может использоваться в тонкоплёночных микрочип-лазерах [27]. А кристаллическая матрица должна обеспечивать подходящие для микрочип-лазера термооптические свойства [70, 71]. В настоящей главе описываются исследования спектрально-люминесцентных и генерационных свойств кристалла двойного калий-иттриевого молибдата с ионами тулия, $Tm:KY(MoO_4)_2$.

4.1 Структура кристалла (Рентгенофазовый анализ)

Выращенный из расплава методом Чохральского кристалл $Tm:KY(MoO_4)_2$ показан на рисунке 4.1.1 (а). Отжиг после выращивания кристалла не применялся. Выращенный кристалл не имел трещин и включений. Ионы Tm^{3+} придали кристаллу слегка желтоватую окраску. Методом дифракции рентгеновских лучей была определена ориентация осей кристалла. Идеальный естественный скол кристалла $Tm:KY(MoO_4)_2$ наблюдается вдоль кристаллографической плоскости (100), то есть перпендикулярно направлению роста кристалла

На рисунке 4.1.1 (б) приведено изображение излома края механически сколотой кристаллической пластины $Tm:KY(MoO_4)_2$, полученное на сканирующем электронном микроскопе. На изображении хорошо видны плоскости естественного скола, идущие параллельно оси c в плоскости (100).

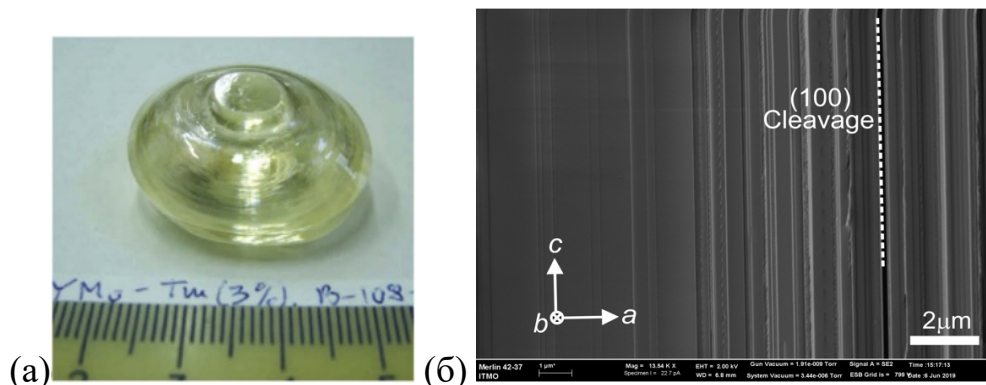


Рисунок 4.1.1 – (а) Фотография выращенной були кристалла 3 ат.% Tm:KY(MoO₄)₂. Направление роста - по оси [100] (вертикально); (б) Изображение излома боковой поверхности кристаллической пластинки, полученное с помощью сканирующего электронного микроскопа (SEM), с указанием кристаллографических осей.

Структура и фазовая чистота кристалла Tm:KY(MoO₄)₂ были подтверждены методом порошкового рентгенофазового анализа (Рис. 4.1.2). Кристалл Tm:KY(MoO₄) относится к классу орторомбических центросимметричных кристаллов с пространственной группой *Pbna* - D^{14}_{2h} , No 60. Следы каких-либо других примесных фаз в кристалле не были обнаружены. Постоянные решетки кристалла, допированного 3 ат.% Tm, были определены с помощью метода уточнения Ритвельда [73] и составили $a = 18.2012(9)$ Å, $b = 7.9301(5)$ Å, $c = 5.0666(4)$ Å, $\alpha = \beta = \gamma = 90^\circ$, расчётная плотность $\rho_{\text{расч}}$ составляет 4.0897(4) г/см³ (количество структурных единиц $Z = 4$). Концентрация ионов Tm³⁺ была рассчитана при условии, что коэффициент сегрегации $K_{\text{Tm}} \approx 1$, таким образом $N_{\text{Tm}} = 1.95 \times 10^{20}$ см⁻³.

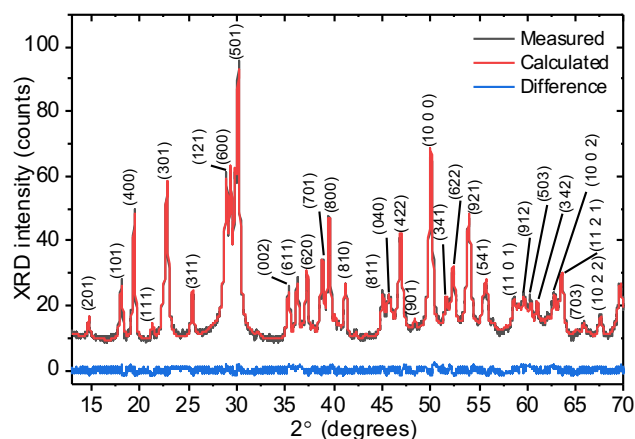


Рисунок 4.1.2 – Дифрактограммы кристалла 3 ат.% Tm:KY(MoO₄); числа обозначают индексы Миллера (*hkl*) (сп. гр. *Pbna*).

Структура Tm:KY(MoO₄) слоистая и она подобна структуре кристалла Eu:KY(MoO₄), которая была подробно описана в разделе 3.1.

Кристалл состоит из непрерывных лент искаженных октаэдров [YO₈], расположенных параллельно оси *b*. В плоскости *a–b* эти октаэдры имеют общие углы с тетраэдрами [MoO₄]. Радикалы [Y(MoO₄)₂][–] образуют пористые слои, параллельные плоскости *b–c*. Связь этих слоёв по оси *a* слабая, что объясняет идеальный скол по плоскости (100). Ионы Tm³⁺ замещают Y³⁺ в одной позиции (координационное число кислорода VIII, симметрия C₂). Этому способствует близость ионных радиусов Tm³⁺ (0,994 Å) и Y³⁺ (1,019 Å).

4.2 Спектроскопия комбинационного рассеяния света

На рисунке 4.2.1 приведены поляризованные спектры КР, которые были измерены для тонкой пластинки кристалла Tm:KY(MoO₄) ориентированной вдоль (100). Длина волны возбуждающего излучения λ_{exc} составила 488 нм.

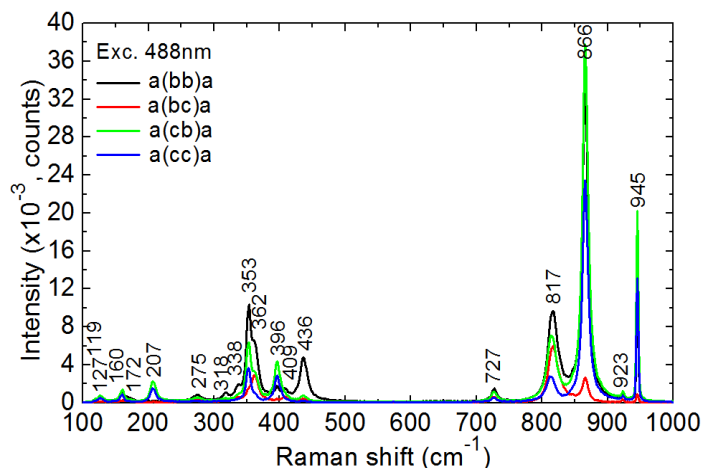


Рисунок 4.2.1 – Спектры КР кристалла $\text{Tm:KY}(\text{MoO}_4)_2$ для геометрии $\mathbf{a}(ij)\mathbf{a}$, где $i, j = \mathbf{b}$ или \mathbf{c} (обозначения Порто), $\lambda_{\text{exc}} = 488$ нм.

Видно, что спектры сильно поляризованы. Они содержат полосы с различной интенсивностью, расположенные в трех диапазонах длин волн [60, 61]. Низкочастотный диапазон ($<275 \text{ cm}^{-1}$) содержит слабые колебания, связанные с поступательными Γ' -модами К, Y|Tm и Mo и вращательными R-модами решетки. Поскольку спектры КР были измерены от 100 cm^{-1} , в них не попали акустооптические моды, лежащие в диапазоне ниже 80 cm^{-1} . Внутренние моды наблюдаются на более высоких частотах, в диапазоне колебаний $318\text{--}436 \text{ cm}^{-1}$. Здесь наблюдаются полосы средней интенсивности, связанные с деформационными (δ) колебаниями мостиковых кислородных тетраэдров $[\text{MoO}_4]^{2-}$. Третий, высокочастотный диапазон $727\text{--}945 \text{ cm}^{-1}$ содержит интенсивные моды, обусловленные валентными (ν) колебаниями колебаниям мостикового кислородного тетраэдра $[\text{MoO}_4]^{2-}$. Наиболее интенсивная и сильно поляризованная полоса комбинационного рассеяния света появляется в спектре на частоте 865.6 cm^{-1} , её полуширина 10.5 cm^{-1} . Она относится к одному из внутренних (ν) колебаний $[\text{MoO}_4]$. Максимальная энергия фононов $\text{Tm:KY}(\text{MoO}_4)$ составляет 945 cm^{-1} .

4.3 Спектры поперечных сечений поглощения

Кристалл $\text{Tm}^{3+}:\text{KY}(\text{MoO}_4)_2$ является ромбическим и, следовательно, оптически двухосным. А значит, для полного исследования анизотропии спектрально-люминесцентных свойств кристалла существует три направления поляризации света $E \parallel a, b, c$. Для кристалла $\text{Tm}^{3+}:\text{KY}(\text{MoO}_4)_2$ известно только среднее значение показателя преломления $\langle n \rangle \approx 2$ [27]. Все спектроскопические исследования для этого кристалла проводились при комнатной температуре (293 К).

Для измерения спектров поглощения и люминесценции был подготовлен образец кристаллической пластины толщиной ~ 1 мм, механически сколотый с целого кристалла. Для такой пластинки возможно было измерить спектры поглощения для поляризаций света $E \parallel b$ и $E \parallel c$, спектры измерялись на спектрофотометре Varian CARY 5000 с использованием призмы Глана-Тейлора в качестве поляризатора. Подготовить полированный образец, ориентированный перпендикулярно плоскости спайности, и таким образом, получить возможность измерения спектров поглощения для поляризации $E \parallel a$ оказалось невозможным, поэтому поглощение для данной поляризации не исследовалось.

Спектр поглощения кристалла $\text{Tm}:\text{KY}(\text{MoO}_4)_2$ для поляризаций света $E \parallel b$ и $E \parallel c$ показан на рис. 4.3.1 (а). Полосы поглощения, наблюдаемые в спектре, обусловлены переходами ионов Tm^{3+} из основного энергетического состояния ($^3\text{H}_6$) в вышележащие возбужденные состояния (от $^3\text{F}_4$ до $^1\text{D}_2$). Край поглощения в УФ-области находится на длине волны $\lambda_{UV} = 327$ нм (для поляризации $E \parallel c$) и $\lambda_{UV} = 340$ нм (для $E \parallel b$). Это соответствует оптической ширине запрещенной зоны E_g 3.64–3.80 эВ.

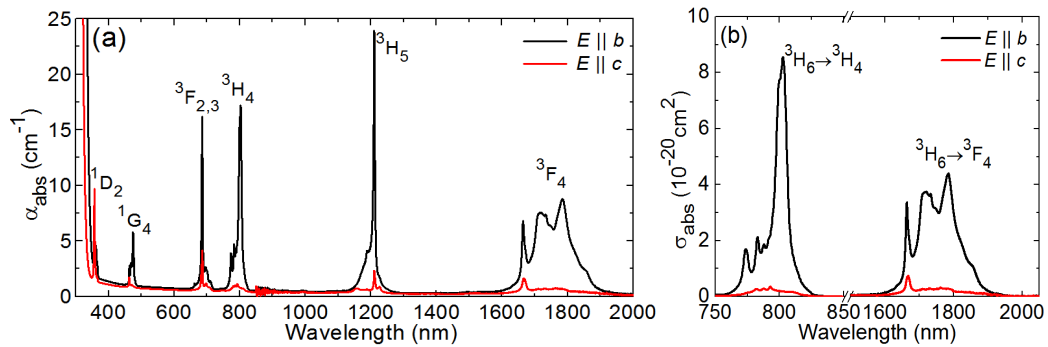


Рисунок 4.3.1 – Поглощение кристалла $\text{Tm:KY}(\text{MoO}_4)_2$ для поляризаций света $E \parallel b$ и $E \parallel c$: (а) полный спектр поглощения; (б) поперечные сечения поглощения, для переходов ${}^3\text{H}_6 \rightarrow {}^3\text{H}_4$ и ${}^3\text{H}_6 \rightarrow {}^3\text{F}_4$.

Поперечные сечения поглощения σ_{abs} для переходов ${}^3\text{H}_6 \rightarrow {}^3\text{H}_4$ и ${}^3\text{H}_6 \rightarrow {}^3\text{F}_4$ показаны на рис. 4.3.1 (б). Для полосы ${}^3\text{H}_6 \rightarrow {}^3\text{H}_4$ максимальное значение σ_{abs} составляет $7.70 \times 10^{-20} \text{ см}^2$ на длине волны 802.8 нм, а соответствующая полуширина полосы поглощения составляет 10.0 нм (для $E \parallel b$). Для второй доступной поляризации света ($E \parallel c$) σ_{abs} на порядок меньше: $0.32 \times 10^{-20} \text{ см}^2$ на 792.9 нм. Переход ${}^3\text{H}_6 \rightarrow {}^3\text{H}_4$ подходит для накачки ионов Tm^{3+} , промышленными и мощными AlGaAs лазерными диодами. Максимальное значение σ_{abs} для перехода ${}^3\text{H}_6 \rightarrow {}^3\text{H}_4$ ионов Tm^{3+} в $\text{KY}(\text{MoO}_4)_2$ аналогично таковому в моноклинном $\text{KLu}(\text{WO}_4)_2$, $\sigma_{\text{abs}} = 9.5 \times 10^{-20} \text{ см}^2$ на 793.6 нм [10], однако полуширина полосы поглощения 1.7 нм (поляризация света: $E \parallel N_p$). Получается, что кристалл $\text{Tm}^{3+}:\text{KY}(\text{MoO}_4)_2$ больше подходит для диодной накачки из-за меньшей чувствительности к температурному дрейфу длины волны излучения диода. Для перехода ${}^3\text{H}_6 \rightarrow {}^3\text{F}_4$ ионов Tm^{3+} в кристалле $\text{KY}(\text{MoO}_4)_2$ значение σ_{abs} достигает $3.95 \times 10^{-20} \text{ см}^2$ на длине волны 1785 нм (поляризация $E \parallel b$). Этот переход подходит для внутриволосной накачки ионов Tm^{3+} непосредственно на верхний лазерный уровень, например, для волоконных КР лазеров на эрбиевом излучении с длиной волны $\sim 1,7 \text{ мкм}$ [74].

Заметная анизотропия сечений поглощения в плоскости (100) не может быть отнесена только к слоистой структуре и, скорее всего, связана с низкой симметрией люминесцентных центров Tm^{3+} (C_2).

4.4 Спектры поперечных сечений испускания и усиления. Времена жизни люминесценции

Спектры люминесценции на длине волны ~ 2 мкм были измерены для трех поляризаций $E \parallel a, b, c$. Источником возбуждения служил непрерывный титан-сапфировый лазер, настроенный на длину волны ~ 802 нм.

Поперечные сечения вынужденного испускания σ_{SE} перехода ${}^3F_4 \rightarrow {}^3H_6$ ионов Tm^{3+} были рассчитаны по методу Фюхтбауэра-Ладенбурга (формула 10). Полученный в результате спектр показан на рисунке 4.4.1.

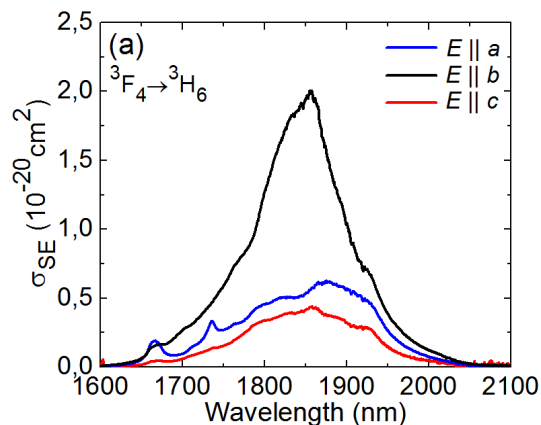


Рисунок 4.4.1 – Поперечные сечения вынужденного испускания σ_{SE} для перехода ${}^3F_4 \rightarrow {}^3H_6$ ионов Tm^{3+} в кристалле $\text{KY}(\text{MoO}_4)_2$. Поляризации света $E \parallel a, b, c$.

Максимальное значение поперечного сечения вынужденного испускания σ_{SE} составляет $2.70 \times 10^{-20} \text{ см}^2$ на длине волны 1856 нм с полушириной > 110 нм (для $E \parallel b$). В спектрах люминесценции и в спектрах поперечных сечений вынужденного испускания кристалла $\text{Tm}:\text{KY}(\text{MoO}_4)_2$ наблюдается заметная анизотропия: отношения $\sigma_{SE}(b):\sigma_{SE}(c) = 7.5$ и $\sigma_{SE}(b):\sigma_{SE}(a) = 5.7$ на длине волны ~ 1.86 мкм. Это

соответствует необходимому условию для получения линейно поляризованного лазерного излучения.

Затухание люминесценции из состояния 3F_4 представлено на рисунке 4.4.2. Оно является моноэкспоненциальным, время жизни люминесценции $\tau_{lum} = 2.29$ мс. Это согласуется с расположением ионов Tm^{3+} в позициях одного типа (симметрия: C_2). Время жизни люминесценции уровня накачки 3H_4 составляет 48 мкс. Оба времени жизни были измерены для тонких пленок, чтобы исключить эффект перепоглощения. Значение τ_{lum} (для уровня 3F_4), полученное для кристаллической пластины, было намного больше 3.35 мс.

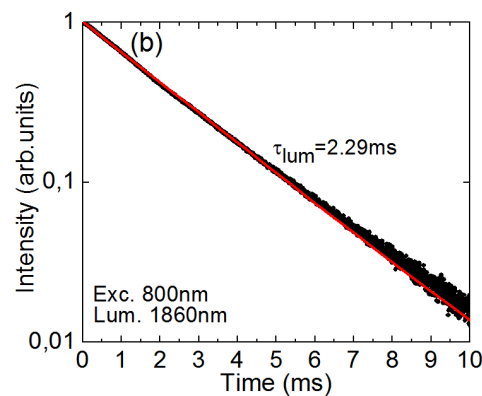


Рисунок 4.4.1 – Кривая затухания люминесценции ионов Tm^{3+} в кристалле $KY(MoO_4)_2$ из состояния 3F_4 , $\lambda_{возб} = 800$ нм, $\lambda_{lum} = 1860$ нм.

Переход ${}^3F_4 \rightarrow {}^3H_6$ ионов Tm^{3+} представляет собой квазитрехуровневую схему лазера с потерями на перепоглощение. Сечения усиления (σ_{gain}) рассчитываются, чтобы получить возможность сделать вывод об ожидаемой длине волны излучения: $\sigma_{gain} = \sigma_{SE} - (1 - \beta)\sigma_{abs}$, где $\beta = N_2({}^3F_4)/N_{Tm}$ – коэффициент инверсии, а N_2 – населенность верхнего лазерного уровня (3F_4). Спектры усиления σ_{gain} для поляризации света с большим усилением ($E \parallel b$) показаны на рис. 4.4.3. Они относительно гладкие и широкие.

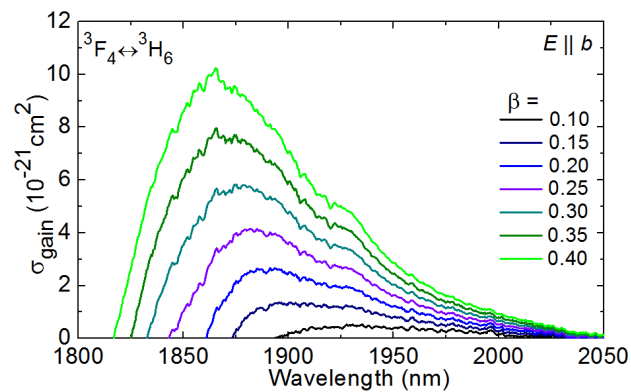


Рисунок 4.4.3 – Сечения усиления, рассчитанные для перехода ${}^3F_4 \leftrightarrow {}^3H_6$ ионов Tm^{3+} в кристалле $\text{KY}(\text{MoO}_4)_2$, поляризация света $E \parallel b$.

4.5 Лазерная генерация в кристаллических пластинках и тонких плёнках $\text{Tm}^{3+}:\text{KY}(\text{MoO}_4)_2$, полученных методом скалывани

4.5.1 Схема лазеров с микрочип-конфигурацией резонатора

Для лазерных экспериментов из кристалла 3 ат.% $\text{Tm}:\text{KY}(\text{MoO}_4)_2$ были подготовлены два образца. Они были изготовлены методом механического откалывания тонкой пластинки кристалла острым лезвием, расположенным вдоль кристаллографической плоскости (100). К лезвию было приложено лишь небольшое давление, в результате чего образовалась начальная трещина, которая в дальнейшем легко распространялась по поперечному сечению кристалла за счёт слоистой структуры и совершенной спайности, приводящей к идеальному сколу. Первый образец, представляющий из себя тонкую кристаллическую плёнку, имел толщину (t) 70 ± 5 мкм. Второй образец – тонкая кристаллическая пластина толщиной 700 ± 10 мкм. Толщина образцов была измерена с помощью микрометра и затем для тонкой плёнки была подтверждена с помощью сканирующей электронной микроскопии. Образцы были однородными по сечению в пределах заданной погрешности. Первый образец был подвержен упругой деформации. Последующая обработка образцов после скола (например, полировка, покрытие и т.д.) не применялась. Чистая

апертура образцов составляла более 1 см^2 . Образцы были изготовлены из объёмного кристалла, так что ориентация осей $[010]$ и $[001]$ была известна.

Образцы были помещены в компактный плоский (микрочип) резонатор, образованный плоским зеркалом накачки (PM) с покрытием для высокого пропускания на длине волны накачки $\sim 0.80 \text{ мкм}$ и для высокого отражения на ожидаемой длине лазерного излучения $1.8\text{--}2.1 \text{ мкм}$, и набором плоских выходных зеркал (OC) с пропусканием $T_{OC} = 0.1\% \text{--}9\%$ на длине волны генерации лазера, рис. 4.5.1 (а). Входное и выходное зеркала резонатора были осторожно прижаты к кристаллической пластине или плёнке, так что геометрическая длина полости $L_{cav} \equiv t$ толщине исследуемого образца активной среды. Лазерный элемент был пассивно охлажден, на рисунке 4.5.1 (б) приведена фотография кристаллической пластины, размещённой в микрочип-резонаторе.

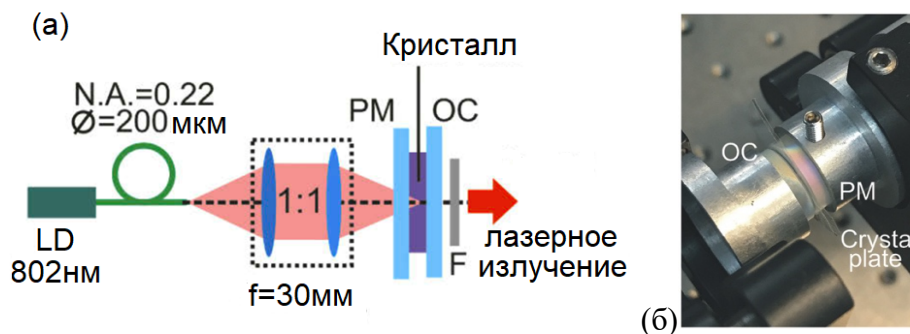


Рисунок 4.5.1 – (а) Схема микрочип-лазера с диодной накачкой на кристалле $\text{Tm:KY}(\text{MoO}_4)_2$ лазера: LD – лазерный диод, PM – зеркало накачки, OC – выходное зеркало, F – отсекающий фильтр; (б) фотография лазера на кристаллической пластинке.

Накачка лазерного элемента осуществлялась с помощью оптоволоконного лазерного диода AlGaAs (диаметр сердцевины волокна: 200 мкм , $N.A. = 0.22$), излучающего до 17 Вт неполяризованного излучения на длине волны 802 нм . Мощность

накачки была ограничена, чтобы избежать оптического повреждения на границах раздела кристалл / зеркало. Луч накачки коллимировался и фокусировался в лазерный элемент с помощью набора линз (фокусное расстояние $f = 30$ мм), в результате чего диаметр пятна накачки $2w_p = 200 \pm 10$ мкм. Из-за частичной отражательной способности выходного зеркала на длине волны накачки ($R \approx 40\%$) накачка была двухпроходной. Выходной сигнал лазера отделялся от остаточной накачки с помощью длиннопроходного фильтра.

4.5.2 Выходные характеристики лазеров

В первом лазерном эксперименте в качестве активного элемента лазера выступала кристаллическая пластина толщиной $t = 700$ мкм, рис. 4.5.2. Максимальная выходная мощность такого лазера составила 0.88 Вт на длине волны 1840–1905 нм с дифференциальной эффективностью в зависимости от поглощенной мощности накачки P_{abs} $\eta = 65.8\%$, а порог лазерной генерации был на уровне $P_{abs} = 210$ мВт (для выходного зеркала с пропусканием $T_{oc} = 5\%$). Для всех выходных зеркал полученные зависимости мощности лазерного излучения от поглощённой мощности были линейными. Поляризация лазера была линейной ($E \parallel b$), и соответствовала поляризации, определённой по анизотропии сечений усиления. Спектры лазерного излучения показаны на рисунке 4.5.2 (б). С увеличением значения T_{oc} спектры сдвигались в более коротковолновую область. Например, при маленькой величине пропускания $T_{oc} = 1.5\%$ лазер генерировал излучение с длиной волны 1970 – 1978 нм, а при высоком значении $T_{oc} = 9\%$ – на 1826 – 1835 нм. Такое смещение хорошо согласуется со спектрами усиления для поляризации света $E \parallel b$, рис.4.4.2.

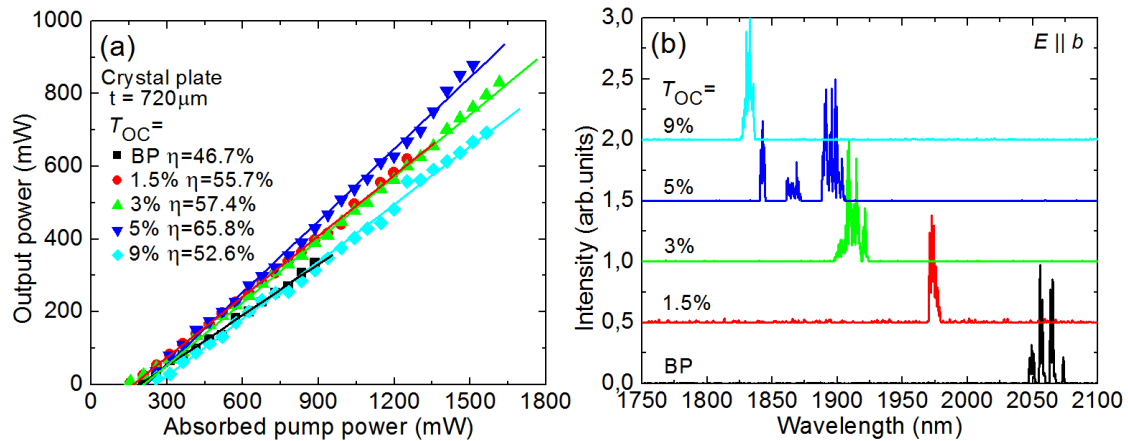


Рисунок 4.5.2 – Характеристики лазера с диодной накачкой для сколотой пластинки 3 ат.% Tm:KY(MoO₄)₂ кристалла с ориентацией (100) ($t = 700$ мкм): а – зависимость выходной мощности от поглощённой мощности, η – дифференциальная эффективность; б – спектры лазерного излучения, измеренные при максимальных P_{abs} . Поляризация лазера $E \parallel b$.

Второй эксперимент заключался в исследовании лазерной генерации на тонкой кристаллической плёнке в качестве активного лазерного элемента, рисунок 4.4.3. Максимальная выходная мощность такого лазера составила 131 мВт на длине волны 1801 – 1872 нм с $\eta = 45.2\%$ и порогом лазерной генерации всего 35 мВт (для $T_{OC} = 1.5\%$). Излучение лазера также было линейно поляризованным ($E \parallel b$). С увеличением пропускания выходного зеркала порог лазерной генерации увеличился: с 13 мВт для наименьшего $T_{OC} = 0.1\%$ до 54 мВт для $T_{OC} = 9\%$, при этом оставаясь относительно низким. Дифференциальная эффективность лазера сначала увеличивалась с увеличением пропускания выходного зеркала, а затем уменьшалась для $T_{OC} > 1.5\%$. Возможно, это связано с сильным ап-конверсионным переносом энергии. Этот перенос энергии напрямую влияет на значение порога лазерной генерации [75], приводит к более сильным термооптическим эффектам в активной среде, что может косвенно влиять на дифференциальную эффективность

Более низкая дифференциальная эффективность лазера на кристаллической плёнке по сравнению с лазером на кристаллической пластинке, объясняется более высокими пассивными потерями, возникающими из-за возможного механического искажения и изгиба пленки. Возможно, такие потери могут быть устранены путём дальнейшей оптимизации процедуры скалывания.

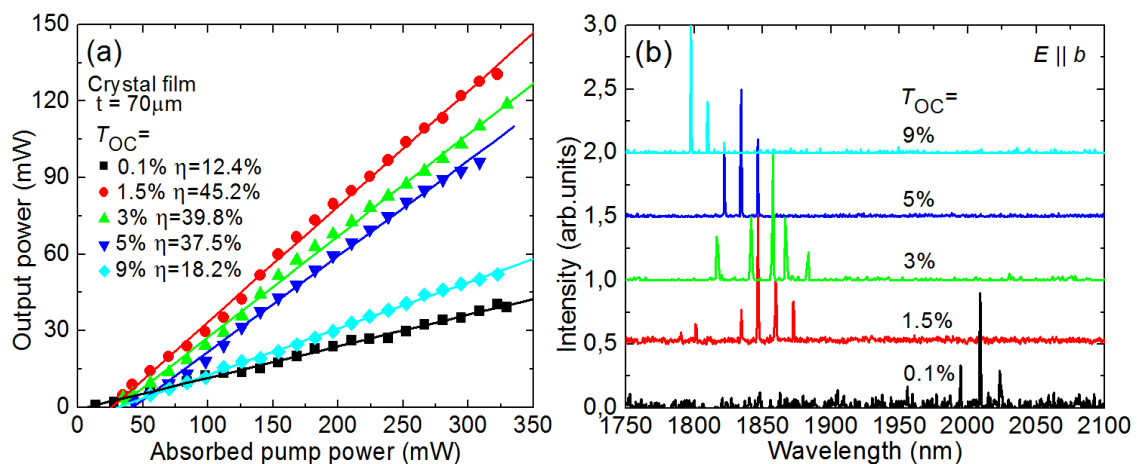


Рисунок 4.5.2 – Характеристики лазера с диодной накачкой для сколотой тонкой плёнки 3 ат.% Tm:KY(MoO₄)₂ кристалла с ориентацией (100) ($t = 70$ мкм): а – зависимость выходной мощности от поглощённой мощности, η – дифференциальная эффективность; б – спектры лазерного излучения, измеренные при максимальных P_{abs} . Поляризация лазера $E \parallel b$.

В данном эксперименте также наблюдался сдвиг длины волны лазерного излучения в сторону коротких волн при увеличении пропускания выходного зеркала резонатора, рис. 4.5.2 (б). В спектрах присутствовали эквидистантные спектральные линии, разделенные расстоянием $\Delta\lambda = 12,2$ нм при $\sim 1,85$ мкм (для $T_{OC} = 1,5\text{--}9\%$). Это можно объяснить эталоном Фабри-Перо. Свободный спектральный диапазон эталона Фабри-Перо толщиной t и с показателем преломления n_g при нормальном падении составляет $\Delta\lambda_{FSR} \approx \lambda_2/(n_g t)$. Из этой формулы получаем толщину эталона 71 мкм при $n = 2.0$, что хорошо согласуется с толщиной кристаллической плёнки.

Лазеры на кристаллических пластинках и плёнках кристалла $Tm:KY(MoO_4)_2$ работали в основной поперечной моде. Параметры качества луча были измерены стандартным методом ISO с фокусирующей линзой $M^2_{x,y} < 1.2$ ($x = b$, $y = c$).

4.6 Краткие выводы по главе 4

Ромбический кристалл калий-иттриевого двойного молибдата $Tm:KY(MoO_4)_2$ является перспективным кристаллом для создания эффективных лазеров, генерирующих в условно-безопасной для глаз спектральной области ~ 2 мкм. В таком кристалле возможно достигать высоких концентраций ионов-активаторов без заметного тушения люминесценции, в кристалле наблюдаются интенсивные, широкие и сильно поляризованные полосы поглощения и испускания, а также такой кристалл является КР активной средой. Слоистая структура кристалла $KY(MoO_4)_2$ способствует анизотропии его оптических свойств, а также позволяет легко изготавливать тонкие кристаллические пластинки и плёнки лазерного качества, подверженные упругой деформации, толщиной от нескольких мм до десятков мкм. Была продемонстрирована генерация лазера на длине волны ~ 2 мкм с пассивным охлаждением на тонких кристаллических пластинках (700 мкм) и плёнках (70 мкм) с дифференциальной эффективностью до 65.8% и выходной мощностью 0,88 Вт.

ГЛАВА 5. Спектрально-люминесцентные и генерационные свойства кристаллов $\text{Yb}^{3+}, \text{Li}^+ : \text{ZnWO}_4$ и $\text{Yb}^{3+} : \text{KY}(\text{MoO}_4)_2$

5.1 Структура кристаллов (Рентгенофазовый анализ)

Кристаллическая структура и фазовая чистота кристаллов были подтверждены с помощью рентгенофазового анализа. На рисунке 5.1.1 приведена рентгенограмма кристалла 5 ат.% $\text{Yb}^{3+}, \text{Li}^+ : \text{ZnWO}_4$. Рентгенофазовый анализ подробно описан в [76], было принято, что кристалл имеет состав $\text{Zn}_{0.964}\text{Yb}_{0.018}\text{Li}_{0.018}\text{WO}_4$. Фактическая концентрация ионов Yb (1.8 ат.%) была определена с помощью микронзондового анализа, и было принято, что ионы Yb и Li имеют равные атомные доли. Относительная интенсивность и положение дифракционных пиков образца хорошо согласуются с картой JCPDS (Объединенный комитет по порошковым дифракционным стандартам) № 96-210-1676 для недопированного кристалла ZnWO_4 . Других фаз, кроме моноклинной, не было обнаружено. Все это указывает на то, что выращенный образец кристалла ZnWO_4 однофазный. Рентгенограмма, измеренная для более широкого диапазона углов дифракции 2θ от 14,5 до 120°, была уточнена методом Ритвельда [77].

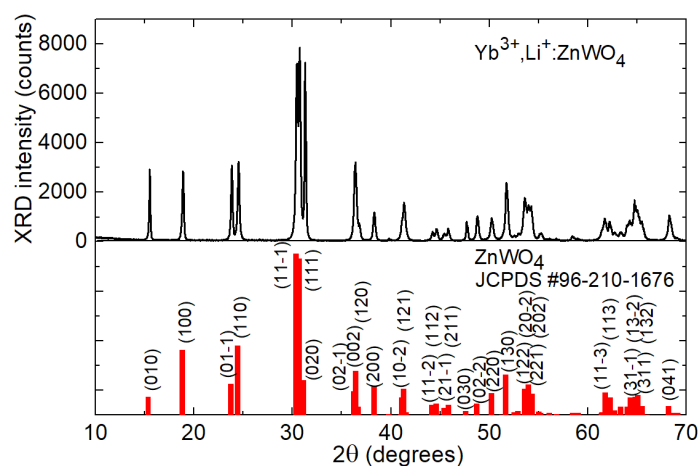


Рисунок 5.1.1 – Рентгенограмма кристалла 5 ат.% $\text{Yb}^{3+}, \text{Li}^+ : \text{ZnWO}_4$ [77]; теоретическая картина недопированного ZnWO_4 показана для сравнения (карта JCPDS № 96-210-1676), числа обозначают индексы Миллера, (hkl).

Кристалл $\text{Yb}^{3+}, \text{Li}^+:\text{ZnWO}_4$ является моноклинным, он принадлежит к пространственной группе $P2/c - C_{2h}^4$, № 13 и centrosymmetric точечной группе $2/m$. Постоянные решетки $a = 4.702(2) \text{ \AA}$, $b = 5.718(6) \text{ \AA}$, $c = 4.930(4) \text{ \AA}$, объём элементарной ячейки $V_{\text{calc}} = 132.571 \text{ \AA}^3$, угол моноклинности составляет $\beta = \alpha^{\wedge}c = 90.713(5)^\circ$ и теоретическая плотность кристалла $\rho_{\text{расч}} = 7.553 \text{ г/см}^3$.

Предполагалось, что ионы Yb^{3+} в кристалле ZnWO_4 заменят катионы Zn^{2+} . А для обеспечения компенсации заряда кристалл соактивировался одновалентными катионами лития (Li^+). Использование одновалентных катионов щелочных металлов в кристаллах с гетеровалентным механизмом компенсации заряда подробно описано в [77-78]. Для исследуемого кристалла ионные радиусы катионов, участвующих в процессе допирования, составляют 0.868 \AA (Yb^{3+}), 0.74 \AA (Zn^{2+}) и 0.76 \AA (Li^+) [79], поэтому ожидается увеличение объёма элементарной ячейки. Также предполагается, что существенное различие ионных радиусов Zn^{2+} , Yb^{3+} и Li^+ , а также различие их валентности приведет к неоднородному уширению спектральных полос поглощения и люминесценции ионов Yb^{3+} .

На рисунке 5.1.2 приведена структура кристалла ZnWO_4 , допированного ионами Yb^{3+} , Li^+ . Структура построена в соответствии с координатами атомов, которые были определены с помощью уточнения Ритвельда. W^{6+} связан с шестью ионами кислорода O^{2-} и образует искажённые октаэдры $[\text{WO}_6]$, которые имеют общие углы с восемью эквивалентными октаэдрами $[(\text{Zn}|\text{Yb}|\text{Li})\text{O}_6]$ и края с двумя эквивалентными октаэдрами $[\text{WO}_6]$, как показано в проекции на кристаллографическую плоскость b - c .

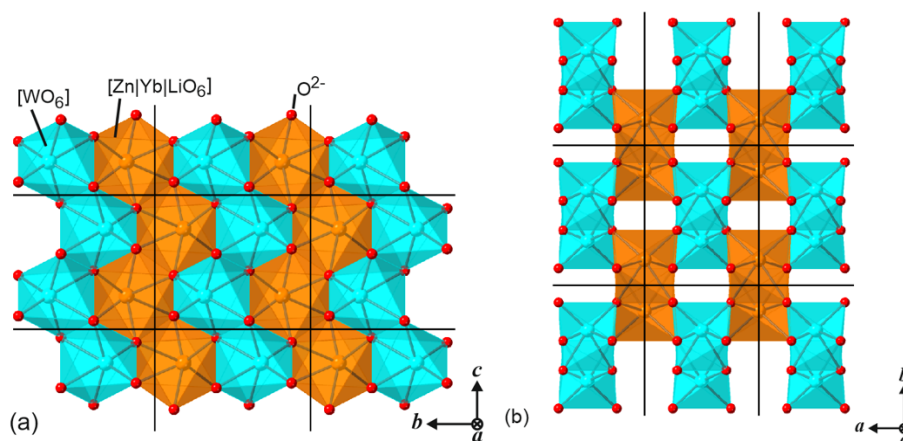


Рисунок 5.1.2 – Схематический фрагмент кристаллической структуры ZnWO_4 , допированного ионами Yb^{3+} и Li^+ : (а) проекция в плоскости b - c ; (б) проекция в плоскости a - b . Черными линиями обозначена элементарная ячейка.

Таким образом структура $\text{Yb}^{3+}, \text{Li}^+:\text{ZnWO}_4$ представляет собой зигзагообразные цепочки, образованные октаэдрами $[(\text{Zn}|\text{Yb}|\text{Li})\text{O}_6]$ с общими ребрами или октаэдрами $[\text{WO}_6]$ с общими ребрами, идущими параллельно оси c . Каждая цепочка, образованная $[(\text{Zn}|\text{Yb}|\text{Li})\text{O}_6]$, связана углами с четырьмя цепочками, образованными $[\text{WO}_6]$. Таким образом, структура содержит открытые каналы, также идущие параллельно оси c . В кристалле $\text{Yb}^{3+}, \text{Li}^+:\text{ZnWO}_4$ наблюдается естественный скол по плоскости (010).

5.2 Спектроскопия комбинационного рассеяния света

Поляризованные спектры КР кристалла 5 ат.% $\text{Yb}^{3+}, \text{Li}^+:\text{ZnWO}_4$ показаны на рис. 5.2.1. Для измерений был подготовлен прямоугольный образец. Были изучены все возможные направления распространения падающего и рассеянного света, для обозначения геометрий использовались обозначения Порто, $m(nk)l$ где m и l - направления распространения падающего и рассеянного света, а n и k - соответствующие состояния поляризации [80].

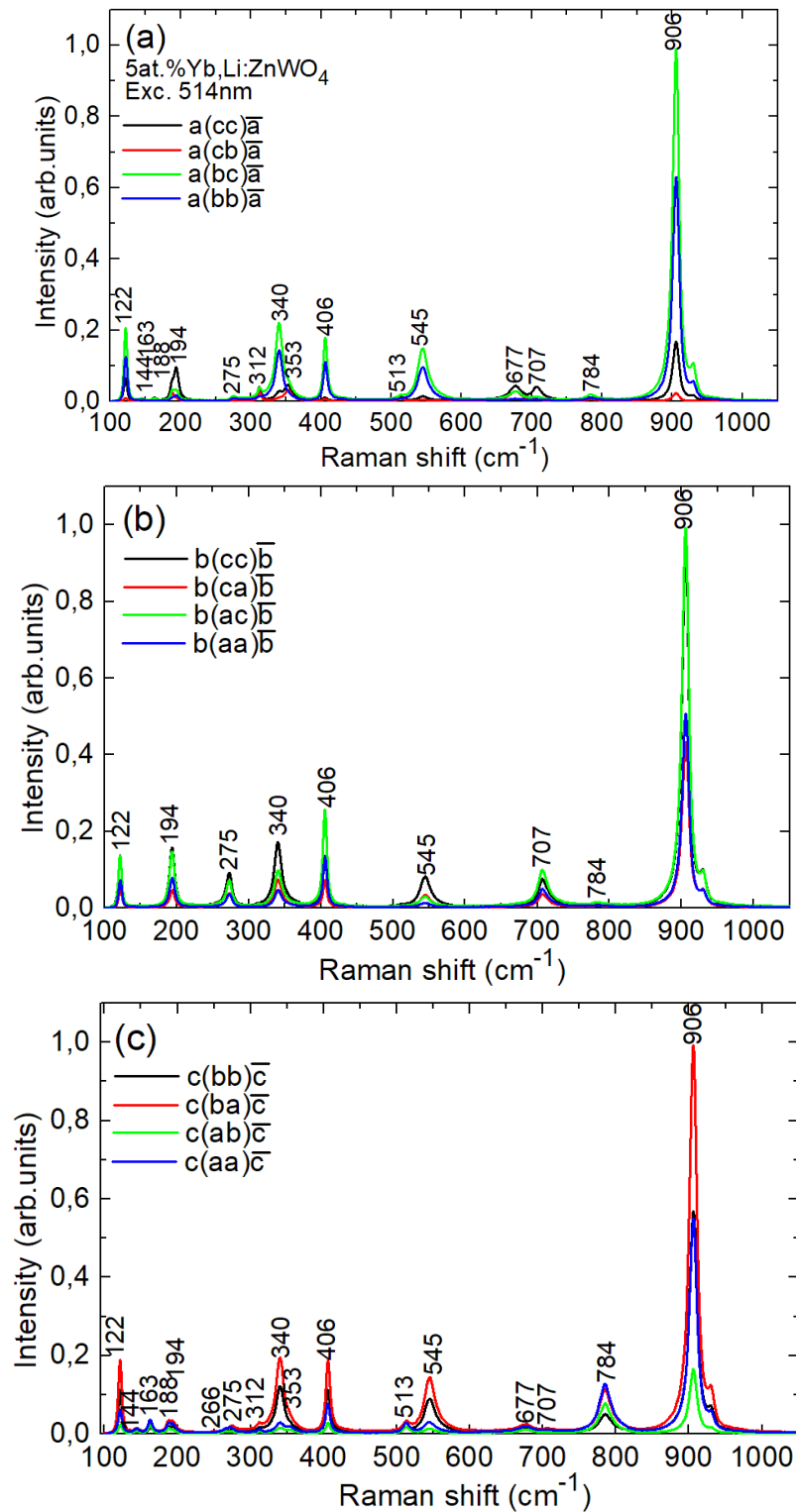


Рисунок 5.2.1 – Спектры КР кристалла 5 ат.% Yb³⁺, Li⁺:ZnWO₄ для геометрии (a) $a(ij)\bar{a}$, (b) $b(ij)\bar{b}$ и (c) $c(ij)\bar{c}$ (обозначения Порто). Цифры указывают частоты полос КР в см⁻¹. Длина волны возбуждающего излучения $\lambda_{\text{возб}} = 514$ нм.

Элементарная ячейка ZnWO₄ содержит две формульные единицы (Z = 2). Фактор-групповой анализ предсказывает в общей сложности 36

степеней свободы для 12 атомов в каждой элементарной ячейке. Соответствующие неприводимые представления в центре зоны Бриллюэна Γ ($k = 0$) равны $8A_g + 10B_g + 8A_u + 10B_u$, из которых четные колебания (g) являются комбинационно-активными, а остальные – ИК-активными [81, 82]. Таким образом, возможны 18 колебательных мод ($8A_g + 10B_g$). На зарегистрированных спектрах КР наблюдалось 17 мод из 18 возможных (кроме низкочастотной $<100 \text{ см}^{-1}$). Частоты колебательных мод обозначены на рис. 5.2.1, а их пиковые частоты и симметрии (A_g или B_g) перечислены в таблице 5.2.1.

Таблица 5.1 – Частоты колебательных мод, зарегистрированные в кристалле $\text{Yb}^{3+}, \text{Li}^+:\text{ZnWO}_4$ при комнатной температуре.

№	Частота, см^{-1}		Симметрия	Внутренняя мода
	$\text{Yb}^{3+}, \text{Li}^+:\text{ZnWO}_4$	ZnWO_4 [81]		
1	906	906.8	A_g	+
2	784	785.9	B_g	+
3	707	709.1	A_g	+
4	677	678.7	B_g	
5	545	546.4	A_g	
6	513	515.3	B_g	
7	406	406.9	A_g	+
8	353	355.4	B_g	
9	340	341.8	A_g	+
10	312	314.6	B_g	
11	275	274.4	A_g	
12	266	267.3	B_g	
13	194	195.3	A_g	
14	188	190.0	B_g	+
15	163	164.5	B_g	
16	144	146.3	B_g	
17	122	123.2	A_g	
18	–	91.5	B_g	

Спектры КР кристалла $\text{Yb}^{3+}, \text{Li}^+:\text{ZnWO}_4$ сильно поляризованы. Наиболее интенсивная полоса в спектрах находится на частоте 906.0 см^{-1} . Её полуширина $\Delta\nu$ составляет 11.9 см^{-1} . Эта полоса немного смещена и уширена по сравнению с нелегированным ZnWO_4 , для которого $\nu_1 = 906,8 \text{ см}^{-1}$ и соответствующее $\Delta\nu = 8,3 \text{ см}^{-1}$ (все значения

указаны для спектров, зарегистрированных при комнатной температуре) [81].

Спектры КР кристалла $\text{Yb:KY}(\text{MoO}_4)_2$ показаны на рис. 5.2.2. Они сильно поляризованы, наибольшая интенсивность полос наблюдается в геометрии $a(bb)a$. Все полосы в спектрах подразделяются на три группы колебаний [59,60]. Низкочастотный диапазон, $80\text{--}272\text{ см}^{-1}$, содержит поступательные T' - и вращательные R -моды катионов K , $Y|Yb$ и Mo . Полосы средней интенсивности, относящиеся к внутренним деформационным колебаниям (δ) мостиковых кислородных тетраэдров $[\text{MoO}_4]^{2-}$ наблюдаются в интервале частот $315\text{--}435\text{ см}^{-1}$. Высокочастотный диапазон $726\text{--}944\text{ см}^{-1}$ содержит интенсивные валентные колебания (ν) этих тетраэдров. Разрыв в спектрах комбинационного рассеяния (в диапазоне $500\text{--}700\text{ см}^{-1}$) обусловлен относительно слабой кислородной связью тетраэдров $[\text{MoO}_4]$ в плоскости слоя. Наиболее интенсивная и сильно поляризованная полоса КР появляется в спектре на частоте 865.6 см^{-1} с полушириной 18.8 см^{-1} . Она относится к одному из внутренних (ν) колебаний $[\text{MoO}_4]$. Максимальная энергия фононов составляет 944 см^{-1} .

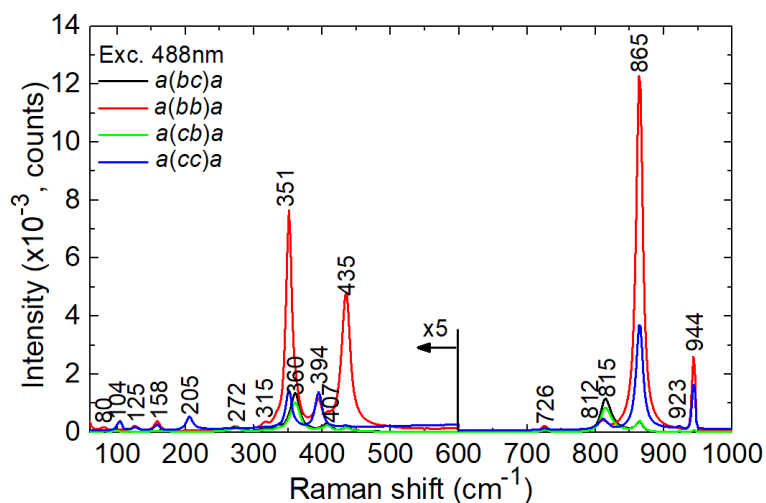


Рисунок 5.2.2 – Спектры КР кристалла 3 ат.% Yb^{3+} : $\text{KY}(\text{MoO}_4)_2$ для геометрии $a(ij)\bar{a}$, $i, j = b$ или c . Цифры указывают частоты полос КР в см^{-1} . Длина волны возбуждающего излучения $\lambda_{\text{возб}} = 514\text{ нм}$.

5.3 Спектры поперечных сечений поглощения

Кристалл $\text{Yb}^{3+}, \text{Li}^+:\text{ZnWO}_4$ является оптически двухосным [83]. Его оптические свойства описываются в рамках взаимно ортогональных осей оптической индикатрисы, обозначенных как N_p , N_m и N_g . Кристаллографическая ось b параллельна оси симметрии C_2 , а две другие расположены в ортогональной плоскости a - c , составляющей определенные углы с кристаллографическими осями.

Поперечные сечения поглощения ионов Yb^{3+} в кристалле 1.8 ат.% $\text{Yb}^{3+}, \text{Li}^+:\text{ZnWO}_4$ были определены по спектрам поглощения, измеренными при комнатной температуре. Результаты показаны на рисунке 5.3.1. Максимальное значение $\sigma_{\text{abs}} = 2.40 \times 10^{-20} \text{ см}^2$ на длине волны 972.7 нм, а соответствующая полуширина полосы поглощения составляет 8.3 нм (для поляризации света $E \parallel N_g$). Эта полоса поглощения соответствует бесфононной линии (ZPL) при комнатной температуре. В кристалле $\text{Yb}^{3+}, \text{Li}^+:\text{ZnWO}_4$ наблюдается заметная анизотропия сечений поглощения, что выражается отношениями $\sigma_{\text{abs}}(N_g) : \sigma_{\text{abs}}(N_p) = 2.6 : 1$ и $\sigma_{\text{abs}}(N_g) : \sigma_{\text{abs}}(N_m) = 4.7 : 1$ на длине волны ~ 0.97 мкм. Другая интенсивная и немного более широкая полоса поглощения появляется на длине волны 958.4 нм ($\sigma_{\text{abs}} = 1.84 \times 10^{-20} \text{ см}^2$ с полушириной 9.8 нм для $E \parallel N_g$). Обе полосы поглощения подходят для накачки лазерными диодами InGaAs. Можно предположить, что из-за широких линий поглощения $\text{Yb}^{3+}, \text{Li}^+:\text{ZnWO}_4$ будет менее чувствительным к температурному дрейфу длины волны лазерного диода.

По сравнению с другим хорошо известным моноклинным лазерным кристаллом вольфрамата, $\text{Yb}^{3+}, \text{Li}^+:\text{ZnWO}_4$, исследуемый материал показывает более низкие значения поперечного сечения пикового поглощения при гораздо более широких пиках поглощения.

Для кристалла $\text{Yb}^{3+}:\text{KLu}(\text{WO}_4)_2$ значение σ_{abs} достигает $11.8 \times 10^{-20} \text{ см}^2$ на 981.0 нм с полушириной всего 3.5 нм для поляризации света $E \parallel N_m$ [10]. В работе по исследованию $\text{Yb}^{3+}:\text{ZnWO}_4$ (без Li^+) сообщалось о максимальном сечении поглощения $2,6 \times 10^{-20} \text{ см}^2$ на $\sim 972 \text{ нм}$ [84]. Это согласуется с настоящими исследованиями для кристалла $\text{Yb}^{3+}, \text{Li}^+:\text{ZnWO}_4$.

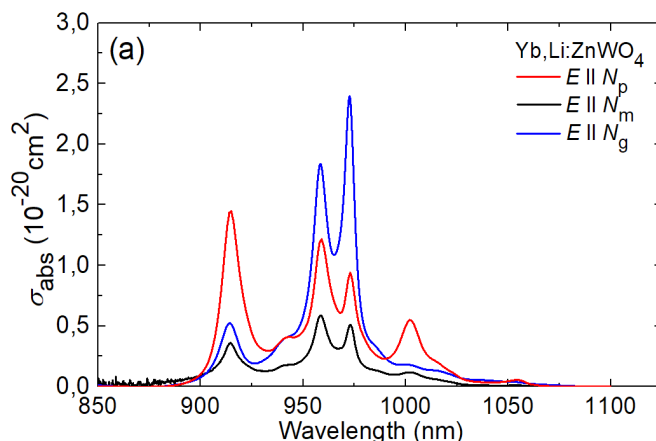


Рисунок 5.3.1 – Спектры поперечных сечений поглощения кристалла 1,8 ат.% $\text{Yb}^{3+}, \text{Li}^+:\text{ZnWO}_4$ при комнатной температуре (293 К): Поляризации света $E \parallel N_p, N_m, N_g$.

Для орторомбического кристалла $\text{KY}(\text{MoO}_4)_2$ известно только среднее значение показателя преломления ≈ 1.95 . В нём наблюдается сильное двулучепреломление $\Delta n = 0.018\text{--}0.087$ [84]. Оси оптической индикатрисы совпадают с кристаллографическими осями.

Спектр пропускания кристалла 3 ат.% $\text{Yb}:\text{KY}(\text{MoO}_4)_2$ был измерен для образца толщиной $\sim 1 \text{ см}$, рисунок 5.3.2 (а). Диапазон прозрачности кристаллической матрицы от 0.33 до 3.4 мкм. Структурированное поглощение на более длинных волнах (до 5 мкм) связано с ν -колебаниями тетраэдров MoO_4 .

Поглощение на длине волны $\sim 1 \text{ мкм}$ относится к энергетическому переходу ${}^2F_{7/2} \rightarrow {}^2F_{5/2}$ иона Yb^{3+} . Спектры поперечных сечений поглощения этого перехода для основных поляризаций света $E \parallel a, b, c$, рассчитанные по спектрам поглощения, приведены на

рисунке 5.3.2 (б). В спектрах наблюдается сильная поляризационная анизотропия.

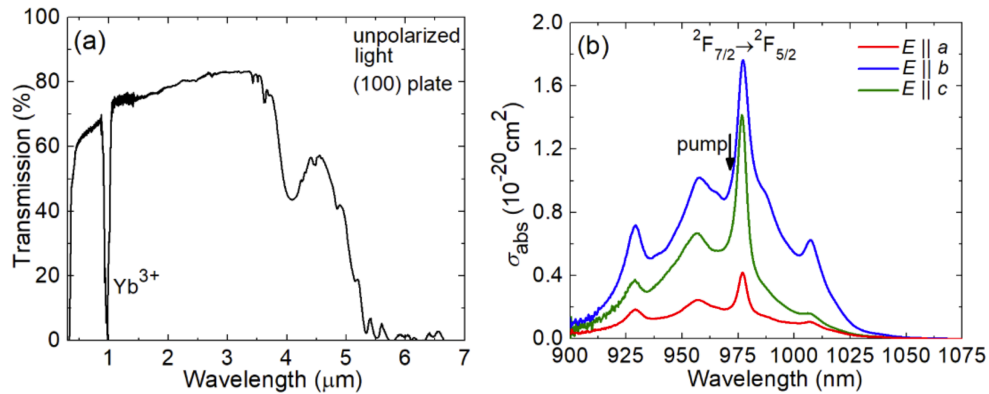


Рисунок 5.3.2 – Свойства поглощения кристалла 3 ат.% Yb:KY(MoO₄)₂: (а) неполяризованный спектр пропускания кристаллической пластинки с ориентацией (100) толщиной ~1 см; (б) спектры поперечных сечений поглощения σ_{abs} , поляризации света $E \parallel a$, b и c . Стрелка указывает длину волны накачки, использованную в лазерных экспериментах.

Максимальное значение σ_{abs} составляет $1.77 \times 10^{-20} \text{ см}^2$ на длине волны 977.1 нм, а полуширина полосы равна 19.6 нм для поляризации света $E \parallel b$. Эта длина волны соответствует переходу в бесфононную линию при комнатной температуре. Для двух других поляризаций света значения поперечных сечений поглощения ниже, что выражается отношениями $\sigma_{\text{abs}}(b) : \sigma_{\text{abs}}(c) = 1.26$ и $\sigma_{\text{abs}}(b) : \sigma_{\text{abs}}(a) = 4.2$ на длине волны ~980 нм. Эта анизотропия частично возникает из-за слоистой кристаллической структуры (значительное падение оптического поглощения света, поляризованного ортогонально плоскости слоя b-c) и частично из-за низкой симметрии позиции ионов Yb³⁺. Наблюдаемые широкие спектры поглощения Yb:KY(MoO₄)₂ показывают возможность использования лазерных диодов InGaAs, излучающих на длине волны ~980 нм для накачки активных лазерных сред, изготовленных из данного кристалла.

Наблюдаемые в кристалле Yb:KY(MoO₄)₂ поперечные сечения поглощения ниже, чем в моноклинном кристалле Yb:KY(WO₄)₂, для которого значение $\sigma_{\text{abs}} = 10.8 \times 10^{-20} \text{ см}^2$ на длине волны 981.0 нм, с

соответствующей полушириной линии 4.0 нм для поляризации света $E \parallel N_m$ [85].

5.4 Спектры поперечных сечений испускания и усиления.

Времена жизни люминесценции

Поперечные сечения вынужденного испускания, σ_{SE} , были определены из измеренных поляризованных спектров люминесценции с использованием уравнения Фюхтбауэра – Ладенбурга (формула 10). Чтобы избежать нежелательного влияния перепоглощения для измерения спектров люминесценции использовались тонкие (менее 100 мкм) сколотые пластинки кристалла $\text{Yb}^{3+}, \text{Li}^+:\text{ZnWO}_4$. Результаты показаны на рис. 5.4.1.

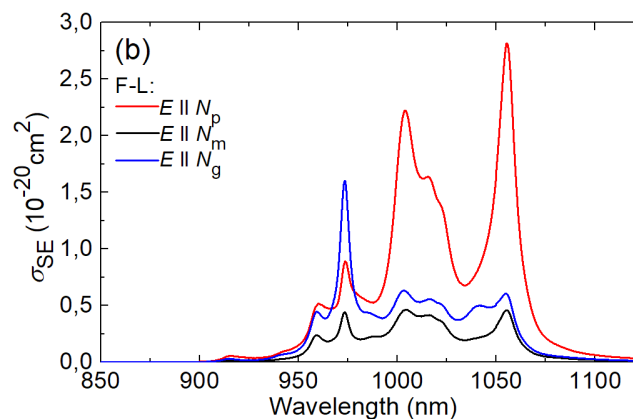


Рисунок 5.4.1 – Поперечные сечения вынужденного испускания кристалла 1,8 ат.% $\text{Yb}^{3+}, \text{Li}^+:\text{ZnWO}_4$. Поляризации света $E \parallel N_p, N_m, N_g$.

Поперечные сечения вынужденного испускания были так же рассчитаны с использованием альтернативного метода расчёта, то есть метода соответствия (формула 11) [50, 51].

Сравнение результатов рассчитанных поперечных сечений вынужденного испускания, полученных с помощью Фюхтбауэра – Ладенбурга (формула 10) и метода соответствия (формула 11), для поляризации света $E \parallel N_p$ показано на рисунке 5.4.2.

Два использованных метода расчёта достаточно хорошо согласуются, что свидетельствует о правильности выбранного значения τ_{rad} (0.37 ± 0.02 мс), а также о слабом влиянии перепоглощения на измеренные спектры люминесценции.

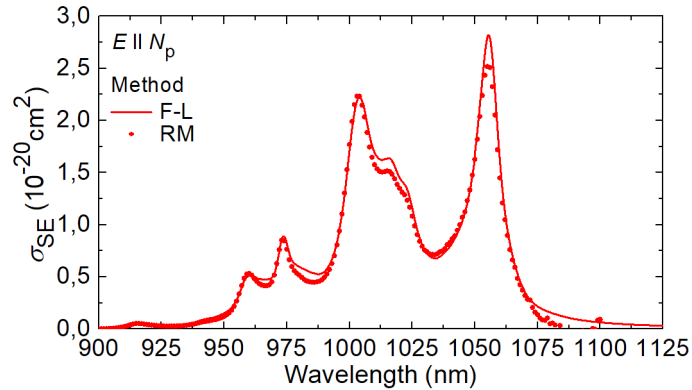


Рисунок 5.4.2 – Поперечные сечения вынужденного испускания, σ_{SE} , ионов Yb^{3+} в кристалле $\text{Yb}^{3+}, \text{Li}^+ : \text{ZnWO}_4$, рассчитанные с использованием уравнения Фюхтбауэра – Ладенбурга (F-L) и методом соответствия (RM). Поляризация света $\mathbf{E} \parallel N_p$.

Максимальное значение поперечного сечения вынужденного испускания $\sigma_{\text{SE}} = 2.81 \times 10^{-20} \text{ см}^2$ наблюдается на длине волны 1055.6 нм и соответствующая полуширина полосы $\Delta\lambda_{\text{em}} = 12.1$ нм (для $\mathbf{E} \parallel N_p$). Аналогично переходам в поглощении наблюдается сильная анизотропия поперечных сечений вынужденного испускания, а именно $\sigma_{\text{SE}}(N_p) : \sigma_{\text{SE}}(N_g) = 4.6 : 1$ и $\sigma_{\text{SE}}(N_p) : \sigma_{\text{SE}}(N_m) = 6.2 : 1$ на ~ 1.06 мкм. Это свидетельствует о том, что излучение лазера на кристалле $\text{Yb}^{3+}, \text{Li}^+ : \text{ZnWO}_4$ будет линейно поляризованным. В спектрах σ_{SE} наблюдается ещё одна более широкая полоса с центром на длине волны 1004.1 нм с полушириной = 28.5 нм (для $\mathbf{E} \parallel N_p$).

По сравнению с кристаллом $\text{Yb}^{3+} : \text{KLu}(\text{WO}_4)_2$ максимальные значения σ_{SE} в кристалле $\text{Yb}^{3+}, \text{Li}^+ : \text{ZnWO}_4$ близки, но спектры излучения намного шире. Для $\text{Yb}^{3+} : \text{KLu}(\text{WO}_4)_2$ $\sigma_{\text{SE}} = 2.64 \times 10^{-20} \text{ см}^2$ на 1026.6 нм, а соответствующая полуширина $\Delta\lambda_{\text{em}} = 10.2$ нм [10]. Максимальное

значение σ_{SE} в кристалле $Yb^{3+}:MgWO_4$ $\sigma_{SE} = 2.64 \times 10^{-20} \text{ cm}^2$ на 1056.7 нм (для $E \parallel N_m$), полуширина 19 нм [86].

На рисунке 5.4.3 приведены рассчитанные по спектрам люминесценции поперечные сечения вынужденного испускания, σ_{SE} , для кристалла $Yb:KY(MoO_4)_2$. Максимум σ_{SE} составляет $3.70 \times 10^{-20} \text{ cm}^2$ на длине волны 1008.0 нм, а полуширина $\Delta\lambda_{em} = 37.0$ нм для поляризации света с высоким коэффициентом усиления $E \parallel b$. Спектры излучения также сильно поляризованы, что выражается отношениями $\sigma_{SE}(b): \sigma_{SE}(c) = 3.9$ и $\sigma_{SE}(b): \sigma_{SE}(a) = 6.0$ на длине волны ~ 1.01 мкм. Это является предпосылкой для генерации линейно поляризованного лазерного излучения.

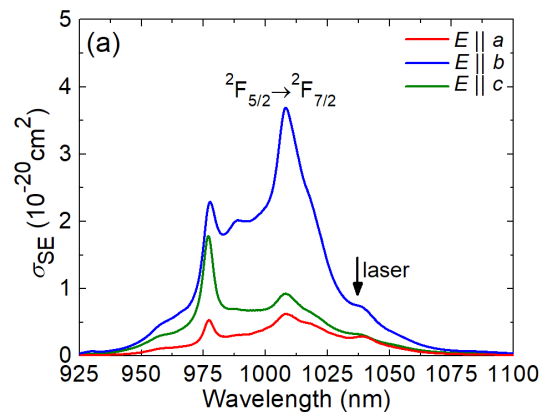


Рисунок 5.4.3 – Спектры поперечных сечений вынужденного испускания ионов Yb^{3+} в кристалле $KY(MoO_4)_2$ для поляризаций света $E \parallel a, b$ и c . Стрелка указывает наблюдаемую длину волны лазера.

По сравнению с аналогичным кристаллу $Yb^{3+}:KY(MoO_4)_2$ моноклинным кристаллом двойного вольфрамата $Yb^{3+}:KY(WO_4)_2$, для которого $\sigma_{SE} = 3.2 \times 10^{-20} \text{ cm}^2$ при 1021.9 нм с $\Delta\lambda_{em} = 30.2$ нм для $E \parallel N_m$ [85], кристалл $Yb:KY(MoO_4)_2$ обладает более высокими значениями поперечных сечений вынужденного испускания и более широкой полосой излучения. Эти особенности являются очень привлекательными для изготовления широко настраиваемых лазеров и лазеров с ультракороткими импульсами на длине волны ~ 1 мкм.

Результаты расчёта поперечных сечений усиления, выполненные для перехода ${}^2F_{5/2} \leftrightarrow {}^2F_{7/2}$ ионов Yb^{3+} в кристалле ZnWO_4 показаны на рисунке 5.4.4 для поляризаций света с высоким коэффициентом усиления $\mathbf{E} \parallel N_p$ и $\mathbf{E} \parallel N_g$. Они вычисляются для прогнозирования возможных длин волн лазера для различных отношений инверсии β . Для поляризации с большим усилением $\mathbf{E} \parallel N_p$, в спектрах усиления доминирует локальный пик на длине волны ~ 1056 нм. Полуширина полосы усиления $\Delta\lambda_{\text{gain}}$ составляет 11.6 нм (для $\beta = 0.15$). Для поляризации $\mathbf{E} \parallel N_g$, при увеличении степени инверсии наблюдается несколько локальных максимумов в спектрах усиления на $\sim 1056, 1040, 1022$ и 1003 нм. Полуширина полосы усиления шире, $\Delta\lambda_{\text{gain}} = 22.2$ нм (при том же $\beta = 0.15$).

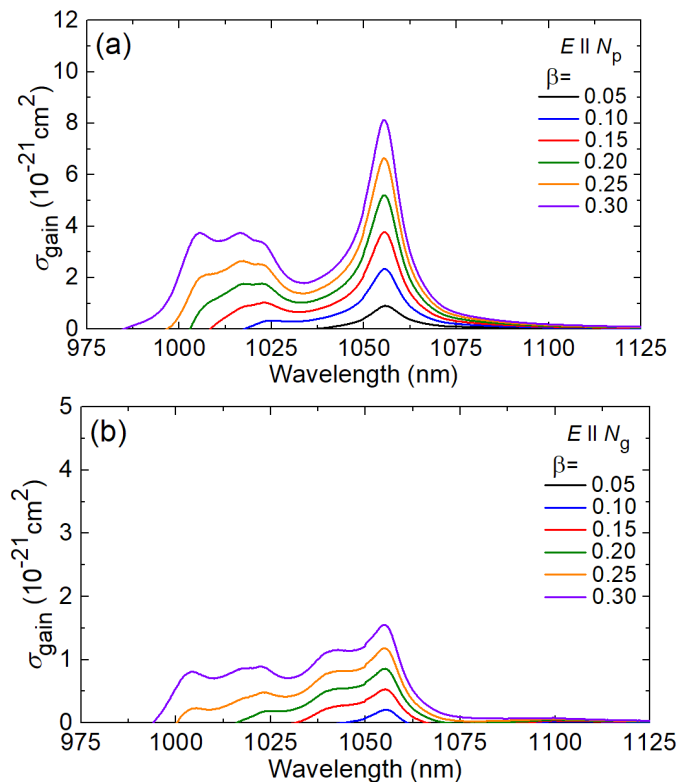


Рисунок 5.4.4 – Спектры поперечных сечений усиления перехода ${}^2F_{5/2} \leftrightarrow {}^2F_{7/2}$ ионов Yb^{3+} в кристалле ZnWO_4 . Спектры рассчитаны для поляризации света: (а) $\mathbf{E} \parallel N_p$ и (б) $\mathbf{E} \parallel N_g$.

Затухание люминесценции ионов Yb^{3+} в кристалле 1.4 ат.% $\text{Yb}^{3+}, \text{Li}^+:\text{ZnWO}_4$ было исследовано при комнатной температуре. Для

измерения использовались тонкие (менее 100 мкм) сколотые пластины, чтобы избежать перепоглощения люминесценции. Люминесценция возбуждалась излучением на длине волны 960 нм. Затухание люминесценции исследовалось с уровня ${}^2F_{7/2}$ на длине волны ~ 1030 нм, рисунок 5.4.5.

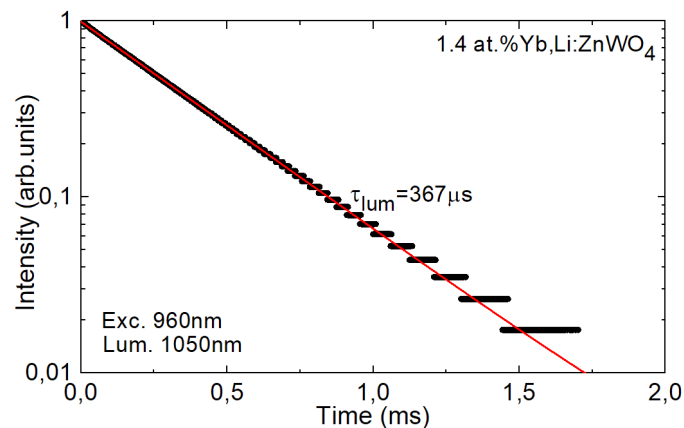


Рисунок 5.4.5 – Кривая затухания люминесценции кристалла 1.4 ат.% $\text{Yb}^{3+}, \text{Li}^+:\text{ZnWO}_4$, $\lambda_{\text{возб}} = 960$ нм, $\lambda_{\text{lum}} = 1050$ нм. Символы – экспериментальные данные, линия – моноэкспоненциальная аппроксимация.

Кривая затухания носит моноэкспоненциальный характер, аппроксимируется выражением $I_{\text{lum}}(t) = I_0 \times \exp(-t/\tau_{\text{lum}})$, где $\tau_{\text{lum}} = 367$ мкс – время жизни люминесценции. Такое поведение согласуется расположением ионов Yb^{3+} в позициях одного типа (симметрия: C_2).

Для кристалла $\text{Yb}^{3+}:\text{ZnWO}_4$ (без ионов Li^+) [84] время жизни люминесценции было определено как 644 мкс, измерения в [84] проводились на объёмном кристалле, поэтому это значение может быть завышено из-за эффекта перепоглощения.

Согласно расчёту поперечных сечений вынужденного испускания двумя независимыми методами (уравнение Фюхтбауэра – Ладенбурга и метод соответствия), было получено радиационное время жизни $\tau_{\text{rad}} = 0.37 \pm 0.02$ мс. Таким образом, квантовая эффективность люминесценции, рассчитанная для кристалла $\text{Yb}^{3+}, \text{Li}^+:\text{ZnWO}_4$ $\eta_q = \tau_{\text{lum}}/\tau_{\text{rad}}$

близка к единице. Это согласуется с постулатом [87] о том, что безызлучательная релаксация является слабой, когда запрещенная зона до нижележащего мультиплета ($\Delta E = 9481 \text{ см}^{-1}$ для $\text{Yb}^{3+}, \text{Li}^+:\text{ZnWO}_4$) как минимум в 4 раза больше, чем максимальная энергия фононов основной матрицы ($h\nu_{\text{ph}} = 906 \text{ см}^{-1}$ для $\text{Yb}^{3+}, \text{Li}^+:\text{ZnWO}_4$).

На рисунке 5.4.6 приведены результаты расчёта поперечных сечений усиления, выполненные для перехода ${}^2\text{F}_{5/2} \leftrightarrow {}^2\text{F}_{7/2}$ ионов Yb^{3+} в кристалле: $\text{KY}(\text{MoO}_4)_2$ для поляризации света $\mathbf{E} \parallel \mathbf{b}$. Для малых значений $\beta < 0.03$ спектры усиления очень плоские и широкие (от ~ 1040 до 1100 нм). Для промежуточных отношений инверсии $0.05 < \beta < 0.10$ в спектрах появляется локальный пик на длине волны $\sim 1039 \text{ нм}$. Для еще более высоких отношений инверсии наблюдается еще один максимум на более короткой длине волны $\sim 1019 \text{ нм}$. В соответствии с исследованиями люминесценции для $\beta = 0.15$ ширина полосы усиления $\Delta\lambda_g$ составляет 33.0 нм .

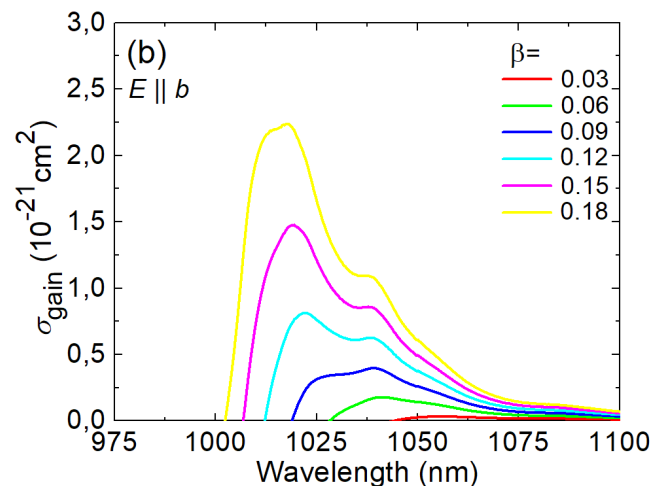


Рисунок 5.4.5 – Спектры поперечных сечений усиления, выполненные для перехода ${}^2\text{F}_{5/2} \leftrightarrow {}^2\text{F}_{7/2}$ ионов Yb^{3+} в кристалле: $\text{KY}(\text{MoO}_4)_2$, поляризация света $\mathbf{E} \parallel \mathbf{b}$.

Кривая затухания люминесценции кристаллической плёнки, сколотой от объёмного кристалла $\text{Yb}^{3+}:\text{KY}(\text{MoO}_4)_2$, построенная в полулогарифмическом масштабе, приведена на рисунке 5.4.6. Люминесценция возбуждалась нс импульсами от генератора,

настроенного на длину волны 930 нм. Для исключения эффекта перепоглощения люминесценции в измерениях использовалась тонкая (~30 мкм) сколотая плёнка. Затухание люминесценции регистрировалось на длине волны $\lambda_{lum} = 1030$ нм. Кривая затухания носит моноэкспоненциальный характер, что соответствует одному типу позиций расположения ионов Yb^{3+} . Время затухания люминесценции $\tau_{lum} = 458$ мкс больше, чем у моноклинных кристаллов $Yb:KY(WO_4)_2$ ($\tau_{lum} = 231$ мкс [85]).

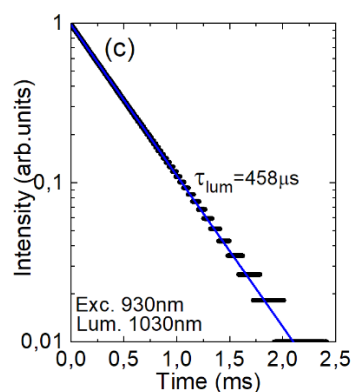


Рисунок 5.4.6 – Кривая затухания люминесценции для сколотой плёнки кристалла $Yb^{3+}:KY(MoO_4)_2$, $\lambda_{exc} = 930$ нм, $\lambda_{lum} = 1030$ нм, символы: экспериментальные данные, линия: одноэкспоненциальная аппроксимация.

5.5 Низкотемпературная спектроскопия

5.5.1 Штарковское расщепление уровней энергии ионов Yb^{3+}

Для определения штарковского расщепления мультиплетов Yb^{3+} в $ZnWO_4$ были измерены поляризованные спектры поглощения и люминесценции в интервале температур 6–300 К, рис. 5.5.1. Исследования проводились для следующих поляризаций света: $E \parallel a$ и $E \parallel b$ (N_p) в поглощении и $E \parallel c$ и $E \parallel b$ (N_p) в люминесценции. Для ионов Yb^{3+} в позициях с симметрией C_2 существует всего $J+1/2$ штарковских подуровня для каждого мультиплета $^{2S+1}L_J$, обозначаемых как 0..3 для $^2F_{7/2}$ и 0'..2' для $^2F_{5/2}$ соответственно. Интерпретация электронных переходов проводилась с учетом спектров КР.

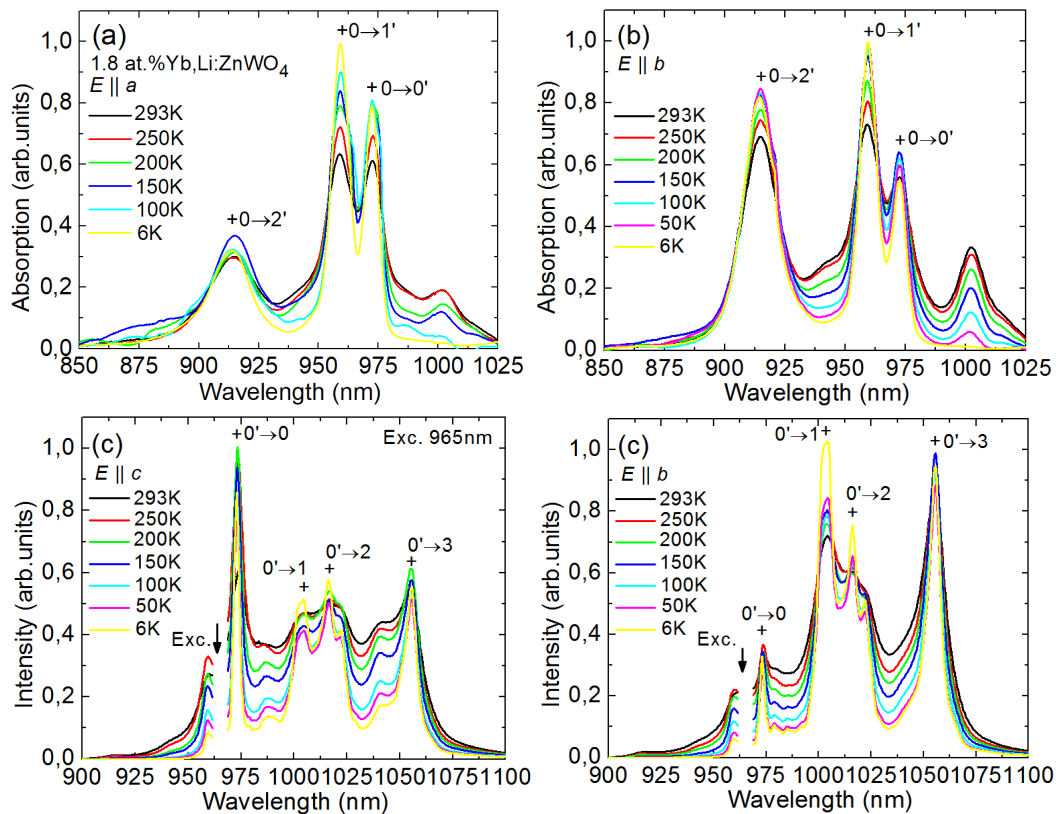


Рисунок 5.5.1 – Низкотемпературная (6–293 К) спектроскопия кристалла 1,8 ат.% $\text{Yb}^{3+}, \text{Li}^+:\text{ZnWO}_4$: (а, б) спектры поглощения для поляризаций света (а) $E \parallel a$ и (б) $E \parallel b$; (в, г) спектры люминесценции для поляризаций света (в) $E \parallel c$ и (г) $E \parallel b$, $\lambda_{\text{возб}} = 965$ нм.

При температуре 6 К электрон-фононная связь сильно подавляется, однако для ионов Yb^{3+} в кристалле ZnWO_4 наблюдается большая ширина бесфононной линии ($\Delta\lambda_{\text{ZPL}} = 3,0$ нм), т.е. перехода между нижними штарковскими подуровнями двух мультиплетов, или $0 \leftrightarrow 0'$ переход.

По сравнению с моноклинным кристаллом $\text{Yb}^{3+}:\text{KY}(\text{WO}_4)_2$ ($\Delta\lambda_{\text{ZPL}} < 0.1$ нм для $E \parallel N_p$) [88], бесфононная линия в кристалле $\text{Yb}^{3+}, \text{Li}^+:\text{ZnWO}_4$ намного шире. Это заметное различие можно объяснить неоднородным уширением перехода бесфононной линии, связанным с различием ионных радиусов ионов Yb^{3+} , Li^+ и Zn^{2+} ($R_{\text{Yb}} = 0,868$, $R_{\text{Li}} = 0,76$ Å и $R_{\text{Zn}} = 0,74$ Å для VI-кратной координации кислорода [79]). Бесфононная линия в поглощении имеет плохо

разрешенную слегка асимметричную форму. Подобное уширение бесфоновой линии недавно было обнаружено для изоструктурного кристалла MgWO_4 , допированного ионами Yb^{3+} , в котором $\Delta\lambda_{\text{ZPL}} = 3.3$ нм для $E \parallel N_m$ [86].

Схема энергетических уровней ионов Yb^{3+} в кристалле ZnWO_4 показана на рисунке 5.5.2 (а). Бесфоновая линия имеет энергию $E_{\text{ZPL}} = 10285 \text{ см}^{-1}$. При температуре 6 К соответствующая переходу длина волны $\lambda = 972.3$ нм.

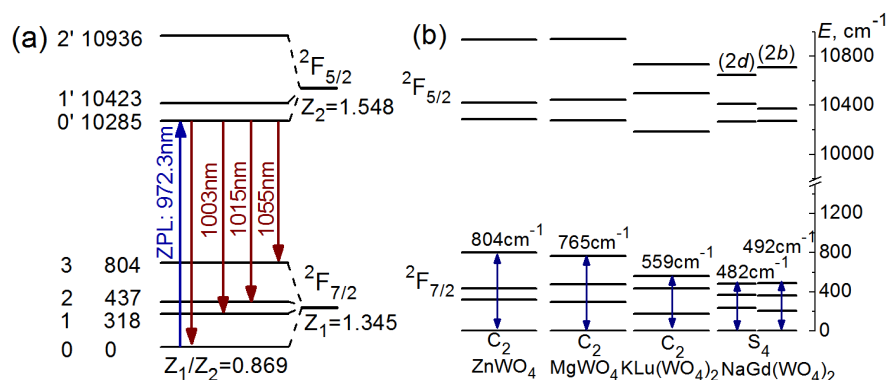


Рисунок 5.5.2 – Расщепление энергетических уровней ионов Yb^{3+} в кристаллическом поле кристалла ZnWO_4 : (а) Схема штарковских подуровней; синяя стрелка обозначает бесфоновую линию (ZPL) при поглощении, красные стрелки обозначают люминесцентные переходы при 6 К. $Z_1(Z_2)$ - статистические суммы для нижних (верхних) мультиплетов; (б) сравнение расщепления кристаллического поля для ионов Yb^{3+} в кристаллах вольфрамата ZnWO_4 , MgWO_4 [86], $\text{KLu(WO}_4)_2$ [10] и $\text{NaGd(WO}_4)_2$ [89].

Полное штарковское расщепление основного состояния $\Delta E(^2F_{7/2}) = 804 \text{ см}^{-1}$. В целом, большее значение $\Delta E(^2F_{7/2})$ подразумевает лучшие возможности для настройки длины волны и более длинные достижимые длины волны лазера. Расщепление основного состояния ионов Yb^{3+} в кристалле ZnWO_4 превосходит расщепление других известных кристаллов вольфраматы, используемых для лазеров с диодной накачкой на ~ 1 мкм, таких как моноклинный (пр. гр. $P2/c$) упорядоченный Yb:MgWO_4 , 765 см^{-1} [86], моноклинный (пр. гр. $C2/c$) упорядоченный $\text{Yb:KLu(WO}_4)_2$, 559 см^{-1} [10], и тетрагональный (пр. гр.

$I4_1/a$) неупорядоченный кристалл $\text{Yb}:\text{NaGd}(\text{WO}_4)_2$, 482 cm^{-1} ($2d$ позиции) и 492 cm^{-1} ($2b$ позиции) [89], рис. 5.5.2 (б). Для всех рассмотренных моноклинных кристаллов симметрия позиций ионов Yb^{3+} одинакова – C_2 , для тетрагонального кристалла – с S_4 .

Так же, как и в кристалле ZnWO_4 , для ионов Yb^{3+} в кристалле $\text{Yb}^{3+}:\text{KY}(\text{MoO}_4)_2$ каждый мультиплет $^{2S+1}L_J$ разбивается на $J + 1/2$ штарковских подуровня, которые пронумерованы как $0 \dots 3$ для основного состояния ($^2F_{7/2}$) и $0' \dots 2'$ для возбужденного состояния ($^2F_{5/2}$). Для определения их энергий были измерены спектры неполяризованного поглощения и люминесценции при низкой температуре (6 К), рис. 5.5.3.

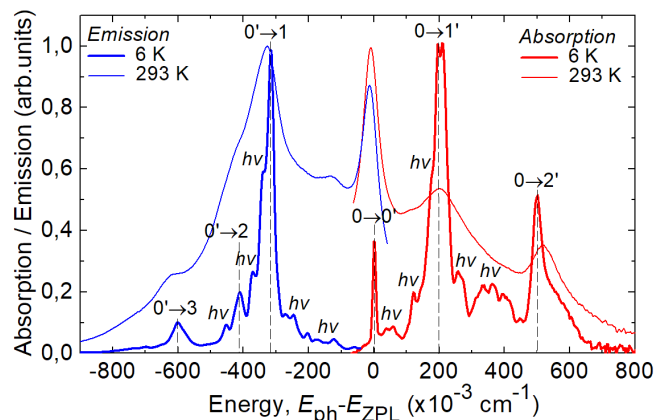


Рисунок 5.5.3 – Спектры поглощения и люминесценции кристалла $\text{Yb}^{3+}:\text{KY}(\text{MoO}_4)_2$ в зависимости от разности энергий ($E_{\text{ph}} - E_{\text{ZPL}}$), где $E_{\text{ph}} = h(c/\lambda)$ – энергия фотона, а $E_{\text{ZPL}} = 10246 \text{ cm}^{-1}$ – энергия бесфононной линии (ZPL), измеренная при низкой (6 К) и комнатной (293 К) температурах в неполяризованном свете. $\lambda_{\text{возб}} = 976 \text{ nm}$. Электронные переходы обозначены как $i \leftrightarrow j'$, фононные полосы – как $h\nu$.

Бесфононная линия ионов Yb^{3+} в кристалле $\text{Yb}^{3+}:\text{KY}(\text{MoO}_4)_2$ наблюдается на уровне энергии 10246 cm^{-1} , что соответствует длине волны 976.0 nm (при температуре 6 К). Полный набор уровней энергии в кристалле $\text{Yb}^{3+}:\text{KY}(\text{MoO}_4)_2$ равен $^2F_{7/2} = (0, 315, 411, 601) \text{ cm}^{-1}$ и $^2F_{5/2} = (10246, 10440, 10749) \text{ cm}^{-1}$. На рисунке 5.5.4 приведена схема уровней энергии и длины волн электронных переходов ионов Yb^{3+} в кристалле

КУ(МоО₄)₂ при поглощении и испускании. Полученное для кристалла Yb³⁺:КУ(МоО₄)₂ значение расщепления основного и возбуждённого состояния отличается от расщепления в моноклинном кристалле Yb:КУ(WO₄)₂, для которого ²F_{7/2} = (0, 169, 407, 568) см⁻¹ и ²F_{5/2} = (10187, 10476, 10695) см⁻¹ [90]. Штарковское расщепление основного состояния ΔE (²F_{7/2}) ионов Yb³⁺ в кристалле КУ(МоО₄)₂ составляет 60 см⁻¹.

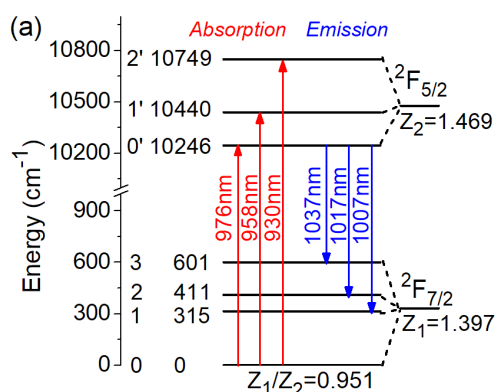


Рисунок 5.5.4 – Расщепление энергетических уровней иона Yb³⁺ в кристаллическом поле кристалла КУ(МоО₄)₂, стрелки указывают переходы в поглощении и в испускании при 6 К.

5.5.2 Применимость «правила барицентров» для исследуемых кристаллов

Известно, что для всех редкоземельных ионов энергия барицентра любого изолированного мультиплета ^{2S+1}L_J 4ⁿ линейно изменяется с энергией барицентра любого другого мультиплета. Это выражается так называемым графиком барицентров [91], На рисунке 5.5.5. эта связь выражается графиком зависимости барицентра возбуждённого уровня от основного. Энергии барицентров $\langle E(^2F_{5/2}) \rangle$ и $\langle E(^2F_{7/2}) \rangle$ для кристаллов Yb³⁺,Li⁺:ZnWO₄ и Yb³⁺:КУ(МоО₄)₂ хорошо согласуются с линейной аппроксимацией этого графика, выраженного уравнением $E(^2F_{5/2}) = 10166.6 + 0.997 \times E(^2F_{7/2})$ [в см⁻¹], описывающего зависимость барицентра возбуждённого уровня редкоземельного иона от основного состояния. В выражении $E_0 = 10166.6$ см⁻¹ имеет смысл

энергии возбужденного Yb^{3+} состояния, предполагающее свободный ион. Этот анализ подтверждает правильность построенной схемы уровней энергии.

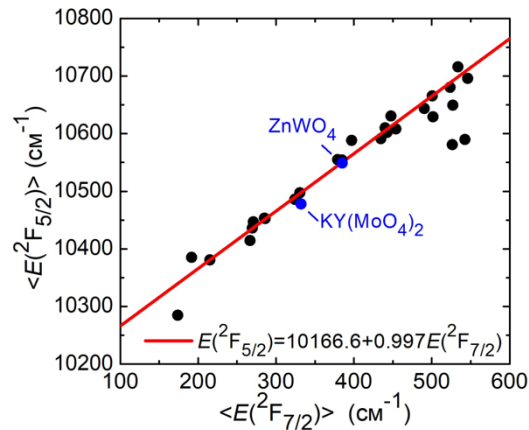


Рисунок 5.5.5 – Зависимость барицентра возбуждённого уровня от основного, показывающая положение кристаллов $\text{Yb}^{3+}, \text{Li}^+:\text{ZnWO}_4$ и $\text{Yb}^{3+}:\text{KY}(\text{MoO}_4)_2$ (синие кружки).

5.6 Лазерные эксперименты

5.6.1 Экспериментальная лазерная установка

Для проведения лазерных экспериментов на кристаллах вольфраматов из выращенного кристалла были подготовлены образцы с полированными входными и выходными гранями. Для исследования генерационных свойств была собрана установка, в которой исследуемый образец был помещён в полусферический резонатор, образованный плоским зеркалом накачки и набором вогнутых выходных зеркал (OCs) с пропусканием на длине волны предполагаемой лазерной генерации ТОС = 3%, 5% и 10%. Активный элемент был обмотан индиевой фольгой со всех четырёх боковых сторон для эффективного теплоотвода и установлен в медный держатель (рис. 5.6.1), охлаждаемый циркулирующей водой ($T = 12^\circ\text{C}$). Накачка лазерного элемента осуществлялась с использованием InGaAs лазерного диода на 968 нм.

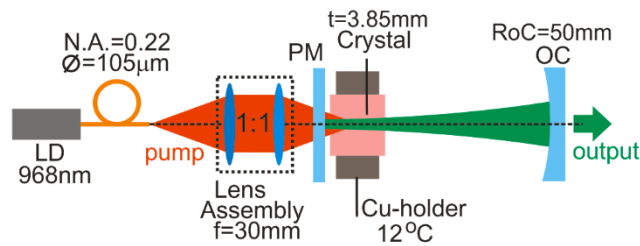


Рисунок 5.6.1 – Схема лазера на 1.8 ат.% $\text{Yb}^{3+}, \text{Li}^+:\text{ZnWO}_4$ с диодной накачкой: LD – лазерный диод, PM – зеркало накачки, OC – выходное зеркало.

Структурные особенности кристаллов двойных вольфраматов (в том числе кристалла $\text{Yb}^{3+}:\text{KY}(\text{MoO}_4)_2$), а именно совершенная спайность, позволяют изготовить для лазерных экспериментов образцы кристаллических плёнок и пластинок толщиной до нескольких десятков мкм. В настоящем эксперименте изготовленный образец имел толщину $t = 286$ мкм. Образец был получен методом механического откалывания вдоль плоскости естественного скола с использованием острого лезвия. Никаких последующих обработок (например, полировок и диэлектрических покрытий поверхностей, полученных после скола) не применялось.

Схема лазерной установки для проведения экспериментов по получению генерации на кристаллической пластинке, полученной из кристалла $\text{KY}(\text{MoO}_4)_2$ показана на рис. 5.6.2 (а). Кристаллическая пластина была установлена в компактном лазерном резонаторе с микрочип-конфигурацией, образованном плоским зеркалом накачки (PM) с высоким пропусканием на длине волны накачки и высоким отражением в диапазоне ожидаемых длин волн лазера, а также набором плоских выходных зеркал (OC) с пропусканием 0,5%, 1%, 2,5%, 5% и 10% (T_{OC}). Входное и выходное зеркала резонатора были аккуратно прижаты к кристаллической пластине. Фотография стенда с экспериментальной лазерной установкой и реализованным на ней лазером на кристалле $\text{KY}(\text{MoO}_4)_2$ показана на рисунке 5.6.2 (б)

Использовалось только пассивное охлаждение. Кристаллическая пластина накачивалась с торца лазерным диодом на основе InGaAs, излучающем на длине волны 968 нм.

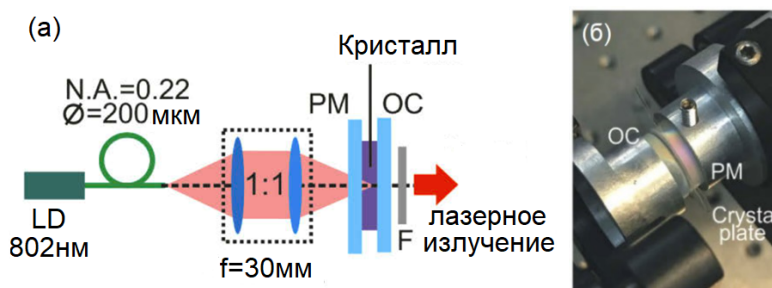


Рисунок 5.6.2 – (а) Схема микрочип-лазера с диодной накачкой на кристалле $\text{Yb:KY}(\text{MoO}_4)_2$: LD – лазерный диод, PM – входное зеркало резонатора, OC – выходное зеркало, F – фильтр; (б) фотография лазера на кристаллической пластинке $\text{KY}(\text{MoO}_4)_2$.

5.6.2 Выходные характеристики микрочип-лазера на основе кристаллических пластинок $\text{Yb}^{3+}:\text{KY}(\text{MoO}_4)_2$

Зависимость выходной мощности от поглощенной мощности накачки была линейной для всех значений пропускания выходного зеркала, рис. 5.6.3. Максимальная выходная мощность $\text{Yb}^{3+}:\text{KY}(\text{MoO}_4)_2$ лазера на кристаллической пластинке в микрочип-конфигурации резонатора составила 0,81 Вт на длине волны 1021-1044 с высоким дифференциальным КПД $\eta = 76,4\%$ в зависимости от поглощенной мощности накачки. Порог лазерной генерации составил всего 56 мВт.

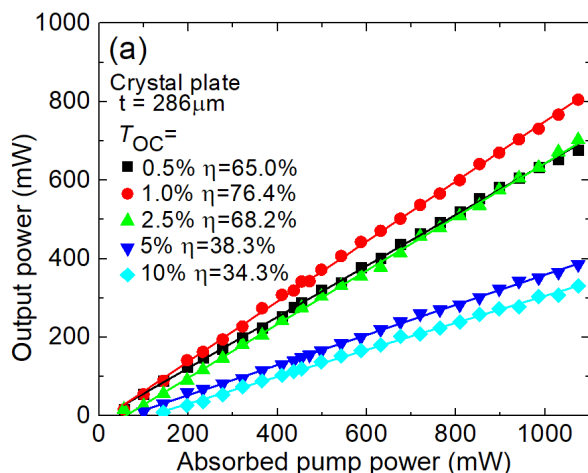


Рисунок 5.6.3 – Выходные характеристики микрочип-лазера на кристалле на кристалле $\text{Yb}^{3+}:\text{KY}(\text{MoO}_4)_2$ с диодной накачкой.

Лазер работал на основной поперечной моде с естественно выбранной линейной поляризацией ($E \parallel b$). Спектры лазерного излучения показаны на рис. 5.6.4. Длина волны, на которой работал лазер, значительно сдвигалась с уменьшением пропускания выходного зеркала T_{OC} (с 1010-1022 нм до 1021-1047 нм).

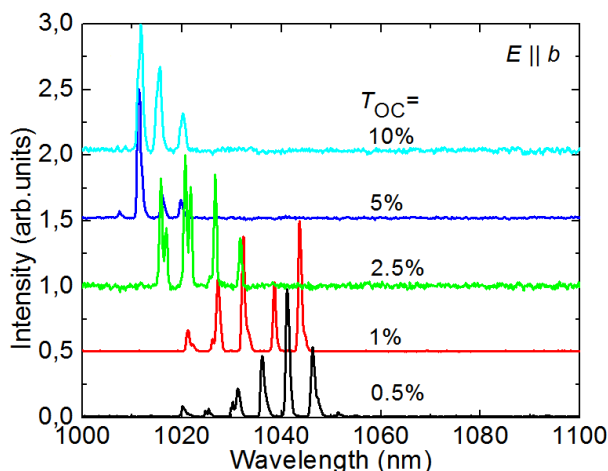


Рисунок 5.6.4 – Спектры лазерного излучения микрочип-лазера на кристалле $\text{Yb}^{3+}:\text{KY}(\text{MoO}_4)_2$, измеренные при $P_{abs} = 1.0$ Вт. Поляризация лазера $E \parallel b$.

5.6.3 Выходные характеристики лазера на кристалле $\text{Yb}^{3+},\text{Li}^+:\text{ZnWO}_4$

Лазер на кристалле $\text{Yb}^{3+},\text{Li}^+:\text{ZnWO}_4$ генерировал максимальную выходную мощность 2,90 Вт на длине волны ~ 1059 нм с дифференциальной эффективностью $\eta = 57.9\%$ (по отношению к

поглощенной мощности накачки) и порогом лазерной генерации $P_{th} = 0.41$ Вт, рис. 5.6.5 (а). Для всех выходных зеркал зависимость выходной мощности лазера от поглощенной мощности была линейной до $P_{abs} = 5$ Вт, при значениях $P_{abs} > 5$ Вт зависимость переставала быть линейной. Это связано с неоптимизированным охлаждением лазерного элемента.

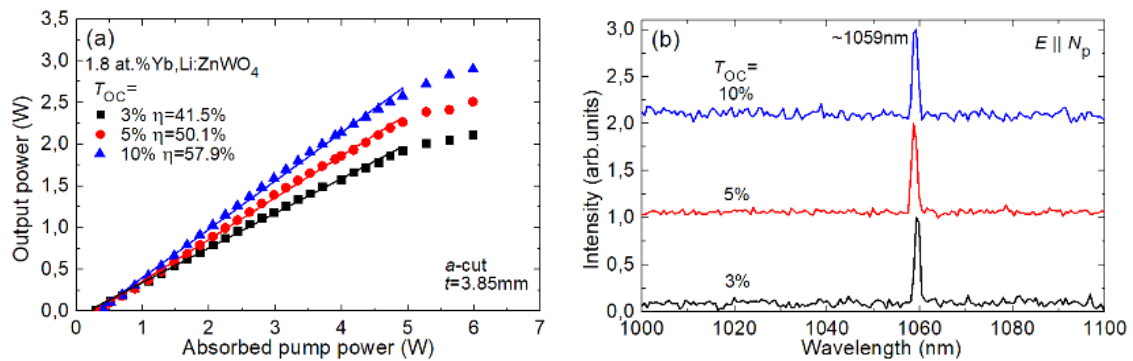


Рисунок 5.6.5 – Лазер на кристалле 1.8 ат.% Yb³⁺, Li⁺:ZnWO₄ с диодной накачкой: (а) выходные характеристики лазера; (б) спектры лазерного излучения. Лазерное излучение линейно поляризовано ($E \parallel N_p$).

Излучение лазера было линейно поляризованным ($E \parallel N_p$), поляризация выбиралась естественным образом по анизотропии усиления. Спектры излучения, рис. 5.6.5 (б), слабо зависели от пропускания выходного зеркала. Лазер работал на длине волны около 1.06 мкм, что соответствовало рассчитанным спектрам усиления.

5.7 Краткие выводы по главе 5

В данной главе было проведено исследование спектрально-люминесцентных, колебательных и генерационных свойств двух кристаллов с ионами Yb^{3+} : орторомбического кристалла калий-иттриевого двойного молибдата $\text{KY}(\text{MoO}_4)_2$ и моноклинного кристалла цинкового вольфрамата ZnWO_4 , содопированного ионами Li^+ . Было определено Штарковское расщепление уровней ионов Yb^{3+} в кристаллах ZnWO_4 и $\text{KY}(\text{MoO}_4)_2$, было установлено, что в кристалле цинкового вольфрамата ZnWO_4 , соактивированного ионами Yb^{3+} и Li^+ (обеспечивающими локальную компенсацию заряда), наблюдается большое (804 см^{-1}) Штарковское расщепление нижнего мультиплета ионов иттербия, в то время как для кристалла $\text{KY}(\text{MoO}_4)_2$ эта величина составляет 601 см^{-1} . Также в кристалле ZnWO_4 наблюдается значительное увеличение ширины безфононной линии $\Delta\lambda_{\text{ZPL}} = 3.0 \text{ нм}$, что намного шире, чем в кристалле $\text{Yb}:\text{KY}(\text{WO}_4)_2$ ($\Delta\lambda_{\text{ZPL}} < 0.1 \text{ нм}$).

Была продемонстрирована эффективная лазерная генерации на данных кристаллах. Лазер на кристаллической пластине $\text{Yb}^{3+}:\text{KY}(\text{MoO}_4)_2$ толщиной 286 мкм генерировал максимальную выходную мощность 0.81 Вт на длине волны 1021–1044 нм с дифференциальной эффективностью 76.4%. Лазер на кристалле $\text{Yb}^{3+}, \text{Li}^{3+}:\text{ZnWO}_4$ генерировал максимальную выходную мощность 2,90 Вт на длине волны $\sim 1059 \text{ нм}$ с дифференциальной эффективностью $\eta = 57.9\%$.

Заклучение

В диссертационной работе было проведено комплексное исследование спектрально-люминесцентных свойств новых ромбических и моноклинных кристаллов $KY(WO_4)_2$, $KLu(WO_4)_2$, $KY(MoO_4)_2$, $CsGd(MoO_4)_2$ и $ZnWO_4$, активированных ионами европия, тербия, тулия и иттербия, а также была продемонстрирована эффективная лазерная генерация в ИК области спектра, в том числе в микрочип-лазере.

Было показано, что кристаллы двойных молибдатов, к которым относятся кристаллы калий-иттриевого двойного молибдата $KY(MoO_4)_2$ и цезий-гадолиниевого двойного молибдата $CsGd(MoO_4)_2$, характеризуются исключительно сильной для редкоземельных ионов анизотропией поперечных сечений поглощения и вынужденного испускания. Например, для кристалла $Tm^{3+}:KY(MoO_4)_2$ величина поперечного сечения поглощения для поляризации $E \parallel b$ на порядок выше, чем для поляризации $E \parallel c$, и составляет 7.70×10^{-20} см². А величина поперечного сечения вынужденного испускания для этой поляризации в 6-8 раз больше, чем для остальных поляризаций. Такая анизотропия прежде всего связана с низкой локальной симметрией люминесцентных центров (C_2), а также со слоистой структурой кристаллов.

Были сформулированы поляризационные правила отбора для магнитно-дипольных переходов в оптически двухосных кристаллах с локальной симметрией люминесцентных центров C_2 . Они определяются взаимной ориентацией вектора напряжённости магнитного поля и магнитного диполя относительно оси симметрии второго порядка. При детальном исследовании анизотропии люминесценции магнитно-дипольного перехода $^5D_0 \rightarrow ^7F_1$ ионов Eu^{3+} в кристаллах $Eu^{3+}:KY(WO_4)_2$ и $Eu^{3+}:KY(MoO_4)_2$ было обнаружено

влияние поляризации возбуждающего света и ориентации кристалла на форму спектра люминесценции. Таким образом, было получено первое экспериментальное подтверждение поляризационных правил отбора.

Впервые было определено Шарковское расщепление уровней ионов Yb^{3+} в кристаллах ZnWO_4 и $\text{KY}(\text{MoO}_4)_2$, было установлено, что в кристалле цинкового вольфрамата ZnWO_4 , соактивированного ионами Yb^{3+} и Li^+ (обеспечивающими локальную компенсацию заряда), наблюдается большое (804 см^{-1}) Шарковское расщепление нижнего мультиплета ионов иттербия, в то время как для кристалла $\text{KY}(\text{MoO}_4)_2$ эта величина составляет 601 см^{-1} . Также в кристалле ZnWO_4 наблюдается значительное увеличение ширины безфононной линии $\Delta\lambda_{\text{ZPL}} = 3.0 \text{ нм}$, что намного шире, чем в кристалле $\text{Yb:KY}(\text{WO}_4)_2$ ($\Delta\lambda_{\text{ZPL}} < 0.1 \text{ нм}$). Также кристаллу ZnWO_4 свойственна высокая анизотропия поперечных сечений вынужденного испускания в поляризованном свете и широкими спектрами усиления.

Было показано, что слоистая структура и совершенная спайность кристаллов калий-иттриевого двойного молибдата $\text{KY}(\text{MoO}_4)_2$, позволяет изготавливать тонкие кристаллические пластинки и плёнки, подверженные упругой деформации, толщиной до нескольких десятков микрометров. Такие плёнки и пластинки обладают лазерным качеством и пригодны для использования в качестве активных элементов микрочип-лазеров без какой-либо последующей обработки. Впервые была продемонстрирована работа лазера на тонких кристаллических пластинках и плёнках кристаллов $\text{Tm:KY}(\text{MoO}_4)_2$ и $\text{Yb}^{3+}:\text{KY}(\text{MoO}_4)_2$. Максимальная выходная мощность лазера на кристаллической пластинке толщиной 286 мкм изготовленной из $\text{Yb}^{3+}:\text{KY}(\text{MoO}_4)_2$, составила $0,81 \text{ Вт}$ на длине волны $1021\text{-}1044 \text{ нм}$ с высоким дифференциальным КПД = $76,4\%$. Максимальная выходная мощность лазера на $\text{Tm:KY}(\text{MoO}_4)_2$ кристаллической пластинке

толщиной 700 мкм составила 0,88 Вт. Лазер генерировал излучение на длине волны 1840–1905 нм с дифференциальной эффективностью $\eta = 65,8\%$. Лазер на тонкой Tm:KY(MoO₄)₂ кристаллической плёнке генерировал излучение с максимальной выходной мощностью 131 мВт на длине волны 1801–1872 нм с $\eta = 45,2\%$.

Список литературы:

1. Klevtsov P. V. et al. Polymorphism of the double molybdates and tungstates of mono- and trivalent metals with the composition $M^+R^{3+}(EO_4)_2$ // *Journal of Structural Chemistry*. – 1977. – Vol. 18. – №. 3. – PP. 339-355.
2. Liu J. et al. Efficient high-power laser operation of Yb:KLu(WO₄)₂ crystals cut along the principal optical axes // *Optics letters*. – 2007. – Vol. 32. – №. 14. – PP. 2016-2018
3. Serres J. M. et al. Diode-pumped microchip Tm:KLu(WO₄)₂ laser with more than 3 W of output power // *Optics letters*. – 2014. – Vol. 39. – №. 14. – PP. 4247-4250.
4. Loiko P. et al. In-band-pumped Ho:KLu(WO₄)₂ microchip laser with 84% slope efficiency // *Optics letters*. – 2015. – Vol. 40. – №. 3. – PP. 344-347.
5. Griebner U. et al. Passively mode-locked Yb:KLu(WO₄)₂ oscillators // *Optics Express*. – 2005. – Vol. 13. – №. 9. – PP. 3465-3470.
6. Pujol M. C. et al. Growth, optical characterization, and laser operation of a stoichiometric crystal KYb(WO₄)₂ // *Physical Review B*. – 2002. – Vol. 65. – №. 16. – PP. 165121.
7. Mateos X. et al. Crystal growth, spectroscopic studies and laser operation of Yb³⁺-doped potassium lutetium tungstate // *Optical Materials*. – 2006. – Vol. 28. – №. 5. – PP. 519-523.
8. Lagatsky A. A. et al. Diode-pumped CW lasing of Yb:KYW and Yb:KGW // *Optics communications*. – 1999. – Vol. 165. – №. 1-3. – PP. 71-75.
9. Silvestre Ò. et al. Thermal properties of monoclinic KLu(WO₄)₂ as a promising solid state laser host // *Optics express*. – 2008. – Vol. 16. – №. 7. – PP. 5022-5034.
10. Petrov V. et al. Growth and properties of KLu(WO₄)₂, and novel ytterbium and thulium lasers based on this monoclinic crystalline host // *Laser & Photonics Reviews*. – 2007. – Vol. 1. – №. 2. – PP. 179-212.
11. Cascales C. et al. Structural, spectroscopic, and tunable laser properties of Yb³⁺-doped NaGd(WO₄)₂ // *Physical Review B*. – 2006. – Vol. 74. – №. 17. – PP. 174114.

12. Voron'ko Y. K. et al. Growth and spectroscopic investigations of Yb³⁺-doped NaGd(MoO₄)₂ and NaLa(MoO₄)₂—new promising laser crystals // *Optical Materials*. – 2006. – Vol. 29. – №. 2-3. – PP. 246-252.
13. Wakefield G. et al. Luminescence properties of nanocrystalline Y₂O₃:Eu // *Advanced Materials* – 2001, Vol. 13, №. 20, PP. 1557-1560.
14. Neeraj S. et al. Novel red phosphors for solid-state lighting: the system NaM(WO₄)_{2-x}(MoO₄)_x:Eu³⁺ (M=Gd, Y, Bi) // *Chemical Physics Letters* – 2004. – Vol. 387. – №. 1-3. – PP. 2-6.
15. Wang Z. et al. Luminescence of (Li_{0.333}Na_{0.334}K_{0.333})Eu(MoO₄)₂ and its application in near UV InGaN-based light-emitting diode // *Chemical Physics Letters* – 2005. – Vol. 412. – №. 4-6 – PP. 313-316.
16. Bagaev S. N. et al. 25% Eu:KGd(WO₄)₂ laser crystal: spectroscopy and lasing on the ⁵D₀→⁷F₄ transition // *Quantum Electronics* – 2011. – Vol. 41. – №3. – PP. 189-192.
17. Dashkevich V. I. et al. Red Eu, Yb:KY(WO₄)₂ laser at ~ 702 nm // *Laser Physics Letters* – 2015. – Vol. 12. – №. 8. – PP. 085001.
18. Loiko P. A. et al. Spectroscopic characterization and pulsed laser operation of Eu³⁺:KGd(WO₄)₂ crystal // *Laser Physics* – 2013. – Vol. 23. – №. 10. – PP. 105811-1-7.
19. Kränkel C. et al. Out of the blue: semiconductor laser pumped visible rare-earth doped lasers // *Laser & photonics reviews* – 2016. – Vol. 10. – №. 4. – PP. 548-568.
20. Metz P. W. et al. Efficient continuous wave laser operation of Tb³⁺-doped fluoride crystals in the green and yellow spectral regions // *Laser & Photonics Reviews* – 2016. – Vol. 10. – №. 2. – PP. 335-344.
21. Metz P. W. et al. Performance and wavelength tuning of green emitting terbium lasers // *Optics express* – 2017. – Vol. 25. – №. 5. – PP. 5716-5724.
22. Hayakawa T. et al. Visible emission characteristics in Tb³⁺-doped fluorescent glasses under selective excitation // *Journal of luminescence* – 1996. – Vol. 68. – №. 2-4. – PP. 179-186.

23. Sun X. et al. Luminescence behavior of Tb^{3+} ions in transparent glass and glass-ceramics containing CaF_2 nanocrystals // Journal of Luminescence – 2009. – Vol. 129. – №. 8. – PP. 773-777.
24. Hao Z. et al. Blue-green-emitting phosphor $CaSc_2O_4:Tb^{3+}$: tunable luminescence manipulated by cross-relaxation // Journal of The Electrochemical Society – 2009. – Vol. 156. – №. 3. – PP. H193-H196.
25. Liao J. et al. Synthesis and luminescence properties of $Tb^{3+}:NaGd(WO_4)_2$ novel green phosphors // Journal of luminescence – 2009. – Vol. 129. – №. 7. – PP. 668-671.
26. Ju X. et al. Luminescence properties of $ZnMoO_4:Tb^{3+}$ green phosphor prepared via co-precipitation // Materials Letters – 2011. – Vol. 65. – №. 17-18. – PP. 2642-2644.
27. Kaminskii A. A. et al. Ribbon and sheet miniature crystal laser // Quantum Electronics – 1994. – Vol. 24. – №. 12. – PP. 1029.
28. Bünzli J. C. G., Choppin G. R. Lanthanide probes in life, chemical and earth sciences. – 1989.
29. Carnall W. T. et al. Electronic energy levels in the trivalent lanthanide aquo ions. I. Pr^{3+} , Nd^{3+} , Pm^{3+} , Sm^{3+} , Dy^{3+} , Ho^{3+} , Er^{3+} , and Tm^{3+} // The Journal of Chemical Physics. – 1968. – Vol. 49. – №. 10. – PP. 4424-4442
30. Binnemans K. et al. Application of the Eu^{3+} ion for site symmetry determination // Journal of rare earths. – 1996. – Vol. 14. – №. 3. – PP. 173-180.
31. Kirby A. F., Richardson F. S. Detailed analysis of the optical absorption and emission spectra of europium ($3+$) in the trigonal (C3) $Eu(DBM)_3 \cdot H_2O$ system // The Journal of Physical Chemistry. – 1983. – Vol. 87. – №. 14. – PP. 2544-2556.
32. Jia G. et al. Eu^{3+} spectroscopy: a structural probe for yttrium orthoborate phosphors // The Journal of Physical Chemistry C. – 2010. – Vol. 114. – №. 6. – PP. 2769-2775.
33. Sardar D. K. et al. Absorption intensities and emission cross sections of $Tb^{3+}(4f^8)$ in $TbAlO_3$ // Journal of applied physics. – 2006. – Vol. 100. – №. 8. – PP. 083108.
34. Mateos X. et al. Efficient 2- μm continuous-wave laser oscillation of $Tm^{3+}:KLu(WO_4)_2$ // IEEE journal of quantum electronics. – 2006. – Vol. 42. – №. 10. – PP. 1008-1015.

35. Troshin A. E. et al. Spectroscopy and laser properties of $\text{Tm}^{3+}:\text{KY}(\text{WO}_4)_2$ crystal // *Applied Physics B*. – 2007. – Vol. 86. – №. 2. – PP. 287-292.
36. Silvestre O. et al. Thulium doped monoclinic $\text{KLu}(\text{WO}_4)_2$ single crystals: growth and spectroscopy // *Applied Physics B*. – 2007. – Vol. 87. – №. 4. – PP. 707-716.
37. Loiko P. et al. Sub-nanosecond $\text{Yb}:\text{KLu}(\text{WO}_4)_2$ microchip laser // *Optics letters*. – 2016. – Vol. 41. – №. 11. – PP. 2620-2623.
38. Pekarek S. et al. Diode-pumped gigahertz femtosecond $\text{Yb}:\text{KGW}$ laser with a peak power of 3.9 kW // *Optics express*. – 2010. – Vol. 18. – №. 16. – PP. 16320-16326.
39. Rico M. et al. Tunable laser operation of ytterbium in disordered single crystals of $\text{Yb}:\text{NaGd}(\text{WO}_4)_2$ // *Optics express*. – 2004. – Vol. 12. – №. 22. – PP. 5362-5367.
40. Liu H. et al. Diode-pumped Kerr-lens mode-locked $\text{Yb}:\text{KY}(\text{WO}_4)_2$ laser // *Optics letters*. – 2001. – Vol. 26. – №. 21. – PP. 1723-1725
41. Zhao H., Major A. A continuous wave $\text{Yb}:\text{KGW}$ laser with polarization-independent pump absorption // *Laser Physics*. – 2013. – Vol. 23. – №. 9. – PP. 095001.
42. Judd B. R. Optical absorption intensities of rare-earth ions // *Physical review*. – 1962. – Vol. 127. – №. 3. – PP. 750.
43. Ofelt G. S. Intensities of crystal spectra of rare-earth ions // *The journal of chemical physics*. – 1962. – Vol. 37. – №. 3. – PP. 511-520.
44. Loiko P. A. et al. Spectroscopic and photoluminescence characterization of Eu^{3+} -doped monoclinic $\text{KY}(\text{WO}_4)_2$ crystal // *Journal of luminescence*. – 2014. – Vol. 153. – PP. 221-226.
45. Kornienko A. A. et al. Dependence of the line strength of f-f transitions on the manifold energy. II. Analysis of Pr^{3+} in $\text{KPrP}_4\text{O}_{12}$ // *physica status solidi (b)*. – 1990. – Vol. 157. – №. 1. – PP. 267-273.
46. Loiko P. A. et al. Growth, spectroscopic and thermal properties of Nd-doped disordered $\text{Ca}_9(\text{La/Y})(\text{VO}_4)_7$ and $\text{Ca}_{10}(\text{Li/K})(\text{VO}_4)_7$ crystals // *Journal of luminescence*. – 2013. – Vol. 137. – PP. 252-258.

47. Loiko P. et al. Judd-Ofelt modelling and stimulated-emission cross-sections for Tb^{3+} ions in monoclinic $KYb(WO_4)_2$ crystal //Journal of Luminescence. – 2017. – Vol. 190. – PP. 37-44.
48. Aull B., Janssen H. Vibronic interactions in Nd:YAG resulting in nonreciprocity of absorption and stimulated emission cross sections //IEEE Journal of Quantum Electronics. – 1982. – Vol. 18. – №. 5. – PP. 925-930.
49. Ясюкевич А. РР. и др. Интегральный метод соответствия в спектроскопии лазерных кристаллов с примесными центрами //Журнал прикладной спектроскопии. – 2004. – Т. 71. – №. 2. – С. 187-192.
50. McCumber D. E. Einstein relations connecting broadband emission and absorption spectra //Physical Review. – 1964. – Vol. 136. – №. 4A. – PP. A954.
51. Payne S. A. et al. Infrared cross-section measurements for crystals doped with Er^{3+} , Tm^{3+} , and Ho^{3+} //IEEE Journal of Quantum Electronics. – 1992. – Vol. 28. – №. 11. – PP. 2619-2630&
52. Garcia-Cortes A. et al. Spectroscopy and Lasing of Yb-Doped $NaY(WO_4)_2$: Tunable and Femtosecond Mode-Locked Laser Operation //IEEE Journal of Quantum Electronics. – 2007. – Vol. 43. – №. 9. – PP. 758-764
53. Klevtsova R. F., Borisov S. V. X-ray structural study of the double molybdate $KY(MoO_4)_2$ //Soviet Physics Doklady. – 1968. – Vol. 12. – PP. 1095.
54. Chen Y. et al. Polarized spectral characteristics of $Nd^{3+}:KY(MoO_4)_2$ crystal with perfect cleavage planes: a promising microchip gain medium //JOSA B. – 2007. – Vol. 24. – №. 3. – PP. 496-503.
55. Kaminskii A. A. et al. Investigation of stimulated emission in the ${}^4F_{3/2} \rightarrow {}^4I_{13/2}$ transition of Nd^{3+} ions in crystals (III) //physica status solidi (a). – 1973. – Vol. 15. – №. 2. – PP. K141-K144
56. Kaminskii A. A., Verdun H. R. New high power, high efficient quasi-cw and cw single-mode $KY(MoO_4)_2:Nd^{3+}$ laser end-pumped by a GaAlAs laser-diode array //Physica Status Solidi A (Applied Research);(Germany). – 1993. – Vol. 138. – №. 1
57. Kaminskii A. A. et al. Optical spectroscopy and visible stimulated emission of Dy^{3+} ions in monoclinic $\alpha-KY(WO_4)_2$ and

- α -KGd(WO₄)₂ crystals //Physical Review B: Condensed Matter and Materials Physics. – 2002. – Vol. 65. – №. 12. – PP. 1-29.
58. Bennett J. M. Polarizers Handbook of Optics ed M Bass. – 1995.
59. Volokitina A. et al. Eu³⁺:KY(MoO₄)₂: A novel anisotropic red-emitting material with a layered structure //Journal of Alloys and Compounds. – 2018. – Vol. 762. – PP. 786-796.
60. Hanuza J., Łabuda L. Polarized Raman and infrared spectra of a multilayer KY(MoO₄)₂ crystal //Journal of Raman Spectroscopy. – 1981. – Vol. 11. – №. 4. – PP. 231-237.
61. Hanuza J., Macalik L. Polarized ir and Raman spectra of orthorhombic KLn(MoO₄)₂ crystals (Ln= Y, Dy, Ho, Er, Tm, Yb, Lu) //Spectrochimica Acta Part A: Molecular Spectroscopy. – 1982. – Vol. 38. – №. 1. – PP. 61-72.
62. Macalik L., Hanuza J., Kaminskii A. A. Polarized Raman spectra of the oriented NaY(WO₄)₂ and KY(WO₄)₂ single crystals //Journal of Molecular Structure. – 2000. – Vol. 555. – №. 1-3. – PP. 289-297.
63. Loiko P. A. et al. Europium doping in monoclinic KYb(WO₄)₂ crystal //Journal of Luminescence. – 2017. – Vol. 183. – PP. 217-225.
64. Colak S. et al. Transition rates of Tb³⁺ in TbP₅O₁₄, TbLiP₄O₁₂, and TbAl₃(BO₃)₄: An evaluation for laser applications //Journal of applied physics. – 1983. – Vol. 54. – №. 5. – PP. 2156-2166.
65. Dodson C. M., Zia R. Magnetic dipole and electric quadrupole transitions in the trivalent lanthanide series: Calculated emission rates and oscillator strengths //Physical Review B. – 2012. – Vol. 86. – №. 12. – PP. 125102.
66. Schwung S. et al. The crystal structure and luminescence quenching of poly- and single-crystalline KYW₂O₈:Tb³⁺ //Journal of Luminescence. – 2015. – Vol. 166. – PP. 289-294.
67. Каминский А. А. и др. Физика и спектроскопия лазерных кристаллов. Наука. – 1986.
68. Görller-Walrand C. K. Binnemans Handbook on the Physics and Chemistry of rare Earths, 25. – 1998.
69. Aminov L. K., Kaminskii A. A., Malkin B. Z. Anisotropy of radiation intensity of activator ions in crystals //Physics and Spectroscopy of Laser Crystals. – 1986

70. Gaponenko M. S. et al. Thermal lensing and microchip laser performance of N g-cut $\text{Tm}^{3+}:\text{KY}(\text{WO}_4)_2$ crystal // *Applied Physics B*. – 2012. – Vol. 108. – №. 3. – PP. 603-607.
71. Serres J. M. et al. Diode-pumped microchip $\text{Tm}:\text{KLu}(\text{WO}_4)_2$ laser with more than 3 W of output power // *Optics letters*. – 2014. – Vol. 39. – №. 14. – PP. 4247-4250.
72. Borovlev Y. A. et al. Progress in growth of large sized BGO crystals by the low-thermal-gradient Czochralski technique // *Journal of crystal growth*. – 2001. – Vol. 229. – №. 1-4. – PP. 305-311.
73. Volokitina A. et al. Laser operation of cleaved single-crystal plates and films of $\text{Tm}:\text{KY}(\text{MoO}_4)_2$ // *Optics express*. – 2020. – Vol. 28. – №. 7. – PP. 9039-90.
74. Loiko P. et al. In-band pumping of $\text{Tm}:\text{LiYF}_4$ channel waveguide: a power scaling strategy for $\sim 2 \mu\text{m}$ waveguide lasers // *Optics letters*. – 2019. – Vol. 44. – №. 12. – PP. 3010-3013.
75. So S. et al. A power-scaling strategy for longitudinally diode-pumped $\text{Tm}:\text{YLF}$ lasers // *Applied Physics B*. – 2006. – Vol. 84. – №. 3. – PP. 389-393.
76. Subbotin K. et al. Monoclinic zinc monotungstate $\text{Yb}^{3+}, \text{Li}^+:\text{ZnWO}_4$: Part I. Czochralski growth, structure refinement and Raman spectra // *Journal of Luminescence*. – 2020. – Vol. 228. – PP. 117601.
77. Serrano M. D. et al. Design of Yb^{3+} optical bandwidths by crystallographic modification of disordered calcium niobium gallium laser garnets // *Journal of Materials Chemistry C*. – 2017. – Vol. 5. – №. 44. – PP. 11481-11495.
78. Pan Z. et al. Disordered $\text{Tm}^{3+}, \text{Ho}^{3+}$ -codoped CNGG garnet crystal: Towards efficient laser materials for ultrashort pulse generation at $\sim 2 \text{mm}$. – 2021.
79. Shannon R. D. Revised effective ionic radii and systematic studies of interatomic distances in halides and chalcogenides // *Acta crystallographica section A: crystal physics, diffraction, theoretical and general crystallography*. – 1976. – Vol. 32. – №. 5. – PP. 751-767.
80. Damen T. C., Porto S. P. S., Tell B. Raman effect in zinc oxide // *Physical Review*. – 1966. – Vol. 142. – №. 2. – PP. 570.

81. Wang H. et al. Temperature dependence of the polarized Raman spectra of ZnWO_4 single crystals //physical review B. – 1992. – Vol. 45. – №. 18. – PP. 1035.
82. Liu Y. et al. Analysis of Raman spectra of ZnWO_4 single crystals //Journal of applied physics. – 1988. – Vol. 64. – №. 9. – PP. 4651-465.
83. Spengler C. J., O'Hara S. Zinc Tungstate—Some Optical Properties //Applied Optics. – 1964. – Vol. 3. – №. 9. – PP. 1084-1085.
84. Yang F. The spectroscopic investigation of $\text{ZnWO}_4:\text{Yb}^{3+}$ single crystal //Journal of Materials Research. – 2012. – Vol. 27. – №. 16. – PP. 2096-2100.
85. Kulakova L. A. Acoustooptical and elastic properties of laminated $\text{KY}(\text{MoO}_4)_2$ crystals //Physics of the Solid State. – 2000. – Vol. 42. – №. 1. – PP. 55-58.
86. Loiko P. et al. Spectroscopy and high-power laser operation of a monoclinic $\text{Yb}^{3+}:\text{MgWO}_4$ crystal //Optics letters. – 2020. – Vol. 45. – №. 7. – PP. 1770-1773.
87. Scheife H. et al. Advances in up-conversion lasers based on Er^{3+} and Pr^{3+} //Optical Materials. – 2004. – Vol. 26. – №. 4. – PP. 365-37.
88. Castellano-Hernández E. et al. Mode-locked laser operation of Indium-modified $\text{Yb}:\text{KY}(\text{WO}_4)_2$ single crystal //Optics express. – 2015. – Vol. 23. – №. 9. – PP. 11135-11140.
89. Cascales C. et al. Structural, spectroscopic, and tunable laser properties of Yb^{3+} -doped $\text{NaGd}(\text{WO}_4)_2$ //Physical Review B. – 2006. – Vol. 74. – №. 17. – PP. 174114.
90. Lagatsky A. A., Kuleshov N. V., Mikhailov V. P. Diode-pumped CW lasing of $\text{Yb}:\text{KYW}$ and $\text{Yb}:\text{KGW}$ //Optics communications. – 1999. – Vol. 165. – №. 1-3. – PP. 71-75.
91. Haumesser P. H. et al. Spectroscopic and crystal-field analysis of new Yb-doped laser materials //Journal of Physics: Condensed Matter. – 2001. – Vol. 13. – №. 23. – PP. 5427.
92. Borovlev Y. A. et al. Progress in growth of large sized BGO crystals by the low-thermal-gradient Czochralski technique //Journal of crystal growth. – 2001. – Vol. 229. – №. 1-4. – PP. 305-311

ПРИЛОЖЕНИЕ А

Оттиски статей



ELSEVIER

Contents lists available at ScienceDirect

Journal of Alloys and Compounds

journal homepage: <http://www.elsevier.com/locate/jalcom>



Eu³⁺:KY(MoO₄)₂: A novel anisotropic red-emitting material with a layered structure

Anna Volokitina^a, Pavel Loiko^{a,*}, Elena Vilejshikova^b, Xavier Mateos^c, Elena Dunina^d, Alexey Kornienko^d, Nikolai Kuleshov^b, Anatoly Pavlyuk^e

^a ITMO University, Kronverkskiy pr., 49, Saint-Petersburg 197101, Russia

^b Center for Optical Materials and Technologies (COMT), Belarusian National Technical University, 65/17 Nezavisimosti Ave., Minsk 220013, Belarus

^c Física i Cristal·lografia de Materials i Nanomaterials (FICMA-FICNA)-EMaS, Dept. Química Física i Inorgànica, Universitat Rovira i Virgili (URV), Campus Sescelades, E-43007 Tarragona, Spain

^d Vitebsk State Technological University, 72 Moskovskaya Ave., 210035 Vitebsk, Belarus

^e A.V. Nikolaev Institute of Inorganic Chemistry, Siberian Branch of Russian Academy of Sciences, 3 Lavrentyev Ave., Novosibirsk 630090, Russia

ARTICLE INFO

Article history:

Received 13 March 2018

Received in revised form

14 May 2018

Accepted 20 May 2018

Available online 21 May 2018

Keywords:

Double molybdate

Europium ions

Crystal structure

Spectroscopy

Judd-Ofelt theory

Stimulated emission

ABSTRACT

We report on the crystal growth, structure determination and the vibronic and spectroscopic properties of a novel red-emitting anisotropic crystal featured by a layered structure, the Eu³⁺-doped orthorhombic potassium yttrium double molybdate crystal, KY(MoO₄)₂. The transition probabilities of Eu³⁺ ions are determined within the Judd-Ofelt theory. The stimulated-emission cross-sections are calculated for the ⁵D₀ → ⁷F_J transitions of Eu³⁺ with polarized light. The maximum σ_{SE} reaches 11.4×10^{-20} cm² at 613.9 nm for *E* || *c*. The strong anisotropy of the spectroscopic properties of Eu³⁺ is attributed to the layered structure of KY(MoO₄)₂. The lifetime of the ⁵D₀ state is 0.65 ms. Under UV excitation, Eu:KY(-MoO₄)₂ provides red emission (CIE 1931 coordinates, *x* = 0.665 and *y* = 0.335) with almost unity color purity. Eu³⁺ ions are studied as structural probes, revealing a single type of site (C₂ symmetry). The polarization-anisotropy of the purely magnetic-dipole ⁵D₀ → ⁷F₁ transition is discussed. Eu:KY(MoO₄)₂ is promising for red phosphors and deep-red lasers.

© 2018 Elsevier B.V. All rights reserved.

1. Introduction

The tungstate and molybdate crystals represent an important class of oxide host matrices for doping with trivalent rare-earth (RE) ions. The most prominent examples are the double tungstates (DTs), and double molybdates (DMos), A⁺R³⁺(X⁶⁺O₄)₂, where A⁺ stands for a univalent alkali cation, K, Li, Na, Rb or Cs, R³⁺ - for a trivalent cation including RE (Sc, Y, La-Lu), Bi, In, etc., and X⁶⁺ = W or Mo, respectively. The DTs and DMos exhibit a variety of crystalline systems [1]. In recent years, multiple studies have been dedicated to monoclinic potassium rare-earth DTs [2], KRE(WO₄)₂, and tetragonal sodium rare-earth DTs [3] and DMos, NaRE(W/MoO₄)₂. These crystals have been found to be very suitable for efficient continuous-wave (CW) [4–6] and mode-locked [7,8] lasers emitting in the near-IR spectral range based on Yb³⁺, Tm³⁺ or Ho³⁺ ions.

In the visible spectral range, the search for active ions is focused on Sm³⁺, Eu³⁺, Tb³⁺ and Dy³⁺ [9]. In particular, trivalent europium ions (Eu³⁺, electronic configuration: [Xe]4f⁶) are well-known for their red emissions due to the ⁵D₀ → ⁷F_J (*J* = 0 ... 6) 4f-4f electronic transitions. The most intense transition to the ⁷F₂ state typically occurs at ~610 nm resulting in red luminescence of high color purity; the property which is widely used in commercial red phosphors, e.g. based on Eu³⁺:Y₂O₃ [10]. Eu³⁺-doped DT and DMO phosphors are also known [11,12]. Eu³⁺ ions are laser-active as well. It is worth noting that the first room temperature (RT) lasing of Eu³⁺ ions (⁵D₀ → ⁷F₄ transition) was achieved using monoclinic DT crystals, namely, Eu:KGd(WO₄)₂ and Eu:KY(WO₄)₂ (shortly Eu:KYW) [13,14]. Eu³⁺-doped monoclinic DTs show high transition cross-sections for polarized light and high luminescence quantum yield (>99%) due to the weak non-radiative (NR) relaxation [15]. Besides phosphor and laser applications, Eu³⁺ ions are recognized as structural probes [16]. This is because the ⁵D₀ → ⁷F₁ transition is purely magnetic dipole (MD) and it is almost not sensitive to the symmetry of the crystal field which is not the case of the purely electric-dipole (ED) ⁵D₀ → ⁷F₂ one [17].

* Corresponding author.

E-mail addresses: pavel_loiko@corp.ifmo.ru, kinetic@tut.by (P. Loiko).

The orthorhombic potassium yttrium DMO crystal, $KY(MoO_4)_2$ (shortly KYMo) is known for decades but poorly investigated as compared to its monoclinic DT counterpart, KYW. The early studies of KYMo crystals focused on their structure [18]. Later on, laser action [19,20] and spectroscopy [21,22] of Nd^{3+} -doped KYMo were reported. Due to their structure features (a layered structure), KYMo crystals exhibit a perfect cleavage limiting, to a certain extent, their applications in bulk lasers. However, using these materials, the concept of thin-film lasers was proposed [23]. A detailed study of the vibronic properties of undoped KYMo crystals was performed [24]. In addition, Dy^{3+} , Pr^{3+} , Er^{3+} and Tm^{3+} doped KYMo crystals are known [25–28]. In recent years, KYMo microcrystalline phosphors doped with Eu^{3+} ions as well as stoichiometric $KEu(MoO_4)_2$ (KEuMo) have been studied [29,30]. Note that KEuMo has a different structure (it is triclinic or monoclinic, depending on the synthesis conditions) [31].

In the present study, we aimed to grow large-volume Eu:KYM o single-crystals and to perform a detailed study of their structural, vibronic and spectroscopic properties, for the first time, to the best of our knowledge.

2. Crystal growth and structure

The family of potassium double molybdate crystals with general chemical formula $K^+R^{3+}(MoO_4)_2$, where R includes rare-earths ($RE = Sc, Y, La-Lu$), Bi and In, exhibits a variety of structural types, see Fig. 1 [1]. One of them is the orthorhombic KYMo-type phase which is observed for potassium rare-earth double molybdates with R varying from Sm to Lu. For $R = Dy, Ho, Y, Er, Tm$ this is the only possible phase. The KYMo-type crystals are orthorhombic [18].

KYM o is chemically stable, it possesses a relatively low melting temperature ($\sim 970^\circ C$) and it does not exhibit any polymorphic transformation below the melting point as in the case of its DT counterpart, KYW [1]. Thus, KYMo can be grown by the conventional Czochralski (Cz) method. The preliminary growth studies of KYMo by the Cz method indicated a partial dissociation of the KYMo melt resulting in the formation of yttrium oxomolybdate (Y_2MoO_6) and a low melting point ($\sim 560^\circ C$) phase of potassium trimolybdate ($K_2Mo_3O_{10}$) according to the equation: $2KY(MoO_4)_2 \rightarrow Y_2MoO_6 + K_2Mo_3O_{10}$ [32]. Y_2MoO_6 has a high melting point and high density and its solubility in the KYMo melt is low. Thus, it prevents the growth of high-quality KYMo crystals. The dissociation of the melt depends strongly on the evaporation of $K_2Mo_3O_{10}$. Thus, to stabilize the growth, 5–7 mol% of $K_2Mo_3O_{10}$ were added to the melt.

As raw materials, Eu_2O_3 (purity: 4N) Y_2O_3 (5N), MoO_3 (4N) and

K_2CO_3 (5N) were taken according to the composition 100 mol% $KY_{0.9}Eu_{0.1}(MoO_4)_2 - 5-7\text{ mol}\% K_2Mo_3O_{10}$ (e.g., the Eu^{3+} atomic fraction with respect to the replaced Y^{3+} was 10 at.%) They were carefully grinded, mixed and placed in a Pt crucible (volume: 140 cm^3 , diameter: 50 mm). The crucible was heated until $1050^\circ C$ in air and kept at this temperature for 2–3 h to homogenize the melt. Then, the melt was cooled to $\sim 960^\circ C$. The seed from an undoped KYMo crystal oriented with its [001] crystallographic axis being perpendicular to the melt was rotated at ~ 20 rpm (revolutions per minute); the pulling rate was 1–2 mm/h; the cooling rate for the melt was $\sim 2^\circ C/day$. The temperature gradient in the melt was below $3^\circ C/cm$. The growth rate was 5–10 g/day. After the growth, the crystal was removed from the melt and slowly cooled down to RT. No post-growth annealing was performed. The grown crystal exhibited a perfect cleavage along the (100) plane.

The photograph of the as-grown Eu:KYM o crystal boule is shown in Fig. 2. The boule has a slightly elliptic cross-section extended along the [010] axis. The boule is free of cracks and inclusions and it is transparent. The crystal has a slight rose coloration due to the Eu^{3+} ions. The actual Eu^{3+} concentration was determined with the Energy-Dispersive X-ray emission spectroscopy (EDX) to be $N_{Eu} = 2.4 \times 10^{20}\text{ cm}^{-3}$ (6 at.%). The stoichiometric formula of the crystal is then $KY_{0.94}Eu_{0.06}(MoO_4)_2$ and the segregation coefficient for Eu^{3+} ions K_{Eu} is about 0.60 ± 0.05 . The Eu^{3+} doping was almost the same, $6.0 \pm 0.5\text{ at.}\%$, over the cylindrical part of the boule. As mentioned above, the Eu^{3+} ions (ionic radius: 1.066 \AA for VIII-fold O^{2-} coordination [33]) in the KYMo lattice replaces the Y^{3+} ones (ionic radius: 1.019 \AA [33]). The difference in ionic radii determines the value of $K_{Eu} < 1$. It is known that $KEu(MoO_4)_2$ has a different structure, Fig. 1.

The phase purity and the structure of the grown Eu:KYM o crystals was confirmed by X-ray diffraction (XRD), see Fig. 3. The Eu:KYM o sample was fine powdered to avoid the orientation effects in the measured XRD patterns. The Eu:KYM o crystal is orthorhombic (space group $Pbna - D_{2h}^{14}$, No. 60, point group mmm). Its lattice constants are $a = 18.1976(6)\text{ \AA}$, $b = 7.9528(7)\text{ \AA}$ and $c = 5.0832(4)\text{ \AA}$, $\alpha = \beta = \gamma = 90^\circ$, the volume of the unit-cell $V = 735.65(9)\text{ \AA}^3$ and the calculated density ρ_{calc} is 4.083 g/cm^3 (the number of the structural units $Z = 4$), according to the performed Rietveld refinement, Fig. 3. The initial set of atomic coordinates (for undoped KYMo) used for the structure optimization was taken from Ref. [18]. The reduced chi-squared value of $\chi^2 = (R_{wp}/R_{exp})^2$ for this sample is 1.291 ($R_{wp} = 7.00\%$, $R_{exp} = 6.16\%$).

Note that the nonconventional crystallographic setting $Pbna$ was initially introduced for KYMo according to the growth forms and single-crystal XRD studies, while another (standard) setting $Pbnc$ was also used in later works [18,20]. The rule for equivalence

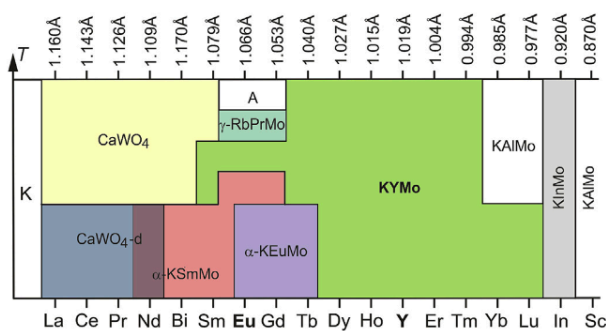


Fig. 1. Structural types of potassium double molybdates, $K^+R^{3+}(MoO_4)_2$, where R includes rare-earths (Sc, Y, La-Lu), Bi and In, see Ref. [1]. The vertical arrow indicates the temperature. The numbers on top – ionic radii of the R^{3+} ions for VIII-fold O^{2-} coordination. A – unknown structure.

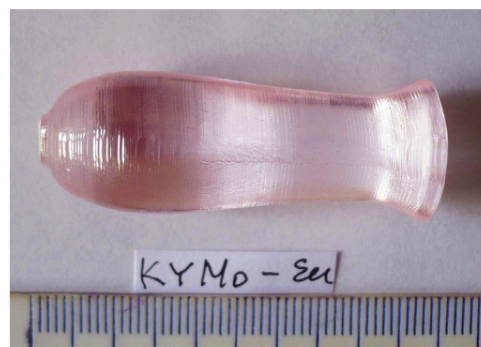


Fig. 2. Photograph of the as-grown 6 at.% Eu:KYM o crystal; the growth direction is along the [001] axis.

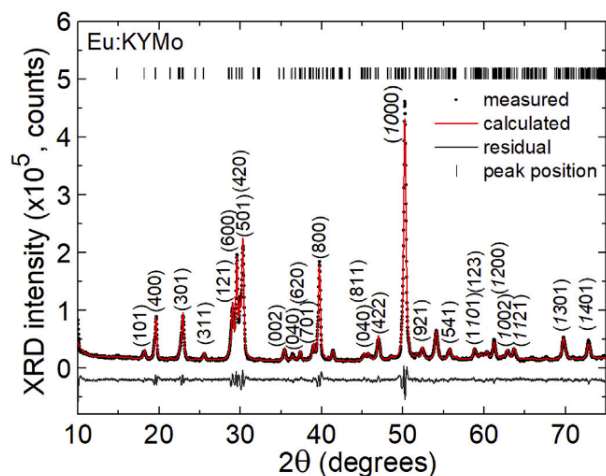


Fig. 3. X-ray powder diffraction (XRD) pattern of the as-grown 6 at.% Eu:KYMo crystal, the numbers denote the Miller's indices (*hkl*) (sp. gr. *Pbna*). The rule of equivalence of Miller's indices between *Pbnc* → *Pbna* crystallographic settings is *h'* → *l*, *k'* → *h* and *l'* → *k*. Symbols – experimental data, red curve – result of the Rietveld refinement, grey curve – the residual plot, vertical dashes – calculated peak positions. (For interpretation of the references to color in this figure legend, the reader is referred to the Web version of this article.)

of crystallographic axes between these two settings (*Pbnc* → *Pbna*) is *a'* → *c*, *b'* → *a* and *c'* → *b*. This situation is similar to the case of monoclinic KYW crystal (space group *C*_{2h}, No. 15) for which two crystallographic settings (*C*₂/*c* and *I*₂/*c*) were used. The latter one is more suitable for the description of the crystal habit [15].

The fractional atomic coordinates and interatomic distances determined with the Rietveld analysis are listed in Tables 1 and 2, respectively.

The structure of Eu:KYMo is schematically illustrated in Fig. 4 according to the results from the Rietveld refinement. In the structure of KYMo, the coordination number (C.N.) for the K⁺, Y³⁺ and Mo⁶⁺ cations is 6 + 4, 8 and 4 + 1, respectively. Here, the C.N. 4 + 1 for Mo⁶⁺ refers to a distorted tetrahedral coordination with 4 closely located O²⁻ ions (interatomic distances: 1.48–1.84 Å) and one additional O²⁻ cation positioned at slightly longer distance (2.53 Å). A similar effect is observed for the [K₂O₆] polyhedra. The continuous belts of edge-sharing distorted [YO₈] octahedrons (distorted Thomson cubes) are parallel to the *b*-axis, Fig. 4(a). In the *a*-*b* plane, they share corners with the [MoO₄] tetrahedra. The radical [Y(MoO₄)₂]⁻ forms porous layers parallel to the *b*-*c* plane. The linkage of these layers separated by *a*/*2* is provided only by the [K₂O₆] polyhedra, Fig. 4(a). This explains the perfect cleavage along the (100) plane in this crystal. The sites for the K⁺ and Y³⁺ cations in KYMo are different (e.g., this is an ordered crystal) which is

Table 1
Fractional atomic coordinates for the 6 at.% Eu:KYMo crystal (sp. gr. *Pbna*).

Atom	Wyckoff symbol	Site symmetry	<i>x/a</i>	<i>y/b</i>	<i>z/c</i>
K	4c	C ₂	0.273(2)	1/4	0
Y Eu	4c	C ₂	0.504(2)	1/4	0
Mo	8d	C ₁	0.101(5)	0.006(7)	0.025(9)
O1	8d	C ₁	0.181(5)	0.524(7)	0.114(2)
O2	8d	C ₁	0.080(8)	0.706(8)	0.198(6)
O3	8d	C ₁	0.069(8)	0.155(4)	0.205(4)
O4	8d	C ₁	0.447(4)	0.002(1)	0.275(8)

The rule for equivalence of atomic coordinates between *Pbnc* → *Pbna* settings is *x'* → *z*, *y'* → *x* and *z'* → *y*.

Table 2
Selected interatomic distances for the 6 at.% Eu:KYMo crystal.

Atoms	Number	Distance, Å	Atoms	Number	Distance, Å
Y Eu – O3	×2	1.82(1)	K – O1	×2	2.75(1)
Y Eu – O2	×2	2.46(1)	K – O1'	×2	2.79(2)
Y Eu – O4	×2	2.50(1)	K – O2	×2	2.99(1)
Y Eu – O4	×2	2.50(2)	K – O1''	×2	3.70(2)
Mo – O2	×1	1.48(1)	K – O3	×2	4.03(1)
Mo – O1	×1	1.66(0)	Y Eu – Y Eu	×2	3.98(3)
Mo – O4	×1	1.82(1)	K – K	×4	4.79(3)
Mo – O3	×1	1.84(1)	K – K'	×2	5.08(4)
Mo – O4'	×1	2.53(1)			

different from the case of disordered tetragonal scheelite (CaWO₄) type NaY(WO₄)₂ (NaYW) crystal for which the Na⁺ and Y³⁺ cations statistically occupy the 2b and 2d sites (both possessing the same S₄ symmetry).

For KYMo, the interatomic Y-O distances in the [YO₈] polyhedra are in the range 1.82–2.50 Å and the shortest Y³⁺-Y³⁺ distance is 3.98 Å which is close to that in monoclinic KYW, 4.06 Å. The shortest Y³⁺-Y³⁺ distance is observed along the *b*-axis for cations lying in the *b*-*c* “layer” plane. Note that along the *c*-axis (in the “layer” plane) and along the *a*-axis (layer-to-layer), these distances are much longer, namely 5.08 Å and 9.49 Å, respectively.

The symmetry of the Y³⁺ site is C₂ (no center of inversion symmetry). In KYMo, the C₂ axis is perpendicular to the cleavage plane (100) (parallel to the *a*-axis) [24].

3. Experimental

The Eu:KYMo crystal is orthorhombic and thus optically biaxial. Its optical properties are characterized in the frame of the optical indicatrix, with the three orthogonal axes (*N_p*, *N_m*, *N_g*) [2] being parallel to the crystallographic *a*, *b*, *c* ones. The exact values of the principal refractive indices (*n_p*, *n_m* and *n_g*) are unknown for KYMo (only a mean value of ~2 was reported [21]). Thus, the assignment of the optical indicatrix axes was performed to date. Because of this, we will describe the spectroscopic properties of the Eu³⁺ ions for the principal light polarizations *E* || *a*, *b*, *c*.

All spectroscopic studies were performed at RT (293 K). We carefully cut a rectangular sample from the Eu:KYMo boule oriented in the {*a*, *b*, *c*} frame. It was polished from all lateral sides thus giving access to all three principal polarizations.

The RT polarized absorption spectrum in the visible (0.33–0.63 μm) was measured with a Varian CARY-5000 spectrophotometer (Agilent). The spectral bandwidth (SBW) was 0.01 nm. The absorption cross-section was calculated from the absorption coefficient, $\sigma_{\text{abs}} = \alpha_{\text{abs}}/N_{\text{Eu}}$. The RT polarized absorption spectrum in the near-IR (2000–5500 cm⁻¹) was measured using a FTIR spectrometer Bruker Tensor 27 with a spectral resolution of 1 cm⁻¹. For the polarization-resolved measurements, a Glan-Taylor polarizer was used.

The polarized RT emission spectra of Eu:KYMo were measured with a Renishaw inVia confocal micro-Raman microscope with a ×50 objective and an 1800 gr/mm grating. The excitation wavelength λ_{exc} was 458 nm (Ar⁺ ion laser). The spectral resolution was ~1 cm⁻¹. The unpolarized RT excitation spectrum was measured with a Cary Eclipse fluorescence spectrometer (Agilent). The luminescence was monitored at 612 nm and the spectral resolution was ~1 nm.

For the RT luminescence decay studies, the same Cary Eclipse spectrometer was employed. The excitation wavelength λ_{exc} was 400 or 532 nm. The decay from the ³D₀ state was monitored at

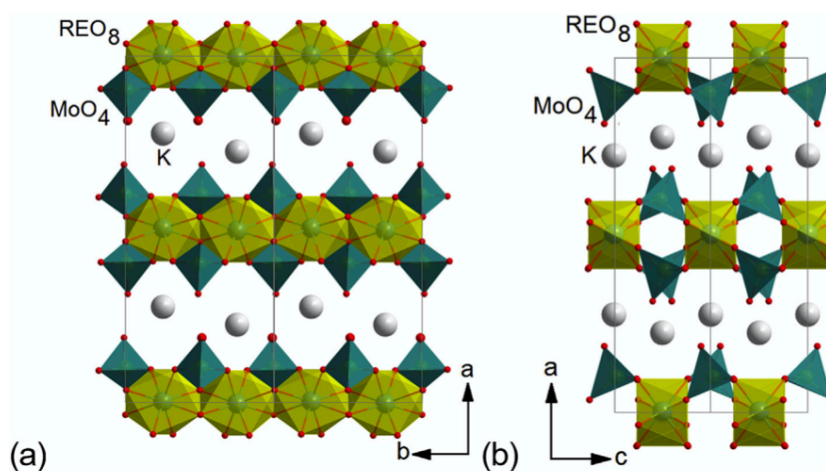


Fig. 4. Structure of Eu:KY(MoO₄)₂ (the axes are indicated according to the *Pbna* crystallographic setting) in projection on the *a-b* and *a-c* crystallographic planes. Yellow and green polyhedra indicate the [Y/EuO₈] and [MoO₄] groups, respectively. For Mo⁶⁺ cations, only the closest coordination polyhedron (C.N. = IV) is shown. (For interpretation of the references to color in this figure legend, the reader is referred to the Web version of this article.)

612 nm. The luminescence decay time τ_{lum} was determined according to a single-exponential law, $I_{lum}(t) = I_0 \exp(-t/\tau_{lum})$.

The polarized Raman spectra were measured for *a-*, *b-* and *c-* cut Eu:KYMo crystals using the same Renishaw inVia confocal micro-Raman microscope as used for the polarized RT emission spectra, λ_{exc} was 488 nm (Ar⁺ ion laser). The spectral resolution was $\sim 1 \text{ cm}^{-1}$.

4. Results and discussion

4.1. Raman spectroscopy

The polarized Raman spectra of the Eu:KYMo crystal for the *a*(xx)*a*, *b*(xx)*b* and *c*(xx)*c* geometries are shown in Fig. 5. Here, the standard $k_{exc}(E_{exc}E_{sc})k_{sc}$ notations are used where $E_{exc}|E_{sc}$ and $k_{exc}|k_{sc}$ vectors stand for the polarization and direction of propagation of the excitation and scattered light, respectively. The spectra are strongly polarized as a result of the layered structure feature of KYMo. The vibronic properties of undoped KYMo were described previously in detail [24,34]. Thus, we will discuss only the main features of the Raman spectra of Eu:KYMo.

The main features of KYMo concerning its vibration properties are the layered structure, causing vibrational branches in the Raman spectrum for layer-perpendicular wave vectors at relatively low frequencies, and the necessity to consider interactions between isolated tetrahedra [MoO₄]²⁻ [24]. The primitive unit-cell of the orthorhombic KYMo contains 48 atoms giving rise to $48 \times 3 = 144$ fundamental vibrations. According to the factor group analysis for KYMo, the symmetries of these vibrations can be described by irreducible representation at the center of the Brillouin zone ($k = 0$) as

$\Gamma = 17A_g + 19B_{1g} + 17B_{2g} + 19B_{3g} + 17A_u + 19B_{1u} + 17B_{2u} + 19B_{3u}$. Only 72 modes of even (gerade, g) parity are Raman active, including 17 symmetric vibrations of A_g , 72 antisymmetric odd (ungerade, u) modes B_{1u} , B_{2u} and B_{3u} are IR active and 17 vibrations of A_u symmetry are silent both in Raman and in IR spectra.

The selection rules allow vibrations of B_{1g} symmetry only for $k_{exc}(ac)k_{sc}$ and $k_{exc}(ca)k_{sc}$ geometries, B_{2g} - for $k_{exc}(bc)k_{sc}$ and $k_{exc}(cb)k_{sc}$, and B_{3g} - for $k_{exc}(ab)k_{sc}$ and $k_{exc}(ba)k_{sc}$ ones. For symmetric vibrations A_g , only diagonal elements of polarizability tensor are non-zero, corresponding to $k_{exc}(aa)k_{sc}$, $k_{exc}(bb)k_{sc}$ and

$k_{exc}(cc)k_{sc}$ geometries, Fig. 5. Applying structural model, in which pairs of [MoO₄]²⁻ tetrahedra linked through the oxygen bridges are considered as polyatomic ionic groups, the factor-group analysis distributes the 72 Raman-active vibrations over the $n(T') = 18$ translational modes, $n(R) = 6$ librational ones and $n(\text{Mo}_2\text{O}_8) = 48$ internal modes of the [Mo₂O₈]⁴⁻ ionic group. The simplified consideration within the model where the [MoO₄]²⁻ tetrahedra are isolated gives only 36 Raman-active internal modes of [MoO₄]²⁻, insufficient for interpretation of all observed vibrations.

The Raman spectra of Eu:KYMo contain bands located in three ranges, being different by their intensity. The first range (at 57–275 cm^{-1}) contains weak vibrations related to T' modes of K, Y and Mo, R modes and acousto-optic coupled modes (at $< 80 \text{ cm}^{-1}$). Internal modes are observed at higher frequencies $> 300 \text{ cm}^{-1}$. The second range is at 319–435 cm^{-1} containing bands of intermediate intensity related to the bending (δ) vibrations of the oxygen bridged [MoO₄]²⁻ tetrahedra. The last range, 726–1006 cm^{-1} , contains very intense modes due to the stretching (ν) vibrations of the oxygen bridged [MoO₄]²⁻. The most intense and strongly polarized Raman peaks appear at 866 and 945 cm^{-1} . The maximum phonon energy of Eu:KYMo $h\nu_{max}$ is 955 cm^{-1} .

The DT counterpart of KYMo, namely the monoclinic KYW, has a lower maximum phonon energy of 905 cm^{-1} . More specifically, its Raman spectrum does not contain a gap at 450–700 cm^{-1} being characteristic for scheelite-type crystals, e.g., tetragonal NaYW [35]. This gap appears due to the isolated nature of the [WO₄] tetrahedra in such crystals. In contrast, for KYW, the [WO₆] polyhedra are double-oxygen-bridge connected (WOOW) [2]. In KYMo, only a partial oxygen bridge of the [MoO₄] tetrahedra appears in the *b-c* plane. Thus, the vibronic properties of KYMo are intermediate between those for tetragonal NaYW and monoclinic KYW.

4.2. Optical absorption

The polarized absorption spectra of Eu:KYMo crystal in the visible are shown in Fig. 6(a and b). In general, for Eu³⁺ ions, all transitions for the absorption falling in the visible are spin-forbidden and thus their probability is relatively low. Note that for Eu³⁺ ions, the lower-lying excited states (⁷F₁ and ⁷F₂) are separated by a relatively small energy-gap from the ground-state, ⁷F₀ (360 cm^{-1} and 1020 cm^{-1} , respectively, compare with the *kT*

The absorption spectra of Eu:KYMo exhibit a strong polarization-anisotropy and the strongest absorption corresponds to $E \parallel c$. Fig. 6(c) presents an overview of the absorption spectrum for this polarization with a color fill indicating the possibilities for Eu^{3+} excitation. Eu lasers were pumped in the green by frequency-doubled (2ω) Nd ones, at $0.53 \mu\text{m}$ (${}^7\text{F}_{0,1} \rightarrow {}^5\text{D}_1$) [37]. This scheme is also beneficial because of the smallest quantum defect. Similarly to the blue pumping of visible lasers (e.g., Tb^{3+} ones) by 2ω optically pumped semiconductor lasers [38], the Eu^{3+} ions can be potentially excited at $0.46 \mu\text{m}$ (${}^7\text{F}_{0,1} \rightarrow {}^5\text{D}_2$). Finally, the strongest absorption band of Eu^{3+} in the visible, at $0.40 \mu\text{m}$ (${}^7\text{F}_{0,1} \rightarrow {}^5\text{L}_6$), is well matching the emission of blue GaN diodes.

For the ${}^7\text{F}_{0,1} \rightarrow {}^5\text{D}_1$ transition, the maximum absorption cross-section σ_{abs} is $0.37 \times 10^{-20} \text{cm}^2$ at 533.9nm for $E \parallel c$. The full width at the half maximum (FWHM) of the corresponding absorption peak is $< 2 \text{nm}$. For the same transition, the σ_{abs} values are much lower for light polarizations $E \parallel a$ ($0.11 \times 10^{-20} \text{cm}^2$ at 537.2nm) and for $E \parallel b$ ($0.03 \times 10^{-20} \text{cm}^2$ at 533.9nm). These values are lower than those for the monoclinic Eu:KYW crystal for which the maximum $\sigma_{\text{abs}} = 1.71 \times 10^{-20} \text{cm}^2$ at 534.3nm for $E \parallel N_m$ [15]. This can be ascribed to the lower symmetry of the latter host. Indeed, the FWHM of the corresponding absorption peak for Eu:KYW is only 0.5nm [15].

The polarized absorption spectra of Eu:KYMo in the near-IR are shown in Fig. 7. As mentioned above, the feature of Eu^{3+} is a series of lower-lying excited-states, from ${}^7\text{F}_1$ – ${}^7\text{F}_6$. The transitions to these states are spin-allowed and thus the corresponding absorption bands are rather intense (as compared to those in the visible). The IR absorption edge of Eu:KYMo is at $5.14 \mu\text{m}$ ($\sim 1950 \text{cm}^{-1}$). Thus, only the ${}^7\text{F}_{0,1} \rightarrow {}^7\text{F}_6$, ${}^7\text{F}_5$, ${}^7\text{F}_4$ and partially ${}^7\text{F}_3$ transitions are observed in the spectra.

The unpolarized excitation spectrum of the Eu:KYMo crystal (for $\lambda_{\text{lum}} = 612 \text{nm}$) is shown in Fig. 8. It is in good agreement with the measured absorption spectra.

4.3. Judd-Ofelt analysis based on the absorption spectra

The measured absorption spectra were analyzed within the standard Judd-Ofelt (J-O) theory [39,40] with thermal correction. The details of the J-O analysis for Eu^{3+} ions in a biaxial crystal can be found elsewhere [41]. We will describe only the main steps. The absorption transitions of Eu^{3+} mostly originate from the ${}^7\text{F}_0$ and ${}^7\text{F}_1$

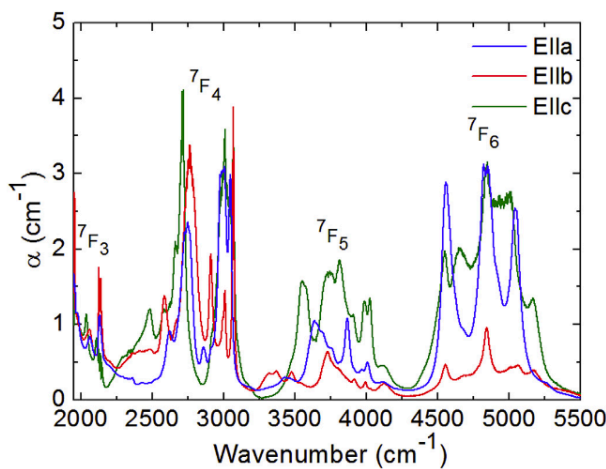


Fig. 7. Polarized absorption spectra of a 6 at.% Eu:KYMo crystal in the near-IR: light polarizations are $E \parallel a, b, c$.

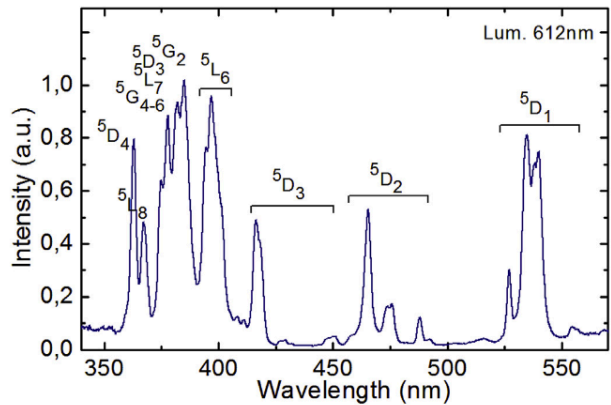


Fig. 8. Unpolarized excitation spectrum of a 6 at.% Eu:KYMo crystal, $\lambda_{\text{lum}} = 612 \text{nm}$.

states for which the corresponding fractional thermal populations X_j have to be taken into account:

$$X_j = \frac{B_j}{\sum_{j''=0-6} B_{j''}}, \text{ where } B_j = (2J + 1)e^{-E_j/(kT)}, \quad (1)$$

where B_j is the Boltzmann factor of the ${}^7\text{F}_j$ state for which the actual population N_j is $X_j N_{\text{Eu}}$. For most of the absorption transitions in Eu:KYMo, it was difficult to separate the contribution of the transitions from the ${}^7\text{F}_0$ and ${}^7\text{F}_1$ states to the integrated absorption. Thus, we considered its total value and, accordingly, effective experimental absorption oscillator strengths:

$$\langle f_{\text{exp}}^{\Sigma} \rangle (J)J' = \frac{m_e c^2}{\pi e^2 N_{\text{Eu}} \langle \lambda \rangle^2} \langle \Gamma((J)J') \rangle, \quad (2)$$

where m_e and e are the electron mass and charge, respectively, c is the speed of light, $\langle \Gamma((J)J') \rangle$ is the total integrated absorption coefficient for the transitions from the ${}^7\text{F}_{0,1}$ states (indicated by J), $\langle \lambda \rangle$ is the “center of gravity” of the absorption band. All parameters are considered as averaged over the three principal light polarizations, e.g., $\langle f_{\text{exp}}^{\Sigma} \rangle = 1/3(f_{\text{exp}}^{\Sigma}(\mathbf{a}) + f_{\text{exp}}^{\Sigma}(\mathbf{b}) + f_{\text{exp}}^{\Sigma}(\mathbf{c}))$. The $\langle f_{\text{exp}}^{\Sigma} \rangle$, $\langle \lambda \rangle$ and $\langle \Gamma \rangle$ values are listed in Table 3. Here and below, the Σ superscript indicates the total (ED + MD) value.

The absorption oscillator strengths can be also calculated from the ED line strengths ($S_{\text{calc}}^{\text{ED}}$):

$$\langle f_{\text{calc}}^{\Sigma} \rangle (J)J' = \frac{8}{3h\langle \lambda \rangle} \frac{(\langle n \rangle^2 + 2)^2}{9\langle n \rangle} \langle S_{\text{calc}}^{\text{ED}} \rangle (J)J' + \langle f_{\text{calc}}^{\text{MD}} \rangle (J)J', \quad (3)$$

Here, h is the Planck constant and $\langle n \rangle$ is the mean refractive index. The contribution of magnetic-dipole (MD) transitions with $J - J' = 0, \pm 1$ can be found elsewhere [42] and they should be thermally corrected. The ED line strengths can be calculated theoretically as:

$$\langle S_{\text{calc}}^{\text{ED}} \rangle (J)J' = \sum_{k=2,4,6} U^{(k)}(J)J' \Omega_k. \quad (4)$$

Here, Ω_2 , Ω_4 and Ω_6 are the J-O (intensity) parameters and $U^{(k)}(J)J'$ are the effective squared reduced matrix elements for the transitions in absorption:

Table 3

Experimental and calculated polarization-averaged absorption oscillator strengths ($f_{\text{exp}}^{\text{p}}$ and $f_{\text{calc}}^{\text{p}}$) for Eu^{3+} ions in KYMo.

Transition ${}^7\text{F}_{0,1} \rightarrow$	$\langle \lambda \rangle$, nm	$\langle I \rangle$, cm^{-1}nm	$U^{(k)}(\langle JJ' \rangle)$			$f_{\text{exp}}^{\text{p}}$ $\times 10^6$	$f_{\text{calc}}^{\text{p}}$ $\times 10^6$
			$U^{(2)}$	$U^{(4)}$	$U^{(6)}$		
${}^7\text{F}_4$	3473	1079	0	0.10966	0	3.887	3.975 ^{ED}
${}^7\text{F}_5$	2637	281.7	0	0.01395	0.00637	1.76	0.853 ^{ED}
${}^7\text{F}_6$	1999	474.7	0	0	0.13461	5.162	5.215 ^{ED}
${}^5\text{D}_1$	526.5	1.45	0.000283	0	0	0.206	0.160 ^{ED} +0.021 ^{MD}
${}^5\text{D}_2$	464.9	1.48	0.000533	0	0	0.295	0.346 ^{ED} +0.002 ^{MD}
${}^5\text{D}_3$	409.2	0.83	0.000047	0.00013	0	0.215	0.081 ^{ED}
${}^5\text{L}_6$	394.5	7.41	0	0	0.01083	2.068	2.344 ^{ED}
${}^5\text{G}_{4,5,6}, {}^5\text{L}_7, {}^5\text{D}_{3,5}, {}^5\text{G}_2$	376.4	6.63	0.00047	0.00067	0.00596	2.036	2.018 ^{ED}
${}^5\text{D}_4$	362.5	0.876	0	0.00077	0	0.29	0.303 ^{ED}
rms dev.							0.432

Averaging $\langle \rangle$ is performed over the three principal polarizations, $\mathbf{E} \parallel \mathbf{a}, \mathbf{b}, \mathbf{c}$; $\langle \lambda \rangle$ - barycenter of the absorption band, $\langle I \rangle$ - integrated absorption coefficient, $U^{(k)}(\langle JJ' \rangle)$ - effective squared reduced matrix elements (accounting for the transitions from both the ${}^7\text{F}_0$ ground-state and the thermally populated ${}^7\text{F}_1$ excited-state), ED and MD stand for the electric-dipole and magnetic-dipole contributions, respectively, rms dev. - root-mean-square deviation between $f_{\text{exp}}^{\text{p}}$ and $f_{\text{calc}}^{\text{p}}$.

$$U^{(k)}(\langle JJ' \rangle) = \sum_{J=0,1} \frac{X_J}{2J+1} U^{(k)}(JJ'), \quad (5)$$

The calculated ($f_{\text{calc}}^{\text{p}}$) values are shown in Table 3. The root-mean-square (rms) deviation between ($f_{\text{exp}}^{\text{p}}$) and ($f_{\text{calc}}^{\text{p}}$) is 0.432. The J-O parameters Ω_k determined from the absorption spectra are listed in Table 4.

4.4. Photoluminescence

We measured the unpolarized photoluminescence (PL) spectrum of Eu:KYMo, see Fig. 9 where the spectrum is color-filled according to the emission color. The intense and narrow line at ~614 nm (${}^5\text{D}_0 \rightarrow {}^7\text{F}_2$ Eu^{3+} transition) dominates in the spectrum and determines the red-orange color of the luminescence. The inset in Fig. 9 shows a photograph of the crystal under excitation by an UV lamp. The color coordinates of this emission was determined in the CIE 1931 (*Commission internationale de l'éclairage*) color space, $x = 0.665$ and $y = 0.335$ (red color). The dominant wavelength λ_d was 612 nm and the color purity p is >99%.

4.5. Stimulated-emission cross-sections

Using the J-O parameters determined from the absorption spectra (cf. Table 4), we calculated the probabilities of spontaneous radiative transitions from the ${}^5\text{D}_0$ and ${}^5\text{D}_1$ excited states A_{JJ}^{Σ} :

$$A_{\text{calc}}^{\Sigma}(JJ') = \frac{64\pi^4 e^2}{3h(2J+1)\langle \lambda \rangle^3} \langle n \rangle \left(\frac{\langle n \rangle^2 + 2}{3} \right)^2 S_{\text{calc}}^{\text{ED}}(JJ') + A^{\text{MD}}(JJ'), \quad (6)$$

the MD contribution was taken from Ref. [42]. On the basis of A_{JJ}^{Σ} , the total probabilities of radiative decay A^{tot} , the radiative lifetimes τ_{rad} and the luminescence branching ratios $B(JJ')$ were determined:

Table 4
Calculated J-O parameters for Eu^{3+} ions in KYMo.

Calculation based on:	$\Omega_k, 10^{-20} \text{cm}^2$		
	Ω_2	Ω_4	Ω_6
Absorption	13.16	5.86	3.60
Emission	13.47	6.61	3.61

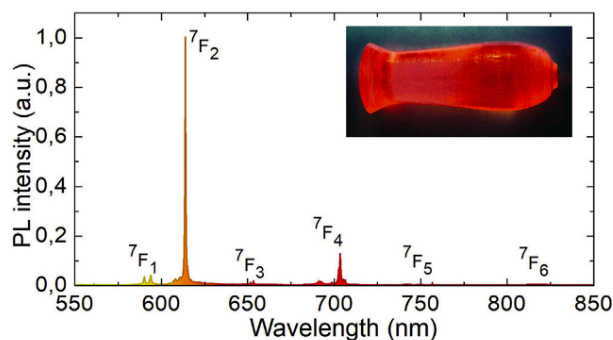


Fig. 9. Unpolarized photoluminescence (PL) spectrum of a 6 at.% Eu:KYMo crystal, $\lambda_{\text{exc}} = 458$ nm, the color fill corresponds to the emission wavelength. Inset - photograph of the crystal under excitation by an UV lamp.

$$\tau_{\text{rad}} = \frac{1}{A_{\text{calc}}^{\text{tot}}}, \text{ where } A_{\text{calc}}^{\text{tot}} = \sum_J A_{\text{calc}}^{\Sigma}(JJ'), \quad (7a)$$

$$B(JJ') = \frac{A_{\text{calc}}^{\Sigma}(JJ')}{A_{\text{calc}}^{\text{tot}}}, \quad (7b)$$

see Table 5. The radiative lifetime of the ${}^5\text{D}_0$ state is 0.658 ms. This lifetime is longer than that for Eu:KYW (0.464 ms) that can be ascribed to the structure features of KYMo composed of isolated layers containing the $[\text{YO}_8]$ polyhedra.

The PL spectra for each ${}^5\text{D}_0 \rightarrow {}^7\text{F}_J$ ($J = 1 \dots 6$) transition were measured with polarized light, W_{JJ}^i ($i = a, b, c$). Here, the index i numbers the orientation of the electric field vector \mathbf{E} and the magnetic field vector \mathbf{H} for ED ($J = 2 \dots 6$) and MD ($J = 1$) transitions, respectively, see more details below. From these spectra and the $\tau_{\text{rad}}({}^5\text{D}_0)$ value determined above, we calculated the stimulated-emission (SE) cross-sections, σ_{SE} . For this, the Füchtbauer–Ladengurg (F-L) formula was used [43]:

$$\sigma_{\text{SE}}^i(\lambda) = \frac{\lambda^5}{8\pi \langle n \rangle^2 \tau_{\text{rad}} c} \frac{W_{JJ}^i(\lambda)}{1/3 \sum_{i=a,b,c} \int \lambda W_{JJ}^i(\lambda) d\lambda}, \quad (8)$$

where c is the speed of light, λ is the light wavelength and the integration is performed within the spectral range covering all ${}^5\text{D}_0 \rightarrow {}^7\text{F}_J$ transitions. Note that typically in Eq. (8), only separate

Table 5
 Calculated emission probabilities for Eu^{3+} ions in KYMo (within the J-O theory, based on the absorption spectrum).

Transition	$\langle \lambda \rangle$, nm	A_{JJ}^{Σ} , s^{-1}	B_{JJ} , %	A_{tot} , s^{-1}	τ_{rad} , ms	
${}^5\text{D}_0 \rightarrow$	${}^7\text{F}_1$	591.0	127.95 ^{MD}	8.4	1521	0.658
	${}^7\text{F}_2$	614.1	1140.87 ^{ED}	75.0		
	${}^7\text{F}_4$	700.2	242.07 ^{ED}	15.9		
	${}^7\text{F}_6$	816.4	9.92 ^{ED}	0.65		
${}^5\text{D}_1 \rightarrow$	${}^7\text{F}_0$	528.6	11.306 ^{MD}	0.3	4327	0.231
	${}^7\text{F}_1$	539.3	1388.20 ^{ED} +0.03 ^{MD}	32.1		
	${}^7\text{F}_2$	553.8	378.10 ^{ED} +104.5 ^{MD}	11.2		
	${}^7\text{F}_3$	585.2	1917.43 ^{ED}	44.3		
	${}^7\text{F}_4$	623.6	415.45 ^{ED}	9.6		
	${}^7\text{F}_5$	661.2	90.09 ^{ED}	2.1		
	${}^7\text{F}_6$	718.6	19.85 ^{ED}	0.5		
	${}^5\text{D}_0$	5934.7	2.15 ^{MD}	0.05		

$\langle \lambda \rangle$ – estimated barycenter of emission band, A_{JJ}^{Σ} – probability of spontaneous radiative transition, B_{JJ} – luminescence branching ratios, A_{tot} – total probability of radiative spontaneous transitions from the excited-state, τ_{rad} – radiative lifetime of the excited-state; ED and MD stand for the electric-dipole and magnetic-dipole contributions, respectively.

emission channels ($J \rightarrow J'$) are considered and W_{JJ}^i is multiplied by the corresponding B_{JJ} value. However, for Eu^{3+} ions, the J-O theory does not allow for the calculation of the B_{JJ} values for some of the ${}^5\text{D}_0 \rightarrow {}^7\text{F}_J$ transitions (for $J = 0, 3$ and 5). The $0 \rightarrow 0'$ is both ED and MD forbidden, as mentioned above. According to the Wigner-Eckart theorem, the possible k indices for the Ω_k parameters satisfy the relation:

$$|J - J'| \leq k \leq |J + J'|, \quad (9)$$

and thus, for the $0 \rightarrow 3'$ and $0 \rightarrow 5'$ transitions, the corresponding $A_{JJ}^{\text{ED}} = 0$ (as $\Omega_3 = \Omega_5 = 0$) [44]. Obviously, the corresponding A_{JJ}^{MD} values are also zero. Because of this, we used the whole measured emission spectrum or, in other words, the experimental $B(JJ)_{\text{exp}}$ values (see Section 4.6).

The results achieved for σ_{SE} are shown in Fig. 10. The spectra are

strongly polarized. For the ${}^5\text{D}_0 \rightarrow {}^7\text{F}_2$ and ${}^5\text{D}_0 \rightarrow {}^7\text{F}_4$ transitions, which are of interest for laser applications, the highest σ_{SE} values correspond to $\mathbf{E} \parallel \mathbf{c}$ polarization, namely $11.4 \times 10^{-20} \text{ cm}^2$ at 613.9 nm and $2.5 \times 10^{-20} \text{ cm}^2$ at 703.5 nm, respectively. Despite the longer radiative lifetime of the ${}^5\text{D}_0$ state for Eu^{3+} ions in KYMo, the peak σ_{SE} values are larger than those for Eu^{3+} in monoclinic KYW (e.g., $4.0 \times 10^{-20} \text{ cm}^2$ at 613.4 nm) [15]. This is related to a stronger polarization-anisotropy of the SE properties of Eu:KYMo. Indeed, for the ${}^5\text{D}_0 \rightarrow {}^7\text{F}_2$ transition, the ratios of the peak σ_{SE} values are as high as $\sigma_{\text{SE}}(\text{c}):\sigma_{\text{SE}}(\text{a}) = 22.7$ and $\sigma_{\text{SE}}(\text{c}):\sigma_{\text{SE}}(\text{b}) = 8.6$. For Eu:KYW, these ratios are $\sigma_{\text{SE}}(\text{m}):\sigma_{\text{SE}}(\text{g}) = 5.6$ and $\sigma_{\text{SE}}(\text{m}):\sigma_{\text{SE}}(\text{p}) = 2.6$ [15].

For the Eu:KYMO crystal, several weak emissions in the 525–580 nm spectral range were also observed, Fig. 11. They are related to the transitions from the higher-lying ${}^5\text{D}_1$ excited-state to the ${}^7\text{F}_0$, ${}^7\text{F}_1$, ${}^7\text{F}_3$ and ${}^7\text{F}_3$ states [45]. We have not calculated the σ_{SE} spectra for these transitions because they are not suitable for laser

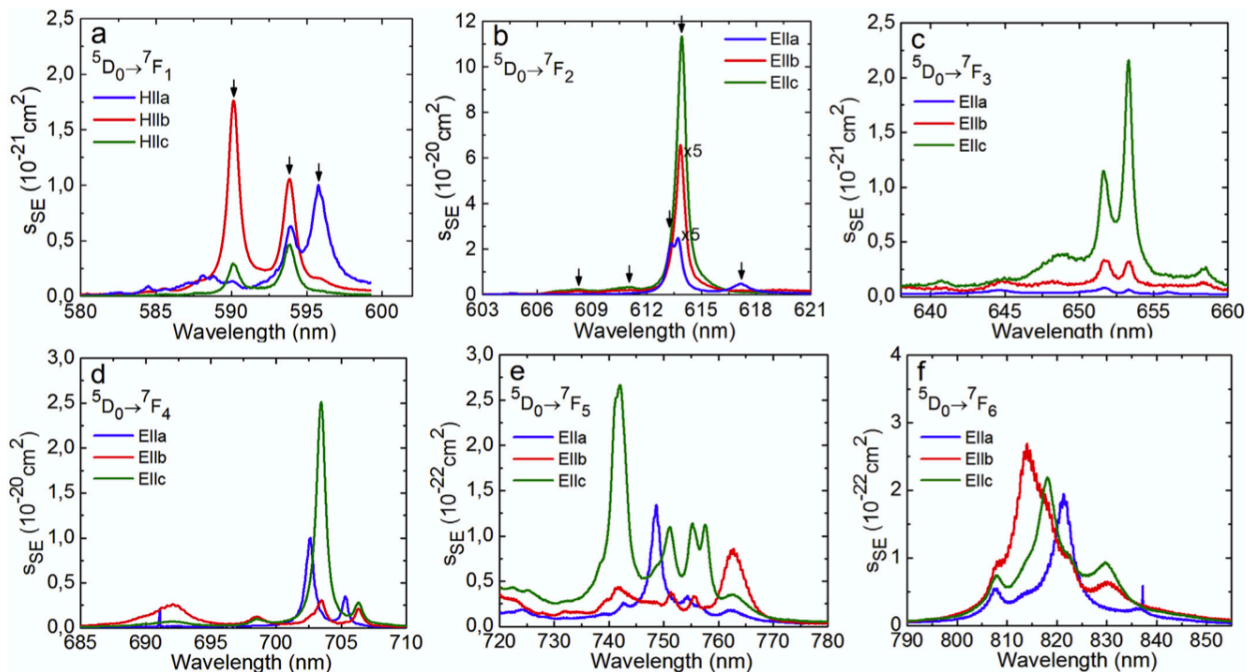


Fig. 10. Polarized stimulated-emission (SE) cross-section, σ_{SE} , spectra for Eu^{3+} ions in the Eu:KYMo crystal, plotted for the orientations of the electric field vector $\mathbf{E} \parallel \mathbf{a}, \mathbf{b}, \mathbf{c}$ (a–f) and magnetic field vector $\mathbf{H} \parallel \mathbf{a}, \mathbf{b}, \mathbf{c}$ (a). The arrows in (a,b) indicate the Stark-to-Stark transitions.

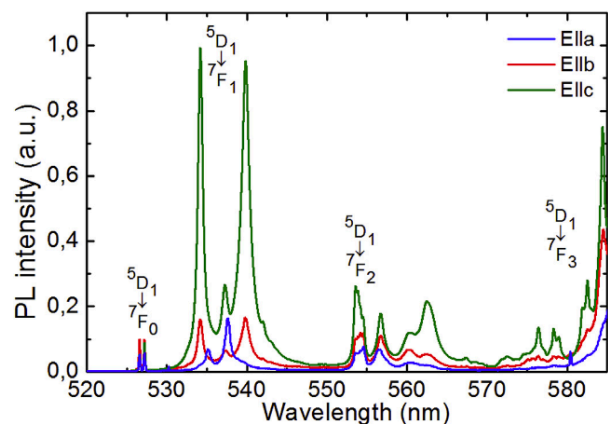


Fig. 11. Emissions of Eu^{3+} ions originating from the ${}^5\text{D}_1$ state in Eu:KYMo, light polarizations are $E \parallel a, b, c$, $\lambda_{\text{exc}} = 458 \text{ nm}$.

operation due to the strong NR relaxation for the ${}^5\text{D}_1 \rightarrow {}^5\text{D}_0$ channel (see also Section 4.8).

4.6. Judd-Ofelt analysis based on the emission spectra

Eu^{3+} ions are known for their purely MD transition ${}^5\text{D}_0 \rightarrow {}^7\text{F}_1$. The probability of this transition is weakly dependent on the host and can be calculated as:

$$A_{\text{calc}}^{\text{MD}}(01') = A_{\text{calc}}^{\text{MD}}(01')_{\text{vac}} \langle n \rangle^3, \quad (10)$$

where the first term is the vacuum probability, 14.5 s^{-1} [41]. Thus, one can calculate the probabilities of all spontaneous transitions ${}^5\text{D}_0 \rightarrow {}^7\text{F}_j$ from the experimental luminescence branching ratios $B(JJ')_{\text{exp}}$:

$$A_{\text{calc}}^{\Sigma}(0J') = A_{\text{calc}}^{\text{MD}}(01') \frac{B(0J')_{\text{exp}}}{B(01')_{\text{exp}}}, \quad (11a)$$

$$B(JJ')_{\text{exp}} = \frac{\int \langle W_{JJ'} \rangle(\nu) d\nu}{\sum_j \int \langle W_{JJ'} \rangle(\nu) d\nu}. \quad (11b)$$

Here, ν is the light frequency. From the set of values, a derivation of the J-O parameters is possible with Eq. (6) and (4). The $\tau_{\text{rad}}({}^5\text{D}_0)$ value can be directly determined with Eq. (7a). More details can be found in Ref. [46]. The results are presented in Table 6. The radiative lifetime of the ${}^5\text{D}_0$ state is 0.640 ms. The determined Ω_k parameters are listed in Table 4 showing a good agreement with the values determined from the absorption spectra (see Section 4.2). This confirms the accuracy of the performed J-O modelling.

Table 6

Calculated emission probabilities for Eu^{3+} ions in KYMo (within the J-O theory, based on the luminescence spectrum).

Transition	$\langle \lambda \rangle$, nm	$A_{JJ'}$, s^{-1}	$\langle B_{JJ'} \rangle$, %	A_{tot} , s^{-1}	τ_{rad} , ms	
${}^5\text{D}_0 \rightarrow$	${}^7\text{F}_1$	591	127.95 ^{MD}	8.191	1562	0.640
	${}^7\text{F}_2$	614	1168.18 ^{ED}	74.787		
	${}^7\text{F}_4$	700	255.94 ^{ED}	16.385		
	${}^7\text{F}_6$	816	9.938 ^{ED}	0.636		

$\langle B_{JJ'} \rangle$ – polarization-averaged luminescence branching ratios calculated from the measured emission spectra.

4.7. Asymmetry parameter

The feature of the purely MD transition ${}^5\text{D}_0 \rightarrow {}^7\text{F}_1$ generating the emission at $\sim 590 \text{ nm}$ is that the adjacent emission band is due to the purely ED transition ${}^5\text{D}_0 \rightarrow {}^7\text{F}_2$. The latter is known to be hyper-sensitive to the symmetry of the Eu^{3+} site [17]. If the site has no inversion center, this transition will be dominant over the ${}^5\text{D}_0 \rightarrow {}^7\text{F}_1$ one. The ratio of the integral intensities of the corresponding emission bands is known as an asymmetry parameter:

$$\langle R \rangle = \frac{\int \langle W_{02'}^{\text{ED}} \rangle(\nu) d\nu}{\int \langle W_{01'}^{\text{MD}} \rangle(\nu) d\nu}. \quad (12)$$

For Eu:KYMo, a polarization-averaged $\langle R \rangle$ parameter is 9.6 (a strong prevalence of the ED transition, in agreement with the C_2 site symmetry for $\text{Eu}^{3+}/\text{Y}^{3+}$ ions). This value is only slightly smaller than that for Eu:KYW, $R = 12$ [15].

4.8. Luminescence decay

The measured luminescence decay curves for Eu:KYMo with excitation at $\lambda_{\text{exc}} = 400 \text{ nm}$ and 532 nm are shown in Fig. 12. For both studied excitation wavelengths, these curves are linear when plotted in a semi-log scale. This indicates a single-exponential decay and agrees well with the assumption of a single type of site for Eu^{3+} ions. The mean measured luminescence decay time τ_{lum} is 0.652 ms. Thus, the intrinsic efficiency of luminescence from the ${}^5\text{D}_0$ state $\eta_q = \tau_{\text{lum}}/\tau_{\text{rad}}$ is $>99\%$. This is in agreement with the large energy-gap from the metastable ${}^5\text{D}_0$ state to the lower-lying ${}^7\text{F}_6$ one ($\sim 12200 \text{ cm}^{-1}$ [36]) even for a relatively high maximum phonon frequency of Eu:KYMo, $h\nu_{\text{max}} = 955 \text{ cm}^{-1}$, so that the NR relaxation is almost zero. Under this point of view, Eu:KYMo is an excellent luminescent material. Note that the actual value of the luminescence quantum yield should be measured using an integration

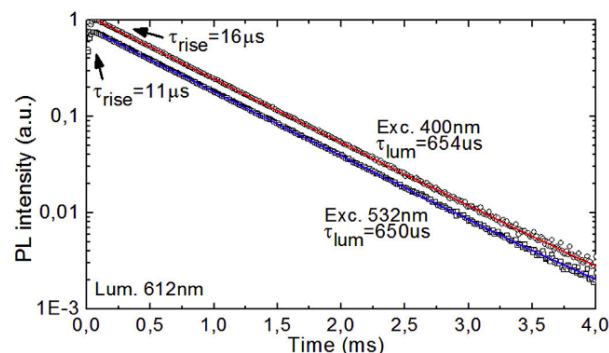


Fig. 12. Luminescence decay curves for a 6 at.% Eu:KYMo crystal, $\lambda_{\text{exc}} = 400 \text{ nm}$ or 532 nm , $\lambda_{\text{lum}} = 612 \text{ nm}$, symbols – experimental data, lines – their single-exponential fits.

sphere and a reference luminescent material (e.g., Eu^{3+} -based phosphor).

In Fig. 12, one can see a short rise of luminescence with a characteristic time τ_{rise} of 16 μs and 11 μs for $\lambda_{\text{exc}} = 400$ nm and 532 nm, respectively. It is related to the lifetimes of the excited-states above $^5\text{D}_0$. The two applied excitation wavelengths correspond to the transitions $^7\text{F}_1 \rightarrow ^5\text{L}_6$ and $^7\text{F}_1 \rightarrow ^5\text{D}_1$, respectively. Eu^{3+} ions excited to the $^5\text{L}_6$ or $^5\text{D}_1$ states can emit photons or experience a NR relaxation to the metastable $^5\text{D}_0$ state. The second process is more probable. This is because of small energy-gaps between the $^5\text{L}_6$ and $^5\text{D}_1$ excited-states ($<3000 \text{ cm}^{-1}$) [36]. Thus, the τ_{lum} lifetime of the $^5\text{D}_1$ state is about 11 μs and the lifetimes of the higher-lying states is about few μs . Such a short $\tau_{\text{lum}}(^5\text{D}_1)$ compared to the determined radiative one (0.231 ms) confirms the strong NR relaxation and explains the weakness of the emission bands in Fig. 11.

4.8. Magnetic-dipole $^5\text{D}_0 \rightarrow ^7\text{F}_1$ transition

A polarization-resolved study of the $^5\text{D}_0 \rightarrow ^7\text{F}_1$ emission band, Fig. 13, revealed some specific behavior. For this transition, the number and relative intensity of the corresponding emission peaks was found to depend not only on the light polarization \mathbf{E} , but also on its propagation direction \mathbf{k} . In Fig. 13, we used the $\mathbf{k}_{\text{exc}}(\mathbf{E}_{\text{exc}}\mathbf{E}_{\text{lum}})\mathbf{k}_{\text{lum}}$ notations adopted from the Raman spectra to illustrate it. Note that such an effect is not observed for all the remaining $^5\text{D}_0 \rightarrow ^7\text{F}_j$ ($j = 2 \dots 6$) transitions, which are purely ED.

This behavior can be understood by taking into account that the $^5\text{D}_0 \rightarrow ^7\text{F}_1$ transition is of purely MD nature. The MD transition is caused by interaction of the active ion (e.g., the RE^{3+} ion) with the magnetic field component of the light through a magnetic dipole which orientation is set by the vector \mathbf{M} . In other words, the orientation of the magnetic field vector \mathbf{H} with respect to \mathbf{M} is now relevant.

A similar behavior is known for uniaxial crystals [47] for which the optical axis $\parallel \mathbf{c}$ -axis. In general for both ED and MD transitions, the principal light polarizations are σ ($\mathbf{E} \perp \mathbf{c}, \mathbf{H} \parallel \mathbf{c}$), α ($\mathbf{E} \perp \mathbf{c}, \mathbf{H} \perp \mathbf{c}$) and π ($\mathbf{E} \parallel \mathbf{c}, \mathbf{H} \perp \mathbf{c}$). For ED transitions, the spectra for σ and α are identical, and for the MD ones, the spectra are the same for α and π . For orthorhombic, monoclinic and triclinic crystals (optically biaxial), this approach should be generalized.

For the C_2 site, each $^{2S+1}\text{L}_j$ multiplet of the RE^{3+} ion is split in the crystal field to $2j + 1$ Stark sub-levels, namely 1 for the $^5\text{D}_0$ state and

3 for the $^7\text{F}_1$ one. For the $^5\text{D}_0$ state, it corresponds to an irreducible representation Γ_1 (projection of quasi-momentum: $\mu = 0$). For the $^5\text{D}_1$ state, one sub-level corresponds to Γ_1 and two sub-levels equivalent for the selection rules correspond to Γ_2 (denoted as $\Gamma_2^{(1)}$ and $\Gamma_2^{(2)}$, with $\mu = 1$). The polarization selection rules for the $^5\text{D}_0 \rightarrow ^7\text{F}_1$ MD transition are $\Gamma_1 \rightarrow \Gamma_1$ for the orientation of the \mathbf{M} vector along the C_2 axis ($\mathbf{M} \parallel \mathbf{a}$) and $\Gamma_1 \rightarrow \Gamma_2^{(1)}, \Gamma_2^{(2)}$ for $\mathbf{M} \perp \text{C}_2$ ($\mathbf{M} \parallel \mathbf{b}, \mathbf{c}$).

The probability of MD inter-Stark transition in emission in our case is [48]:

$$dW^{\text{MD}} = \frac{\omega_{if}^3}{2\pi\hbar c^3} |\mathbf{e}_{\rho k} \cdot [\mathbf{k} \times \langle f | \mathbf{M} | i \rangle]|^2 d\Omega, \quad (13)$$

where, $\omega = 2\pi\nu$, $\hbar = h/2\pi$, i and f mark the initial and terminal Stark sub-level, Ω is a solid angle, $\mathbf{e}_{\rho k}$ is the polarization vector, ρ indicates the two possible polarization states. The square brackets [...] stand for a vector product. The latter is maximized when the \mathbf{k} and \mathbf{M} vectors are orthogonal. The whole mixed product $\mathbf{e}_{\rho k} \cdot [\mathbf{k} \times \langle f | \mathbf{M} | i \rangle]$ is maximized when all three vectors are mutually orthogonal. This allowed us to construct the table of polarization selection rules and the corresponding preferred orientations of \mathbf{k} and $\mathbf{e}_{\rho k}$ vectors, Table 7.

Now, let us analyse Fig. 13. For an \mathbf{a} -cut crystal, all spectra in Fig. 13 correspond to geometries 3, 4 from Table 7, so that $\Gamma_1 \rightarrow \Gamma_2^{(1)}, \Gamma_2^{(2)}$. Indeed, only two peaks are detected in the spectra, at 590.1 and 593.8 nm. For a \mathbf{b} -cut crystal, the $\mathbf{b}(\mathbf{ac})\mathbf{b}$ and $\mathbf{b}(\mathbf{cc})\mathbf{b}$ spectra correspond to geometries 1, 5, 6, so that all three $\Gamma_1 \rightarrow \Gamma_1, \Gamma_2^{(1)}, \Gamma_2^{(2)}$ transitions are allowed as indeed observed in the spectra. The additional peak at 595.8 nm is due to the $\Gamma_1 \rightarrow \Gamma_1$ transition. The $\mathbf{b}(\mathbf{ca})\mathbf{b}$ and $\mathbf{b}(\mathbf{aa})\mathbf{b}$ spectra correspond only to geometries 5, 6 ($\Gamma_1 \rightarrow \Gamma_2^{(1)}, \Gamma_2^{(2)}$) and only two peaks are observed. For a \mathbf{c} -cut crystal, the spectra $\mathbf{c}(\mathbf{ab})\mathbf{c}$ and $\mathbf{c}(\mathbf{bb})\mathbf{c}$ correspond to 2, 7, 8 geometries ($\Gamma_1 \rightarrow \Gamma_1, \Gamma_2^{(1)}, \Gamma_2^{(2)}$) and the $\mathbf{c}(\mathbf{ba})\mathbf{c}$ and $\mathbf{c}(\mathbf{aa})\mathbf{c}$ spectra – to the 7, 8 geometries ($\Gamma_1 \rightarrow \Gamma_1$) and indeed three and two lines are observed, respectively.

The analysis Table 7 and Fig. 13 indeed indicates the relevance of the orientation of \mathbf{H} vector (defined by a pair of \mathbf{k} and $\mathbf{e}_{\rho k}$) for the polarization selection rules of MD transitions.

Note that the emission intensity is also determined by crystal absorption. In our case, $\lambda_{\text{exc}} = 458$ nm ($^7\text{F}_0 \rightarrow ^5\text{D}_2$ ED transition), so that the absorption is determined by \mathbf{E}_{exc} . This explains why all spectra in Fig. 13 are different in shape and intensity: all of them correspond to different ($\mathbf{E}_{\text{exc}}, \mathbf{H}_{\text{lum}}$) pairs.

Because the shape of the emission spectra for the MD $^5\text{D}_0 \rightarrow ^7\text{F}_1$ transition is determined by the \mathbf{H}_{lum} vector, we plotted the σ_{SE} spectra in Fig. 10(a) for three \mathbf{H} orientations, along the $\mathbf{a}, \mathbf{b}, \mathbf{c}$ axes.

According to [16], the polarization-resolved analysis of the MD $^5\text{D}_0 \rightarrow ^7\text{F}_1$ and ED $^5\text{D}_0 \rightarrow ^7\text{F}_2$ transitions is a powerful tool to conclude about the site symmetry. If the $^5\text{D}_0 \rightarrow ^7\text{F}_1$ emission band contains 3 spectral lines, this will be an orthorhombic, monoclinic and triclinic crystal. Furthermore, if the $^5\text{D}_0 \rightarrow ^7\text{F}_2$ band contains 5 lines, the site symmetry will be C_1, C_2 or C_s and only C_2 and C_s are kept if this band exhibits polarization-anisotropy. This is in excellent agreement with our observations for C_2 Eu^{3+} site in KYMo.

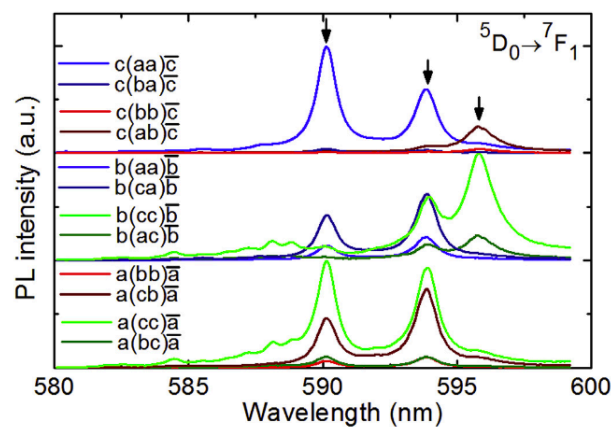


Fig. 13. Polarized photoluminescence (PL) spectra for the purely MD $^5\text{D}_0 \rightarrow ^7\text{F}_1$ transition of Eu^{3+} ions in the Eu:KYMo crystal, $\lambda_{\text{exc}} = 458$ nm. The $\mathbf{k}_{\text{exc}}(\mathbf{E}_{\text{exc}}\mathbf{E}_{\text{lum}})\mathbf{k}_{\text{lum}}$ notations are used. The arrows indicate the Stark-to-Stark transitions.

Table 7
Polarization selection rules for the $^5\text{D}_0 \rightarrow ^7\text{F}_1$ MD transition of Eu^{3+} ions in KYMo.

\mathbf{M} vector (MD)	$^5\text{D}_0 \rightarrow ^7\text{F}_1$	Preferred \mathbf{k}	Possible $\mathbf{e}_{\rho k}$	No.
$\mathbf{M} \parallel \text{C}_2$ ($\mathbf{M} \parallel \mathbf{a}$)	$\Gamma_1 \rightarrow \Gamma_1$	$\parallel \mathbf{b}$	$\parallel \mathbf{c}$	1
		$\parallel \mathbf{c}$	$\parallel \mathbf{b}$	2
$\mathbf{M} \perp \text{C}_2$ ($\mathbf{M} \parallel \mathbf{b}, \mathbf{c}$)	$\Gamma_1 \rightarrow \Gamma_2^{(1)}, \Gamma_2^{(2)}$	$\parallel \mathbf{a}$	$\parallel \mathbf{b}, \mathbf{c}$	3, 4
		$\parallel \mathbf{b}$	$\parallel \mathbf{a}, \mathbf{c}$	5, 6
		$\parallel \mathbf{c}$	$\parallel \mathbf{a}, \mathbf{b}$	7, 8

5. Conclusion

The orthorhombic KYMo double molybdate crystal is a promising host matrix for optically active RE³⁺ ions. In the present work, we have grown, by the Czochralski method, large-volume KYMo crystals doped with Eu³⁺ ions with high optical quality. This was facilitated by a proper melt composition with an addition of potassium trimolybdate (K₂Mo₃O₁₀) and low temperature gradients in the melt, <3 °C/cm. The Eu³⁺ ions were studied both as optical centers and structural probes. KYMo exhibits a layered structure leading to a perfect cleavage along the (100) plane. This structure feature promotes a strong polarization-anisotropy of spectroscopic properties of the Eu³⁺ ions, as well as vibronic properties of the host crystal exceeding those for monoclinic KYW double tungstate. Moreover, the perfect cleavage of KYMo can be used for the preparation of thin-film optical elements. Regarding the structural probing by Eu³⁺ doping, the accommodation of these ions in a single type of site (C₂) was confirmed. A magnetic-field vector dependent spectroscopy of the ⁵D₀ → ⁷F₁ MD Eu³⁺ transition has been described.

Eu:KYMo is of interest for red phosphors of high color purity and for red and deep-red lasers operating at the ⁵D₀ → ⁷F_{2,4} transitions. We believe that this study will motivate the development of KYMo crystals doped with other RE³⁺ ions such as Yb³⁺ or Tm³⁺, for emission in the near-IR. RE³⁺-doped KYMo crystals are expected to feature strong polarization anisotropy of transition cross-sections being beneficial for efficient laser operation.

Acknowledgements

This work was partially supported by Federal Agency for Scientific Organizations (Russia). P.L. acknowledges financial support from the

Government of the Russian Federation (Grant 074-U01) through ITMO Post-Doctoral Fellowship scheme. P.L. thanks Dr. Olga Dymshits for the XRD measurement.

References

[1] P.V. Klevtsov, R.F. Klevtsova, J. Struct. Chem. 18 (1977) 339–355.
[2] V. Petrov, M.C. Pujol, X. Mateos, Ó. Silvestre, S. Rivier, M. Aguiló, R.M. Solé, J.H. Liu, U. Griebner, F. Díaz, Laser Photon. Rev. 1 (2007) 179–212.
[3] J.M. Cano-Torres, M. Rico, X. Han, M.D. Serrano, C. Cascales, C. Zaldo, V. Petrov, U. Griebner, X. Mateos, P. Koopmann, C. Kränkel, Phys. Rev. B 84 (2011), 174207–1–15.
[4] J. Liu, V. Petrov, X. Mateos, H. Zhang, J. Wang, Opt. Lett. 32 (2007) 2016–2018.
[5] J.M. Serres, X. Mateos, P. Loiko, K. Yumashev, N. Kuleshov, V. Petrov, U. Griebner, M. Aguiló, F. Díaz, Opt. Lett. 39 (2014) 4247–4250.
[6] P. Loiko, J.M. Serres, X. Mateos, K. Yumashev, N. Kuleshov, V. Petrov, U. Griebner, M. Aguiló, F. Díaz, Opt. Lett. 40 (2015) 344–347.
[7] U. Griebner, S. Rivier, V. Petrov, M. Zorn, G. Erbert, M. Weyers, X. Mateos, M. Aguiló, J. Massons, F. Díaz, Opt. Express 13 (2005) 3465–3470.
[8] A. García-Cortes, J.M. Cano-Torres, M.D. Serrano, C. Cascales, C. Zaldo, S. Rivier, X. Mateos, U. Griebner, V. Petrov, IEEE J. Quant. Electron. 43 (2007) 758–764.
[9] C. Kränkel, D.-T. Marzahl, F. Moglia, G. Huber, P.W. Metz, Laser Photon. Rev. 10 (2016) 548–568.
[10] G. Wakefield, E. Holland, P.J. Dobson, J.L. Hutchison, Adv. Mater. 13 (2001) 1557–1560.

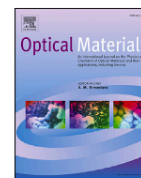
[11] S. Neeraj, N. Kijima, A.K. Cheetham, Chem. Phys. Lett. 387 (2004) 2–6.
[12] Z. Wang, H. Liang, L. Zhou, H. Wu, M. Gong, Q. Su, Chem. Phys. Lett. 412 (2005) 313–316.
[13] S.N. Bagayev, V.I. Dashkevich, V.A. Orlovich, S.M. Vatnik, A.A. Pavlyuk, A.M. Yurkin, Quant. Electron. 41 (2011) 189–192.
[14] V.I. Dashkevich, S.N. Bagayev, V.A. Orlovich, A.A. Bui, P.A. Loiko, K.V. Yumashev, A.S. Yasukevich, N.V. Kuleshov, S.M. Vatnik, A.A. Pavlyuk, Laser Phys. Lett. 12 (2015), 085001.
[15] P.A. Loiko, V.I. Dashkevich, S.N. Bagayev, V.A. Orlovich, A.S. Yasukevich, K.V. Yumashev, N.V. Kuleshov, E.B. Dunina, A.A. Kornienko, S.M. Vatnik, A.A. Pavlyuk, J. Lumin. 153 (2014) 221–226.
[16] K. Binnemans, C. Görrler-Walrand, J. Rare Earths 14 (1996) 173–180.
[17] A.F. Kirby, F.S. Richardson, J. Phys. Chem. 87 (1983) 2544–2556.
[18] R.F. Klevtsova, S.V. Borisov, Sov. Phys. Dokl. 12 (1968) 1095.
[19] A.A. Kaminskii, S.E. Sarkisov, L. Li, Phys. Status Solidi (a) 15 (1973) K141–K144.
[20] A.A. Kaminskii, H.R. Verdun, Phys. Status Solidi (a) 138 (1993) K49–K53.
[21] A.A. Kaminskii, P.V. Klevtsov, A.A. Pavlyuk, Phys. Status Solidi (a) 1 (1970) K91–K94.
[22] Y. Chen, Y. Lin, X. Gong, Q. Tan, Z. Luo, Y. Huang, J. Opt. Soc. Am. B 24 (2007) 496–503.
[23] A.A. Kaminskii, S.N. Bagayev, Quant. Electron. 24 (1994) 1029–1030.
[24] J. Hanuza, L. Łabuda, J. Raman Spectrosc. 11 (1981) 231–237.
[25] J. Hanuza, L. Macalik, W. Ryba-Romanowski, E. Mugeński, R. Cywiński, K. Witke, W. Piltz, P. Reich, J. Solid State Chem. 73 (1988) 488–501.
[26] W. Guo, Y. Lin, X. Gong, Y. Chen, Z. Luo, Y. Huang, J. Phys. Chem. Solid. 69 (2008) 8–15.
[27] Y. Wei, C. Su, H. Zhang, J. Shao, Z. Fu, Phys. B Condens. Matter 525 (2017) 149–153.
[28] L. Macalik, J. Alloys Compd. 41 (2002) 226–232.
[29] L. Li, J. Zhang, W. Zi, S. Gan, G. Ji, H. Zou, X. Xu, Solid State Sci. 29 (2014) 58–65.
[30] T. Wu, Y. Liu, Y. Lu, L. Wei, H. Gao, H. Chen, CrystEngComm 15 (2013) 2761–2768.
[31] V.A. Morozov, A.V. Arakcheeva, P. Pattison, K.W. Meert, P.F. Smet, D. Poelman, N. Gauquelin, Jo. Verbeeck, A.M. Abakumov, J. Hadermann, Chem. Mater. 27 (2015) 5519–5530.
[32] P.V. Klevtsov, A.A. Pavlyuk, Dokl. Akad. Nauk SSSR Kristallogr 203 (1972) 813–815.
[33] R.D. Shannon, Acta Crystallogr. A 32 (1976) 751–767.
[34] J. Hanuza, L. Macalik, Spectrochim. Acta A: Mol. Spectr. 38 (1982) 61–72.
[35] L. Macalik, J. Hanuza, A.A. Kaminskii, J. Mol. Struct. 555 (2000) 289–297.
[36] W.T. Carnall, P.R. Fields, K. Rajnak, J. Chem. Phys. 49 (1968) 4450–4455.
[37] V.I. Dashkevich, S.N. Bagayev, V.A. Orlovich, A.A. Bui, P.A. Loiko, K.V. Yumashev, N.V. Kuleshov, S.M. Vatnik, A.A. Pavlyuk, Laser Phys. Lett. 12 (2015), 015006.
[38] P.W. Metz, D.T. Marzahl, A. Majid, C. Kränkel, G. Huber, Laser Photon. Rev. 10 (2016) 335–344.
[39] B.R. Judd, Phys. Rev. 127 (1962) 750–761.
[40] G.S. Ofelt, J. Chem. Phys. 37 (1962) 511–520.
[41] P.A. Loiko, V.I. Dashkevich, S.N. Bagayev, V.A. Orlovich, X. Mateos, J.M. Serres, E.V. Vilejshikova, A.S. Yasukevich, K.V. Yumashev, N.V. Kuleshov, E.B. Dunina, A.A. Kornienko, S.M. Vatnik, A.A. Pavlyuk, J. Lumin. 168 (2015) 102–108.
[42] C.M. Dodson, R. Zia, Phys. Rev. B 86 (2012), 125102.
[43] B.F. Aull, H.P. Jenssen, IEEE J. Quant. Electron. 18 (1982) 925–930.
[44] P.A. Loiko, G.E. Rachkovskaya, G.B. Zakharevich, A.A. Kornienko, E.B. Dunina, A.S. Yasukevich, K.V. Yumashev, J. Non Cryst. Solids 392–393 (2014) 39–44.
[45] P.A. Loiko, E.V. Vilejshikova, X. Mateos, J.M. Serres, E.B. Dunina, A.A. Kornienko, K.V. Yumashev, M. Aguiló, F. Díaz, J. Lumin. 183 (2017) 217–225.
[46] P. Loiko, E.V. Vilejshikova, A.A. Volokitina, V.A. Trifonov, J.M. Serres, X. Mateos, N.V. Kuleshov, K.V. Yumashev, A.V. Baranov, A.A. Pavlyuk, J. Lumin. 188 (2017) 154–161.
[47] C. Görrler-Walrand, K. Binnemans, Handbook on the Physics and Chemistry of Rare Earths, vol. 25, 1998, pp. 101–264.
[48] L.K. Aminov, A.A. Kaminskii, B.Z. Malkin, Anisotropy of radiation intensity of activator ions in crystals, in: Physics and Spectroscopy of Laser Crystals, 1986. Moscow, Nauka.



Contents lists available at ScienceDirect

Optical Materials

journal homepage: www.elsevier.com/locate/optmat



Spectroscopy of Tb³⁺ ions in monoclinic KLu(WO₄)₂ crystal application of an intermediate configuration interaction theory

Pavel Loiko^a, Anna Volokitina^a, Xavier Mateos^{b,*}, Elena Dunina^c, Alexey Kornienko^c,
Elena Vilejshnikova^d, Magdalena Aguiló^b, Francesc Díaz^b

^a ITMO University, Kronverkskiy Pr., 49, 197101, Saint-Petersburg, Russia

^b Física i Cristal·lografia de Materials i Nanomaterials (FICMA-FICNA)-EMaS, Dept. Química Física i Inòrganica, Universitat Rovira i Virgili (URV), Campus Sescelades, E-43007, Tarragona, Spain

^c Vitebsk State Technological University, 72 Moskovskaya Ave., 210035, Vitebsk, Belarus

^d Center for Optical Materials and Technologies (COMT), Belarusian National Technical University, 65/17 Nezavisimosti Ave., 220013, Minsk, Belarus



ARTICLE INFO

Article history:

Received 5 February 2018

Received in revised form

27 February 2018

Accepted 7 March 2018

Keywords:

Double tungstates

Terbium ions

Absorption

Luminescence

Judd-Ofelt theory

Stimulated emission

ABSTRACT

The spectroscopic properties of Tb³⁺ ions in monoclinic KLu(WO₄)₂ double tungstate crystal are studied with polarized light. The absorption spectra in the visible, near- and mid-IR including the transitions to all lower-lying ⁷F_J (*J* = 0 ... 5) excited states are measured. The maximum absorption cross-section for the ⁷F₆ → ⁵D₄ transition is 3.42 × 10⁻²¹ cm² at 486.7 nm for light polarization *E* || *N*_m. The transition probabilities for Tb³⁺ ions are calculated within the Judd-Ofelt theory modified for the case of an intermediate configuration interaction (ICI). The radiative lifetime of the ⁵D₄ state is 450 μs and the luminescence quantum yield is >90%. The polarized stimulated-emission cross-section spectra for all ⁵D₄ → ⁷F_J (*J* = 0 ... 6) emission channels are evaluated. The maximum σ_{SE} is 11.4 × 10⁻²¹ cm² at 549.4 nm (for *E* || *N*_m). Tb³⁺:KLu(WO₄)₂ features high transition cross-sections for polarized light being promising for color-tunable visible lasers and imaging.

© 2018 Published by Elsevier B.V.

1. Introduction

Among the trivalent rare-earth ions (RE³⁺), Sm³⁺, Eu³⁺, Tb³⁺ and Dy³⁺ are rather attractive for obtaining multi-color laser emission in the visible [1]. In particular, the Tb³⁺ ions (electronic configuration: [Xe]4f⁸) are featuring a higher-lying (energy: ~20500 cm⁻¹) metastable excited state (⁵D₄) and a set of lower-lying ⁷F_J states (*J* = 6 ... 0 in order of increasing energy) [2]. This leads to multiple visible emissions due to the ⁵D₄ → ⁷F_J transitions that fall into the blue, green, yellow and red spectral ranges [3]. The ⁵D₄ state is long-living (from hundreds of μs to few ms) [3] and the corresponding luminescence quantum yield can be high due to the weak non-radiative (NR) processes even in oxide matrices with high phonon energies. The ⁵D₄ → ⁷F₅ transition at ~545 nm is the most probable one and a purely green emission from Tb³⁺ has been observed [4]. The rich structure of higher-lying excited-states of Tb³⁺ allows for efficient UV excitation of these ions.

Aside from the interest to Tb lasers, there are multiple studies of Tb³⁺-based green phosphors based on various matrices, i.e., glasses, glass-ceramics and nanoparticles [5–10]. This extended the understanding of Tb³⁺ spectroscopy. In recent years, the main interest shifted towards (Eu³⁺, Tb³⁺) and (Yb³⁺, Tb³⁺) codoped materials. The former codoped scheme brings the advantage of continuous color tuning (from red for singly Eu³⁺ doping to green for the Tb³⁺ one) [11,12]. The second codoped system is promising for down-conversion (DC) suitable to enhance the efficiency of silicon solar cells [13,14]. Such DC materials provide emission of up to 2 near-IR (~1 μm) photons from Yb³⁺ ions after the absorption of a single UV photon by a Tb³⁺ ion [13].

There are several early reports about the stimulated-emission from a Tb³⁺-doped glass [15], an organic solution [16] and a Tb:LiYF₄ crystal [17] under broadband flashlamp-pumping, and from a Tb³⁺-doped fiber laser [18]. Recently, efficient room-temperature (RT) Tb lasers were demonstrated using various fluoride crystals, namely LiYF₄, LiLuF₄, KY₃F₁₀, BaY₂F₈, CaF₂, LaF₃ and TbF₃ [3,19]. Lasing at ~545 nm (in the green, ⁵D₄ → ⁷F₅ transition) and at ~585 nm (in the yellow, ⁵D₄ → ⁷F₄ transition) were achieved. In the study of Metz et al., a highly-doped (28 at.%)

* Corresponding author.

E-mail address: xavier.mateos@urv.cat (X. Mateos).

Tb:LiLuF₄ laser pumped by a frequency-doubled optically pumped semiconductor laser (2ω-OPSL) at 486 nm (to the ⁵D₄ state) generated a maximum green output power of 1.13 W with a slope efficiency of 52% with respect to the absorbed pump power. In Ref. [19], wavelength tuning of Tb:CaF₂ and Tb:LiLuF₄ lasers between ~540 and 550 nm was also demonstrated.

The physical reason for application of fluoride crystals in Tb lasers is the following. Among the RE³⁺ ions, Tb³⁺ has one of the lowest energy separations between the multiplets of the 4f⁸ configuration and the 4f⁶5d¹ excited one [20]. The 4f⁸ → 4f⁶5d¹ transitions (e.g., the excited-state absorption (ESA)) are parity-allowed and thus more intense than the 4f⁸ → 4f⁸ transitions. Such interconfigurational ESA can strongly affect the laser performance [1,3]. For fluoride crystals, the so-called crystal field depression (CFD), which determines the splitting of the 4f⁶5d¹ levels and depends strongly on the host material) is small [20]. Thus, the unwanted interactions with the excited configuration are diminished. However, as it was shown by Metz et al., different host materials even with high CFD (e.g., oxide crystals) can be potentially suitable for Tb lasers.

Among the oxide crystals, the monoclinic double tungstates (MDTs) having a chemical formula of KRE(WO₄)₂ (shortly KREW) where RE stands for Y, Gd, Lu or Yb, are very attractive for RE³⁺ doping [21]. The two main features of MDTs are the high transition cross-sections for polarized light and high available RE³⁺ doping levels accompanied by weak luminescence quenching. Besides the ions suitable for near-IR lasers (at ~1 μm and at ~2 μm) [21], MDTs are recognized to be promising for visible lasers [22,23]. Dashkevich et al. presented a RT Eu:KGdW laser operating at 702 nm [23]. Stimulated-emission of Dy³⁺ ions in KYW (at 574 nm and 664 nm) was observed by Kaminskii et al. [24] at low temperature. Concerning Tb³⁺-doped MDTs, very scarce data can be found in the literature. The previous work on Tb:KLuW focused only on the crystal growth and thermal properties [25]. In Refs. [26–28], the luminescence of Tb³⁺ ions in isostructural KYW and KYbW crystals was studied. In particular, Loiko et al. reported on the polarized spectroscopy of Tb³⁺ ions in KYbW [28]. However, this is a stoichiometric crystal and it is less attractive for laser applications due to the possible Yb³⁺ ↔ Tb³⁺ energy-transfer processes.

The aim of the present work is to study the optical absorption and emission of Tb³⁺ ions in the monoclinic KLuW crystal with polarized light and to calculate the Tb³⁺ transition probabilities using the modified Judd-Ofelt theory.

2. Crystal growth

The KLuW crystal doped with 3 at.% Tb³⁺ ($N_{Tb} = 1.93 \times 10^{-20} \text{ cm}^{-3}$, crystal density, $\rho = 7.613 \text{ g/cm}^3$) was grown by the Top Seeded Solution Growth (TSSG) Slow-Cooling method using potassium ditungstate, K₂W₂O₇, as a solvent, see more details in Ref. [21]. The starting materials, K₂CO₃, Lu₂O₃, Tb₂O₃ and WO₃, were from Aldrich and Fluka (>99.9% purity). A seed from an undoped KYW crystal was used for starting the nucleation and was oriented along the [010] crystallographic axis. The structure of the grown crystal was confirmed with X-ray powder diffraction. Tb:KLuW is monoclinic (space group C_{2h}⁶ – C_{2/c}, No. 15, point group: 2/m). The as-grown crystal was transparent, it was free of cracks and inclusions. The crystal had a slight yellow-brown coloration due to the Tb³⁺ ions.

3. Experimental

The MDT crystals, including Tb:KLuW, are optically biaxial and have three principal refractive indices, $n_p < n_m < n_g$ [21]. The spectroscopic properties are then characterized in the frame of the

optical indicatrix, with the three orthogonal axes, denoted as N_p , N_m and N_g , respectively. For all monoclinic crystals, one of the optical indicatrix axes (it is N_p for MDTs) is parallel to the C₂ symmetry axis (or **b** crystallographic one). The two remaining optical indicatrix axes are located in the orthogonal mirror plane (the **a-c** plane). For KLuW, the angles $N_m^*a = 59.3^\circ$ and $N_g^*c = 18.5^\circ$ [21].

For the spectroscopic studies, we cut and polished a parallelepiped sample from the 3 at.% Tb:KLuW crystal with thicknesses t of 4.25 mm and 5.00 mm along the N_g - and N_p -axes, respectively, and thus giving access to all three principal polarizations.

The RT (293 K) absorption spectrum in the visible (0.36–0.51 μm) was measured with a Varian CARY-5000 spectrophotometer (Agilent). The spectral bandwidth (SBW) was 0.01 nm. The absorption cross-section was calculated from the absorption coefficient, $\sigma_{abs} = \alpha/N_{Tb}$. The RT absorption spectrum in the near-IR (1800–6200 cm⁻¹) was measured using a FTIR spectrometer Bruker Tensor 27 with a spectral resolution of 1 cm⁻¹. The spectra were measured for polarized light using a Glan-Taylor polarizer.

The polarized RT emission spectra of Tb:KLuW were measured with a Renishaw inVia confocal micro-Raman microscope with a ×50 objective and an 1800 l/mm grating. The excitation wavelength λ_{exc} was 458 nm or 488 nm. The spectra were combined to cover the 0.48–0.7 μm spectral range. The spectral resolution was ~1 cm⁻¹.

For the RT luminescence decay studies, a Cary Eclipse fluorescence spectrometer (Agilent) was used. The excitation wavelength λ_{exc} was 365, 380 or 475 nm. The decay from the ⁵D₄ state was monitored at 545 nm. The decay time τ_{lum} was determined according to a single-exponential law, $I_{lum}(t) = I_0 \exp(-t/\tau_{lum})$.

4. Results and discussion

4.1. Absorption

The absorption spectra of Tb³⁺ ions in KLuW are shown in Fig. 1

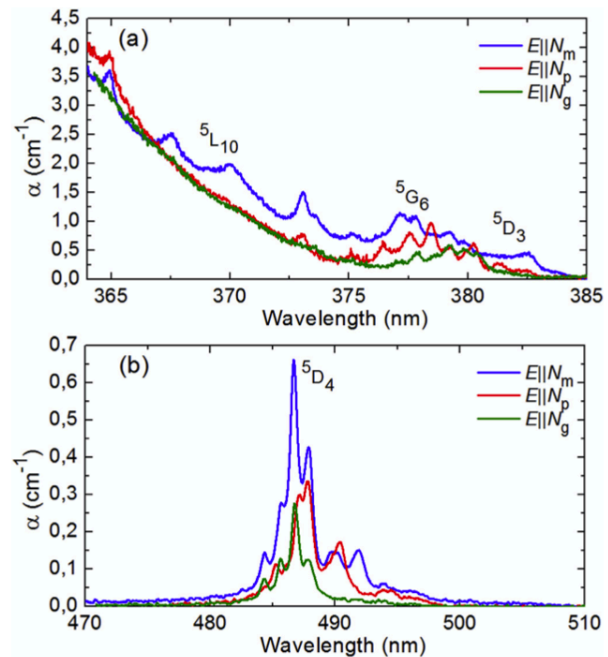


Fig. 1. Visible absorption spectra of a 3 at.% Tb:KLuW crystal with polarized light at RT. Transitions ⁷F₆ → ⁵D₃, ⁵G₆, ⁵L₁₀ (a) and ⁷F₆ → ⁵D₄ (b).

(for visible) and in Fig. 2 (for near-IR). The spectra are plotted for the principal light polarizations $\mathbf{E} \parallel N_p, N_m$ and N_g . Tb:KLuW provides a strong anisotropy of the absorption spectra for polarized light which is inherent for all RE³⁺-doped MDTs due to their low-symmetry structure. The maximum absorption corresponds to the $\mathbf{E} \parallel N_m$ polarization. The shape of the spectra is similar for $\mathbf{E} \parallel N_m$ and $\mathbf{E} \parallel N_g$ polarizations while being different from that for $\mathbf{E} \parallel N_p$. This is because for MDTs, the N_p -axis is parallel to the C_2 symmetry axis while both the N_m and N_g axes are lying in the mirror plane. Because of this, the selection rules for the 4f–4f transitions are different for light polarized along the N_p and (N_m, N_g) axes [29].

For Tb³⁺ ions, all the absorption bands at RT are due to transitions solely from the ground-state (⁷F₆) to excited ones. This behavior is different from that for Eu³⁺ ions featuring very similar structure of the energy-levels while exhibiting transitions in absorption originating not only from the ground-state (⁷F₀) but also from the thermally populated ⁷F₁ and even ⁷F₂ excited ones [30].

For Tb:KLuW, the weak absorption band in the visible (480–500 nm) is due to the spin-forbidden ⁷F₆ → ⁵D₄ transition, Fig. 1(b). The maximum σ_{abs} is $3.42 \times 10^{-21} \text{ cm}^2$ at 486.7 nm with a full width at half maximum (FWHM) of the corresponding absorption peak of 1.0 nm (all values are specified for $\mathbf{E} \parallel N_m$). The σ_{abs} is about two times lower for the light polarizations $\mathbf{E} \parallel N_p$ ($1.73 \times 10^{-21} \text{ cm}^2$ at 487.8 nm) and $\mathbf{E} \parallel N_g$ ($1.43 \times 10^{-21} \text{ cm}^2$ at 486.7 nm). The peak σ_{abs} value is higher than that for the isostructural Tb:KYbW crystal ($\sigma_{\text{abs}} = 2.3 \times 10^{-21} \text{ cm}^2$ at 486.7 nm) [28] and they are much higher than those for Tb³⁺-doped fluorides, e.g., Tb:LiLuF₄ ($0.3 \times 10^{-21} \text{ cm}^2$ at 488.8 nm for π -polarization) [3]. The multiple absorption peaks at 365–385 nm are due to the spin-forbidden transitions to the higher-lying ⁵D₃, ⁵G₆ and ⁵L₁₀ excited-states, Fig. 1(a). The UV absorption edge of Tb:KLuW is at ~360 nm ($E_g = 3.44 \text{ eV}$).

In the near-IR, Fig. 2, the absorption bands of Tb³⁺ are due to the transitions to the lower-lying ⁷F₅ – ⁷F₀ excited-states. As these transitions are spin-allowed, the peak absorption cross-sections σ_{abs} (about $2 \dots 3 \times 10^{-20} \text{ cm}^2$) are one order of magnitude higher than those for the absorption bands in the visible and UV ($1 \dots 2 \times 10^{-21} \text{ cm}^2$). The Tb:KLuW crystal is transparent until ~5.3 μm .

The spectroscopic properties of the Tb³⁺ ions were modeled within the standard Judd–Ofelt (J–O) theory [31,32] and its modifications accounting for the configuration interaction. First, the absorption oscillator strengths for Tb³⁺ ions were determined from the measured absorption spectra as [30]:

$$\langle f_{\text{exp}}^{\Sigma} \rangle (Jf) = \frac{m_e c^2}{\pi e^2 N_{\text{Tb}} \langle \lambda \rangle^2} \langle \Gamma(Jf) \rangle, \quad (1)$$

where m_e and e are the electron mass and charge, respectively, c is

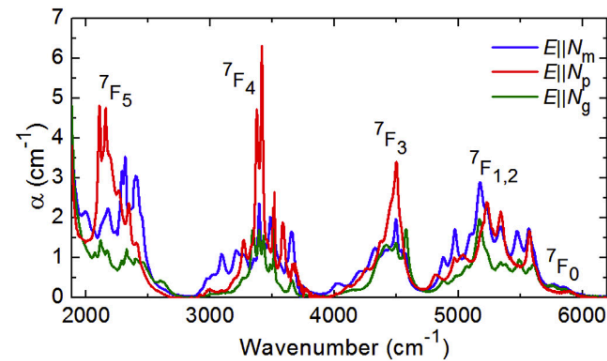


Fig. 2. Near-IR absorption spectra of a 3 at.% Tb:KLuW crystal with polarized light at RT.

the speed of light, $\langle \Gamma(Jf) \rangle$ is the integrated absorption coefficient and $\langle \lambda \rangle$ is the “center of gravity” of the absorption band. In the J–O modeling, we consider all the values as averaged over the three principal light polarizations, e.g., $\langle f_{\text{exp}}^{\Sigma} \rangle = 1/3(f_{\text{exp}}^p + f_{\text{exp}}^m + f_{\text{exp}}^g)$ [30]. The experimental $\langle f_{\text{exp}}^{\Sigma} \rangle$ values are listed in Table 1. The absorption oscillator strengths were also calculated theoretically as [30]:

$$\langle f_{\text{calc}}^{\Sigma} \rangle (Jf) = \frac{8}{3h(2J+1)\langle \lambda \rangle} \frac{(\langle n \rangle^2 + 2)^2}{9\langle n \rangle} \langle S_{\text{calc}}^{\text{ED}} \rangle (Jf) + \langle f_{\text{calc}}^{\text{MD}} \rangle (Jf), \quad (2)$$

Here, h is the Planck constant and $\langle n \rangle$ is the mean refractive index, $\langle S_{\text{calc}}^{\text{ED}} \rangle$ are the ED line strengths. The J–O theory describes electric-dipole (ED) transitions. The contribution of magnetic-dipole (MD) ones with $J - J' = 0, \pm 1$ was calculated separately within the Russell–Saunders approximation on wavefunctions of Tb³⁺ ion under the assumption of a free-ion. For the considered absorption spectrum of Tb³⁺, these are the ⁷F₆ → ⁷F₅ and ⁷F₆ → ⁵G₆ transitions.

In the case of an intermediate configuration interaction (ICI), the ED line strengths are given by Refs. [33,34]:

$$\langle S_{\text{calc}}^{\text{ED}} \rangle (Jf) = \sum_{k=2,4,6} U^{(k)} \tilde{Q}_k, \quad (3)$$

where:

$$\tilde{Q}_k = Q_k [1 + 2R_k (E_j + E_j - 2E_f^0)], \quad (4a)$$

$$U^{(k)} = \langle (4f^n)SLJ || U^{(k)} || (4f^n)S'LJ' \rangle^2 \quad (4b)$$

Here, $U^{(k)}$ are the squared reduced matrix elements for the transitions accounting for the absorption [28], R_k ($k = 2, 4, 6$) are the parameters representing the configuration interaction. In the ICI model, the J–O (intensity) parameters \tilde{Q}_k , Eq. (4a), are the linear functions of the energies of the two multiplets (E_j and E_j) involved in the transition, while E_f^0 is the mean energy of the 4fⁿ configuration. In the ICI model, there are 6 free parameters, namely Ω_k and R_k ($k = 2, 4, 6$). If only the excited configuration with opposite parity 4fⁿ⁻¹5d¹ contributes to the configuration interaction, then $R_2 = R_4 = R_6 = \alpha \approx 1/(2\Delta)$ and Eq. (4a) is simplified to [33]:

$$\tilde{Q}_k = Q_k [1 + 2\alpha (E_j + E_j - 2E_f^0)]. \quad (5)$$

Equation (3) with the intensity parameters given by Eq. (5) is referred as the modified J–O (mj–O) theory. In this case, there are 4 free parameters, namely $\Omega_2, \Omega_4, \Omega_6$ and α . Here, Δ means the energy of the excited configuration 4fⁿ⁻¹5d¹. For the case of higher-lying excited configuration of opposite parity ($\Delta \rightarrow \infty$):

$$\langle S_{\text{calc}}^{\text{ED}} \rangle (Jf) = \sum_{k=2,4,6} U^{(k)} Q_k. \quad (6)$$

This case corresponds to the standard J–O theory. There are three free parameters in this case, namely Ω_2, Ω_4 and Ω_6 .

The calculated absorption oscillator strengths ($f_{\text{calc}}^{\text{ED}}$) for Tb:KLuW crystal using the J–O, mj–O and ICI models are listed in Table 1. The ICI theory provides the smallest root mean square deviation (rms dev.) between the experimental, $\langle f_{\text{exp}}^{\Sigma} \rangle$, and calculated, $\langle f_{\text{calc}}^{\Sigma} \rangle = \langle f_{\text{calc}}^{\text{ED}} \rangle + \langle f_{\text{calc}}^{\text{MD}} \rangle$, absorption oscillator strengths, 0.295 (compare with rms dev. = 0.477 for the J–O theory and 0.482 for the mj–O one). The best-fit parameters of all the used theories are listed in Table 2. In particular, for the ICI model, $\Omega_2 = 18.170$, $\Omega_4 = 23.394$, $\Omega_6 = 13.459 [10^{-20} \text{ cm}^2]$ and $R_2 = -0.102$, $R_4 = 0.203$,

Table 1
Experimental and calculated absorption oscillator strengths for a 3 at.% Tb:KLuW crystal.

Transition	$f_{\text{exp}}^{\text{p}}, 10^{-6}$			$(f_{\text{exp}}^{\text{p}})^{\dagger}, 10^{-6}$	$(f_{\text{calc}}^{\text{ED}})^{\dagger}, 10^{-6}$			$(f_{\text{calc}}^{\text{MD}})^{\dagger}$
	N_p	N_m	N_g		J-O	mJ-O	ICI	
${}^7F_6 \rightarrow {}^7F_5$	7.20	9.45	4.26	6.97	6.38 ^{ED}	6.27 ^{ED}	6.33 ^{ED}	0.57 ^{MD}
${}^7F_6 \rightarrow {}^7F_4$	4.97	5.04	2.15	4.06	4.32 ^{ED}	4.38 ^{ED}	4.28 ^{ED}	–
${}^7F_6 \rightarrow {}^7F_3$	4.33	3.60	2.97	3.63	3.27 ^{ED}	3.22 ^{ED}	3.32 ^{ED}	–
${}^7F_6 \rightarrow {}^7F_{1,2}$	4.98	6.22	3.24	4.81	4.98 ^{ED}	4.95 ^{ED}	4.89 ^{ED}	–
${}^7F_6 \rightarrow {}^7F_0$	0.96	1.07	0.45	0.83	0.86 ^{ED}	0.85 ^{ED}	0.85 ^{ED}	–
${}^7F_6 \rightarrow {}^5D_4$	0.34	0.59	0.16	0.36	0.20 ^{ED}	0.22 ^{ED}	0.24 ^{ED}	–
${}^7F_6 \rightarrow {}^5D_3 + {}^5G_6$	1.42	2.70	1.25	1.79	0.64 ^{ED}	0.76 ^{ED}	1.55 ^{ED}	0.21 ^{MD}
<i>rms dev.</i>					0.477	0.482	0.295	

[†] $f_{\text{exp}}^{\text{p}}$ - experimental oscillator strengths, polarization-averaging: $(f_{\text{exp}}^{\text{p}})^{\dagger} = 1/3(f_{\text{p}}^{\text{p}} + f_{\text{m}}^{\text{p}} + f_{\text{g}}^{\text{p}})$, $(f_{\text{calc}}^{\text{ED}})^{\dagger}$ - calculated ones (ED and MD stand for electric and magnetic dipole contributions, respectively), *rms dev.* - root-mean-square deviation between $(f_{\text{exp}}^{\text{p}})^{\dagger}$ and $(f_{\text{calc}}^{\text{ED}})^{\dagger} = (f_{\text{calc}}^{\text{ED}})^{\dagger} + (f_{\text{calc}}^{\text{MD}})^{\dagger}$.

$R_6 = 0.170 [10^{-4} \text{ cm}]$. The *rms dev.* obtained in the present paper for Tb:KLuW is much lower than that reported for Tb:KYbW (0.887 with the J-O theory and 0.726 with the SCI one) [28]. This is referred mostly to the measurements of the absorption spectra in the near-IR performed in the present work, Fig. 2, where intense spin-allowed transitions ${}^7F_6 \rightarrow {}^7F_j$ are observed.

4.2. Emission

The probabilities for spontaneous radiative transitions are calculated from the line strengths [30]:

$$A_{\Sigma}^{\text{calc}}(JJ') = \frac{64\pi^4 e^2}{3h(2J'+1)\langle\lambda\rangle^3} n \left(\frac{n^2+2}{3} \right)^2 S_{ED}^{\text{calc}}(JJ') + A_{MD}(JJ'). \quad (7)$$

The values of $U^{(k)}$ for the transitions accounting for the emission are listed in Ref. [28]. The MD contributions were calculated in the present paper under the assumption of a free ion as described above. The mean emission wavelengths for each $J \rightarrow J'$ transition, $\langle\lambda\rangle$, were determined from the barycenters of the absorption, Figs. 1 and 2, and emission, Fig. 3, bands of Tb^{3+} ions. From the values of A for separate emission channels $J \rightarrow J'$, we calculated the total probability $A_{\text{tot}}^{\text{calc}}$, the radiative lifetimes of the excited-states τ_{rad} and the luminescence branching ratios for the separate emission channels $B(JJ')$:

$$\tau_{\text{rad}} = \frac{1}{A_{\text{tot}}^{\text{calc}}}, \text{ where } A_{\text{tot}}^{\text{calc}} = \sum_{J'} A_{\Sigma}^{\text{calc}}(JJ'), \quad (8a)$$

$$B(JJ') = \frac{A_{\Sigma}^{\text{calc}}(JJ')}{\sum_{J'} A_{\Sigma}^{\text{calc}}(JJ')} \quad (8b)$$

The results on the probabilities for radiative transitions are listed in Table 3 for transitions from the 5D_4 and 5D_3 excited states (according to the ICI theory). The radiative lifetime of the metastable 5D_4 state is 0.450 ms. In Table 4, we have compared the τ_{rad} values for the 5D_4 and 5D_3 states as determined with the J-O, mJ-O and SCI theories. In our previous study of an isostructural Tb:KYbW crystal [28], the $\tau_{\text{rad}}({}^5D_4)$ was calculated as 2.08 ms using the strong

configuration interaction (SCI) theory. This value is longer than that determined in the present work. We attribute this difference to a lower precision of the analysis in Ref. [28] due to the lack of absorption studies in the near-IR as performed in this work, cf. Fig. 2. Tb:KLuW possesses a shorter radiative lifetime of the 5D_4 state as compared to oxide crystals such as $\text{TbAl}_3(\text{BO}_3)_4$ ($\tau_{\text{rad}}({}^5D_4) = 2.07 \text{ ms}$) [35] and TbAlO_4 ($\tau_{\text{rad}}({}^5D_4) = 3.5 \text{ ms}$) [4].

The photoluminescence (PL) spectrum of Tb:KLuW under excitation at 488 nm (to the 5D_4 state) is shown in Fig. 3 for light polarization $E \parallel N_m$. The band related to the ${}^5D_4 \rightarrow {}^7F_6$ transition was measured separately under 458 nm excitation. The PL spectrum thus includes all the ${}^5D_4 \rightarrow {}^7F_j$ ($J = 6 \dots 0$) transitions: 484–500 nm (blue, $J = 6$), 540–552 nm (green, $J = 5$), 578–593 nm (orange, $J = 4$), 614–627 nm (red, $J = 3$), 639–665 nm (red, $J = 2$), 665–685 nm (deep-red, $J = 1$) and 686–700 nm (deep-red, $J = 0$). The corresponding emission colors are indicated in Fig. 3 by filling the spectra. The most intense emission band is due to the ${}^5D_4 \rightarrow {}^7F_5$ transition that is typical for Tb^{3+} -doped materials [4].

The scheme of energy-levels of Tb^{3+} ions and the observed transitions in absorption and emission are shown in Fig. 4. In this

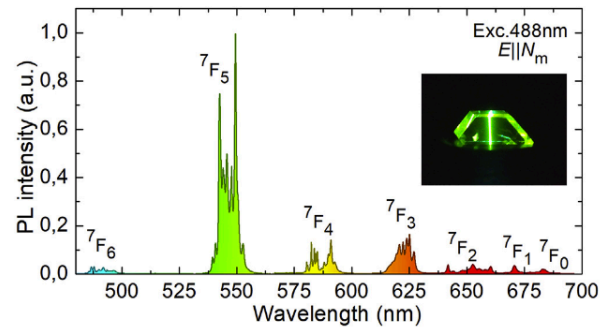


Fig. 3. Combined photoluminescence (PL) spectrum of a 3 at.% Tb:KLuW crystal at RT for light polarization $E \parallel N_m$; the excitation wavelength is 458 nm (${}^5D_4 \rightarrow {}^7F_6$ emission band) and 488 nm (remaining bands). The color fill corresponds to the emission wavelength. *Inset* shows a photo of the crystal under excitation. (For interpretation of the references to color in this figure legend, the reader is referred to the Web version of this article.)

Table 2
Parameters of J-O, mJ-O and ICI theories applied to calculate the absorption oscillator strengths for a Tb:KLuW crystal.

Theory	Parameters	Value: Tb:KLuW
J-O	$\Omega_k [10^{-20} \text{ cm}^2]$	$\Omega_2 = 23.524, \Omega_4 = 8.111, \Omega_6 = 6.918$
mJ-O	$\Omega_k [10^{-20} \text{ cm}^2]; \alpha [10^{-4} \text{ cm}]$	$\Omega_2 = 25.496, \Omega_4 = 9.590, \Omega_6 = 7.589; \alpha = 0.033$
ICI	$\Omega_k [10^{-20} \text{ cm}^2]; R_k [10^{-4} \text{ cm}]$	$\Omega_2 = 18.170, \Omega_4 = 23.394, \Omega_6 = 13.459; R_2 = -0.102, R_4 = 0.203, R_6 = 0.170$

Table 3
 Calculated emission probabilities for Tb³⁺ ions in a 3 at.% Tb:KLuW crystal (for the ICI theory).

Excited state	Terminating state	A _{JJ'} , s ⁻¹	B _{JJ'} , %	A _{tot} , s ⁻¹	τ _{rad} , ms
⁵ D ₄ →	⁷ F ₆	351.4 ^{ED}	15.8	2221.6	0.450
	⁷ F ₅	1076.6 ^{ED} +90.5 ^{MD}	52.5		
	⁷ F ₄	241.3 ^{ED} +0.4 ^{MD}	10.9		
	⁷ F ₃	139.5 ^{ED} +10.8 ^{MD}	6.8		
	⁷ F ₂	65.5 ^{ED}	2.9		
	⁷ F ₁	148.7 ^{ED}	6.7		
	⁷ F ₀	97.9 ^{ED}	4.4		
⁵ D ₃ →	⁷ F ₆	383.2 ^{ED}	8.5	4535.0	0.221
	⁷ F ₅	1227.5 ^{ED}	27.1		
	⁷ F ₄	916.9 ^{ED} +105.2 ^{MD}	22.5		
	⁷ F ₃	340.2 ^{ED} +1.6 ^{MD}	7.5		
	⁷ F ₂	772.2 ^{ED} +30.4 ^{MD}	17.7		
	⁷ F ₁	413.6 ^{ED}	9.1		
	⁷ F ₀	–	–		
	⁵ D ₄	294.5 ^{ED} +49.7 ^{MD}	7.6		

A_{JJ'} - probability of spontaneous transition (ED and MD stand for electric and magnetic dipole contributions, respectively), B_{JJ'} - luminescence branching ratio, A_{tot} - total probability of spontaneous transitions, τ_{rad} - radiative lifetime.

Table 4
 Calculated radiative lifetimes of the ⁵D₄ and ⁵D₃ excited-states of Tb³⁺ ions in KLuW crystal (for J-O, mj-O and ICI theories).

Excited state	τ _{rad} , ms		
	J-O	mj-O	ICI
⁵ D ₄	0.500	0.449	0.450
⁵ D ₃	0.323	0.275	0.221

figure, we have also indicated the efficient resonant cross-relaxation (CR) process, ⁵D₃ + ⁷F₆ → ⁵D₄ + ⁷F_{0,1}, responsible for the depopulation of the ⁵D₃ excited-state [36].

The measured PL decay curves for Tb³⁺ ions in a 3 at.% Tb:KLuW crystal are plotted in Fig. 5. The emission was monitored at 545 nm (from the ⁵D₄ state). Several excitation wavelengths were tested,

namely 475 nm (direct excitation to the emitting state), 380 nm (to the ⁵D₃ excited-state) and 365 nm (to the higher-lying ⁵L₁₀ one). All the measured curves are clearly single-exponential as revealed in Fig. 5 plotted in a semi-log scale. This agrees with the accommodation of Tb³⁺ ions in a single type of site (Lu³⁺ site with a C₂ symmetry and VIII-fold O²⁻ coordination [21], ionic radii: 0.977 Å for Lu³⁺ and 1.04 Å for Tb³⁺). The luminescence decay time τ_{lum} is 411 ± 3 μs. The τ_{lum} is slightly shorter than the radiative one, resulting in a luminescence quantum efficiency η_q = τ_{lum}/τ_{rad} of 91%. Such a high value can be expected for Tb³⁺ ions due to the large energy gap between the ⁵D₄ state and the lower-lying excited-state (⁷F₀) which is about 15000 cm⁻¹ [2]. Indeed, as the maximum phonon frequency hν_{max} of KLuW is 908 cm⁻¹ [21], the non-radiative relaxation from the ⁵D₄ state is not probable. A similar effect is observed for the metastable ⁵D₀ state of Eu³⁺ ions in KLuW [30]. Previously for the isostructural 1 at.% Tb:KYbW and 5 at.% Tb:KYW crystals, τ_{lum}(⁵D₄) was determined to be 395 μs and 460 μs, respectively, which is close to the value measured in the present work [26,28].

The PL spectra of Tb³⁺ ions were measured for all three principal light polarizations, E || N_p, N_m and N_g. Using such spectra, the polarized stimulated-emission (SE) cross-section, σ_{SE}, spectra for Tb³⁺ ions were calculated with the Füchtbauer–Ladenburg (F-L) equation [37]:

$$\sigma_{SE}^i(\lambda) = \frac{\lambda^5}{8\pi n_i^2 \tau_{rad} c} \frac{W_i(\lambda) B(JJ')}{1/3 \sum_{i=p,m,g} \int \lambda W_i(\lambda) d\lambda} \quad (9)$$

Here, W_i(λ) is the measured spectral power density of luminescence for the i-th polarization, i = p, m, g, n_i is the corresponding refractive index taken from Ref. [21], τ_{rad} is the radiative lifetime of the ⁵D₄ state of Tb³⁺ and integration in Eq. (9) is performed within the emission band corresponding to the particular ⁵D₄ → ⁷F_J transition. The σ_{SE} spectra are shown in Fig. 6. The Tb³⁺ ions in KLuW exhibit strong anisotropy for polarized light. The maximum σ_{SE} values correspond to E || N_m (so that this polarization is the most

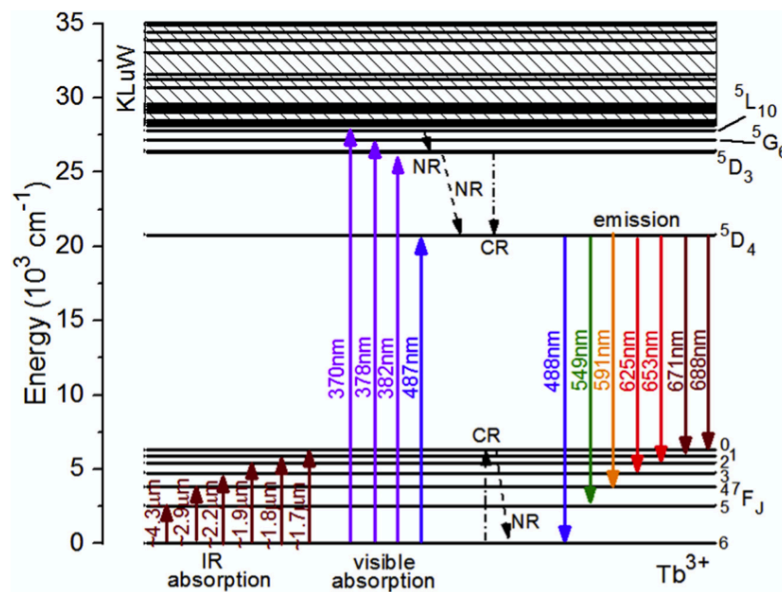


Fig. 4. Scheme of the energy levels of Tb³⁺ ions in KLuW and the observed transitions for absorption and emission (shown by solid arrows). NR – non-radiative relaxation, CR – cross-relaxation. Dashed area – host absorption of KLuW.

500

P. Loiko et al. / Optical Materials 78 (2018) 495–501

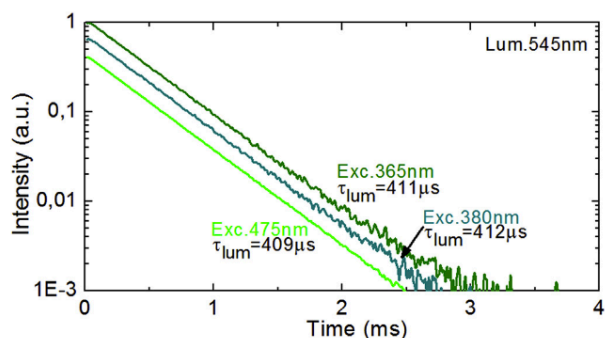


Fig. 5. Decay of the green luminescence of Tb^{3+} ions at 545 nm for a 3 at.% Tb:KLuW crystal at RT, the excitation wavelength is 365 nm, 380 nm or 475 nm, τ_{lum} is the luminescence decay time according to a single-exponential fit. (For interpretation of the references to color in this figure legend, the reader is referred to the Web version of this article.)

attractive for laser operation), the intermediate ones – to $E \parallel N_p$ and the lowest ones – to light polarized parallel to the N_g -axis. This trend is similar for most of the RE^{3+} ions in MDTs [21]. For the $^5D_4 \rightarrow ^7F_5$ transition, the maximum $\sigma_{SE} = 11.4 \times 10^{-21} \text{ cm}^2$ at 549.4 nm (for $E \parallel N_m$). The peak σ_{SE} values for all the $^5D_4 \rightarrow ^7F_J$ transitions are listed in Table 5. The maximum σ_{SE} value for Tb^{3+} ions in KLuW is much larger than those for Tb:LiLuF₄ crystal, namely $\sim 1.6 \times 10^{-21} \text{ cm}^2$ at $\sim 540 \text{ nm}$ for σ -polarization [3].

The unpolarized PL spectra of the Tb:KLuW crystal under blue excitation were characterized in terms of the CIE 1931 (*Commission internationale de l'éclairage*) chromaticity diagram. The color coordinates are $x = 0.380$ and $y = 0.608$ that fall into the yellowish green region. The dominant wavelength λ_d is 561 nm with a color purity p of $>97\%$ (for a 2° observer).

5. Conclusion

The Tb^{3+} -doped monoclinic $KLu(WO_4)_2$ crystal is promising for color tunable visible (green and yellow) lasers. Due to its low-symmetry structure, it features high transition cross-sections for absorption and emission with polarized light. The upper-laser level (5D_4) lifetime of Tb^{3+} ions is 411 μs (for 3 at.% Tb^{3+} doping) and the luminescence quantum yield is $>90\%$. We have successfully applied the J-O theory modified for the case of an intermediate configuration interaction (ICI) for the description of the transition probabilities of Tb^{3+} ions in $KLu(WO_4)_2$. Due to the measurements of the characteristic Tb^{3+} absorption ($^7F_6 \rightarrow ^7F_J, J = 0 \dots 5$) in the near- and mid-IR, we were able to improve the quality of the J-O analysis and to predict a higher luminescence quantum efficiency of Tb^{3+} : $KLu(WO_4)_2$ crystals, similarly to those doped with Eu^{3+} ions. We determine that $KLu(WO_4)_2$ doped with Tb^{3+} is more attractive than the isostructural stoichiometric crystal Tb^{3+} : $KYb(WO_4)_2$ studied recently due to the higher transition cross-sections and the lack of parasitic cooperative $2 Yb^{3+} \leftrightarrow Tb^{3+}$ processes.

As the transitions suitable for Tb^{3+} pumping (e.g., $^7F_6 \rightarrow ^5D_4$, falling in the blue spectral range) are spin-forbidden, relatively high doping concentrations of Tb^{3+} are required to ensure high pump absorption efficiency. The future work will focus on the growth of highly Tb^{3+} -doped $KLu(WO_4)_2$ crystals (the isostructural series of monoclinic $KLu_{1-x}Tb_x(WO_4)_2$ up to the stoichiometric $KTb(WO_4)_2$ exists) and the study of the concentration effects on the Tb^{3+} spectroscopy, e.g., the luminescence quenching and the cross-

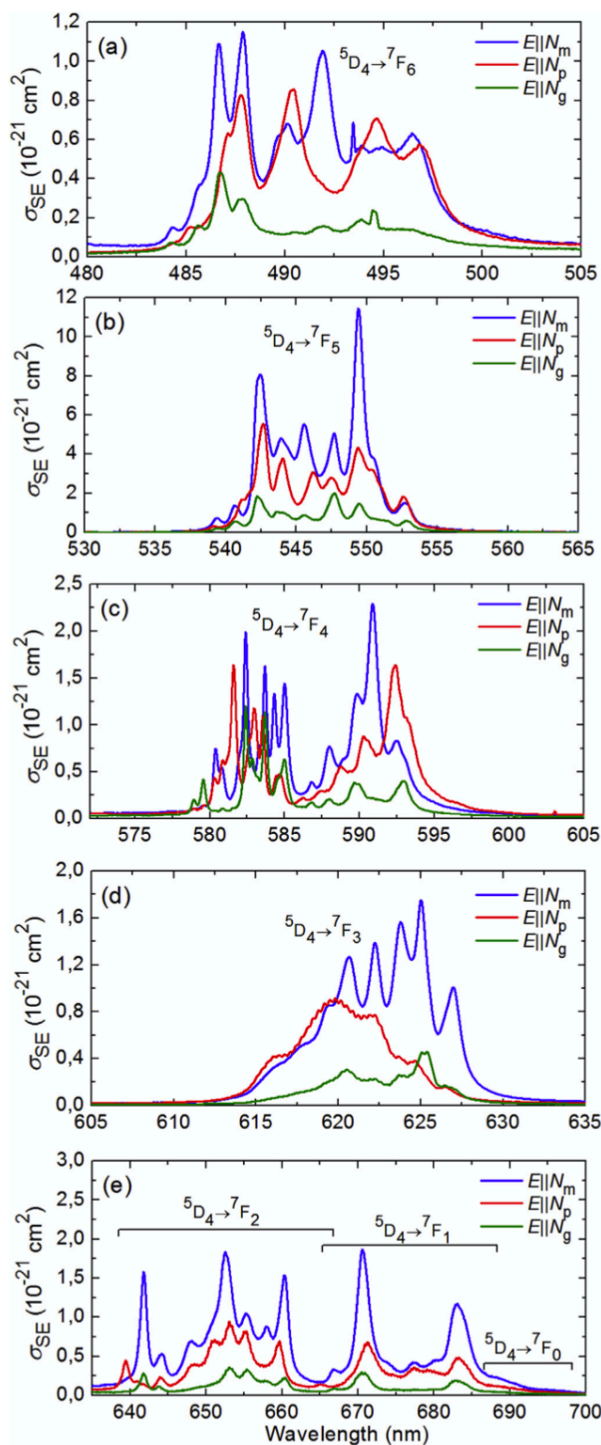


Fig. 6. (a)–(e) Stimulated-emission cross-sections, σ_{SE} , for Tb^{3+} ions in KLuW crystal at RT (for the principal light polarizations, $E \parallel N_p, N_m$ and N_g , as calculated with the F-L formula using the luminescence branching ratios from Table 4).

Table 5

Peak stimulated-emission cross-sections for $E \parallel N_m$, σ_{SE} , for Tb^{3+} ions in $KLuW$ crystal, as calculated with the F-L formula using the luminescence branching ratios from Table 4).

Transition	σ_{SE} , 10^{-21} cm ²	λ_{peak} , nm	Color
$^5D_4 \rightarrow ^7F_6$	1.15	487.9	blue
$^5D_4 \rightarrow ^7F_5$	11.4	549.4	green
$^5D_4 \rightarrow ^7F_4$	2.29	590.9	orange
$^5D_4 \rightarrow ^7F_3$	1.75	625.0	red
$^5D_4 \rightarrow ^7F_2$	1.84	652.5	red
$^5D_4 \rightarrow ^7F_1$	1.88	670.6	deep-red
$^5D_4 \rightarrow ^7F_0$	0.23	688.4	deep-red

relaxation. The study of an excited-state absorption of Tb^{3+} in $KLu(WO_4)_2$ (from the 5D_4 state) to the higher-lying excited states of the $4f^8$ configuration and to the 9D and 7D states of the excited $4f^75d^1$ configuration is also relevant for obtaining lasing in the Tb^{3+} ions.

Acknowledgements

This work was supported by the Spanish Government under projects MAT2016-75716-C2-1-R (AEI/FEDER,UE) and TEC2014-55948-R, and by the Generalitat de Catalunya under project 2014SGR1358. F.D. acknowledges additional support through the ICREA academia award 2010ICREA-02 for excellence in research. P.L. acknowledges financial support from the Government of the Russian Federation (Grant 074-U01) through ITMO Post-Doctoral Fellowship scheme.

References

- [1] C. Kränkel, D.-T. Marzahl, F. Moglia, G. Huber, P.W. Metz, Out of the blue: semiconductor laser pumped visible rare-earth doped lasers, *Laser Photon. Rev.* 10 (2016) 548–568.
- [2] W.T. Carnall, P.R. Fields, K. Rajnak, Electronic energy levels of the trivalent lanthanide aquo ions. III. Tb^{3+} , *J. Chem. Phys.* 49 (1968) 4447–4449.
- [3] P.W. Metz, D.-T. Marzahl, A. Majid, C. Kränkel, G. Huber, Efficient continuous wave laser operation of Tb^{3+} -doped fluoride crystals in the green and yellow spectral regions, *Laser Photon. Rev.* 10 (2016) 335–344.
- [4] D.K. Sardar, K.L. Nash, R.M. Yow, J.B. Gruber, U.V. Valiev, E.P. Kokanyan, Absorption intensities and emission cross sections of $Tb^{3+}(4f^8)$ in $TbAlO_3$, *J. Appl. Phys.* 100 (2006), 083108–1–5.
- [5] T. Hayakawa, N. Kamata, K. Yamada, Visible emission characteristics in Tb^{3+} -doped fluorescent glasses under selective excitation, *J. Lumin.* 68 (1996) 179–186.
- [6] X.Y. Sun, M. Gu, S.M. Huang, X.J. Jin, X.L. Liu, B. Liu, C. Ni, Luminescence behavior of Tb^{3+} ions in transparent glass and glass-ceramics containing CaF_2 nanocrystals, *J. Lumin.* 129 (2009) 773–777.
- [7] G. Lakshminarayana, J. Qiu, M.G. Brik, I.V. Kityk, Photoluminescence of Eu^{3+} , Tb^{3+} , Dy^{3+} and Tm^{3+} -doped transparent GeO_2 - TiO_2 - K_2O glass ceramics, *J. Phys. Condens. Matter* 20 (2008), 335106–1–11.
- [8] X. Ju, X. Li, W. Li, W. Yang, C. Tao, Luminescence properties of $ZnMoO_4:Tb^{3+}$ green phosphor prepared via co-precipitation, *Mater. Lett.* 65 (2011) 2642–2644.
- [9] J. Liao, B. Qiu, H. Lai, Synthesis and luminescence properties of Tb^{3+} : $NaGd(WO_4)_2$ novel green phosphors, *J. Lumin.* 129 (2009) 668–671.
- [10] Z. Hao, J. Zhang, X. Zhang, S. Lu, X. Wang, Blue-green-emitting phosphor $CaSc_2O_4:Tb^{3+}$: tunable luminescence manipulated by cross-relaxation, *J. Electrochem. Soc.* 156 (2009) H193–H196.
- [11] S. Som, S.K. Sharma, Eu^{3+}/Tb^{3+} -codoped Y_2O_3 nanophosphors: Rietveld refinement, bandgap and photoluminescence optimization, *J. Phys. D* 45 (2012), 415102–1–11.
- [12] M. Xu, L. Wang, D. Jia, H. Zhao, Tuning the color emission of $Sr_2P_2O_7:Tb^{3+}, Eu^{3+}$ phosphors based on energy transfer, *J. Am. Ceram. Soc.* 98 (2015) 1536–1541.

- [13] P. Vergeer, T.J. Vlugt, M.H. Kox, M.I. Den Hertog, J.P. Van der Eerden, A. Meijerink, Quantum cutting by cooperative energy transfer in $Yb_xY_{1-x}PO_4:Tb^{3+}$, *Phys. Rev. B* 71 (2005), 014119–1–11.
- [14] J.L. Yuan, X.Y. Zeng, J.T. Zhao, Z.J. Zhang, H.H. Chen, X.X. Yang, Energy transfer mechanisms in Tb^{3+}, Yb^{3+} codoped Y_2O_3 downconversion phosphor, *J. Phys. D* 41 (2008), 105406–1–6.
- [15] S.I. Andreev, M.R. Bedilov, G.O. Karapetyan, V.M. Likhachev, Stimulated emission of glass activated by terbium, *Sov. J. Opt. Technol.* 34 (1967) 819.
- [16] T. Bjorklund, G. Kellermeyer, C.R. Hurt, N. McAvoy, N. Filipescu, Laser action from terbium trifluoroacetylacetonate in *p*-dioxane and acetonitrile at room temperature, *Appl. Phys. Lett.* 10 (1967) 160–162.
- [17] H.P. Jensen, D. Castleberry, D. Gabbe, A. Linz, Stimulated emission at 5445 Å in Tb^{3+} -YLF, *IEEE J. Quant. Electron.* 9 (1973) 665.
- [18] T. Yamashita, Y. Ohishi, Amplification and lasing characteristics of Tb^{3+} -doped fluoride fiber in the 0.54 μm band, *Jpn. J. Appl. Phys.* 46 (2007) L991–L993.
- [19] P.W. Metz, D.T. Marzahl, G. Huber, C. Kränkel, Performance and wavelength tuning of green emitting terbium lasers, *Optic Express* 25 (2017) 5716–5724.
- [20] P. Dorenbos, The 5d level positions of the trivalent lanthanides in inorganic compounds, *J. Lumin.* 91 (2000) 155–176.
- [21] V. Petrov, M.C. Pujol, X. Mateos, Ö. Silvestre, S. Rivier, M. Aguiló, R.M. Solé, J. Liu, U. Griebner, F. Díaz, Growth and properties of $KLu(WO_4)_2$ and novel ytterbium and thulium lasers based on this monoclinic crystalline host, *Laser Photon. Rev.* 1 (2007) 179–212.
- [22] P.A. Loiko, V.I. Dashkevich, S.N. Bagaev, V.A. Orlovich, A.S. Yasukevich, K.V. Yumashev, N.V. Kuleshov, E.B. Dunina, A.A. Kornienko, S.M. Vatrik, A.A. Pavlyuk, Spectroscopic characterization and pulsed laser operation of Eu^{3+} : $KGd(WO_4)_2$ crystal, *Laser Phys.* 23 (2013), 105811–1–7.
- [23] V.I. Dashkevich, S.N. Bagaev, V.A. Orlovich, A.A. Bui, P.A. Loiko, K.V. Yumashev, N.V. Kuleshov, S.M. Vatrik, A.A. Pavlyuk, Quasi-continuous wave and continuous wave laser operation of Eu : $KGd(WO_4)_2$ crystal on a $^5D_0 \rightarrow ^7F_4$ transition, *Laser Phys. Lett.* 12 (2014), 015006–1–6.
- [24] A.A. Kaminskii, J.B. Gruber, S.N. Bagaev, K.I. Ueda, U. Hömmerich, J.T. Seo, D. Temple, B. Zandi, A.A. Kornienko, E.B. Dunina, A.A. Pavlyuk, Optical spectroscopy and visible stimulated emission of Dy^{3+} ions in monoclinic α - $KY(WO_4)_2$ and α - $KGd(WO_4)_2$ crystals, *Phys. Rev. B* 65 (2002), 125108–1–29.
- [25] H. Zhao, J. Wang, J. Li, H. Zhang, J. Zhang, Z. Ling, H. Xia, R.I. Boughton, Optical and thermal properties of crystalline $Tb:KLu(WO_4)_2$, *Mater. Lett.* 61 (2007) 2499–2501.
- [26] S. Schwung, D. Rytz, B. Heying, U.Ch. Rodewald, O. Niehaus, D. Ensling, T. Jüstel, R. Pöttgen, The crystal structure and luminescence quenching of poly- and single-crystalline $KYW_2O_8:Tb^{3+}$, *J. Lumin.* 166 (2015) 289–294.
- [27] W. Strek, P.J. Deren, A. Bednarkiewicz, Cooperative processes in $KYb(WO_4)_2$ crystal doped with Eu^{3+} and Tb^{3+} ions, *J. Lumin.* 87–89 (2000) 999–1001.
- [28] P. Loiko, X. Mateos, E. Dunina, A. Kornienko, A. Volokitina, E. Vilejshikova, J.M. Serres, A. Baranov, K. Yumashev, M. Aguiló, F. Díaz, Judd-Ofelt modelling and stimulated-emission cross-sections for Tb^{3+} ions in monoclinic $KYb(WO_4)_2$ crystal, *J. Lumin.* 190 (2017) 37–44.
- [29] P.A. Loiko, E.V. Vilejshikova, X. Mateos, J.M. Serres, E.B. Dunina, A.A. Kornienko, K.V. Yumashev, M. Aguiló, F. Díaz, Europium doping in monoclinic $KYb(WO_4)_2$ crystal, *J. Lumin.* 183 (2017) 217–225.
- [30] P.A. Loiko, V.I. Dashkevich, S.N. Bagaev, V.A. Orlovich, A.S. Yasukevich, K.V. Yumashev, N.V. Kuleshov, E.B. Dunina, A.A. Kornienko, S.M. Vatrik, A.A. Pavlyuk, Spectroscopic and photoluminescence characterization of Eu^{3+} -doped monoclinic $KY(WO_4)_2$ crystal, *J. Lumin.* 153 (2014) 221–226.
- [31] B.R. Judd, Optical absorption intensities of rare-earth ions, *Phys. Rev.* 172 (1962) 750–761.
- [32] G.S. Ofelt, Intensities of crystal spectra of rare-earth ions, *J. Chem. Phys.* 37 (1962) 511–519.
- [33] A.A. Kornienko, A.A. Kaminskii, E.B. Dunina, Dependence of the line strength of f–f transitions on the manifold energy. II. Analysis of Pr^{3+} in $KPrP4O12$, *Phys. Status Solidi* 157 (1990) 267–273.
- [34] P.A. Loiko, A.S. Yasukevich, A.E. Gulevich, M.P. Demesh, M.B. Kosmyna, B.P. Nazarenko, V.M. Puzikov, A.N. Shekhovtsov, A.A. Kornienko, E.B. Dunina, N.V. Kuleshov, Growth, spectroscopic and thermal properties of Nd-doped disordered $Ca_9(La/Y)(VO_4)_7$ and $Ca_{10}(Li/K)(VO_4)_7$ crystals, *J. Lumin.* 137 (2013) 252–258.
- [35] S. Colak, W.K. Zwicker, Transition rates of Tb^{3+} in TbP_5O_{14} , $TbLiP_4O_{12}$, and $TbAl_3(BO_3)_4$: an evaluation for laser applications, *J. Appl. Phys.* 54 (1983) 2156–2166.
- [36] D.J. Robbins, B. Cockayne, B. Lent, J.L. Gasper, The mechanism of $^5D_3 - ^5D_4$ cross-relaxation in $Y_3Al_5O_{12}:Tb^{3+}$, *Solid State Commun.* 20 (1976) 673–676.
- [37] B.F. Aull, H.P. Jensen, Vibronic interactions in Nd:YAG resulting in non-reciprocity of absorption and stimulated emission cross sections, *IEEE J. Quant. Electron.* 18 (1982) 925–930.



Contents lists available at ScienceDirect

Journal of Luminescence

journal homepage: www.elsevier.com/locate/jlumin



Judd-Ofelt modelling and stimulated-emission cross-sections for Tb³⁺ ions in monoclinic KYb(WO₄)₂ crystal



Pavel Loiko^{a,*}, Xavier Mateos^b, Elena Dunina^c, Alexey Kornienko^c, Anna Volokitina^a, Elena Vilejshikova^d, Josep Maria Serres^b, Alexander Baranov^a, Konstantin Yumashev^d, Magdalena Aguiló^b, Francesc Díaz^b

^a ITMO University, Kronverkskiy pr., 49, 197101 Saint-Petersburg, Russia

^b Física i Cristal·lografia de Materials i Nanomaterials (FiCMA-FiCNA), Universitat Rovira i Virgili (URV), Campus Sescelades, c/ Marcel·lí Domingo, s/n., E-43007 Tarragona, Spain

^c Vitebsk State Technological University, 72 Moskovskaya Ave., 210035 Vitebsk, Belarus

^d Center for Optical Materials and Technologies (COMT), Belarusian National Technical University, 65/17 Nezavisimosti Ave., 220013 Minsk, Belarus

ARTICLE INFO

Keywords:

Monoclinic double tungstates
Terbium ions
Absorption
Luminescence
Stimulated emission

ABSTRACT

Terbium (Tb³⁺) ions are promising for the development of visible lasers. We report on the spectroscopy of Tb³⁺ in the monoclinic KYb(WO₄)₂ (KYbW) crystal, including the Judd-Ofelt (J-O) modelling of the transition probabilities, evaluation of the absorption and stimulated-emission (SE) cross-sections with polarized light, and emission lifetime study. Within the strong configuration interaction (SCI) approximation of the J-O theory, the intensity parameters of Tb³⁺ are $\Omega_2 = 0.864$, $\Omega_4 = 1.657$, $\Omega_6 = 1.975$ [10^{20} cm²] and $\Delta = 38810$ cm⁻¹. The maximum σ_{abs} for the ⁷F₆ → ⁵D₄ transition reaches 2.3×10^{-21} cm² at 486.7 nm and the maximum σ_{SE} for the green emission according to the ⁵D₄ → ⁷F₅ transition is 2.3×10^{-21} cm² at 549.3 nm (both for E || N_m). The measured lifetime of the ⁵D₄ state for a 1 at% Tb³⁺ doping is 395 ± 5 μs. Under blue excitation, Tb: KYbW exhibits intense green emission with the CIE 1931 coordinates of (0.312; 0.644).

1. Introduction

The trivalent terbium ions (Tb³⁺) possess an electronic configuration of [Xe]4f⁸ and have an energy-level scheme featuring a metastable ⁵D₄ excited-state separated by a large energy-gap (~15000 cm⁻¹) from the lower-lying ⁷F_J (J = 6...0) multiplets [1]. This determines the appearance of multiple visible emissions from this ion falling into blue, green, yellow and red spectral ranges, high luminescence quantum efficiency and long lifetime of the emitting state (ranging from hundreds of μs to few ms) [2]. The Tb³⁺ ions can be excited in the blue and UV. Some Tb³⁺-doped materials have been studied for green phosphors and fluorescence imaging [3–6]. The former application is related to the fact that the ⁵D₄ → ⁷F₅ emission of Tb³⁺ at ~545 nm typically dominates in the spectrum resulting in a green emission with high color purity.

The Tb³⁺ ions in single-crystals have also been considered for the development of visible lasers. After the first demonstration of stimulated emission (SE) in Tb:LiYF₄ crystal [7] and a Tb:fluoride fiber [8], efficient room-temperature continuous-wave (CW) Tb³⁺ lasers emitting in the green and yellow (transitions to the ⁷F₅ and ⁷F₄ terminating

states, respectively) have been realized recently [2,9]. For this, various fluoride host crystals, e.g. LiLuF₄, KY₃F₁₀, BaY₂F₈ or LaF₃, were used [2]. Tb³⁺ lasers offer high slope efficiency, > 50%, and certain tunability of the emission wavelength [2,9]. This makes them promising as compared to the conventional ~532 nm green frequency-doubled Nd lasers. As the ground-state absorption transitions in the blue are spin-forbidden for Tb³⁺, the corresponding cross-sections σ_{abs} are about 10^{-21} cm² [9,10]. This determines the necessity of high Tb³⁺ concentrations leading potentially to strong parasitic effects, e.g. cross-relaxation and energy-transfer upconversion [2,11–13].

The development of novel Tb³⁺-doped laser materials using mechanically strong oxide crystals is of high interest [9]. Such matrices should allow for high Tb³⁺ doping levels and keep weak inter-ionic interactions. A crystal family of monoclinic double tungstates (MDTs), having chemical formula KRE(WO₄)₂, where RE = Gd, Y, Lu or Yb (shortly KREW), is well-known for doping with various rare-earth ions (RE³⁺), e.g. Yb³⁺, Tm³⁺ or Ho³⁺, resulting in efficient lasing in the near-IR [14]. The RE³⁺ ions in KREW crystals exhibit high transition cross-sections in polarized light and weak luminescence quenching under high doping levels due to the long RE³⁺-RE³⁺ distances [15].

* Corresponding author.

E-mail address: kinetic@tut.by (P. Loiko).

<http://dx.doi.org/10.1016/j.jlumin.2017.05.031>

Received 9 March 2017; Received in revised form 12 May 2017; Accepted 12 May 2017
Available online 13 May 2017

0022-2313/© 2017 Elsevier B.V. All rights reserved.

Very recently, MDTs were employed for europium (Eu^{3+}) doping [16] resulting in CW deep-red lasers [17]. The similarity of the energy-level structure of Eu^{3+} and Tb^{3+} promotes the study of the Tb^{3+} -doped MDTs.

The information about the Tb^{3+} -doped MDTs is scarce. The Tb^{3+} ions in MDTs replace the RE^{3+} ones which are VIII-fold O^{2-} -coordinated. The ionic radius of Tb^{3+} , $R_{\text{Tb}} = 1.040 \text{ \AA}$, is close to those of the replaced ions [18], which allows for high Tb^{3+} doping levels preserving the monoclinic structure [19]. There exists a monoclinic stoichiometric crystal, KTbW [20]. The crystal growth and thermal properties, as well as luminescence of Tb:KLuW were studied [21]. The crystal structure and luminescence quenching for Tb:KYW have also been reported [19].

In the present work, we report on a detailed polarization-resolved study of Tb^{3+} spectroscopy in a stoichiometric $\text{KYb(WO}_4)_2$ crystal (shortly KYbW), accompanied by a Judd-Ofelt modelling and an evaluation of the SE cross-sections, in order to evaluate the key spectroscopic parameters relevant for the further application of Tb^{3+} -doped MDTs in lasers. Recently, this crystal was studied for Eu^{3+} doping [22]. The previous studies of Tb:KYbW [23,24] focused on cooperative upconversion of this self-activated material. It should be noted that for Tb:KYbW , the Yb^{3+} ions are considered as “passive” (host-forming).

2. Crystal growth

The KYbW crystals doped with 1 at% or 5 at% Tb^{3+} were grown by the Top Seeded Solution Growth (TSSG) Slow-Cooling method using potassium ditungstate, $\text{K}_2\text{W}_2\text{O}_7$, as a solvent. The starting materials, K_2CO_3 , Yb_2O_3 , Tb_2O_3 and WO_3 , were from Aldrich and Fluka (> 99.9% purity). A seed from an undoped KYW was used for starting the nucleation and was oriented along the b crystallographic axis. More details can be found in [14,22]. The phase purity and the structure of the grown crystals were determined with X-ray diffraction. Tb:KYbW is monoclinic (space group $C_{2h}^6 - C2/c$, point group: $2/m$). The as-grown crack- and inclusion-free crystal was of high optical quality and had a slight yellow coloration due to the Tb^{3+} ions, Fig. 1.

3. Experimental

The monoclinic Tb:KYbW is optically biaxial [15]. Its spectroscopic properties are characterized for the principal light polarizations $E \parallel N_p$, N_m and N_g (along the optical indicatrix axes) The N_p -axis is parallel to the b crystallographic axis and the two remaining axes are located in the a - c plane such that the angles $N_m \hat{a} = 59.7^\circ$ and $N_g \hat{c} = 19.0^\circ$ [15]. For the spectroscopic studies, we cut and polished a sample from the 1 at% Tb:KYbW crystal having thickness t of 2.29 mm and 2.62 mm along the N_g - and N_p -axes, respectively, and thus giving access to all

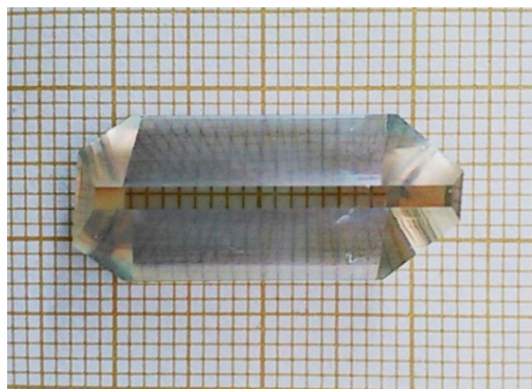


Fig. 1. Image of the as-grown 1 at% Tb:KYbW crystal: b -axis is pointing towards the observer.

three principal polarizations.

The room-temperature (RT, 293 K) absorption spectrum was measured with a Varian CARY-5000 spectrophotometer. The spectral bandwidth (SBW) was 0.01 nm in the visible (0.36–0.5 μm) and 0.1 nm in the near-IR (1.8–3 μm). The absorption cross-section was calculated from the absorption coefficient, $\sigma_{\text{abs}} = a/N_{\text{Tb}}$. The actual Tb^{3+} concentration in the crystal was $N_{\text{Tb}} = 0.65 \times 10^{20} \text{ cm}^{-3}$ (crystal density, $\rho = 7.554 \text{ g/cm}^3$). This value was calculated according to the known segregation coefficient, $K_{\text{Tb}} \approx 1$, determined previously with the Electron Probe Micro-Analysis (EPMA). For low-temperature (LT) absorption measurements at 6 K, we used an Oxford Instruments Ltd. cryostat (SU 12 model) with helium-gas close-cycle flow.

The polarized emission spectra of Tb:KYbW were measured with a Renishaw inVia confocal micro-Raman microscope with a x50 objective and an 1800 l/mm grating. The excitation wavelength λ_{exc} was 458 nm or 488 nm. The spectral resolution was $\sim 1 \text{ cm}^{-1}$. The spectral sensitivity of the set-up was determined by means of a halogen lamp with a calibrated spectral power density.

For the luminescence decay studies, a nanosecond (ns) optical parametric oscillator Lotis TII LT-2214 tuned to $\lambda_{\text{exc}} = 480 \text{ nm}$ was used. The decay curves were detected with a MDR-12 monochromator (SBW $\sim 1 \text{ nm}$), a fast photodetector, Hamamatsu C5460 (response time, 40 ns) and a 500 MHz Textronix TDS-3052B digital oscilloscope. The decay from the $^5\text{D}_4$ state was monitored at 543 nm. The decay time τ was determined according to a single-exponential law, $I(t) = I_0 \exp(-t/\tau)$.

4. Results and discussion

4.1. Absorption

The absorption cross-section, σ_{abs} , spectra of Tb^{3+} ions in KYbW are shown in Fig. 2 (for light polarizations $E \parallel N_p$, N_m and N_g , at RT). Contrary to Eu^{3+} [16], the energy-gap between the ground-state of Tb^{3+} ($^7\text{F}_6$) and the lowest excited-state ($^7\text{F}_5$) is relatively large, $\sim 2100 \text{ cm}^{-1}$, so the thermal population of the latter state is negligible. Thus, all transitions observed in the RT absorption spectra occur from the $^7\text{F}_6$ state. Tb:KYbW exhibits a strong polarization anisotropy of the σ_{abs} which is typical for RE^{3+} ions in MDTs, e.g. as observed before for Eu^{3+} in KYbW [22], and is related to their low-symmetry structure. The maximum σ_{abs} corresponds to the light polarization $E \parallel N_m$.

In the near-IR, Fig. 2(c), the characteristic bands of Tb^{3+} related to the transitions to the lower-lying $^7\text{F}_4$ (with center of gravity of the absorption band at $\sim 2.85 \mu\text{m}$), $^7\text{F}_3$ (2.28 μm), $^7\text{F}_2$ (1.98 μm), $^7\text{F}_1$ (1.85 μm) and $^7\text{F}_0$ (1.78 μm) states are observed. These transitions are spin-allowed and thus the corresponding σ_{abs} values are larger, at about $\sim 1 \dots 2 \times 10^{-20} \text{ cm}^2$. In the visible, Fig. 2(b), the weak absorption band is related to the spin-forbidden transition to the $^5\text{D}_4$ metastable state and it is usually used for the pumping of the Tb lasers, e.g. by using the frequency-doubled optically pumped semiconductor lasers (2ω -OPSL) [2]. The maximum $\sigma_{\text{abs}} = 2.3 \times 10^{-21} \text{ cm}^2$ at 486.7 nm with a full width at half maximum (FWHM) of only 1.0 nm (for $E \parallel N_m$). The σ_{abs} is almost two times lower for $E \parallel N_p$ ($1.3 \times 10^{-21} \text{ cm}^2$ at 487.9 nm) and for $E \parallel N_g$ ($1.2 \times 10^{-21} \text{ cm}^2$ at 486.7 nm). The determined σ_{abs} for Tb:KYbW are much larger than those for fluoride crystals, e.g. $0.3 \times 10^{-21} \text{ cm}^2$ at 488.8 nm for Tb:LiLuF_4 (π -polarization) [2]. In the UV, Fig. 2(a), the weak overlapping bands are assigned to the spin-forbidden transitions to the $^5\text{D}_3$, $^5\text{G}_6$, $^5\text{L}_{10}$, $^5\text{G}_5$ higher-lying excited-states. The UV absorption edge of Tb:KYbW is at $\sim 320 \text{ nm}$ ($E_g \sim 3.9 \text{ eV}$).

The spectroscopic properties of the Tb^{3+} ions were modeled within the standard Judd-Ofelt (J-O) theory [25,26] and its modification for the strong configuration interaction (SCI) approximation [27,28]. The absorption oscillator strengths for Tb^{3+} ions were determined as:

$$f_{\Sigma}^{\text{exp}}(JJ') = \frac{m_e c^2}{\pi e^2 N_{\text{Tb}} \langle \lambda \rangle^2} \Gamma(JJ'), \quad (1)$$

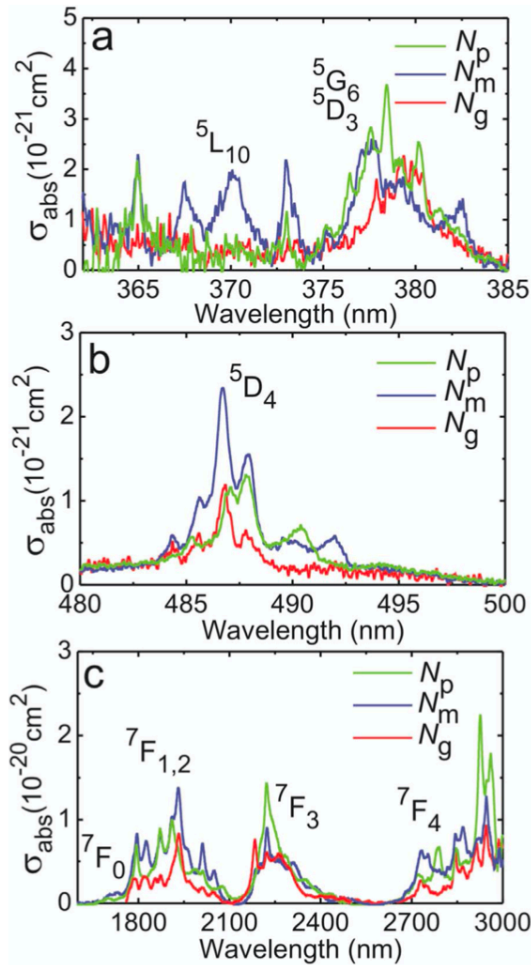


Fig. 2. Absorption cross-sections, σ_{abs} , spectra of 1 at% Tb: KYbW crystal in polarized light at RT: transitions ${}^7F_6 \rightarrow {}^7F_j$ (a), ${}^7F_6 \rightarrow {}^5D_4$ (b) and ${}^7F_6 \rightarrow {}^5D_3, {}^5G_6, {}^5L_{10}$ (c).

Table 1
Experimental and calculated polarization-averaged absorption oscillator strengths for a 1 at% Tb:KYbW crystal^a.

Transition	d , nm \times cm ⁻¹	f_{exp} 10 ⁻⁶	$U^{(2)}$ 10 ⁻³	$U^{(4)}$ 10 ⁻³	$U^{(6)}$ 10 ⁻³	f_{calc} 10 ⁻⁶	
						J-O	SCI
${}^7F_6 \rightarrow {}^7F_4$	123.3	2.68	90.0	515.8	265.3	2.72	2.77
${}^7F_6 \rightarrow {}^7F_3$	75.1	2.64	–	232.3	412.6	2.59	2.54
${}^7F_6 \rightarrow {}^7F_2$	55.3	2.50	–	48.18	469.4	2.42	2.27
${}^7F_6 \rightarrow {}^7F_1$	26.7	1.38	–	–	376.1	1.85	1.72
${}^7F_6 \rightarrow {}^7F_0$	13.4	0.74	–	–	144.2	0.71	0.66
${}^7F_6 \rightarrow {}^5D_4$	0.21	0.15	2.061	0.795	1.310	0.01	0.02
${}^7F_6 \rightarrow {}^5D_3$	1.76 ^b	2.28	–	0.228	1.421	0.45	1.66
${}^7F_6 \rightarrow {}^5G_6$	–	–	2.314	4.543	11.84	–	–
${}^7F_6 \rightarrow {}^5L_{10}$	–	–	–	0.363	59.20	–	–
${}^7F_6 \rightarrow {}^5G_5$	–	–	1.608	1.866	13.53	–	–
RMS dev.	–	–	–	–	–	0.887	0.726

^a Polarization-averaging: $f = 1/3(f_p + f_m + f_g)$, Γ – integrated absorption coefficient, f_{exp} – experimental oscillator strengths f_{calc} – calculated ones, $U^{(k)}$ – calculated squared reduced matrix elements, RMS – root-mean-square deviation.

^b The transitions to the ${}^5D_3 + {}^5G_6 + {}^5L_{10} + {}^5G_5$ states are analyzed together.

where m_e and e are the electron mass and charge, respectively, c is the speed of light, $\Gamma(JJ)$ is the integrated absorption coefficient within the absorption band and $\langle \lambda \rangle$ is the “center of gravity” of the absorption

band. In the J-O modelling, we considered all values as averaged over the three principal light polarizations, e.g. $\langle f \rangle = 1/3(f_p + f_m + f_g)$. The experimental f values are shown in Table 1. The absorption oscillator strengths were also derived from the line strengths:

$$f_{\Sigma}^{\text{calc}}(JJ') = \frac{8}{3h(2J'+1)\langle \lambda \rangle} \frac{(n^2+2)^2}{9n} S_{ED}^{\text{calc}}(JJ') + f_{MD}(JJ'), \quad (2)$$

Here, h is the Planck constant and n is the refractive index of the crystal. The J-O theory describes electric-dipole (ED) transitions. The contribution of magnetic-dipole (MD) ones with $J - J' = 0, \pm 1$ can be found in [29]. For the considered absorption spectrum of Tb³⁺, these are the ${}^7F_6 \rightarrow {}^5G_6$ and 5G_5 transitions. The ED line strengths within the conventional J-O theory are given by [25,26]:

$$S_{ED}^{\text{calc}}(JJ') = \sum_{k=2,4,6} U^{(k)} \Omega_k, \quad U^{(k)} = \langle (4f^n)SL\|U^{(k)}\|(4f^n)S'L'J' \rangle^2. \quad (3)$$

Here, $U^{(k)}$ are the squared reduced matrix elements and Ω_2, Ω_4 and Ω_6 are the intensity parameters (J-O parameters). The values of $U^{(k)}$ for the considered transitions in absorption were calculated in the present paper using the crystal-field parameters from [30], cf. Table 1.

In the previous studies of Eu³⁺ ions in MDTs, a much better agreement between the experimental and calculated absorption oscillator strengths was observed for a modification of the J-O theory for the case of strong configuration interaction (SCI) [22]. The approach by Judd and Ofelt corresponds to the second order of the Perturbation theory in terms of the energies of virtual transitions of a 4f electron to the states with an opposite parity (5d, 6s). The SCI model refines this scheme by incorporating the third-order perturbative effects: it is assumed that the excited configurations have the same average energy Δ . Then, the formula for ED line strengths is [22,27,28]:

$$S_{ED}^{\text{calc}}(JJ') = \frac{1}{4} \sum_{k=2,4,6} U^{(k)} \Omega_k \left(\frac{\Delta}{\Delta - E_j} + \frac{\Delta}{\Delta - E_{j'}} \right)^2. \quad (4)$$

The calculated absorption oscillator strengths for Tb:KYbW using both the standard J-O theory and the SCI approximation are shown in Table 1. The latter approach provides lower root mean square (RMS) deviation between the experimental and calculated f of 0.726 (as compared with the standard J-O theory with RMS = 0.887). The best-fit parameters of both theories are listed in Table 2. For the SCI approximation, $\Omega_2 = 0.864$, $\Omega_4 = 1.657$, $\Omega_6 = 1.975$ [10^{-20} cm²] and $\Delta = 38810$ cm⁻¹. In Table 3, we have compared the J-O parameters for Tb³⁺ in KYbW with the previously reported values for various oxide and fluoride crystals.

To determine the energy of the Stark sub-levels of the multiplets of Tb³⁺ ions, we performed LT absorption measurements, Fig. 3. The Tb³⁺ ion has an even number of active electrons, 4f⁸, and it is located in the C₂ site (in KYbW). The number of Stark sub-levels according to the irreducible representations (Γ_1, Γ_2) for the Tb³⁺ multiplets in KYbW is shown in Table 4. The total splitting of the 7F_6 ground-state of Tb³⁺ is typically large (450–700 cm⁻¹) while the two lowest Stark sub-levels are relatively close and separated by $\delta E \sim 3\text{--}8$ cm⁻¹ [34,35]. At 6 K, the absorption occurs from one of these two lowest Stark sub-levels, depending on the polarization. For Tb³⁺ in KYbW, the polarization-dependent selection rules are different for $E \parallel N_p$ and $E \parallel N_m$ (N_g), see [22], as the corresponding optical indicatrix axes are parallel and orthogonal to the C₂ symmetry axis, respectively. Thus, the peaks

Table 2
Parameters of J-O and SCI theories applied to calculate the absorption oscillator strengths for Tb:KYbW.

Theory	Parameters	Value: 1 at% Tb:KYbW
Judd-Ofelt	Ω_k [10^{-20} cm ²]	$\Omega_2 = 1.909, \Omega_4 = 2.414, \Omega_6 = 4.911$
SCI	Ω_k [10^{-20} cm ²]; Δ_j , cm ⁻¹	$\Omega_2 = 0.864, \Omega_4 = 1.657, \Omega_6 = 1.975; \Delta = 38810$

Table 3
 Judd-Ofelt intensity parameters (Ω_k) and spectroscopic quality factor, $X_{4/6}$, for Tb^{3+} ions in various hosts.

Material	Ref.	$\Omega_k, 10^{-20} \text{ cm}^2$			$X_{4/6}$
		Ω_2	Ω_4	Ω_6	
Tb:KYb(WO ₄) ₂	This work	1.91	2.41	4.91	0.49
Tb:YAlO ₃	[31]	3.25	7.13	2.00	3.57
Tb:YLiF ₄	[10]	28.30	1.65	2.15	0.77
Tb:KY ₃ F ₁₀	[32]	3.92	0.30	3.02	0.10
TbAl ₃ (BO ₃) ₄	[33]	8.15	0.29	2.44	0.12
TbP ₅ O ₁₄	[34]	3.77	1.78	3.43	0.52

observed in the LT absorption spectra can be attributed to the energies of the Stark sub-levels with a precision of the δE . The determined energy level position for the excited-states of Tb^{3+} (from 7F_3 to 5G_4) are listed in Table 4.

4.2. Emission

The probability of spontaneous radiative transitions is calculated from the corresponding line strengths:

$$A_{\Sigma}^{calc}(JJ') = \frac{64\pi^4 e^2}{3h(2J'+1)\langle\lambda\rangle^3} n \left(\frac{n^2+2}{3} \right)^2 S_{ED}^{calc}(JJ') + A_{MD}(JJ'). \quad (5)$$

The set of $U^{(k)}$ for emission transitions, as well as the MD contributions can be found in the literature. The mean emission wavelengths for each $J \rightarrow J'$ transition, $\langle\lambda\rangle$, are estimated from the energies of each multiplet for the Tb^{3+} free-ion. From the values of A for separate emission channels $J \rightarrow J'$, we calculated the total probability A_{tot} , the radiative lifetimes of the excited-states τ_{rad} and luminescence branching ratios for the emission channels $B(JJ')$:

$$\tau_{rad} = \frac{1}{A_{tot}^{calc}}, \text{ where } A_{tot}^{calc} = \sum_{J'} A_{\Sigma}^{calc}(JJ'), \quad (6a)$$

$$B(JJ') = \frac{A_{\Sigma}^{calc}(JJ')}{\sum_{J'} A_{\Sigma}^{calc}(JJ')} \quad (6b)$$

Table 4
 Energies of the Stark sub-levels of excited-states of Tb^{3+} ions in KYbW determined from the LT absorption spectra.

State	Splitting	$E, \text{ cm}^{-1}$	Polariz.	State	Splitting	$E, \text{ cm}^{-1}$	Polariz.
7F_6	$7\Gamma_1 + 6\Gamma_2$	0				26551	p
7F_5	$5\Gamma_1 + 6\Gamma_2$	–				26571	$m, g(p)$
7F_4	$5\Gamma_1 + 4\Gamma_2$	–				26659	m, g
7F_3	$3\Gamma_1 + 4\Gamma_2$	4408	m, g			26662	p
		4503	m, g			26805	m, g
		4542	m, g			26807	p
		4579	m, g	$^5L_{10}$	$11\Gamma_1 + 10\Gamma_2$	26958	m, g
7F_2	$3\Gamma_1 + 2\Gamma_2$	5006	p			26961	p
7F_1	$\Gamma_1 + 2\Gamma_2$	5083	p			26992	p
		5172	$m, g(p)$			26996	m, g
		5231	m, g			27029	m, g
		5273	p			27041	p
		5339	p			27086	m, g
		5606	$m, g(p)$			27152	m, g
		5634	p			27204	m, g
7F_0	Γ_1	?				27445	$m, g(p)$
5D_4	$5\Gamma_1 + 4\Gamma_2$	20529	p	5G_5	$5\Gamma_1 + 6\Gamma_2$	27769	m, g
		20531	m, g			27773	p
		20542	p			27801	m, g
		20545	$m, g(p)$			27809	p
		20953	$m, g(p)$			27823	m, g
		20614	p			27851	$m, g(p)$
		20652	$m, g(p)$			27882	p
5D_3	$3\Gamma_1 + 4\Gamma_2$	26324	p			27894	m, g
		26329	m, g			27941	$m, g(p)$
		26338	m, g			28052	p
		26350	p	5D_2	$3\Gamma_1 + 2\Gamma_2$	28191	m, g
		26359	m, g			28197	p
		26366	p			28225	p
		26372	m, g			28313	m, g
5G_6	$7\Gamma_1 + 6\Gamma_2$	26417	m, g			28317	p
		26429	p	5G_4	$5\Gamma_1 + 4\Gamma_2$	28375	p
		26441	p			28403	p
		26471	m, g			28413	m, g
		26491	p			28455	m, g
		26513	m, g			28495	m, g

The results are presented in Table 5 for transitions from the 5D_4 and 5D_3 excited states. Fig. 4 shows the scheme of energy-levels of Tb^{3+} in

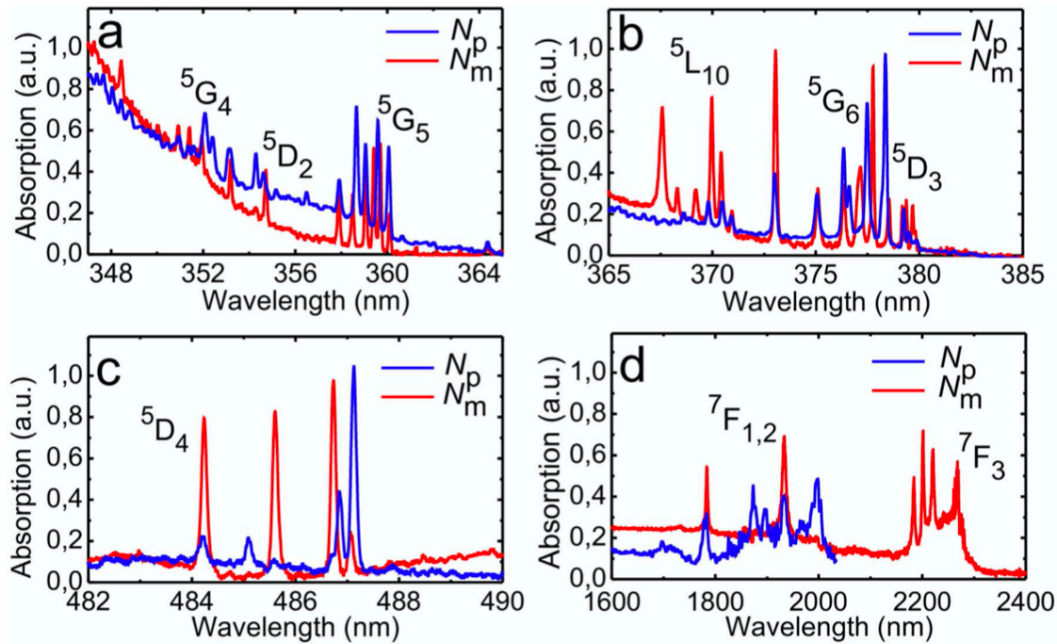


Fig. 3. Absorption spectra of Tb:KYbW crystal at 6 K for light polarizations $E \parallel N_m$ and $E \parallel N_p$.

Table 5
Emission probabilities for Tb^{3+} ions in 1 at% Tb:KYbW crystal (calculated within the SCI theory)*.

Transition	$U^{(2)}$, 10^{-3}	$U^{(4)}$, 10^{-3}	$U^{(6)}$, 10^{-3}	A_{JJ} , s^{-1}	B_{JJ} , %	A_{tot} , s^{-1}	τ_{rad} , ms
$^5D_4 \rightarrow$	7F_6	2.061	0.795	1.310	98.9 ^{ED}	20.6	2.082
	7F_5	15.30	1.354	2.209	103.0 ^{ED} + 98.2 ^{MD}	41.9	
	7F_4	0.303	2.190	1.340	77.8 ^{ED}	16.2	
	7F_3	2.275	0.543	0.586	32.2 ^{ED}	6.8	
	7F_2	1.142	0.400	0.115	12.5 ^{ED}	2.6	
	7F_1	–	2.540	–	34.6 ^{ED}	7.2	
	7F_0	–	1.722	–	22.6 ^{ED}	4.7	
$^5D_3 \rightarrow$	7F_6	–	0.228	1.421	319.5 ^{ED}	18.3	0.573
	7F_5	0.247	2.852	1.537	586.7 ^{ED}	33.6	
	7F_4	6.989	0.169	0.202	138.3 ^{ED} + 90.4 ^{MD}	13.1	
	7F_3	0.812	0.955	0.041	110.0 ^{ED}	6.3	
	7F_2	1.452	2.560	–	239.2 ^{ED}	13.7	
	7F_1	1.129	1.332	–	125.7 ^{ED}	7.2	
	7F_0	–	–	–	–	–	
	5D_4	54.76	27.99	9.159	136.2 ^{ED}	7.8	

λ_0 - mean emission wavelength, $U^{(k)}$ - calculated squared reduced matrix elements, A_{JJ} - probability of spontaneous transition (ED and MD stand for electric and magnetic dipole contributions, respectively), B_{JJ} - luminescence branching ratio, A_{tot} - total probability of spontaneous transitions, τ_{rad} - radiative lifetime.

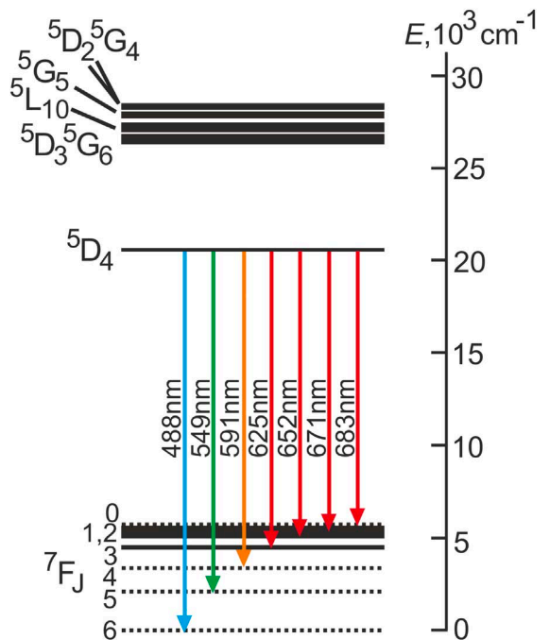


Fig. 4. Scheme of energy levels and emission channels from the 5D_4 metastable level for Tb^{3+} ions in KYbW crystal: solid rectangles – data based on the Stark splitting, dashed horizontal lines – data based on RT emission spectroscopy.

Table 6
Radiative lifetimes (τ_{rad}) of the 5D_4 state of Tb^{3+} ions in various hosts and the corresponding experimental lifetimes (τ_{exp}) for Tb^{3+} ions in various double tungstate compounds.

Material	τ_{rad} , ms	Ref.	Material	τ_{exp} , ms	Ref.
Tb:KYb(WO ₄) ₂	2.08	This work	Tb:KYb(WO ₄) ₂	0.395	This work
TbAlO ₃	3.5	[10]	Tb:KY(WO ₄) ₂	0.50	[19]
Tb:KY ₃ F ₁₀	4.8	[32]	KTb(WO ₄) ₂	0.11	[20]
TbP ₅ O ₁₄	3.82	[33]	NaTb(WO ₄) ₂	0.58	[38]
TbAl ₃ (BO ₃) ₄	2.07	[33]	Tb:NaGd(WO ₄) ₂	1.03	[5]
Tb:YPO ₄	2.6	[36]	Tb:NaLa(WO ₄) ₂	1.40	[39]

KYbW and the transitions from the 5D_4 state observed in our experiments. The radiative lifetime of the 5D_4 state is 2.082 ms (SCI theory). This value is close to the one calculated previously for TbAl₃(BO₃)₄

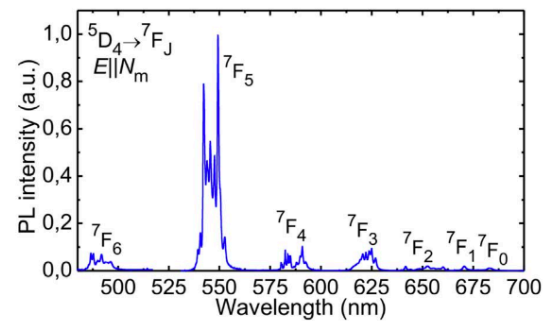


Fig. 5. Photoluminescence (PL) spectrum of Tb:KYbW crystal at RT for light polarization $E \parallel N_m$; the excitation wavelength is 458 nm.

(with the standard J-O theory), 2.07 ms [33], and shorter than for TbAlO₃ (3.5 ms) [10] and Tb:KY₃F₁₀ (4.8 ms) [32], see also Table 6.

The luminescence spectrum of Tb:KYbW under blue excitation at 458 nm is shown in Fig. 5 (for light polarization $E \parallel N_m$). The observed emissions are related to the $^5D_4 \rightarrow ^7F_J$ ($J = 6..0$) transitions. The polarized SE cross-sections for Tb^{3+} ions in KYbW were calculated with the Füchtbauer–Ladenburg (F-L) equation [37]:

$$\sigma_{SE}^i(\lambda) = \frac{\lambda^5}{8\pi n_i^2 \tau_{rad} c} \frac{3W_i(\lambda)B(JJ')}{\sum_{i=p,m,g} \int \lambda W_i(\lambda) d\lambda} \quad (7)$$

Here, $W_i(\lambda)$ is the measured spectral power density of luminescence for the principal polarization states, $i = p, m, g$, n_i is the refractive index corresponding to i -th polarization, τ_{rad} is the radiative lifetime of the emitting state (5D_4 level of Tb^{3+}). The results are shown in Fig. 6 for all seven $^5D_4 \rightarrow ^7F_J$ ($J = 6..0$) transitions. Tb:KYbW exhibits a strong polarization-anisotropy of the σ_{SE} spectra with maximum cross-sections corresponding to $E \parallel N_m$. For the $^5D_4 \rightarrow ^7F_5$ transition, that occurs in the green and it is most interesting for laser operation, the maximum $\sigma_{SE} = 2.3 \times 10^{-21} \text{ cm}^2$ at 549.3 nm (for $E \parallel N_m$). The σ_{SE} is much lower for $E \parallel N_p$ ($1.1 \times 10^{-21} \text{ cm}^2$ at 542.6 nm) and for $E \parallel N_g$ ($0.44 \times 10^{-21} \text{ cm}^2$ at 547.6 nm). The maximum σ_{SE} value for Tb:KYbW also exceeds the one for Tb:LiLuF₄, $\sim 1.6 \times 10^{-21} \text{ cm}^2$ at ~ 540 nm (σ -polarization) [2].

The luminescence decay curves for Tb^{3+} ions for the 1 at% and 5 at% Tb:KYbW crystals are shown in Fig. 7 (direct excitation at 480 nm to the 5D_4 state). They are clearly single-exponential. This agrees with the accommodation of Tb^{3+} ions in a single type of site in the KYbW lattice [15]. The luminescence decay time τ_{exp} equals $395 \pm 5 \mu\text{s}$ (1 at% Tb)

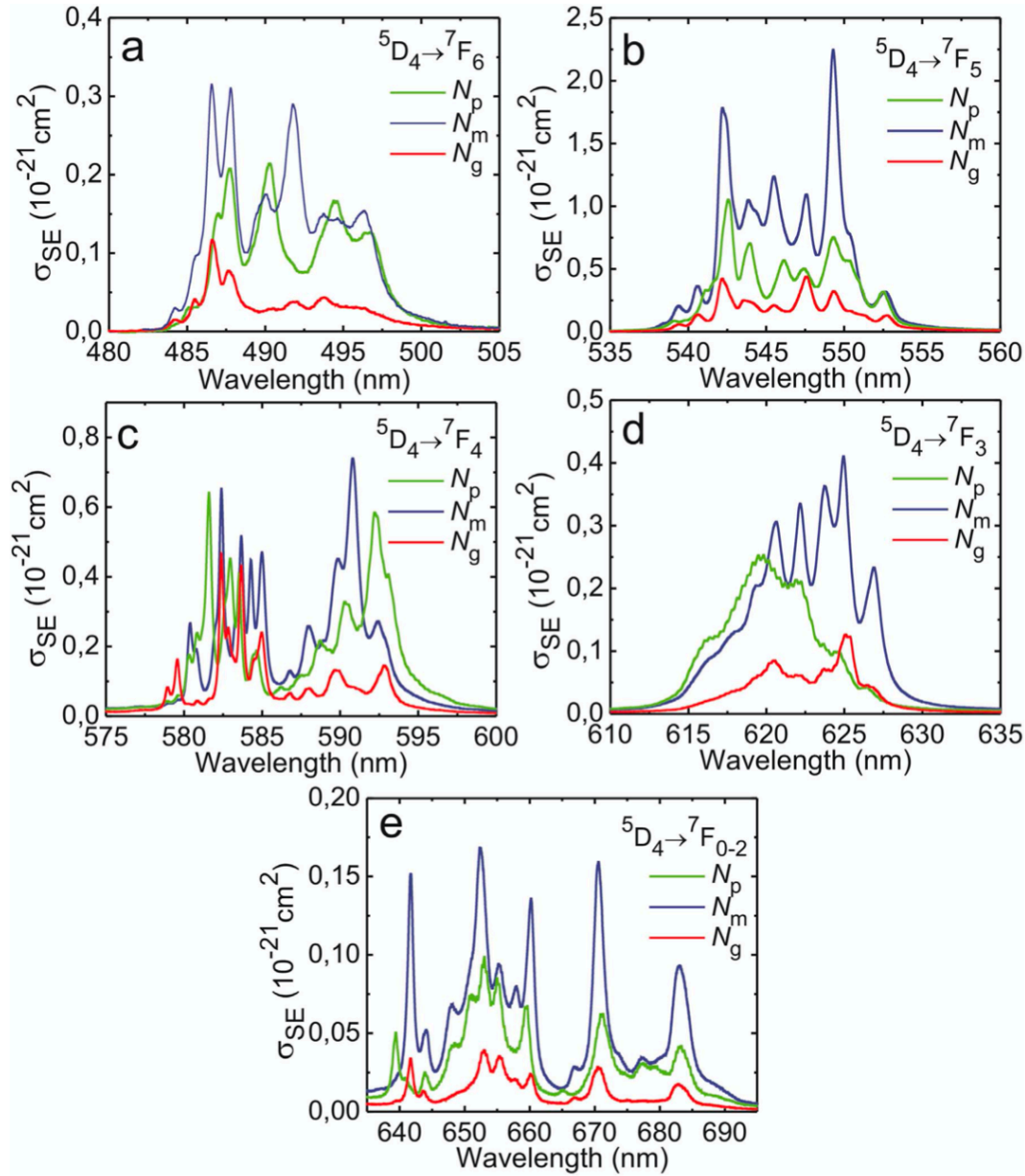


Fig. 6. (a)–(e) Stimulated-emission cross-sections, σ_{SE} , for Tb^{3+} ions in KYbW at RT (for principal light polarizations, $E \parallel N_p, N_m$ and N_g , calculated with the F-L formula).

and $388 \pm 5 \mu s$ (5 at% Tb). The τ_{exp} is shorter than the radiative one, resulting in a luminescence quantum efficiency $\eta_q = \tau_{exp}/\tau_{rad} = 19\%$ (for 1 at% Tb^{3+} doping). This shortening cannot be attributed to the non-radiative relaxation [9], due to the large energy gap between the metastable 5D_4 state and the lower lying excited-state 7F_0 , $\sim 15000 \text{ cm}^{-1}$, as compared with the maximum phonon frequency in KYbW, $\nu_{max} = 911 \text{ cm}^{-1}$ [15]. In Table 6, we compare the τ_{exp} values reported recently for various Tb^{3+} -doped double tungstates. In [19] for a 5 at% Tb:KYW single-crystal, the τ_{exp} was measured to be $\sim 460 \mu s$ that is only slightly longer than the one determined in our work for Tb:KYbW with the same doping. In [20] for a stoichiometric KTbW single-crystal, the τ_{exp} was $114 \mu s$ and it was even longer for a polycrystalline KTbW, $292 \mu s$ [19]. Regarding η_q for Tb^{3+} -doped crystals, the values varying from $\sim 38\%$ (for $TbAl_3(BO_3)_4$ [33] and (Tb: KY₃F₁₀ [32]) to 57% (for $TbAlO_4$ [10]) were reported.

The MDTs exhibit long interionic distances. In particular for KYbW, the shortest $Yb^{3+}-Yb^{3+}$ distance is 4.049 \AA [40]. As shown in [19], the critical doping Tb^{3+} level for KYW in terms of the concentration-quenching is about 40 at%. Further increase of the Tb^{3+} concentration leads to a notable alteration of the optical properties of the host by lowering the band of metal-to-metal charge transfer (M.M.C.T.) between Tb^{3+} and the $[WO_6]$ octahedra. As a result, the overlap between the crystal-field components of the $[Xe]4f^75d^1$ excited configuration and the M.M.C.T. band becomes stronger. It is known that Tb^{3+} has one of the smallest energy separations between the ground-state (7F_6) of the $[Xe]4f^8$ configuration and the lowest excited states (9D) of the $[Xe]4f^75d^1$ one [2,41]. Moreover, the position of these states is strongly dependent on the crystal field [41]. The SCI theory for Tb: KYbW yields a value of $\Delta = 38810 \text{ cm}^{-1}$ that is much lower than that for Eu: KYbW, $\Delta = 50160 \text{ cm}^{-1}$ [22]. These considerations may explain the shortening

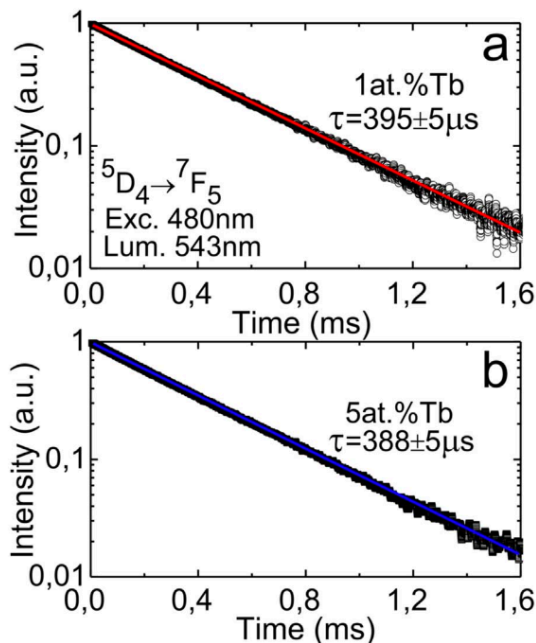


Fig. 7. Decay of the green luminescence of Tb^{3+} ions at 543 nm for 1 at% (a) and 5 at% (b) $Tb:KYbW$ crystals, excitation wavelength is 480 nm: points – experimental data, solid line – single-exponential fit, τ is the decay time.

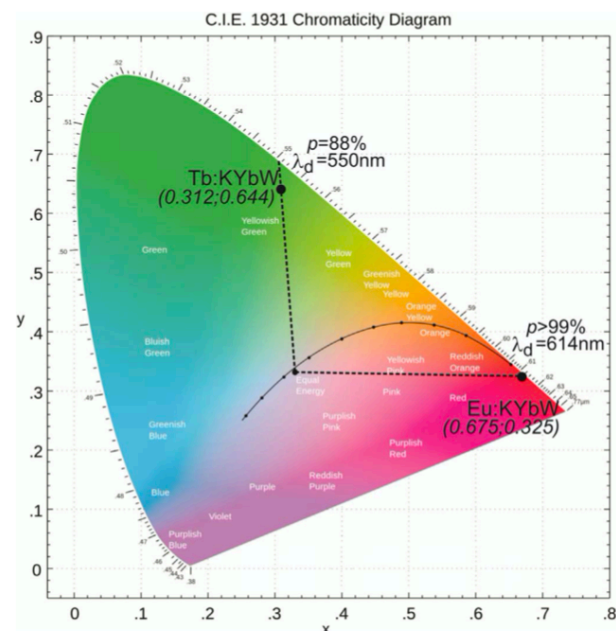


Fig. 8. CIE 1931 color space with the indicated color coordinates (x , y), dominant wavelength (λ_d) and color purity (p) for luminescence of Tb^{3+} and Eu^{3+} ions in $KYbW$ crystals.

of the $\tau_{exp}(^5D_4)$ in $Tb:KYbW$ with respect to the radiative lifetime.

It is known that the host crystals self-activated with Yb^{3+} and doped with the RE^{3+} ions, e.g. Er^{3+} , Eu^{3+} , Tb^{3+} , etc. exhibit up- and down-conversion emissions [24,42]. In the case of Eu^{3+} and Tb^{3+} , they are related to the cooperative energy-transfer involving excited $Yb^{3+}-Yb^{3+}$ ion pairs [24,43]. Such effects have been discussed for $Tb:KYbW$ before [23,24]. In the case of $Tb:KYbW$ and $Eu:KYbW$ this process is rather inefficient due to the large $Yb^{3+}-Yb^{3+}$ distances. Our studies on

luminescence decay of Yb^{3+} ions in $Tb:KYbW$ revealed no significant shortening of the experimental lifetime, $\tau_{exp}(^2F_{5/2}) = 200 \pm 10 \mu s$, as compared with that for undoped $KYbW$. This is similar to the previous findings for $Eu:KYbW$ [22]. Thus, the cooperative effects cannot fully explain the shortening of $\tau_{exp}(^5D_4)$ with respect to τ_{rad} for $Tb:KYbW$. This supports the above-discussed mechanism.

The CIE 1931 (*Commission internationale de l'éclairage*) color coordinates for the luminescence of $Tb:KYbW$ are $x = 0.312$ and $y = 0.644$ that fall into the green region in the chromaticity diagram, see Fig. 8. The dominant wavelength for the emission spectrum λ_d is 550 nm with the purity p of 88%.

5. Conclusion

Monoclinic double tungstates are promising oxide crystals for Tb^{3+} doping. They can provide high Tb^{3+} doping levels (potentially up to 100 at% in the stoichiometric $KTbW$ material) and weak concentration-quenching of luminescence. According to the present study, Tb^{3+} ions in MDTs (on the example of $Tb:KYbW$) also exhibit high transition cross-sections in polarized light for absorption in the blue (the $^7F_6 \rightarrow ^5D_4$ transition) and for SE in the green and yellow (the $^5D_4 \rightarrow ^7F_5, ^7F_4$ transitions). The possible drawback of the Tb^{3+} -doped MDTs is the shortening of the 5D_4 emission lifetime with respect to the radiative one. For $Tb:KYbW$, this process is assigned to the M.M.C.T. involving the $[Xe]4f^75d^1$ excited configuration. Further studies of the Tb^{3+} luminescence in the series of $Tb:K(Gd-Y-Lu-Yb)W$ are required to clarify this effect and to select the optimum host matrix.

Acknowledgements

This work was supported by the Spanish Government under projects MAT2016-75716-C2-1-R (AEI/FEDER,UE), MAT2013-47395-C4-4-R and TEC2014-55948-R, and by the Generalitat de Catalunya under project 2014SGR1358. F.D. acknowledges additional support through the ICREA academia award 2010ICREA-02 for excellence in research. P.L. acknowledges financial support from the Government of the Russian Federation (Grant 074-U01) through ITMO Post-Doctoral Fellowship scheme.

References

- [1] W.T. Carnall, P.R. Fields, K. Rajnak, *J. Chem. Phys.* 49 (1968) 4447–4449.
- [2] P.W. Metz, D.-T. Marzahl, A. Majid, C. Kränkel, G. Huber, *Laser Photon. Rev.* 10 (2016) 335–344.
- [3] S. Pandya, J. Yu, D. Parker, *Dalton Trans.* 23 (2006) 2757–2766.
- [4] X. Ju, X. Li, W. Li, W. Yang, C. Tao, *Mater. Lett.* 65 (2011) 2642–2644.
- [5] J. Liao, B. Qiu, H. Lai, *J. Lumin.* 129 (2009) 668–671.
- [6] R.P. Rao, *J. Electrochem. Soc.* 150 (2003) H165–H171.
- [7] H.P. Jensen, D. Castleberry, D. Gabbe, A. Linz, *IEEE J. Quantum Electron* 9 (1973) 665.
- [8] T. Yamashita, Y. Ohishi, *Jpn. J. Appl. Phys.* 46 (2007) (2007) L991.
- [9] C. Kränkel, D.-T. Marzahl, F. Moglia, G. Huber, P.W. Metz, *Laser Photon. Rev.* 10 (2016) 548–568.
- [10] D.K. Sardar, K.L. Nash, R.M. Yow, J.B. Gruber, U.V. Valiev, E.P. Kokanyan, *J. Appl. Phys.* 100 (2006) (083108-1-5).
- [11] K.S. Sohn, Y.Y. Choi, H.D. Park, Y.G. Choi, *J. Electrochem. Soc.* 47 (2000) 2375–2379.
- [12] D.J. Robbins, B. Cockayne, B. Lent, J.L. Gaspar, *Sol. State Commun.* 20 (1976) 673–676.
- [13] P. Boutinaud, R. Mahiou, J.C. Coussens, *J. Lumin.* 72–74 (1997) 318–320.
- [14] V. Petrov, M.C. Pujol, X. Mateos, O. Silvestre, S. Rivier, M. Aguiló, R.M. Solé, J. Liu, U. Griebner, F. Díaz, *Laser Photon. Rev.* 1 (2007) 179–212.
- [15] M.C. Pujol, M.A. Bursukova, F. Güell, X. Mateos, R. Solé, Jna Gavalda, M. Aguiló, J. Massons, F. Díaz, P. Klopp, U. Griebner, V. Petrov, *Phys. Rev. B* 65 (2002) (165121-1-11).
- [16] P.A. Loiko, V.I. Dashkevich, S.N. Bagaev, V.A. Orlovich, A.S. Yasukevich, K.V. Yumashev, N.V. Kuleshov, E.B. Dunina, A.A. Kornienko, S.M. Vatrik, A.A. Pavlyuk, *J. Lumin.* 153 (2014) 221–226.
- [17] V.I. Dashkevich, S.N. Bagaev, V.A. Orlovich, A.A. Bui, P.A. Loiko, K.V. Yumashev, A.S. Yasukevich, N.V. Kuleshov, S.M. Vatrik, A.A. Pavlyuk, *Laser Phys. Lett.* 12 (2015) (085001-1-5).
- [18] R.D. Shannon, *Acta Crystallogr. A* 32 (1976) 751–767.
- [19] S. Schwung, D. Rytz, B. Heying, U.Ch Rodewald, O. Niehaus, D. Ensling, T. Jüstel,

P. Loiko et al.

Journal of Luminescence 190 (2017) 37–44

- R. Pöttgen, *J. Lumin.* 166 (2015) 289–294.
- [20] J. Li, J. Wang, S. Han, Y. Guo, Y. Wang, *J. Rare Earth* 30 (2012) 967–971.
- [21] H. Zhao, J. Wang, J. Li, H. Zhang, J. Zhang, Z. Ling, H. Xia, R.I. Boughton, *Mater. Lett.* 61 (2007) 2499–2501.
- [22] P.A. Loiko, E.V. Vilejshikova, X. Mateos, J.M. Serres, E.B. Dunina, A.A. Kornienko, K.V. Yumashev, M. Aguiló, F. Díaz, *J. Lumin.* 183 (2017) 217–225.
- [23] W. Strek, A. Bednarkiewicz, P.J. Deren, *J. Lumin.* 92 (2001) 229–235.
- [24] W. Strek, P.J. Deren, A. Bednarkiewicz, *J. Lumin.* 87–89 (2000) 999–1001.
- [25] B.R. Judd, *Phys. Rev.* 172 (1962) 750–761.
- [26] G.S. Ofelt, *J. Chem. Phys.* 37 (1962) 511–519.
- [27] A.A. Kornienko, E.B. Dunina, V.L. Yankevich, *Opt. Spectr.* 81 (1996) 871–874.
- [28] E.B. Dunina, A.A. Kornienko, *Opt. Spectr.* 116 (2014) 706–711.
- [29] C.M. Dodson, R. Zia, *Phys. Rev. B* 86 (2012) 125102-1-10.
- [30] J.B. Gruber, B. Zandi, U.V. Valiev, Sh.A. Rakhimov, *Phys. Rev. B* 69 (2004) 115103-1-9.
- [31] M.J. Weber, T.E. Varitimos, B.H. Matsinger, *Phys. Rev. B* 8 (1973) 47–53.
- [32] J. Zhang, Z. Hao, X. Zhang, Y. Luo, X. Ren, X.-J. Wang, J. Zhang, *J. Appl. Phys.* 106 (2009) 034915-1-6.
- [33] S. Colak, W.K. Zwickler, *J. Appl. Phys.* 54 (1983) 2156–2166.
- [34] R. Bayerer, J. Heber, D. Mateika, *Z. Phys. B* 64 (1986) 201–210.
- [35] K.S. Thomas, S. Singh, G.H. Dieke, *J. Chem. Phys.* 38 (1963) 2180–2190.
- [36] S. Kubiniwa, T. Hoshina, *J. Phys. Soc. Jpn.* 32 (1972) 1059–1068.
- [37] B.F. Aull, H.P. Jensen, *IEEE J. Quantum Electron.* 18 (1982) 925–930.
- [38] Z. Wang, H. Liang, Q. Wang, L. Luo, M. Gong, *Mater. Sci. Eng.* 164 (2009) 120–123.
- [39] J. Gu, Y. Zhu, H. Li, X. Zhang, Y. Qian, *J. Sol. State Chem.* 183 (2010) 497–503.
- [40] M.C. Pujol, X. Mateos, R. Solé, J. Massons, Jna Gavaldà, X. Solans, F. Díaz, M. Aguiló, *J. Appl. Cryst.* 35 (2002) 108–112.
- [41] P. Dorenbos, *J. Lumin* 91 (2000) 155–176.
- [42] P.A. Loiko, N.M. Khaidukov, J. Méndez-Ramos, E.V. Vilejshikova, N.A. Skoptsov, K.V. Yumashev, *J. Lumin.* 170 (2016) 1–7.
- [43] P.A. Loiko, G.E. Rachkovskaya, G.B. Zakharevich, A.A. Kornienko, E.B. Dunina, A.S. Yasukevich, K.V. Yumashev, *J. Non-Cryst. Solids* 392–393 (2014) 39–44.



Contents lists available at ScienceDirect

Journal of Luminescence

journal homepage: www.elsevier.com/locate/jlumin



Growth, structure, Raman spectra and luminescence of orthorhombic $\text{Li}_2\text{Mg}_2(\text{MoO}_4)_3$ crystals doped with Eu^{3+} and Ce^{3+} ions



P. Loiko^{a,*}, E.V. Vilejshikova^b, A.A. Volokitina^a, V.A. Trifonov^c, J.M. Serres^d, X. Mateos^d,
N.V. Kuleshov^b, K.V. Yumashev^b, A.V. Baranov^a, A.A. Pavlyuk^c

^a ITMO University, Kronverkskiy pr., 49, Saint-Petersburg 197101, Russia

^b Center for Optical Materials and Technologies (COMT), Belarusian National Technical University, 65/17 Nezavisimosti Ave., Minsk 220013, Belarus

^c A.V. Nikolaev Institute of Inorganic Chemistry, Siberian Branch of Russian Academy of Sciences, 3 Lavrentyev Ave., Novosibirsk 630090, Russia

^d Física i Cristal·lografia de Materials i Nanomaterials (FiCMA-FiCNA), Universitat Rovira i Virgili (URV), Campus Sescelades, c/ Marcel·lí Domingo, s/n., Tarragona E-43007, Spain

ARTICLE INFO

Keywords:

Molybdate crystals
Crystal growth
Crystal structure
Raman spectra
Europium ions
Luminescence

ABSTRACT

We report on the growth and the structural, thermal, vibronic and spectroscopic properties of a complex molybdate single-crystal, $\text{Li}_2\text{Mg}_2(\text{MoO}_4)_3$ (LiMgMo), doped with Eu^{3+} or Ce^{3+} ions. Few cm size crystals were grown from the flux using Li_2MoO_4 as a solvent. Eu:LiMgMo is orthorhombic (sp. gr. $Pnma$, $a=5.085$ Å, $b=10.482$ Å, $c=17.614$ Å). It exhibits strongly polarized Raman spectra with the most intense band at 905.2 cm^{-1} . Eu:LiMgMo possesses positive thermal expansion. Using the Eu^{3+} ion as a structural probe, we argue its predominant accommodation in a single type of site A(3) with a trigonal prismatic coordination. The spectroscopy of Eu^{3+} is characterized by the lifetime measurement ($\tau(^3\text{D}_0)=537$ μs), Judd-Ofelt modeling ($\Omega_2=21.811$, $\Omega_4=7.805$ and $\Omega_6=1.203$ [10^{-20} cm^2]) and the calculation of stimulated-emission cross-sections for the $^3\text{D}_0 \rightarrow ^7\text{F}_J$ ($J=0..6$) transitions. The LiMgMo crystals are promising for rare-earth-ion doping with application as laser materials and Raman shifters.

1. Introduction

Complex tungstates and molybdates crystals are attractive as laser host materials for doping with trivalent rare-earth ions (RE^{3+}) [1] and they are Raman-active [2]. Due to their (typically) low-symmetry structure and specific structure features (in particular, large interionic distances), they provide broad and intense spectral bands of the RE^{3+} ions with a strong polarization-anisotropy [3,4], as well as RE^{3+} doping in high concentrations [5]. The most known example is the crystal family of monoclinic double tungstates (MDTs) [1], $\text{KRE}(\text{WO}_4)_2$ where $\text{RE} = \text{Gd}, \text{Y}$ or Lu , studied with Nd^{3+} [6], Yb^{3+} [7], Tm^{3+} [3], Ho^{3+} [8], etc. that have been used in efficient near-IR lasers, see [1] and Refs. therein. Double and triple molybdate crystals, e.g. the orthorhombic $\text{KY}(\text{MoO}_4)_2$ [9] and $\text{Gd}_2(\text{MoO}_4)_3$ [10] and tetragonal $\text{ALn}(\text{MoO}_4)_2$ where $\text{A} = \text{Na}$ or Li and $\text{Ln} = \text{Gd}, \text{La}$, etc. [4,11], have been also studied as promising laser hosts for RE^{3+} ions and as Raman shifters.

The crystals of lithium metal triple molybdates with chemical formula $\text{Li}_2\text{M}_2(\text{MoO}_4)_3$ where $\text{M}^{2+} = \text{Mg}, \text{Zn}, \text{Mn}, \text{Ni}, \text{Co}$ (shortly LiMMo) [12] have been poorly studied as hosts for RE^{3+} ions. These crystals have a lyonsite-type structure and they are orthorhombic [13].

The incorporation of the RE^{3+} ions into the LiMMo lattice is due to the replacement of the divalent M^{2+} cation that may limit the doping range for the RE^{3+} ions. Because of this, the first studies on the LiMMo single-crystals were devoted to their doping with divalent transition-metal ions, e.g. Co^{2+} [14,15]. Later on, the LiZnMo [16] and isostructural LiMgW [17] crystals doped with europium (Eu^{3+}) ions were prepared in the form of μm -sized crystals. It was found that doping with Eu^{3+} up to 10 at% is possible without alteration of the crystal symmetry (despite the fact that the Eu^{3+} incorporation requires a charge compensation mechanism). The intense red long-living luminescence was detected and no signs of Eu^{2+} ions were observed.

Among the RE^{3+} ions, the Eu^{3+} ones are known for their red emission of high color purity that makes them highly suitable for red phosphors [18–22]. Recently, they have also attracted interest for the development of visible (red) lasers operating at the $^5\text{D}_0 \rightarrow ^7\text{F}_J$ transitions [23]. Such lasers were based on Eu^{3+} -doped MDTs. Consequently, a further search of suitable laser hosts for Eu^{3+} doping is of high relevance. In the present paper, we report on the growth, structure and spectroscopy of orthorhombic LiMgMo single crystals doped with Eu^{3+} and Ce^{3+} ions, for the first time, to the best of our knowledge.

* Corresponding author.

E-mail address: kinetic@tut.by (P. Loiko).

<http://dx.doi.org/10.1016/j.jlumin.2017.04.021>

Received 9 February 2017; Received in revised form 11 April 2017; Accepted 13 April 2017

Available online 14 April 2017

0022-2313/ © 2017 Elsevier B.V. All rights reserved.

2. Growth and structure

2.1. Crystal growth

The LiMgMo crystal melts incongruently at 1060 °C and it cannot be grown by the conventional Czochralski method. In the present work, Eu³⁺ and Ce³⁺-doped LiMgMo crystals were grown by the modified Czochralski method (from the flux) using [010]-oriented undoped LiMgMo seeds. Lithium molybdate Li₂MoO₄ was used as a solvent. The solubility of LiMgMo in Li₂MoO₄ decreases from ~50–20 mol% on the temperature decrease from ~1020 to 910 °C. First, the Li₂MoO₄ was prepared by melting and then the Li₂CO₃, MgO, MoO₃ and RE₂O₃ (RE = Eu or Ce) reagents (5N purity, Soviet supplier) were added in stoichiometric proportion. The concentration of the RE³⁺ ions in the growth charge was 10 at% (with respect to the Mg²⁺ content).

For the crystal growth, a Pt crucible (diameter: 70 mm, height: 120 mm) was used. It was covered by Pt lid with a small hole. The solution (solute (LiMgMo): solvent (Li₂MoO₄) = 2:3 ratio in mol%) was heated at ~1000 °C in air and homogenized with a Pt stirrer. Then, it was cooled to 994 °C and the rotating seed (35 rev/min) was put in contact to the solution surface. The growth was performed under low thermal gradients (< 1 °C/cm) [24–27]; the temperature was controlled with a precision of 0.1 °C. During the growth, the temperature was decreased at about 1–2 °C/day, the pulling rate was 1–5 mm/day and the rotation rate was 20–30 rev/min. The growth period was nearly 30 days. When the growth was completed, the crystal was carefully removed from the flux and slowly cooled to room temperature (RT) at a cooling rate of 30 °C/h. No subsequent annealing of the crystals was implemented. The photographs of the as-grown crystals are presented in Fig. 1. They were transparent, crack- and inclusion-free. The cross-section of the grown boules is extended along the [100] direction. The Eu³⁺-doped crystal was colorless and the Ce³⁺-doped one had a slight yellowish coloration.

2.2. Structure

The crystal structure and phase purity of the grown RE³⁺-doped LiMgMo crystals were confirmed with XRD. The XRD measurements were made using a Siemens D5000 diffractometer (Bragg-Brentano parafocusing geometry and vertical θ - θ goniometer) fitted with a curved graphite diffracted-beam monochromator, incident and diffracted beam Soller slits, a 0.06° receiving slit and scintillation counter as a detector. The 2θ diffraction range was between 10° and 70°. The data were collected with an angular step of 0.05° at 3 s per step and

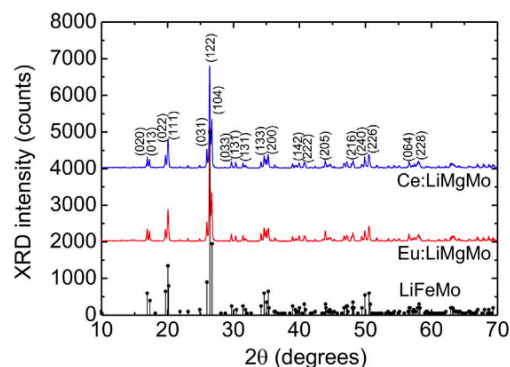


Fig. 2. X-ray powder diffraction (XRD) patterns of the Eu:LiMgMo and Ce:LiMgMo crystals, points represent relative intensities of XRD peaks for a Li₃Fe(MoO₄)₃ crystal (ICCD card 01-072-0754), numbers are the Miller's indices (hkl).

sample rotation. The Cu K α radiation (1.54184 Å) was used. For the XRD studies, the crystal samples were finely powdered.

The obtained XRD patterns are shown in Fig. 2 and compared with the known pattern of a Li₃Fe(MoO₄)₃ crystal (ICCD card 01-072-0754) [28]. The grown Eu:LiMgMo and Ce:LiMgMo crystals are orthorhombic (point group: *mmm*, space group: D_{2h}¹⁶ - *Pnma* (No. 62)). The determined lattice constants are $a = 5.085 \pm 0.002$ Å, $b = 10.482 \pm 0.004$ Å, $c = 17.614 \pm 0.004$ Å, $Z = 4$, the unit-cell volume $V = 938.8$ Å³, and the calculated density $\rho = 3.837$ g/cm³ (for Eu:LiMgMo, the lattice parameters of Ce:LiMgMo are the same within the error interval). In Table 1, we have compared the lattice parameters of various lyonsite-type complex molybdates and tungstates.

The following description of the structure of LiMgMo is according to the previous structural studies [12,13,29]. The complex molybdate LiMgMo belongs to the structural type of the vanadate mineral lyonsite Cu₃Fe₄(VO₄)₆, which includes a number of complex oxides with the general formula A₁₆B₁₂O₄₈, where A and B are lower oxidation-state (+1, +2, +3) and high oxidation-state (+5, +6) metal cations, respectively [12]. In the LiMgMo structure, the B = Mo⁶⁺ cations occupy two different tetrahedral sites (4d and 8c Wyckoff positions). The lower oxidation-state cations A = Li⁺, Mg²⁺ occupy three different low-symmetry sites that form chains of octahedral polyhedrons (A(1) site), face-sharing highly distorted octahedrons (A(2) site) and edge-sharing trigonal prisms (A(3) site) [12,29], see Fig. 3(a). The mean A–O distances for the three sites are 2.09, 2.05 and 2.1 Å,

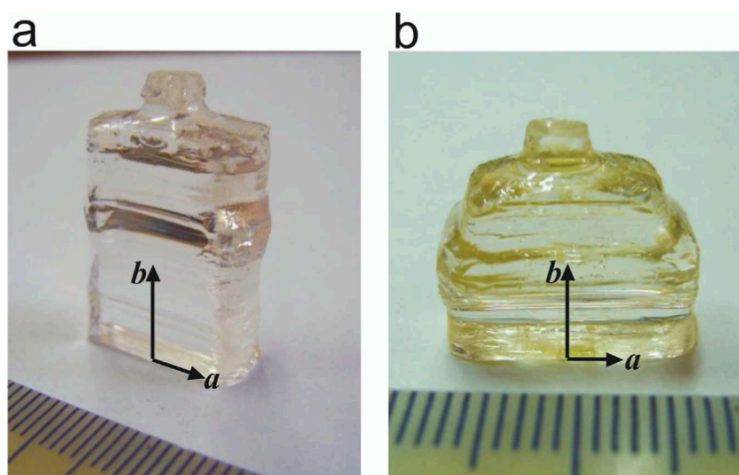


Fig. 1. Photographs of the as-grown 0.4 at% Eu:LiMgMo (a) and 0.5 at% Ce:LiMgMo crystals.

Table 1
Unit-cell parameters (*a*, *b*, *c*) of the orthorhombic lyonsite-type complex molybdates and tungstates.

Crystal	<i>a</i> , Å	<i>b</i> , Å	<i>c</i> , Å	Ref.
Eu:Li ₂ Mg ₂ (MoO ₄) ₂	5.085	10.482	17.614	This work
Li ₂ Mg ₂ (MoO ₄) ₂	5.1167	10.4646	17.6228	[13]
Li ₂ Mg ₂ (WO ₄) ₃	5.1129	10.462	17.612	[29]
Li ₂ Zn ₂ (MoO ₄) ₃	5.1042	10.506	17.638	[14]
FeLi ₃ (MoO ₄) ₃	5.07	10.48	17.64	[30]
Co ₂ Li ₂ (MoO ₄) ₃	5.086	10.484	17.606	[31]
Li ₃ V(MoO ₄) ₃	5.0575	10.4562	17.5105	[32]
Li ₃ Al(MoO ₄) ₃	5.0372	10.32	17.272	[33]

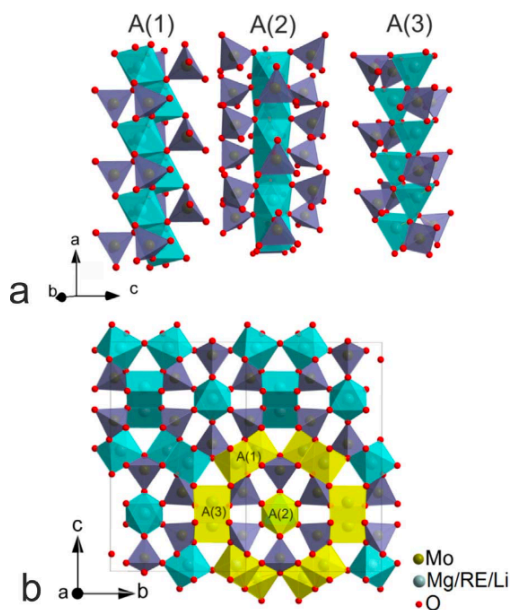


Fig. 3. Structure of the Eu/Ce:LiMgMo crystals: (a) linkages between the [Mg/LiO₆] and [MoO₄] polyhedrons for three types of sites for Mg/Li, A(1), A(2) and A(3); (b) projection of a structure within one unit-cell on the *b*-*c* plane, green and blue polyhedrons represent [Mg/LiO₆] and [MoO₄], yellow polyhedrons – fragment of the tunnel-like hexagonal structure.

respectively. In the chains of the face-sharing octahedrons A(2)O₆, the Li⁺ and Mg²⁺ ions are very close: the interionic distance A–A is about 2.5 Å. In the edge-sharing zigzag-like chains of the AO₆ octahedrons and prismatic polyhedrons, the A–A distances are 3.0–3.2 Å, as calculated from the structural data from [13].

In the LiMgMo structure, the isolated [MoO₄]²⁻ tetrahedrons are linked by AO₆ chains creating a tunnel-like hexagonal structure, as shown in Fig. 3(b). The sides of the hexagonal “tunnel” consist of the

above mentioned chains of octahedrons of the A(1) sites and edge-sharing trigonal prisms of the A(3) sites, and the face-sharing octahedral polyhedrons of the A(2) sites pass through the center of this tunnel-like structure.

Though the Li⁺ and Mg²⁺ cations in LiMgMo are randomly distributed on the VI-fold O²⁻-coordinated cationic positions A(1), A(2) and A(3), the occupation factors of the A-sites are different. For undoped LiMgMo, the occupation factors of the A(1), A(2) and A(3) sites for the Mg²⁺/Li⁺ ions are 0.659/0.341, 0.471/0.529 and 0.210/0.790, respectively [13]. In the rare-earth doped LiMgMo, the trivalent RE³⁺ ions predominantly replace the Mg²⁺ ions in the A sites. This process is accompanied by a cationic redistribution over these sites.

The concentration of RE³⁺ ions in the grown crystals was determined by Energy-Dispersive X-ray (EDX) spectroscopy using an Electron Scanning Environmental Microscope (ESEM) equipped with an Inca microanalyzer (Oxford Instruments) to be 0.4 ± 0.2 at% Eu³⁺ and 0.5 ± 0.2 at% Ce³⁺. Thus, the segregation coefficient for the RE³⁺ ions in LiMgMo, $K_{RE} = N_{crystal}/N_{flux} \sim 0.045 \pm 0.02$. Such a low value is explained by the difference of the ionic radii of Mg²⁺ ions (0.72 Å for VI-fold O²⁻-coordination) and Eu³⁺ (0.947 Å), Ce³⁺ (1.01 Å) [34].

By performing the XRD studies at various elevated temperatures over the range of 303 – 773 K, we have determined the linear thermal expansion coefficients α , which are $\alpha_a = 17.87$, $\alpha_b = 14.02$ and $\alpha_c = 15.63 \times 10^{-6} K^{-1}$, and the volumetric thermal expansion $\alpha_{vol} = \alpha_a + \alpha_b + \alpha_c = 47.52 \times 10^{-6} K^{-1}$ (for Eu:LiMgMo). The values of α are large and positive for LiMgMo (while negative α are known for some complex molybdates along certain crystallographic directions, e.g. for Sc₂(MoO₄)₃ [35]). In Table 2, we have compared the α values for various complex molybdates and tungstates. The anisotropy of the thermal expansion is very weak for LiMgMo, $\alpha_a : \alpha_b : \alpha_c = 1.27 : 1 : 1.11$, e.g. as compared with the MDTs [40].

3. Experimental

For the spectroscopic studies, two polished rectangular samples from Eu:LiMgMo and Ce:LiMgMo oriented along the *a*, *b*, *c* axes were prepared. All the studies were performed at RT. It should be noted, that during the processing of the samples (cut and polishing), tiny cracks along the {001} plane appeared when some amount of pressure was applied to the crystal. Such a behavior related to a perfect cleavage is typical for complex molybdates [41–44].

Raman spectra were measured in polarized light using a Renishaw inVia confocal Raman microscope with a x50 objective. The excitation wavelength λ_{exc} was 514 nm and an edge filter was used. The accumulation time was 10 s and the number of accumulations – 30.

The absorption spectra were measured in the visible spectral range with a Varian CARY-5000 spectrophotometer. The unpolarized emission spectra were measured under the excitation of a blue GaN laser diode ($\lambda_{exc} \sim 400$ nm) using a lock-in amplifier (Stanford Research Systems, model SR810), a grating monochromator (model MDR-23) and an avalanche photodiode (Hamamatsu, model C5460-01). The polarized emission spectra of the Eu³⁺ ions were measured with the

Table 2
Thermal expansion coefficients α [$10^{-6} K^{-1}$] along the *a*, *b* and *c* axes for complex molybdates and tungstates (orthorhombic and monoclinic).

Crystal	Crystal class	Temperature range, K	α , $10^{-6} K^{-1}$			Ref.
			α_a	α_b	α_c	
Eu:Li ₂ Mg ₂ (MoO ₄) ₃	orthorhombic	303–773	17.87	14.02	15.63	This work
Gd ₂ (MoO ₄) ₃	orthorhombic	320–480	18.3	16.7	–4.7	[36]
Fe ₂ (MoO ₄) ₃	monoclinic	305–780	10.6	10.38	14.45	[37]
	orthorhombic	820–1070	–1.94	4.57	0.71	
Sc ₂ (MoO ₄) ₃	orthorhombic	180–300	–8.41	10.82	–8.73	[35]
Lu ₂ (MoO ₄) ₃	orthorhombic	470–1070	–8.88	–1.23	–6.62	[38]
Li ₂ Ba ₂ Gd ₃ (MoO ₄) ₈	monoclinic	400–1000	16.2	17.3	21.5	[39]
KY(WO ₄) ₂	monoclinic	293–473	10.3	2.0	20.3	[40]

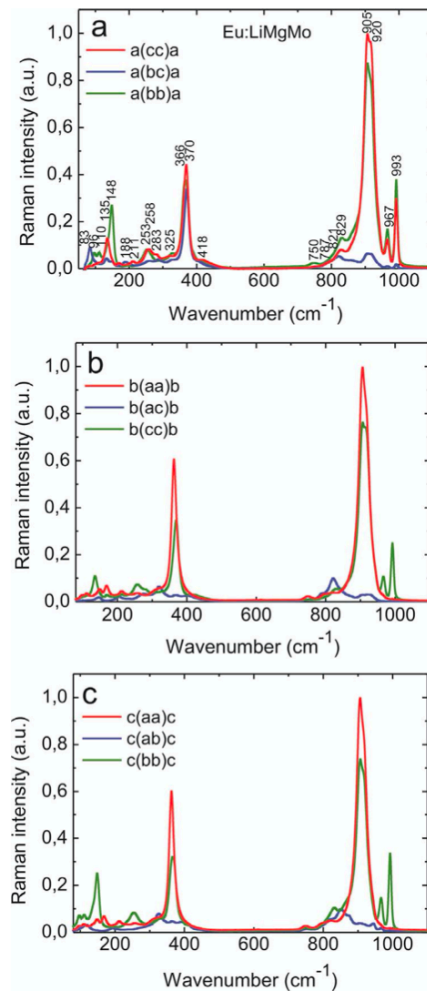


Fig. 4. Polarized Raman spectra for the Eu:LiMgMo crystal for the $a(xy)a$ (a), $b(xy)b$ (b) and $c(xy)c$ (c) geometries where $x, y = a, b$ or c (directions of the crystallographic axes); $\lambda_{\text{exc}} = 514$ nm. Numbers in (a) denote the peak positions in cm^{-1} . For each graph, the spectra are in scale.

Renishaw inVia confocal Raman microscope with a x50 objective, λ_{exc} was 488 nm.

To measure the luminescence decay curve of the Eu^{3+} ions, a ns optical parametric oscillator Lotis TII LT-2214 tuned to 534 nm was used as excitation source. The detection system included a monochromator (model MDR-12) set at 610 nm, a fast Hamamatsu C5460 photodetector (response time, 40 ns) and a 500 MHz Textronix TDS-3052B digital oscilloscope. The luminescence decay of Ce^{3+} was studied with a laser scanning confocal microscope MicroTime 100 (PicoQuant), which implements the method of time-correlated single photon counting ($\lambda_{\text{exc}} \sim 400$ nm, duration of the pump pulse: ~ 200 ps).

4. Raman spectra

For Raman spectroscopy, a polished rectangular Eu:LiMgMo sample oriented along the a, b, c axes was used. The spectra corresponded to the configurations $a(xy)a, b(xy)b$ and $c(xy)c$ where $x, y = a, b$ or c . The results are shown in Fig. 4(a–c) (for each configuration, the spectra are normalized to unity). The Raman spectra of Ce:LiMgMo were very similar.

The interpretation of the Raman spectra of Eu:LiMgMo is performed

according to [45,46]. The free $[\text{MoO}_4]^{2-}$ tetrahedral (T_d) units have four fundamental modes of vibration: $\nu_1(A_1)$ – non-degenerated symmetric stretching at 894 cm^{-1} , $\nu_2(E)$ – doubly degenerated symmetric bending at 318 cm^{-1} , $\nu_3(T_2)$ – triply degenerated asymmetric stretching at 833 cm^{-1} , and $\nu_4(T_2)$ – triply degenerated asymmetric bending at 381 cm^{-1} . In the crystal structure of LiMgMo, the MoO_4 tetrahedrons are distorted and their symmetry is lowered lifting the degeneracy of the modes. The factor group analysis leads to 228 vibrational modes of which 114 are Raman-active, distributed among the irreducible representations as $31A_g + 26B_{1g} + 31B_{2g} + 26B_{3g}$.

The Raman spectra of LiMgMo are strongly polarized. The observed Raman bands can be classified into three groups of vibrations: (i) translational and rotational modes of the MoO_4 tetrahedrons and Li/Mg–O external modes at $< 300 \text{ cm}^{-1}$; (ii) symmetric and asymmetric O–Mo–O bending vibrations at $300\text{--}450 \text{ cm}^{-1}$; (iii) Mo–O stretching modes at $750\text{--}850 \text{ cm}^{-1}$ (asymmetric) and at $850\text{--}1000 \text{ cm}^{-1}$ (symmetric). The most intense band consists of two closely located peaks centered at 905.3 and 919.9 cm^{-1} attributed to the ν_1 mode; the full width at half maximum (FWHM) of these peaks are 27.4 and 19.4 cm^{-1} , respectively. It should be noted that for LiMgMo, no bands at $> 1000 \text{ cm}^{-1}$ (which are related to the cation vacancies [47]) are observed.

5. Optical spectroscopy (absorption and emission)

LiMgMo is orthorhombic and, thus, it is optically biaxial. Its optical properties are described in the optical indicatrix frame. The optical indicatrix axes for orthorhombic crystals coincide with the crystallographic a, b, c axes [48] while their exact assignment for LiMgMo is still unknown. The reported mean value of n for LiMgMo is ~ 1.87 [49] and the birefringence for the isostructural LiZnMo is $\Delta n \sim 0.02$ [50].

The absorption spectra of the Eu:LiMgMo and Ce:LiMgMo crystals are shown in Fig. 5. Due to the low doping level of the RE^{3+} ions, the corresponding absorption bands are weak and the spectra are shown in unpolarized light. For Eu:LiMgMo, the UV absorption edge is at $\lambda_g = 324 \text{ nm}$ ($E_g = 3.82 \text{ eV}$). In the visible, two weak absorption bands at $\sim 398 \text{ nm}$ (the ${}^7F_0 \rightarrow {}^5L_6$ transition of Eu^{3+}) and at $\sim 466 \text{ nm}$ (${}^7F_0 \rightarrow {}^5D_2$) are observed. For Ce:LiMgMo, the feature of the absorption spectrum is the long-wavelength shift of the UV absorption edge ($\lambda_g = 365 \text{ nm}$) that is partially ascribed to the Ce^{3+} doping.

The emission spectra of the studied crystals in unpolarized light are shown in Fig. 6 ($\lambda_{\text{exc}} = 400 \text{ nm}$). The red emission of Eu:LiMgMo is related to the transitions of Eu^{3+} ions from the metastable 5D_0 state to the upper-lying 7F_J ones (denoted as $0 \rightarrow J'$ transitions in Fig. 6(a)). No signs of blue emission from the divalent europium, Eu^{2+} , are detected. The bluish-green emission of Ce:LiMgMo detected as a single broad band centered at $\sim 490 \text{ nm}$ is related to the $5d \rightarrow {}^2F_{5/2}$ ($4f$) transitions of

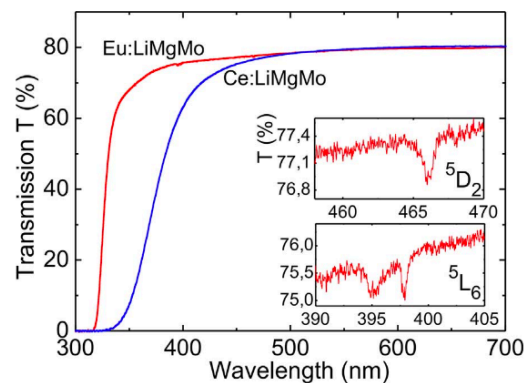


Fig. 5. Unpolarized transmission spectra of 0.4 at% Eu:LiMgMo and 0.5 at% Ce:LiMgMo crystals in the visible (sample thickness, $t = 3.7 \text{ mm}$).

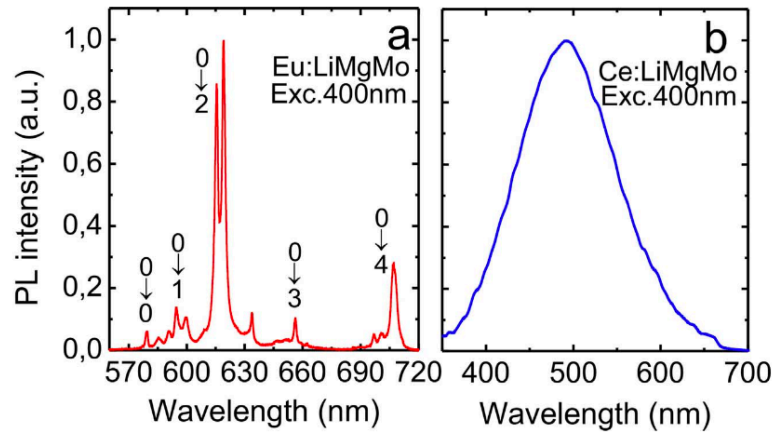


Fig. 6. Photoluminescence (PL) spectra of 0.4 at% Eu:LiMgMo (a) and 0.5 at% Ce:LiMgMo (b) crystals in unpolarized light; $\lambda_{exc} = 400$ nm.

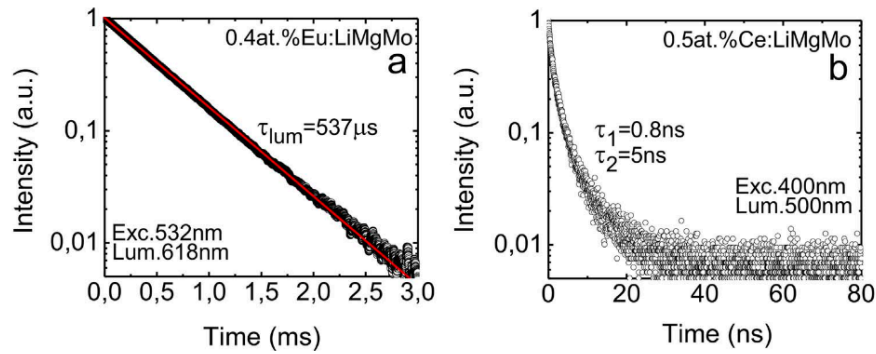


Fig. 7. Luminescence decay curve for 0.4 at% Eu:LiMgMo (a) and 0.5 at% Ce:LiMgMo (b) crystals: points are the experimental data, red curve in (a) represent a single-exponential fit.

Table 3
 Lifetime of the metastable 5D_0 state of Eu^{3+} ions in complex molybdates and tungstates.

Crystal	Crystal class (sp. gr.)	τ , ms	Ref.
Eu:Li ₂ Mg ₂ (MoO ₄) ₃	orthorhombic (<i>Pnma</i>)	0.537	This work
Eu:Li ₂ Mg ₂ (WO ₄) ₃	orthorhombic (<i>Pnma</i>)	0.86	[17]
Eu:LiKGd ₂ (MoO ₄) ₄	monoclinic (<i>C2/c</i>)	0.385	[54]
Eu:La ₂ (MoO ₄) ₃	monoclinic (<i>C2/c</i>)	0.99	[55]
Eu:Y ₂ (MoO ₄) ₃	monoclinic (<i>C2/c</i>)	0.55	[56]
Eu:Li ₃ Ba ₂ Gd ₃ (MoO ₄) ₈	monoclinic (<i>C2/c</i>)	0.471	[57]
Eu: KY(WO ₄) ₂	monoclinic (<i>C2/c</i>)	0.43	[52]

Table 4
 Emission properties of the Eu^{3+} ions in LiMgMo.

Parameters	Value
Judd-Ofelt parameters [10^{-20} cm ²]	$\Omega_2 = 21.811$, $\Omega_4 = 7.805$, $\Omega_6 = 1.203$
Calculated luminescence branching ratios ($^5D_0 \rightarrow ^7F_j$)	$B_{0-1} = 5.8\%$, $B_{0-2} = 85.3\%$, $B_{0-4} = 14.7\%$, $B_{0-6} = 0.14\%$
Asymmetry parameter	$R = 5.2$
Lifetime (5D_0)	$\tau_{rad} = 578 \mu s$, $\tau_{exp} = 537 \mu s$
Luminescence quantum efficiency	$\eta_q = 93\%$

the Ce^{3+} ions.

Eu^{3+} is known for its hyper-sensitive purely electric-dipole (ED) transition $^5D_0 \rightarrow ^7F_2$ that is an indicator of the site symmetry of the ion

[51]. If the site has no inversion center, this transition will be dominant over the $^5D_0 \rightarrow ^7F_1$ transition that is of pure magnetic dipole (MD) nature. The ratio of the integral intensities of the corresponding emission bands is typically calculated and referred as an asymmetry parameter R [52]:

$$R = \frac{I_{ED}(^5D_0 \rightarrow ^7F_2)}{I_{MD}(^5D_0 \rightarrow ^7F_1)} \quad (1)$$

For Eu:LiMgMo, $R = 5.2$ which means a strong prevalence of the ED transition or, in other words, the lack of center of inversion for the Eu^{3+} sites. This value is lower than that for Eu^{3+} -doped MDTs ($R = 10 \dots 13$) where the Eu^{3+} ions accommodate in the C_2 symmetry sites [53] and it is close to the results reported previously for Eu:LiZnMo phosphors ($R = 5.6 \dots 6.2$, depending on the Li/Zn cationic ratio) [16].

The luminescence decay curve for the Eu:LiMgMo crystal is shown in Fig. 7(a). The decay is clearly single-exponential indicating that the Eu^{3+} ions accommodate in a single type of site, similarly to the case of the isostructural Eu:LiMgW [17]. The obtained data on the asymmetry parameter for the Eu^{3+} emission and the luminescence decay indicate that the Eu^{3+} ions mostly accommodate in the trigonal prismatic A(3) sites without the inversion center. For Eu:LiMgMo, the characteristic decay time $\tau_{lum} = 537 \mu s$ corresponding to the lifetime of the 5D_0 excited-state of the Eu^{3+} ions. In Table 3, we compare the $\tau_{lum}(^5D_0)$ for various complex molybdate and tungstate crystals. The $\tau_{lum}(^5D_0)$ for Eu:LiMgMo is shorter than that for a 6 at% Eu:LiMgW crystal synthesized in the form of phosphor (860 μs) [17] while it is longer than for another well-known host for Eu^{3+} doping, Eu: KY(WO₄)₂, for which $\tau_{lum}(^5D_0) = 430 \mu s$ [52].

The luminescence decay of Ce^{3+} ions in LiMgMo is shown in Fig. 7(b). The decay curve can be fitted with a double-exponential law

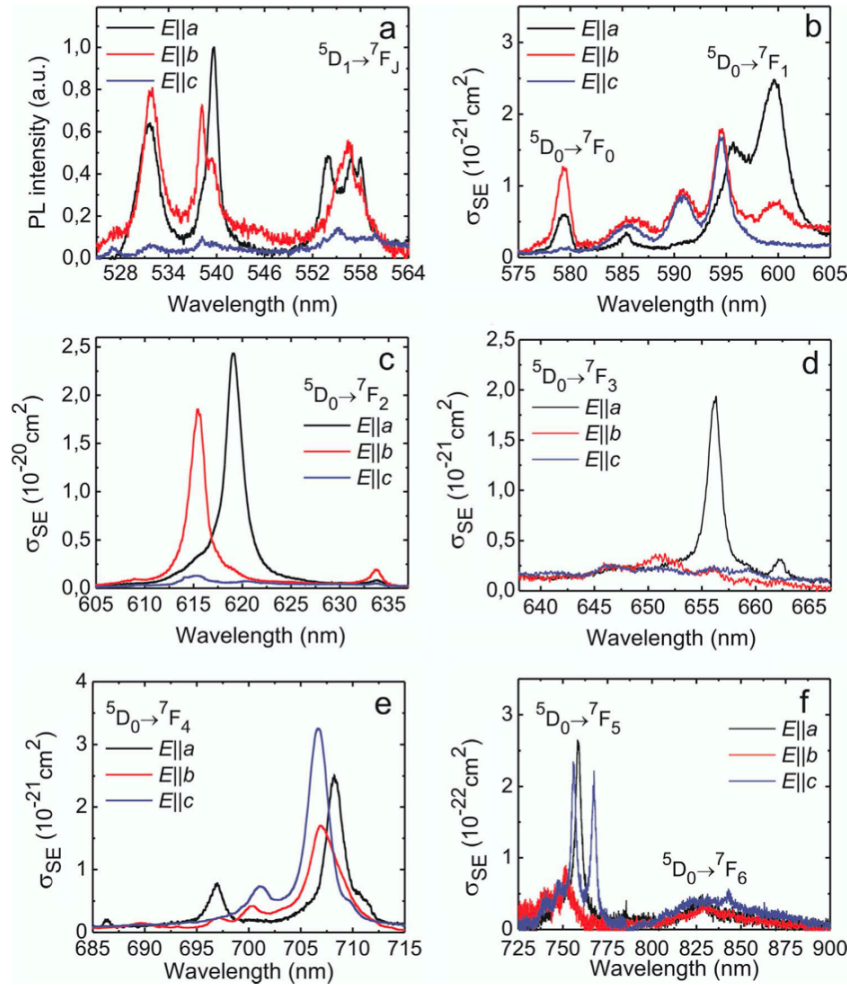


Fig. 8. Polarization-resolved emission spectroscopy of Eu^{3+} ions in the LiMgMo crystal: (a) emissions from the ${}^5\text{D}_1$ state; (b-f) stimulated-emission cross-sections, σ_{SE} , for the ${}^5\text{D}_0 \rightarrow {}^7\text{F}_J$ transitions calculated with the F-L formula, Eq. (7). The principal light polarizations are $E \parallel a, b$ and c .

Table 5

Color coordinates (x, y) , dominant wavelength λ_d , and color purity p (CIE 1931) of the luminescence of Eu^{3+} and Ce^{3+} ions in LiMgMo under blue excitation.

Crystal	x	y	λ_d , nm	p , %
$\text{Eu}^{3+}:\text{Li}_2\text{Mg}_2(\text{MoO}_4)_3$	0.667	0.333	608.6	100
$\text{Ce}^{3+}:\text{Li}_2\text{Mg}_2(\text{MoO}_4)_3$	0.156	0.349	491.1	62.0

corresponding to two characteristic lifetimes, $\tau_1 = 0.8$ ns and $\tau_2 \sim 5$ ns. This can be explained by a possible accommodation of relatively large number of Ce^{3+} ions in several A sites.

Due to the weakness of the absorption bands of Eu^{3+} in LiMgMo , Fig. 5, it was difficult to evaluate its radiative properties within the Judd-Ofelt (J-O) theory [58,59] solely based on the absorption oscillator strengths [52]. Thus, we involved an additional consideration. As mentioned above, the ${}^5\text{D}_0 \rightarrow {}^7\text{F}_1$ transition is of purely MD nature. Its probability A_{MD} is independent on the crystal-field and can be derived as [60]:

$$A_{\text{MD}}(01') = A_{\text{MD}(\text{vac})}(01') \cdot n^3, \quad (2)$$

where $A_{\text{MD}(\text{vac})}(01') = 14.5 \text{ s}^{-1}$ is the vacuum probability [60]. By

calculating the experimental luminescence branching ratios $B_{\text{exp}}(JJ')$ for the ${}^5\text{D}_0 \rightarrow {}^7\text{F}_J$ transitions:

$$B_{\text{exp}}(JJ') = 1/3 \sum_{i=a,b,c} \frac{\int_{JJ'} W_i(\nu) d\nu}{\int W_i(\nu) d\nu}, \quad (3)$$

where $W_i(\nu)$ is the luminescence spectrum for the i -th polarization (measured with a spectrally calibrated detector in the spectral range covering all the ${}^5\text{D}_0 \rightarrow {}^7\text{F}_J$ transitions for $J' = 0 \dots 6$), ν is the light frequency, one can derive the probabilities of spontaneous transitions ${}^5\text{D}_0 \rightarrow {}^7\text{F}_J$ and the radiative lifetime of the ${}^5\text{D}_0$ state:

$$A(JJ') = A_{\text{MD}}(01') \frac{B_{\text{exp}}(JJ')}{B_{\text{exp}}(01')}, \quad (4a)$$

$$\tau_{\text{rad}} = \frac{1}{\sum_{J'} A(JJ')}. \quad (4b)$$

Finally, the probabilities of the ED spontaneous transitions can be expressed as [53]:

$$A_{\text{ED}}(JJ') = \frac{64\pi^4 e^2}{3h(\lambda)^3} n \left(\frac{n^2 + 2}{3} \right)^2 S(JJ'). \quad (5)$$

Here, $\langle \lambda_{JJ'} \rangle$ is the mean emission wavelength, h is the Planck constant, e is the electron charge, and $S(JJ')$ is the line strength. The latter, according to the standard J-O theory [58,59], is expressed as:

$$S(JJ') = \sum_{k=2,4,6} \Omega_k U_{JJ'}^{(k)}. \quad (6)$$

Here, $U^{(k)}$ are the squared reduced matrix elements for the $J \rightarrow J'$ transition and Ω_k are the intensity parameters (J-O parameters).

The results on the radiative properties of the Eu^{3+} ions in LiMgMo are summarized in Table 4. The J-O parameters are $\Omega_2 = 21.811$, $\Omega_4 = 7.805$, $\Omega_6 = 1.203$ [10^{-20} cm^2] and the radiative lifetime of the ${}^5\text{D}_0$ state is $\tau_{\text{rad}} = 578 \mu\text{s}$. Thus, the luminescence quantum efficiency, $\eta_q = \tau_{\text{lum}}/\tau_{\text{rad}} = 93\%$.

By using the measured polarized emission spectra for the ${}^5\text{D}_0 \rightarrow {}^7\text{F}_J$ transitions and the determined $\tau_{\text{rad}}({}^5\text{D}_0)$, we have derived the stimulated-emission (SE) cross-sections, σ_{SE} . For this, the Fichtbauer-Ladenburg (F-L) equation for biaxial crystals [53,61] was used:

$$\sigma_{\text{SE}}^{(i)}(\lambda) = \frac{\lambda^5}{8\pi n^2 \tau_{\text{rad}} c} \frac{W_i(\lambda) B_{\text{exp}}(JJ')}{1/3 \sum_{i=a,b,c} \int \lambda W_i(\lambda) d\lambda}. \quad (7)$$

Here, c is the speed of light. The results on σ_{SE} are presented in Fig. 8. The σ_{SE} spectra for Eu:LiMgMo are strongly polarized. For the ${}^5\text{D}_0 \rightarrow {}^7\text{F}_2$ transition, the highest SE cross-sections correspond to light polarizations $\mathbf{E} \parallel \mathbf{a}$ ($2.5 \times 10^{-20} \text{ cm}^2$ at 619.1 nm) and $\mathbf{E} \parallel \mathbf{b}$ ($1.8 \times 10^{-20} \text{ cm}^2$ at 615.5 nm). For the ${}^5\text{D}_0 \rightarrow {}^7\text{F}_4$ transition, that was recently used to achieve lasing at RT in Eu^{3+} -doped MDTs [62], the maximum $\sigma_{\text{SE}} = 3.3 \times 10^{-21} \text{ cm}^2$ at 706.7 nm for $\mathbf{E} \parallel \mathbf{c}$. In Fig. 8(a), we also show emissions related to the transitions from the short-living ${}^5\text{D}_1$ state [52].

The accommodation of Eu^{3+} ions in the sites without center of inversion may potentially lead to observation of ultranarrow ${}^5\text{D}_0 \rightarrow {}^7\text{F}_0$ and ${}^5\text{D}_1 \rightarrow {}^7\text{F}_0$ emission lines like in monoclinic $\text{Eu}_2(\text{MoO}_4)_3$ [20]. In Fig. 8(b), the peak at 579.4 nm (17259 cm^{-1}) is assigned to the ${}^5\text{D}_0 \rightarrow {}^7\text{F}_0$ transition of Eu^{3+} ions in orthorhombic LiMgMo while its FWHM is larger than that of monoclinic $\text{Eu}_2(\text{MoO}_4)_3$ [20] and $\text{Eu:KLu}(\text{WO}_4)_2$ [63] probably due to the higher symmetry of the former host.

The CIE 1931 (*Commission internationale de l'éclairage*) color coordinates for the luminescence of Eu:LiMgMo and Ce:LiMgMo under blue excitation are presented in Table 5. For the former crystal, $x = 0.667$ and $y = 0.333$ that fall into the red region; the dominant wavelength in the emission spectrum is 609 nm with almost 100% purity. The color coordinates for the emission of Eu:LiMgMo are close to those of the $\text{Eu:KY}(\text{WO}_4)_2$ crystal, $x = 0.670$ and $y = 0.329$ [40].

6. Conclusions

Orthorhombic lyonsite-type lithium magnesium complex molybdate, $\text{Li}_2\text{Mg}_2(\text{MoO}_4)_3$, is a promising host material for RE^{3+} doping potentially suitable for laser applications and for Raman frequency conversion. In the present work, we have successfully grown large-volume and high optical quality LiMgMo single-crystals doped with Eu^{3+} and Ce^{3+} ions and studied their structural, thermal, vibrational and spectroscopic properties, for the first time, to the best of our knowledge. The Raman spectroscopy of LiMgMo shows a significant polarization-anisotropy of the vibronic properties with the most intense Raman band at 905.3 cm^{-1} . LiMgMo exhibits a positive thermal expansion along all three \mathbf{a} , \mathbf{b} and \mathbf{c} axes. Using the Eu^{3+} ion as a probe, we argued the predominant accommodation of Eu^{3+} in a single site (the A(3) site of $\text{Mg}^{2+}/\text{Li}^+$ with a trigonal prismatic coordination and without inversion center). The spectroscopy of Eu^{3+} is further characterized in detail, including the lifetime measurement, the J-O modeling and the calculation of the SE cross-section spectra.

Further work on LiMgMo and the isostructural LiZnMo will focus on their doping with the Yb^{3+} laser-active rare-earth ion at higher

concentrations (up to 10 at%) than the one studied in the present paper for Eu^{3+} (0.4 at%). A relatively long interionic A-A distances for the A(3) sites and a strong polarization-anisotropy of the spectroscopic properties will favor a weak concentration quenching of the luminescence and naturally polarized laser output. In addition, Raman self-conversion is expected in such Yb lasers.

Acknowledgments

P.L. acknowledges financial support from the Government of the Russian Federation (Grant 074-U01) through ITMO Post-Doctoral Fellowship scheme. P.L. also thanks Dr. E. Ushakova (ITMO University) for the help with the decay measurements for Ce:LiMgMo crystal.

References

- [1] V. Petrov, M.C. Pujol, X. Mateos, Ò. Silvestre, S. Rivier, M. Aguiló, R.M. Solé, J. Liu, U. Griebner, F. Díaz, Laser Photon. Rev. 1 (2007) 179–212.
- [2] T.T. Basiev, A.A. Sobol, P.G. Zverev, L.I. Ivleva, V.V. Osiko, R.C. Powell, Opt. Mater. 11 (1999) 307–314.
- [3] O. Silvestre, M.C. Pujol, M. Rico, F. Güell, M. Aguiló, F. Díaz, Appl. Phys. B 87 (2007) 707–716.
- [4] Yu.K. Voron'ko, K.A. Subbotin, V.E. Shukshin, D.A. Lis, S.N. Ushakov, A.V. Popov, E.V. Zharikov, Opt. Mater. 29 (2006) 246–252.
- [5] M.C. Pujol, M.A. Bursukova, F. Güell, X. Mateos, R. Solé, J. Gavalda, M. Aguiló, J. Massons, F. Díaz, P. Klopp, U. Griebner, V. Petrov, Phys. Rev. B 65 (2002) (165121-1-11).
- [6] Y. Chen, Y. Lin, X. Gong, Q. Tan, J. Zhuang, Z. Luo, Y. Huang, J. Lumin. 126 (2007) 653–660.
- [7] X. Mateos, R. Solé, J. Gavalda, M. Aguiló, J. Massons, F. Díaz, V. Petrov, U. Griebner, Opt. Mater. 28 (2006) 519–523.
- [8] V. Jambunathan, X. Mateos, P.A. Loiko, J.M. Serres, U. Griebner, V. Petrov, K.V. Yumashev, M. Aguiló, F. Díaz, J. Lumin. 179 (2016) 50–58.
- [9] A.A. Kaminskii, H.R. Verdun, Phys. Stat. Sol. (a) 138 (1993) K49–K53.
- [10] A.A. Kaminskii, H.-J. Eichler, D. Grebe, R. Macdonald, S.N. Bagaev, A.A. Pavlyuk, F.A. Kuznetsov, Phys. Stat. Sol. (a) 153 (1996) 281–285.
- [11] A.V. Mandrik, A.E. Troshin, V.E. Kisel, A.S. Yasukevich, G.N. Klavust, N.V. Kuleshov, A.A. Pavlyuk, Appl. Phys. B 81 (2005) 1119–1121.
- [12] J.P. Smit, P.C. Stair, K.R. Poeppelmeier, Chem. Eur. J. 12 (2006) 5944–5953.
- [13] L. Sebastian, Y. Piffard, A.K. Shukla, F. Taulelle, J. Gopalakrishnan, J. Mater. Chem. 13 (2003) 1797–1802.
- [14] L. Xue, Y. Wang, P. Lv, D. Chen, Z. Lin, J. Liang, F. Huang, Z. Xie, Cryst. Growth Des. 9 (2009) 914–920.
- [15] V.A. Trifonov, A.A. Pavlyuk, K.N. Gorbachenya, A.S. Yasyukevich, N.V. Kuleshov, Inorg. Mater. 49 (2013) 517–519.
- [16] X. He, M. Guan, C. Zhang, T. Shang, N. Lian, Y. Yao, J. Alloy Compd. 509 (2011) L341–L343.
- [17] Z. Mu, E. Song, D. Zhu, J. Feng, Y. Yang, Displays 43 (2016) 18–22.
- [18] G. Wakefield, E. Holland, P.J. Dobson, J.L. Hutchison, Adv. Mater. 13 (2001) 1557–1560.
- [19] P. Shi, Z. Xia, M.S. Molokeev, V.V. Atuchin, Dalton Trans. 43 (2014) 9669–9676.
- [20] V.V. Atuchin, A.S. Aleksandrovsky, O.D. Chimitova, T.A. Gavrilova, A.S. Krylov, M.S. Molokeev, A.S. Oreshonkov, B.G. Bazarov, J.G. Bazarova, J. Phys. Chem. C. 118 (2014) 15404–15411.
- [21] V.V. Atuchin, A.P. Yeliseyev, E.N. Galashov, M.S. Molokeev, Mater. Chem. Phys. 147 (2014) 1191–1194.
- [22] H. Ji, Z. Huang, Z. Xia, M.S. Molokeev, X. Jiang, Z. Lin, V.V. Atuchin, Dalton Trans. 44 (2015) 7679–7686.
- [23] P.A. Loiko, V.I. Dashkevich, S.N. Bagaev, V.A. Orlovich, A.S. Yasukevich, K.V. Yumashev, N.V. Kuleshov, E.B. Dunina, A.A. Kornienko, S.M. Vatnik, A.A. Pavlyuk, Laser Phys. 23 (2013) (105811-1-7).
- [24] Y.A. Borovlev, N.V. Ivannikova, V.N. Shlegel, Y.V. Vasiliev, V.A. Gusev, J. Cryst. Growth 229 (2001) 305–311.
- [25] V.V. Atuchin, E.N. Galashov, A.S. Kozhukhov, L.D. Pokrovsky, V.N. Shlegel, J. Cryst. Growth 318 (2011) 1147–1150.
- [26] T.A. Gavrilova, N.V. Ivannikova, V.N. Shlegel, V.D. Grigorieva, S.F. Solodovnikov, T.B. Bekker, V.V. Atuchin, Solid State Phenom. 213 (2014) 160–164.
- [27] V.V. Atuchin, E.N. Galashov, O.Y. Khyzhun, V.L. Bekenev, L.D. Pokrovsky, Y.A. Borovlev, V.N. Zhdankov, J. Solid State Chem. 236 (2016) 24–31.
- [28] R.F. Klevtsova, S.A. Magarill, Sov. Phys. Crystallogr. 15 (1971) 611.
- [29] Z. Fu, W. Li, Powder Diffr. 9 (1994) 158–160.
- [30] R.F. Klevtsova, S.A. Magarill, Krist. SSSR 15 (1970) 710–715.
- [31] M. Wiesmann, I. Svoboda, H. Weitzel, H. Fuess, Z. fur Krist. 210 (1995) (525-525).
- [32] D. Mikhailova, A. Sarapulova, A. Voss, A. Thomas, S. Oswald, W. Gruner, D.M. Trots, N.N. Brannik, H. Ehrenberg, Chem. Mater. 22 (2010) 3165–3173.
- [33] D.E. Bugaris, H.C. Loye, Acta Cryst. C. 68 (2012) i34–i36.
- [34] R.D. Shannon, Acta Cryst. A32 (1976) 751–767.
- [35] J.S. Evans, T.A. Mary, Int. J. Inorg. Mater. 2 (2000) 143–151.
- [36] J. Kobayashi, Y. Sato, T. Nakamura, Phys. Stat. Sol. (a) 14 (1972) 259–264.

P. Loiko et al.

Journal of Luminescence 188 (2017) 154–161

- [37] Y.Z. Cheng, M.M. Wu, J. Peng, X.L. Xiao, Z.X. Li, Z.B. Hub, R. Kiyonagi, J.S. Fieramosca, S. Short, J. Jorgensen, *Sol. State Sci.* 9 (2007) 693–698.
- [38] W. Mei-Mei, P. Jie, Z. Yong, L. Rong-Deng, H. Zhong-Bo, L. Yun-Tao, C. Dong-Feng, *Chin. Phys. B* 21 (2012) 116102.
- [39] M. Song, W. Zhao, G. Wang, M. Zhao, L. Wang, *J. Alloy Compd.* 509 (2011) 2164–2169.
- [40] P.A. Loiko, K.V. Yumashev, N.V. Kuleshov, G.E. Rachkovskaya, A.A. Pavlyuk, *Opt. Mater.* 34 (2011) 23–26.
- [41] A.A. Kaminskii, S.N. Bagaev, *Quantum Electron.* 24 (1994) 1029–1030.
- [42] V.V. Atuchin, O.D. Chimitova, T.A. Gavrilova, M.S. Molokeyev, S.J. Kim, N.V. Surovtsev, B.G. Bazarov, *J. Cryst. Growth* 318 (2011) 683–686.
- [43] V.V. Atuchin, T.A. Gavrilova, T.I. Grigorjeva, N.V. Kuratieva, K.A. Okotrub, N.V. Pervukhina, N.V. Surovtsev, *J. Cryst. Growth* 318 (2011) 987–990.
- [44] V.V. Atuchin, N.V. Ivannikova, A.I. Komonov, N.V. Kuratieva, I.D. Loshkarev, N.V. Pervukhina, L.D. Pokrovsky, V.N. Shlegel, *CrystEngComm* 17 (2015) 4512–4516.
- [45] H. Bih, L. Bih, B. Manoun, M. Azrou, S. Benmokhtar, P. Lazor, *J. Molec. Struct.* 965 (2010) 7–13.
- [46] N.K. James, R. Ratheesh, *J. Am. Ceram. Soc.* 93 (2010) 931–933.
- [47] J.P. Smit, H.S. Kim, J.D. Pless, P.C. Stair, K.R. Poeppelmeier, *Inorg. Chem.* 45 (2006) 521–528.
- [48] P.A. Loiko, A. Major, *Opt. Mater. Express* 6 (2016) 2177–2183.
- [49] L. Li, Y. Yu, G. Wang, L. Zhang, *RSC Adv.* 4 (2014) 37041–37046.
- [50] N.V. Bashmakova, et al., *Funct. Mater.* 16 (2009) 266–274.
- [51] A.F. Kirby, F.S. Richardson, *J. Phys. Chem.* 87 (1983) 2544–2556.
- [52] P.A. Loiko, V.I. Dashkevich, S.N. Bagaev, V.A. Orlovich, A.S. Yasukevich, K.V. Yumashev, N.V. Kuleshov, E.B. Dunina, A.A. Kornienko, S.M. Vatrik, A.A. Pavlyuk, *J. Lumin.* 153 (2014) 221–226.
- [53] P.A. Loiko, E.V. Vilejshikova, X. Mateos, J.M. Serres, E.B. Dunina, A.A. Kornienko, K.V. Yumashev, M. Aguiló, F. Díaz, *J. Lumin.* 183 (2017) 217–225.
- [54] A. Xie, X. Yuan, F. Wang, *Sci. China* 54 (2011) 70–75.
- [55] Y. Tian, B. Chen, R. Hua, J. Sun, L. Cheng, H. Zhong, X. Li, J. Zhang, Y. Zheng, T. Yu, L. Huang, H. Yu, *J. Appl. Phys.* 109 (2011) 053511.
- [56] Y. Tian, X. Qi, X. Wu, R. Hua, B. Chen, *J. Phys. Chem. C* 113 (2009) 10767–10772.
- [57] Y. Chang, C. Liang, S. Yan, Y. Chang, *J. Phys. Chem. C* 114 (2010) 3645–3652.
- [58] B.R. Judd, *Phys. Rev.* 172 (1962) 750–761.
- [59] G.S. Ofelt, *J. Chem. Phys.* 37 (1962) 511–519.
- [60] C.M. Dodson, R. Zia, *Phys. Rev. B* 86 (2012) (125102-1-10).
- [61] B.F. Aull, H.P. Janssen, *IEEE J. Quantum Electron.* 18 (1982) 925–930.
- [62] V.I. Dashkevich, S.N. Bagaev, V.A. Orlovich, A.A. Bui, P.A. Loiko, K.V. Yumashev, A.S. Yasukevich, N.V. Kuleshov, S.M. Vatrik, A.A. Pavlyuk, *Laser Phys. Lett.* 12 (2015) (085001-1-5).
- [63] P.A. Loiko, V.I. Dashkevich, S.N. Bagaev, V.A. Orlovich, X. Mateos, J.M. Serres, E.V. Vilejshikova, A.S. Yasukevich, K.V. Yumashev, N.V. Kuleshov, E.B. Dunina, A.A. Kornienko, S.M. Vatrik, A.A. Pavlyuk, *J. Lumin.* 168 (2015) 102–108.

Orthorhombic $\text{Yb:Li}_2\text{Zn}_2(\text{MoO}_4)_3$ —a novel potential crystal for broadly tunable lasers

This content has been downloaded from IOPscience. Please scroll down to see the full text.

View [the table of contents for this issue](#), or go to the [journal homepage](#) for more

Download details:

IP Address: 207.162.240.147

This content was downloaded on 20/07/2017 at 14:32

Please note that [terms and conditions apply](#).

You may also be interested in:

[Crystal growth, polarized spectra, and laser performance of Yb:CaGdAlO₄ crystal](#)

J Q Di, X D Xu, C T Xia et al.

[Growth, crystal structure, spectral properties and laser performance of Yb³⁺:NaLu\(MoO₄\)₂ crystal](#)

Yi Yu, Lizhen Zhang, Yisheng Huang et al.

[Spectroscopic characterization and pulsed laser operation of Eu³⁺:KGd\(WO₄\)₂ crystal](#)

P A Loiko, V I Dashkevich, S N Bagaev et al.

[Polarized spectral properties of Yb³⁺:Li₂Gd₄\(MoO₄\)₇ crystal](#)

Haomiao Zhu, Yujin Chen, Yanfu Lin et al.

[Growth and spectroscopic characteristics of Yb:GSO single crystal](#)

Chengfeng Yan, Guangjun Zhao, Liangbi Su et al.

[Tm,Ho:KY\(WO₄\)₂ planar waveguide laser](#)

C V Ruiz Madroñero, X Mateos, P Loiko et al.

[Optical properties of chromium \(III\) in MIIIn\(WO₄\)₂ hosts, where MI = Li, Na, K,Rb](#)

K Hermanowicz

[Efficient end-pumped multi-wavelength laser operation of disordered Nd:LiGd\(WO₄\)₂ crystal](#)

Shan Xu, Xinyang Huang, Bingxuan Li et al.

[Red Eu,Yb:KY\(WO₄\)₂ laser at ~702nm](#)

V I Dashkevich, S N Bagayev, V A Orlovich et al.

Letter

Orthorombic Yb:Li₂Zn₂(MoO₄)₃—a novel potential crystal for broadly tunable lasers

Sergei Kurilchik^{1,2}, Pavel Loiko^{3,6}, Anatol Yasukevich¹,
Vyacheslav Trifonov⁴, Anna Volokitina³, Elena Vilejshikova¹, Viktor Kisel¹,
Xavier Mateos⁵, Alexander Baranov³, Oleg Goriev², Nikolay Kuleshov¹ and
Anatoly Pavlyuk⁴

¹ Center for Optical Materials and Technologies (COMT), Belarusian National Technical University, 65/17 Nezavisimosti Ave., 220013 Minsk, Belarus

² Kazan Federal University, 18 Kremlevskaya St., 420008 Kazan, Russia

³ ITMO University, 49 Kronverkskiy pr., 197101 St. Petersburg, Russia

⁴ A.V. Nikolaev Institute of Inorganic Chemistry, Siberian Branch of Russian Academy of Sciences,

⁵ Lavrentyev Ave., 630090 Novosibirsk, Russia

⁶ Física i Cristal·lografia de Materials i Nanomaterials (FiCMA-FiCNA), Universitat Rovira i Virgili (URV), Campus Sescelades, c/ Marcel·lí Domingo, s/n., E-43007 Tarragona, Spain

E-mail: kinetic@tut.by

Received 2 May 2017, revised 6 May 2017

Accepted for publication 16 May 2017

Published 20 July 2017



CrossMark

Abstract

Crystal with composition Li₂Zn₂(MoO₄)₃ doped with 0.7 at.% Yb (Yb:LiZnMo), with high optical quality and a length of a few cm is grown from the flux using Li₂MoO₄ as a solvent. Yb:LiZnMo is orthorombic (sp. gr. *Pnma*, *a* = 5.0843 Å, *b* = 10.4927 Å, *c* = 17.6742 Å, *Z* = 4). Polarized Raman spectra are studied for this crystal; the most intense band is observed at 898 cm⁻¹. The absorption, stimulated-emission and gain cross-sections of Yb³⁺ ions are determined for the principal light polarizations, *E* ∥ *a*, *b*, *c*. The maximum $\sigma_{SE} = 6.6 \times 10^{-21}$ cm² at 1011 nm for *E* ∥ *b*. The gain bandwidth for Yb:LiZnMo is up to ~50 nm. The radiative lifetime of the Yb³⁺ ions is 1.55 ms. The Yb:LiZnMo crystals are very promising for broadly tunable lasers.

Keywords: molybdate crystals, ytterbium, laser materials, stimulated-emission, Raman spectra

(Some figures may appear in colour only in the online journal)

1. Introduction

Ytterbium (Yb³⁺) ions are attractive for the development of efficient lasers emitting at ~1 μm due to the ²F_{5/2} → ²F_{7/2} transition. They possess a simple energy-level scheme exempt of excited-state absorption (ESA) and upconversion (UC), thus leading to weak heat loading, they can be pumped at 0.94–0.98 μm by commercial and powerful InGaAs laser diodes resulting in high laser efficiency and offer a certain tuning of the laser emission wavelength. When embedded in low-symmetry [1] or disordered [2] crystals, Yb³⁺ ions can

provide additional benefits arising from the broadening of their absorption and emission spectral bands. This effect is relevant, e.g. for broadly tunable [3, 4] or mode-locked (ML) lasers [5–8] capable of generating sub-100 fs pulses.

Complex tungstate and molybdate crystals are well-known hosts for Yb³⁺ doping. The most prominent examples are monoclinic double tungstates (DTs), KRE(WO₄)₂ [1], and tetragonal scheelite-like DTs [2, 9] and double molybdates [10] (DMos), ARE(XO₄)₂ (*A* = Na or Li, *X* = W or Mo), where RE³⁺ is a rare-earth element. Monoclinic DTs offer a higher Yb³⁺ doping levels' possibility [11], better thermal properties [12] and stronger anisotropy of the transition cross-sections [13, 14] which determine their use in power-scalable

⁶ Author to whom any correspondence should be addressed.

continuous-wave (CW) [15, 16], passively Q-switched (PQS) [17] and especially ML lasers [5–8, 18]. Tetragonal Yb^{3+} -doped DTs and DMos feature broader spectral bands due to their locally disordered structure [2, 10].

Besides tetragonal DMos, there are many complex molybdates of different crystal class. For example, orthorhombic lithium metal triple molybdates exist with chemical formula $\text{Li}_2\text{M}_2(\text{MoO}_4)_3$ (shortly LiMMo), where $\text{M}^{2+} = \text{Mg}, \text{Zn}, \text{Mn}, \text{Ni},$ or Co [19]. To date, studies of LiMMo single-crystals focused mostly on their possible applications as scintillators [20] and hosts for transition-metal ions, e.g. Co^{2+} [21, 22]. It was shown that it is possible to grow large-volume LiMMo crystals of good optical quality. The lyonsite-type structure [19] of these materials was refined [21, 23] and the elastic properties are also known [24]. Recently, the authors of [25] prepared powders of powdered $\text{Eu}:\text{LiZnMo}$ via the solid-state reaction method showing an intense red luminescence from Eu^{3+} . Later on, a LiMgMo single-crystal doped with Eu^{3+} was grown [26]. Using Eu^{3+} as a structural probe, it was argued that the rare-earth ions accommodate in a single type of site.

In the present work, we aimed to grow and study the spectroscopic properties of Yb^{3+} -doped LiZnMo single-crystal as a promising laser material, for the first time, to the best of our knowledge.

2. Crystal growth and structure

2.1. Crystal growth

The $\text{Li}_2\text{Zn}_2(\text{MoO}_4)_3$ compound melts incongruently at 885 °C and during the melting, it is partially decomposed: $\text{Li}_2\text{Zn}_2(\text{MoO}_4)_3 \rightarrow \text{Li}_2\text{MoO}_4 + 2\text{ZnMoO}_4$. Thus, it cannot be grown by the conventional Czochralski method. In the present work, Yb^{3+} -doped LiZnMo crystals were grown from the flux using [010]-oriented ($\pm 1^\circ$) undoped LiZnMo seeds with dimensions $5 \times 5 \times 25 \text{ mm}^3$. Lithium molybdate Li_2MoO_4 was used as a solvent. The solubility C of LiZnMo in Li_2MoO_4 decreases from ~95 to 50 mol% with a decrease of temperature T from ~875 to 845 °C according to the equation $C = -0.0086T^2 + 1.9929T + 765.39$ (C is in mol% and T is in °C) [27]. First, the Li_2MoO_4 solvent was prepared and then the Li_2CO_3 , ZnO , MoO_3 and Yb_2O_3 reagents (3–4 N purity) were added with an excess of Li_2CO_3 and MoO_3 (5–15 mol%) over the stoichiometry. The concentration of Yb^{3+} in the growth charge was 2 or 10 at.% (with respect to the Zn^{2+} content).

For the crystal growth, a Pt crucible (diameter: 70 mm, height: 120 mm) was used. It was covered by a Pt lid with a small hole. The solution ($\text{Li}_2\text{Zn}_2(\text{MoO}_4)_3$ –5–15 mol% Li_2MoO_4) was heated at ~20–30 °C above the equilibrium temperature and homogenized with a Pt stirrer for 1–2 h. Then, it was cooled down to 880 °C and the seed (rotating at 12 rev min^{-1}) was put in contact to the solution surface. The growth was performed under low thermal gradients ($< 1 \text{ }^\circ\text{C cm}^{-1}$). During the growth, the temperature was controlled and decreased for 10–15 °C with a precision of 0.1 °C, the pulling rate was 1.5–5 mm d^{-1} and the rotation speed was 10–20 rev min^{-1} . The crystallization rate was ~0.3–10 g



Figure 1. Photograph of the as-grown boule of the LiZnMo crystal doped with (nominally) 2 at.% Yb ; the growth direction is along the [010] axis.

d^{-1} . The crystal weight was 150–200 g. When the growth was completed, the crystal was carefully removed from the flux and slowly cooled to room temperature (RT) at a cooling rate of 30 °C h^{-1} . No annealing of the grown crystals was applied. A photograph of the as-grown 2 at.% (nominal) $\text{Yb}:\text{LiZnMo}$ is shown in figure 1. It was transparent, crack-and inclusion-free and had a slight brown coloration. For 10 at.% (nominal) Yb^{3+} doping, the as-grown crystal contained numerous inclusions oriented along the [100] axis.

2.2. Crystal structure

The crystal structure and phase purity of the grown $\text{Yb}:\text{LiZnMo}$ crystals were confirmed with x-ray powder diffraction (XRD). The XRD measurements were performed using a Shimadzu XRD-6000 diffractometer, $\text{Cu K}\alpha$ radiation with a Ni filter. The obtained XRD pattern for the 2 at.% (nominal) $\text{Yb}:\text{LiZnMo}$ crystal is shown in figure 2 and compared with that of the parent compound— $\text{Li}_3\text{Fe}(\text{MoO}_4)_3$ (ICCD card 01-072-0754) [28]. The grown $\text{Yb}:\text{LiZnMo}$ crystals are orthorhombic (point group: mmm , space group: $D_{2h}^{16}-Pnma$ (No. 62)). The determined lattice constants are $a = 5.0843 \text{ \AA}$, $b = 10.4927 \text{ \AA}$, $c = 17.6742 \text{ \AA}$, $Z = 4$, the unit-cell volume $V = 942.89 \text{ \AA}^3$, and the calculated density $\rho = 4.22 \text{ g cm}^{-3}$ (for 2 at.% (nominal) Yb^{3+} doping). They are relatively close to those for undoped LiZnMo with a stoichiometric composition, $a = 5.1139 \text{ \AA}$, $b = 10.4926 \text{ \AA}$, $c = 17.645 \text{ \AA}$ [29].

The habit of the as-grown boule of $\text{Yb}:\text{LiZnMo}$ is schematically represented in figure 3. The bottom part of the boule is formed by the (010) pinacoid surrounded by (011) and (013) prismatic faces. The density of dislocations on the (010) plane measured after etching with 10% HCl is $\sim 4 \times 10^2 \text{ cm}^{-2}$. The boule cross-section extends along the [100] axis. The central part of the boule is formed by the (001) pinacoids and (110) prisms.

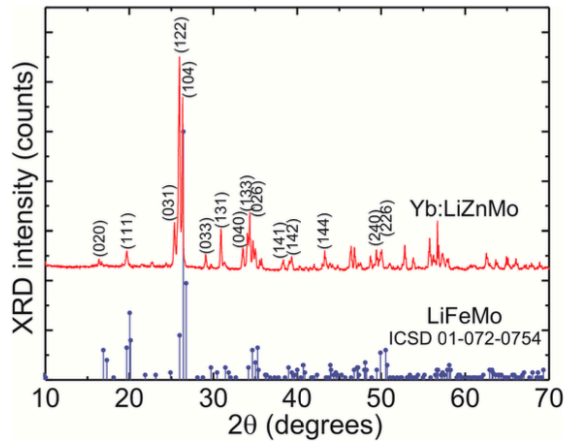


Figure 2. X-ray diffraction (XRD) pattern of a finely powdered 0.7 at.% Yb:LiZnMo crystal, the numbers indicate the Miller indices (*hkl*).

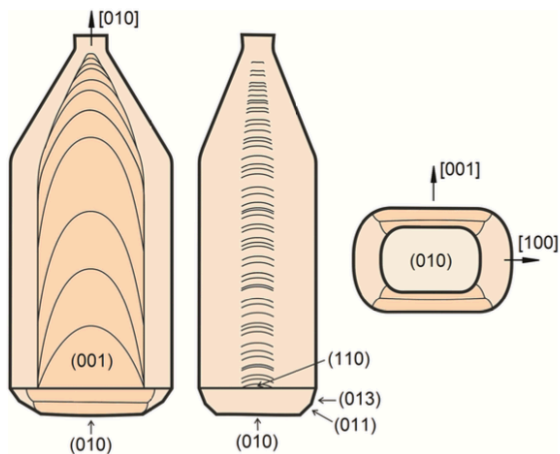


Figure 3. Habit of the as-grown 0.7 at.% Yb:LiZnMo crystal, the numbers indicate the crystallographic planes (*hkl*) and axes (*hkl*).

The fragment of the LiZnMo structure in projection on the *b*-*c* plane is shown in figure 4. The LiZnMo crystal belongs to the vanadate mineral lyonsite $\text{Cu}_3\text{Fe}_4(\text{VO}_4)_6$ structural type. The Mo^{6+} cations occupy tetrahedral sites. The lower oxidation-state cations Li^+ , Zn^{2+} occupy three different low-symmetry sites forming chains of octahedral polyhedrons (A(1) site), face-sharing highly distorted octahedrons (A(2) site) and edge-sharing trigonal prisms (A(3) site). According to our previous study of an isostructural LiMgMo crystal doped with Eu^{3+} ions serving as a structural probe, the rare-earth dopants will replace the Zn^{2+} ions in a single type of site, A(3) [26]. This process will be accompanied by a cationic redistribution over the A sites to maintain the charge compensation. The A–O distances for the A(3) site are 1.95–2.25 Å and in the chains formed by trigonal prisms, the interionic distance A–A is ~ 2.78 Å, as calculated from the Rietveld refinement data. In the LiZnMo structure, the isolated

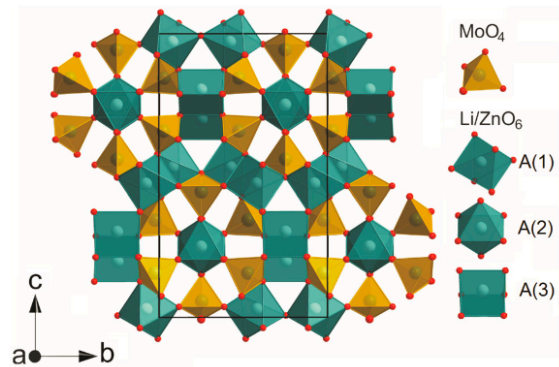


Figure 4. A fragment of the Yb:LiZnMo crystal structure in projection on the *b* and *c* plane. The Yb^{3+} ions replace the Zn^{2+} ones in the A(3) sites. The black rectangle indicates the unit-cell.

$[\text{MoO}_4]^{2-}$ tetrahedrons are linked by AO_6 chains creating a tunnel-like hexagonal structure, figure 4. The surrounding of the hexagonal ‘tunnel’ consists of chains formed by the A(1) octahedrons and edge-sharing A(3) trigonal prisms, and the face-sharing A(2) octahedral polyhedrons pass through the center of this ‘tunnel’.

The concentration of Yb^{3+} ions in the grown crystals was determined by energy-dispersive x-ray (EDX) spectroscopy using an electron scanning environmental microscope (ESEM) equipped with an Inca microanalyzer (Oxford Instruments) to be 0.7 ± 0.2 at.% and 3.6 ± 0.2 at.% for the nominal doping levels of 2 and 10 at.% Yb ($N_{\text{Yb}} = 0.60$ and $3.1 \times 10^{-20} \text{ cm}^{-2}$, respectively). Thus, the segregation coefficient for the Yb^{3+} ions in LiZnMo, $K_{\text{RE}} = N_{\text{crystal}}/N_{\text{solution}} \sim 0.35 \pm 0.02$. This low value is attributed to the difference of the ionic radii for Zn^{2+} (0.74 Å for VI-fold O^{2-} -coordination), Li^+ (0.76 Å) and Yb^{3+} (0.868 Å).

3. Raman spectroscopy

The Raman spectra were measured in polarized light using a Renishaw inVia confocal Raman microscope with a $\times 50$ Leica objective. The excitation wavelength λ_{exc} was 514 nm (Ar^+ laser) and an edge filter was used. A polished 0.7 at.% Yb:LiZnMo sample cut along the growth direction (*b*-axis) was used. The spectra corresponded to the configurations *b*(*aa*)*b*, *b*(*ac*)*b* and *b*(*cc*)*b*, see figure 5.

The Raman spectra of Yb:LiZnMo are strongly polarized. The observed Raman bands can be classified into three groups of vibrations [26]: (i) translational and rotational modes of the MoO_4 tetrahedrons and Li/Zn–O external modes at $< 300 \text{ cm}^{-1}$; (ii) symmetric and asymmetric O–Mo–O bending vibrations at $300\text{--}450 \text{ cm}^{-1}$; (iii) Mo–O stretching modes at $750\text{--}850 \text{ cm}^{-1}$ (asymmetric) and at $850\text{--}1000 \text{ cm}^{-1}$ (symmetric). The most intense band consists of two closely located peaks centered at 898 and 912 cm^{-1} attributed to the ν_1 mode of the $[\text{MoO}_4]^{2-}$ tetrahedrons (non-degenerated symmetric stretching); the full width at half maximum (FWHM) of these peaks is 26 and 17 cm^{-1} , respectively.

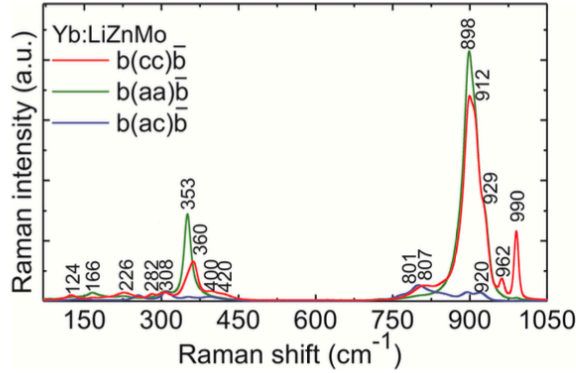


Figure 5. Polarized Raman spectra of the 0.7 at.% Yb:LiZnMo crystal for $b(xy)b$ geometry, $x, y = a$ or c . The numbers indicate the most intense Raman bands.

4. Optical spectroscopy

The orthorhombic LiZnMo crystal is optically biaxial. Consequently, the optical indicatrix axes coincide with the a, b, c crystallographic ones [30] while their exact assignment is still unknown. In [20], the refractive index of undoped LiZnMo was measured to be ~ 1.97 at 579 nm and the birefringence was determined to be ~ 0.02 .

The absorption spectra of the 0.7 at.% Yb:LiZnMo crystal were measured with polarized light ($E \parallel a, b, c$) using a Varian CARY 5000 spectrophotometer. The absorption cross-sections, σ_{abs} , were calculated as $\alpha_{\text{abs}}/N_{\text{Yb}}$, where α_{abs} is the absorption coefficient and $N_{\text{Yb}} = 0.60 \times 10^{20} \text{ cm}^{-3}$ (0.7 at.%). The results are shown in figure 6(a). The Yb:LiZnMo crystal exhibits a strong anisotropy of the spectroscopic properties. The maximum $\sigma_{\text{abs}} = 11.1 \times 10^{-19} \text{ cm}^2$ at 972.6 nm for light polarization $E \parallel a$. The corresponding FWHM of the absorption peak is 7.3 nm. For $E \parallel b$ and $E \parallel c$, the peak σ_{abs} are lower, 5.5 and $5.1 \times 10^{-19} \text{ cm}^2$, respectively. These values are lower than those for Yb³⁺-doped tetragonal DMOs, NaLa(MoO₄)₂ (NaLaMo) and LiLa(MoO₄)₂ (LiLaMo), namely 2.1 and $1.9 \times 10^{-20} \text{ cm}^2$ at 976 nm for $E \parallel c$, respectively [10, 31]. A broad absorption band for Yb:LiZnMo relaxes the effect of the temperature drift of a laser diode wavelength in the pumping process for the realization of a diode-pumped solid-state laser (DPSSL). Physically, it is attributed to the distortion of the crystal field due to the large difference of ionic radii for Zn²⁺ and Yb³⁺.

The luminescence spectra were measured with polarized light using a lock-in amplifier (Stanford Research Systems, model SR810), a monochromator MDR-23 and an InGaAs PIN photodiode (Hamamatsu, model G5851). The excitation was from an InGaAs laser diode emitting at 940 nm. The stimulated-emission (SE) cross-sections were calculated from the measured luminescence spectra using the Füchtbauer–Ladenburg (F–L) equation [32] adopted for biaxial crystals [33]:

$$\sigma_{\text{SE}}^{(i)}(\lambda) = \frac{\lambda^5}{8\pi n^2 \tau_{\text{rad}} c} \frac{3W_i(\lambda)}{\sum_{i=a,b,c} \int \lambda W_i(\lambda) d\lambda}. \quad (1)$$

Here, $i = a, b, c$ indicates the light polarization, $\sigma_{\text{SE}}^{(i)}$ are the SE cross-sections for the i th polarization, λ is the light wavelength,

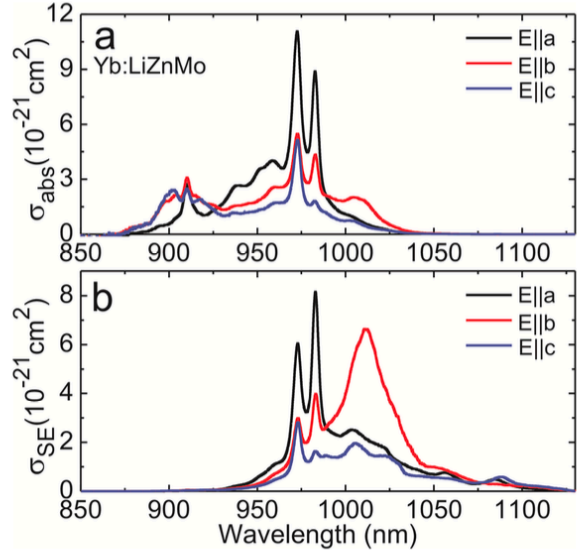


Figure 6. (a) Absorption, σ_{abs} , and (b) SE, σ_{SE} , cross-section spectra for the 0.7 at.% Yb:LiZnMo crystal and light polarizations $E \parallel a, b, c$.

$n = 1.93$ is the mean refractive index of the crystal at $\sim 1 \mu\text{m}$ (as estimated from the dispersion [20]), c is the speed of light, $\tau_{\text{rad}} = 1.55 \text{ ms}$ is the radiative lifetime of the emitting state (the ${}^2F_{5/2}$ state of Yb³⁺, see below), $W_i(\lambda)$ is the luminescence spectrum for the i th polarization. The results are shown in figure 6(b).

The maximum $\sigma_{\text{SE}} = 8.2 \times 10^{-19} \text{ cm}^2$ at 982.9 nm for light polarization $E \parallel a$. However, as Yb³⁺ represents a quasi-three-level laser scheme, the laser operation is expected at longer wavelengths than the zero-phonon-line (ZPL, $E_{\text{ZPL}} = 10176 \text{ cm}^{-1}$ (982.7 nm) for Yb:LiZnMo). In this case, the largest $\sigma_{\text{SE}} = 6.6 \times 10^{-21} \text{ cm}^2$ is observed at 1011 nm for $E \parallel b$. This is lower than for tetragonal DMOs, Yb:NaLaMo and Yb:LiLaMo, $2.6 \times 10^{-20} \text{ cm}^2$ at $\sim 1000 \text{ nm}$ and $1.5 \times 10^{-20} \text{ cm}^2$ at $\sim 1011 \text{ nm}$ for $E \parallel c$, respectively [10, 31].

Considering the quasi-three-level nature of the Yb³⁺ laser, the gain cross-sections, $\sigma_{\text{g}} = \beta\sigma_{\text{SE}} - (1 - \beta)\sigma_{\text{abs}}$, where $\beta = N_2({}^2F_{5/2})/N_{\text{Yb}}$ is the inversion ratio, were calculated for the Yb:LiZnMo crystal for the high-gain light polarizations $E \parallel a$ and b , figure 7. The gain bandwidth (FWHM) is $\sim 51 \text{ nm}$ and 30 nm for the two polarizations, respectively (for $\beta = 0.3$). Such a broad gain spectra for the Yb:LiZnMo crystal make it very promising for broadly tunable lasers with a potential tuning range of $>90 \text{ nm}$ and for mode-locked lasers generating sub-100 fs pulses. The determined gain bandwidths for Yb:LiZnMo are broader than for tetragonal DMO, Yb:NaLaMo ($\sim 41 \text{ nm}$) [10].

To measure the luminescence decay, we used a ns optical parametric oscillator Lotis TII LT-2214 tuned to 972 nm as an excitation source and a monochromator MDR-12, the same photodiode (response time, $<100 \text{ ns}$) and a 500 MHz Tektronix TDS-3052B digital oscilloscope as a detection system. To avoid the radiation trapping effects, the crystal sample was finely powdered and immersed in glycerin with a powder/solvent ratio varying from 10 to 70 wt.%.

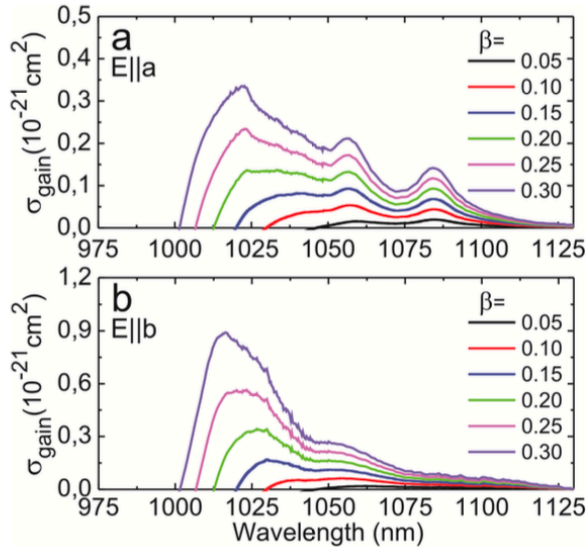


Figure 7. Gain cross-section, $\sigma_g = \beta\sigma_{SE} - (1 - \beta)\sigma_{abs}$, spectra for the 0.7 at.% Yb:LiZnMo crystal and light polarizations $E \parallel a$ (a) and $E \parallel b$ (b), $\beta = N_2(^2F_{5/2})/N_{Yb}$ is the inversion ratio.

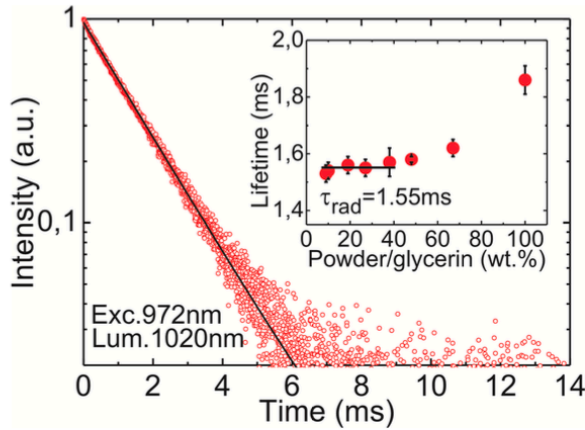


Figure 8. Luminescence decay curve for the 0.7 at.% Yb:LiZnMo crystal (circles—experimental data; black line—single-exponential fit); inset: dependence of the measured decay time on the powder/solution ratio for 3.6 at.% Yb:LiZnMo.

The 0.7 at.% Yb-doped crystal did not show any notable dependence of the measured decay curve on the powder/solvent ratio, the typical decay curve plotted in a semi-log scale is shown in figure 8. It is clearly linear supporting the previous conclusion about a single type of site for Yb^{3+} ions and the characteristic decay time τ_{exp} is 1.55 ms. For the 3.6 at.% Yb-doped crystal, $\tau_{exp} = 1.86$ ms for the bulk crystal and it decreased to ~ 1.55 ms for powder/solvent ratios < 30 wt.%.

For Yb^{3+} ions, one can estimate the radiative lifetime with the modified reciprocity method adopted for biaxial crystals [34]:

$$\tau_{rad} = 8\pi n^2 c \frac{Z_2}{Z_1} \frac{3e^{-hc/kT\lambda}}{\sum_{i=a,b,c} \int \sigma_{abs}^{(i)}(\lambda) \lambda^{-4} e^{-hc/kT\lambda} d\lambda}. \quad (2)$$

Here, h is the Planck constant, k is the Boltzmann constant, T is the crystal temperature (RT), and $Z_{1(2)}$ are the partition

functions for the lower and upper states, respectively. The ratio Z_1/Z_2 can be determined from the Stark splitting of both multiplets. According to our low-temperature (6 K) studies employing an Oxford Instruments Ltd cryostat (SU 12 model) with helium-gas close-cycle flow, $Z_1/Z_2 = 0.909$ for Yb:LiZnMo. This value is very close to that of another complex molybdate, trigonal Yb:K₅Bi(MoO₄)₄ (Yb:KBiMo), $Z_1/Z_2 = 0.889$ [35]. From equation (2), $\tau_{rad} = 1.55 \pm 0.05$ ms and the luminescence quantum yield $\eta_q = \tau_{exp}/\tau_{rad} > 99\%$. Such a high value is in good agreement with the large phonon energies of the host matrix, figure 5, minimizing the non-radiative relaxation. The determined τ_{rad} for Yb:LiZnMo is much longer than that for the tetragonal DMos, LiGd(MoO₄)₂ (Yb:LiGdMo) (250 μ s), Yb:NaLaMo (290 μ s), and Yb:LiLaMo (390 μ s) [10, 31, 36], and slightly shorter than for trigonal Yb:KBiMo (1.93 ms) [35].

5. Conclusion

To conclude, we report on the growth, structure, Raman and optical spectroscopic characterization of a novel complex molybdate crystal—orthorhombic Yb:Li₂Zn₂(MoO₄)₃. This crystal exhibits strong anisotropy of the transition cross-sections of Yb^{3+} ions in polarized light favoring linearly polarized laser output, broad emission bands (the gain bandwidth is up to ~ 50 nm) which is of interest for broadly tunable lasers at ~ 1 μ m and good energy storage capability (the lifetime of the upper laser level is ~ 1.55 ms). The latter is of interest for Q-switched lasers. Further work will focus on the laser operation with Yb:LiZnMo. For this, *c*-cut crystals are of interest as they will give access to the high-gain polarizations $E \parallel a$ and $E \parallel b$. The low solubility of Yb^{3+} ions in LiZnMo limits the available doping level (0.7 at.% Yb^{3+} for crystals of high optical quality), so further optimization of the growth conditions is necessary to achieve > 3 at.% Yb^{3+} -doped crystals. We believe that it can be reached by a proper control of the solute/solvent concentration and the temperature gradients in the crucible.

Acknowledgments

This work was funded by the subsidy allocated to Kazan Federal University for the state assignment in the sphere of scientific activities and Russian Government Program of Competitive Growth of Kazan Federal University. PL acknowledges financial support from the Government of the Russian Federation (Grant 074-U01) through ITMO Post-Doctoral Fellowship scheme. PL also thanks Dr Olga Dymshits (St. Petersburg) for the XRD measurement.

References

- [1] Petrov V, Pujol M C, Mateos X, Silvestre Ò, Rivier S, Aguiló M, Solé R, Liu J, Griebner U and Díaz F 2007 *Laser Photon. Rev.* **1** 179–212
- [2] Cascales C et al 2006 *Phys. Rev. B* **74** 174114
- [3] Rico M, Liu J, Griebner U, Petrov V, Serrano M D, Esteban-Betegón F, Cascales C and Zaldo C 2004 *Opt. Express* **12** 5362–7

- [4] Jacobsson B, Hellström J E, Pasiskevicius V and Laurell F 2007 *Opt. Express* **15** 1003–10
- [5] Griebner U, Rivier S, Petrov V, Zorn M, Erbert G, Weyers M, Mateos X, Aguiló M, Massons J and Diaz F 2005 *Opt. Express* **13** 3465–70
- [6] Liu H, Nees J and Mourou G 2001 *Opt. Lett.* **26** 1723–5
- [7] Castellano-Hernández E, Han X, Rico M, Roso L, Cascales C and Zaldo C 2015 *Opt. Express* **23** 11135–40
- [8] Zhao H and Major A 2013 *Opt. Express* **21** 31846–51
- [9] Loiko P A, Xan X, Yumashev K V, Kuleshov N V, Serrano M D, Casales C and Zaldo C 2013 *Appl. Phys. B* **111** 279–87
- [10] Voronko Yu K, Subbotin K A, Shukshin V E, Lis D A, Ushakov S N, Popov A V and Zharikov E V 2006 *Opt. Mater.* **29** 246–52
- [11] Pujol M C et al 2002 *Phys. Rev. B* **65** 165121
- [12] Silvestre O et al 2006 *Opt. Express* **16** 5022–34
- [13] Mateos X, Solé R, Gavaldà J, Aguiló M, Massons J, Díaz F, Petrov V and Griebner U 2006 *Opt. Mater.* **28** 519–23
- [14] Lagatsky A A, Kuleshov N V and Mikhailov V P 1999 *Opt. Commun.* **165** 71–5
- [15] Liu J, Petrov V, Zhang H and Wang J 2007 *Appl. Phys. B* **88** 527–30
- [16] Loiko P A, Kisel V E, Konsratuk N V, Yumashev K V, Kuleshov N V and Pavlyuk A A 2013 *Opt. Mater.* **35** 582–5
- [17] Loiko P, Serres J M, Mateos X, Yumashev K, Yasyukevich A, Petrov V, Griebner U, Aguiló M and Díaz F 2016 *Opt. Lett.* **41** 2620–3
- [18] Pekarek S, Fiebig C, Stumpf M C, Oehler A E H, Paschke K, Erbert G, Sudmeyer T and Keller U 2010 *Opt. Express* **18** 16320–6
- [19] Smit J P, Stair P C and Poepfelmeier K R 2006 *Chem. Eur. J.* **12** 5944–53
- [20] Bashmakova N V et al 2009 *Funct. Mater.* **16** 266–74
- [21] Xue L, Wang Y, Lv P, Chen D, Lin Z, Liang J, Huang F and Xie Z 2009 *Cryst. Growth Design* **9** 914–20
- [22] Trifonov V A, Pavlyuk A A, Gorbachenya K N, Yasyukevich A S and Kuleshov N V 2013 *Inorg. Mater.* **49** 517–9
- [23] Sebastian L, Piffard Y, Shukla A K, Taulelle F and Gopalakrishnan J 2003 *J. Mater. Chem.* **13** 1797–802
- [24] Mazur L I, Mazur M M, Pavlyuk A A and Solodovnikov S F 2010 *Inorg. Mater.* **46** 1353–8
- [25] He X, Guan M, Zhang C, Shang T, Lian N and Yao Y 2011 *J. Alloys Compd.* **509** L341–3
- [26] Loiko P, Vilejshikova E V, Volokitina A A, Trifonov V A, Serres J M, Mateos X, Kuleshov N V, Yumashev K V, Baranov A V and Pavlyuk A A 2017 *J. Lumin.* **188** 154–61
- [27] Trifonov V A and Pavlyuk A A 2012 *BSU Bull. Phys. Chem.* **3** 13–7 (in Russian)
- [28] Klevtsova R F and Magarill S A 1971 *Sov. Phys.-Crystallogr.* **15** 611
- [29] Solodovnikov S F, Solodovnikova Z A, Zolotova E S, Yudanova L I, Kardash T Yu, Pavlyuk A A and Nadolnny V A 2009 *J. Solid State Chem.* **182** 1935–43
- [30] Loiko P A and Major A 2016 *Opt. Mater. Express* **6** 2177–83
- [31] Huang X, Lin Z, Zhang L and Wang G 2007 *J. Cryst. Growth* **306** 208–11
- [32] Aull B F and Jenssen H P 1982 *IEEE J. Quantum Electron.* **18** 925–30
- [33] Mateos X, Serres J M, Loiko P, Griebner U, Petrov V, Yumashev K, Aguiló M and Díaz F 2017 *J. Lumin.* **183** 391–400
- [34] Yasyukevich A S, Shcherbitskii V G, Kisel' V É, Mandrik A V and Kuleshov N V 2004 *J. Appl. Spectr.* **71** 202–8
- [35] Canibano H, Boulon G, Palatella L, Guyot Y, Brenier A, Voda M, Balda R and Fernandez J 2003 *J. Lumin.* **102** 318–26
- [36] Rico M, Griebner U, Petrov V, Ortega P, Han X, Cascales C and Zaldo C 2006 *J. Opt. Soc. Am. B* **23** 1083–90

PAPER • OPEN ACCESS

Growth and spectroscopy of orthorhombic Yb:KY(MoO₄)₂ laser crystal with a layered structure

To cite this article: A Volokitina *et al* 2019 *J. Phys.: Conf. Ser.* **1410** 012149

View the [article online](#) for updates and enhancements.



IOP | ebooks™

Bringing you innovative digital publishing with leading voices to create your essential collection of books in STEM research.

Start exploring the collection - download the first chapter of every title for free.

Growth and spectroscopy of orthorhombic Yb:KY(MoO₄)₂ laser crystal with a layered structure

A Volokitina¹, P Loiko¹, J M Serres², X Mateos², N Kuleshov³, V Trifonov⁴,
and A Pavlyuk⁴

¹ITMO University, 49 Kronverkskiy Pr., 197101 St. Petersburg, Russia

²Física i Cristal·lografia de Materials i Nanomaterials (FiCMA-FiCNA)-EMaS, Dept. Química Física i Inòrganica, Universitat Rovira i Virgili (URV), Campus Sescelades, E-43007 Tarragona, Spain

³Center for Optical Materials and Technologies (COMT), Belarusian National Technical University, 65/17 Nezavisimosti Ave., 220013 Minsk, Belarus

⁴A.V. Nikolaev Institute of Inorganic Chemistry, Siberian Branch of Russian Academy of Sciences, 3 Lavrentyev Ave., Novosibirsk 630090, Russia

Abstract. We report on the growth, structure, vibronic and spectroscopic properties of novel Yb³⁺-doped orthorhombic potassium yttrium double molybdate crystal, Yb:KY(MoO₄)₂. The layered structure of this material determines a strong polarization-anisotropy of absorption and emission bands of Yb³⁺ ions. The maximum stimulated-emission cross-section is 3.7×10^{-20} cm² at ~ 1.01 μ m for light polarization $E \parallel b$ and the lifetime of the ²F_{5/2} state is 0.46 ms. Naturally cleaved Yb:KY(MoO₄)₂ plates are suitable for microchip lasers at ~ 1 μ m.

1. Introduction

Among the oxide host crystals, potassium (rare-earth) double tungstates (DTs) and double molybdates (DMos) with a general chemical formula of KLn(XO₄)₂ (where X = W or Mo, respectively, and Ln = Y, Gd, Lu, etc.) are attractive for doping with laser-active trivalent rare-earth ions (RE³⁺) [1,2] because they provide ordered structure, high available RE³⁺ doping concentrations, intense and strongly polarized absorption and emission bands, weak non-radiative relaxation and strong Raman response.

Ytterbium (Yb³⁺) ions are well-known for their emission at ~ 1 μ m according to the ²F_{5/2} \rightarrow ²F_{7/2} electronic transition. They exhibit a simple energy-level scheme eliminating the unwanted processes such as energy-transfer upconversion or excited-state absorption leading to low heat loading and high laser efficiencies. Yb³⁺-doped materials can be pumped by high-power InGaAs laser diodes emitting at ~ 0.98 μ m. To date, Yb³⁺-doped monoclinic DTs have been implemented for efficient continuous-wave (CW) [3], passively Q-switched [4] and especially mode-locked oscillators at ~ 1 μ m [5,6].

Contrary to DT crystals, their molybdate counterparts, KLn(MoO₄)₂, are less widespread [2,7]. However, these crystals do not exhibit a polymorphic phase transition below the melting point (like in DTs) and thus they can be grown by the conventional Czochralski (Cz) method [8,9]. KLn(MoO₄)₂ crystals belong to the orthorhombic class and they feature a layered structure leading to a perfect cleavage feature. This allows one to fabricate thin crystalline films [10] suitable for microchip or thin-disk lasers.

In the present work, we report on the growth, structure, vibronic and spectroscopic characterization of a novel crystal in the orthorhombic DMO family – Yb³⁺-doped potassium yttrium double molybdate, Yb:KY(MoO₄)₂.



2. Crystal growth and structure

KY(MoO₄)₂ crystals are chemically stable, they have a relatively low melting temperature (about 970 °C) and do not show any polychromic transformation below the melting point. In this work, a 3 at.% Yb:KY(MoO₄)₂ crystal was grown by the Cz method using a [100]-oriented undoped seed. 5–7 mol% of potassium trimolybdate (K₂Mo₃O₁₀) were added to the melt to prevent its partial dissociation. The seed rotation speed was 20 rpm, the pulling rate was 1-2 mm/h and the cooling rate was 2 °C/day. The temperature gradient in the melt was below 3 °C/mm. The growth rate was 5–10 g/day.

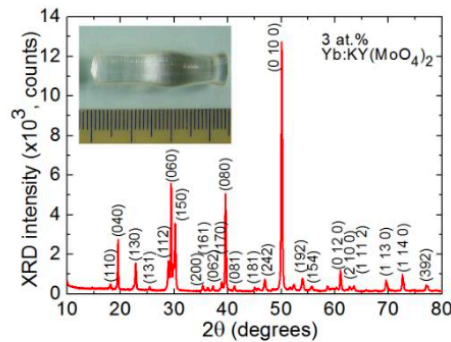


Figure 1. X-ray powder diffraction (XRD) pattern of 3 at.% Yb:KY(MoO₄)₂, numbers indicate the Miller's indices, (hkl) , inset – photograph of the as-grown crystal; the growth direction is [100].

The as-grown crystal of good optical quality was transparent and free of cracks and inclusions, see inset in Fig. 1. No post-growth annealing was applied. The crystal was colorless. The phase purity and the structure of the as-grown crystal were confirmed by X-ray powder diffraction (XRD), see Fig. 1. Yb:KY(MoO₄)₂ is orthorhombic (sp. gr. *Pbna* – D¹⁴_{2h}, No. 60). The Yb³⁺ ions in KY(MoO₄)₂ replaces the Y³⁺ ones in a single type of crystallographic sites (symmetry: C₂, VIII-fold O²⁻ coordination). Briefly, the structure of Yb:KY(MoO₄)₂ is as following [8]: continuous belts of edge-sharing distorted [Y|YbO₈] octahedrons are parallel to the *b*-axis. In the *a*-*b* plane, they share corners with the [MoO₄] tetrahedra. The [Y|Yb(MoO₄)₂]⁻ radicals form porous layers in the *b*-*c* plane. Because of this, the crystal exhibits a perfect cleavage along the (100) plane.

3. Raman spectra

All members of the DT and DMo crystal families are Raman-active [1]. This feature may be used for self-Raman conversion of the laser output. To characterize the vibronic properties of Yb:KY(MoO₄)₂, the room temperature (RT) Raman spectra were measured with polarized light using a Raman microscope (Renishaw inVia). The excitation wavelength was 488 nm (an Ar⁺ laser line). A cleaved crystal plate (i.e., an *a*-cut) was used and the studied excitation / collection geometries were *a(bb)a*, *a(bc)a*, *a(cb)a* and *a(cc)a* (according to Porto's notations).

The Raman spectra are shown in Fig. 2. They are strongly polarized with the most intense Raman response in the *a(bb)a* geometry. The observed bands are classified into three groups of vibrations [8]. The low-frequency range, 80-272 cm⁻¹, contains translational (*T'*) and rotational (*R'*) modes of the K, Y and Mo cations. Internal bending vibrations (*δ*) of the oxygen bridged [MoO₄]²⁻ tetrahedral are observed in the intermediate range, 300–435 cm⁻¹. The high-frequency range, 726-944 cm⁻¹, contains intense stretching vibrations (*ν*) of these tetrahedra.

The most intense Raman mode is at 865 cm⁻¹. The full width at half maximum (FWHM) of this mode is 18.8 cm⁻¹. The maximum phonon frequency, $h\nu_{\max} = 944 \text{ cm}^{-1}$.

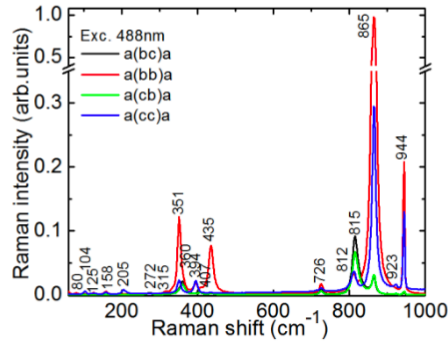


Figure 2. Polarized Raman spectra of an *a*-cut Yb:KY(MoO₄)₂, $\lambda_{\text{exc}} = 488$ nm, *numbers* indicate the frequencies of the Raman peaks in cm⁻¹.

4. Optical spectroscopy

Orthorhombic Yb:KY(MoO₄)₂ crystal is optically biaxial. The optical indicatrix axes coincide with the crystallographic ones while the assignment of the refractive indices is still unknown. We characterized the spectroscopic properties for the principal light polarizations indicated as $E \parallel a$, $E \parallel b$ and $E \parallel c$. All the studies were performed at RT (20 °C).

The absorption spectra were measured using a Varian CARY 5000 spectrophotometer and a Glan-Taylor polarizer. The absorption cross-sections, σ_{abs} , were then calculated using the Yb³⁺ ion density of 2.29×10^{20} cm⁻³, as shown in Fig. 3(a). The maximum $\sigma_{\text{abs}} = 1.77 \times 10^{-20}$ cm² at 977.1 nm for $E \parallel b$ and the corresponding FWHM of the absorption peak is 19 nm which is advantageous for diode-pumping. Note that the absorption cross-sections for the light polarizations $E \parallel b$ and $E \parallel c$ are much higher than that for $E \parallel a$ (orthogonal to the cleavage plane) which is due to the layered crystal structure. The UV absorption edge λ_{UV} is at 334 nm and in the IR, the transparency window is until 5.3 μ m.

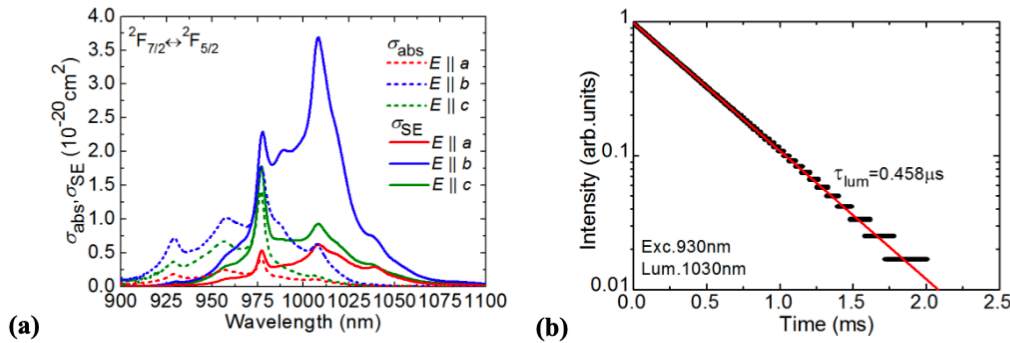


Figure 3(a, b). Spectroscopy of Yb³⁺ ions in orthorhombic KY(MoO₄)₂ crystal: **(a)** absorption, σ_{abs} , and stimulated-emission (SE) cross-sections, σ_{SE} , for the ${}^2F_{5/2} \leftrightarrow {}^2F_{7/2}$ transition, light polarizations are $E \parallel a$, $E \parallel b$ and $E \parallel c$; **(b)** the luminescence decay curve.

The luminescence spectra were measured using an optical spectrum analyser (OSA, Hamamatsu, model AQ6373) and a Glan-Taylor polarizer; a Ti:Sapphire laser tuned to 928 and 977 nm was used as an excitation source. The stimulated-emission (SE) cross-section were calculated by the Fichtbauer-Ladenburg (F-L) formula [11]:

$$\sigma_{SE}^i(\lambda) = \frac{\lambda^5}{8\pi \langle n \rangle^2 c \tau_{rad}} \frac{W_i(\lambda)}{1/3 \sum_{i=a,b,c} \int \lambda W_i(\lambda) d\lambda} \quad (1)$$

where, $i = a, b, c$ is the light polarization, λ is the light wavelength, $\langle n \rangle \approx 1.9$ is the mean refractive index of the crystal, c is the speed of light, τ_{rad} is the radiative lifetime of the emitting state (${}^2F_{5/2}$, see below), $W_i(\lambda)$ is the measured luminescence spectrum for i -th polarization. The SE cross-section spectra are shown in Fig. 3(a). The maximum σ_{SE} for the ${}^2F_{5/2} \rightarrow {}^2F_{7/2}$ transition of Yb^{3+} ions is $3.70 \times 10^{-20} \text{ cm}^2$ at 1008.0 nm for the light polarization $E \parallel b$. The FWHM of the emission band is >35 nm. The strong polarization anisotropy of the SE cross-sections is a prerequisite for linearly polarized laser emission from the $Yb:KY(MoO_4)_2$ crystal.

The luminescence decay curve for $Yb:KY(MoO_4)_2$ was measured under ns pulse excitation from an optical parametric oscillator using a fast InGaAs photodetector and an 8 GHz digital oscilloscope. A thin ($\sim 100 \mu\text{m}$) cleaved film was used to avoid the effect of reabsorption. The excitation wavelength λ_{exc} was 930 nm, the luminescence from the ${}^2F_{5/2}$ Yb^{3+} multiplet was monitored at 1030 nm. The decay curve plotted in a semi-log scale is shown in Fig. 3(b). It is clearly single-exponential in agreement with a single type of sites for Yb^{3+} ions. The luminescence decay time ($\tau_{lum} = 458 \mu\text{s}$) was determined according to a single-exponential law, $I_{lum}(t) = I_0 \exp(-t/\tau_{lum})$.

5. Conclusion

Orthorhombic $Yb:KY(MoO_4)_2$ crystals featuring simple growth by the standard Cz method, easy Yb^{3+} doping, strongly polarized absorption and stimulated-emission cross-section spectra due to the layered structure and a perfect cleavage feature are very promising for microchip lasers based on crystalline films with a thickness of few hundreds of μm and emitting at $\sim 1 \mu\text{m}$. Further work will focus on laser characterization of this material.

Acknowledgments

This work was partly supported by Russian Science Foundation (Agreement # 18-13-00200). P.L. acknowledges financial support from the Government of the Russian Federation (Grant 074-U01) through ITMO Post-Doctoral Fellowship scheme. P.L. would like to thank Dr. Olga Dymshits for the XRD measurement.

References

- [1] Petrov V, Pujol M C, Mateos X, Silvestre O, Rivier S, Aguiló M, Solé R M, Liu J, Griebner U, Díaz F 2007 *Laser & Photon. Rev.* **1** 179
- [2]. Kaminskii A A, Sarkisov S E, Li L 1973 *Phys. Stat. Sol. (a)* **15** K141
- [3] Liu J, Petrov V, Mateos X, Zhang H, Wang J 2007 *Opt. Lett.* **32** 2016
- [4] Loiko P, Serres J M, Mateos X, Yumashev K, Yasukevich A, Petrov V, Griebner U, Aguiló M, Díaz F 2016 *Opt. Lett.* **41** 2620
- [5] Griebner U, Rivier S, Petrov V, Zorn M, Erbert G, Weyers M, Mateos X, Aguiló M, Massons J, Díaz F 2005 *Opt. Express* **13** 3465
- [6] Pekarek S, Fiebig C, Stumpf M C, Oehler A E H, Paschke K, Erbert G, Südmeyer T, Keller U 2010 *Opt. Express* **18** 16320
- [7] Kaminskii A A, Klevtsov P V, Pavlyuk A A 1970 *Phys. Stat. Sol. (a)* **1** K91
- [8] Volokitina A A, Loiko P A, Vilejshikova E V, Mateos X, Dunina E B, Kornienko A A, Kuleshov N V, Pavlyuk A A 2018 *J. Alloys Compd.* **762** 786
- [9] Loiko P A, Kifle E, Serres J M, Mateos X, Aguiló M, Díaz F, Vilejshikova E V, Kuleshov N V, Pavlyuk A 2018 *Laser Phys. Lett.* **15** 065002
- [10] Kaminskii A A, Bagayev S N 1944 *Quantum Electron.* **24** 1029
- [11] Aull B F, Janssen H P 1982 *IEEE J. Quantum Electron.* **18** 925



Laser operation of cleaved single-crystal plates and films of Tm:KY(MoO₄)₂

ANNA VOLOKITINA,^{1,2} PAVEL LOIKO,³ ANATOLY PAVLYUK,⁴
SAMI SLIMI,^{1,5} ROSA MARIA SOLÉ,¹ EZZEDINE BEN SALEM,⁴
ESROM KIFLE,¹ JOSEP MARIA SERRES,^{1,6} UWE GRIEBNER,⁷
VALENTIN PETROV,⁷ MAGDALENA AGUILÓ,¹ FRANCESC DÍAZ,¹ AND
XAVIER MATEOS^{1,*}

¹Física i Cristal·lografia de Materials i Nanomaterials (FiCMA-FiCNA)-EMaS, Dept. Química Física i Inorgànica, Universitat Rovira i Virgili (URV), Campus Sescelades, E-43007 Tarragona, Spain

²ITMO University, 49 Kronverkskiy Pr., 197101 St. Petersburg, Russia

³Centre de recherche sur les Ions, les Matériaux et la Photonique (CIMAP), UMR 6252

CEA-CNRS-ENSICAEN, Université de Caen, 6 Boulevard du Maréchal Juin, 14050 Caen Cedex 4, France

⁴A. V. Nikolaev Institute of Inorganic Chemistry, Siberian Branch of Russian Academy of Sciences, 3 Lavrentyev Ave., Novosibirsk 630090, Russia

⁵I.P.E.I. of Monastir, Unit of Materials and Organic Synthesis Monastir 5019, UR17ES31, Tunisia

⁶Eurecat, Centre Tecnològic de Catalunya, Unitat Advanced Manufacturing Systems (AMS), Campus Sescelades, E-43007 Tarragona, Spain

⁷Max Born Institute for Nonlinear Optics and Short Pulse Spectroscopy, Max-Born-Str. 2a, D-12489 Berlin, Germany

*xavier.mateos@urv.cat

Abstract: We report on the crystal growth, spectroscopy and first laser operation of a novel double molybdate compound – Tm:KY(MoO₄)₂. This orthorhombic (sp. gr. *Pbna*) crystal exhibits strong anisotropy of the spectroscopic properties due to its layered structure. The maximum stimulated emission cross-section for the ³F₄ → ³H₆ transition is 2.70×10⁻²⁰ cm² at 1856nm with a bandwidth of >110 nm (for *E* || *b*). The lifetime of the ³F₄ state is 2.29 ms. Crystalline films and plates (thickness down to 70 μm) of high optical quality are obtained by mechanical cleavage along the (100) plane. Continuous-wave diode-pumped laser operation is achieved in such thin films and plates yielding a maximum output power of 0.88 W at ~1.9 μm with a slope efficiency of 65.8% and a linearly polarized laser output. Vibronic lasing is demonstrated at ~2.06 μm. Tm:KY(MoO₄)₂ is promising for microchip and thin-disk lasers.

© 2020 Optical Society of America under the terms of the [OSA Open Access Publishing Agreement](#)

1. Introduction

Monoclinic (sp. gr. *C2/c*) double tungstate (DT) crystals, KRE(WO₄)₂ (where RE = Gd, Y, Lu), doped with rare-earth ions (RE³⁺), and, in particular, with trivalent thulium (Tm³⁺) ions are known for efficient lasing in the eye-safe spectral range of ~2 μm according to the ³F₄ → ³H₆ electronic transition [1–3]. This is due to the high achievable Tm doping concentrations, strong cross-relaxation for neighboring Tm³⁺ ions, ³H₄(Tm₁) + ³H₆(Tm₂) → ³F₄(Tm₁) + ³F₄(Tm₂) [4], even at moderate doping levels, broad and intense emission bands at ~2 μm with polarized light [5], weak non-radiative relaxation from the upper laser level (³F₄) and Raman activity. The host crystals themselves also provide suitable thermo-optical properties enabling microchip laser operation [6,7]. Monoclinic DTs exhibit a polymorphic phase transformation below the melting point. Thus, they are typically grown by the Top-Seeded Solution Growth (TSSG) method (from the flux) [1].

Such attractive spectroscopic properties are also expected for their double molybdate (DMo) counterparts, KRE(MoO₄)₂. One representative of this crystal family is the potassium yttrium

double molybdate, $\text{KY}(\text{MoO}_4)_2$ [8]. It belongs to the orthorhombic crystal class (sp. gr. *Pbna*) and does not exhibit polymorphism [9]. Thus, it can be easily grown by the Czochralski (Cz) method (from the melt). Moreover, $\text{KY}(\text{MoO}_4)_2$ features a layered structure further enhancing the polarization-anisotropy of vibronic [10,11] and spectroscopic properties [12,13] and leading to a perfect cleavage feature that can be utilized in microchip or thin-film lasers [14]. The structure of undoped $\text{KY}(\text{MoO}_4)_2$ is known [8].

The previous studies of laser properties of RE^{3+} -doped $\text{KY}(\text{MoO}_4)_2$ crystals focused solely on Nd^{3+} ions. The first laser operation of $\text{Nd}:\text{KY}(\text{MoO}_4)_2$ at the wavelengths of 1.067 μm and 1.349 μm was obtained in the free-running regime (flashlamp pumping) [15,16]. Continuous-wave (CW) operation with *bulk* crystals was later achieved in [17,18]. Kaminski *et al.* also proposed the concept of a thin-film or a *belt-shaped* laser using thin crystalline films (thickness: down to 50 μm) of $\text{Nd}:\text{KY}(\text{MoO}_4)_2$ pumped by flash-lamps and Ar^+ ion laser [14].

Recently, efficient lasers operating at $\sim 1 \mu\text{m}$ based on single-crystal plates were demonstrated using other cleaving crystals such as $\text{Yb}:\text{LuPO}_4$ or $\text{Yb}:\text{BaGd}_2(\text{MoO}_4)_4$ [19,20].

In the present work, we report on the crystal growth by the Czochralski method, structural and spectroscopic characterization as well as the first laser operation of a novel representative of the DMo crystal family – the orthorhombic $\text{Tm}:\text{KY}(\text{MoO}_4)_2$ crystal.

2. Crystal growth and structure

2.1. Crystal growth

The crystal growth was performed by the Low Temperature Gradient (LTG) Cz method [21]. The $\text{Tm}:\text{KY}(\text{MoO}_4)_2$ crystal melts at $\sim 1243 \text{ K}$. The starting materials for preparing the growth charge were Y_2O_3 (purity: 5N), Tm_2O_3 (4N), MoO_3 (4N) and K_2CO_3 (5N) taken for the composition 100 mol% $\text{KY}_{0.97}\text{Tm}_{0.03}(\text{MoO}_4)_2$ –5–7 mol% $\text{K}_2\text{Mo}_3\text{O}_{10}$. Potassium trimolybdate ($\text{K}_2\text{Mo}_3\text{O}_{10}$) was added to prevent partial dissociation of the melt and to stabilize the growth process. The raw materials were carefully mixed and placed in a Pt crucible with a cylindrical shape (diameter: 70 mm, height: 120 mm). The crucible was first heated until $\sim 1320 \text{ K}$ in air and kept at this temperature for 2–3 h to homogenize the melt. Then, the melt was cooled to $\sim 1240 \text{ K}$ (the starting growth temperature). The crucible was placed in a three-zone resistive heating furnace having good bottom and top heat insulation [21]. A seed prepared from an undoped $\text{KY}(\text{MoO}_4)_2$ crystal was oriented orthogonal to the cleavage plane (i.e., along the [100] crystallographic axis). It was rotated at 20 rpm (revolutions per minute); the pulling rate was 1–2 mm/h; the cooling rate was $\sim 2 \text{ K/day}$. The temperature gradient in the melt was below 3 K/cm as measured by a Pt/Pt-Rh thermocouple along the crystal growth direction. After the growth process was completed, the crystal was removed from the melt and slowly cooled down to room temperature (RT, 293 K). No post-grown annealing was applied.

The as-grown 3 at.% $\text{Tm}:\text{KY}(\text{MoO}_4)_2$ crystal boule is shown in Fig. 1(a). The Tm^{3+} concentration was calculated to be $N_{\text{Tm}} = 1.95 \times 10^{20} \text{ cm}^{-3}$ (assuming a segregation coefficient $K_{\text{Tm}} \approx 1$). The crystal boule had a donut shape and contained no cracks and inclusions. The crystal had a slight yellowish coloration due to the Tm^{3+} doping. $\text{Tm}:\text{KY}(\text{MoO}_4)_2$ exhibits a perfect natural cleavage along the crystallographic (100) plane (i.e., orthogonal to the growth direction in the present work), as verified by single-crystal X-ray diffraction (XRD). The orientation of the [010] and [001] axes was also determined by single-crystal XRD. It can be also found in a different way. The (100) cleaved thin crystal plates of $\text{Tm}:\text{KY}(\text{MoO}_4)_2$ brake under bending along the [001] axis. Along the orthogonal [010] axis, the plates exhibit elastic deformation. The anisotropy of the thermal properties of $\text{Tm}:\text{KY}(\text{MoO}_4)_2$ in the (100) plane also determines a slight ellipticity of the cross-section of the crystal boule with the principal directions along the [010] and [001] axes.

A Scanning Electron Microscope (SEM) image of the fracture edge of a mechanically cleaved single-crystal plate of $\text{Tm}:\text{KY}(\text{MoO}_4)_2$ is shown in Fig. 1(b). Note that the whole boule of

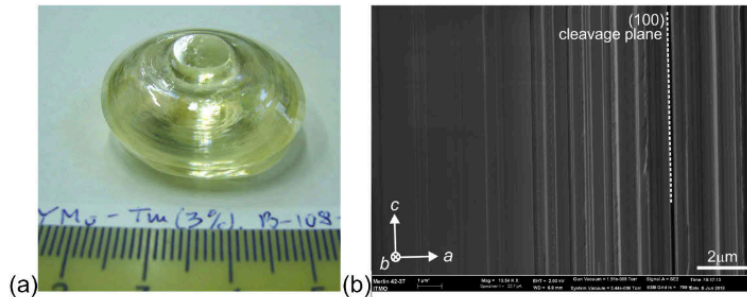


Fig. 1. (a) Photograph of the as-grown 3 at.% Tm:KY(MoO₄)₂ crystal boule. The growth direction is along the [100] axis (vertical); (b) Scanning Electron Microscope (SEM) image of the side surface of a cleaved single-crystal film indicating the crystallographic directions.

Tm:KY(MoO₄)₂ has single-crystalline nature. The fracture of crystal-plates occurs along the [001] axis. The SEM image reveals the natural cleavage feature as the fracture edge represents multiple “stairs” running parallel to the *c*-axis in the (100) plane.

2.2. Crystal structure and Raman spectra

The structure and phase purity of Tm:KY(MoO₄)₂ were confirmed by powder XRD, see Fig. 2(a). Tm:KY(MoO₄)₂ belongs to the orthorhombic centrosymmetric crystal class (sp. gr. *Pbna* – D¹⁴_{2h}, No. 60). No traces of any other impurity phases are found. The lattice constants for the 3 at.% Tm-doped crystal were determined using the Rietveld refinement to be *a* = 18.2012(9) Å, *b* = 7.9301(5) Å, *c* = 5.0666(4) Å, $\alpha = \beta = \gamma = 90^\circ$, the calculated density ρ_{calc} is 4.0897(4) g/cm³ (the number of the structural units *Z* = 4). The reduced chi-squared value of $\chi^2 = (R_{\text{wp}}/R_{\text{exp}})^2$ for this fit is 1.802 (*R*_{wp} = 8.65%, *R*_{exp} = 4.80%). The initial set of atomic coordinates for undoped KY(MoO₄)₂ was taken from [8].

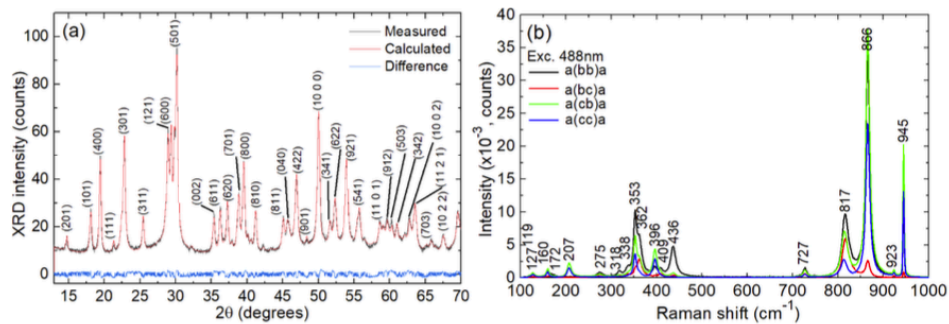


Fig. 2. (a) Rietveld refinement of the X-ray powder diffraction (XRD) pattern of the 3 at.% Tm:KY(MoO₄)₂ crystal; numbers indicate the Miller’s indices (*hkl*) (sp. gr. *Pbna*); (b) Polarized Raman spectra of the Tm:KY(MoO₄)₂ crystal for the *a*(*ij*)*a* geometries, where *i*, *j* = *b* or *c* (Porto’s notations), $\lambda_{\text{exc}} = 488 \text{ nm}$.

The structure of Tm:KY(MoO₄)₂ consists of continuous belts of edge-sharing distorted [YO₈] octahedra arranged parallel to the *b*-axis. In the *a*-*b* plane, they share corners with the [MoO₄] tetrahedra. The radicals [Y(MoO₄)₂]⁻ form porous layers parallel to the *b*-*c* plane. The linkage of these layers along the *a*-axis is weak, which explains the excellent cleavage along the (100) plane. Tm³⁺ ions substitute for Y³⁺ in a single site (coordination number (C.N.) by oxygen is VIII, C₂ symmetry). This is favored by the closeness of ionic radii of Tm³⁺ (0.994 Å) and Y³⁺ (1.019 Å).

The polarized Raman spectra were measured using a Renishaw inVia confocal Raman microscope with a $\times 50$ objective. The excitation wavelength λ_{exc} was 488 nm (Ar⁺ ion laser line). The spectral resolution was ~ 1 cm⁻¹. The Raman spectra of an (100)-oriented plate from the Tm:KY(MoO₄)₂ crystal are shown in Fig. 2(b). The spectra contain bands localized in three ranges showing different intensity. The low-frequency range (at < 275 cm⁻¹) contains weak vibrations related to translational (T') modes of K, Y|Tm and Mo and rotational (R) lattice modes. Internal modes are observed at higher frequencies. The second intermediate-frequency range at 318-436 cm⁻¹ exhibits bands of medium intensity related to the bending (δ) vibrations of the oxygen bridged [MoO₄] tetrahedra. Finally, the high-frequency range, 727-945 cm⁻¹, contains intense modes due to the stretching (ν) vibrations of [MoO₄]. The most intense and strongly polarized Raman peak appears at 865.6 cm⁻¹ with a full width at half maximum (FWHM) of 10.5 cm⁻¹. It is assigned to one of the internal (ν) vibrations of [MoO₄]. The maximum phonon energy of Tm:KY(MoO₄)₂ is 945 cm⁻¹. More details can be found elsewhere [10,11].

3. Spectroscopic study

3.1. Experimental

The KY(MoO₄)₂ crystal is orthorhombic and, thus, optically biaxial. The frame of the optical indicatrix axes (X, Y, Z) coincides with the (*a*, *b*, *c*) crystallographic frame (not necessarily respectively). Only a mean value of the refractive index $\langle n \rangle \approx 2$ is known [15]. Thus, the anisotropic absorption and luminescence properties were characterized for the *E* || *a*, *b*, *c* light polarizations. All the spectroscopic studies were performed at RT (293 K).

For measuring the absorption and luminescence spectra, we used a ~ 1 mm-thick cleaved crystal plate. The absorption spectra were measured for the available light polarizations *E* || *b* and *E* || *c* using a Varian CARY 5000 spectrophotometer and a Glan-Taylor polarizer. The spectral resolution was 0.1–0.5 nm. It was complicated to prepare a polished sample oriented orthogonal to the cleavage plane thus accessing the *E* || *a* polarization in absorption.

The luminescence spectra at ~ 2 μ m for the polarizations *E* || *a*, *b*, *c* were measured using an optical spectrum analyzer (AQ6375B, Yokogawa, spectral resolution: 1 nm) and a Glan-Taylor polarizer. The spectral response of the set-up was calibrated employing a quartz iodine lamp. The excitation source was a CW Ti:Sapphire laser tuned to ~ 802 nm.

The luminescence decay of Tm³⁺ ions was studied using a 1/4 m monochromator (Oriel 77200), an InGaAs detector and a 8 GHz digital oscilloscope (DSA70804B, Tektronix). The luminescence was excited by the output of a ns optical parametric oscillator tuned to ~ 802 nm (Horizon, Continuum).

3.2. Optical absorption and luminescence

The absorption spectrum of the Tm:KY(MoO₄)₂ crystal for light polarizations *E* || *b* and *E* || *c* is shown in Fig. 3(a). In the spectrum, the absorption bands are due to transitions of Tm³⁺ ions from the ground-state (³H₆) to the excited-states (³F₄ to ¹D₂). There is no color center absorption in the visible. The UV absorption edge is found at $\lambda_{\text{UV}} = 327$ nm (for *E* || *c*) and 340 nm (for *E* || *b*), corresponding to an optical bandgap *E_g* of 3.64–3.80 eV.

The absorption cross-sections, σ_{abs} , for the ³H₆ → ³H₄ and ³H₆ → ³F₄ transitions are shown in Fig. 3(b). For the ³H₆ → ³H₄ one, the maximum σ_{abs} is 7.70×10^{-20} cm² at 802.8 nm and the corresponding FWHM of the absorption peak is 10.0 nm (for *E* || *b*). For the second available light polarization (*E* || *c*), σ_{abs} is by one order of magnitude smaller: 0.32×10^{-20} cm² at 792.9 nm. This transition is suitable for pumping of Tm³⁺ ions, e.g., by commercial and high-power AlGaAs laser diodes (the “conventional” pump scheme). The maximum σ_{abs} value for the ³H₆ → ³H₄ Tm³⁺ transition in KY(MoO₄)₂ is similar to that in monoclinic Tm:KLu(WO₄)₂, $\sigma_{\text{abs}} = 9.5 \times 10^{-20}$ cm² at 793.6 nm [1] however providing a FWHM of the absorption peak of 1.7

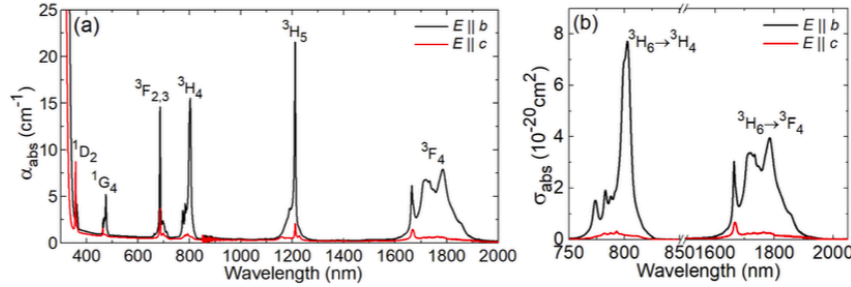


Fig. 3. Absorption of the Tm:KY(MoO₄)₂ crystal: (a) full absorption spectrum; (b) absorption cross-sections, σ_{abs} , for the ${}^3\text{H}_6 \rightarrow {}^3\text{F}_4$ and ${}^3\text{H}_4$ transitions for polarizations $E \parallel b$ and $E \parallel c$.

nm (light polarization: $E \parallel N_p$). As a result, Tm:KY(MoO₄)₂ is more suitable for diode-pumping because of weaker sensitivity to the temperature drift of the diode emission wavelength. For the ${}^3\text{H}_6 \rightarrow {}^3\text{F}_4$ Tm³⁺ transition in KY(MoO₄)₂, σ_{abs} reaches $3.95 \times 10^{-20} \text{ cm}^2$ at 1785 nm (again for $E \parallel b$). This transition is suitable for in-band pumping of Tm³⁺ ions directly to the upper laser level, e.g., by erbium Raman fiber lasers emitting at $\sim 1.7 \mu\text{m}$ [22].

The notable anisotropy of the absorption cross-sections in the (100) plane cannot be assigned to the layered structure and is most probably related to the low symmetry of the Tm³⁺ site (C_2).

The stimulated-emission (SE) cross-sections, σ_{SE} , for the ${}^3\text{F}_4 \rightarrow {}^3\text{H}_6$ transition of Tm³⁺ were calculated using the Füchtbauer–Ladenburg (F-L) formula [23]:

$$\sigma_{\text{SE}}^i(\lambda) = \frac{\lambda^5}{8\pi \langle n \rangle^2 \tau_{\text{rad}} c} \frac{W_i(\lambda)}{\sum_{i=a,b,c} \int \lambda W_i(\lambda) d\lambda}, \quad (1)$$

where λ is the light wavelength, $\langle n \rangle$ is the refractive index, c is the speed of light, τ_{rad} is the radiative lifetime of the emitting state (${}^3\text{F}_4$), $W_i(\lambda)$ is the measured luminescence spectrum for the i -th polarization calibrated for the spectral response of the set-up and $i = a, b, c$. The results are shown in Fig. 4(a). The maximum σ_{SE} is $2.70 \times 10^{-20} \text{ cm}^2$ at 1856 nm with an emission bandwidth (FWHM) of $> 110 \text{ nm}$ (for $E \parallel b$). Tm:KY(MoO₄)₂ exhibits a notable anisotropy of the SE cross-sections: the ratios $\sigma_{\text{SE}}(b) : \sigma_{\text{SE}}(c) = 7.5$ and $\sigma_{\text{SE}}(b) : \sigma_{\text{SE}}(a) = 5.7$ at $\sim 1.86 \mu\text{m}$, which is a prerequisite for a linearly polarized laser output.

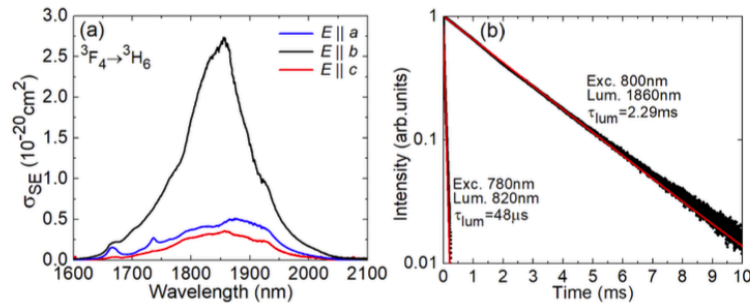


Fig. 4. Emission properties of the Tm:KY(MoO₄)₂ crystal: (a) stimulated-emission (SE) cross-sections, σ_{SE} , for the ${}^3\text{F}_4 \rightarrow {}^3\text{H}_6$ transition, light polarizations are $E \parallel a, b, c$; (b) luminescence decay curve from the ${}^3\text{F}_4$ state, $\lambda_{\text{exc}} = 800 \text{ nm}$, $\lambda_{\text{lum}} = 1860 \text{ nm}$.

The luminescence decay from the ${}^3\text{F}_4$ state is single-exponential yielding a luminescence lifetime τ_{lum} of 2.29 ms, see Fig. 4(b). This agrees with the accommodation of Tm³⁺ ions in a

single type of sites (symmetry: C_2). The luminescence lifetime of the 3H_4 pump level is 48 μs . This value is expected to be quenched by the cross-relaxation. Both lifetimes were measured for thin (tens of μm) films eliminating the effect of reabsorption (radiation trapping). Indeed, the $\tau_{lum}(^3F_4)$ value obtained using a crystal-plate was much longer, 3.35 ms.

The $^3F_4 \rightarrow ^3H_6$ Tm^{3+} transition represents a quasi-three-level laser scheme with reabsorption losses. Thus, the gain cross-sections, $\sigma_{gain} = \sigma_{SE} - (1 - \beta)\sigma_{abs}$, are typically calculated to conclude about the expected emission wavelength, where $\beta = N_2(^3F_4)/N_{Tm}$ is the inversion ratio and N_2 is the population of the upper laser level (3F_4). The σ_{gain} spectra for the high-gain light polarization $E \parallel b$ are shown in Fig. 5. They are relatively smooth and broad.

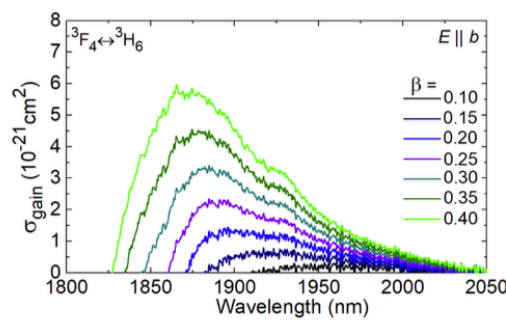


Fig. 5. Gain cross-sections, $\sigma_{gain} = \sigma_{SE} - (1 - \beta)\sigma_{abs}$, for the $^3F_4 \leftrightarrow ^3H_6$ transition of Tm^{3+} in $KY(MoO_4)_2$: $\beta = N_2(^3F_4)/N_{Tm}$ is the inversion ratio, the light polarization is $E \parallel b$.

4. Laser operation

4.1. Laser set-up

For the laser experiments, we prepared two samples from the 3 at.% $Tm:KY(MoO_4)_2$ crystal. They were fabricated by mechanical cleaving the crystal using a thin razor blade placed along the (100) crystallographic plane. Only a slight pressure was applied to the blade producing the initial crack which further easily propagated through the crystal cross-section. The samples had thicknesses (t) of $70 \pm 5 \mu m$ and $700 \pm 10 \mu m$, referred further as a thin-film and a crystal-plate, respectively. The thickness was measured using a micrometer and confirmed by SEM for the thin-film. It was uniform along the sample cross-section within the specified error. The first sample exhibited elastic deformation at naked eye. No post-cleavage processing (e.g., polishing or coating) was applied. The clean aperture of the samples was more than $1 cm^2$. The samples were fabricated from the bulk crystal oriented by means of single-crystal XRD so that the orientation of the [010] and [001] axes was known.

The samples were placed in a compact plano-plano (microchip) cavity formed by a flat pump mirror (PM) coated for high transmission (HT) at the pump wavelength, $\sim 0.80 \mu m$, and for high reflection (HR) at 1.8–2.1 μm , and a set of flat output couplers (OCs) having a transmission T_{OC} of 0.1%–9% at the laser wavelength, Fig. 6(a). A special band-pass (BP) OC coated for HT at $< 2 \mu m$ and for partial reflection ($T_{OC} = 1.5\%$) at 2.05–2.20 μm was also used. Both the PM and OC were gently pressed towards the crystalline sample, so that the geometrical cavity length $L_{cav} \equiv t$. The laser element was passively cooled, Fig. 6(b).

The laser element was pumped by a fiber-coupled (fiber core diameter: 200 μm , N.A. = 0.22) AlGaAs laser diode emitting up to 17 W of unpolarized output at 802 nm ($M^2 \approx 86$). The incident pump power was limited to avoid optical damage at the crystal / mirror interfaces. The pump beam was collimated and focused into the laser element by a lens assembly (1:1 reimaging ratio, focal length $f = 30 mm$) resulting in a pump spot diameter $2w_p = 200 \pm 10 \mu m$. Due to the partial

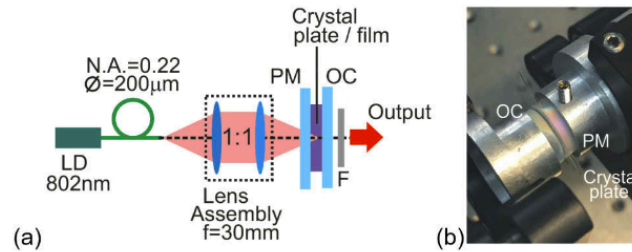


Fig. 6. (a) Scheme of the diode-pumped microchip Tm:KY(MoO₄)₂ lasers: LD – laser diode, PM – pump mirror, OC – output coupler, F – cut-off filter; (b) photograph of the laser.

reflectivity of the OCs at the pump wavelength ($R \approx 40\%$), the pumping was in a double-pass. The total pump absorption was taken at its small-signal value, $\eta_{\text{abs},0} = 6.4\%$ and 47.6% for the thin-film and crystal-plate, respectively. This value does not account for the possible ground-state bleaching; however, it does not overestimate the slope efficiency of the laser. The laser output was separated from the residual pump using a long-pass filter (FEL1000, Thorlabs).

4.2. Laser performance

First, we studied the laser performance of the crystal-plate ($t = 700 \mu\text{m}$), Fig. 7(a),(b). The laser generated a maximum output power of 0.88 W at $1840\text{--}1905 \text{ nm}$ with a slope efficiency η of 65.8% (vs. the absorbed pump power P_{abs}) and the laser threshold was at $P_{\text{abs}} = 210 \text{ mW}$ (for $T_{\text{OC}} = 5\%$). For higher output coupling, the performance slightly deteriorated probably due to the upconversion losses. For all OCs, the input-output dependences were linear indicating weak thermal effects. The laser polarization was linear ($E \parallel b$); it was naturally selected by the anisotropy of the gain. Typical spectra of the laser emission are shown in Fig. 7(b). With the increase of T_{OC} , the spectra experienced a blue-shift due to the quasi-three-level nature of the ${}^3\text{F}_4 \rightarrow {}^3\text{H}_6$ Tm³⁺ laser scheme. For example, for small $T_{\text{OC}} = 1.5\%$, the laser operated at $1970\text{--}1978 \text{ nm}$ and for high $T_{\text{OC}} = 9\%$ - at $1826\text{--}1835 \text{ nm}$. This behavior agrees well with the gain spectra for light polarization $E \parallel b$, Fig. 5.

By implementing the band-pass OC, laser emission beyond $2 \mu\text{m}$ was achieved. The output power reached 0.34 W at $2047\text{--}2074 \text{ nm}$ with $\eta = 46.7\%$ and a laser threshold of 205 mW . Such a long wavelength emission is ascribed to the electron-phonon coupling with the low-energy Raman modes of the KY(MoO₄)₂ lattice [24,25].

The second experiment consisted of inserting the crystal-film into the laser cavity, Fig. 7(c),(d). The maximum output power was 131 mW at $1801\text{--}1872 \text{ nm}$ with $\eta = 45.2\%$ and a threshold of only 35 mW (for $T_{\text{OC}} = 1.5\%$). The emission was linearly polarized ($E \parallel b$). With the increase of the output coupling, the laser threshold increased: from 13 mW for the smallest $T_{\text{OC}} = 0.1\%$ up to 54 mW for $T_{\text{OC}} = 9\%$ still remaining relatively low. The slope efficiency first increased with T_{OC} (so that the optimum transmission of the OC is expected to lie between $T_{\text{OC}} = 0.1\%$ and 1.5%) and, furthermore, decreased for $T_{\text{OC}} > 1.5\%$. The latter effect is probably due to stronger energy-transfer upconversion (ETU) associated with higher population of the upper laser level ${}^3\text{F}_4$ (higher inversion rate β) at increased output coupling. The ETU has a direct influence on the laser threshold [26]. However, it also leads to a stronger heat dissipation and more severe thermo-optic effects in the gain medium thus affecting the slope efficiency in an indirect way.

The lower slope efficiency achieved with the crystal-film laser as compared to the crystal-plate one is ascribed to higher passive losses originating from possible mechanical distortion and bending of the film. We expect that such losses can be eliminated by further optimizing the cleaving procedure.

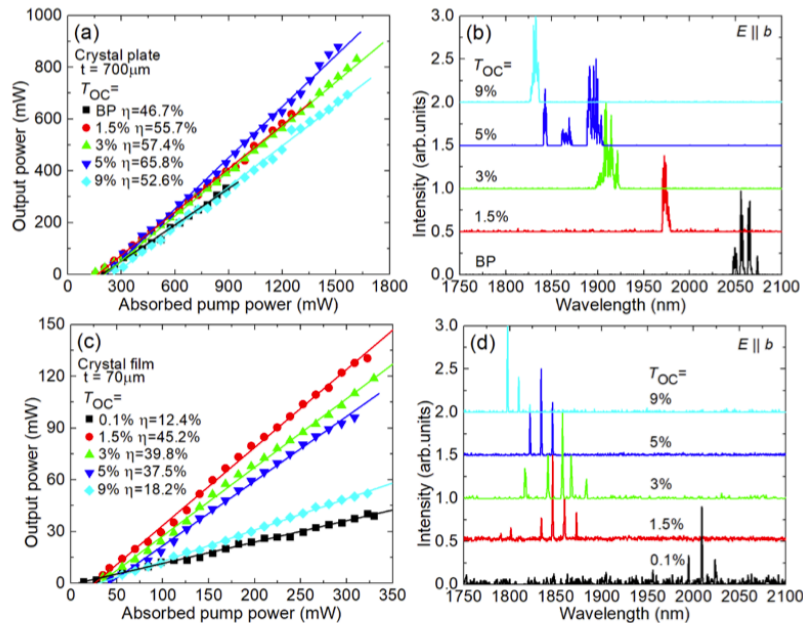


Fig. 7. Diode-pumped laser performance of (100)-oriented cleaved (a,b) thin-film ($t = 70 \mu\text{m}$) and (c,d) crystal-plate ($t = 700 \mu\text{m}$) 3 at.% Tm:KY(MoO₄)₂ crystal: (a,c) input-output dependences, η – slope efficiency; (b,d) typical spectra of the laser emission measured at maximum P_{abs} . The laser polarization is $E \parallel b$.

The blue-shift of the emission spectra with the output coupling was also detected, Fig. 7(d). The spectra contained equidistant spectral lines separated by $\Delta\lambda = 12.2 \text{ nm}$ at $\sim 1.85 \mu\text{m}$ (for $T_{\text{OC}} = 1.5\% - 9\%$). This is ascribed to the etalon effect of the uncoated laser element. The free spectral range (FSR) of the Fabry-Perot etalon with a thickness t and a refractive index n_g ($n_g \approx n$ assuming a weak dispersion) at normal incidence is $\Delta\lambda_{\text{FSR}} \approx \lambda^2 / (n_g t)$. From this formula, we get the etalon thickness of $71 \mu\text{m}$ for $n = 2.0$ in good agreement with the measured thickness.

The Tm:KY(MoO₄)₂ lasers operated in the fundamental transverse mode. The beam quality parameters measured using an ISO-standard method employing a focusing lens $M^2_{x,y} < 1.2$ ($x = b, y = c$).

5. Conclusion

To conclude, the orthorhombic double molybdate crystal Tm:KY(MoO₄)₂ is a promising material for efficient $\sim 2 \mu\text{m}$ lasers owing to its easy growth, high available doping levels, intense, broad and strongly polarized absorption and emission bands and Raman activity. The layered structure of KY(MoO₄)₂ promotes the anisotropy of its optical properties and allows one to fabricate easily laser-quality crystal plates and films with a thickness ranging from few mm down to tens of μm . This feature is of interest for microchip and thin-disk lasers. In particular, the long lifetime of the upper laser level of Tm³⁺ is attractive for passively Q-switched sub-nanosecond microchip lasers. In the present work, we achieved $\sim 2 \mu\text{m}$ CW laser action in single-crystal plates (sub-mm) and films (sub-100 μm) featuring up to 65.8% slope efficiency and almost watt-level output for passively-cooled devices.

Funding

Ministerio de Economía y Competitividad (MAT2016-75716-C2-1-R (AEI/FEDER,UE)); Agència de Gestió d'Ajuts Universitaris i de Recerca (2017SGR755); Russian Foundation for Basic Research (19-32-90199).

Disclosures

The authors declare no conflicts of interest.

References

1. V. Petrov, M. C. Pujol, X. Mateos, O. Silvestre, S. Rivier, M. Aguiló, R. M. Solé, J. Liu, U. Griebner, and F. Díaz, "Growth and properties of $\text{KLu}(\text{WO}_4)_2$, and novel ytterbium and thulium lasers based on this monoclinic crystalline host," *Laser Photonics Rev.* **1**(2), 179–212 (2007).
2. X. Mateos, V. Petrov, J. Liu, M. C. Pujol, U. Griebner, M. Aguiló, F. Díaz, M. Galan, and G. Viera, "Efficient 2- μm continuous-wave laser oscillation of $\text{Tm}^{3+}:\text{KLu}(\text{WO}_4)_2$," *IEEE J. Quantum Electron.* **42**(10), 1008–1015 (2006).
3. A. E. Troshin, V. E. Kisel, A. S. Yasukevich, N. V. Kuleshov, A. A. Pavlyuk, E. B. Dunina, E. B. and A., and A. Kornienko, "Spectroscopy and laser properties of $\text{Tm}^{3+}:\text{KY}(\text{WO}_4)_2$ crystal," *Appl. Phys. B* **86**(2), 287–292 (2007).
4. K. van Dalmsen, S. Aravazhi, C. Grivas, S. M. García-Blanco, and M. Pollnau, "Thulium channel waveguide laser with 1.6 W of output power and ~80% slope efficiency," *Opt. Lett.* **39**(15), 4380–4383 (2014).
5. Ò. Silvestre, M. C. M. Rico, F. Güell, M. Aguiló, and F. Díaz, "Thulium doped monoclinic $\text{KLu}(\text{WO}_4)_2$ single crystals: growth and spectroscopy," *Appl. Phys. B* **87**(4), 707–716 (2007).
6. M. S. Gaponenko, P. A. Loiko, N. V. Gusakova, K. V. Yumashev, N. V. Kuleshov, and A. A. Pavlyuk, "Thermal lensing and microchip laser performance of N_g -cut $\text{Tm}^{3+}:\text{KY}(\text{WO}_4)_2$ crystal," *Appl. Phys. B* **108**(3), 603–607 (2012).
7. J. M. Serres, X. Mateos, P. Loiko, K. Yumashev, N. Kuleshov, V. Petrov, U. Griebner, M. Aguiló, and F. Díaz, "Diode-pumped microchip $\text{Tm}:\text{KLu}(\text{WO}_4)_2$ laser with more than 3 W of output power," *Opt. Lett.* **39**(14), 4247–4250 (2014).
8. R. F. Klevtsova and S. V. Borisov, "X-ray structural study of the double molybdate $\text{KY}(\text{MoO}_4)_2$," *Sov. Phys. Dokl.* **12**, 1095 (1968) [Transl. from *Dokl. Akad. Nauk SSSR* **177**(6), 1333–1336 (1967)].
9. P. V. Klevtsov and R. F. Klevtsova, "Polymorphism of the double molybdates and tungstates of mono- and trivalent metals with the composition $\text{M}^+\text{R}^{3+}(\text{EO}_4)_2$," *J. Struct. Chem.* **18**(3), 339–355 (1977).
10. J. Hanuza and L. Ľabuda, "Polarized Raman and infrared spectra of a multilayer $\text{KY}(\text{MoO}_4)_2$ crystal," *J. Raman Spectrosc.* **11**(4), 231–237 (1981).
11. J. Hanuza and L. Macalik, "Polarized IR and Raman spectra of orthorhombic $\text{KLn}(\text{MoO}_4)_2$ crystals ($\text{Ln} = \text{Y}, \text{Dy}, \text{Ho}, \text{Er}, \text{Tm}, \text{Yb}, \text{Lu}$)," *Spectrochim. Acta A: Mol. Spectr.* **38**(1), 61–72 (1982).
12. A. Volokitina, P. Loiko, E. Vilejshikova, X. Mateos, E. Dunina, A. Kornienko, N. Kuleshov, and A. Pavlyuk, " $\text{Eu}^{3+}:\text{KY}(\text{MoO}_4)_2$: A novel anisotropic red-emitting material with a layered structure," *J. Alloys Compd.* **762**, 786–796 (2018).
13. Y. Chen, Y. Lin, X. Gong, Q. Tan, Z. Luo, and Y. Huang, "Polarized spectral characteristics of $\text{Nd}^{3+}:\text{KY}(\text{MoO}_4)_2$ crystal with perfect cleavage planes: a promising microchip gain medium," *J. Opt. Soc. Am. B* **24**(3), 496–503 (2007).
14. A. A. Kaminskii and S. N. Bagayev, "Ribbons and sheet miniature crystal laser," *Quantum Electron.* **24**(12), 1029–1030 (1994).
15. A. A. Kaminskii, P. V. Klevtsov, and A. A. Pavlyuk, "Stimulated emission from $\text{KY}(\text{MoO}_4)_2\text{-Nd}^{3+}$ crystal laser," *Phys. Status Solidi A* **1**(3), K91–K94 (1970).
16. A. A. Kaminskii, S. E. Sarkisov, and L. Li, "Investigation of stimulated emission in the ${}^4\text{F}_{3/2} \rightarrow {}^4\text{I}_{13/2}$ transition of Nd^{3+} ions in crystals (III)," *Phys. Status Solidi A* **15**(2), K141–K144 (1973).
17. A. A. Kaminskii and H. R. Verdun, "New high power, high efficient quasi-CW and CW single-mode $\text{KY}(\text{MoO}_4)_2:\text{Nd}^{3+}$ laser end-pumped by a GaAlAs laser-diode array," *Phys. Status Solidi A* **138**(1), K49–K53 (1993).
18. P. Loiko, E. Kifle, J. M. Serres, X. Mateos, M. Aguiló, F. Díaz, E. Vilejshikova, N. Kuleshov, and A. Pavlyuk, "Efficient continuous-wave in-band pumped $\text{Nd}:\text{KY}(\text{MoO}_4)_2$ laser," *Laser Phys. Lett.* **15**(6), 065002 (2018).
19. J. Liu, W. Han, X. Chen, D. Zhong, B. Teng, C. Wang, and Y. Li, "Spectroscopic properties and continuous-wave laser operation of $\text{Yb}:\text{LuPO}_4$ crystal," *Opt. Lett.* **39**(20), 5881–5884 (2014).
20. H. Zhu, Y. Chen, Y. Lin, X. Gong, Q. Tan, Z. Luo, and Y. Huang, "Growth, spectral properties, and laser demonstration of $\text{Yb}^{3+}:\text{BaGd}_2(\text{MoO}_4)_4$ cleavage crystal," *J. Appl. Phys.* **101**(6), 063109 (2007).
21. Y. A. Borovlev, N. V. Ivannikova, V. N. Shlegel, Y. V. Vasiliev, and V. A. Gusev, "Progress in growth of large sized BGO crystals by the low-thermal-gradient Czochralski technique," *J. Cryst. Growth* **229**(1-4), 305–311 (2001).
22. P. Loiko, R. Thouroude, R. Souillard, L. Guillemot, G. Brasse, B. Guichardaz, A. Braud, A. Hideur, M. Laroche, H. Gilles, and P. Camy, "In-band pumping of $\text{Tm}:\text{LiYF}_4$ channel waveguide: a power scaling strategy for ~2 μm waveguide lasers," *Opt. Lett.* **44**(12), 3010–3013 (2019).

23. B. Aull and H. Jenssen, "Vibronic interactions in Nd:YAG resulting in nonreciprocity of absorption and stimulated emission cross sections," *IEEE J. Quantum Electron.* **18**(5), 925–930 (1982).
24. P. Loiko, X. Mateos, S. Y. Choi, F. Rotermund, J. M. Serres, M. Aguiló, F. Díaz, K. Yumashev, U. Griebner, and V. Petrov, "Vibronic thulium laser at 2131 nm Q-switched by single-walled carbon nanotubes," *J. Opt. Soc. Am. B* **33**(11), D19–D27 (2016).
25. P. Loiko, L. Zhang, J. M. Serres, Y. Wang, M. Aguiló, F. Díaz, Z. Lin, H. Lin, G. Zhang, E. Vilejshikova, E. Dunina, A. Kornienko, L. Fomicheva, V. Petrov, U. Griebner, W. Chen, and X. Mateos, "Monoclinic Tm:MgWO₄ crystal: Crystal-field analysis, tunable and vibronic laser demonstration," *J. Alloys Compd.* **763**, 581–591 (2018).
26. S. So, J. I. Mackenzie, D. P. Sheperd, W. A. Clarkson, J. G. Betterton, and E. K. Gorton, "A power-scaling strategy for longitudinally diode-pumped Tm:YLF lasers," *Appl. Phys. B* **84**(3), 389–393 (2006).

PROCEEDINGS OF SPIE

[SPIDigitalLibrary.org/conference-proceedings-of-spie](https://spiedigitallibrary.org/conference-proceedings-of-spie)

Efficient laser operation in cleaved single-crystal plates of Yb:KY(MoO₄)₂: A novel molybdate compound

Volokitina, Anna, Loiko, Pavel, Pavlyuk, Anatoly, Serres, Josep Maria, Slimi, Sami, et al.

Anna Volokitina, Pavel Loiko, Anatoly Pavlyuk, Josep Maria Serres, Sami Slimi, Ezzedine Ben Salem, Rosa Maria Solé, Mikhail Baranov, Esrom Kifle, Magdalena Aguiló, Francesc Díaz, Uwe Griebner, Valentin Petrov, Xavier Mateos, "Efficient laser operation in cleaved single-crystal plates of Yb:KY (MoO₄)₂: A novel molybdate compound," Proc. SPIE 11357, Fiber Lasers and Glass Photonics: Materials through Applications II, 113571T (1 April 2020); doi: 10.1117/12.2555416

SPIE.

Event: SPIE Photonics Europe, 2020, Online Only

Efficient laser operation in cleaved single-crystal plates of Yb:KY(MoO₄)₂: A novel molybdate compound

Anna Volokitina^{a,b*}, Pavel Loiko^c, Anatoly Pavlyuk^d, Josep Maria Serres^a, Sami Slimi^{a,e}, Ezzedine Ben Salem^e, Rosa Maria Solé^a, Mikhail Baranov^b, Esrom Kifle^a, Magdalena Aguiló^a, Francesc Díaz^a, Uwe Griebner^f, Valentin Petrov^f, and Xavier Mateos^a

^aUniversitat Rovira i Virgili (URV), Física i Cristal·lografia de Materials i Nanomaterials (FiCMA-FiCNA), Dept. Química Física i Inòrganica, Campus Sescelades, E-43007 Tarragona, Spain

^bITMO University, 49 Kronverkskiy Pr., 197101 St. Petersburg, Russia

^cCentre de Recherche sur les Ions, les Matériaux et la Photonique (CIMAP), UMR 6252 CEA-CNRS-ENSICAEN, Université de Caen Normandie, 6 Boulevard du Maréchal Juin, 14050 Caen Cedex 4, France

^dA.V. Nikolaev Institute of Inorganic Chemistry, Siberian Branch of Russian Academy of Sciences, 3 Lavrentyev Ave., 630090 Novosibirsk, Russia

^eI.P.E.I. of Monastir, Unit of Materials and Organic Synthesis, 5019 Monastir, UR17ES31, Tunisia

^fMax Born Institute for Nonlinear Optics and Short Pulse Spectroscopy, Max-Born-Str. 2a, D-12489 Berlin, Germany

ABSTRACT

We report on the first laser operation of a novel double molybdate compound, Yb:KY(MoO₄)₂. Single-crystals were grown by the Low Temperature Gradient (LTG) Czochralski method. The crystal structure (orthorhombic, sp. gr. *Pbna* – *D*¹⁴_{2h}) was refined with the Rietveld method. Yb:KY(MoO₄)₂ exhibits a layered structure leading to a strong optical anisotropy and a perfect cleavage along the (100) plane. The stimulated-emission cross-section for Yb³⁺ ions is 3.70×10⁻²⁰ cm² at 1008.0 nm and the emission bandwidth is 37 nm (for light polarization *E* || *b*). Continuous-wave laser operation is achieved in a 3 at.% Yb:KY(MoO₄)₂ crystal plate (thickness: 286 μm) under diode pumping. The microchip laser generated a maximum output power of 0.81 W at 1021-1044 nm with a slope efficiency of 76.4% and linear polarization. Yb:KY(MoO₄)₂ crystal films / plates are attractive for sub-ns passively Q-switched microchip lasers and thin-disk lasers.

Keywords: double molybdate, ytterbium doping, crystalline plates, crystal structure, laser operation.

1. INTRODUCTION

Ytterbium (Yb³⁺) doped materials are known for efficient laser operation at ~1 μm according to the ²F_{5/2} → ²F_{7/2} electronic transition [1]. The Yb³⁺ ion can be easily pumped by commercial and high-power InGaAs laser diodes emitting at ~0.96-0.98 μm [2]. It also exhibits a simple energy level scheme eliminating the parasitic processes such as excited-state absorption or energy-transfer upconversion. The in-band pumping scheme of Yb³⁺ leads to high pump Stokes efficiency, and, thus, reduced heat loading. Moreover, as compared to Nd³⁺, Yb³⁺ shows larger Stark splitting of the ground-state (²F_{7/2}) and, consequently, broader emission at ~1 μm, which is utilized in broadly tunable and mode-locked lasers [3].

Among the host materials for Yb³⁺ doping, monoclinic (sp. gr. *C2/c*) double tungstate (MDT) crystals are attracting a lot of attention. The general chemical formula of MDTs is KLn(WO₄)₂, where Ln = Gd, Y or Lu.

*e-mail: anna.itmo@gmail.com

Fiber Lasers and Glass Photonics: Materials through Applications II, edited by Maurizio Ferrari,
Jacob I. Mackenzie, Stefano Taccheo, Proc. of SPIE Vol. 11357, 113571T · © 2020 SPIE
CCC code: 0277-786X/20/\$21 · doi: 10.1117/12.2555416

Proc. of SPIE Vol. 11357 113571T-1

Their advantages include: (i) high attainable Yb^{3+} doping concentrations (up to the stoichiometric composition $\text{KYb}(\text{WO}_4)_2$) [4]; (ii) weak luminescence quenching, (iii) low non-radiative path from the excited-state, (iv) polarized intense and broad absorption and emission bands around $1 \mu\text{m}$ [5,6] and (v) Raman activity. Moreover, MDTs exhibit satisfactory thermo-optical properties [7,8]. As a result, efficient continuous-wave (CW) [2,9], passively Q-switched [10] and especially mode-locked [3,11] Yb :MDT lasers were reported. Thin-disk lasers based on these materials were also demonstrated using thin bulk or epitaxial samples [12,13].

Compared to above mentioned potassium double tungstates, their double molybdate (DMo) counterparts with chemical formula $\text{KLn}(\text{MoO}_4)_2$ have been barely studied. One example of the DMo crystal family is potassium yttrium double molybdate, $\text{KY}(\text{MoO}_4)_2$. This crystal is orthorhombic [14] and it exhibits an interesting layered structure [15,16] together with a low-symmetry site for the rare-earth ions (C_2) leading to a strong anisotropy of the optical properties as well as to the natural cleavage habit which is interesting for microchip and thin-disk lasers [17]. The structure and vibronic properties of undoped $\text{KY}(\text{MoO}_4)_2$ have been already reported [18]. The RE^{3+} site symmetry was revealed using Eu^{3+} as a structural probe [16].

Regarding the laser applications of rare-earth doped $\text{KY}(\text{MoO}_4)_2$ crystals, there exist only few studies. Kaminskii *et al.* reported on CW laser operation in diode-pumped *bulk* $\text{Nd}:\text{KY}(\text{MoO}_4)_2$ [19]. Later on, Loiko *et al.* improved the laser performance using the in-band pumping scheme [20]. A $\text{Nd}:\text{KY}(\text{MoO}_4)_2$ laser generated 0.43 W at 1067 nm with a slope efficiency of 71%. Kaminskii *et al.* also proposed the concept of a *thin-film* laser using cleaved $\text{Nd}:\text{KY}(\text{MoO}_4)_2$ [21].

In the present work, we aimed to achieve the first laser operation in the new DMo compound, $\text{Yb}:\text{KY}(\text{MoO}_4)_2$, and to demonstrate the proof-of-concept of crystal-plate DMo lasers utilizing their natural cleavage feature.

2. CRYSTAL GROWTH AND CHARACTERIZATION

2.1 Crystal growth and structure

Crystals with composition of 3 at.% $\text{Yb}:\text{KY}(\text{MoO}_4)_2$ in the melt (Yb^{3+} ions are substituting for the Y^{3+} ones) were grown by the Low Temperature Gradient (LTG) Czochralski method [22]. As raw materials, we used Yb_2O_3 , Y_2O_3 , MoO_3 and K_2CO_3 . About 5-7 mol% of potassium trimolybdate ($\text{K}_2\text{Mo}_3\text{O}_{10}$) was added to the melt to prevent its possible partial dissociation resulting in the formation of yttrium oxomolybdate (Y_2MoO_6) and, thus, to stabilize the growth process. The growth was performed in a Pt crucible; the starting temperature was $\sim 970^\circ\text{C}$. A [100]-oriented seed from undoped $\text{KY}(\text{MoO}_4)_2$ was used. More details can be found elsewhere [16].

Once the growth was completed, the crystal was removed from the melt and slowly cooled down to room temperature (RT, 20°C). It was transparent and colorless; no post-growth annealing was applied. The crystal boule was oriented by means of single-crystal X-ray diffraction (XRD). It had a cylindrical shape and could be easily cleaved along the (100) crystallographic plane, resulting in a mirror-quality surfaces.

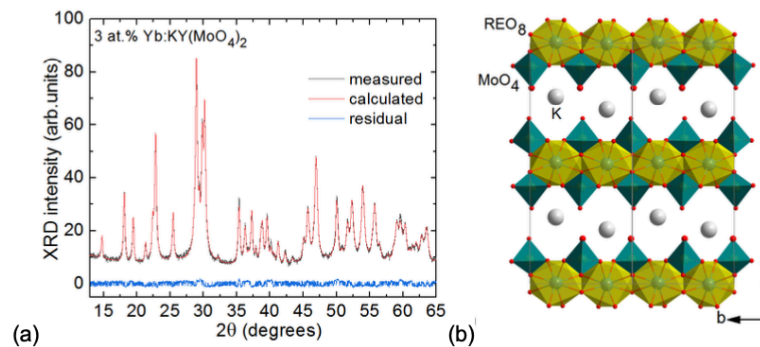


Figure 1. Rietveld analysis of the X-ray powder diffraction (XRD) pattern of 3 at.% $\text{Yb}:\text{KY}(\text{MoO}_4)_2$; (b) Fragment of $\text{Yb}:\text{KY}(\text{MoO}_4)_2$ crystal structure in projection onto the a - b plane.

The structure and phase purity of $\text{Yb}:\text{KY}(\text{MoO}_4)_2$ was confirmed by powder XRD, Fig. 1(a). The crystal belongs to the orthorhombic class (space group $Pbna - D_{2h}^{14}$). The crystal structure was refined using the Rietveld method. The

determined lattice constants are $a = 18.223(5) \text{ \AA}$, $b = 7.938(1) \text{ \AA}$, $c = 5.075(7) \text{ \AA}$, (number of the formula units in the unit-cell $Z = 4$). The R-factors obtained were $R_{wp} = 6.44\%$ and $R_{exp} = 5.19\%$. The volume of the unit cell is $732.7(1) \text{ \AA}^3$ and the calculated crystal density is 4.018 g/cm^3 .

According to the refined atomic coordinates, the crystal structure projection on the a - b plane was drawn, Fig. 1(b).

The Yb^{3+} ions in $\text{KY}(\text{MoO}_4)_2$ replace the Y^{3+} ones in a single type of sites (C_2 symmetry). The structure of $\text{Yb:KY}(\text{MoO}_4)_2$ consists of $[\text{Y}|\text{YbO}_8]$ polyhedra with shared edges which form continuous belts parallel to the b -axis. In the a - b plane, they share corners with the $[\text{MoO}_4]$ tetrahedra. Due to the weak linkage of the $[\text{Y}(\text{MoO}_4)_2]^-$ layers along the a -axis, the $\text{Yb:KY}(\text{MoO}_4)_2$ crystal exhibits a perfect cleavage feature along the (100) crystallographic plane.

By mechanical cleavage, we produced thin crystal-plates and crystal-films of $\text{Yb:KY}(\text{MoO}_4)_2$ with a thickness (t) down to $\sim 30 \text{ \mu m}$. The Scanning Electron Microscope (SEM) images of a fracture edge of such a crystal-plate and one of its (100) surfaces are shown in Fig. 2.

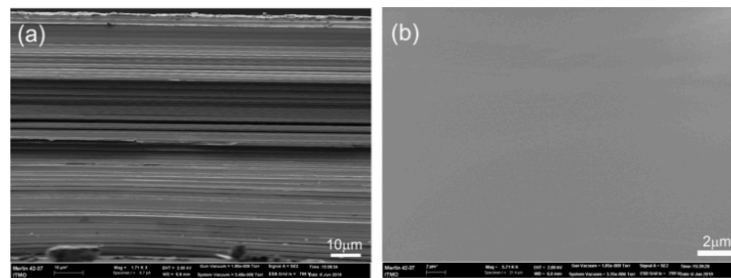


Figure 2. Scanning Electron Microscope (SEM) images of a cleaved crystal-plate of 3 at.% $\text{Yb:KY}(\text{MoO}_4)_2$: (a) the fracture edge of the plate, the a -axis is vertical; (b) the plate surface parallel to the (100) plane.

2.2 Optical spectroscopy

Prior to the laser experiments, we briefly describe the polarized spectroscopic properties of Yb^{3+} ions in $\text{KY}(\text{MoO}_4)_2$. The orthorhombic $\text{KY}(\text{MoO}_4)_2$ crystal is optically biaxial with high refractive index ($n \sim 1.95$). The optical indicatrix axes coincide with the crystallographic ones, so that the three principal light polarizations can be defined as $E \parallel a, b, c$.

The polarized absorption spectra in the 900-1100 nm range (the ${}^2F_{7/2} \rightarrow {}^2F_{5/2}$ Yb^{3+} transition) were measured using a Shimadzu UV-3600 spectrophotometer and a Glan-Taylor polarizer. The absorption cross-sections, σ_{abs} , were calculated as $\alpha_{\text{abs}}/N_{\text{Yb}}$ (where α_{abs} is the absorption coefficient and $N_{\text{Yb}} = 2.29 \times 10^{20} \text{ cm}^{-3}$ is the Yb^{3+} ion density).

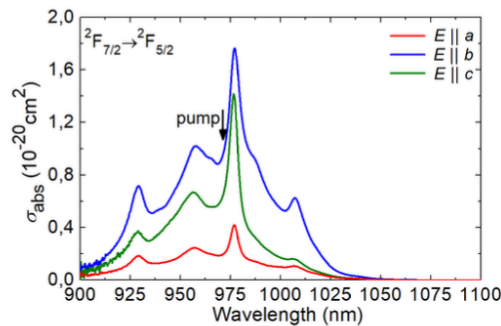


Figure 3. RT absorption cross-section, σ_{abs} , spectra of Yb^{3+} ions in $\text{KY}(\text{MoO}_4)_2$ for light polarizations $E \parallel a, b$ and c . The arrow indicates the pump wavelength used in the laser experiments.

The absorption spectra exhibit strong polarization anisotropy, Fig. 3. The maximum σ_{abs} is $1.77 \times 10^{-20} \text{ cm}^2$ at 977.1 nm and the full width at half maximum (FWHM) of the absorption peak is 19.6 nm for light polarization $E \parallel b$. For the other two light polarizations, the absorption cross-sections are lower, as expressed by the ratios $\sigma_{\text{abs}}(b) : \sigma_{\text{abs}}(c) = 1.26$ and $\sigma_{\text{abs}}(b) : \sigma_{\text{abs}}(a) = 4.2$ at $\sim 0.98 \text{ \mu m}$. This anisotropy arises, in part, from the layered crystal structure (note a significant drop of the optical absorption for light polarized orthogonal to the b - c layer plane) and, in part, from the low symmetry

of the Yb^{3+} ion site. The relatively broad absorption spectra make $\text{Yb:KY}(\text{MoO}_4)_2$ attractive for diode-pumping by InGaAs laser diodes emitting at $\sim 0.98 \mu\text{m}$.

The polarized luminescence spectra of $\text{Yb:KY}(\text{MoO}_4)_2$ around $\sim 1 \mu\text{m}$ were measured using an optical spectrum analyzer (Hamamatsu, AQ6373) and a Glan-Taylor polarizer. The stimulated-emission (SE) cross-sections, σ_{SE} , were calculated from the measured luminescence spectra calibrated for the spectral response of the set-up using the Füchtbauer-Ladenburg (F-L) formula [23]. The radiative lifetime τ_{rad} of the ${}^2\text{F}_{5/2}$ Yb^{3+} multiplet was taken as $458 \mu\text{s}$, as determined from the luminescence decay studies with thin (tens of μm) crystal films eliminating the radiation trapping effect [24].

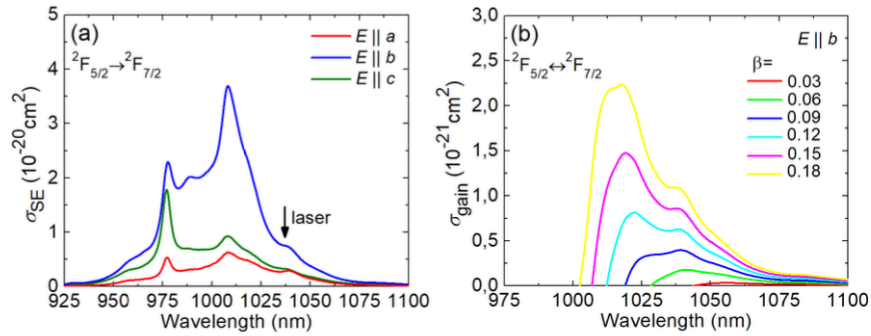


Figure 4. Emission properties of Yb^{3+} ions in $\text{KY}(\text{MoO}_4)_2$ crystal: (a) stimulated-emission (SE) cross-sections, σ_{SE} , for light polarizations $E \parallel a$, b and c . The arrow indicates the observed laser wavelength; (b) gain cross-sections, $\sigma_{\text{gain}} = \beta\sigma_{\text{SE}} - (1 - \beta)\sigma_{\text{abs}}$, $\beta = N_2({}^2\text{F}_{5/2})/N_{\text{Yb}}$ is the inversion ratio, the light polarization is $E \parallel b$.

For $\text{Yb:KY}(\text{MoO}_4)_2$, the maximum σ_{SE} amounts to $3.70 \times 10^{-20} \text{ cm}^2$ at 1008.0 nm and the emission bandwidth $\Delta\lambda_{\text{em}}$ is 37.0 nm for the high-gain light polarization $E \parallel b$. The emission spectra are also strongly polarized, as expressed by the ratios $\sigma_{\text{SE}}(b) : \sigma_{\text{SE}}(c) = 3.9$ and $\sigma_{\text{SE}}(b) : \sigma_{\text{SE}}(a) = 6.0$ at $1.08 \mu\text{m}$. This is a prerequisite for linearly polarized laser emission. Note that (100)-oriented crystal plates give access to the preferable light polarization $E \parallel b$.

For Yb^{3+} ions exhibiting reabsorption at the laser wavelength, the spectral behavior of the laser depends on the output-coupling losses via the level of inversion in the gain medium, expressed by the inversion ratio $\beta = N_2({}^2\text{F}_{5/2})/N_{\text{Yb}}$, where N_2 is the population of the upper level (${}^2\text{F}_{5/2}$) and $N_1 + N_2 = N_{\text{Yb}}$. Thus, the gain cross-sections, $\sigma_{\text{gain}} = \beta\sigma_{\text{SE}} - (1 - \beta)\sigma_{\text{abs}}$, are calculated to predict the possible laser wavelengths for different β . The σ_{gain} spectra for $E \parallel b$ are shown in Fig. 4(b). For small $\beta < 0.03$, the gain spectra are flat and broad extending from 1.05 to $1.1 \mu\text{m}$. For higher β up to 0.10 , there is a local maximum in the spectra at $\sim 1.04 \mu\text{m}$. For even higher inversion ratios, another maximum at a shorter wavelength of $\sim 1.02 \mu\text{m}$ is observed.

3. LASER OPERATION

3.1 Laser setup

The active elements for the laser experiments were obtained by mechanical cleavage of the 3 at.% $\text{Yb:KY}(\text{MoO}_4)_2$ crystal along the (100) plane. In this way, we produced a thin crystal-plate. No post-cleavage treatment (e.g., polishing) was applied to both surfaces which remained uncoated. The measured thickness of the crystal-plate was $t = 286 \mu\text{m}$ and it was very uniform ($\pm 2 \mu\text{m}$) over the clear aperture which exceeded 1 cm^2 . The crystal orientation corresponded to light propagation along the a -axis (a -cut). It is beneficial in regard to the pump absorption because it gives access to the light polarizations $E \parallel b$ and $E \parallel c$ corresponding to higher σ_{abs} values, cf. Fig. 3.

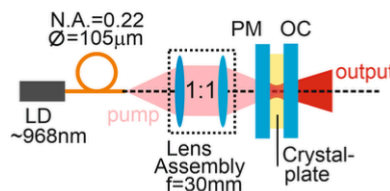


Figure 5. Scheme of the diode-pumped 3 at.% $\text{Yb:KY}(\text{MoO}_4)_2$ crystal-plate microchip laser: LD – laser diode, PM – pump mirror, OC – output coupler.

For laser experiments, we selected a plano-plano (microchip) laser cavity, Fig. 5. It was formed by a flat pump mirror (PM) coated for high transmission (HT) at $\sim 0.97 \mu\text{m}$ and for high reflection (HR) at $1.02\text{--}1.2 \mu\text{m}$, and a set of flat output couplers (OCs) providing a transmission at the laser wavelength T_{OC} of 0.5%–10%. Both cavity mirrors were gently pressed towards the crystal-film resulting in a nearly monolithic design. The geometrical cavity length L_{cav} was thus $\approx t$. The whole stack (cavity mirrors and crystal-plate) was passively cooled.

As a pump source, we employed an InGaAs fiber coupled laser diode (fiber core diameter: $105 \mu\text{m}$; numerical aperture (N.A.): 0.22) emitting unpolarized output at a central wavelength of $\sim 968 \text{ nm}$. The pump was collimated and focused into the crystal through the PM using a lens assembly (reimaging ratio: 1:1, focal length: $f = 30 \text{ mm}$). The pump spot size $2W_{\text{p}}$ in the focus was $100 \pm 10 \mu\text{m}$. The crystal-plate was pumped in a double-pass, as all the used OCs provided reflection at the pump wavelength, $R \sim 90\%$. The total pump absorption in two passes was estimated from the small-signal value as $\eta_{\text{abs},0} = 9.4\%$. This value does not account for the possible ground-state bleaching but at the same time does not overestimate the laser slope efficiency.

3.2 Laser performance

Laser operation in the CW regime was achieved for all employed OCs. The input-output dependences of the diode-pumped microchip crystal-plate Yb:KY(MoO₄)₂ laser are shown in Fig. 6(a). The laser generated a maximum output power of 0.81 W at 1021–1044 nm (the spectrum was modulated by etalon (Fabry-Perot) effects) with a high slope efficiency (η) of 76.4% vs. the absorbed pump power. The laser threshold P_{th} was as low as 56 mW whilst the optical-to-optical efficiency (vs. the pump power incident on the crystal) η_{opt} was relatively low, 7.0%, owing to the low pump absorption in the thin crystal. These characteristics were measured for $T_{\text{OC}} = 1.0\%$. With increasing the output coupling, the laser threshold gradually increased, from 55 mW for $T_{\text{OC}} = 0.5\%$ to 143 mW for $T_{\text{OC}} = 10\%$. The input-output dependences were linear for all the OCs. The absorbed pump power in the crystal-plate P_{abs} was limited to below 1.1 W in order to avoid thermal fracture of the passively cooled crystal.

The typical laser emission spectra are shown in Fig. 6(b). The spectra experienced a blue-shift with the increase of the output coupling: from 1020–1051 nm for $T_{\text{OC}} = 0.5\%$ to 1012–1020 nm for $T_{\text{OC}} = 10\%$. This is due to the quasi-three level nature of the Yb³⁺ laser transition ${}^2F_{5/2} \rightarrow {}^2F_{7/2}$ exhibiting reabsorption. The observed spectral behavior is in agreement with the gain spectra for $E \parallel b$, cf. Fig. 4(b). The laser output was linearly polarized ($E \parallel b$) and the polarization state was naturally selected by the anisotropy of the gain, Fig. 4(a). As pointed out above, the multi-peak spectral behavior was due to the etalon effect. The broad laser spectra originated from the broadband emission properties of Yb³⁺ in KY(MoO₄)₂.

The laser operation in the plano-plano cavity indicated a positive thermal lens for *a*-cut Yb:KY(MoO₄)₂.

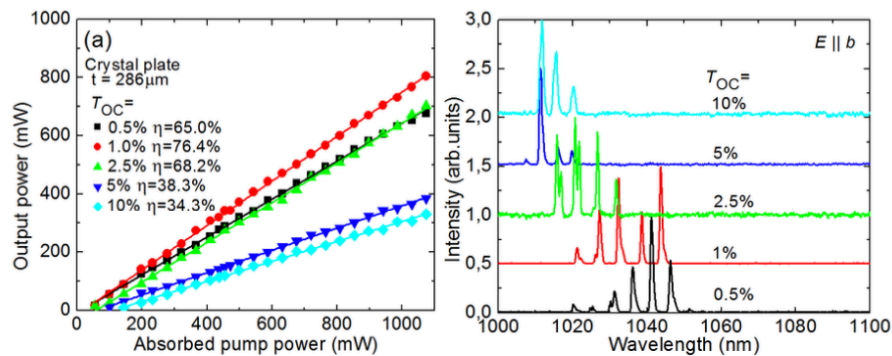


Figure 6. Diode-pumped Yb:KY(MoO₄)₂ crystal-plate microchip laser: (a) input-output dependences, η – slope efficiency; (b) typical laser emission spectra measured at $P_{\text{abs}} = 1.0 \text{ W}$. The laser polarization is $E \parallel b$.

4. CONCLUSIONS

To conclude, we report on the structure refinement, polarized room-temperature spectroscopy and first laser operation of a novel double molybdate compound with a layered structure, orthorhombic Yb:KY(MoO₄)₂. The structure of this crystal dictates a strong polarization-anisotropy of transition cross-sections for Yb³⁺ ions and a perfect natural cleavage habit along the (100) plane. As a result, mechanically cleaved thin crystal films and plates (with a thickness down to tens

of μm) can be directly used for efficient laser operation. We report on a watt-level output from a diode-pumped microchip 3 at.% Yb:KY(MoO₄)₂ laser operating with a high slope efficiency (76.4%) almost approaching the Stokes limit. Highly Yb³⁺-doped KY(MoO₄)₂ crystal plates and films are attractive for short-pulse (sub-ns) passively Q-switched microchip lasers [10], as well as thin-disk lasers.

ACKNOWLEDGMENTS

The reported study was partially supported by RFBR (project No. 19-32-90199). The authors acknowledge financial support from the Spanish Government under Project MAT2016-75716-C2-1-R (AEI/FEDER,UE) and from the Catalan Government under Project 2017 SGR 755.


REFERENCES

- [1] Petrov, V., Pujol, M. C., Mateos, X., Silvestre, O., Rivier, S., Aguiló, M., Solé, R., Liu, J., Griebner, U., and Díaz, F., "Growth and properties of KLu(WO₄)₂, and novel ytterbium and thulium lasers based on this monoclinic crystalline host," *Laser & Photon. Rev.* 1(2), 179–212 (2007).
- [2] Liu, J., Petrov, V., Mateos, X., Zhang, H., and Wang, J., "Efficient high-power laser operation of Yb:KLu(WO₄)₂ crystals cut along the principal optical axes," *Opt. Lett.* 32(14), 2016-2018 (2007).
- [3] Griebner, U., Rivier, S., Petrov, V., Zorn, M., Erbert, G., Weyers, M., Mateos, X., Aguiló, M., Massons, J. and Díaz, F., "Passively mode-locked Yb:KLu(WO₄)₂ oscillators," *Opt. Express* 13(9), 3465-3470 (2005).
- [4] Pujol, M. C., Bursukova, M. A., Güell, F., Mateos, X., Solé, R., Gavalda, J., Aguiló, M., Massons, J., Díaz, F., Klopp, P., Griebner, U., and Petrov, V., "Growth, optical characterization and laser operation of a stoichiometric crystal KYb(WO₄)₂," *Phys. Rev. B* 65(16), 165121-1-11 (2002).
- [5] Mateos, X., Solé, R., Gavalda, J., Aguiló, M., Massons, J., Díaz, F., Petrov, V., and Griebner, U., "Crystal growth, spectroscopic studies and laser operation of Yb³⁺-doped potassium lutetium tungstate," *Opt. Mater.* 28(5), 519-523 (2006).
- [6] Kuleshov, N. V., Lagatsky, A. A., Shcherbitsky, V. G., Mikhailov, V. P., Heumann, E., Jensen, T., Diening, A., and Huber, G., "CW laser performance of Yb and Er,Yb doped tungstates," *Appl. Phys. B* 64(4), 409-413 (1997).
- [7] Serres, J. M., Loiko, P., Mateos, X., Yumashev, K., Kuleshov, N., Petrov, V., Griebner, U., Aguiló, M., and Díaz, F., "Prospects of monoclinic Yb:KLu(WO₄)₂ crystal for multi-watt microchip lasers," *Opt. Mater. Express* 5(3), 661-667 (2015).
- [8] Loiko, P., Manjoran, S., Yumashev, K., and Major, M., "Polarization anisotropy of thermal lens in Yb:KY(WO₄)₂ laser crystal under high-power diode pumping," *Appl. Opt.* 56(10), 2937-2945 (2017).
- [9] Loiko, P. A., Kisel, V. E., Kondratuk, N. V., Yumashev, K. V., Kuleshov, N. V., and Pavlyuk, A. A., "14 W high-efficiency diode-pumped cw Yb:KGd(WO₄)₂ laser with low thermo-optic aberrations," *Opt. Mat.* 35(3), 582-585 (2013).
- [10] Loiko, P., Serres, J. M., Mateos, X., Yumashev, K., Yasukevich, A., Petrov, V., Griebner, U., Aguiló, M., and Díaz, F., "Sub-nanosecond Yb:KLu(WO₄)₂ microchip laser," *Opt. Lett.* 41(11), 2620-2623 (2016).
- [11] Klopp, P., Petrov, V., Griebner, U., and Erbert, G., "Passively mode-locked Yb:KYW laser pumped by a tapered diode laser," *Opt. Express* 10(2), 108-113 (2002).
- [12] Rivier, S., Mateos, X., Silvestre, O., Petrov, V., Griebner, U., Pujol, M. C., Aguiló, M., Díaz, F., Vernay, S., and Rytz, D., "Thin-disk Yb:KLu(WO₄)₂ laser with single-pass pumping," *Opt. Lett.* 33(7), 735-737 (2008).
- [13] Brunner, F., Südmeyer, T., Innerhofer, E., Morier-Genoud, F., Paschotta, R., Kisel, V. E., Shcherbitsky, V. G., Kuleshov, N. V., Gao, J., Contag, K., Giesen, A., and Keller, U., "240-fs pulses with 22-W average power from a mode-locked thin-disk Yb:KY(WO₄)₂ laser," *Opt. Lett.* 27(13), 1162-1164 (2002).
- [14] Klevtsova, R. F. and Borisov, S. V., "X-ray structural study of the double molybdate KY(MoO₄)₂," *Sov. Phys. Dokl.* 12, 1095 (1968) [Transl. from *Dokl. Akad. Nauk SSSR* 177(6), 1333-1336 (1967)].
- [15] Kaminskii, A. A., Klevtsov, P. V., and Pavlyuk, A. A., "Stimulated emission from KY(MoO₄)₂-Nd³⁺ crystal laser," *Phys. Status Solidi A* 1(3), K91-K94 (1970).
- [16] Volokitina, A., Loiko, P., Vilejshikova, E., Mateos, X., Dunina, E., Kornienko, A., Kuleshov, N., and Pavlyuk, A., "Eu³⁺:KY(MoO₄)₂: A novel anisotropic red-emitting material with a layered structure," *J. Alloy Compd.* 762, 786-796 (2018).

- [17] Chen, Y., Lin, Y., Gong, X., Tan, Q., Luo, Z., and Huang, Y., "Polarized spectral characteristics of $\text{Nd}^{3+}:\text{KY}(\text{MoO}_4)_2$ crystal with perfect cleavage planes: a promising microchip gain medium," *J. Opt. Soc. Am. B* 24(3), 496-503 (2007).
- [18] Hanuza, J. and Łabuda, L., "Polarized Raman and infrared spectra of a multilayer $\text{KY}(\text{MoO}_4)_2$ crystal," *J. Raman Spectr.* 11(4), 231-237 (1981).
- [19] Kaminskii, A. A. and Verdun, H. R., "New high power, high efficient quasi-CW and CW single-mode $\text{KY}(\text{MoO}_4)_2:\text{Nd}^{3+}$ laser end-pumped by a GaAlAs laser-diode array," *Phys. Status Solidi A* 138(1), K49-K53 (1993).
- [20] Loiko, P., Kifle, E., Serres, J.M., Mateos, X., Aguiló, M., Díaz, F., Vilejshikova, E., Kuleshov, N., and Pavlyuk, A., "Efficient continuous-wave in-band pumped $\text{Nd}:\text{KY}(\text{MoO}_4)_2$ laser," *Laser Phys. Lett.* 15(6), 065002-1-5 (2018).
- [21] Kaminskii A. A. and Bagayev, S. N., "Ribbon and sheet miniature crystal laser," *Quantum Electron.* 24(12), 1029-1030 (1994).
- [22] Borovlev, Y. A., Ivannikova, N. V., Shlegel, V. N., Vasiliev, Y. V., and Gusev, V. A., "Progress in growth of large sized BGO crystals by the low-thermal-gradient Czochralski technique," *J. Cryst. Growth* 229(1-4), 305-311 (2001).
- [23] Aull, B. and Jenssen, H., "Vibronic interactions in $\text{Nd}:\text{YAG}$ resulting in nonreciprocity of absorption and stimulated emission cross sections," *IEEE J. Quantum Electron.* 18(5), 925-930 (1982).
- [24] Volokitina, A., Loiko, P., Serres, J.M., Mateos, X., Kuleshov, N., Trifonov, V. and Pavlyuk, A., "Growth and spectroscopy of orthorhombic $\text{Yb}:\text{KY}(\text{MoO}_4)_2$ laser crystal with a layered structure," *J. Phys.: Conf. Ser.* 1410(1), 012149 (2019).



Spectroscopy and efficient laser operation of cleaving Yb:KY(MoO₄)₂ crystal

ANNA VOLOKITINA,^{1,2}  PAVEL LOIKO,³ ANATOLY PAVLYUK,⁴
JOSEP MARIA SERRES,¹  SAMI SLIMI,^{1,5} EZZEDINE BEN SALEM,⁵
ESROM KIFLE,¹ UWE GRIEBNER,⁶ VALENTIN PETROV,⁶ LI WANG,⁶
WEIDONG CHEN,^{6,7}  ROSA MARIA SOLÉ,¹ MAGDALENA AGUILÓ,¹
FRANCESC DÍAZ,¹ AND XAVIER MATEOS^{1,*} 

¹Universitat Rovira i Virgili (URV), Física i Cristal·lografia de Materials i Nanomaterials (FiCMA-FiCNA)-EMaS, Marcel·li Domingo 1, 43007 Tarragona, Spain

²ITMO University, 49 Kronverkskiy Pr., 197101 St. Petersburg, Russia

³Centre de Recherche sur les Ions, les Matériaux et la Photonique (CIMAP), UMR 6252 CEA-CNRS-ENSICAEN, Université de Caen Normandie, 6 Boulevard du Maréchal Juin, 14050 Caen Cedex 4, France

⁴A. V. Nikolaev Institute of Inorganic Chemistry, Siberian Branch of Russian Academy of Sciences, 3 Lavrentyev Ave., 630090 Novosibirsk, Russia

⁵I.P.E.I. of Monastir, Unit of Materials and Organic Synthesis, UR17ES31, 5019 Monastir, Tunisia

⁶Max Born Institute for Nonlinear Optics and Short Pulse Spectroscopy, Max-Born-Str. 2a, 12489 Berlin, Germany

⁷Key Laboratory of Optoelectronic Materials Chemistry and Physics, Fujian Institute of Research on the Structure of Matter, Chinese Academy of Sciences, Fuzhou, 350002 Fujian, China

*xavier.mateos@urv.cat

Abstract: We report on the first laser operation of ytterbium-doped potassium yttrium double molybdate crystal (Yb:KY(MoO₄)₂). Single-crystals containing 3 at.% Yb³⁺-ions were grown by the low temperature gradient Czochralski method. The crystal structure (orthorhombic, sp. gr. D¹⁴_{2h} – *Pbna*) was refined with the Rietveld method. Yb:KY(MoO₄)₂ exhibits a layered structure leading to a strong optical anisotropy and a perfect cleavage along the crystallographic (100) plane. The maximum stimulated-emission cross-section amounts to 3.70×10⁻²⁰ cm² at 1008.0 nm with an emission bandwidth of 37 nm (for light polarization *E* || *b*). The Stark splitting is determined at 6 K. Continuous-wave laser operation is achieved in a thin Yb:KY(MoO₄)₂ crystal plate (thickness: 286 μm) under diode pumping. The microchip laser generated a maximum output power of 0.81 W at 1021-1044 nm with a slope efficiency of 76.4% and polarized emission. Yb:KY(MoO₄)₂ crystal lamellae / plates are attractive for sub-ns passively Q-switched microchip lasers and thin-disk lasers.

© 2020 Optical Society of America under the terms of the [OSA Open Access Publishing Agreement](#)

1. Introduction

Cleavage is the property of crystalline materials to split along certain crystallographic planes. The simplest case is basal or pinacoidal cleavage when this happens along only a single plane. It may result from a weaker bond strength or larger lattice spacing perpendicular to the plane, and it is frequently observed in crystals with a regular location of atoms forming “layers”. As a result, crystalline plates with continuous, smooth and flat faces, both strictly parallel to the so-called cleavage plane are easily obtained. An example of a cleaving mineral is mica showing perfect (or even “eminent”) cleavage. Crystals with perfect cleavage can cleave without leaving any rough surface (mirror-quality) [1]. Cleavage is used for identification of minerals. It is also useful for chipping of wafers of semiconductor crystals (e.g., silicon).

Laser crystals exhibiting perfect cleavage along a crystallographic plane are known [1–3]. On the one hand, this complicates their mechanical processing (cutting and polishing). On the other hand, it can turn out to be a useful feature for applications where thin laser elements with a large aperture and good parallelism / optical quality of the faces are required. Moreover, this simplifies fabrication of laser elements, especially for soft crystals. Two examples are the microchip and thin-disk lasers. In particular, a microchip laser consists of a thin (typically, few hundred μm thick) gain medium placed in a simple plano-plano cavity without air gaps, leading to a highly-compact and monolithic design (optionally, one or both of the cavity mirrors are coated on the crystal faces) [4]. Note a positive thermal lens of the gain material for stabilizing the laser mode of microchip lasers is an important requirement [5]. This robust design is almost insensitive to misalignment and leads to low intracavity losses, low laser threshold, good cavity stability and very short cavity roundtrip time beneficial for achieving sub-ns pulses in passively Q-switched lasers [6].

So far, only few crystals doped with rare-earth ions (RE^{3+}) such as Nd^{3+} , Yb^{3+} or Tm^{3+} showing perfect cleavage have been applied for lasers in the near-IR, cf. Table 1. These include borates (LaB_3O_6) [7], phosphates (YPO_4 and LuPO_4) [8,9] and molybdates ($\text{BaGd}_2(\text{MoO}_4)_4$) [10]. Other cleaving crystals were proposed as potential laser materials (e.g., $\text{CsGd}(\text{MoO}_4)_2$) [11] but no laser operation has been reported so far. Yb^{3+} -doped materials are known for efficient laser operation at $\sim 1 \mu\text{m}$ on the ${}^2\text{F}_{5/2} \rightarrow {}^2\text{F}_{7/2}$ electronic transition. The Yb^{3+} ion can be easily pumped by commercially available high-power InGaAs laser diodes emitting at $\sim 0.96\text{--}0.98 \mu\text{m}$ [12]. It also exhibits a simple energy level scheme eliminating parasitic energy-transfer processes. In-band pumping of Yb^{3+} leads to high pump Stokes efficiency, and, thus, reduced heat load and slope efficiencies up to $\sim 80\%$ [13]. Moreover, as compared to Nd^{3+} , Yb^{3+} shows larger Stark splitting of the ground-state (${}^2\text{F}_{7/2}$) and, consequently, broader emission at $\sim 1 \mu\text{m}$, beneficial for broadly tunable and mode-locked lasers. Liu *et al.* reported on a diode-pumped $\text{Yb}:\text{LuPO}_4$ laser based on a (100)-oriented unprocessed as-grown crystal plate delivering 1.61 W at 1036–1040 nm with a slope efficiency of 75% [8]. Zhu *et al.* used cleaved plates of $\text{Yb}:\text{BaGd}_2(\text{MoO}_4)_4$ and produced a similar output power (1.16 W at 1046–1054 nm) albeit with much lower slope efficiency (20%) [1].

Table 1. Laser Performance^a of RE^{3+} -doped Cleaving Crystals

Crystal	Plane	t , mm	P_{out} , W	λ_L , nm	η , %	P_{th} , W	Ref.
Nd: LaB_3O_6	(101)	0.5	0.53	1060	49	~ 0.03	[7]
Nd: YPO_4	(010)	0.6	2.16	1063	56.4	0.22	[9]
Nd: $\text{BaGd}_2(\text{MoO}_4)_4$	(010)	1.1	0.70	1061	51	< 0.01	[14]
$\text{Yb}:\text{LuPO}_4$	(100)	0.3	1.61	1036–1040	75	0.17	[8]
$\text{Yb}:\text{BaGd}_2(\text{MoO}_4)_4$	(010)	4.0	1.16	1046–1054	20	5.8	[1]
$\text{Yb}:\text{KY}(\text{MoO}_4)_2$	(100)	0.29	0.81	1021–1044	76.4	0.06	This work
$\text{Tm}:\text{KY}(\text{MoO}_4)_2$	(100)	0.70	0.88	1840–1905	65.8	0.21	[3]
$\text{Tm}:\text{BaGd}_2(\text{MoO}_4)_4$	(010)	1.6	0.35	1905–1921	49	0.1	[10]

^a t - thickness, P_{out} - output power, λ_L - laser wavelength, η - slope efficiency, P_{th} - laser threshold.

Among the host crystals for Yb^{3+} doping, complex tungstates and molybdates are attracting a lot of attention. Their advantages include: (i) high attainable Yb^{3+} doping concentrations; (ii) weak luminescence quenching, (iii) low non-radiative relaxations and luminescence quantum yields approaching unity, (iv) polarized, intense and broad absorption and emission bands at $1 \mu\text{m}$, and (v) Raman activity. A prominent example is the crystal family of monoclinic double tungstates with chemical formula $\text{KLn}(\text{WO}_4)_2$, where $\text{Ln} = \text{Gd}, \text{Y}$ or Lu [15,16]. Efficient continuous-wave [12,17], passively Q-switched [6] and especially mode-locked [18,19] $\text{Yb}:\text{KLn}(\text{WO}_4)_2$ lasers

are known. Thin-disk lasers based on these materials were also demonstrated using thin bulk or epitaxial samples [20,21].

Compared to the above mentioned potassium double tungstates, their double molybdate (DMo) counterparts with chemical formula $\text{KLn}(\text{MoO}_4)_2$ have been barely studied. One example of the DMo crystal family is potassium yttrium double molybdate, $\text{KY}(\text{MoO}_4)_2$ [22–24]. It is orthorhombic and exhibits an interesting layered structure together with a low-symmetry site for the RE ions (C_2) leading to a strong anisotropy of the optical properties as well as to the natural cleavage habit [22]. The structure and vibronic properties of undoped $\text{KY}(\text{MoO}_4)_2$ have been reported [25,26]. The RE^{3+} site symmetry was revealed using Eu^{3+} as a structural probe [22]. Very recently, we achieved laser operation in cleaved single-crystalline plates and thin films of $\text{Tm:KY}(\text{MoO}_4)_2$ [3]. A crystal-plate laser generated 0.88 W at 1840-1905nm with a slope efficiency of 65.8%. The concept of the *thin-film* laser using cleaved $\text{Nd:KY}(\text{MoO}_4)_2$ was first proposed [27] by Kaminski *et al.*

In the present work, we demonstrate laser operation of a $\text{Yb:KY}(\text{MoO}_4)_2$ crystal, for the first time to the best of our knowledge, by using its perfect cleavage feature.

2. Crystal growth

The $\text{Yb:KY}(\text{MoO}_4)_2$ compound melts at ~ 1243 K. The single crystals were grown by the Low Temperature Gradient (LTG) Czochralski method [28]. As raw materials, we used Y_2O_3 (purity: 5N), Yb_2O_3 (4N), MoO_3 (4N) and K_2CO_3 (5N) taken according to the composition 95-93mol% $\text{KY}_{0.97}\text{Yb}_{0.03}(\text{MoO}_4)_2$ solute – 5-7 mol% $\text{K}_2\text{Mo}_3\text{O}_{10}$ solvent assuming substitution of Y^{3+} ions by the Yb^{3+} dopants (3 at.% Yb). The potassium trimolybdate ($\text{K}_2\text{Mo}_3\text{O}_{10}$) was added to the melt to prevent its partial dissociation resulting in the formation of yttrium oxomolybdate (Y_2MoO_6) and, thus, to stabilize the growth process [22]. The raw materials were mixed and placed in a Pt crucible. It was heated up to ~ 1320 K in air and kept at this temperature for 2–3 hours to homogenize the melt. Then, it was cooled to ~ 1240 K (the temperature where the growth started). A [100]-oriented seed from an undoped $\text{KY}(\text{MoO}_4)_2$ was used. It was rotated at 20 rpm, the pulling rate was 1–2 mm/h and the cooling rate was ~ 2 K/day. The temperature gradient in the melt was below 3 K/cm (in the vertical direction). After completing the growth, the crystal was removed from the melt and slowly cooled down to room temperature (RT, 293 K). No annealing was applied. More details can be found elsewhere [3,22].

The as-grown crystals were transparent and colorless, Fig. 1. They had a cylindrical shape with an elliptic cross-section with the semiaxes oriented along the [010] and [001] directions. Neither cracks nor inclusions were observed. The crystals showed an easy cleavage along the (100) plane (orthogonal to the growth direction). The orientation of the [010] and [001] axes was determined by single-crystal X-ray diffraction.

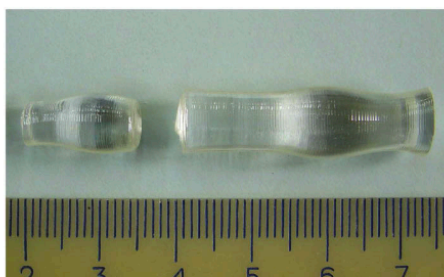


Fig. 1. A photograph of as-grown 3 at.% $\text{Yb:KY}(\text{MoO}_4)_2$ crystals. The growth direction is along the [100] crystallographic axis.

The actual Yb^{3+} doping concentration was determined by Energy Dispersive X-ray (EDX) spectroscopy to be $N_{\text{Yb}} = 2.3 \pm 0.5 \times 10^{20} \text{ cm}^{-3}$ (~ 3.0 at.% Yb), so that the segregation coefficient for Yb^{3+} doping $K_{\text{Yb}} = N_{\text{crystal}}/N_{\text{melt}}$ was close to unity.

3. Crystal structure

3.1. Rietveld refinement

The structure and phase purity of the 3 at.% Yb:KY(MoO₄)₂ was confirmed by X-ray powder diffraction (XRD), Fig. 2(a). The measurements were carried out in a θ - θ Bragg Brentano configuration using a Siemens D-5000 powder X-ray diffractometer with Cu K α (1.5406 Å) radiation. The XRD pattern was recorded in a 2θ range from 10° to 65°, a step size of 0.02° and a step time of 16 s. The crystal belongs to the orthorhombic class (sp. gr. *Pbna* – D¹⁴_{2h}, centrosymmetric point group *2/m*). Note that we use the non-conventional space group (the standard one is *Pbcn*, No. 60), following the early publications [25,29]. The unit cell parameters refined using the Le Bail method are: $a = 18.212(2)$ Å, $b = 7.9343(6)$ Å, $c = 5.0705(5)$ Å (number of the formula units in the unit-cell $Z = 4$). The obtained R -factors were $R_{\text{wp}} = 6.44\%$ and $R_{\text{exp}} = 5.19\%$ (the reduced χ -squared value $\chi^2 = (R_{\text{wp}}/R_{\text{exp}})^2 = 1.54$). The calculated volume of the unit cell V is $732.7(1)$ Å³ and the crystal density $\rho_{\text{calc}} = 4.083(6)$ g/cm³. The structure from [22] was taken as the starting one for the refinement. The fractional atomic coordinates were refined by the Rietveld method using the TOPAS software, see the results in Table 2, with the fixed unit cell parameters obtained by the Le Bail's method and considering the (100) preferred orientation. For this refinement, $R_{\text{wp}} = 8.90\%$ and $R_{\text{exp}} = 5.19\%$ ($\chi^2 = 2.94$). Figure 2 shows the Rietveld refinement plot with the observed, calculated and difference patterns. No other phases except the orthorhombic one are found in the pattern. The min / max residual electron densities are $-0.6 \text{ e}/\text{Å}^3$ and $+0.1 \text{ e}/\text{Å}^3$, respectively.

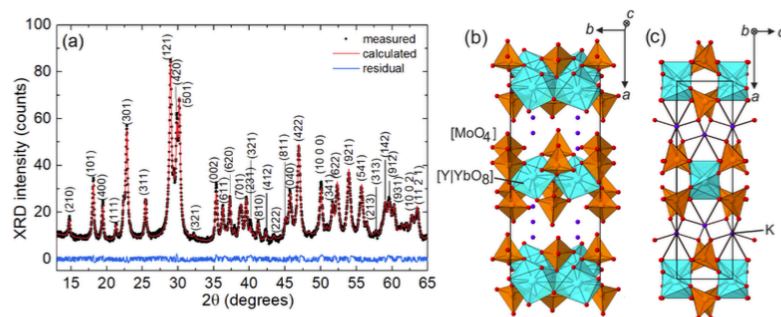


Fig. 2. (a) Rietveld analysis of the RT X-ray powder diffraction (XRD) pattern of a 3 at.% Yb:KY(MoO₄)₂ crystal, the numbers denote the Miller's indices (*hkl*) for the sp. gr. *Pbna*; (b,c) Illustration of the layered structure of the Yb:KY(MoO₄)₂ crystal: (b) three-dimensional view, (c) a projection of the *a-c* plane. Black rectangle denotes the unit-cell.

The unit-cell parameters are slightly smaller than those for undoped KY(MoO₄)₂, $a = 18.23$ Å, $b = 7.95$ Å, $c = 5.07$ Å [25]. In KY(MoO₄)₂, the Yb^{3+} ions substitute for the Y^{3+} ones in a single type of crystallographic sites (Wyckoff symbol: 4c, site symmetry: C_2 , coordination number (C.N.): VIII). The corresponding ionic radii are $R_{\text{Yb}} = 0.985$ Å and $R_{\text{Y}} = 1.019$ Å for VIII-fold oxygen coordination [30], explaining the observed decrease of the lattice constants. The closeness of the ionic radii of Yb^{3+} and Y^{3+} , the existence of the orthorhombic stoichiometric KYb(MoO₄)₂ phase [31] and the homovalent doping mechanism also explain the observed $K_{\text{Yb}} \approx 1$.

Table 2. Fractional Atomic Coordinates (x, y, z), Occupancy Factors (O.F.) and Temperature Factors (B_{iso}) for 3 at.% Yb:KY(MoO₄)₂ (Space Group Pbn_a)

Atom	Wyckoff symbol	x	y	z	O.F.	B_{iso}
K	4c	0.2713(4)	0.25	0	1	2.6(3)
Y	4c	0.5060(2)	0.25	0	0.97	0.94(1)
Yb	4c	0.5060(2)	0.25	0	0.03	0.94(1)
Mo	8d	0.1014(1)	-0.0163(3)	0.0204(6)	1	0.83(8)
O1	8d	0.1885(6)	0.531(2)	0.102(2)	1	1.6(2)
O2	8d	0.1001(1)	0.834(2)	0.245(2)	1	1.6(2)
O3	8d	0.1039(1)	0.164(2)	0.230(2)	1	1.6(2)
O4	8d	0.4716(7)	-0.034(4)	0.2804(2)	1	1.6(2)

Using the refined atomic coordinates, the structure of Yb:KY(MoO₄)₂ is illustrated in Fig. 2(b,c). The corresponding interatomic distances are listed in Table 3. The C.N. for Mo⁶⁺ cations is 4 + 1: a distorted tetrahedral coordination (with 4 closely located oxygens, with the Mo – O distances lying in the range 1.644(8) – 1.847(6) Å and 1 more distant oxygen at 2.5735 Å). For K⁺, the C.N. is 6 + 4, defined in a similar manner. The closest 6 oxygens are at 2.742(1) – 2.759(6) Å, while the other oxygens are at 3.335(2) – 4.223(0) Å. Such a coordination behavior is common for tungstates and molybdates with a C.N. of W (or Mo) of V or VI, where the cation – anion distances may vary in a broad range, so that a formal definition of the C.N. is not possible [25]. For the distorted [Y|YbO₈] polyhedra (bicapped octahedra), the bond lengths are in the range 2.26(2) – 2.74(3) Å. The belts of edge-sharing [Y|YbO₈] polyhedra run along the *b*-axis. Along the *c*-axis, they are separated by an empty polyhedron which is sharing 4 edges with four [MoO₄] tetrahedra. Each Mo-tetrahedron connects two translationally identical belts of Y-polyhedra and, simultaneously, it connects the corners of two adjacent Y-polyhedra (within the belt). Thus, the multi-layer structure of Yb:KY(MoO₄)₂ is determined by [Y|Yb(MoO₄)₂] layers (lying in the *b-c* plane) formed by [MoO₄] tetrahedra and [Y|YbO₈] polyhedra and containing cavities, as well as zigzag K⁺-layers separating two neighboring [Y|Yb(MoO₄)₂] layers. The zigzag K⁺-layers are more loose than the [Y|Yb(MoO₄)₂] ones. Moreover, the latter are separated by a relatively large *a*/2 spacing of 9.106 Å. This determines the natural cleavage along the (100) plane.

Table 3. Selected Interatomic Distances in 3 at.% Yb:KY(MoO₄)₂

Distances (Å)		
[Y Yb]O ₈	[Mo]O ₄₊₁	[K]O ₆₊₄
Y Yb – O4 = 2.261(2) × 2	Mo – O3 = 1.784(6) × 1	K – O1 = 2.742(1) × 2
Y Yb – O3 = 2.348(0) × 2	Mo – O4 = 1.847(6) × 1	K – O1' = 2.759(6) × 2
Y Yb – O2 = 2.418(9) × 2	Mo – O2 = 1.644(8) × 1	K – O2 = 2.756(2) × 2
Y Yb – O4' = 2.743(1) × 2	Mo – O1 = 1.708(7) × 1	K – O2' = 3.335(2) × 1
Y Yb – Y Yb = 3.973(2) × 2 ^a	Mo – O4 = 2.5735 × 1	K – O1'' = 3.587(6) × 2
Y Yb – Y Yb = 5.071(5) × 2 ^b		K – O3 = 4.223(0) × 1

^{a,b}The shortest Y|Yb – Y|Yb distances are added for comparison.

^aAlong the *b*-axis.

^bAlong the *c*-axis (sp. gr. Pbn_a).

The shortest Y|Yb – Y|Yb distance is 3.973 Å (along the *b*-axis, in the layer plane). It is relatively long and similar to that (Y – Y) in the monoclinic KY(WO₄)₂ crystal (4.06 Å) [22]. This distance determines the weak cross-talk of Yb³⁺ ions (weak concentration quenching of luminescence) along the *a*-axis (orthogonal to the layer plane), 9.45 Å.

The coefficients of thermal expansion (CTE) of Yb:KY(MoO₄)₂ were calculated from the temperature dependence of the lattice constants determined by high-temperature powder XRD. For the XRD studies in the temperature range of 300–550 K, we used a temperature chamber (HTK10). The heating rate was 0.17 K/s with a delay of 300 s before each measurement. The 2θ angle varied from 10° to 70° with a step size of 0.03° and a step time of 5 s. The relative evolution of the unit cell parameters with temperature is shown in Fig. 3. The linear thermal expansion tensor (α_{ij}) in *abc* frame was obtained from the slopes of the linear fits shown in Fig. 3. Thus, (α_{ij}) is:

$$(\alpha_{ij}) = \begin{pmatrix} 38.3 & 0 & 0 \\ 0 & 23.4 & 0 \\ 0 & 0 & 5.36 \end{pmatrix} \times 10^{-6} \text{K}^{-1}. \quad (1)$$

The coefficient of the volumetric thermal expansion, $\alpha_{\text{vol}} = \alpha_a + \alpha_b + \alpha_c$ is $67.1 \times 10^{-6} \text{K}^{-1}$.

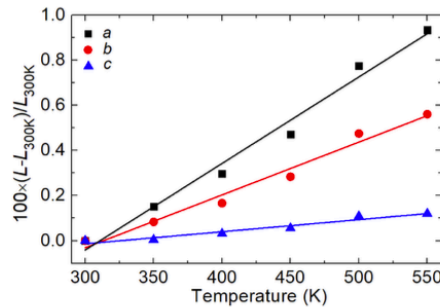


Fig. 3. Relative thermal evolution of the unit cell parameters of 3 at.% Yb:KY(MoO₄)₂ with the temperature up to 550 K.

The anisotropy of the thermal expansion in Yb:KY(MoO₄)₂ is relatively strong, as expressed by the ratios $\alpha_a : \alpha_b = 1.64$ and $\alpha_a : \alpha_c = 7.15$. The thermal expansion in KY(MoO₄)₂ is stronger than in its double tungstate counterpart. Indeed, for KY(WO₄)₂, $\alpha_a = 8.4$, $\alpha_b = 2.0$ and $\alpha_{c^*} = 19.8$ [10^{-6}K^{-1}] [32].

The thermal conductivity of KY(MoO₄)₂ is unknown but it is expected to be higher in the layer plane.

By mechanical cleavage orthogonal to the crystal growth direction (along the (100) plane), we produced single-crystalline plates of Yb:KY(MoO₄)₂ with a thickness (*t*) as thin as 100 μm. They were studied by Scanning Electron Microscopy (SEM) using a MERLIN microscope (Carl Zeiss). Under bending, the plates exhibited an elastic deformation along the [010] axis and broke with the fracture edge running parallel to the [001] axis, Fig. 4(a). This SEM image shows multiple “steps” parallel to the (100) cleavage plane. Both surfaces of the cleaved plates had mirror-quality. No polishing was applied to them. The SEM study in the μm-scale revealed dark flower-like defects, Fig. 4(b); however, the concentration of these defects was low. The clean aperture of the obtained crystal-plates was > 1 cm². They contained no macroscopic cracks.

3.2. Raman spectra

Molybdate crystals are known as efficient Raman-active materials. Thus, Yb:KY(MoO₄)₂ can serve for self-frequency Raman conversion. The RT polarized Raman spectra were measured using a confocal Raman microscope (Renishaw inVia) equipped with an ×50 objective, an edge filter and an Ar⁺ ion laser (488 nm). A cleaved crystal plate (*a*-cut) was used and the excitation / collection geometries were *a*(*mn*)*a*, where *m*, *n* = *b*, *c* (according to Porto’s notations).

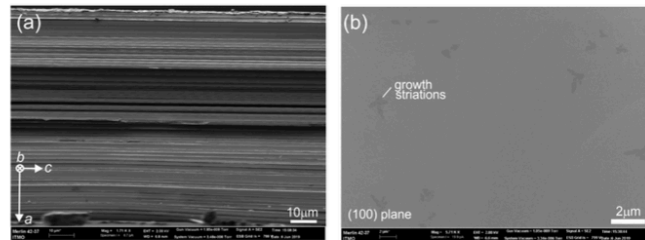


Fig. 4. Scanning Electron Microscope (SEM) images of a cleaved single-crystal plate of 3 at.% Yb:KY(MoO₄)₂: (a) the fracture edge of the plate running along the *c*-axis, the *a*-axis is vertical; (b) the plate surface parallel to the (100) plane showing flower-like defects.

The Raman spectra are shown in Fig. 5. They are strongly polarized with the most intense Raman response in the *a(bb)a* geometry. The observed bands are classified into three groups of vibrations [22,26]. The low-frequency range, 80-272 cm⁻¹, contains translational (*T'*) and rotational (*R'*) modes of the K, Y|Yb and Mo cations. Internal bending vibrations (δ) of the oxygen bridged [MoO₄] tetrahedra are observed in the intermediate frequency range, 315–435 cm⁻¹. The high-frequency range, 726-944 cm⁻¹, contains intense stretching vibrations (ν) of these tetrahedra. The gap in the Raman spectra (500-700 cm⁻¹) is due to the relatively weak oxygen linkage of the [MoO₄] tetrahedra in the layer plane. This feature is similar to the one found in scheelite (CaWO₄) type double tungstate and molybdate crystals with isolated [WO₄] tetrahedra [33].

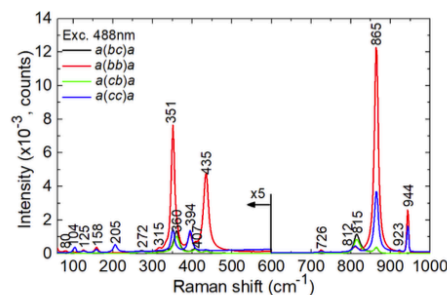


Fig. 5. RT Raman spectra of the 3 at.% Yb:KY(MoO₄)₂ crystal for the *a(mn)a*, *m*, *n* = *b*, *c* geometries (Porto's notations), $\lambda_{\text{exc}} = 488$ nm, numbers indicate the peak frequencies in cm⁻¹.

The most intense Raman mode is at 865 cm⁻¹ with a width at half maximum (FWHM) of 18.8 cm⁻¹. The maximum phonon energy $h\nu_{\text{max}}$ is 944 cm⁻¹.

4. Optical spectroscopy

4.1. Optical absorption

Orthorhombic KY(MoO₄)₂ is an optically biaxial crystal. Only a mean value of its refractive index is known, ≈ 1.95 . KY(MoO₄)₂ shows a strong birefringence, $\Delta n = 0.018\text{--}0.087$ [34]. The optical indicatrix axes coincide with the crystallographic axes. We will denote the principal light polarizations as *E* || *a*, *b* and *c*.

The absorption spectra were measured using a Varian CARY-5000 spectrophotometer (0.3-2 μm) and a FTIR spectrometer Bruker Tensor 27 (2-7 μm). A Glan-Taylor prism was used for polarization-resolved studies.

The transmission spectrum of a ~ 1 cm-thick 3 at.% Yb:KY(MoO₄)₂ crystal sample is shown in Fig. 6(a) revealing a transparency range from 0.33 to 3.4 μm (extending up to 5 μm to some extent). The structured absorption at longer wavelengths is related to the ν vibrations of the MoO₄ tetrahedra. The infrared cut-off is due to the $2\nu_1$ overtone peak of the [MoO₄]²⁻ group fundamental vibration.

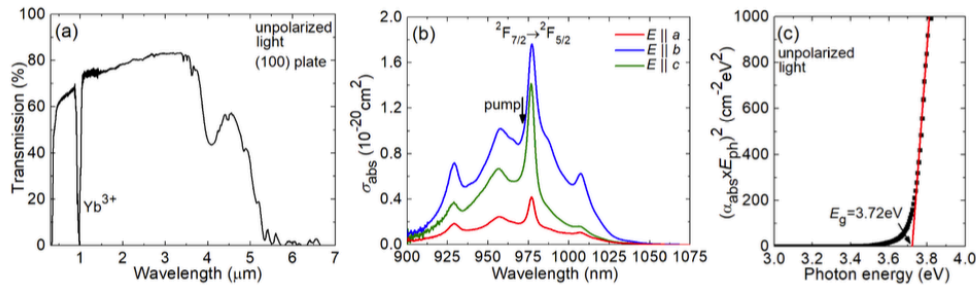


Fig. 6. RT absorption properties of a 3 at.% Yb:KY(MoO₄)₂ crystal: (a) unpolarized transmission spectrum of a ~ 1 cm-thick (100)-oriented crystal plate; (b) absorption cross-section, σ_{abs} , spectra for light polarizations $E \parallel a, b, c$. The arrow indicates the pump wavelength used in the laser experiments; (c) Tauc plot for the evaluation of the optical bandgap (E_g), E_{ph} – photon energy.

The absorption at ~ 1 μm originates from the $^2F_{7/2} \rightarrow ^2F_{5/2}$ transition of Yb³⁺ ions. It is analyzed in Fig. 6(b) in terms of absorption cross-sections, $\sigma_{\text{abs}} = \alpha_{\text{abs}}/N_{\text{Yb}}$ (α_{abs} - absorption coefficient) for the principal light polarizations $E \parallel a, b, c$. The absorption spectra exhibit strong polarization anisotropy. The maximum σ_{abs} is 1.77×10^{-20} cm² at 977.1 nm and the FWHM of the absorption peak is 19.6 nm for light polarization $E \parallel b$. This wavelength corresponds to the zero-phonon line (ZPL, see below) transition at RT. For the other two light polarizations, the absorption cross-sections are lower, as expressed by the ratios $\sigma_{\text{abs}}(b) : \sigma_{\text{abs}}(c) = 1.26$ and $\sigma_{\text{abs}}(b) : \sigma_{\text{abs}}(a) = 4.2$ at ~ 980 nm. This anisotropy arises, in part, from the layered crystal structure (note the significant drop of the optical absorption for light polarized orthogonal to the b - c layer plane) and, in part, from the low symmetry of the Yb³⁺ site. The observed broad absorption spectra qualify Yb:KY(MoO₄)₂ for diode-pumping by InGaAs laser diodes emitting at ~ 980 nm.

The absorption cross-sections in Yb:KY(MoO₄)₂ are lower than those for the monoclinic Yb:KY(WO₄)₂ crystal: $\sigma_{\text{abs}} = 10.8 \times 10^{-20}$ cm² at 981.0 nm corresponding a narrower FWHM of 4.0 nm (for light polarization $E \parallel N_m$) [35].

The optical bandgap of Yb:KY(MoO₄)₂ was evaluated with the Tauc plot, i.e. by plotting $(\alpha_{\text{abs}} \times E_{\text{ph}})^2$ vs. the photon energy $E_{\text{ph}} = h(c/\lambda)$. The intersection of the linear fit of the obtained plot with the horizontal axis yields $E_g = 3.72$ eV (the wavelength of the UV absorption edge is ~ 330 nm).

4.2. Luminescence: spectra and lifetime

The polarized luminescence spectra were measured using an optical spectrum analyzer (OSA, Hamamatsu, AQ6373) and a Glan-Taylor polarizer. The stimulated-emission (SE) cross-sections, σ_{SE} , for i -th polarization ($i = a, b, c$) were calculated from the measured luminescence spectra calibrated for the spectral response of the set-up $W'(\lambda)$ using the Füchtbauer–Ladenburg (F-L) formula [36]:

$$\sigma_{\text{SE}}^i(\lambda) = \frac{\lambda^5}{8\pi \langle n \rangle^2 \tau_{\text{rad}} c} \frac{3W'_i(\lambda)}{\sum_{i=a,b,c} \int \lambda W'_i(\lambda) d\lambda}, \quad (2)$$

where λ is the wavelength, ≈ 1.95 is the refractive index, c is the speed of light in vacuum and $\tau_{\text{rad}} = 458 \mu\text{s}$ is the radiative lifetime of the emitting level (${}^2F_{5/2}$), see below. The results are shown in Fig. 7(a).

For $\text{Yb:KY}(\text{MoO}_4)_2$, the maximum σ_{SE} amounts to $3.70 \times 10^{-20} \text{ cm}^2$ at 1008.0 nm and the emission bandwidth (FWHM) $\Delta\lambda_{\text{em}}$ is 37.0 nm for the high-gain light polarization $E \parallel b$. The emission spectra are also strongly polarized, as expressed by the ratios $\sigma_{\text{SE}}(b) : \sigma_{\text{SE}}(c) = 3.9$ and $\sigma_{\text{SE}}(b) : \sigma_{\text{SE}}(a) = 6.0$ at $\sim 1.01 \mu\text{m}$. These high ratios are a prerequisite for linearly polarized laser emission. Note that (100)-oriented crystal plates give access to the preferable light polarization $E \parallel b$. Compared to its monoclinic double tungstate counterpart, $\text{Yb:KY}(\text{WO}_4)_2$, for which $\sigma_{\text{SE}} = 3.2 \times 10^{-20} \text{ cm}^2$ at 1021.9 nm with $\Delta\lambda_{\text{em}} = 30.2 \text{ nm}$ for $E \parallel N_m$ [35], $\text{Yb:KY}(\text{MoO}_4)_2$ provides higher SE cross-sections and broader emission bandwidth. These are attractive features for broadly tunable and ultrashort-pulse lasers at $\sim 1 \mu\text{m}$.

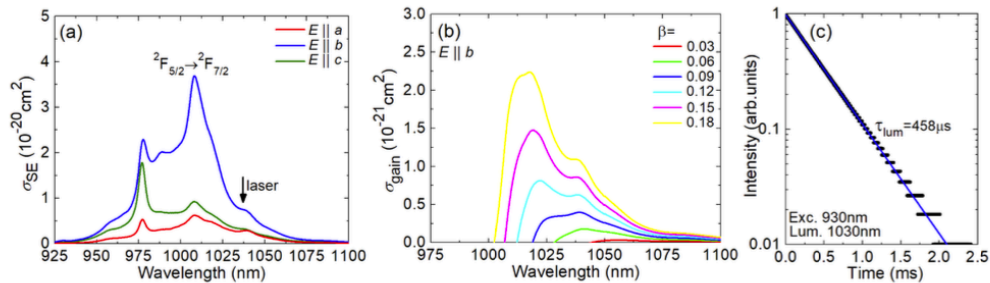


Fig. 7. Emission properties of $\text{Yb}^{3+}:\text{KY}(\text{MoO}_4)_2$: (a) stimulated-emission (SE) cross-sections, σ_{SE} , for light polarizations $E \parallel a$, b and c . The arrow indicates the observed laser wavelength; (b) gain cross-sections, $\sigma_{\text{gain}} = \sigma_{\text{SE}} - (1 - \beta)\sigma_{\text{abs}}$, $\beta = N_2({}^2F_{5/2})/N_{\text{Yb}}$ is the inversion ratio, the light polarization is $E \parallel b$; (c) luminescence decay curve for a cleaved film, $\lambda_{\text{exc}} = 930 \text{ nm}$, $\lambda_{\text{lum}} = 1030 \text{ nm}$, symbols: experimental data, line: single-exponential fit.

For the Yb^{3+} ion, exhibiting reabsorption at the laser wavelength, the spectral behavior of the laser depends on the output-coupling losses via the rate of inversion in the gain medium, expressed by the inversion ratio $\beta = N_2({}^2F_{5/2})/N_{\text{Yb}}$, where N_2 is the population of the upper level (${}^2F_{5/2}$) and $N_1 + N_2 = N_{\text{Yb}}$. Thus, the gain cross-sections, $\sigma_{\text{gain}} = \sigma_{\text{SE}} - (1 - \beta)\sigma_{\text{abs}}$, are calculated to predict the possible laser wavelengths for different β . The gain spectra for light polarization $E \parallel b$ are shown in Fig. 7(b). For small $\beta < 0.03$, the gain spectra are very flat and broad extending from $\sim 1040 \text{ nm}$ to 1100 nm . For intermediate inversion ratios $0.05 < \beta < 0.10$, a local peak in the spectra appears at $\sim 1039 \text{ nm}$. For even higher inversion ratios, another maximum at a shorter wavelength of $\sim 1019 \text{ nm}$ is observed. For $\beta = 0.15$, the gain bandwidth $\Delta\lambda_g$ is 33.0 nm in agreement with the luminescence studies.

The luminescence decay curve of the sample was measured using an InGaAs photodetector under ns pulse excitation from an optical parametric oscillator (Horizon, Continuum) tuned to 930 nm , a $1/4 \text{ m}$ monochromator (Oriel 77200) and an 8 GHz oscilloscope (DSA70804B, Tektronix). A thin ($\sim 30 \mu\text{m}$) cleaved film was used to avoid the effect of radiation trapping. The decay curve plotted in a semi-log scale, Fig. 7(c), is single-exponential in agreement with a single type of Yb^{3+} sites. The luminescence decay time $\tau_{\text{lum}} = 458 \mu\text{s}$ is longer than that of monoclinic $\text{Yb:KY}(\text{WO}_4)_2$ crystals ($\tau_{\text{lum}} = 231 \mu\text{s}$ [35]).

4.3. Crystal-field splitting

For Yb^{3+} ions in C_2 sites, each ${}^{2S+1}L_J$ multiplet is split into $J + 1/2$ Stark sub-levels which are numbered as $0 \dots 3$ for the ground-state (${}^2F_{7/2}$) and $0' \dots 2'$ for the excited-state (${}^2F_{5/2}$). To

resolve their energies, we measured the unpolarized absorption and luminescence spectra at low temperature (LT, 6 K) using an Oxford Instruments Ltd. cryostat (model SU 12) with helium-gas close-cycle flow. The results are shown in Fig. 8. The LT spectra were interpreted accounting for the Raman spectra in order to assign the possible vibronic sidebands.

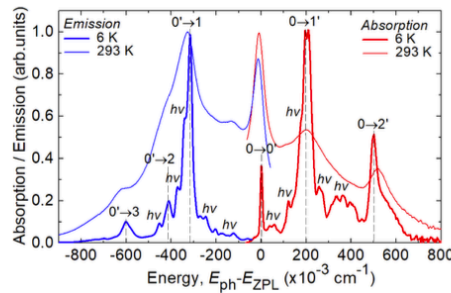


Fig. 8. Absorption and luminescence spectra of $\text{Yb}^{3+}:\text{KY}(\text{MoO}_4)_2$ plotted vs. the energy difference ($E_{\text{ph}} - E_{\text{ZPL}}$), where $E_{\text{ph}} = h(c/\lambda)$ is the photon energy and $E_{\text{ZPL}} = 10246 \text{ cm}^{-1}$ is the zero-phonon line (ZPL) energy, measured at LT (6 K) and RT (293 K) with unpolarized light. For LT emission spectra, $\lambda_{\text{exc}} = 976 \text{ nm}$. Electronic transitions are indicated as $i \leftrightarrow j'$, phonon sidebands – as hv .

The zero-phonon line (ZPL) is the transition between the lowest Stark sub-levels of both multiplets, designated as $0 \leftrightarrow 0'$. It is observed at 10246 cm^{-1} corresponding to the wavelength of 976.0 nm (at 6 K). The full set of energy-levels of $\text{Yb}^{3+}:\text{KY}(\text{MoO}_4)_2$ is ${}^2\text{F}_{7/2} = (0, 315, 411, 601) \text{ cm}^{-1}$ and ${}^2\text{F}_{5/2} = (10246, 10440, 10749) \text{ cm}^{-1}$, see Fig. 9(a), showing the energy-level scheme and the wavelengths of the electronic transitions in absorption and emission. In particular, the emission peak at $\sim 1007 \text{ nm}$ corresponding to the maximum SE cross-sections is assigned to the $0' \rightarrow 1$ transition. The partition functions for the lower ($m = 1$) and upper ($m = 2$) manifolds are $Z_1 = 1.397$ and $Z_2 = 1.469$ (the ratio $Z_1/Z_2 = 0.951$). The determined crystal-field splitting is different from that in monoclinic $\text{Yb}:\text{KY}(\text{WO}_4)_2$ for which ${}^2\text{F}_{7/2} = (0, 169, 407, 568) \text{ cm}^{-1}$ and ${}^2\text{F}_{5/2} = (10187, 10476, 10695) \text{ cm}^{-1}$ [16]. In particular, the total Stark splitting of the ground-state, $\Delta E({}^2\text{F}_{7/2})$, is larger for $\text{Yb}:\text{KY}(\text{MoO}_4)_2$ (601 cm^{-1}), which explains the broadband emission properties of this material.

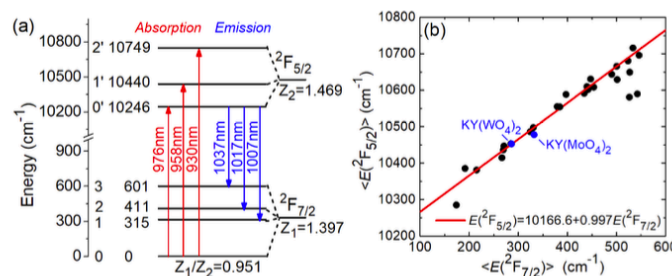


Fig. 9. (a) Crystal-field splitting of the Yb^{3+} ion in the $\text{KY}(\text{MoO}_4)_2$ crystal (site symmetry: C_2), $Z_{1(2)}$ are the partition functions for the ground- and excited-state, respectively, arrows indicate the transitions in absorption / emission at 6 K; (b) barycenter plot [37] for the Yb^{3+} ion showing the position of $\text{Yb}:\text{KY}(\text{WO}_4)_2$ and $\text{Yb}:\text{KY}(\text{MoO}_4)_2$ crystals (blue circles).

Previously, for the isostructural $\text{KYb}(\text{MoO}_4)_2$, it was pointed out that even at LT, the spectra of the Yb^{3+} ion revealed a strong electron-phonon coupling [31]. Thus, the assignment of the

Stark levels was complicated. The following splitting for the ground-state ($^2F_{7/2}$) was proposed: (0, 240, 460, 460) cm^{-1} . This poorly agrees with our data.

For all RE ions, the barycenter energy of any isolated $^{2S+1}L_J 4f^n$ multiplet depends linearly on the barycenter energy of any other isolated multiplet. This relation is expressed by the barycenter plot [37], Fig. 9(b). The determined barycenter energies $\langle E(^2F_{5/2}) \rangle$ and $\langle E(^2F_{7/2}) \rangle$ agree well with the linear fit to this plot, expressed by the equation $E(^2F_{5/2}) = 10166.6 + 0.997 \times E(^2F_{7/2})$ cm^{-1} , where $E_0 = 10166.6 \text{ cm}^{-1}$ denotes the energy of the Yb^{3+} excited-state for a free-ion. This confirms the correctness of the constructed energy-level scheme.

5. Laser operation

5.1. Laser set-up

The active elements for the laser experiments were fabricated by mechanical cleavage of the 3 at.% bulk $\text{Yb:KY}(\text{MoO}_4)_2$ crystal along the (100) plane. In this way, we produced a thin cleaved crystal-plate with a thickness $t = 286 \mu\text{m}$ and a high uniformity of $\pm 2 \mu\text{m}$ over the clear aperture. No post-cleavage treatment (e.g., polishing) was applied to both surfaces which remained uncoated. The crystal orientation corresponded to light propagation along the *a*-axis (*a*-cut) which is beneficial for the pump absorption providing access to light polarizations $\mathbf{E} \parallel \mathbf{b}$ and $\mathbf{E} \parallel \mathbf{c}$ with higher σ_{abs} values, Fig. 6(b).

For laser experiments, we selected a plano-plano (microchip) laser cavity, Fig. 10, formed by a flat pump mirror (PM) coated for high transmission (HT) at $\sim 0.97 \mu\text{m}$ and for high reflection (HR) at $1.02\text{--}1.2 \mu\text{m}$, and a set of flat output couplers (OCs) with a transmission at the laser wavelength T_{OC} of 0.5%–10%. Both cavity mirrors were gently pressed towards the crystal-plate resulting in a nearly monolithic design. The geometrical cavity length L_{cav} nearly equaled the crystal-plate thickness t . The whole stack (cavity mirrors and crystal-plate) was passively cooled.

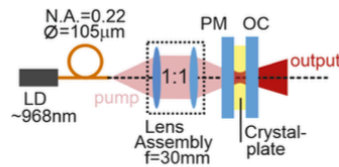


Fig. 10. Scheme of the diode-pumped 3 at.% $\text{Yb:KY}(\text{MoO}_4)_2$ cleaved crystal-plate microchip laser: LD – laser diode, PM – pump mirror, OC – output coupler.

As a pump source, we employed an InGaAs fiber coupled laser diode (fiber core diameter: $105 \mu\text{m}$; numerical aperture (N.A.): 0.22) emitting unpolarized output at a central wavelength of $\sim 968 \text{ nm}$. The pump was collimated and focused into the crystal through the PM using a lens assembly (reimaging ratio: 1:1, focal length: $f = 30 \text{ mm}$). The pump spot diameter $2w_p$ in the focus was $100 \pm 10 \mu\text{m}$. The crystal-plate was pumped in a double-pass, as all the used OCs provided reflection at the pump wavelength, $R \approx 90\%$. The total pump absorption in two passes was estimated from the small-signal value accounting for the Fresnel losses at the uncoated crystal surfaces and amounted to 9.4%. In one pass, $\eta_{\text{abs},0} = 1 - \exp(-\langle \sigma_{\text{abs}} \rangle N_{\text{Yb}} t) = 4.8\%$, where $\langle \sigma_{\text{abs}} \rangle = 0.75 \times 10^{-20} \text{ cm}^2$ is the polarization-averaged absorption cross-section. This value does not account for the ground-state bleaching but at the same time it does not overestimate the laser slope efficiency. Due to the small leakage of the residual pump through the OC, it was difficult to estimate the pump absorption under lasing conditions.

A long-pass filter (FEL1000, Thorlabs) separated the laser output and the residual pump. The laser emission spectra were measured with an accuracy of $\pm 0.2 \text{ nm}$.

5.2. Laser performance

Laser operation was achieved for all the employed OCs. The CW input-output dependences of the diode-pumped microchip cleaved crystal-plate Yb:KY(MoO₄)₂ laser are shown in Fig. 11(a). For the 1% OC, the laser generated a maximum output power of 0.81 W at 1021-1044 nm with a high slope efficiency (η) of 76.4% vs. the absorbed pump power P_{abs} . The laser threshold P_{th} was as low as 56 mW whilst the optical-to-optical efficiency (vs. the pump power incident on the crystal) η_{opt} was rather low, 7.0%, owing to the low pump absorption in the thin crystal. With increasing the output coupling, the laser threshold gradually increased, from 55 mW for $T_{\text{OC}} = 0.5\%$ to 143 mW for $T_{\text{OC}} = 10\%$. The input-output dependences were linear for all the OCs. The absorbed pump power in the crystal-plate P_{abs} was limited to below 1.1 W in order to avoid thermal fracture of the passively cooled crystal.

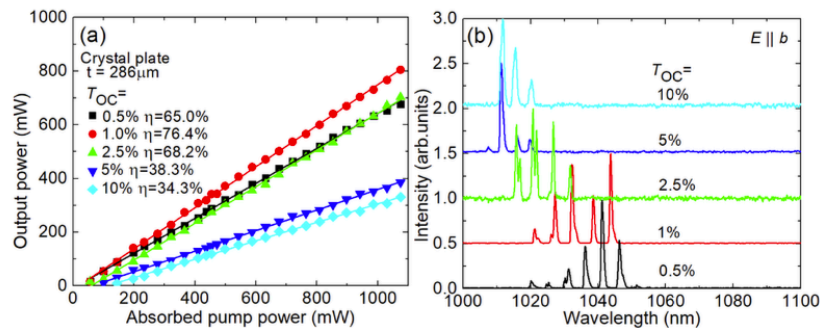


Fig. 11. Diode-pumped Yb:KY(MoO₄)₂ cleaved crystal-plate microchip laser: (a) input-output dependences, η – slope efficiency; (b) typical laser emission spectra measured at $P_{\text{abs}} = 1.0 \text{ W}$. The laser polarization is $E \parallel b$.

Typical laser emission spectra are shown in Fig. 11(b). The spectra experienced a blue-shift with the increase of the output coupling: from 1020-1051 nm for $T_{\text{OC}} = 0.5\%$ to 1012-1020 nm for $T_{\text{OC}} = 10\%$. This is due to the quasi-three level nature of the Yb³⁺ laser transition ${}^2F_{5/2} \rightarrow {}^2F_{7/2}$ exhibiting reabsorption. The observed spectral behavior agrees with the gain spectra for $E \parallel b$, Fig. 7(b). The laser output was linearly polarized ($E \parallel b$) naturally selected by the anisotropy of the gain.

The laser spectra were modulated by etalon (Fabry-Perot) effects showing two wavelength separations, $\Delta\lambda_1 = 1.0 \pm 0.1 \text{ nm}$ and $\Delta\lambda_2 = 6.2 \pm 0.5 \text{ nm}$. The smaller one is attributed to the etalon effect of the crystal itself and the larger one – to the residual small airgap between the crystal and one of the cavity mirrors. The free spectral range (FSR) of the Fabry-Perot etalon with a thickness t and a refractive index n at normal incidence is $\Delta\lambda_{\text{FSR}} \approx \lambda^2/(2nt)$ which yields 0.95 nm for the crystal ($t = 286 \mu\text{m}$ and $\langle\lambda\rangle = 1030 \text{ nm}$). The thickness of the equivalent airgap is $\sim 90 \mu\text{m}$. The roughly 20 nm broad laser spectra originated from the large gain bandwidth of Yb³⁺ in KY(MoO₄)₂.

The laser operation in the plano-plano cavity indicated a positive thermal lens for a -cut Yb:KY(MoO₄)₂. Positive thermal lens was observed also for monoclinic Yb:KY(WO₄)₂ crystal [38] and ascribed to the counteraction of negative thermo-optic coefficients dn/dT [39] and the positive thermal expansion. Negative dn/dT values were also measured for tetragonal double molybdates [40]. Note that for Yb:KY(MoO₄)₂, the largest coefficient of linear thermal expansion ($38.3 \times 10^{-6} \text{ K}^{-1}$) is along the a -axis which may explain the positive thermal lens for the present crystal cut.

6. Conclusion

To conclude, we report on the growth, structure refinement by the Rietveld method, polarized room-temperature spectroscopy and crystal-field splitting (at 6 K), and first laser operation of Yb³⁺-doped potassium yttrium double molybdate, Yb:KY(MoO₄)₂. Its layered crystal structure dictates a strong polarization-anisotropy of the transition cross-sections for the Yb³⁺ dopant and a perfect natural cleavage habit along the (100) plane. Mechanically cleaved thin crystal films and plates with a thickness as thin as tens of μm can be directly applied as gain medium for laser operation. We report on a watt-level output from a diode-pumped microchip 3 at.% Yb:KY(MoO₄)₂ crystal-plate laser operating with a high slope efficiency (76.4%) almost approaching the Stokes limit. Highly Yb³⁺-doped KY(MoO₄)₂ crystal plates and films (e.g., up to 10 at.%, as obtained in our preliminary growth experiments) are attractive for short-pulse (sub-ns) passively Q-switched microchip lasers, as well as thin-disk lasers.

Funding

Russian Foundation for Basic Research (19-32-90199); Ministerio de Economía y Competitividad (MAT2016-75716-C2-1-R (AEI/FEDER,UE)); Agència de Gestió d'Ajuts Universitaris i de Recerca (2017 SGR 755); National Natural Science Foundation of China (51761135115, 61850410533, 61875199, 61975208); Deutsche Forschungsgemeinschaft (PE 607/14-1).

Acknowledgments

P. L. thanks Ms. Liza Basyrova for the help with the SEM studies.

Disclosures

The authors declare no conflicts of interest.

References

1. H. Zhu, Y. Chen, Y. Lin, X. Gong, Q. Tan, Z. Luo, and Y. Huang, "Growth, spectral properties, and laser demonstration of Yb³⁺:BaGd₂(MoO₄)₄ cleavage crystal," *J. Appl. Phys.* **101**(6), 063109 (2007).
2. Y. J. Chen, Y. D. Huang, X. Q. Lin, Q. G. Tan, Z. D. Luo, and Y. F. Lin, "Laser emission from unprocessed cleavage microchip," *Appl. Phys. Lett.* **86**(2), 021115 (2005).
3. A. Volokitina, P. Loiko, A. Pavlyuk, S. Slimi, R. M. Solé, E. B. Salem, E. Kifle, J. M. Serres, U. Griebner, V. Petrov, M. Aguiló, F. Díaz, and X. Mateos, "Laser operation of cleaved single-crystal plates and films of Tm:KY(MoO₄)₂," *Opt. Express* **28**(7), 9039–9048 (2020).
4. J. J. Zayhowski, "Microchip lasers," *Opt. Mater.* **11**(2-3), 255–267 (1999).
5. J. M. Serres, X. Mateos, P. Loiko, K. Yumashev, N. Kuleshov, V. Petrov, U. Griebner, M. Aguiló, and F. Díaz, "Diode-pumped microchip Tm:KLu(WO₄)₂ laser with more than 3 W of output power," *Opt. Lett.* **39**(14), 4247–4250 (2014).
6. P. Loiko, J. M. Serres, X. Mateos, K. Yumashev, A. Yasukevich, V. Petrov, U. Griebner, M. Aguiló, and F. Díaz, "Sub-nanosecond Yb:KLu(WO₄)₂ microchip laser," *Opt. Lett.* **41**(11), 2620–2623 (2016).
7. Y. Chen, X. Gong, Y. Lin, Q. Tan, Z. Luo, and Y. Huang, "Continuous-wave laser characteristics of a Nd³⁺:LaB₃O₆ cleavage microchip and the influence of thermal effects," *Appl. Opt.* **45**(32), 8338–8345 (2006).
8. J. Liu, W. Han, X. Chen, D. Zhong, B. Teng, C. Wang, and Y. Li, "Spectroscopic properties and continuous-wave laser operation of Yb:LuPO₄ crystal," *Opt. Lett.* **39**(20), 5881–5884 (2014).
9. X. Zhang, J. He, T. Tang, B. Teng, D. Zhong, X. Xu, and Z. Wang, "Efficient laser operations of unprocessed thin plate of Nd:YPO₄ crystal," *Opt. Express* **26**(20), 26179–26187 (2018).
10. Y. J. Chen, Y. F. Lin, X. H. Gong, H. M. Zhu, Z. D. Luo, and Y. D. Huang, "805-nm diode-pumped continuous-wave 2-μm laser performance of Tm³⁺:BaGd₂(MoO₄)₄ cleavage plate," *Appl. Phys. B* **98**(1), 55–60 (2010).
11. W. Zhao, Y. S. Huang, Z. B. Lin, B. Wei, F. W. Wang, M. Xu, X. Zhao, Q. H. Zheng, and W. W. Zhou, "Spectra and energy levels of a layered Yb³⁺:CsGd(MoO₄)₂ crystal with perfect cleavage: a candidate for microchip lasers," *RSC Adv.* **5**(44), 34730–34736 (2015).
12. J. Liu, V. Petrov, H. Zhang, and J. Wang, "Power scaling of a continuous-wave and passively Q-switched Yb:KLu(WO₄)₂ laser end-pumped by a high-power diode," *Appl. Phys. B* **88**(4), 527–530 (2007).
13. P. Loiko, J. M. Serres, X. Mateos, X. Xu, J. Xu, V. Jambunathan, P. Navratil, A. Lucianetti, T. Mocek, X. Zhang, U. Griebner, V. Petrov, M. Aguiló, F. Díaz, and A. Major, "Microchip Yb:CaLnAlO₄ lasers with up to 91% slope efficiency," *Opt. Lett.* **42**(13), 2431–2434 (2017).

14. H. Zhu, Y. Chen, Y. Lin, X. Gong, Z. Luo, and Y. Huang, "Polarized spectral properties and laser demonstration of $\text{Nd}^{3+}:\text{BaGd}_2(\text{MoO}_4)_4$ cleavage crystal," *J. Opt. Soc. Am. B* **24**(10), 2659–2665 (2007).
15. V. Petrov, M. C. Pujol, X. Mateos, O. Silvestre, S. Rivier, M. Aguiló, R. M. Solé, J. Liu, U. Griebner, and F. Díaz, "Growth and properties of $\text{KLu}(\text{WO}_4)_2$, and novel ytterbium and thulium lasers based on this monoclinic crystalline host," *Laser Photonics Rev.* **1**(2), 179–212 (2007).
16. A. A. Lagatsky, N. V. Kuleshov, and V. P. Mikhailov, "Diode-pumped CW lasing of Yb:KYW and Yb:KGW," *Opt. Commun.* **165**(1-3), 71–75 (1999).
17. J. M. Serres, P. Loiko, X. Mateos, K. Yumashev, N. Kuleshov, V. Petrov, U. Griebner, M. Aguiló, and F. Díaz, "Prospects of monoclinic Yb:KLu(WO₄)₂ crystal for multi-watt microchip lasers," *Opt. Mater. Express* **5**(3), 661–667 (2015).
18. U. Griebner, S. Rivier, V. Petrov, M. Zorn, G. Erbert, M. Weyers, X. Mateos, M. Aguiló, J. Massons, and F. Díaz, "Passively mode-locked Yb:KLu(WO₄)₂ oscillators," *Opt. Express* **13**(9), 3465–3470 (2005).
19. S. Pekarek, C. Fiebig, M. C. Stumpf, A. E. H. Oehler, K. Paschke, G. Erbert, T. Südmeyer, and U. Keller, "Diode-pumped gigahertz femtosecond Yb:KGW laser with a peak power of 3.9 kW," *Opt. Express* **18**(16), 16320–16326 (2010).
20. F. Brunner, T. Südmeyer, E. Innerhofer, F. Morier-Genoud, R. Paschotta, V. E. Kisel, V. G. Shcherbitsky, N. V. Kuleshov, J. Gao, K. Contag, A. Giesen, and U. Keller, "240-fs pulses with 22-W average power from a mode-locked thin-disk Yb:KY(WO₄)₂ laser," *Opt. Lett.* **27**(13), 1162–1164 (2002).
21. S. Rivier, X. Mateos, O. Silvestre, V. Petrov, U. Griebner, M. C. Pujol, M. Aguiló, F. Díaz, S. Vernay, and D. Rytz, "Thin-disk Yb:KLu(WO₄)₂ laser with single-pass pumping," *Opt. Lett.* **33**(7), 735–737 (2008).
22. A. Volokitina, P. Loiko, E. Vilejshikova, X. Mateos, E. Dunina, A. Kornienko, N. Kuleshov, and A. Pavlyuk, " $\text{Eu}^{3+}:\text{KY}(\text{MoO}_4)_2$: A novel anisotropic red-emitting material with a layered structure," *J. Alloys Compd.* **762**, 786–796 (2018).
23. Y. Chen, Y. Lin, X. Gong, Q. Tan, Z. Luo, and Y. Huang, "Polarized spectral characteristics of $\text{Nd}^{3+}:\text{KY}(\text{MoO}_4)_2$ crystal with perfect cleavage planes: a promising microchip gain medium," *J. Opt. Soc. Am. B* **24**(3), 496–503 (2007).
24. P. Loiko, E. Kifle, J. M. Serres, X. Mateos, M. Aguiló, F. Díaz, E. Vilejshikova, N. Kuleshov, and A. Pavlyuk, "Efficient continuous-wave in-band pumped Nd:KY(MoO₄)₂ laser," *Laser Phys. Lett.* **15**(6), 065002 (2018).
25. R. F. Klevtsova and S. V. Borisov, "X-ray structural study of the double molybdate KY(MoO₄)₂," *Sov. Phys. Dokl.* **12**, 1095 (1968) [Transl. from Dokl. Akad. Nauk SSSR **177**(6), 1333–1336 (1967)].
26. J. Hanuza and L. Łabuda, "Polarized Raman and infrared spectra of a multilayer KY(MoO₄)₂ crystal," *J. Raman Spectrosc.* **11**(4), 231–237 (1981).
27. A. A. Kaminskii and S. N. Bagayev, "Ribbon and sheet miniature crystal laser," *Quantum Electron.* **24**(12), 1029–1030 (1994).
28. Y. A. Borovlev, N. V. Ivannikova, V. N. Shlegel, Y. V. Vasiliev, and V. A. Gusev, "Progress in growth of large sized BGO crystals by the low-thermal-gradient Czochralski technique," *J. Cryst. Growth* **229**(1-4), 305–311 (2001).
29. A. A. Kaminskii, P. V. Klevtsov, and A. A. Pavlyuk, "Stimulated emission from KY(MoO₄)₂-Nd³⁺ crystal laser," *Phys. Status Solidi A* **1**(3), K91–K94 (1970).
30. R. D. Shannon, "Revised effective ionic radii and systematic studies of interatomic distances in halides and chalcogenides," *Acta Crystallogr., Sect. A: Cryst. Phys., Diff., Theor. Gen. Crystallogr.* **32**(5), 751–767 (1976).
31. G. I. Frolova, L. E. Reznik, and I. E. Paukov, "Crystal-field effects on the thermodynamic properties of the KLn(MoO₄)₂ isostructural compounds," *J. Chem. Thermodyn.* **21**(1), 25–36 (1989).
32. P. A. Loiko, K. V. Yumashev, N. V. Kuleshov, G. E. Rachkovskaya, and A. A. Pavlyuk, "Detailed characterization of thermal expansion tensor in monoclinic KRe(WO₄)₂ (where Re = Gd, Y, Lu, Yb)," *Opt. Mater.* **34**(1), 23–26 (2011).
33. L. Macalik, J. Hanuza, and A. A. Kaminskii, "Polarized Raman spectra of the oriented NaY(WO₄)₂ and KY(WO₄)₂ single crystals," *J. Mol. Struct.* **555**(1-3), 289–297 (2000).
34. L. A. Kulakova, "Acoustooptical and elastic properties of laminated KY(MoO₄)₂ crystals," *Phys. Solid State* **42**(1), 55–58 (2000) [transl. from Fizika Tverdogo Tela **42**(1), 53–56 (2000)].
35. X. Mateos, J. M. Serres, P. Loiko, U. Griebner, V. Petrov, K. Yumashev, M. Aguiló, and F. Díaz, "Indium-modified Yb:KLu(WO₄)₂ crystal: Growth, spectroscopy and laser operation," *J. Lumin.* **183**, 391–400 (2017).
36. B. Aull and H. Jenssen, "Vibronic interactions in Nd:YAG resulting in nonreciprocity of absorption and stimulated emission cross sections," *IEEE J. Quantum Electron.* **18**(5), 925–930 (1982).
37. P. H. Haumesser, R. Gaumé, B. Viana, E. Antic-Fidancev, and D. Vivien, "Spectroscopic and crystal-field analysis of new Yb-doped laser materials," *J. Phys.: Condens. Matter* **13**(23), 5427–5447 (2001).
38. P. A. Loiko, S. Manjooran, K. V. Yumashev, and A. Major, "Polarization-anisotropy of thermal lens in Yb:KY(WO₄)₂ laser crystal under high-power diode pumping," *Appl. Opt.* **56**(10), 2937–2945 (2017).
39. P. A. Loiko, K. V. Yumashev, N. V. Kuleshov, and A. A. Pavlyuk, "Thermo-optical properties of pure and Yb-doped monoclinic KY(WO₄)₂ crystals," *Appl. Phys. B* **106**(3), 663–668 (2012).
40. P. A. Loiko, X. Han, K. V. Yumashev, N. V. Kuleshov, M. D. Serrano, C. Cascales, and C. Zaldo, "Thermo-optical properties of uniaxial NaT(XO₄)₂ laser host crystals, (where T = Y, La, Gd or Bi and X = W or Mo)," *Appl. Phys. B* **111**(2), 279–287 (2013).

Laser Operation of Cleaved Single-Crystal Plates and Films of Tm:KY(MoO₄)₂

Pavel Loiko^{1,*}, Anna Volokitina¹, Josep Maria Serres², Vyacheslav Trifonov³, Anatoly Pavlyuk³,
Sami Slimi^{2,4}, Ezzedine Ben Salem⁴, Rosa Maria Solé², Magdalena Aguiló², Francesc Díaz², and Xavier Mateos²

¹ITMO University, 49 Kronverkskiy Pr., 197101 Saint-Petersburg, Russia

²Física i Cristal·lografia de Materials i Nanomaterials (FiCMA-FiCNA)-EMaS, Dept. Química Física i Inòrganica,
Universitat Rovira i Virgili (URV), Campus Sescelades, E-43007 Tarragona, Spain

³A.V. Nikolaev Institute of Inorganic Chemistry, Siberian Branch of Russian Academy of Sciences, 3 Lavrentyev Ave., Novosibirsk 630090, Russia

⁴I.P.E.I. of Monastir, Unit of Materials and Organic Synthesis Monastir 5019, UR17ES31, Tunisia

*kinetic@tut.by

Abstract: We report on the crystal growth and spectroscopy of novel orthorhombic Tm:KY(MoO₄)₂ crystals with a layered structure. CW 2- μ m laser operation in cleaved single-crystal plates and films of Tm:KY(MoO₄)₂ (thickness: down to 70 μ m) is achieved. © 2019 The Author(s)

OCIS codes: (140.3380) Laser materials; (140.3070) Infrared and far-infrared lasers; (310.6845) Thin film devices and applications.

1. Introduction

Monoclinic double tungstate crystals, KRE(WO₄)₂ (where RE = Gd, Y, Lu) are known for doping with rare-earth ions, e.g., Yb³⁺ or Tm³⁺ leading to efficient lasing in the near-IR [1]. This is because of high available doping concentrations, broad and intense emission bands for polarized light, weak non-radiative path and Raman activity. Similar properties are expected for their double molybdate (DMo) counterparts, KRE(MoO₄)₂. Such crystals are orthorhombic and they feature a layered structure enhancing the polarization-anisotropy of the spectroscopic properties [2] and leading to a perfect cleavage feature that can be utilized in microchip or thin-film lasers [3]. Recently, efficient ~1 μ m lasers based on single-crystal plates were demonstrated [4]. However, orthorhombic DMo are poorly studied especially for ~2 μ m emission.

In the present work, we report on the crystal growth by the Czochralski (Cz) method, structural and spectroscopic characterization as well as the first laser operation of a novel representative of the DMo crystal family – the orthorhombic Tm:KY(MoO₄)₂ crystal.

2. Growth and Structure

The 3 at.% Tm:KY(MoO₄)₂ crystal (melting temperature: ~970 °C) was grown by A. Pavlyuk by the Cz method using a [100]-oriented seed. 5–7 mol% of potassium trimolybdate (K₂Mo₃O₁₀) were added to the melt to prevent its partial dissociation. No post-growth annealing was applied. High optical quality crystal with a weak yellow coloration due to Tm³⁺ ions was obtained, Fig. 1(a). Its structure and phase purity were confirmed by XRD, Fig. 1(b). The crystal is orthorhombic (sp. gr. D_{2h}¹⁴ – *Pbna*) with lattice constants $a = 5.0782(4)$ Å, $b = 18.2206(6)$ Å, $c = 7.9506(6)$ Å. The crystal exhibits a perfect cleavage along the (100) plane, see Fig. 1(c), due to its layered structure. We produced (100)-oriented crystal plates and films (showing elastic deformation) with a thickness down to 70 μ m. The crystal features intense and strongly polarized Raman spectra with the most intense line at ~865 cm⁻¹.

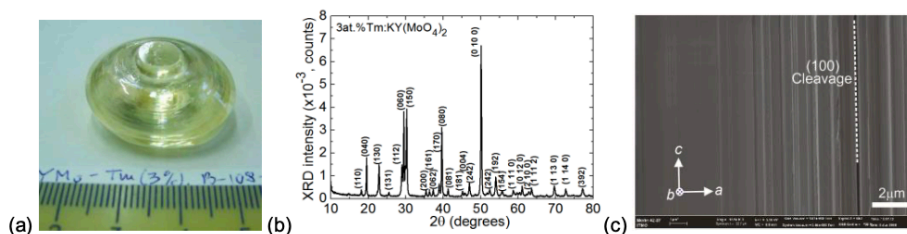


Fig. 1. Growth and structure of orthorhombic 3 at.% Tm:KY(MoO₄)₂ crystal: (a) as-grown boules, the growth direction is along the [100] axis; (b) X-ray powder diffraction (XRD) pattern, numbers denote the Miller's indices, (hkl); (c) Scanning Electron Microscope (SEM) image of the side surface of a cleaved single-crystal film.

3. Results and Discussion

KY(MoO₄)₂ is an optically biaxial crystal with the optical indicatrix axes being parallel to the a , b , c ones. It has a high refractive index ($n \approx 2$). For (100)-oriented plates, there are two principal light polarizations available, $E \parallel b$ and $E \parallel c$.

The maximum absorption cross-section, σ_{abs} , for the ${}^3\text{H}_6 \rightarrow {}^3\text{H}_4$ Tm^{3+} transition is $8.6 \times 10^{-20} \text{ cm}^2$ at 802.8 nm (the FWHM of the absorption peak is 10.0 nm) for the light polarization $\mathbf{E} \parallel \mathbf{b}$, Fig. 2(a). The stimulated-emission cross-sections, σ_{SE} , were calculated using the Füchtbauer–Ladenburg (F-L) formula, Fig. 2(b). The maximum σ_{SE} is $2.01 \times 10^{-20} \text{ cm}^2$ at 1856.4 nm (for $\mathbf{E} \parallel \mathbf{b}$) with an emission bandwidth of $>110 \text{ nm}$. The luminescence decay from the ${}^3\text{F}_4$ state is single-exponential, Fig. 2(c). The Tm^{3+} ions replace the Y^{3+} ones in a single type of sites with the C_2 symmetry.

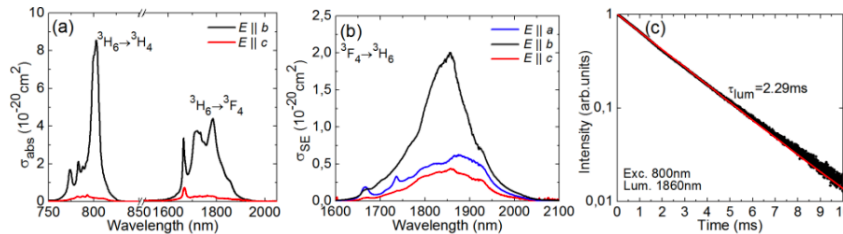


Fig. 2. Spectroscopy of Tm^{3+} ions in orthorhombic $\text{KY}(\text{MoO}_4)_2$ crystal: (a) absorption cross-sections, σ_{abs} , for the ${}^3\text{H}_6 \rightarrow {}^3\text{H}_4$ and ${}^3\text{H}_6 \rightarrow {}^3\text{F}_4$ transition; (b) stimulated-emission cross-sections, σ_{SE} , for the ${}^3\text{F}_4 \rightarrow {}^3\text{H}_6$ transition; (c) luminescence decay curve, $\lambda_{\text{exc}} = 800 \text{ nm}$, $\lambda_{\text{lum}} = 1850 \text{ nm}$.

The laser operation was first studied with Ti:Sapphire laser pumping tuned at 802 nm. A 700 μm -thick cleaved crystal plate was used. It was not repolished and remained uncoated. The plate was pressed between a flat pump mirror (PM) coated for HT at $\sim 0.8 \mu\text{m}$ and for HR at $1.8\text{--}2.1 \mu\text{m}$ and a set of flat output couplers (OCs) with a transmission of 1.5%...20% at the laser wavelength, Fig. 3(a). The pump radiation was focused into the crystal by a spherical lens ($f = 60 \text{ mm}$). The pump absorption (2-passes of the pump) η_{abs} was 49.8%. The crystal-plate microchip laser generated a maximum output power of 352 mW at $\sim 1.95 \mu\text{m}$ with a slope efficiency $\eta = 57.6\%$ and a laser threshold of 125 mW (for $T_{\text{OC}} = 1.5\%$, vs. P_{abs}), Fig. 3(b,c). The laser output was linearly polarized ($\mathbf{E} \parallel \mathbf{b}$) and spatially single-mode ($M_{x,y}^2 < 1.1$). Using a special “bandpass” OC, the laser operation at $>2 \mu\text{m}$ (2052-2069 nm, in “vibronic” regime) was achieved.

Moreover, we fabricated a 70 μm -thick crystal plate which was studied in a similar cavity under pumping by a fiber-coupled AlGaAs laser diode at 802 nm. The pump was focused to a spot of 200 μm in diameter; η_{abs} was 9.0%. For $T_{\text{OC}} = 1.5\%$, the laser generated 46 mW at 1861 nm with $\eta = 12.1\%$ and a laser threshold of only $\sim 60 \text{ mW}$ (vs. P_{abs}).

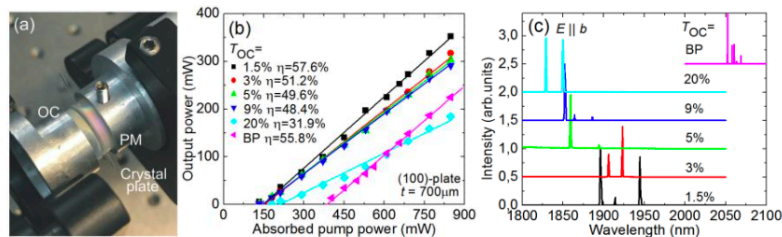


Fig. 3. $\text{Tm}:\text{KY}(\text{MoO}_4)_2$ single-crystal-plate laser: (a) photograph of the laser (PM – pump mirror, OC – output coupler); (b) input-output dependences, η – slope efficiency; (c) typical laser emission spectra measured at $P_{\text{abs}} = 0.85 \text{ W}$. The (100)-oriented plate is 700 μm -thick; the laser polarization is $\mathbf{E} \parallel \mathbf{b}$. BP is a bandpass OC for laser operation $>2 \mu\text{m}$.

4. Conclusion

To conclude, the orthorhombic double molybdate crystal $\text{Tm}:\text{KY}(\text{MoO}_4)_2$ is a promising material for efficient $\sim 2 \mu\text{m}$ lasers because of its easy growth, high available doping levels, intense, broad and strongly polarized absorption and emission bands and Raman activity. The layered structure of $\text{KY}(\text{MoO}_4)_2$ promotes the anisotropy of its optical properties and allows one to fabricate easily laser-quality crystal plates and films with a thickness ranging from few mm down to tens of μm . This feature is of interest for microchip and thin-disk lasers. In particular, the long lifetime of the upper laser level of Tm^{3+} is attractive for passively Q-switched microchip lasers. In the present work, we achieved $\sim 2 \mu\text{m}$ CW laser action in single-crystal plates (sub-mm) and films (sub-100 μm) featuring up to 57.6% slope efficiency.

- [1] V. Petrov, M. C. Pujol, X. Mateos, O. Silvestre, S. Rivier, M. Aguiló, R. M. Solé, J. Liu, U. Griebner, and F. Díaz, “Growth and properties of $\text{KLu}(\text{WO}_4)_2$, and novel ytterbium and thulium lasers based on this monoclinic crystalline host,” *Laser & Photon. Rev.* **1**(2), 179–212 (2007).
- [2] A. Volokitina, P. Loiko, E. Vilejshikova, X. Mateos, E. Dunina, A. Kornienko, N. Kuleshov, and A. Pavlyuk, “ $\text{Eu}^{3+}:\text{KY}(\text{MoO}_4)_2$: A novel anisotropic red-emitting material with a layered structure,” *J. Alloy Compd.* **762**, 786–796 (2018).
- [3] A. A. Kaminskii and S. N. Bagayev, “Ribon and sheet miniature crystal laser,” *Quantum Electron.* **24**(12), 1029–1030 (1994).
- [4] J. Liu, W. Han, X. Chen, D. Zhong, B. Teng, C. Wang, and Y. Li, “Spectroscopic properties and continuous-wave laser operation of $\text{Yb}:\text{LuPO}_4$ crystal,” *Opt. Lett.* **39**(20), 5881–5884 (2014).



Contents lists available at ScienceDirect

Journal of Luminescence

journal homepage: <http://www.elsevier.com/locate/jlumin>



Monoclinic zinc mon tungstate $\text{Yb}^{3+}, \text{Li}^+:\text{ZnWO}_4$: Part II. Polarized spectroscopy and laser operation

Anna Volokitina^{a,b}, Samuel Paul David^c, Pavel Loiko^d, Kirill Subbotin^{e,f}, Anatoly Titov^{e,f}, Denis Lis^e, Rosa Maria Solé^a, Venkatesan Jambunathan^c, Antonio Lucianetti^c, Tomas Mocek^c, Patrice Camy^d, Weidong Chen^{g,h}, Uwe Griebner^g, Valentin Petrov^g, Magdalena Aguiló^a, Francesc Díaz^a, Xavier Mateos^{a,*}

^a Universitat Rovira I Virgili (URV), Física I Cristal·lografia de Materials I Nanomaterials (FICMA-FICNA)-EMaS, Marcel·li Domingo 1, Tarragona, 43007, Spain

^b ITMO University, Kronverkskiy Pr., 49, Saint-Petersburg, 197101, Russia

^c HiLASE Centre, Institute of Physics of the Czech Academy of Sciences, Za Radnicí 828, Dolní Brežany, 25241, Czech Republic

^d Centre de Recherche sur Les Ions, Les Matériaux et La Photonique (CIMAP), UMR 6252 CEA-CNRS-ENSICAEN, Université de Caen Normandie, 6 Boulevard Du Maréchal Juin, Caen Cedex 4, 14050, France

^e Prokhorov General Physics Institute, Russian Academy of Sciences, 38 Vavilova St., Moscow, 119991, Russia

^f Mendeleev University of Chemical Technology of Russia, 9 Miusskaya Sq., Moscow, 125047, Russia

^g Max Born Institute for Nonlinear Optics and Short Pulse Spectroscopy, Max-Born-Str. 2a, Berlin, 12489, Germany

^h Key Laboratory of Optoelectronic Materials Chemistry and Physics, Fujian Institute of Research on the Structure of Matter, Chinese Academy of Sciences, Fuzhou, Fujian, 350002, China

ARTICLE INFO

Keywords:

Zinc tungstate
Ytterbium lasers
Optical spectroscopy
Stark splitting
Luminescence
Laser operation

ABSTRACT

Monoclinic ytterbium-lithium codoped zinc mon tungstate crystal ($\text{Yb}^{3+}, \text{Li}^+:\text{ZnWO}_4$) is a promising material for laser operation at $\sim 1.06 \mu\text{m}$. Absorption, σ_{abs} , and stimulated-emission, σ_{SE} , cross-sections are determined for light polarized along the optical indicatrix axes, $E \parallel N_p, N_m$ and N_g . At room temperature, the maximum σ_{SE} amounts to $2.81 \times 10^{-20} \text{ cm}^2$ at 1055.6 nm (for $E \parallel N_p$) and the gain bandwidth reaches $\sim 22 \text{ nm}$ (for $E \parallel N_g$). The radiative lifetime of the upper laser level is 0.37 ms. The Stark splitting of Yb^{3+} multiplets is resolved with low-temperature (6 K) spectroscopy revealing a relatively large total splitting of the ground-state, $\Delta E(^2F_{7/2}) = 804 \text{ cm}^{-1}$, being remarkably high as compared to other Yb^{3+} -doped tungstate crystals. A notable inhomogeneous broadening of the zero-phonon line is detected at 6 K. A continuous-wave diode-pumped 1.8 at.% $\text{Yb}^{3+}, \text{Li}^+:\text{ZnWO}_4$ laser generated a maximum output power of 2.90 W at $\sim 1059 \text{ nm}$ with a slope efficiency of 57.9% and a linearly polarized output ($E \parallel N_p$). $\text{Yb}^{3+}, \text{Li}^+:\text{ZnWO}_4$ is attractive for broadly tunable and mode-locked oscillators.

1. Introduction

The ytterbium (Yb^{3+}) ion (electronic configuration: $[\text{Xe}]4f^{13}$) is a major subject of research on laser emission at $\sim 1 \mu\text{m}$ owing to its $^2F_{5/2} \rightarrow ^2F_{7/2}$ transition. This is because of the following advantages: (i) easy pumping by commercial InGaAs laser diodes emitting at $\sim 0.96\text{--}0.98 \mu\text{m}$ [1–3], (ii) simple energy-level scheme leading to high laser efficiencies and weak heat loading [4,5], (iii) larger Stark splitting of the ground-state ($^2F_{7/2}$) as compared with Nd^{3+} ion, leading to broader wavelength tunability and the generation of ultrashort pulses in mode-locked (ML) lasers [6], (iv) the absence of parasitic energy-transfer processes [7].

Tungstate crystals with different crystallographic structures are known as excellent hosts for Yb^{3+} doping [8–11]. In general, they benefit from high transition cross-sections for polarized light [8], broad emission bands which are attractive for sub-100 fs ML lasers [6,9] and strong Raman activity making self-frequency Raman conversion feasible [12].

A prominent example is the crystal family of monoclinic (sp. gr. $C2/c$) potassium (rare-earth) double tungstates $\text{Yb:KRE}(\text{WO}_4)_2$ where RE = Gd, Y or Lu [8,13]. These crystals feature a substitutional rare-earth site (symmetry: C_2) and easy Yb^{3+} doping. Efficient continuous-wave (CW) [14,15], passively Q-switched (PQS) [16] and ML [6,17] $\text{Yb:KRE}(\text{WO}_4)_2$ lasers are known. The drawback of these materials as laser gain media is

* Corresponding author.

E-mail address: xavier.mateos@urv.cat (X. Mateos).

<https://doi.org/10.1016/j.jlumin.2020.117811>

Received 24 June 2020; Received in revised form 22 November 2020; Accepted 24 November 2020

Available online 27 November 2020

0022-2313/© 2020 Published by Elsevier B.V.

their moderate thermal conductivity ($\langle\kappa\rangle = 3.1 \text{ Wm}^{-1}\text{K}^{-1}$ for $\text{KLu}(\text{WO}_4)_2$ [18]) and strong anisotropic thermal expansion [19]. Another difficulty is that all the $\text{KRE}(\text{WO}_4)_2$ representatives exhibit a polymorphic phase transformation below the melting point and the monoclinic low-temperature phase (α -phase) of interest for lasing cannot be directly obtained from the melt, therefore the Top-Seeded Solution Growth (TSSG) method (using a flux) [8] is needed for the growth of these crystals.

A second family of tungstate crystals deeply studied for Yb^{3+} doping comprises materials with a general chemical formula of $\text{ARE}(\text{WO}_4)_2$ (where $A = \text{Li}$ or Na and $\text{RE} = \text{La}, \text{Gd}, \text{Y}, \text{Lu}$ or Bi) [9,20–22]. These crystals belong to the tetragonal class (having a scheelite-like structure, sp. gr. $I\bar{4}$) and they are structurally disordered, as the A^+ and RE^{3+} cations share two non-equivalent sites ($2b$ and $2d$) [22]. This leads to a significant inhomogeneous broadening of Yb^{3+} emission bands. Laser action in Yb^{3+} -doped $\text{ARE}(\text{WO}_4)_2$ crystals was demonstrated and they were found particularly attractive for ML oscillators [9]. The majority of scheelite-like double tungstate crystals can be grown by the Czochralski (Cz) method (from the melt) [23]. Because of the disordered structure, the thermal conductivity of these crystals is relatively low, $\langle\kappa\rangle \sim 1.6 \text{ Wm}^{-1}\text{K}^{-1}$, however, an “S” shaped dependence of thermal conductivity on the temperature is observed leading to higher κ values above room temperature [24].

Recently, another crystal family of monoclinic (sp. gr. $P2_1/c$) divalent-metal monotungstates M^{2+}WO_4 (where $M = \text{Mg}, \text{Cu}, \text{Ni}, \text{Co}, \text{Fe}, \text{Zn}, \text{Mn}$ or Cd) has attracted attention for doping with rare-earth ions (RE^{3+}) with laser applications [10,25,26]. Two examples of such host crystals are magnesium and zinc monotungstates, MgWO_4 [27] and ZnWO_4 [28], respectively. These crystals offer better thermo-mechanical properties in comparison with two above mentioned families of tungstates, in particular, higher thermal conductivity ($\langle\kappa\rangle = 8.7 \text{ Wm}^{-1}\text{K}^{-1}$ for MgWO_4 [29]) and weaker anisotropy of the thermal expansion [25], that is important for power scaling of lasers. The large RE^{3+} ions in the M^{2+}WO_4 crystals substitute for the smaller divalent-metal cations (e.g., Mg^{2+} or Zn^{2+}) via a heterovalent mechanism, so that the segregation coefficients K_{RE} of the RE^{3+} dopants between the crystals and the fluxes are typically well below 1, and large RE^{3+} doping concentrations are hardly achievable in these materials [26]. However, the differences in ionic radii and valence of the active ions and the host-forming cations promote enlarged Stark splitting of the RE^{3+} multiplets and inhomogeneous broadening of the absorption and emission bands [25,30].

So far, laser operation with RE^{3+} -doped MgWO_4 crystals has been demonstrated at $\sim 1 \mu\text{m}$ (with Yb^{3+}) [5,10] and at $\sim 2 \mu\text{m}$ (with Tm^{3+} and Ho^{3+}) [25,31,32]. In the first report on Yb:MgWO_4 , the crystal growth by the TSSG method, room-temperature (RT) spectroscopy and preliminary laser experiment were described [10]. Later on, low temperature (LT) spectroscopy and highly-efficient laser operation were reported: a diode-pumped 1.25 at.% Yb:MgWO_4 laser generated 18.2 W at $\sim 1056 \text{ nm}$ with a slope efficiency of 89% and a linearly polarized output [5]. In Ref. [33], an Yb:MgWO_4 oscillator was mode-locked by a Semiconductor Saturable Absorber Mirror (SESAM) delivering 125 fs pulses at 1065 nm with a repetition rate of 117 MHz. In Ref. [34], a diode-pumped Yb:MgWO_4 laser generated an optical vortex beam corresponding to the first-order Laguerre–Gaussian doughnut beam (LG_{01}).

Compared to the research on RE^{3+} -doped MgWO_4 crystals for laser applications, much less attention has been paid to their zinc counterparts. However, unlike MgWO_4 , ZnWO_4 crystals melt congruently at 1486 K and thus they can be easily grown by the conventional Czochralski (Cz) method [35,36]. The thermal conductivity of undoped ZnWO_4 is slightly higher than that for monoclinic double tungstates ($\langle\kappa\rangle$ up to $4.3 \text{ Wm}^{-1}\text{K}^{-1}$) [24,37]. Undoped ZnWO_4 is well-known during many years as a promising scintillating material [35,36]. So far, one group repetitively presented the results on the growth and brief optical characterization of ZnWO_4 crystals doped with Yb^{3+} , Tm^{3+} ,

Er^{3+} , Ho^{3+} and Dy^{3+} [38–42]. Yang reported on laser operation of Yb:ZnWO_4 yielding 0.5 W at 1017 nm with an estimated slope efficiency of only $\sim 6\%$ [38]. Tm:ZnWO_4 and Dy:ZnWO_4 lasers are also known [43, 44].

In the first part of this work [45], we presented the results on the Cz crystal growth, its coloration, structure refinement and vibronic properties. In the present work, we assess the potential of Yb^{3+} -doped zinc tungstate as a promising laser material at $\sim 1 \mu\text{m}$. The polarized room temperature (RT, 293 K) and low temperature (LT, down to 6 K) spectroscopy of $\text{Yb}^{3+}, \text{Li}^+:\text{ZnWO}_4$ crystals are studied and efficient diode-pumped laser operation is achieved.

2. Experimental

2.1. Crystal growth

For spectroscopic and laser studies, two ZnWO_4 crystals codoped with (5 at.% Yb^{3+} , 5 at.% Li^+) and (3 at.% Yb^{3+} , 3 at.% Li^+) ions (nominal composition, in the growth charge) were grown by the Czochralski method. The growth was performed in Pt/Rh crucibles. The starting materials were WO_3 , ZnO , Li_2CO_3 (as the source of Li^+ ions) and Yb_2O_3 . The Li^+ ions were added as charge compensators of heterovalent Zn^{2+} to Yb^{3+} substitution. The starting composition was calculated assuming that the Yb^{3+} and Li^+ ions substitute for the Zn^{2+} ones in the ZnWO_4 structure. For the growth, a [100]-oriented undoped seed was used. The pulling rate was 1 mm/h and the rotation speed was 6 rpm. Once the growth was completed, the crystal was separated from the melt and slowly (at a rate of 8 K/h) cooled down to RT to avoid its cracking. The as-grown crystals were black-colored with a well-developed natural faceting parallel to the (010) cleavage plane. The crystals were oriented by means of the single-crystal X-ray diffraction. The crystal exhibited cleavage on the (010) plane.

The crystal coloration was removed by oxidizing annealing at a temperature of 800 °C. The duration at the maximum temperature was 24 h. After annealing, thin (few mm) crystal plates became transparent having a weak rose coloration. More details about the crystal growth, cleavage, coloration and the ways of its removal can be found in the parallel paper [45].

The actual Yb^{3+} concentration N_{Yb} in the crystals was measured by the microprobe analysis using a Cameca Camebax SX-100 analyzer. It amounted to $N_{\text{Yb}} = 2.0 \pm 0.7 \times 10^{20} \text{ cm}^{-3}$ (~ 1.4 at.% Yb) and $2.7 \pm 0.5 \times 10^{20} \text{ cm}^{-3}$ (~ 1.8 at.% Yb) for the crystals with the nominal doping level of 3 at.% and 5 at.% Yb^{3+} , respectively.

2.2. Optical spectroscopy

The polarized RT absorption spectra were measured using a Varian CARY-5000 spectrophotometer and a Glan-Taylor polarizer. To measure the absorption spectra at LT, the sample was fixed within an Oxford Instruments Ltd. cryostat (model SU 12) with helium-gas close-cycle flow. The spectral bandwidth (SBW) was 0.6 nm.

The polarized RT (293 K) luminescence spectra were measured using an Ando AQ6315-E optical spectrum analyzer (OSA) and a Glan-Taylor polarizer. As an excitation source, we used a CW Ti:Sapphire laser tuned to 940 and 972 nm (the two measurements were combined to eliminate the excitation peak). For the LT studies, a Yokogawa AQ6373 OSA was employed using a 965 nm InGaAs laser diode as a pump source. The same cryostat was used.

The luminescence decay of $\text{Yb}^{3+}:\text{ZnWO}_4$ at $\sim 1030 \text{ nm}$ was studied using a 1/4 m monochromator (Oriel 77200), an InGaAs detector and a 300 MHz digital oscilloscope (TDS 3032B, Tektronix). The luminescence was excited by the output of a ns optical parametric oscillator (OPO, Horizon, Continuum) tuned to 960 nm.

3. Optical spectroscopy

3.1. Optical indicatrix

According to the Rietveld refinement of the X-ray powder diffraction patterns (see Part I of this paper), $\text{Yb}^{3+}, \text{Li}^+:\text{ZnWO}_4$ belongs to the monoclinic crystal class (sp. gr. $P2/c - C_{2h}^4$, wolframite-type structure). The lattice constants for the 1.8 at.% $\text{Yb}^{3+}, \text{Li}^+:\text{ZnWO}_4$ crystal are $a = 4.702(2) \text{ \AA}$, $b = 5.718(6) \text{ \AA}$, $c = 4.930(4) \text{ \AA}$ and $\beta = 90.713(5)^\circ$ with $Z = 2$ [45]. This crystal is optically biaxial [46]. Its optical properties are described in the frame of mutually orthogonal optical indicatrix axes, denoted as X, Y and Z. Note that, in general, no relation for the n_x , n_y and n_z refractive indices is placed. One axis is parallel to the 2-fold monoclinic axis (the crystallographic b -axis) and the other two are located in the orthogonal a - c plane making certain angles with the crystallographic axes.

The dispersion of the principal refractive indices of undoped ZnWO_4 was studied in Ref. [47] yielding the following values at 1.0 \mu m : $n_p = 2.1299$, $n_m = 2.1447$ and $n_g = 2.2790$. Here, we use the notations for monoclinic laser crystals, where the optical indicatrix axes are labeled as N_p , N_m and N_g according to the relation between the refractive indices: $n_p < n_m < n_g$. If the intermediate refractive index (n_m) is nearer in magnitude to the smallest one (n_p) than to n_g , the crystal is biaxial positive which is the case of ZnWO_4 . The optical axes are located in the N_p - N_g plane and the angle between them, containing N_g , is $2V_g < 45^\circ$ (for ZnWO_4 , $2V_g = 38.4^\circ$ at 1.0 \mu m , and this crystal is quasi-uniaxial). Here, V_g is the angle between each of the optical axes and the N_g -axis.

There exists a discrepancy in the assignment between the (X, Y, Z) and (N_p , N_m , N_g) axes for ZnWO_4 in the literature. The only work where the axes are unambiguously assigned is [48]. We will follow their convention: the N_p axis is parallel to the b -axis and the N_m and N_g ones are located in the a - c plane, Fig. 1. According to Refs. [48], the angle between the N_g -axis and the c -axis $\rho = 11.93^\circ$ (at the longest available wavelength of 0.69 \mu m), measured within the monoclinic angle β . This assignment is in agreement with the early paper of Spengler and O'Hara where the (X, Y, Z) notations for the optical indicatrix axes were used assuming that the authors followed the $n_x < n_y < n_z$ convention [46]. However, both these studies disagree with the repetitive publications on

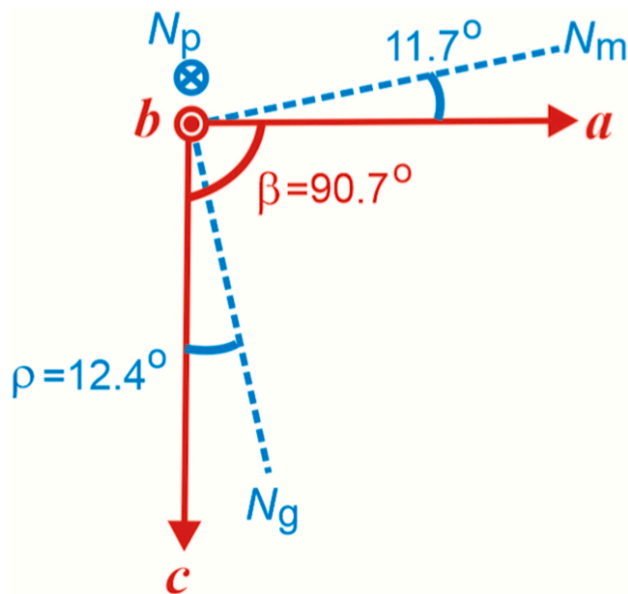


Fig. 1. Orientation of the optical indicatrix axes (N_p , N_m , N_g) with respect to the crystallographic frame (a , b , c) in monoclinic ZnWO_4 . The angle ρ is specified at the wavelength of $\sim 1 \text{ \mu m}$.

RE^{3+} -doped ZnWO_4 crystals published more recently [39,42].

An overview of the reported refractive indices for ZnWO_4 is shown in Fig. 2(a). The data from different authors agree well. The experimental data on the dispersion of the n_p , n_m and n_g refractive indices were fitted using a single-pole Sellmeier formula with an IR correction term:

$$n_i^2(\lambda) = A_i + \frac{B_i \lambda^2}{\lambda^2 - C_i} - D_i \lambda^2, \quad (1)$$

Here, $A_i - D_i$ are the Sellmeier coefficients, λ is the light wavelength [in \mu m], and $i = p, m, g$. The obtained best-fit Sellmeier curves are shown in Fig. 2(a) and the corresponding $A_i - D_i$ coefficients are listed in Table 1. The average deviation between the experimental data and their fits is about 0.0002.

The optical bandgap of undoped ZnWO_4 E_g is $3.9\text{--}4.4 \text{ eV}$ [50].

Similarly to other monoclinic tungstates [49], a rotation of the dielectric frame with the wavelength was determined for ZnWO_4 in the angular range of $\rho = 6.88^\circ\text{--}11.93^\circ$ for wavelengths between 0.40 and 0.69 \mu m [48]. Slightly different values of the ρ angle can be found in the literature: Spengler and O'Hara specified $\rho = 9.80^\circ$ at 0.59 \mu m [46] and Bond gave $\rho = 8.20^\circ$ at $\sim 1 \text{ \mu m}$ [47]. The literature data on ρ are summarized in Fig. 2(b) while the data from Bond [47] are shifted along the vertical axis to correspond to two other sources. They were fitted with the following formula [49]:

$$\rho(\lambda) = A + \frac{B}{\lambda} + \frac{C}{\lambda^2}, \quad (2)$$

where ρ is expressed in deg and λ is in \mu m . The best-fitting parameters $A = 12.792 \text{ deg}$ (it corresponds to the rotation angle in the long-wavelength limit, $\lambda \rightarrow \infty$), $B = 1.0294 \text{ deg} \times \text{\mu m}$ and $C = -1.4239 \text{ deg} \times \text{\mu m}^2$. At $\sim 1 \text{ \mu m}$ relevant for the Yb^{3+} ion, Eq. (2) gives $\rho = 12.40^\circ$. This value is indicated in Fig. 1.

3.2. RT absorption cross-sections

The transition cross-sections were determined at RT using a 1.8 at.% $\text{Yb}^{3+}, \text{Li}^+:\text{ZnWO}_4$ crystal ($N_{\text{Yb}} = 2.7 \times 10^{20} \text{ cm}^{-3}$).

The absorption cross-sections were calculated from the measured absorption coefficient, $\sigma_{\text{abs}}^i = \alpha_{\text{abs}}^i / N_{\text{Yb}}$ (where $i = N_p, N_m, N_g$ is the light polarization). The results are shown in Fig. 3(a). The maximum $\sigma_{\text{abs}} = 2.40 \times 10^{-20} \text{ cm}^2$ at 972.7 nm and the corresponding full width at half maximum (FWHM) of the absorption peak is 8.3 nm (for light polarization $E \parallel N_g$). This absorption peak corresponds to the zero-phonon line (ZPL) at RT (see below). The $\text{Yb}^{3+}, \text{Li}^+:\text{ZnWO}_4$ crystal exhibits a notable anisotropy of the absorption cross-sections, as expressed by the ratios $\sigma_{\text{abs}}(N_g) : \sigma_{\text{abs}}(N_p) = 2.6 : 1$ and $\sigma_{\text{abs}}(N_g) : \sigma_{\text{abs}}(N_m) = 4.7 : 1$ at the wavelength of $\sim 970 \text{ nm}$. Another intense and slightly broader absorption peak occurs at 958.4 nm ($\sigma_{\text{abs}} = 1.84 \times 10^{-20} \text{ cm}^2$ and FWHM = 9.8 nm again for $E \parallel N_g$). Both absorption peaks are suitable for pumping with InGaAs laser diodes. Due to the broad absorption lines, $\text{Yb}^{3+}, \text{Li}^+:\text{ZnWO}_4$ lasers are expected to be less sensitive to the temperature drift of the diode wavelength.

Compared to its magnesium counterpart ($\text{Yb}^{3+}:\text{MgWO}_4$ [5], for which $\sigma_{\text{abs}} = 6.16 \times 10^{-20} \text{ cm}^2$ at 974.0 nm with FWHM = 5.6 nm for $E \parallel N_g$), the studied material exhibits lower peak absorption cross-section values whilst much broader absorption peaks. This effect is even more pronounced when comparing with the monoclinic double tungstate crystal $\text{Yb}^{3+}:\text{KLu}(\text{WO}_4)_2$ [8] (for which σ_{abs} is as high as $11.8 \times 10^{-20} \text{ cm}^2$ at 981.0 nm with a FWHM of only 3.5 nm for the light polarization $E \parallel N_m$).

In a previous work on $\text{Yb}^{3+}:\text{ZnWO}_4$ (without Li^+), a maximum absorption cross-section of $2.6 \times 10^{-20} \text{ cm}^2$ at $\sim 972 \text{ nm}$ was reported [38]. This agrees with the present results. However, due to the probable confusion with the optical orientation of the sample, it is difficult to compare the polarized absorption spectra with those from Ref. [38].

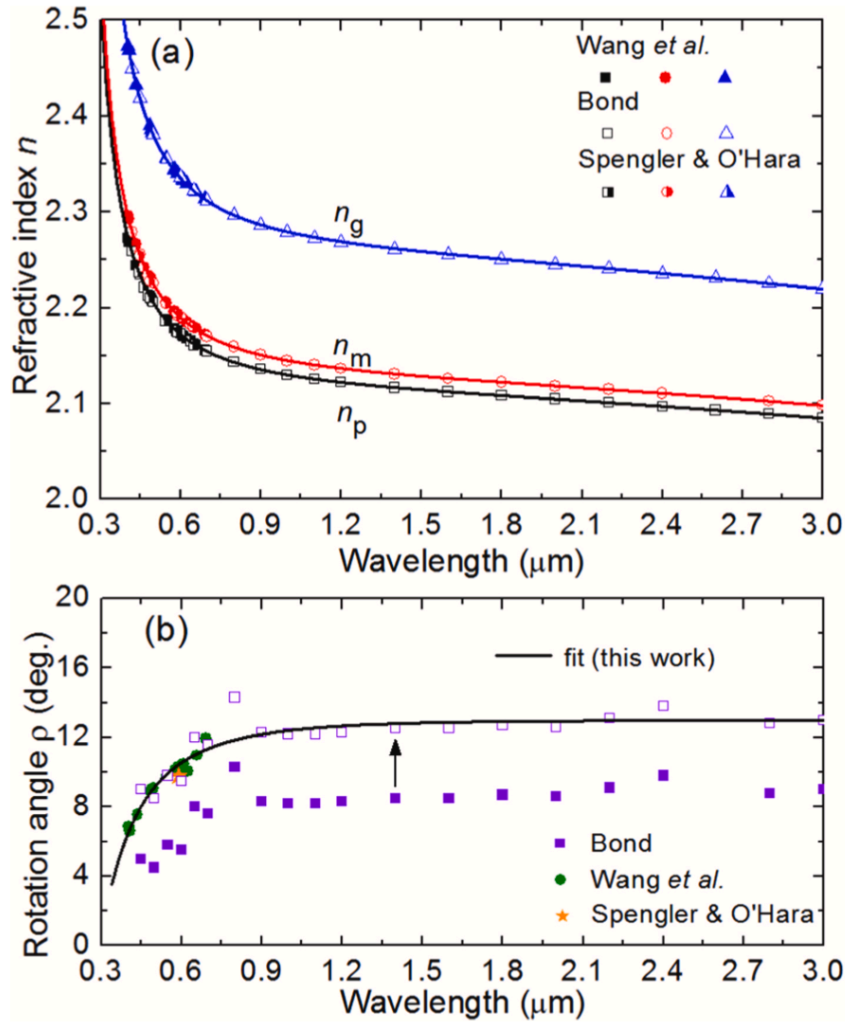


Fig. 2. (a) Dispersion of the principal refractive indices (n_p , n_m , n_g) in monoclinic ZnWO_4 ; symbols – literature data [46–48], curves – their fitting using Eq. (1). The best-fit parameters are listed in Table 1; (b) rotation of the dielectric frame (expressed by the angle ρ between the N_g and c axes in the a - c plane, Fig. 1) as a function of wavelength, filled symbols – literature data [46–48], curve – their fitting using Eq. (2). Open squares – data from Ref. [47] shifted along the vertical axis.

Table 1
 RT Sellmeier coefficients for the principal refractive indices of undoped ZnWO_4 crystal (this work).

n_i	A_i	B_i	$C_i, \mu\text{m}$	$D_i, \mu\text{m}^{-2}$
n_p	2.8443	1.6224	0.2222	0.01432
n_m	2.7334	1.7911	0.2195	0.01467
n_g	3.0034	2.0939	0.2312	0.02044

3.3. RT stimulated-emission and gain cross-sections

The stimulated-emission (SE) cross-sections, σ_{SE} , were determined from the measured luminescence spectra for polarized light calibrated for the spectral response of the set-up using the Füchtbauer–Ladenburg (F-L) equation [51]:

$$\sigma_{\text{SE}}^i(\lambda) = \frac{\lambda^5}{8\pi(n)^2\tau_{\text{rad}}c} \frac{W_i(\lambda)}{(1/3) \sum_{i=p,m,g} \int \lambda W_i(\lambda) d\lambda}, \quad (3)$$

where, λ is the light wavelength, $\langle n \rangle = 2.184$ is the mean refractive index at the mean emission wavelength $\langle \lambda_{\text{lum}} \rangle = 1010.0$ nm, c is the

speed of light, $\tau_{\text{rad}} = 0.37$ ms is the radiative lifetime of the emitting state (${}^2F_{5/2}$), see below, and $W_i(\lambda)$ is the luminescence spectrum for i -th polarization ($i = p, m, g$). To avoid the unwanted effect of reabsorption on the measured luminescence spectra, thin (thickness: $t < 100$ μm) (010)-oriented cleaved plates of $\text{Yb}^{3+}, \text{Li}^+:\text{ZnWO}_4$ were used. The results are shown in Fig. 3(b).

The SE cross-sections can be calculated alternatively by the reciprocity method (RM), or McCumber equation [52,53]:

$$\sigma_{\text{SE}}^i(\lambda) = \sigma_{\text{abs}}^i(\lambda) \frac{Z_1}{Z_2} \exp\left(-\frac{(hc/\lambda) - E_{\text{ZPL}}}{kT}\right), \quad (4)$$

where h is the Planck constant, (hc/λ) is the photon energy (in cm^{-1}), k is the Boltzmann constant, T is the crystal temperature (RT), E_{ZPL} is energy of the ZPL transition, and Z_m are the partition functions of the lower ($m = 1$) and upper ($m = 2$) manifolds:

$$Z_m = \sum_k g_k^m \exp(-E_k^m / kT) \quad (5)$$

Here, $g_k^m = 1$ is the degeneracy of the sub-level with the number k and energy E_k^m measured from the lowest sub-level of each multiplet.

Using the crystal-field splitting for the Yb^{3+} ion in ZnWO_4 (see

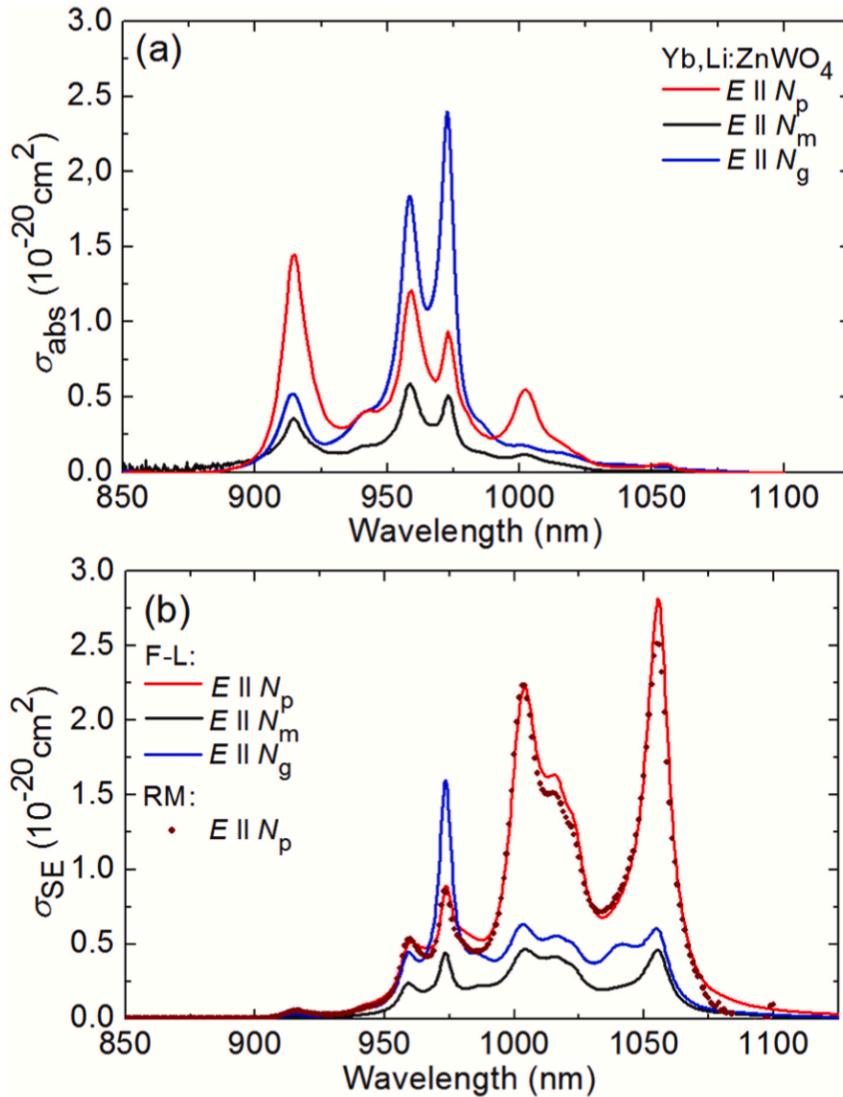


Fig. 3. RT spectroscopy of a 1.8 at.% $\text{Yb}^{3+}, \text{Li}^+:\text{ZnWO}_4$ crystal: (a) absorption cross-section, σ_{abs} , spectra; (b) stimulated-emission cross-section, σ_{SE} , spectra. The light polarizations are $E \parallel N_p, N_m, N_g$. The σ_{SE} values are calculated using the F-L formula, Eq. (3). For light polarization $E \parallel N_p$, the results on σ_{SE} calculated with the reciprocity method (RM), Eq. (4), are given for comparison.

Section 3.5), we calculated the SE cross-sections via Eq. (4). A comparison of the results obtained with the F-L equation and the RM for the light polarization $E \parallel N_p$ is shown in Fig. 3(b). Note that due to the exponential term in Eq. (4), the precision of the SE cross-sections calculated by the RM is lower at longer wavelengths. The two methods used give a satisfactory agreement indicating the correctness of the selected τ_{rad} value (0.37 ± 0.02 ms), as well as the weak influence of the reabsorption on the measured luminescence spectra.

The maximum $\sigma_{\text{SE}} = 2.81 \times 10^{-20} \text{ cm}^2$ at 1055.6 nm and the corresponding emission bandwidth $\Delta\lambda_{\text{em}}$ (FWHM) is ~ 12 nm (for $E \parallel N_p$). Similarly to the absorption transition, strong anisotropy of the SE cross-sections is observed, namely $\sigma_{\text{SE}}(N_p) : \sigma_{\text{SE}}(N_g) = 4.6 : 1$ and $\sigma_{\text{SE}}(N_p) : \sigma_{\text{SE}}(N_m) = 6.2 : 1$ at $\sim 1.06 \mu\text{m}$. This will determine a linearly polarized output in the $\text{Yb}^{3+}, \text{Li}^+:\text{ZnWO}_4$ lasers. Note that at the wavelength of ~ 973 nm (ZPL at RT in emission), the relation for the SE cross-sections is different, $\sigma_{\text{SE}}(N_g) > \sigma_{\text{SE}}(N_p) > \sigma_{\text{SE}}(N_m)$, i.e., in agreement with the one discussed in Section 3.2. There exists another broader peak in the σ_{SE} spectra centered at 1004.1 nm featuring a FWHM of ~ 28 nm (again for E

$\parallel N_p$). The two other polarizations ($E \parallel N_g$ and $E \parallel N_m$) feature broader emission bandwidths at $>1 \mu\text{m}$, however, the spectra are rather structured. Thus, direct laser studies are needed to determine the optimum polarization for generation of ultrashort pulses in ML operation.

The peak σ_{SE} values in $\text{Yb}^{3+}, \text{Li}^+:\text{ZnWO}_4$ are lower than those for its magnesium counterpart ($\text{Yb}^{3+}, \text{MgWO}_4$ [5], for which σ_{SE} reaches $6.2 \times 10^{-20} \text{ cm}^2$ at 1056.7 nm for $E \parallel N_m$ and the emission bandwidth $\Delta\lambda_{\text{em}}$ (FWHM) is 19 nm) and similar to the SE cross-sections for monoclinic double tungstate $\text{Yb}^{3+}:\text{KLu}(\text{WO}_4)_2$ (for which $\sigma_{\text{SE}} = 2.64 \times 10^{-20} \text{ cm}^2$ at 1026.6 nm and $\Delta\lambda_{\text{em}}$ is ~ 10 nm [8]). The emission bandwidth for $\text{Yb}^{3+}, \text{Li}^+:\text{ZnWO}_4$ is similar or even better than in the two above mentioned tungstate crystals. Note that here, we consider the SE cross-sections at wavelengths longer than the ZPL since such wavelengths are typically expected in bulk Yb lasers (see below).

The Yb^{3+} ion represents a quasi-three-level laser scheme with reabsorption at the laser wavelength. Thus, the gain cross-sections:

$$\sigma_{\text{gain}} = \beta\sigma_{\text{SE}} - (1 - \beta)\sigma_{\text{abs}}, \quad (6)$$

where $\beta = N_2(^2F_{5/2})/N_{Yb}$ is the inversion ratio and N_2 is the population of the upper laser level ($^2F_{5/2}$), are calculated to conclude about the possible laser wavelength and gain bandwidths $\Delta\lambda_{\text{gain}}$. The results are shown in Fig. 4 for the high-gain light polarizations $E \parallel N_p$ and $E \parallel N_g$. For $E \parallel N_p$, the local peak at ~ 1056 nm dominates in the gain spectra. The gain bandwidth $\Delta\lambda_{\text{gain}}$ (FWHM) is 11.6 nm (for $\beta = 0.15$). For the $E \parallel N_g$ polarization, with increasing the inversion ratio, several local maxima in the gain spectra are observed at ~ 1056 , 1040, 1022 and 1003 nm. The gain bandwidth is larger, $\Delta\lambda_{\text{gain}} = 22.2$ nm (for the same $\beta = 0.15$).

Note that the strongest emission peak of Yb^{3+} ions in the $\text{Yb}^{3+}, \text{Li}^+$: ZnWO_4 crystal (at the wavelength of ~ 1056 nm for $E \parallel N_p$) corresponds to almost zero absorption (the reabsorption cross-section, $\sigma_{\text{abs}} = 0.05 \times 10^{-20}$ cm²). This causes positive gain around this wavelength even at low β , that gives a hope for obtaining low threshold lasing at ~ 1056 nm in the $\text{Yb}^{3+}, \text{Li}^+$: ZnWO_4 crystal.

3.4. Luminescence decay

The luminescence decay of $\text{Yb}^{3+}, \text{Li}^+$: ZnWO_4 was studied at RT. Very thin ($t < 100$ μm) cleaved plates were used to avoid the radiation trapping effect. The decay curve, Fig. 5, is single-exponential and the luminescence lifetime τ_{lum} is 367 μs . This agrees with the presence of a single site for Yb^{3+} ions in ZnWO_4 (symmetry: C_2). Previously for Yb^{3+} :

ZnWO_4 (without Li^+ codoping), τ_{lum} was determined to be 644 μs using a bulk crystal [38]. This value may be overestimated due to the reabsorption effect.

The calculation of the SE cross-sections by two independent methods (the F-L equation and the RM, Section 3.3), yields an estimation for the radiative lifetime $\tau_{\text{rad}} = 0.37 \pm 0.02$ ms. Thus, the luminescence quantum efficiency for $\text{Yb}^{3+}, \text{Li}^+$: ZnWO_4 $\eta_q = \tau_{\text{lum}}/\tau_{\text{rad}}$ is close to unity. This agrees with the ‘‘energy-gap law’’ for non-radiative relaxation [54] postulating that it is weak when the energy-gap to the lower-lying multiplet ($\Delta E = 9481$ cm⁻¹, in our case) is at least 4 times higher than the maximum phonon energy of the host ($h\nu_{\text{ph}} = 906$ cm⁻¹ [45]).

3.5. Crystal-field splitting

To resolve the Stark splitting of the Yb^{3+} multiplets in ZnWO_4 , the polarized absorption and luminescence spectra were measured in the temperature range of 6–293 K, Fig. 6. The studies were performed for the following light polarizations: $E \parallel a$ ($\approx N_m$) and $E \parallel b$ (N_p) in absorption and $E \parallel c$ ($\approx N_g$) and $E \parallel b$ (N_p) in emission. For Yb^{3+} ions in sites with the C_2 symmetry, there is a total of $J + 1/2$ Stark sub-levels for each $2^{5+1}L_J$ multiplet, denoted as 0..3 for $^2F_{7/2}$ and 0'..2' for $^2F_{5/2}$, respectively. The interpretation of the electronic transitions was performed accounting for the Raman spectra (see Part I of this paper).

At the temperature of 6 K, the populations of all the Stark sub-levels of the ground multiplet (except of the lowest one) are greatly reduced.

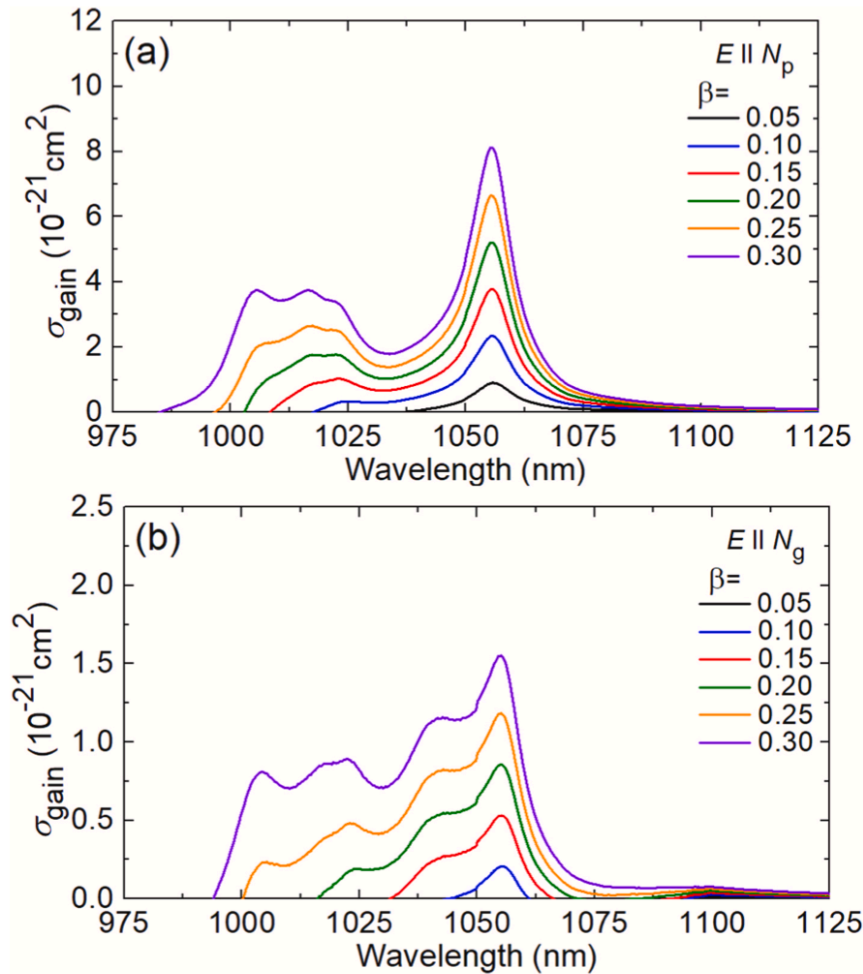


Fig. 4. RT gain cross-section, $\sigma_{\text{gain}} = \beta\sigma_{\text{SE}} - (1 - \beta)\sigma_{\text{abs}}$, spectra for the $^2F_{5/2} \leftrightarrow ^2F_{7/2}$ transition of Yb^{3+} : ZnWO_4 . The light polarizations are (a) $E \parallel N_p$ and (b) $E \parallel N_g$. $\beta = N_2(^2F_{5/2})/N_{Yb}$ is the inversion ratio, N_2 is the population of the upper laser level ($^2F_{5/2}$).

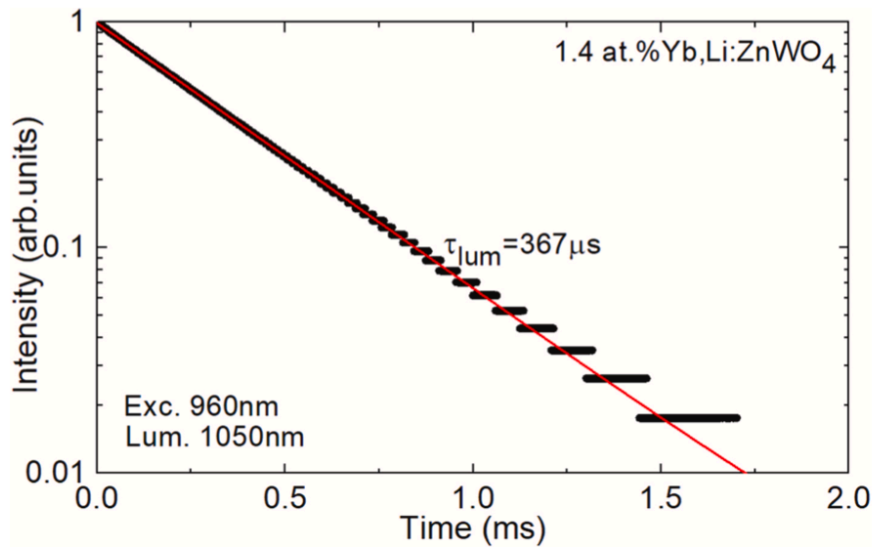


Fig. 5. RT luminescence decay curve for thin ($t < 100 \mu\text{m}$) cleaved plates of 1.4 at.% $\text{Yb}^{3+}, \text{Li}^+:\text{ZnWO}_4$ crystal, $\lambda_{\text{exc}} = 960 \text{ nm}$, $\lambda_{\text{lum}} = 1050 \text{ nm}$. Symbols – experimental data, line – single-exponential fit.

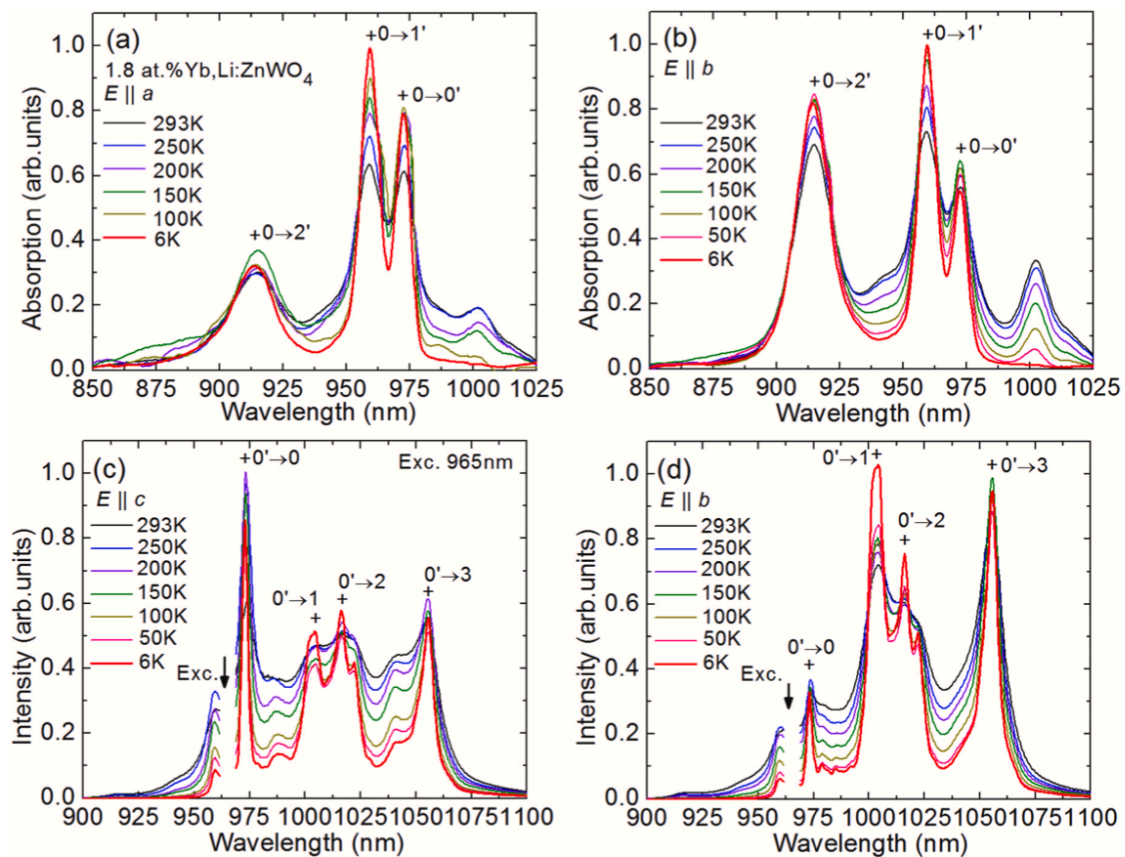


Fig. 6. LT (6–293 K) spectroscopy of a 1.8 at.% $\text{Yb}^{3+}, \text{Li}^+:\text{ZnWO}_4$ crystal: (a,b) absorption spectra for light polarizations (a) $E \parallel a$ and (b) $E \parallel b$; (c,d) luminescence spectra for light polarizations (c) $E \parallel c$ and (d) $E \parallel b$, $\lambda_{\text{exc}} = 965 \text{ nm}$.

Moreover, the electron-phonon coupling is also suppressed. Nevertheless, Yb^{3+} ions in ZnWO_4 exhibit large bandwidth of the zero-phonon line (ZPL), i.e., the transition between the lowest Stark sub-levels of two multiplets, or $0 \leftrightarrow 0'$. Indeed, $\Delta\lambda_{\text{ZPL}} = 3.0 \text{ nm}$ (for $E \parallel N_p$, as

determined from the luminescence spectrum measured with a better resolution of $\text{SBW} = 0.6 \text{ nm}$). Compared to the monoclinic $\text{Yb:KY}(\text{WO}_4)_2$ crystal ($\Delta\lambda_{\text{ZPL}} < 0.1 \text{ nm}$ for $E \parallel N_p$) [55], this is much broader. Besides that, the ZPL in absorption has a poorly resolved slightly asymmetric

shape. The notable inhomogeneous broadening of the ZPL transition in the $\text{Yb}^{3+}, \text{Li}^+:\text{ZnWO}_4$ crystal can be explained both by the difference in the ionic radii of Yb^{3+} , Li^+ and Zn^{2+} ions ($R_{\text{Yb}} = 0.868 \text{ \AA}$, $R_{\text{Li}} = 0.76 \text{ \AA}$ and $R_{\text{Zn}} = 0.74 \text{ \AA}$ for VI-fold oxygen coordination [56]), and by heterovalent mechanism of substitution of Zn^{2+} by Yb^{3+} and Li^+ ions.

Formally, ZnWO_4 is an ordered crystal; the Zn^{2+} ions accommodate in a single type of sites (Wyckoff symbol: 2e). However, in reality, each Li^+ , and, especially, Yb^{3+} ion in the Zn^{2+} sub-lattice is a charged point defect, which brings both the spatial distortions (due to the difference in ionic radii), and the distortions in distribution of the electron density (due to the difference in formal charges) in its local environment. Besides that, as it was shown in the first part of this work [45], the actual Li^+ amount in the crystal is lower than the content of Yb^{3+} ions. It means that essential part of Yb^{3+} remains uncompensated by Li^+ ions. Thus, there additionally should be some amount of another kind charge compensators, probably, zinc vacancies. It is the third kind of point defects, acting in a similar way, as Yb^{3+} and Li^+ ions do. Each Yb^{3+} active center has its own kind of surrounding by these three kinds of points defects, and, consequently, its own kind of crystal field, very slightly differing from that of other Yb^{3+} active centers. In other words, some (rather slight) extent of the structural disordering do exist in the crystal. A similar behavior was detected recently for Yb^{3+} -doped isostructural MgWO_4 crystal, revealing $\Delta\lambda_{\text{ZPL}} = 3.3 \text{ nm}$ for $E \parallel N_m$ [5].

The energy-level scheme of Yb^{3+} in ZnWO_4 is shown in Fig. 7(a). The ZPL has an energy of $E_{\text{ZPL}} = 10285 \text{ cm}^{-1}$. The corresponding transition wavelength at 6 K is 972.3 nm. At RT, the partition functions Z_m for the lower ($m = 1$) and upper ($m = 2$) manifolds are $Z_1 = 1.345$ and $Z_2 = 1.548$ (the ratio: $Z_1/Z_2 = 0.869$).

The total Stark splitting of the ground-state $\Delta E(^2F_{7/2})$ is 804 cm^{-1} . In general, larger $\Delta E(^2F_{7/2})$ supports wavelength tuning, shorter pulses under ML operation regime, longer achievable laser wavelengths, as well as lower lasing threshold and its weaker sensitivity to the temperature increase. The ground-state splitting for Yb^{3+} in ZnWO_4 exceeds those of other known tungstate crystals employed for diode-pumped lasers at $\sim 1 \mu\text{m}$, such as monoclinic ordered $\text{Yb}:\text{MgWO}_4$, 765 cm^{-1} [5], monoclinic ordered $\text{Yb}:\text{KLu}(\text{WO}_4)_2$, 559 cm^{-1} [8], and tetragonal disordered $\text{Yb}:\text{NaGd}(\text{WO}_4)_2$, 482 cm^{-1} (2d sites) and 492 cm^{-1} (2b sites) [22], Fig. 7(b). Note that the local symmetry of the site (sites) for Yb^{3+} ions is the same for all the considered monoclinic crystals (C_2) and it is different for the tetragonal scheelite-type one (S_4).

For all the RE^{3+} ions, it is known that the barycenter energy of any isolated $^{2S+1}L_J 4f^n$ multiplet shows a linear variation with the barycenter

energy of any other multiplet. This is expressed by the so-called barycenter plot [57], Fig. 8. The barycenter energies $\langle E(^2F_{5/2}) \rangle$ and $\langle E(^2F_{7/2}) \rangle$ for $\text{Yb}^{3+}, \text{Li}^+:\text{ZnWO}_4$ agree well with the linear fit of this plot, expressed by equation $E(^2F_{5/2}) = 10166.6 + 0.997 \times E(^2F_{7/2})$ [in cm^{-1}], where $E_0 = 10166.6 \text{ cm}^{-1}$ has the meaning of the energy of the Yb^{3+} excited-state assuming a free ion. This analysis confirms the correctness of the constructed energy-level scheme.

4. Laser operation

4.1. Laser set-up

For laser experiments, we fabricated a rectangular active element from the 1.8 at.% $\text{Yb}^{3+}, \text{Li}^+:\text{ZnWO}_4$ crystal ($t = 3.85 \text{ mm}$, aperture: $7.3 \times 6.5 \text{ mm}^2$). It was cut for light propagation along the a -axis (a -cut). Its input and output facets were polished to laser quality and remained uncoated. The element was wrapped with In foil from all four lateral sides to improve the thermal contact and mounted in a Cu-holder. The latter was cooled by circulating water ($T = 12 \text{ }^\circ\text{C}$). The laser crystal was placed in a linear plano-concave (hemispherical) cavity formed by a flat pump mirror (PM) coated for high transmission (HT) at the pump wavelength ($\sim 0.97 \mu\text{m}$) and for high reflectance (HR) at 1.02–1.2 μm , and a set of concave output couplers (OCs) with a transmission $T_{\text{OC}} = 3\%–10\%$ at the laser wavelength ($\sim 1.06 \mu\text{m}$) and a radius of curvature (RoC) of 50 mm. The scheme of the experimental set-up is shown in Fig. 9. The PM was placed at $\sim 1 \text{ mm}$ separation from the laser element. The geometrical cavity length was 49 mm.

The pump source was a fiber-coupled (N.A. = 0.22, fiber core diameter: 105 μm) InGaAs laser diode emitting up to 54 W of unpolarized output at a central wavelength of 968 nm (emission bandwidth: 1.5 nm, $M^2 \approx 37$). The pump was reimaged into the crystal using a lens assembly (imaging ratio: 1:1, $f = 30 \text{ mm}$) leading to a pump spot diameter $2w_p \approx 100 \mu\text{m}$ and a confocal parameter $2z_R \approx 1 \text{ mm}$ (in the crystal). Despite the reflectivity of the OCs at the pump wavelength, the counter-propagating pump beam was focused before the crystal, so that the second pass of the pump did not contribute to the laser output. The small-signal pump absorption η_{abs0} was calculated from the unpolarized transmission spectrum to be 32.8%. The value determined from the pump-transmission measurement at the threshold pump power and accounting for the absorption saturation was smaller, $\eta_{\text{abs,L}} = 23.2\%$. It was used to determine the absorbed pump power, P_{abs} . Here, we took into account the Fresnel losses at the uncoated crystal surfaces.

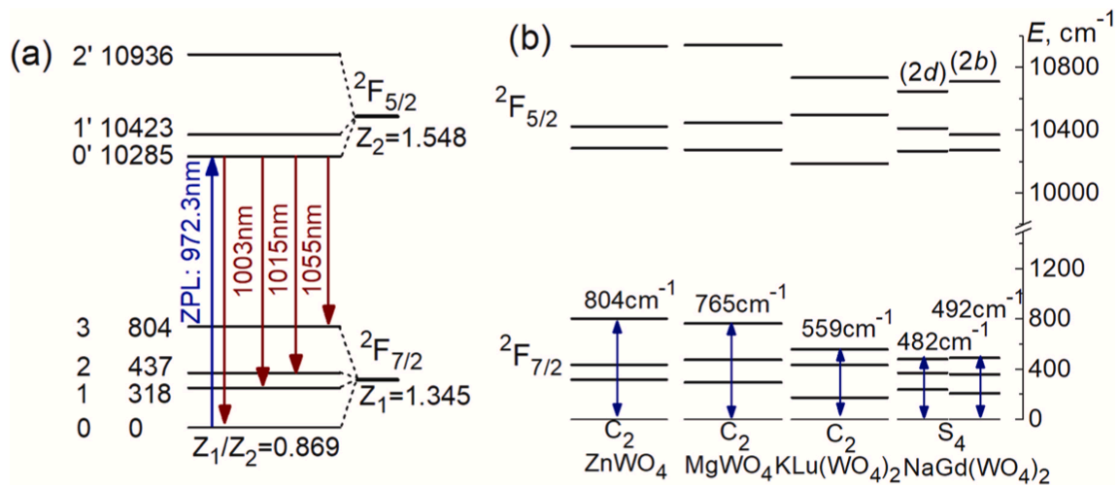


Fig. 7. Crystal-field splitting for Yb^{3+} ions in ZnWO_4 : (a) Scheme of the Stark sub-levels; the blue arrow denotes the zero-phonon line (ZPL) transition in absorption, red arrows denote the transitions in emission at 6 K. Z_1 (Z_2) are the partition functions for the lower (upper) multiplets; (b) a comparison of the crystal-field splitting for Yb^{3+} ions in ZnWO_4 , MgWO_4 [5], $\text{KLu}(\text{WO}_4)_2$ [8] and $\text{NaGd}(\text{WO}_4)_2$ [22] tungstate crystals, C_2 and S_4 – site symmetries.

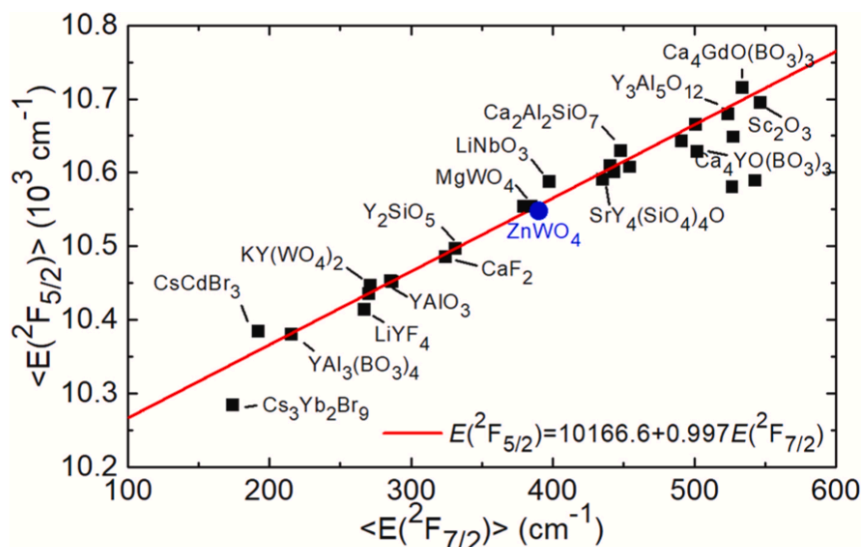


Fig. 8. Barycenter plot for Yb^{3+} ions in various crystals. The blue circle denotes ZnWO_4 . The red line denotes a linear fit through all the points.

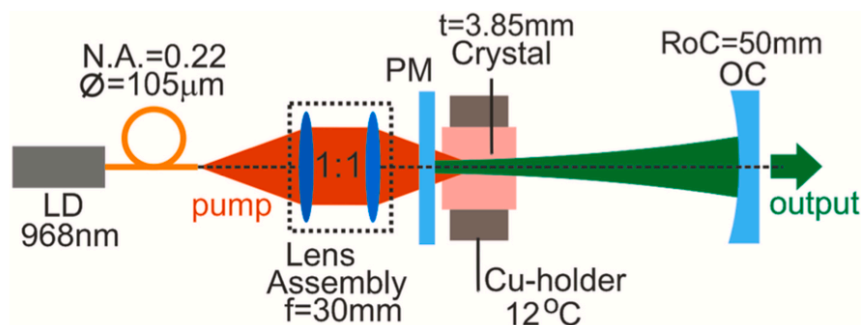


Fig. 9. Scheme of the diode-pumped 1.8 at.% $\text{Yb}^{3+}, \text{Li}^+:\text{ZnWO}_4$ laser: LD – laser diode, PM – pump mirror, OC – output coupler, RoC – radius of curvature.

4.2. Laser performance

The $\text{Yb}^{3+}, \text{Li}^+:\text{ZnWO}_4$ laser generated a maximum output power of 2.90 W at ~ 1059 nm with a slope efficiency $\eta = 57.9\%$ (with respect to the absorbed pump power) and a laser threshold P_{th} of 0.41 W, Fig. 10 (a). The optical-to-optical efficiency η_{opt} (vs. the pump power incident on the crystal) reached 11.2% (all the values are specified for $T_{\text{OC}} = 10\%$). For smaller output coupling transmission, the slope efficiency was inferior while the laser threshold slightly decreased ($\eta = 41.5\%$ and $P_{\text{th}} = 0.29$ W for $T_{\text{OC}} = 3\%$). For all OCs, a thermal roll-over in the input-output dependences was observed for $P_{\text{abs}} > 5$ W and assigned to non-optimized cooling of the laser element.

The laser emission was linearly polarized ($E \parallel N_p$), the polarization was naturally selected by the gain anisotropy. The emission spectra, Fig. 10(b), were weakly dependent on the output coupling being an interesting advantage. The laser operated around 1.06 μm in agreement with the gain spectra, Fig. 4(a).

In a previous study of a 1.25 at.% $\text{Yb}:\text{MgWO}_4$ crystal in the hemispherical cavity under diode pumping, the laser performance was similar: 2.52 W at ~ 1060 nm with $\eta = 61\%$ (vs. P_{abs}) [10]. However, the laser threshold was higher than in our case, $P_{\text{th}} = 0.97$ W. Note that much better CW laser performance was achieved with a microchip $\text{Yb}:\text{MgWO}_4$ laser [5] because of the optimized dimensions of the crystal leading to its efficient cooling and good mode-matching efficiency determined by the positive thermal lens.

No thermal fracture of the crystal was observed up to at least P_{abs} of

6 W. It is known that M^{2+}WO_4 crystals exhibit high thermal fracture limit [5].

5. Conclusions

To conclude, the $\text{Yb}^{3+}, \text{Li}^+:\text{ZnWO}_4$ crystal is promising for ~ 1 μm lasers since it combines (i) good thermal properties (high thermal conductivity and weak anisotropy of thermal expansion) enabling power scaling, (ii) intense spectral bands with polarized light leading to linearly polarized laser emission, (iii) broad emission bands and large total Stark splitting of the ground-state ($^2F_{7/2}$) - largest among other Yb^{3+} -doped tungstate laser crystals and (iv) weak reabsorption at the laser wavelength. The attractive spectroscopic properties of $\text{Yb}^{3+}, \text{Li}^+:\text{ZnWO}_4$ are attributed to the low symmetry of the Yb^{3+} site (C_2) and inhomogeneous broadening arising from the difference in the valence and ionic radius of the cations participating in the doping mechanism (Yb^{3+} , Li^+ and Zn^{2+}). Some of the above characteristics make $\text{Yb}^{3+}, \text{Li}^+:\text{ZnWO}_4$ very attractive for tunable and ML lasers as well as ultrafast amplifiers.

We report on efficient diode-pumped RT laser operation of a 1.8 at.% $\text{Yb}^{3+}, \text{Li}^+:\text{ZnWO}_4$ crystal generating multi-watt output with a slope efficiency of 57.9%. This result well overcomes the previous report (which, in addition, was not supported by the laser power transfer characteristics) [38], proving that Yb^{3+} -doped zinc tungstate is an efficient laser material.

Regarding CW laser operation, further power scaling and improvement of the slope efficiency are possible. One direction of research to

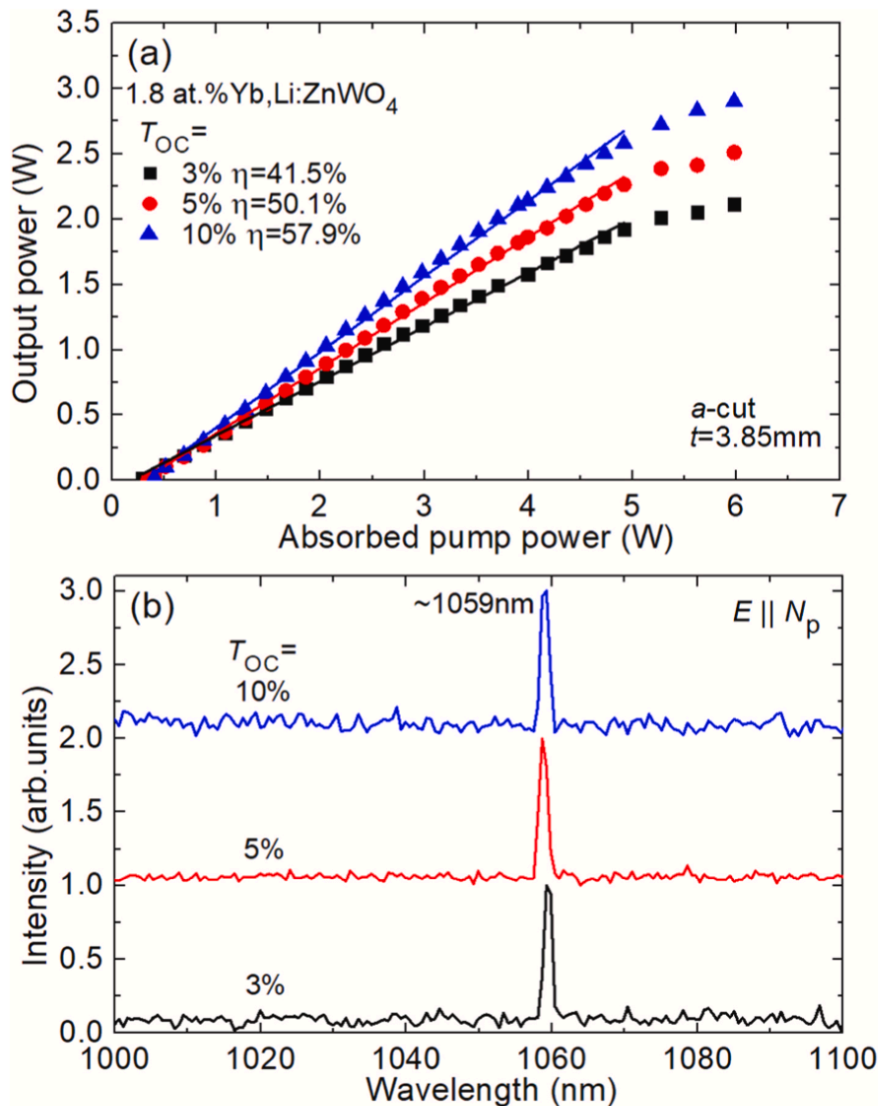


Fig. 10. Diode-pumped 1.8 at.% $\text{Yb}^{3+}, \text{Li}^+:\text{ZnWO}_4$ laser: (a) input-output dependences, η – slope efficiency; (b) typical laser emission spectra. The crystal is *a*-cut. The laser emission is linearly polarized ($E \parallel N_p$).

reach this goal is the elimination of the residual (rose) crystal coloration, e.g., by using Pt crucibles and high-purity reagents during the crystal growth. Another important issue is the control of the charge compensation during Yb^{3+} doping, e.g., by introducing larger amount of Li^+ cations or by using other ions ($\text{Na}^+, \text{Nb}^{5+}$). This may help to improve the segregation coefficient of Yb^{3+} ions in ZnWO_4 leading to higher achievable doping levels and, thus, better pump absorption efficiency. The design of the laser cavity for diode-pumped $\text{Yb}^{3+}, \text{Li}^+:\text{ZnWO}_4$ lasers requires additional knowledge about the thermo-optical properties, such as the dn/dT coefficients and thermal lensing.

CRediT authorship contribution statement

Anna Volokitina: Investigation, Data curation. **Samuel Paul David:** Investigation. **Pavel Loiko:** Conceptualization, Investigation, Methodology, Writing - original draft. **Kirill Subbotin:** Conceptualization, Investigation, Resources, Writing - original draft. **Anatoly Titov:** Investigation, Resources. **Denis Lis:** Investigation, Resources. **Rosa María Solé:** Investigation, Methodology. **Venkatesan Jambunathan:** Investigation. **Antonio Lucianetti:** Resources. **Tomas Mocek:**

Resources. **Patrice Camy:** Resources. **Uwe Griebner:** Writing - review & editing. **Valentin Petrov:** Methodology, Writing - review & editing. **Magdalena Aguiló:** Methodology, Resources. **Francesc Díaz:** Resources. **Xavier Mateos:** Writing - review & editing, Supervision.

Declaration of competing interest

The authors declare that they have no known competing financial interests or personal relationships that could have appeared to influence the work reported in this paper.

Acknowledgements

This work was supported by the Spanish Government (project No. MAT2016-75716-C2-1-R (AEI/FEDER,UE)) and by Generalitat de Catalunya (project No. 2017SGR755). It was funded by the Russian Foundation for Basic Research (RFBR, grant No. 18-02-01058). It was co-financed by the European Regional Development Fund and the state budget of the Czech Republic (project HiLASE CoE: Grant No. CZ.02.1.01/0.0/0.0/15_006/0000674) and by the European Union's

Horizon 2020 research and innovation programme under grant agreement No. 739573. This work was also supported by the Ministry of Education, Youth and Sports of the Czech Republic (Programm NPU I Project No. LO1602).

References

- [1] J. Liu, V. Petrov, H. Zhang, J. Wang, Power scaling of a continuous-wave and passively Q-switched Yb:KLu(WO₄)₂ laser end-pumped by a high-power diode, *Appl. Phys. B* 88 (2007) 527–530.
- [2] J.M. Serres, V. Jambunathan, P. Loiko, X. Mateos, H. Yu, H. Zhang, J. Liu, A. Lucianetti, T. Mocek, K. Yumashev, U. Griebner, V. Petrov, M. Aguiló, F. Díaz, Microchip laser operation of Yb-doped gallium garnets, *Opt. Mater. Express* 6 (2016) 46–57.
- [3] J. Liu, V. Petrov, H. Zhang, J. Wang, M. Jiang, High-power laser performance of a-cut and c-cut Yb:LuVO₄ crystals, *Opt. Lett.* 31 (2006) 3294–3296.
- [4] P. Loiko, J.M. Serres, X. Mateos, X. Xu, J. Xu, V. Jambunathan, P. Navratil, A. Lucianetti, T. Mocek, X. Zhang, U. Griebner, V. Petrov, M. Aguiló, F. Díaz, A. Major, Microchip Yb, CaLnAlO₄ lasers with up to 91% slope efficiency, *Opt. Lett.* 42 (2017) 2431–2434.
- [5] P. Loiko, M. Chen, J.M. Serres, M. Aguiló, F. Díaz, H. Lin, G. Zhang, L. Zhang, Z. Lin, P. Camy, S.B. Dai, Z. Chen, Y. Zhao, L. Wang, W. Chen, U. Griebner, V. Petrov, X. Mateos, Spectroscopy and high-power laser operation of a monoclinic Yb³⁺:MgWO₄ crystal, *Opt. Lett.* 45 (2020) 1770–1773.
- [6] U. Griebner, S. Rivier, V. Petrov, M. Zorn, G. Erbert, M. Weyers, X. Mateos, M. Aguiló, F. Massons, F. Díaz, Passively mode-locked Yb:KLu(WO₄)₂ oscillators, *Optic Express* 13 (2005) 3465–3470.
- [7] F. Auzel, D. Meichenin, F. Pelle, P. Goldner, Cooperative luminescence as a defining process for RE-ions clustering in glasses and crystals, *Opt. Mater.* 4 (1994) 35–41.
- [8] V. Petrov, M.C. Pujol, X. Mateos, Ò. Silvestre, S. Rivier, M. Aguiló, R.M. Solé, J. H. Liu, U. Griebner, F. Díaz, Growth and properties of KLu(WO₄)₂ and novel ytterbium and thulium lasers based on this monoclinic crystalline host, *Laser Photon. Rev.* 1 (2007) 179–212.
- [9] A. García-Cortés, J.M. Cano-Torres, M.D. Serrano, C. Cascales, C. Zaldo, S. Rivier, X. Mateos, U. Griebner, V. Petrov, Spectroscopy and lasing of Yb-doped NaY(WO₄)₂: tunable and femtosecond mode-locked laser operation, *IEEE J. Quant. Electron.* 43 (2007) 758–764.
- [10] L. Zhang, W. Chen, J. Lu, H. Lin, L. Li, G. Wang, G. Zhang, Z. Lin, Characterization of growth, optical properties, and laser performance of monoclinic Yb:MgWO₄ crystal, *Opt. Mater. Express* 6 (2016) 1627–1634.
- [11] K.A. Subbotin, E.V. Zharikov, V.A. Smirnov, Yb- and Er-doped single crystals of double tungstates NaGd(WO₄)₂, NaLa(WO₄)₂, and NaBi(WO₄)₂ as active media for lasers operating in the 1.0 and 1.5 μm ranges, *Opt. Spectra* 92 (2002) 601–608 [transl. from *Optika i Spektroskopiya* 92 (2002) 657–664].
- [12] J. Liu, U. Griebner, V. Petrov, H. Zhang, J. Zhang, J. Wang, Efficient continuous-wave and Q-switched operation of a diode-pumped Yb:KLu(WO₄)₂ laser with self-Raman conversion, *Opt. Lett.* 30 (2005) 2427–2429.
- [13] A.A. Lagatsky, N.V. Kuleshov, V.P. Mikhailov, Diode-pumped CW lasing of Yb:KYW and Yb:KGW, *Optic Commun.* 165 (1999) 71–75.
- [14] P.A. Loiko, V.E. Kisel, N.V. Kondratuk, K.V. Yumashev, N.V. Kuleshov, A. A. Pavlyuk, 14 W high-efficiency diode-pumped cw Yb:KGe(WO₄)₂ laser with low thermo-optic aberrations, *Opt. Mater.* 35 (2013) 582–585.
- [15] J.M. Serres, P. Loiko, X. Mateos, K. Yumashev, N. Kuleshov, V. Petrov, U. Griebner, M. Aguiló, F. Díaz, Prospects of monoclinic Yb:KLu(WO₄)₂ crystal for multi-watt microchip lasers, *Opt. Mater. Express* 5 (2015) 661–667.
- [16] P. Loiko, J.M. Serres, X. Mateos, K. Yumashev, A. Yasukevich, V. Petrov, U. Griebner, M. Aguiló, F. Díaz, Sub-nanosecond Yb:KLu(WO₄)₂ microchip laser, *Opt. Lett.* 41 (2016) 2620–2623.
- [17] S. Pekarek, C. Fiebig, M.C. Stumpf, A.E.H. Oehler, K. Paschke, G. Erbert, T. Südmeyer, U. Keller, Diode-pumped gigahertz femtosecond Yb:KGW laser with a peak power of 3.9 kW, *Optic Express* 18 (2010) 16320–16326.
- [18] O. Silvestre, J. Grau, M.C. Pujol, J. Massons, M. Aguiló, F. Díaz, M.T. Borowiec, A. Szewczyk, M.U. Gutowska, M. Massot, A. Salazar, V. Petrov, Thermal properties of monoclinic KLu(WO₄)₂ as a promising solid state laser host, *Optic Express* 16 (2008) 5022–5034.
- [19] P.A. Loiko, K.V. Yumashev, N.V. Kuleshov, G.E. Rachkovskaya, A.A. Pavlyuk, Detailed characterization of thermal expansion tensor in monoclinic KRe(WO₄)₂ (where Re = Gd, Y, Lu, Yb), *Opt. Mater.* 34 (2011) 23–26.
- [20] Y.K. Voron'ko, E.V. Zharikov, D.A. Lis, A.A. Sobol, K.A. Subbotin, S.N. Ushakov, V. E. Shukshin, Spectroscopic investigations of NaGd(WO₄)₂ and NaLa(MoO₄)₂ single crystals doped by Yb³⁺ ions, *Proc. SPIE* 5478 (2004) 60–68.
- [21] A. García-Cortés, C. Zaldo, C. Cascales, Site selective spectroscopy of Yb³⁺ in NaT(WO₄)₂, T = Bi, Gd, Y, Lu, laser crystals: assessment with simulated crystal field effects, *Opt. Mater.* 31 (2009) 1096–1100.
- [22] C. Cascales, M.D. Serrano, F. Esteban-Betegón, C. Zaldo, R. Peters, K. Petermann, G. Huber, L. Ackermann, D. Rytz, C. Dupré, M. Rico, J. Liu, U. Griebner, V. Petrov, Structural, spectroscopic, and tunable laser properties of Yb³⁺-doped NaGd(WO₄)₂, *Phys. Rev. B* 74 (2006) 174114.
- [23] Y.K. Voron'ko, E.V. Zharikov, D.A. Lis, K.A. Subbotin, S.N. Ushakov, V.E. Shukshin, S. Dröge, Growth and luminescent properties of NaGd(WO₄)₂:Yb³⁺ crystals, *Inorg. Mater.* 39 (2003) 1308–1314 [transl. from *Neorganicheskie Materialy* 39 (2003) 1509–1516].
- [24] M.D. Serrano, C. Cascales, X. Han, C. Zaldo, A. Jezowski, P. Stachowski, K. Ter-Gabrielyan, V. Fromzel, M. Dubinskii, Thermal characterization, crystal field analysis and in-band pumped laser performance of Er doped NaY(WO₄)₂ disordered laser crystals, *PLoS One* 8 (2013), e59381.
- [25] L. Zhang, P. Loiko, J.M. Serres, E. Kifle, H. Lin, G. Zhang, E. Vilejshikova, E. Dunina, A. Kornienko, L. Fomicheva, U. Griebner, V. Petrov, Z. Lin, W. Chen, K. Subbotin, M. Aguiló, F. Díaz, X. Mateos, Growth, spectroscopy and first laser operation of monoclinic Ho³⁺:MgWO₄ crystal, *J. Lumin.* 213 (2019) 316–325.
- [26] L. Zhang, H. Lin, G. Zhang, X. Mateos, J.M. Serres, M. Aguiló, F. Díaz, U. Griebner, V. Petrov, Y. Wang, P. Loiko, E. Vilejshikova, K. Yumashev, Z. Lin, W. Chen, Crystal growth, optical spectroscopy and laser action of Tm³⁺-doped monoclinic magnesium tungstate, *Optic Express* 25 (2017) 3682–3693.
- [27] L. Li, Y. Yu, G. Wang, L. Zhang, Z. Lin, Crystal growth, spectral properties and crystal field analysis of Cr³⁺:MgWO₄, *CrystEngComm* 15 (2013) 6083–6089.
- [28] X. Wang, Z. Fan, H. Yu, H. Zhang, J. Wang, Characterization of ZnWO₄ Raman crystal, *Opt. Mater. Express* 7 (2017) 1732–1744.
- [29] L. Zhang, Y. Huang, S. Sun, F. Yuan, Z. Lin, G. Wang, Thermal and spectral characterization of Cr³⁺:MgWO₄—a promising tunable laser material, *J. Lumin.* 169 (2016) 161–164.
- [30] P. Loiko, Y. Wang, J.M. Serres, X. Mateos, M. Aguiló, F. Díaz, L. Zhang, Z. Lin, H. Lin, G. Zhang, E. Vilejshikova, E. Dunina, A. Kornienko, L. Fomicheva, V. Petrov, U. Griebner, W. Chen, Monoclinic Tm³⁺:MgWO₄ crystal: crystal-field analysis, tunable and vibronic laser demonstration, *J. Alloys Compd.* 763 (2018) 581–591.
- [31] P. Loiko, J.M. Serres, X. Mateos, M. Aguiló, F. Díaz, L. Zhang, Z. Lin, H. Lin, G. Zhang, K. Yumashev, V. Petrov, U. Griebner, Y. Wang, S.Y. Choi, F. Rotermund, W. Chen, Monoclinic Tm³⁺:MgWO₄: a promising crystal for continuous-wave and passively Q-switched lasers at ~2 μm, *Opt. Lett.* 42 (2017) 1177–1180.
- [32] Y. Wang, W. Chen, M. Mero, L. Zhang, H. Lin, Z. Lin, G. Zhang, F. Rotermund, Y. J. Cho, P. Loiko, X. Mateos, U. Griebner, V. Petrov, Sub-100 fs Tm:MgWO₄ laser at 2017 nm mode locked by a graphene saturable absorber, *Opt. Lett.* 42 (2017) 3076–3079.
- [33] H. Lin, G. Zhang, L. Zhang, Z. Lin, F. Pirzio, A. Agnesi, V. Petrov, W. Chen, Continuous-wave and SESAM mode-locked femtosecond operation of a Yb:MgWO₄ laser, *Optic Express* 25 (2017) 11827–11832.
- [34] J. Lu, H. Lin, G. Zhang, B. Li, L. Zhang, Z. Lin, Y.F. Chen, V. Petrov, W. Chen, Direct generation of an optical vortex beam from a diode-pumped Yb:MgWO₄ laser, *Laser Phys. Lett.* 14 (2017), 085807.
- [35] L.L. Nagornaya, A.M. Dubovik, Y.Y. Vostretsov, B.V. Grinyov, F.A. Danevich, K. A. Katrunov, V.M. Mokina, G.M. Onishchenko, D.V. Poda, N.G. Starzhinskiy, I. A. Tupitsyna, Growth of ZnWO₄ crystal scintillators for high sensitivity ββ experiments, *IEEE Trans. Nucl. Sci.* 55 (2008) 1469–1472.
- [36] E.N. Galashov, V.A. Gusev, V.N. Shlegel, Y.V. Vasiliev, The growth of ZnWO₄ and CdWO₄ single crystals from melt by the low thermal gradient Czochralski technique, *Crystallogr. Rep.* 54 (2009) 689–691 [transl. from *Kristallografiya* 54 (2009) 733–735].
- [37] P.A. Popov, S.A. Skrobov, A.V. Matovnikov, N.V. Mitroshenkov, Y.A. Borovlev, Thermal conductivity and heat capacity of a ZnWO₄ crystal, *Phys. Solid State* 58 (2016) 853–856 [transl. from *Fizika Tverdogo Tela* 58 (2016) 827–830].
- [38] F. Yang, The spectroscopic investigation of ZnWO₄:Yb³⁺ single crystal, *J. Mater. Res.* 27 (2012) 2096–2100.
- [39] F. Yang, C. Tu, J. Li, G. Jia, H. Wang, Y. Wei, Z. You, Z. Zhu, Y. Wang, X. Lu, Growth and optical property of ZnWO₄:Er³⁺ crystal, *J. Lumin.* 126 (2007) 623–628.
- [40] F. Yang, C. Tu, H. Wang, Y. Wei, Z. You, G. Jia, J. Li, Z. Zhu, X. Lu, Y. Wang, Growth and spectroscopy of Dy³⁺ doped in ZnWO₄ crystal, *Opt. Mater.* 29 (2007) 1861–1865.
- [41] F. Yang, C. Tu, H. Wang, Y. Wei, Z. You, G. Jia, J. Li, Z. Zhu, X. Lu, Y. Wang, Growth and spectroscopy of ZnWO₄:Ho³⁺ crystal, *J. Alloys Compd.* 455 (2008) 269–273.
- [42] F. Yang, C. Tu, The spectroscopy investigation of ZnWO₄:Tm³⁺ single crystal, *J. Alloys Compd.* 535 (2012) 83–86.
- [43] Z. Xia, F. Yang, L. Qiao, F. Yan, End pumped yellow laser performance of Dy³⁺:ZnWO₄, *Optic Commun.* 387 (2017) 357–360.
- [44] F.G. Yang, Z.Y. You, C.Y. Tu, End-pumping ZnWO₄:Tm³⁺ at ~1.9 μm eye-safe laser, *Laser Phys. Lett.* 9 (2012) 204–206.
- [45] K. Subbotin, P. Loiko, A. Volokitina, A. Titov, D. Lis, E. Chernova, S. Slimi, R. M. Solé, U. Griebner, V. Petrov, M. Aguiló, F. Díaz, X. Mateos, E. Zharikov, Monoclinic zinc monotungstate Yb³⁺:Li⁺:ZnWO₄: Part I. Czochralski growth, structure refinement and Raman spectra, *J. Lumin.* 228 (2020) 117601, <https://doi.org/10.1016/j.jlumin.2020.117601>.
- [46] C.J. Spengler, S. O'Hara, Zinc tungstate - some optical properties, *Appl. Optic.* 3 (1964) 1084–1085.
- [47] W.L. Bond, Measurement of the refractive indices of several crystals, *J. Appl. Phys.* 36 (1965) 1674–1677.
- [48] H. Wang, Y. Lin, Y.-D. Zhou, G. Chen, T. Zhou, J.H. Wang, B.-Q. Hu, Optical characteristics of ZnWO₄ single crystals, *Acta Phys. Sin.* 38 (1989) 670–674.
- [49] B. Zysset, I. Biaggio, P. Günter, Refractive indices of orthorhombic KNbO₃. I. Dispersion and temperature dependence, *J. Opt. Soc. Am. B* 9 (1992) 380–386.
- [50] R. Lacombe-Perales, J. Ruiz-Fuertes, D. Errandonea, D. Martínez-García, A. Segura, Optical absorption of divalent metal tungstates: correlation between the band-gap energy and the cation ionic radius, *Europhys. Lett.* 83 (2008) 37002.
- [51] B. Aull, H. Jenssen, Vibronic interactions in Nd:YAG resulting in nonreciprocity of absorption and stimulated emission cross sections, *IEEE J. Quant. Electron.* 18 (1982) 925–930.

A. Volokitina et al.

Journal of Luminescence 231 (2021) 117811

- [52] D.E. McCumber, Einstein relations connecting broadband emission and absorption spectra, *Phys. Rev.* 136 (1964) A954–A957.
- [53] S.A. Payne, L.L. Chase, L.K. Smith, W.L. Kway, W.F. Krupke, Infrared cross-section measurements for crystals doped with Er^{3+} , Tm^{3+} and Ho^{3+} , *IEEE J. Quant. Electron.* 28 (1992) 2619–2630.
- [54] H. Scheife, G. Huber, E. Heumann, S. Bär, E. Osiać, Advances in up-conversion lasers based on Er^{3+} and Pr^{3+} , *Opt. Mater.* 26 (2004) 365–374.
- [55] E. Castellano-Hernández, X. Han, M. Rico, L. Roso, C. Cascales, C. Zaldo, Mode-locked laser operation of Indium-modified $\text{Yb:KY}(\text{WO}_4)_2$ single crystal, *Optic Express* 23 (2015) 11135–11140.
- [56] R.D. Shannon, Revised effective ionic radii and systematic studies of interatomic distances in halides and chalcogenides, *Acta Crystallogr. A* 32 (1976) 751–767.
- [57] P.H. Haumesser, R. Gaumé, B. Viana, E. Antic-Fidancev, D. Vivien, Spectroscopic and crystal-field analysis of new Yb-doped laser materials, *J. Phys. Condens. Matter* 13 (2001) 5427–5447.



Contents lists available at ScienceDirect

Journal of Luminescence

journal homepage: <http://www.elsevier.com/locate/jlumin>



Monoclinic zinc monotungstate $\text{Yb}^{3+}, \text{Li}^+:\text{ZnWO}_4$: Part I. Czochralski growth, structure refinement and Raman spectra

Kirill Subbotin^{a,b}, Pavel Loiko^c, Sami Slimi^{d,f}, Anna Volokitina^{d,e}, Anatoly Titov^{a,b}, Denis Lis^a, Elena Chernova^a, Sergei Kuznetsov^a, Rosa Maria Solé^d, Uwe Griebner^g, Valentin Petrov^g, Magdalena Aguiló^d, Francesc Díaz^d, Patrice Camy^c, Evgenii Zharikov^a, Xavier Mateos^{d,*}

^a Prokhorov General Physics Institute, Russian Academy of Sciences, 38 Vavilova St., 119991, Moscow, Russia

^b Mendeleev University of Chemical Technology of Russia, 9 Miusskaya Sq., 125047, Moscow, Russia

^c Centre de Recherche sur les Ions, les Matériaux et la Photonique (CIMAP), UMR 6252 CEA-CNRS-ENSICAEN, Université de Caen Normandie, 6 Boulevard du Maréchal Juin, 14050, Caen Cedex 4, France

^d Universitat Rovira i Virgili (URV), Física i Cristal·lografia de Materials i Nanomaterials (FICMA-FICNA)-EMaS, Marcel·li Domingo 1, 43007, Tarragona, Spain

^e I.P.E.I. of Monastir, Unit of Materials and Organic Synthesis UR17ES31, 5019, Monastir, Tunisia

^f ITMO University, Kronverkskiy Pr., 49, 197101, Saint-Petersburg, Russia

^g Max Born Institute for Nonlinear Optics and Short Pulse Spectroscopy, Max-Born-Str. 2a, 12489, Berlin, Germany

ARTICLE INFO

Keywords:

Tungstate crystals
Czochralski method
Impurities
Crystal structure
Ytterbium lasers
Stimulated Raman scattering
Coloration

ABSTRACT

We report on the growth of a co-doped divalent-metal monotungstate crystal, $\text{Yb}^{3+}, \text{Li}^+:\text{ZnWO}_4$, its structure refinement, thermo-mechanical properties and polarized Raman spectra. $\text{Yb}^{3+}, \text{Li}^+:\text{ZnWO}_4$ crystals are grown by the Czochralski method using Pt/Rh and Pt crucibles. The nature of crystal coloration is discussed and assigned to color centers based on oxygen vacancies as well as $\text{Fe}^{2+}(\text{Fe}^{3+})$ species and, possibly, other uncontrolled impurities of transition metal ions. Oxidizing annealing at 800 °C helps to improve the transparency of $\text{Yb}^{3+}, \text{Li}^+:\text{ZnWO}_4$ leading to a weak residual pink coloration. $\text{Yb}^{3+}, \text{Li}^+:\text{ZnWO}_4$ was confirmed to be monoclinic (sp. gr. $P2_1/c - C^4_{2h}$, No. 13) with lattice constants $a = 4.702(2)$ Å, $b = 5.718(6)$ Å, $c = 4.930(4)$ Å and $\beta = 90.713(5)^\circ$. The coefficients of linear thermal expansion are $\alpha_{[100]} = 11.71$, $\alpha_{[010]} = 9.90$ and $\alpha_{[001]} = 7.01$ [10^{-6}K^{-1}]. The melting point of the crystal is at 1166 °C and no thermal effects are found below the melting point. The $\text{Yb}^{3+}, \text{Li}^+:\text{ZnWO}_4$ crystal shows intense and strongly polarized Raman spectra with the most intense mode at 906.0 cm^{-1} assigned to the W – O stretching vibrations in the $[\text{WO}_6]$ octahedra. It is thus a promising gain medium for laser emission at ~ 1 μm and for self-Raman frequency conversion.

1. Introduction

The crystal family of monoclinic divalent-metal monotungstates M^{2+}WO_4 (where $\text{M} = \text{Mg}, \text{Zn}, \text{Cd}, \text{etc.}$) is attracting a lot of attention in recent years for optical applications [1–5]. These compounds possess the so-called wolframite $[(\text{Fe}, \text{Mn})\text{WO}_4]$ type structure belonging monoclinic crystal class, sp. gr. $P2_1/c$ [6]. The M^{2+}WO_4 crystals are ordered and exhibit a single crystallographic site for the M^{2+} cations with a VI-fold oxygen coordination (site symmetry: C_2) [7]. Two promising examples of this crystal family are magnesium monotungstate (MgWO_4 , called huanzalaite in the natural mineral form) and zinc monotungstate (ZnWO_4 , or sanmartinite).

Undoped M^{2+}WO_4 crystals and, in particular, MgWO_4 and ZnWO_4 ,

are known as scintillators [8–11]. ZnWO_4 exhibits a relatively wide transmission range (for oxide crystals) of 0.3–5.5 μm , a broad bandgap (~ 4.5 eV) and an intense luminescence at ~ 480 nm with a relatively high quantum yield comparable with that for CdWO_4 [10]. As a result, ZnWO_4 crystals are promising for low-counting experiments to search for double beta (2β) decay, dark matter and also to study rare alpha (α) and beta (β) decays [12,13]. From the point of view of the thermo-mechanical properties, the MgWO_4 and ZnWO_4 crystals are also attractive because they possess weak anisotropy of thermal expansion [5], satisfactory thermal conductivity κ [14,15] and attractive elastic properties. For example, the thermal conductivity of undoped ZnWO_4 at room temperature along the crystallographic axes is $\kappa_{[100]} = 4.76$, $\kappa_{[010]} = 3.17$ and $\kappa_{[001]} = 4.54 \text{ Wm}^{-1}\text{K}^{-1}$ [15].

* Corresponding author.

E-mail address: xavier.mateos@urv.cat (X. Mateos).

<https://doi.org/10.1016/j.jlumin.2020.117601>

Received 24 June 2020; Received in revised form 31 July 2020; Accepted 15 August 2020

Available online 15 August 2020

0022-2313/© 2020 Elsevier B.V. All rights reserved.

Thanks to these attractive optical and thermal properties, the MgWO_4 and ZnWO_4 crystals were considered for doping with transition-metal (TM) and rare-earth (RE) ions with the goal of laser operation. Up to now, laser operation was achieved with MgWO_4 crystals doped with Yb^{3+} (at $\sim 1 \mu\text{m}$) [3,16], Tm^{3+} [17,18] and Ho^{3+} [5] ions (both at $\sim 2 \mu\text{m}$), as well as with ZnWO_4 crystals doped with Yb^{3+} (at $\sim 1 \mu\text{m}$) [19], Tm^{3+} (at $\sim 2 \mu\text{m}$) [20] and Dy^{3+} ions (at $\sim 0.58 \mu\text{m}$) [21]. These studies revealed some advantageous spectroscopic properties of RE^{3+} -doped M^{2+}WO_4 crystals, such as large values and strong anisotropy of transition cross-sections with polarized light, relatively high Stark splitting of the ground states of RE^{3+} -dopants, as well as inhomogeneous broadening of the spectral bands. These features originate from the low-symmetry of the RE^{3+} site (the dopant ions replace for the M^{2+} host-forming cations) and the difference in the ionic radius and valence state of the dopant and the host-forming cations leading to distortion of the local crystal field [22]. A key role of the charge compensation mechanism, presumably involving monovalent alkali-metal cations (e. g., Na^+ from the flux in the case of MgWO_4) for the spectroscopic properties of the crystals was also suggested [5,22].

The $\text{Yb}^{3+}:\text{MgWO}_4$ crystals for 1- μm lasers were grown by the Top Seeded Growth (TSSG) method (from the flux) [3]. Polarized optical spectroscopy and highly-efficient laser operation were reported in Ref. [16]. Unlike MgWO_4 , its zinc counterpart melts congruently at 1188°C [23] without any polymorphic phase transitions below the melting point, and thus large ZnWO_4 crystals can be easily grown from melt by the conventional Czochralski (Cz) method [24–26]. Yang reported on the Cz growth of $\text{Yb}^{3+}:\text{ZnWO}_4$ and briefly on its spectroscopic characterization and first laser operation [19].

Despite the growth of undoped ZnWO_4 crystals is well documented [24,26], the information about the growth, coloration, doping mechanism, and structure of Yb^{3+} -doped crystals is scarce. Moreover, the use of charge compensators for Yb^{3+} -doped ZnWO_4 was not studied so far. On the other hand, it is known from the early studies that the ZnWO_4 crystals may exhibit a notable coloration (ranging from almost colorless to pink and black) affecting their optical properties [24,27,28]. It is clear that the color centers and defects may also play a key role in preventing the desired laser operation in Yb^{3+} -doped ZnWO_4 crystals. In the present work, we report, for the first time, to the best of our knowledge, on Cz growth of $\text{Yb}^{3+},\text{Li}^+$ -co-doped ZnWO_4 crystals, as well as on a detailed study of the nature of their coloration and the ways of removing them, Yb^{3+} doping, structure refinement, thermal expansion and polarized Raman spectra. The parallel paper [29] is dedicated to the polarization-resolved spectroscopy of Yb^{3+} ions and first laser operation.

To ensure the charge compensation (the Yb^{3+} ions replace for the Zn^{2+} ones, so that the doping is heterovalent), the crystals were co-doped with monovalent lithium cations (Li^+). The use of monovalent alkali-metal cations in crystals with a heterovalent doping is well documented [30,31].

2. Experimental

2.1. Equipment for the crystal growth

$\text{Yb}^{3+},\text{Li}^+:\text{ZnWO}_4$ single crystals were grown by the Cz method at the “Kristall-2” (former USSR) industrial growth facility at Prokhorov General Physics Institute. The growth was performed in air in Pt/Rh or Pt crucibles with a diameter of 30 mm and a height of 30 mm. The pulling rate was 1 mm/h and the rotation speed was 6 rpm. The first undoped single-crystal was obtained by spontaneous nucleation on an Ir wire, so that the growth direction was spontaneous. The seeds for the following growth runs of co-doped crystals were cut from this crystal parallel to the crystallographic plane (010). It is the easiest cleavage plane of ZnWO_4 . After completing the growth process and separating the crystal from the melt, it was slowly cooled (at a rate of 8 K/h) down to room temperature (RT) in order to avoid cracking.

To prepare the charge for the crystal growth, we used the following reagents: WO_3 , ZnO , Li_2CO_3 (as a source of Li^+ ions) and Yb_2O_3 (source of Yb^{3+} ions). WO_3 and ZnO were weighted according to the molar ratio 1:1 with an accuracy of ± 0.01 g. The amounts of Yb^{3+} and Li^+ dopant ions were calculated assuming the substitution of the equimolar amounts of Zn^{2+} in the crystal. In particular, we prepared charge compositions with 5 at.% Yb^{3+} , 5 at.% Li^+ and 3 at.% Yb^{3+} , 3 at.% Li^+ , as well as the charge for the undoped ZnWO_4 crystal. The chemicals were dried at 700°C before weighting. The weighted amounts of the chemicals were thoroughly mixed and the obtained mixtures were calcined at 700°C for 5 h to perform a solid phase synthesis of the compound in order to avoid selective evaporation of individual components of the mixture during melting.

We have used WO_3 from two different batches of the same supplier (Lankhit, Ltd., Russia). The batches (labeled as WO_3 #1 and #2) had a supplier-specified purity of 4 N and 5 N, respectively. ZnO reagent from two suppliers was used. The first one (ZnO #1) was Roanal, Hungary (the purity was not explicitly specified by the supplier). The second source (ZnO #2) was the reagent with a composition of $2\text{ZnCO}_3 \times 3\text{Zn}(\text{OH})_2 \times \text{H}_2\text{O}$ (old stock from Krasnyi Khimik, former USSR), with a specified purity of “OSCh 14-2” (4 N). This powder was calcined at 900°C for 10 h before usage. According to the X-ray powder diffraction (XRD) analysis (Siemens D-5000 equipment) and weighting before and after the calcination, the calcined powder contained solely the ZnO phase (within the precision limits of these methods).

The only source of Yb^{3+} ions in our experiments was Yb_2O_3 (YbO-D, Industry Branch Standard 48-206-81, old stock – p/b M – 5649, former USSR, purity: 4 N). The source of Li^+ ions was Li_2CO_3 , again from Krasnyi Khimik with a specified purity of “OSCh 20-2” (4 N). LiCO_3 was added to the crystal compositions for charge compensation of heterovalent Yb^{3+} entering the Zn^{2+} sub-lattice.

The additional post-growth annealing was performed for color elimination in a vertical cylindrical furnace with Kanthal AF heater. The boules were annealed for 24 h at 800°C . The heating and cooling was at a rate of 40 K/h to avoid thermal shocks.

2.2. Crystal characterization

The actual Yb^{3+} concentration N_{Yb} in the crystals was measured by the microprobe analysis using a Cameca Camebax SX-100 analyzer. The impurity composition of the crystals was also analyzed by the spark-source mass-spectrometry (SSMS) using a JEOL JMS-01-BM2 mass-spectrometer.

Differential thermal analysis (DTA) experiment was carried out on a MOM Q-1500 D derivatograph. A Pt-Rh thermocouple and a Pt crucible were used. The heating and cooling rates were $15^\circ\text{C}/\text{min}$. The sample weight was 350–400 mg. The accuracy for temperature measurement was about $\pm 5^\circ\text{C}$.

The structural characterization of the $\text{Yb}^{3+},\text{Li}^+:\text{ZnWO}_4$ crystals was performed by X-ray powder diffraction. The measurements were carried out in a $\theta - \theta$ Bragg Brentano configuration using a Siemens D-5000 powder X-ray diffractometer with $\text{Cu K}\alpha$ (1.5406 \AA) radiation. For structure identification, the XRD pattern was recorded in a 2θ range from 10° to 70° , a step size of 0.02° and a step time of 16 s. For the structure refinement, the XRD pattern was recorded over a broad range of diffraction angles $2\theta = 14.5\text{--}120^\circ$ in three subranges: (a) 14.5° to 60° (step size: 0.02° , step time: 16 s), (b) 60° to 92° (step size: 0.02° , step time: 23 s), (c) and 92° to 120° (step size: 0.02° , step time: 32 s). For the Rietveld refinement, the merged diffractogram was converted to counts per second. For temperature dependent (303–773 K) XRD studies, we used the same diffractometer with a temperature chamber (HTK10). A heating rate of 0.17 K/s was applied, with a delay of 300 s before each measurement. The 2θ angle varied from 10° to 70° with a step size of 0.03° and a step time of 5 s.

In order to study the coloration of crystals, we measured their unpolarized RT absorption spectra in the wavelength range of 0.3–2.0 μm

using a Varian Cary 5000 spectrophotometer.

The Raman spectra were measured with polarized light using a Renishaw inVia Raman microscope with a $\times 50$ objective. The excitation wavelength was 514 nm (Ar^+ laser) and the spectral resolution was $\sim 1 \text{ cm}^{-1}$. The sample for Raman studies was oriented by means of single-crystal XRD.

3. Crystal growth

3.1. Growth of single-crystals

As noted above, the growth direction for the first undoped crystal was spontaneous, whereas the growth direction of all the following samples was lying in the (010) crystallographic plane. A clear trend for natural faceting and cleavage along the (010) plane was observed in all the grown crystals, Fig. 1(a). The faceting and cleavage along other

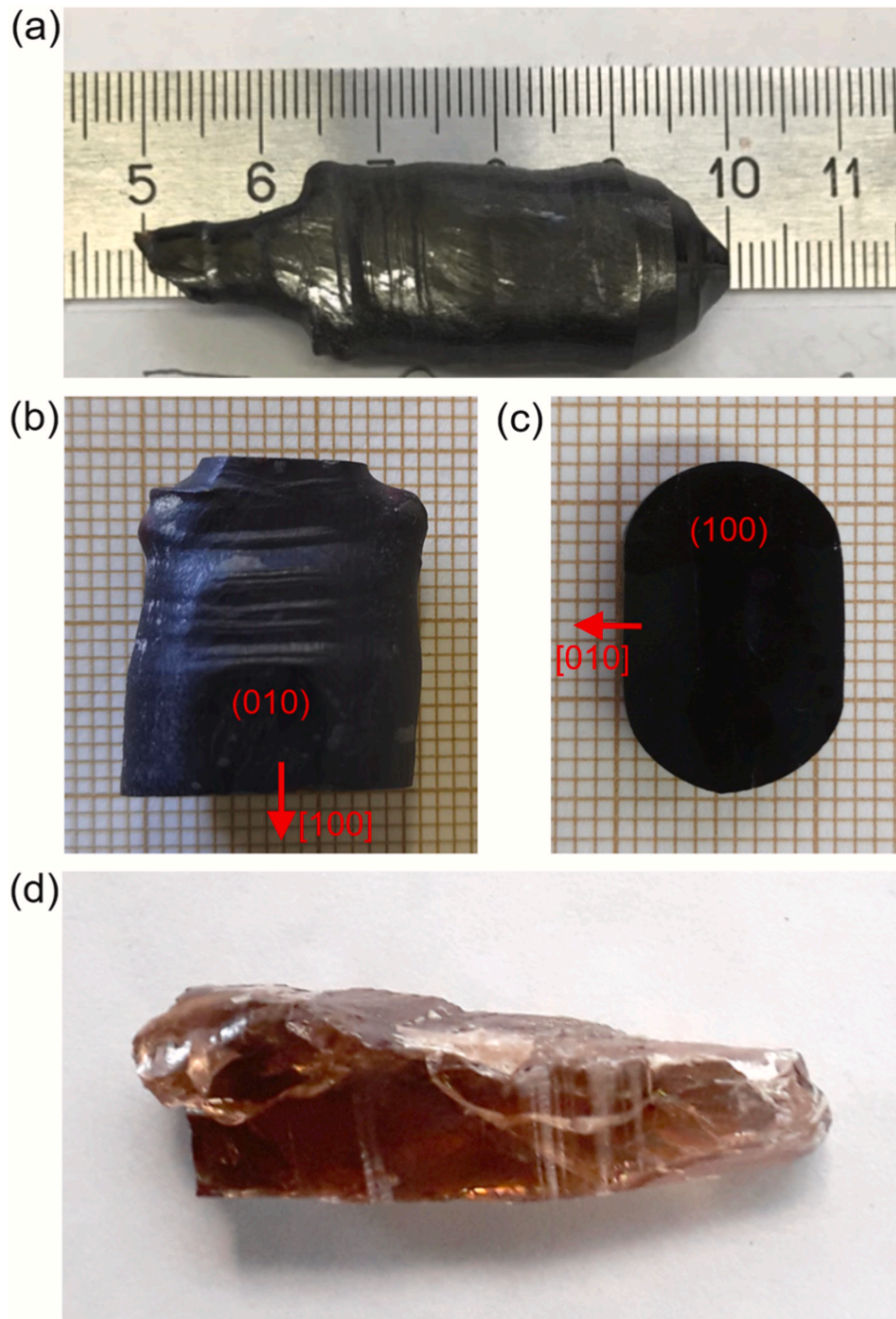


Fig. 1. Photograph of the as-grown 5 at.% Yb^{3+} , 5 at.% Li^+ : ZnWO_4 crystal (nominal composition): (a–c) Pt/Rh crucible, ZnO (#1) and WO_3 (#2) batches, (a) as-grown boule; (b) central part oriented by means of single-crystal XRD; (c) thick ($t = 5 \text{ mm}$) plate cut orthogonal to the growth direction. The growth direction is along the [100] axis; (d) Pt crucible, ZnO (#1) and WO_3 (#2) batches.

crystallographic planes was less pronounced. The cross-section of the boules had a shape essentially strangulated along the [010] direction, Fig. 1(b and c), as compared to the round one being common for the Cz method. This behavior is assigned to considerably lower thermal conductivity of $ZnWO_4$ along this direction [15].

Using the single-crystalline seeds fabricated from undoped $ZnWO_4$ crystal, first, 5 at.% Yb^{3+} , 5 at.% Li^+ : and 3 at.% Yb^{3+} , 3 at.% Li^+ : $ZnWO_4$ crystals (nominal compositions) were grown using the available Pt/Rh crucibles. The crystals had a deep black coloration, Fig. 1(a), almost independent of the WO_3 and ZnO batches used. In very thin layers, the crystals were transparent with deep red or brown color. The reasons for this coloration and the ways for its elimination are discussed in Section 3.2. Higher Yb^{3+} content increased the tendency for cracking of the grown crystal boules along the (010) cleavage plane. Note that a crack-free nominally pure (undoped) $ZnWO_4$ crystal has been easily grown using the same procedure.

Later on, we grew several Yb^{3+}, Li^+ -co-doped crystals using Pt crucibles (without Rh). The shape and the cracking behavior of the crystals was similar to those obtained using the Pt/Rh crucibles. However, the coloration of these samples was different, Fig. 1(d). Even thick (~1 cm) crystal plates were transparent and slightly red-brown colored.

The actual Yb^{3+} doping concentration (in the crystal) N_{Yb} was measured by the microprobe method for the crystal with a nominal composition of 3 at.% Yb^{3+} , 3 at.% Li^+ : $ZnWO_4$. It amounted to $2.0 \pm 0.7 \times 10^{20} \text{ cm}^{-3}$ (~1.4 at.% Yb), so that the Yb^{3+} segregation coefficient between the crystal and the melt in the presence of Li^+ charge compensator was evaluated by the equation $K_{Yb} = K_{crystal}/K_{melt}$ to be 0.45 ± 0.16 .

The study of the same crystal by the SSMS method yielded the value of $0.54 \times 10^{20} \text{ cm}^{-3}$ ($K_{Yb} \geq 0.12$) which is however close to the upper detection limit of the method (about 2000 ppm) and thus it can be considered only as a lower-limit estimate. For the Li^+ ions, the SSMS analysis gave 20 ppm, or, equivalently, $N_{Li} = 0.13 \times 10^{20} \text{ cm}^{-3}$ (0.09 at.% Li). Thus, the actual amount of Li^+ is essentially lower than that of Yb^{3+} and charge compensation is in part maintained by other ways, probably, by zinc vacancies.

In Fig. 2, we plotted the dopant segregation coefficients K_D for several TM (Ni, Fe) [32,33] and RE (Yb, Tm, Er, Ho, Dy) [19–21,34–36] ions in $ZnWO_4$. The K_D values show a clear dependence on the dopant ionic radius R_D for VI-fold oxygen coordination [37] (assuming substitution of the Zn^{2+} cations). This dependence is close to $K_D \propto -(R_D - R_{Zn})^2$ in accordance with well-known Onuma's principle [38]. According to previous studies by inductively coupled plasma atomic emission spectrometry (ICP-AES) performed for a series of RE^{3+} -doped $ZnWO_4$

crystals grown without charge compensators [19,20,34–36], $K_{RE} = 0.10$ – 0.30 , depending on the cation size and, in particular, $K_{Yb} = 0.30$ [19]. This value agrees with our observations within the specified error. The residual difference may originate from the use of the Li^+ charge compensator.

Previously, for the isostructural $Yb^{3+}:MgWO_4$ crystal grown by the TSSG method, the Yb^{3+} segregation coefficient between the crystal and the used high-temperature solution K_{Yb} was determined to be 0.13 using ICP-AES [3]. However, in that case, no charge compensators were intentionally added (only some Na^+ cations might have entered from the melt, as Na_2WO_4 was used as a solvent for the crystal growth [5]).

3.2. Crystal coloration

The unpolarized absorption spectra of Yb^{3+}, Li^+ : $ZnWO_4$ crystals grown using different combinations of ZnO and WO_3 batches in Pt/Rh crucibles are presented in Fig. 3. Here and below, the crystal plates were oriented with their surfaces along the (010) cleavage plane. For all the crystals, absorption related to the ${}^2F_{7/2} \rightarrow {}^2F_{5/2}$ Yb^{3+} transition is observed at ~1 μm . Besides, intense and broad absorption bands in the visible and near-IR occur. The variation of the ZnO/ WO_3 batches leads to a change both in the intensity and position of local maxima of these bands. This effect is more sensitive to the kind of the WO_3 batch. The crystal obtained using the WO_3 (#1) reagent with 4 N purity had a superintense absorption in the visible (at ~500 nm, absorption coefficient $\alpha_{abs} > 100 \text{ cm}^{-1}$) making it completely black. Besides that, it had an additional band in the near-IR (at ~1.36 μm). The use of the WO_3 (#2) reagent with 5N-purity greatly reduced this absorption yielding a different spectrum. Depending on the ZnO batch, the resolved absorption peaks were at 450 nm (for both batches), at 545 nm ($\alpha_{abs} = 25 \text{ cm}^{-1}$, for ZnO #1) or 520 and 600 nm ($\alpha_{abs} \sim 18 \text{ cm}^{-1}$, for ZnO #2). Note that the Yb^{3+} band remained unchanged for all the studied crystals.

Uncontrolled impurities. The study of the impurity composition of the grown crystals by SSMS reveals that the main spectroscopically active uncontrolled impurities in all the crystals are the 3d transition-metal (TM) ions of the iron group: Fe, Mn, Ni, Cr and Cu. The content of each of these ions in the crystals exceeded 2 ppm. Their presence is facilitated by the fact that $FeWO_4$, $MnWO_4$, $NiWO_4$, etc., crystallize with the same structure as $ZnWO_4$ and form isostructural series with it. In particular, the crystal grown using WO_3 #1 contained a lot of Fe (200 ppm) and Ni (20 ppm), see Table 1, as compared to crystals grown with WO_3 #2. On the contrary, the use of the WO_3 #2 reagent led to a higher content of Cu (20 ppm). The concentrations of Cr and Mn were comparable in both cases, ~6–10 ppm. One should also note the essential amount of Rh in both crystals, 40–80 ppm. Obviously, the used Pt/Rh crucible is the source of this impurity.

Annealing. Relatively thick (thickness $t = 3.6 \text{ mm}$) crystalline plates

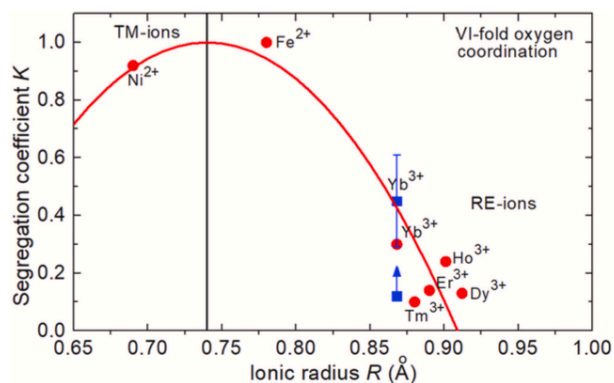


Fig. 2. Segregation coefficients of transition-metal (TM) and rare-earth (RE) ions in monoclinic $ZnWO_4$ vs. their ionic radius for VI-fold oxygen coordination: this work (blue squares) and literature data (red circles) [23,29–34]. Curve: parabolic fit of the data according to the Onuma's principle, $K_D = 1 - C(R_D - R_{Zn})^2$, $C = 35 \pm 3 \text{ \AA}^{-2}$.

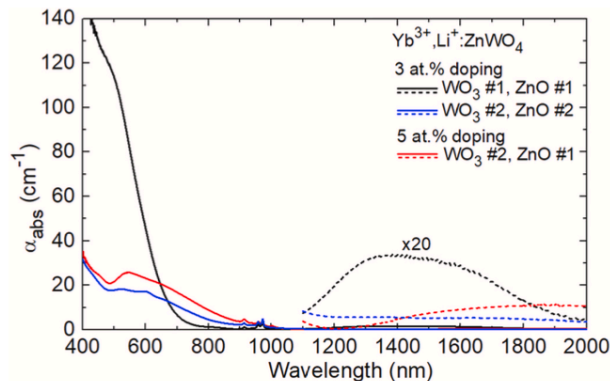


Fig. 3. Unpolarized absorption spectra of Yb^{3+}, Li^+ : $ZnWO_4$ crystals (nominal composition) at RT (293 K) grown using different ZnO and WO_3 reagents.

Table 1

Results of the impurity compositional analysis of the as-grown zinc tungstate crystals: 3 at.% Yb³⁺, 3 at.% Li⁺:ZnWO₄ (nominal composition; reagents: ZnO (#1) and WO₃ (#1)) and undoped ZnWO₄ (reagents: ZnO (#2) and WO₃ (#2)) by the SSMS method.

Element	ppm, weight		Element	ppm, weight	
	Yb ³⁺ ,Li ⁺ :ZnWO ₄	ZnWO ₄		Yb ³⁺ ,Li ⁺ :ZnWO ₄	ZnWO ₄
Li	20	0.8	Zn	host-forming	
O	host-forming		Zr	<0.05	<0.05
Na	0.6		Nb	40	10
Mg	2	6	Mo	10	60
Si	20	10	Ru	<0.1	<0.1
Cl	800	1000	Rh	40	80
K	0.4	2	Cd	2	<0.1
Ca	2	30	In	<0.1	<0.1
Sc	0.2	0.2	Sn	<0.1	<0.1
Ti	<0.01	<0.01	Er	<0.1	<0.1
V	0.4	<0.01	Tm	<0.1	<0.1
Cr	9	10	Yb	>2000	20
Mn	8	6	W	host-forming	
Fe	200	50	Re	<0.2	<0.2
Co	<0.02	<0.02	Os	<0.2	<0.2
Ni	20	2	Ir	<0.2	<0.2
Cu	2	20	Pt	<0.2	<0.2

cut from the 5 at.% Yb³⁺, 5 at.% Li⁺:ZnWO₄ crystal (nominal composition) grown from the Pt/Rh crucible using WO₃ #2 and ZnO #1 were annealed in air at 800 °C for 3 weeks. After annealing, the crystalline plates changed their coloration from black to brownish-red, as shown at the inset of Fig. 4(a). The comparison of the absorption spectra before and after annealing, Fig. 4(a), indicates that the intensity of the broad absorption band in the visible (centered at ~545 nm) is drastically reduced after this treatment. The calculated differential absorption spectrum ($\Delta\alpha_{\text{abs}} = \alpha_{\text{as-grown}} - \alpha_{\text{annealed}}$) is similar to that of black-colored scheelite-like double molybdate crystals grown in oxygen-deficient atmospheres [39–41]. It contains an intense band spanning from 0.5 to 1 μm and centered at ~580 nm ($\Delta\alpha_{\text{abs}} = 21 \text{ cm}^{-1}$). In Ref. [39–41], a similar absorption band was assigned to F-centers (free electrons localized at oxygen vacancies). After annealing, the absorption spectrum contains two distinct peaks at ~440 and ~530 nm ($\alpha_{\text{abs}} \sim 8\text{--}9 \text{ cm}^{-1}$).

For comparison, we also studied an undoped ZnWO₄ crystal grown in a Pt/Rh crucible with the use of WO₃ #2 and ZnO #2 reagents. The absorption spectra of the crystal plate ($t = 0.7 \text{ mm}$) before and after the annealing at 800 °C for 3 weeks (the same regime as applied above), see Fig. 4(b), were similar to those shown in Fig. 4(a) except for the lack of Yb³⁺ absorption at ~1 μm . The intensity of the bands at ~430 and 520 nm was redistributed and their peak wavelengths slightly shifted. This indicates a possible indirect effect of Yb³⁺ ions on the nature of these optical centers, probably via the alteration of the local multi-ligands.

In Fig. 4(c), we compare two samples of different thickness ($t = 0.9 \text{ mm}$ and 3.6 mm) cut from the same sample grown using the ZnO (#1) and WO₃ (#2) reagents. Accordingly, different duration of the oxidizing annealing was needed: 24 h and 3 weeks, respectively. After this time, no noticeable change in the absorption spectrum was detected. The spectra are very similar and the peak absorption at ~520–530 nm ($\alpha_{\text{abs}} \sim 8 \text{ cm}^{-1}$) is nearly the same.

Crucible composition. Finally, we studied the influence of the crucible composition on the crystal coloration. We grew a 5 at.% Yb³⁺, 5 at.% Li⁺:ZnWO₄ crystal (nominal composition) from a rhodium free Pt crucible with the use of the WO₃ #2 and ZnO #1 batches. Unlike all the previous samples grown from the Pt/Rh crucible, this crystal appeared to be transparent with only light pink-brown coloration (even without oxidizing annealing), Fig. 1(d). A similar coloration of undoped ZnWO₄ is presented in Refs. [42]. The absorption spectrum of the as-grown crystal is shown in Fig. 5. In the spectrum, a weak and broad band centered at ~450 nm ($\alpha_{\text{abs}} \sim 1.8 \text{ cm}^{-1}$) is present.

For the Yb³⁺,Li⁺:ZnWO₄ crystals grown using the Pt/Rh crucibles,

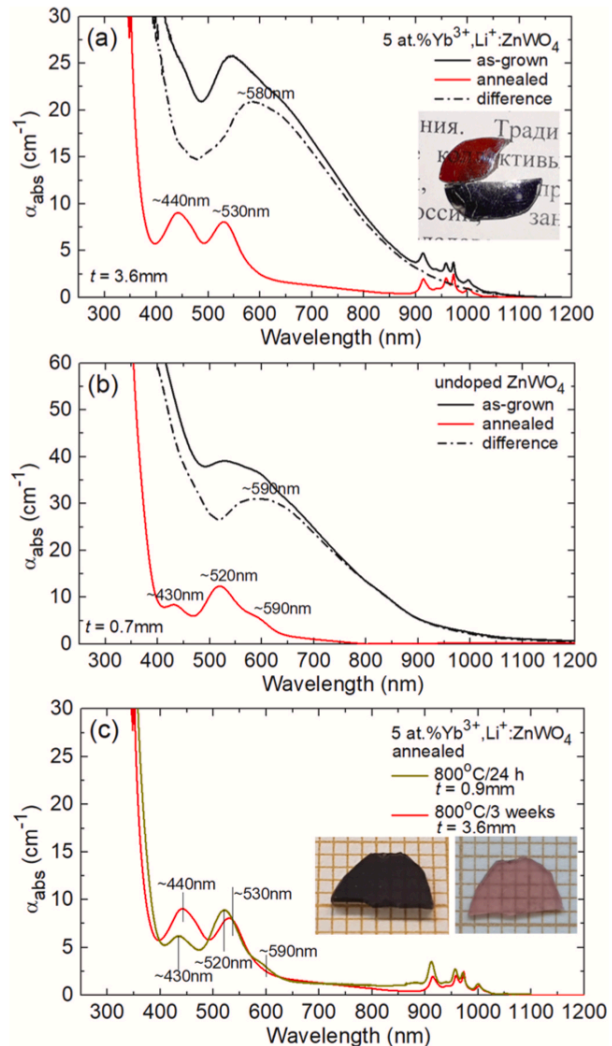


Fig. 4. Effect of oxidizing annealing on the unpolarized absorption spectra of ZnWO₄ crystals at RT (293 K): (a) 5 at.% Yb³⁺, 5 at.% Li⁺:ZnWO₄ (nominal composition) grown using the ZnO (#1) and WO₃ (#2) reagents, annealing at 800 °C for 3 weeks; (b) undoped ZnWO₄ grown using the ZnO (#2) and WO₃ (#2) reagents, annealing at 800 °C for 3 weeks; (c) 5 at.% Yb³⁺, 5 at.% Li⁺:ZnWO₄ (nominal composition) grown using the ZnO (#1) and WO₃ (#2) reagents and annealed at 800 °C for 24 h or for 3 weeks. t – sample thickness. Inset: (a) photograph of the thinner crystal plates before (lower) and after (upper) the annealing, (c) photograph of the crystal plates before (left) and after (right) the annealing at 800 °C for 24 h.

the UV absorption edge λ_{UV} is at ~380 nm (after the oxidizing annealing). For the crystals grown from a Pt crucible, it is shorter, $\lambda_{\text{UV}} \sim 340 \text{ nm}$, corresponding to an optical bandgap of 3.65 eV. The electronic structure of ZnWO₄ was studied in Ref. [43] revealing that it is a direct bandgap material with the minimum of the conduction band and the maximum of the valence band at the same Y point of the Brillouin zone (calculated $E_g \sim 4.65 \text{ eV}$). Experimental optical studies of undoped ZnWO₄ gave the E_g value of 3.9–4.4 eV [44]. Thus, the observed difference in the position of the UV absorption edge may be associated with some local optical centers (see Section 3.3).

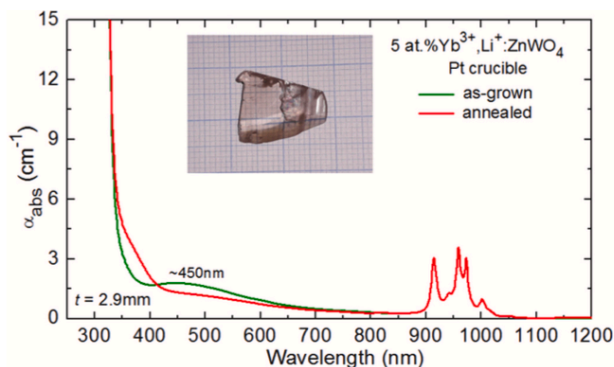


Fig. 5. Unpolarized absorption spectrum at RT (293 K) of a 5 at.% Yb³⁺, 5 at.% Li⁺:ZnWO₄ crystal (nominal composition) grown in a Pt crucible using the ZnO (#1) and WO₃ (#2) reagents, before and after the annealing at 800 °C for 3 weeks. Inset: photo of the polished sample ($t = 2.9$ mm).

3.3. Discussion

The coloration of Yb³⁺-doped ZnWO₄ crystals is a relevant issue because it may affect their laser performance. Let us discuss existing literature on the topic (mostly, for nominally pure (undoped) ZnWO₄ crystals) and interpret the findings of the present work.

The growth of *undoped* ZnWO₄ crystals by the Cz method is known for many years. One of the first reports devoted to this crystal is the paper by O'Hara [45]. It was revealed that the use of Rh crucibles (unlike Pt ones) gave rise to black melts and opaque crystals. However, neither absorption spectra, nor any discussion about the reasons of black coloration nor attempts to eliminate it by oxidizing annealing are given in this paper. Nagornaya et al. reported on the Cz growth of large and transparent ZnWO₄ crystals from Pt crucibles [25]. The authors annealed the as-grown boules at 800–1000 °C in oxygen leading to a change of the crystal coloration from brownish to slightly pink-violet without giving details. Galashov et al. reported on further improvement of the quality of undoped ZnWO₄ crystals [26]. The authors used for the growth performed in Pt crucibles high-purity reagents (a home-made WO₃ and commercial ZnO with concentration of impurity TM ions down to 1 ppm). In Ref. [26], the transmission spectra of ZnWO₄ before and after annealing were presented without giving many details. Despite the excellent purity of the starting growth charge, the as-grown crystals exhibited weak absorption at ~500 nm ($\alpha_{\text{abs}} \sim 0.10$ cm⁻¹). The discussion about the nature of residual coloration is absent in this paper. A systematic study of the optical absorption of ZnWO₄ crystals with various coloration was performed by Limarenko et al. [28]: from almost colorless to pink, dark pink and yellow. The authors discussed such aspects as the possible assignment of the observed absorption bands to different optical active centers (mainly, iron ions), the influence of the crystal annealing in different atmospheres on its residual coloration and the effect of various decolorating agents (Sb, Bi, Ag, etc.) onto such a coloration.

There also exist studies of ZnWO₄ in which the colorating and decolorating impacts of various impurities were studied by a *deliberate doping* of the crystal by such impurities. One clear example is iron doping. The segregation coefficient of iron (Fe) in ZnWO₄ is close to unity [33] and, as a result, it is easily introduced in the crystal in its both valent forms (Fe²⁺ and Fe³⁺). FeWO₄ crystallizes with the same structure as zinc oxide and forms a solid solution with it. Both ions substitute for the Zn²⁺ ones in the lattice. Földvári et al. studied Fe-doped ZnWO₄ crystals [46]. The absorption at ~460 and 350 nm was assigned to Fe²⁺ and Fe³⁺ species, respectively. Watterich et al. have also assigned the absorption of ZnWO₄ crystals at ~460 nm to the divalent iron, Fe²⁺ [27, 33]. Therefore, one of the absorption peaks revealed in our crystals (around 430–440 nm) can be assigned to Fe²⁺ impurity. Bencs et al.

discussed the possible ways to remove the coloration of ZnWO₄ induced by Fe²⁺ and Cr³⁺ impurity ions, i.e., by (i) applying an electric field during growth, (ii) using a subsequent oxidizing treatment (iii) adding decoloration agents (e.g., Sb⁵⁺), to the melt or (iv) using chemical purification of the starting materials [47]. Kornlyo et al. investigated Fe, Li-co-doped ZnWO₄ [48]. This study reported on a reduction in the crystal coloration owing to the Li⁺ codoping, as highlighted by the decrease of the absorption at ~460 nm due to the Fe²⁺ → Fe³⁺ transformation. The same effect was also assumed in Ref. [27]. Therefore, it can be suggested that in our case, besides acting as a charge compensator, the addition of Li⁺ into the ZnWO₄ crystals may be in part responsible for the reduced absorption at 430–440 nm. Another impurity ion, which was proposed as a source of ZnWO₄ coloration is trivalent chromium. In particular, Cr³⁺ was considered as the main source of pinkish coloration of undoped ZnWO₄ crystals in Ref. [27].

The *point defects* in ZnWO₄ and their effect on the crystal coloration have also been studied. In particular, in the papers [27,33], the crystals still presented slight pink coloration with an optical absorption at ~510 nm after removing Fe²⁺. Oxygen vacancies, OH⁻ groups, or W⁵⁺ ions were proposed as possible sources of this absorption in Ref. [33] although they were ruled out in Ref. [27]. As a result, Cr³⁺ was suggested as the possible source of pinkish coloration of undoped crystals. The electron spin resonance studies of ZnWO₄ crystals revealed impurity centers with small concentrations (few ppm) such as Cr³⁺, Mn²⁺, Fe³⁺, Co²⁺, Cu²⁺, Rh²⁺ and Pt³⁺ [33]. The latter two ions may enter into the crystal from the crucible material (Pt or Rh), while the TM ions are associated with the growth charge as impurities from the reagents. In the presence of Li⁺ as a charge compensator, as mentioned above, divalent iron is suppressed at the expense of raising the amount of Fe³⁺, and, moreover, Cr³⁺ impurity ions may be promoted to enter the lattice. Thus, the pink coloration of Li⁺-doped ZnWO₄ was assigned in Refs. [27, 28] to Cr³⁺. Wang et al. reported on the growth of both clear and colored ZnWO₄ crystals [49]. In the latter case, two bands in the excitation spectra centered at ~496 and 520 nm were observed. The corresponding emission was assigned to defects. It was pointed out that annealing of the colored crystals in oxygen atmosphere can remove their coloration, as expressed by the disappearance of the absorption in the visible.

Thus, the problem of coloration of undoped ZnWO₄ crystals is well-known and it can be eliminated to a great extent by (i) using specially purified WO₃ and ZnO reagents, (ii) applying annealing in oxygen atmosphere and (iii) introducing decolorating agents. However, the influence of the crucible composition (in particular, the role of Rh) has been barely studied. Moreover, such analysis has never been performed for Yb³⁺-doped crystals.

The information about the coloration and defects of RE-doped ZnWO₄ crystals is scarce. There is a series of studies dedicated to the growth and characterization of ZnWO₄ crystals with various RE³⁺ dopants (RE = Yb, Er, Tm, Ho, Dy) [19,20,34–36], however, without giving details about their coloration. Nevertheless, in the absorption spectra of Ho³⁺:ZnWO₄ given in Refs. [36], a strong absorption band in the visible, at ~500 nm ($\alpha_{\text{abs}} \sim 5$ cm⁻¹) is shown. Kowalski et al. reported on the growth of undoped, Ca²⁺-doped and Ca²⁺,Eu³⁺-co-doped ZnWO₄ crystals [50]. Particularly in the latter case, a dark internal part of the grown boule was detected indicating the effect of the RE³⁺ ions.

Taking into account the literature data and our results, we can assume that for the as-grown crystals obtained using relatively pure reagents (e.g., ZnO #1 and WO₃ #2) and Pt/Rh crucibles, there are probably two main sources of absorption in the visible, namely (i) the iron ions (the band from Fe³⁺ at ~350 nm, manifested by the red-shift of the UV absorption edge, and the band from Fe²⁺ at ~450 nm) and (ii) the F-centers based on free electrons localized at oxygen vacancies (the broad band centered at ~580 nm spanning into the near-IR). The latter defects result from a partial reduction of the crystal composition that leads to losing a part of oxygen. Moreover, it is obvious that rhodium from the crucible acts as a catalyst for such a reduction. Rhodium (like all other metals of platinum group) is well-known to have a strong

K. Subbotin et al.

catalytic activity in respect to many redox chemical reactions, which is widely used in chemical industry. Note that in Ref. [51], the coloration of oxide crystals with oxygen vacancies was assigned to small polarons rather than F-centers while there is no evidence of such assignment for tungstate crystals.

A combination of the above mentioned optical centers leads to black coloration of the as-grown crystals. The oxidizing annealing removes the oxygen vacancies and reduces the amount of the Fe^{2+} species simultaneously giving rise to the Fe^{3+} ones. As a result, the annealed crystalline samples are pinkish. This color is determined by the residual Fe^{2+} species (the band at $\sim 440\text{--}450$ nm) and by the band at $\sim 520\text{--}530$ nm the nature of which is still unknown. This band cannot be assigned to Cr^{3+} (see Refs. [27,28]) due to the following reasons: (i) the absorption spectra of ZnWO_4 crystals intentionally doped by chromium revealed two almost equal in intensity absorption bands at ~ 520 and 700 nm and the latter one is not observed in our case, and (ii) the absorption cross-section obtained by dividing the peak absorption coefficient at ~ 520 nm by the actual Cr^{3+} concentration in our crystals (see Section 3.2) is by order of magnitude higher than the values commonly accepted for parity forbidden ${}^4A_2 \rightarrow {}^4T_1$ vibronic transition of Cr^{3+} . In addition, it seems that the use of the Pt crucibles (instead of the Pt/Rh ones) somehow diminishes the concentration of TM ion-related defects (for the same composition of the growth charge).

4. Crystal structure

4.1. Differential thermal analysis

The DTA curves for the 5 at.% Yb^{3+} , 5 at.% $\text{Li}^+:\text{ZnWO}_4$ crystal (nominal composition) corresponding to sample heating and cooling are shown in Fig. 6. One can see just one strong and reversible endothermic (at heating) and exothermic (at cooling) effect, which, certainly, corresponds to the congruent melting of the compound. The starting temperature of melting and that of crystallization well correspond to each other at 1166°C , in contrast to the DTA curve for undoped ZnWO_4 given in Ref. [42], where these two temperatures differed by more than 30°C . The determined melting point for 5 at.% Yb^{3+} , 5 at.% $\text{Li}^+:\text{ZnWO}_4$ is by 22°C lower as compared with the data given for the undoped crystal [23]. Lowering of the melting point of a crystal with introduction of impurities into its composition is a usual situation. The absence of any additional thermal effects reflects the absence of polymorphic phase transformations of the 1st type below the melting point.

4.2. Structure refinement

The crystal structure and the phase purity of the crystals were confirmed using XRD. The RT XRD pattern of the 5 at.% Yb^{3+} , 5 at.%

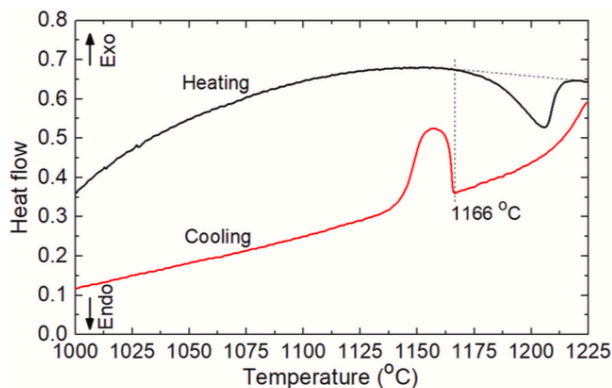


Fig. 6. Differential thermal analysis (DTA) curves for the 5 at.% Yb^{3+} , 5 at.% $\text{Li}^+:\text{ZnWO}_4$ crystal (nominal composition).

Journal of Luminescence 228 (2020) 117601

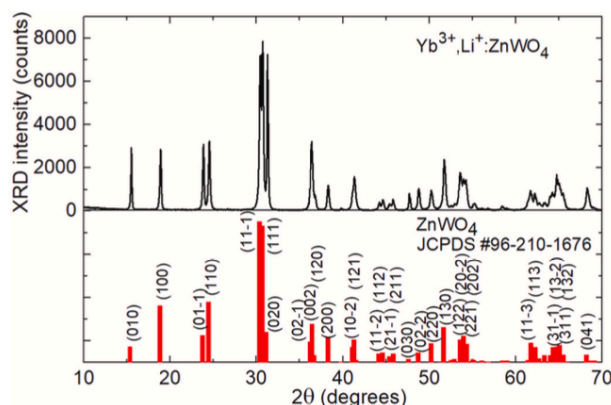


Fig. 7. RT X-ray powder diffraction (XRD) pattern of the as-grown 5 at.% Yb^{3+} , 5 at.% $\text{Li}^+:\text{ZnWO}_4$ crystal (nominal composition); the theoretical pattern of undoped ZnWO_4 is shown for comparison, JCPDS card #96-210-1676, numbers indicate the Miller's indices, (hkl) .

$\text{Li}^+:\text{ZnWO}_4$ crystal (nominal composition) is shown in Fig. 7. The crystal composition of $\text{Zn}_{0.964}\text{Yb}_{0.018}\text{Li}_{0.018}\text{WO}_4$ was assumed. The actual concentration of Yb (1.8 at.%) was determined by the micro-probe analysis and an equal atomic fraction of Yb and Li was considered. The relative intensity and position of the diffraction peaks of the sample agree well with the JCPDS (Joint Committee on Powder Diffraction Standards) card #96-210-1676 for undoped ZnWO_4 . No other phases except the monoclinic one are found. All this indicates that the sample is of single-phase nature. The XRD pattern measured for a broader range of diffraction angles 2θ of $14.5\text{--}120^\circ$ was refined by the Rietveld method using the FULLPROF package; the calculated pattern showed a good matching with the experimental one, Fig. 8. The crystal structure of undoped ZnWO_4 [52] was taken as the starting model for the Rietveld refinement.

$\text{Yb}^{3+},\text{Li}^+:\text{ZnWO}_4$ is monoclinic belonging to the space group $P2_1/c - C^4_{2h}$, No. 13 and the centrosymmetric point group $2/m$. The lattice constants are $a = 4.702(2) \text{ \AA}$, $b = 5.718(6) \text{ \AA}$, $c = 4.930(4) \text{ \AA}$, the unit cell volume $V_{\text{calc}} = 132.571 \text{ \AA}^3$, the monoclinic angle $\beta = \alpha^\circ c = 90.713 (5)^\circ$ and the theoretical crystal density $\rho_{\text{calc}} = 7.553 \text{ g/cm}^3$ (the number of the formula units $Z = 2$). The R -factors were $R_{\text{wp}} = 11.6$ and $R_p = 8.11$ (the reduced chi-squared value $\chi^2 = (R_{\text{wp}}/R_{\text{exp}})^2 = 7.03$ and the Bragg factor $R_b = 0.89$), cf. Table 2. The obtained fractional atomic coordinates are listed in Table 3.

The determined lattice constants are slightly higher than those for an undoped ZnWO_4 crystal ($a = 4.69263(5) \text{ \AA}$, $b = 5.72129(7) \text{ \AA}$, $c =$

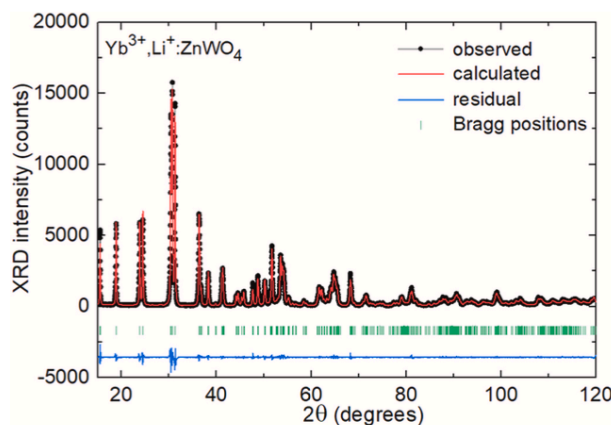


Fig. 8. Results of the Rietveld refinement of the RT X-ray powder diffraction (XRD) pattern of the as-grown $\text{Zn}_{0.964}\text{Yb}_{0.018}\text{Li}_{0.018}\text{WO}_4$ crystal.

K. Subbotin et al.

Journal of Luminescence 228 (2020) 117601

Table 2
Parameters of the Rietveld refinement of the structure of the as-grown $\text{Zn}_{0.964}\text{Yb}_{0.018}\text{Li}_{0.018}\text{WO}_4$ crystal.

Parameters	Values
System	Monoclinic
Space group	$P2/c - C_{2h}^4$
Laue class	$2/m$
Space group IT number	13
Lattice constants ($a - b - c$) (Å)	4.702(2) – 5.718(6) – 4.930(4)
Angles $\alpha - \beta - \gamma$ (deg)	90–90.713(5) – 90
Cell volume V_{calc} (Å ³)	132.571
Number of the formula units Z	2
Crystal density ρ_{calc} (g/cm ³)	7.553
2θ range (deg)	14.5–120
Radiation	Cu-K α 1 ($\lambda = 1.5406$ Å)
No. of reflections	399
No. of points	5270
Background Parameters – No.	Linear interpolation – 72
Refinement	Rietveld (FullProf)
Reliability factors	$R_p = 8.11, R_{wp} = 11.6, \chi^2 = 7.03,$ $R_b = 0.89, R_f = 0.38$

Table 3
Fractional atomic coordinates (x, y, z), occupancy factors (O-F.) and isotropic displacement parameters (B_{iso}) of the as-grown $\text{Zn}_{0.964}\text{Yb}_{0.018}\text{Li}_{0.018}\text{WO}_4$ crystal.

Atom	Site	x	y	z	B_{iso}	O-F.
Zn	2e	1/2	0.687(8)	1/4	0.978	0.964
Yb	2e	1/2	0.687(8)	1/4	0.978	0.018
Li	2e	1/2	0.687(8)	1/4	0.978	0.018
W	2f	0	0.189(9)	1/4	0.552	1
O1	4g	0.256(4)	0.365(0)	0.412(0)	1.513	1
O2	4g	0.220(8)	0.894(2)	0.429(0)	1.722	1

Table 4
Lattice constants of undoped and RE³⁺-doped ZnWO_4 crystals reported so far.

Crystal	$a, \text{Å}$	$b, \text{Å}$	$c, \text{Å}$	$\beta, ^\circ$	Ref.
ZnWO_4	4.69263(5)	5.72129(7)	4.92805(5)	90.6321(9)	[7]
ZnWO_4	4.6902(1)	5.7169(1)	4.9268(1)	90.626(1)	[28]
$\text{Yb}^{3+}, \text{Li}^+ : \text{ZnWO}_4$	4.702(2)	5.718(6)	4.930(4)	90.713(5)	This work
$\text{Eu}^{3+}, \text{Ca}^{2+} : \text{ZnWO}_4$	4.697	5.727	4.938	90.69	[47]

4.92805(5) Å and $\beta = 90.6321(9)^\circ$ [7], see also Table 4. The higher precision in the reported lattice constants for undoped ZnWO_4 is explained by the use of neutron diffraction in Ref. [7].

The Yb^{3+} ions in ZnWO_4 are expected to replace the Zn^{2+} cations. The charge compensation is partially maintained by Li^+ cations and the excessive charge difference originating from the remaining Yb^{3+} ions is most likely compensated by cationic (probably, zinc) vacancies (see Section 3.1). There is a single crystallographic site for Zn^{2+} in the structure of ZnWO_4 (Wyckoff symbol: 2e, symmetry: C_2). The Zn^{2+} cations are located in the $[\text{ZnO}_6]$ octahedra and, consequently, they are VI-fold oxygen-coordinated. The ionic radii of the cations involved in the doping process are 0.868 Å (Yb^{3+}), 0.74 Å (Zn^{2+}) and 0.76 Å (Li^+) [37], so that an increase of the unit-cell volume is expected. The significant difference of the ionic radii of Zn^{2+} , Yb^{3+} and Li^+ , as well as the difference of their valence are expected to result in inhomogeneous broadening of the absorption and luminescence spectral bands of Yb^{3+} ions.

The structure of $\text{Yb}^{3+}, \text{Li}^+$ -doped ZnWO_4 is shown in Fig. 9 according to the atomic coordinates determined by the Rietveld refinement. The metal – oxygen (M – O) interatomic distances in the $[\text{WO}_6]$ and $[(\text{Zn}|\text{Yb}|\text{Li})\text{O}_6]$ polyhedra determined by the analysis of the cif file by VESTA software are listed in Table 5. W^{6+} is bonded to six oxygen ions O^{2-} forming distorted $[\text{WO}_6]$ octahedra that share corners with eight

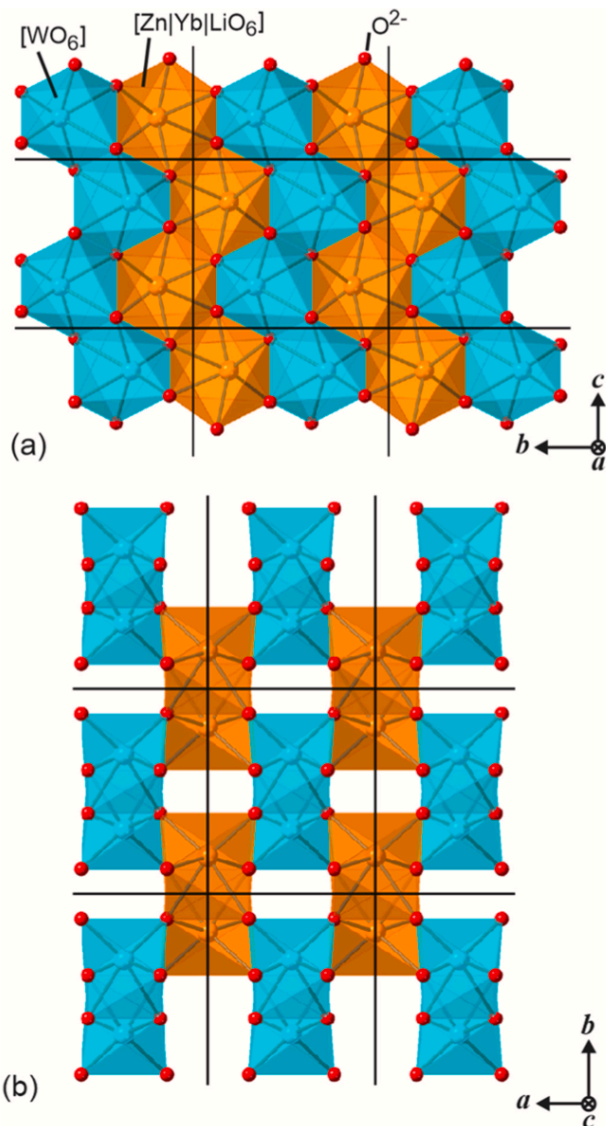


Fig. 9. Fragment of crystal structure of Yb^{3+} -doped ZnWO_4 : (a) projection in the b - c plane; (b) projection in the a - b plane. Black lines indicate the unit-cell.

equivalent $[(\text{Zn}|\text{Yb}|\text{Li})\text{O}_6]$ octahedra, and edges with two equivalent $[\text{WO}_6]$ octahedra in the crystallographic plane b - c . The W – O bond lengths are in the range 1.752(2) – 2.166(4) Å, see Fig. 10(a). $\text{Zn}^{2+}|\text{Yb}^{3+}|\text{Li}^+$ is bonded to six oxygen cations O^{2-} to form $[(\text{Zn}|\text{Yb}|\text{Li})\text{O}_6]$ octahedra which, in their turn, share corners with eight equivalent $[\text{WO}_6]$ octahedra and edges with two equivalent $[(\text{Zn}|\text{Yb}|\text{Li})\text{O}_6]$ ones. There are two shorter (1.981(0) Å), two intermediate (2.032(9) Å) and two longer (2.319(5) Å) Zn–O bond lengths, Fig. 10(b).

As a result, the structure of $\text{Yb}^{3+}, \text{Li}^+ : \text{ZnWO}_4$ is a chain structure determined by zig-zag chains formed by edge-sharing $[(\text{Zn}|\text{Yb}|\text{Li})\text{O}_6]$ octahedra or edge-sharing $[\text{WO}_6]$ octahedra running parallel to the c -axis. Each chain formed by $[(\text{Zn}|\text{Yb}|\text{Li})\text{O}_6]$ is corner-linked to four chains formed by $[\text{WO}_6]$. Thus, the structure contains open channels also going parallel to the c -axis. The shortest distance $\text{Zn}|\text{Yb} - \text{Zn}|\text{Yb}$ observed in $\text{Yb}^{3+}, \text{Li}^+ : \text{ZnWO}_4$ is 3.269(6) Å along the vector $[\text{u v w}] = [0 - 0.3756 \ 0.5]$.

Besides, it is clear from Fig. 9(b) that the structure of ZnWO_4 contains $[\text{WO}_6]$ layers bonded to each other by Zn^{2+} ions only. These ions are not

Table 5
 Characterization of the [WO₆] and [(Zn|Yb|Li)O₆] polyhedra in the 5 at.% Yb³⁺, 5 at.% Li⁺:ZnWO₄ crystal (nominal composition).

Polyhedron	[WO ₆]	[(Zn Yb)O ₆]
Interatomic distances	(W-O2) = 2.166(4) × 2	(Zn Yb-O2) = 1.981(0) × 2
M – O, Å	(W-O2) = 1.963(4) × 2	(Zn Yb-O1) = 2.032(9) × 2
	(W-O1) = 1.752(2) × 2	(Zn Yb-O1) = 2.319(5) × 2
Average bond length, Å	1.9607	2.1112
Polyhedral volume, Å ³	9.5065	12.1496
Distortion index (bond length)	0.07089	0.06581
Quadratic elongation	1.0455	1.0267
Bond angle variance, deg. ²	128.863	73.8797
Effective coordination number	4.0237	4.9634

very strong bonders and the breaking energy of the [O–Zn–O] chemical bond (which is predominantly ionic) is not very high. Therefore, the existence of very well expressed cleavage plane in this crystal is easily explainable. Moreover, when the crystal is doped with Yb³⁺ ions with not enough amount of the charge compensator (that is somehow valid in our case), a substantial concentration of zinc vacancies may appear. It should additionally weaken the bonds between the neighboring [WO₆] layers in the crystal structure leading to enhanced cleavage ability. This phenomenon occurred in the Yb³⁺,Li⁺-co-doped ZnWO₄ crystals grown in the present work. An increase of the crystal cracking was observed previously for CdWO₄ crystals [42] which are isostructural to ZnWO₄ in the case of Cd²⁺ deficiency. Thus, optimization of charge compensation during the crystal growth will probably help to reduce the cracking of Yb³⁺-doped ZnWO₄ crystals in further studies.

4.3. Thermal expansion

The unit-cell parameters as a function of temperature *T* were refined with the FULLPROF program. The relative evolution of the parameters *L* = *a*, *b*, *c* and *c** = *c* × cos(β–90°) with respect to their values at 303 K (*L*_{303K}), Fig. 11, was used to determine the components of the linear thermal expansion tensor, $\alpha = (\Delta L/L_{303K})/\Delta T$, in the crystallophysical frame with the mutually orthogonal axes (i.e., X₁ || *a*, X₂ || *b* and X₃ || *c**). All the unit-cell parameters increase nearly linearly with temperature indicating a positive thermal expansion. The monoclinic angle β slightly increases with *T*.

The linear thermal expansion tensor in the crystallophysical frame is:

$$\alpha_{ij} = \begin{pmatrix} 11.710 & 0 & -0.006 \\ 0 & 9.901 & 0 \\ -0.006 & 0 & 7.009 \end{pmatrix} \times 10^{-6} \text{K}^{-1}.$$

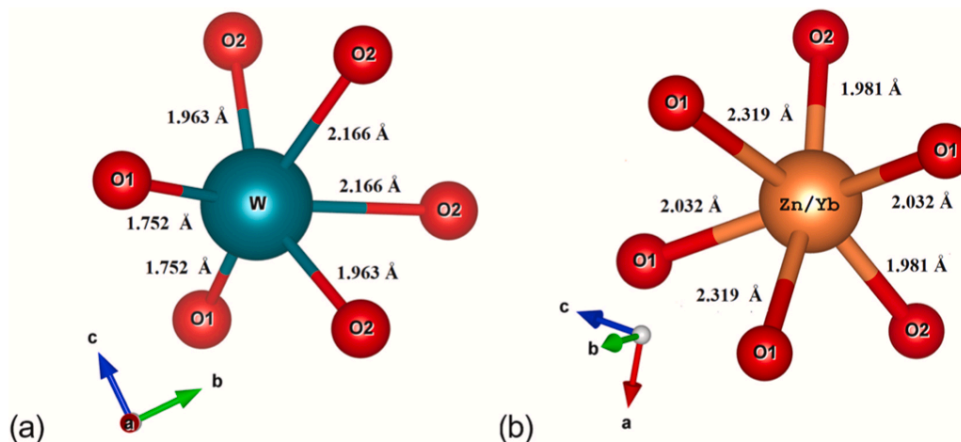


Fig. 10. Nearest-neighbor coordination of (a) tungsten and (b) zinc | ytterbium | lithium cations in the monoclinic Yb³⁺,Li⁺:ZnWO₄ crystal.

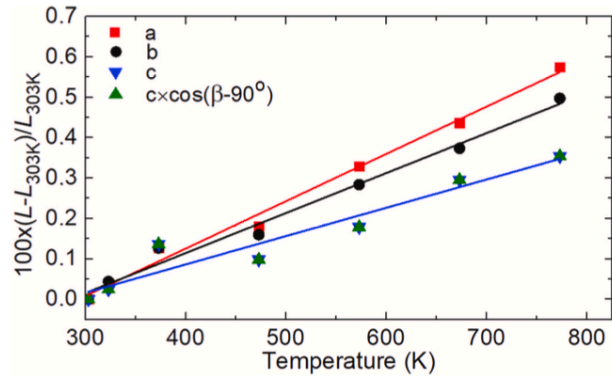


Fig. 11. Temperature evolution of the unit-cell parameters (*L* = *a*, *b*, *c* and *c**) of 5 at.% Yb³⁺, 5 at.% Li⁺:ZnWO₄ (nominal composition) according to the data of high-temperature XRD.

The non-diagonal $\alpha_{13} = \alpha_{31}$ elements are very small and the tensor is quasi-diagonal. The eigen-frame of this tensor in which it takes the diagonal form is very close to the crystallophysical one, X₁ || *a*, X₂ || *b* and X₃ || *c**, see Fig. 12.

The eigen-values of the thermal expansion tensor of Yb³⁺,Li⁺:ZnWO₄ are $\alpha'_{11} \approx \alpha_a = 11.71 \times 10^{-6} \text{K}^{-1}$, $\alpha'_{22} = \alpha_b = 9.90 \times 10^{-6} \text{K}^{-1}$ and $\alpha'_{33} \approx \alpha_{c^*} = 7.01 \times 10^{-6} \text{K}^{-1}$. Thus, the anisotropy of the thermal expansion is relatively weak, as expressed by the ratios $\alpha'_{11}:\alpha'_{33} = 1.67$ and $\alpha'_{22}:\alpha'_{33} = 1.41$. The coefficient of the volumetric thermal expansion $\alpha_{\text{vol}} = \alpha'_{11} + \alpha'_{22} + \alpha'_{33} = 28.62 \times 10^{-6} \text{K}^{-1}$.

In Table 6, we compare the thermal expansion coefficients for various M²⁺WO₄ crystals reported so far [4,5,14,53]. Our results are close to previously reported values for a Ho³⁺:MgWO₄ crystal, $\alpha_a = 11.22 \times 10^{-6} \text{K}^{-1}$, $\alpha_b = 8.09 \times 10^{-6} \text{K}^{-1}$ and $\alpha_c = 8.77 \times 10^{-6} \text{K}^{-1}$ [5].

5. Raman spectra

The polarized RT Raman spectra of the 5 at.% Yb³⁺, 5 at.% Li⁺:ZnWO₄ crystal (nominal composition) are shown in Fig. 13. The measurements were carried out using a rectangular sample cut in the crystallophysical frame {*a*, *b*, *c**}. For simplicity, we will designate *c** as *c* due to the closeness of the monoclinic angle to the right angle, within the accuracy of the sample orientation. The Porto's notations for Raman spectroscopy, *m*(*nk*) \bar{l} , are used, where *m* and *l* are the directions of propagation of the incident and scattered light, and *n* and *k* are the corresponding polarization states [54]. We studied all three principal

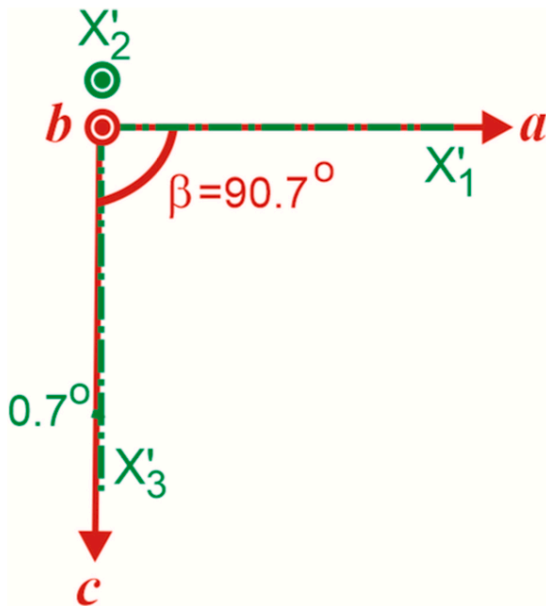


Fig. 12. Mutual orientation of the crystallographic axes (a , b , c) and principal axes of the thermal expansion tensor (X'_1 , X'_2 , X'_3) in $\text{Yb}^{3+}, \text{Li}^+:\text{ZnWO}_4$.

Table 6

Thermal expansion coefficients for M^{2+}WO_4 crystals reported so far.

Crystal	α , 10^{-6} K^{-1}			Method*	Ref.
	[100]	[010]	[001]		
$\text{Cr}^{3+}:\text{MgWO}_4$	10.5	15.7	10.8	DIL	[14]
$\text{Ho}^{3+}:\text{MgWO}_4$	11.22	8.09	8.77	XRD	[5]
CdWO_4	6.39	10.9	6.45	DIL	[49]
ZnWO_4	9.64	8.63	6.45	DIL	[4]
$\text{Yb}^{3+}, \text{Li}^+:\text{ZnWO}_4$	11.71	9.90	7.01	XRD	This work

* XRD – high-temperature XRD, DIL – dilatometry.

crystal cuts: a -cut, b -cut and c -cut.

The primitive cell of ZnWO_4 contains two formula units ($Z = 2$). The factor group analysis predicts a total of 36° of freedom for 12 atoms in each primitive cell. The corresponding irreducible representations at the center of the Brillouin zone Γ ($\mathbf{k} = 0$) are $8A_g + 10B_g + 8A_u + 10B_u$ of which the even (*gerade*, *g*) vibrations are Raman-active and the others are IR-active [55]. Thus, 18 Raman modes ($8A_g + 10B_g$) are possible. We observed 17 modes out of 18 possible ones (except for the low-frequency one at $<100 \text{ cm}^{-1}$). The modes are labeled in Fig. 13 and their peak frequencies and symmetries (A_g or B_g) are listed in Table 7. Here, the assignment is according to Ref. [56,57].

Monotungstates are well-known Raman-active materials. One prominent example is CaWO_4 , having a tetragonal (scheelite-type) structure (sp. gr. $I4_1/a$). For this material, the Raman spectra can be divided into two sets of frequencies at $0\text{-}409 \text{ cm}^{-1}$ and $797\text{-}912 \text{ cm}^{-1}$, showing a characteristic “gap” at intermediate frequencies. This “gap” is related to tightly bound atoms in the $[\text{WO}_4]^{2-}$ molecular group with internal vibrations generally occurring at higher frequencies. In contrast, the external vibrations due to the loosely bound Ca^{2+} and $[\text{WO}_4]^{2-}$ occur at lower frequencies. Such a behavior is not observed in ZnWO_4 due to the closeness of two tungstate groups $[\text{WO}_4]$ corresponding to the octahedra $[\text{WO}_6]$. It is only possible to attribute the high-frequency modes at 707 cm^{-1} (A_g) and 785 cm^{-1} (B_g) (both assigned as ν_2) and at 906 cm^{-1} (A_g) (assigned as ν_1) to internal (stretching) vibrations of the W – O atoms in the $[\text{WO}_6]$ octahedra [55, 56].

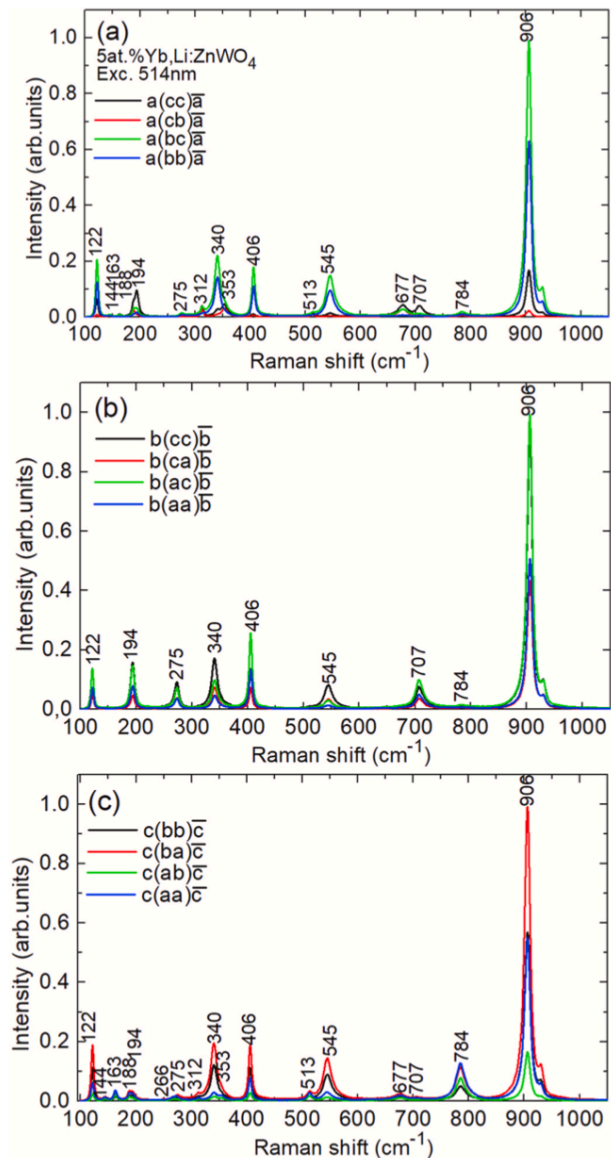


Fig. 13. Polarized Raman spectra of the as-grown 5 at.% Yb^{3+} , 5 at.% $\text{Li}^+:\text{ZnWO}_4$ crystal (nominal composition) for the (a) $a(ij)\bar{a}$, (b) $b(ij)\bar{b}$ and (c) $c(ij)\bar{c}$ geometries (Porto's notations). The numbers indicate the frequencies of Raman bands in cm^{-1} . $\lambda_{\text{exc}} = 514 \text{ nm}$.

The Raman spectra are strongly polarized. The most intense band in the spectra is found at 906.0 cm^{-1} . Its full width at half maximum (FWHM) $\Delta\nu$ is 11.9 cm^{-1} . This band is slightly shifted and broadened as compared to undoped ZnWO_4 for which $\nu_1 = 906.8 \text{ cm}^{-1}$ and the corresponding $\Delta\nu = 8.3 \text{ cm}^{-1}$ (all the values specified at RT) [56]. $\text{Yb}^{3+}, \text{Li}^+:\text{ZnWO}_4$ is a high phonon energy material.

The $\text{Yb}^{3+}, \text{Li}^+:\text{ZnWO}_4$ crystals are promising for self-Raman conversion of the fundamental radiation ($\sim 1.05 \mu\text{m}$, the ${}^2F_{5/2} \rightarrow {}^2F_{7/2}$ Yb^{3+} transition) to the spectral range of $\sim 1.16 \mu\text{m}$. Kaminski et al. demonstrated Stokes and anti-Stokes stimulated Raman scattering relying on the $\sim 906 \text{ cm}^{-1}$ mode in undoped ZnWO_4 using pulses with picosecond duration [57].

Table 7
 Raman-active modes observed in $\text{Yb}^{3+}, \text{Li}^+:\text{ZnWO}_4$ (at RT).

No.	Frequency, cm^{-1}		Symmetry	Internal mode
	$\text{Yb}^{3+}, \text{Li}^+:\text{ZnWO}_4$	ZnWO_4 [55]		
1	906	906.8	A_g	+
2	784	785.9	B_g	+
3	707	709.1	A_g	+
4	677	678.7	B_g	
5	545	546.4	A_g	
6	513	515.3	B_g	
7	406	406.9	A_g	+
8	353	355.4	B_g	
9	340	341.8	A_g	+
10	312	314.6	B_g	
11	275	274.4	A_g	
12	266	267.3	B_g	
13	194	195.3	A_g	
14	188	190.0	B_g	+
15	163	164.5	B_g	
16	144	146.3	B_g	
17	122	123.2	A_g	
18	–	91.5	B_g	

6. Conclusions

To conclude, we have grown for the first time $\text{Yb}^{3+}, \text{Li}^+$ -co-doped ZnWO_4 crystals with the goal of developing a novel laser gain material at $\sim 1 \mu\text{m}$. This compound melts congruently at 1166°C and large-volume crystals were obtained by the conventional Czochralski method. $\text{Yb}^{3+}, \text{Li}^+:\text{ZnWO}_4$ crystallizes in the monoclinic system (sp. gr. $P2_1/c$). The main issues for fabrication of laser-quality crystals are (i) suppressing the unwanted crystal coloration; (ii) avoiding excessive crystal cracking which seems to be enhanced by Yb^{3+} doping despite the relatively weak anisotropy of thermal expansion; and (iii) reaching high actual Yb^{3+} doping concentrations for efficient optical pumping.

We studied in detail the coloration of as-grown $\text{Yb}^{3+}, \text{Li}^+:\text{ZnWO}_4$ crystals as a function of the purity of the reagents (WO_3 and ZnO) and crucible composition (Pt/Rh and Pt). For crystals grown from the Pt/Rh crucibles, the coloration caused mainly by the oxygen vacancies can be greatly eliminated by oxidizing annealing at $\sim 800^\circ\text{C}$ for 1–20 days (depending on the sample thickness). The nature of the residual pink coloration of samples is probably due to iron ions, as well as other uncontrolled impurities. Therefore, it can be further eliminated by special purification of the growth charge. The material of the crucible seems to affect the coloration of the crystals acting as a catalyst of a partial reduction of the crystal-forming compound and promoting formation of other impurity centers, such as $\text{Fe}^{2+}(\text{Fe}^{3+})$, etc. in the case of Rh. Thus, there exist two possibilities for obtaining laser-quality $\text{Yb}^{3+}, \text{Li}^+:\text{ZnWO}_4$: (i) the use of Pt/Rh crucibles and a subsequent oxidizing annealing, or (ii) the use of pure Pt crucibles.

Our studies indicate a moderately high segregation coefficient for Yb^{3+} ions in ZnWO_4 ($K_{\text{Yb}} = 0.45 \pm 0.16$), despite the heterovalent doping mechanism and the notable difference of ionic radii of Yb^{3+} and Zn^{2+} . Indeed, K_{Yb} well exceeds that for the isostructural MgWO_4 crystal. This is assigned in part to the used charge compensator (Li^+). Further studies are needed to clarify the role of oxygen vacancies and Li^+ cations in the doping mechanism of ZnWO_4 . An optimization of the Li^+ content in the charge, and/or the search of a more appropriate charge compensator should be performed.

The quality of obtained crystals was sufficient to achieve diode-pumped laser operation with $\text{Yb}^{3+}, \text{Li}^+:\text{ZnWO}_4$ at $\sim 1 \mu\text{m}$ (see the parallel paper [29]).

CRedit authorship contribution statement

Kirill Subbotin: Conceptualization, Investigation, Resources, Writing - original draft. **Pavel Loiko**: Conceptualization, Investigation,

Methodology, Writing - original draft. **Sami Slimi**: Formal analysis, Data curation, Methodology. **Anna Volokitina**: Investigation. **Anatoly Titov**: Investigation, Resources. **Denis Lis**: Investigation, Resources. **Elena Chernova**: Investigation, Resources. **Rosa Maria Solé**: Methodology. **Uwe Griebner**: Writing - review & editing. **Valentin Petrov**: Methodology, Writing - review & editing. **Magdalena Aguiló**: Methodology, Resources. **Francesc Díaz**: Resources. **Patrice Camy**: Writing - review & editing. **Evgenii Zharikov**: Writing - review & editing, Supervision. **Xavier Mateos**: Writing - review & editing, Supervision.

Declaration of Competing interest

The authors declare that they have no known competing financial interests or personal relationships that could have appeared to influence the work reported in this paper.

Acknowledgements

This work was supported by the Spanish Government (project No. MAT2016-75716-C2-1-R (AEI/FEDER,UE)) and by Generalitat de Catalunya (project No. 2017SGR755). The research work of the authors from Prokhorov General Physics Institute was supported by Russian Science Foundation (grant # 18-12-00517).

References

- [1] E. Cavalli, A. Belletti, M.G. Brik, Optical spectra and energy levels of the Cr^{3+} ions in MWO_4 ($M = \text{Mg}, \text{Zn}, \text{Cd}$) and MgMoO_4 crystals, *J. Phys. Chem. Solid.* 69 (2008) 29–34.
- [2] L. Li, Y. Yu, G. Wang, L. Zhang, Z. Lin, Crystal growth, spectral properties and crystal field analysis of $\text{Cr}^{3+}:\text{MgWO}_4$, *CrystEngComm* 15 (2013) 6083–6089.
- [3] L. Zhang, W. Chen, J. Lu, H. Lin, L. Li, G. Wang, G. Zhang, Z. Lin, Characterization of growth, optical properties, and laser performance of monoclinic $\text{Yb}:\text{MgWO}_4$ crystal, *Opt. Mater. Express* 6 (2016) 1627–1634.
- [4] X. Wang, Z. Fan, H. Yu, H. Zhang, J. Wang, Characterization of ZnWO_4 Raman crystal, *Opt. Mater. Express* 7 (2017) 1732–1744.
- [5] L. Zhang, P. Loiko, J.M. Serres, E. Kifle, H. Lin, G. Zhang, E. Vilejshikova, E. Dunina, A. Kornienko, L. Fomicheva, U. Griebner, V. Petrov, Z. Lin, W. Chen, K. Subbotin, M. Aguiló, F. Díaz, X. Mateos, Growth, spectroscopy and first laser operation of monoclinic $\text{Ho}^{3+}:\text{MgWO}_4$ crystal, *J. Lumin.* 213 (2019) 316–325.
- [6] V.B. Kravchenko, Crystal structure of the monoclinic form of magnesium tungstate MgWO_4 , *J. Struct. Chem.* 10 (1969) 139–140.
- [7] P.F. Schofield, K.S. Knight, G. Cressey, Neutron powder diffraction study of the scintillator material ZnWO_4 , *J. Mater. Sci.* 31 (1996) 2873–2877.
- [8] V.B. Mikhailik, H. Kraus, V. Kapustyanyk, M. Panasyuk, P. Yu, V. Tsybulskiy, L. Vasylechko, Structure, luminescence and scintillation properties of the MgWO_4 - MgMoO_4 system, *J. Phys. Condens. Matter* 20 (2008) 365219.
- [9] F.A. Danevich, D.M. Chernyak, A.M. Dubovik, B.V. Grinyov, S. Henry, H. Kraus, V. M. Kudovbenko, V.B. Mikhailik, L.L. Nagornaya, R.B. Podviyanuk, O.G. Polischuk, I.A. Tupitsyna, Y.Y. Vostretsov, MgWO_4 – a new crystal scintillator, *Nucl. Instrum. Methods A* 608 (2009) 107–115.
- [10] T. Oi, K. Takagi, T. Fukazawa, Scintillation study of ZnWO_4 single crystals, *Appl. Phys. Lett.* 36 (1980) 278–279.
- [11] L.L. Nagornaya, B.V. Grinyov, A.M. Dubovik, Y.Y. Vostretsov, I.A. Tupitsyna, F. A. Danevich, V.M. Mokina, S.S. Nagorniy, O.G. Shkulkova, H. Kraus, V.B. Mikhailik, Large volume ZnWO_4 crystal scintillators with excellent energy resolution and low background, *IEEE Trans. Nucl. Sci.* 56 (2009) 994–997.
- [12] H. Kraus, V.B. Mikhailik, Y. Ramachers, D. Day, K.B. Hutton, J. Telfer, Feasibility study of a ZnWO_4 scintillator for exploiting materials signature in cryogenic WIMP dark matter searches, *Phys. Lett. B* 610 (2005) 37–44.
- [13] P. Belli, R. Bernabei, F. Cappella, R. Cerulli, C.J. Dai, F.A. Danevich, B.V. Grinyov, A. Incicchitti, V.V. Kobychov, L.L. Nagornaya, S.S. Nagorniy, Search for 2β processes in ^{64}Zn with the help of ZnWO_4 crystal scintillator, *Phys. Lett. B* 658 (2008) 193–197.
- [14] L. Zhang, Y. Huang, S. Sun, F. Yuan, Z. Lin, G. Wang, Thermal and spectral characterization of $\text{Cr}^{3+}:\text{MgWO}_4$ – a promising tunable laser material, *J. Lumin.* 169 (2016) 161–164. Part A.
- [15] P.A. Popov, S.A. Skrobov, A.V. Matovnikov, N.V. Mitroshenkov, Y.A. Borovlev, Thermal conductivity and heat capacity of a ZnWO_4 crystal, *Phys. Solid State* 58 (2016) 853–856 [transl. from *Fizika Tverdogo Tela* 58 (2016) 827–830].
- [16] P. Loiko, M. Chen, J.M. Serres, M. Aguiló, F. Díaz, H. Lin, G. Zhang, L. Zhang, Z. Lin, P. Camy, S.-B. Dai, Z. Chen, Y. Zhao, L. Wang, W. Chen, U. Griebner, V. Petrov, X. Mateos, Spectroscopy and high-power laser operation of a monoclinic $\text{Yb}^{3+}:\text{MgWO}_4$ crystal, *Opt. Lett.* 45 (2020) 1770–1773.
- [17] P. Loiko, J.M. Serres, X. Mateos, M. Aguiló, F. Díaz, L. Zhang, Z. Lin, H. Lin, G. Zhang, K. Yumashev, V. Petrov, U. Griebner, Y. Wang, S.Y. Choi, F. Rotermund, W. Chen, Monoclinic $\text{Tm}^{3+}:\text{MgWO}_4$: a promising crystal for continuous-wave and passively Q-switched lasers at $\sim 2 \mu\text{m}$, *Opt. Lett.* 42 (2017) 1177–1180.

K. Subbotin et al.

Journal of Luminescence 228 (2020) 117601

- [18] Y. Wang, W. Chen, M. Mero, L. Zhang, H. Lin, Z. Lin, G. Zhang, F. Rotermund, Y. J. Cho, P. Loiko, X. Mateos, U. Griebner, V. Petrov, Sub-100 fs Tm:MgWO₄ laser at 2017 nm mode locked by a graphene saturable absorber, *Opt. Lett.* 42 (2017) 3076–3079.
- [19] F. Yang, The spectroscopic investigation of ZnWO₄:Yb³⁺ single crystal, *J. Mater. Res.* 27 (2012) 2096–2100.
- [20] F. Yang, C. Tu, The spectroscopy investigation of ZnWO₄:Tm³⁺ single crystal, *J. Alloys Compd.* 535 (2012) 83–86.
- [21] Z. Xia, F. Yang, L. Qiao, F. Yan, End pumped yellow laser performance of Dy³⁺:ZnWO₄, *Optic Commun.* 387 (2017) 357–360.
- [22] P. Loiko, L. Zhang, J.M. Serres, Y. Wang, M. Aguiló, F. Díaz, Z. Lin, H. Lin, G. Zhang, E. Vilejshikova, E. Dunina, A. Kornienko, L. Fomicheva, V. Petrov, U. Griebner, W. Chen, X. Mateos, Monoclinic Tm³⁺:MgWO₄ crystal: crystal-field analysis, tunable and vibronic laser demonstration, *J. Alloys Compd.* 763 (2018) 581–591.
- [23] D.M. Trots, A. Senyshyn, L. Vasylechko, R. Niewa, T. Vad, V.B. Mikhailik, H. Kraus, Crystal structure of ZnWO₄ scintillator material in the range of 3–1423 K, *J. Phys. Condens. Matter* 21 (2009) 325402.
- [24] S. O'hara, G.M. McManus, Czochralski growth of low-dislocation-density zinc tungstate crystals, *J. Appl. Phys.* 36 (1965) 1741–1746.
- [25] L.L. Nagornaya, A.M. Dubovik, Y.Y. Vostretsov, B.V. Grinyov, F.A. Danevich, K. A. Katrunov, V.M. Mokina, G.M. Onishchenko, D.V. Poda, N.G. Starzhinskiy, I. A. Tupitsyna, Growth of ZnWO₄ crystal scintillators for high sensitivity 2p experiments, *IEEE Trans. Nucl. Sci.* 55 (2008) 1469–1472.
- [26] E.N. Galashov, V.A. Gusev, V.N. Shlegel, Y.V. Vasiliev, The growth of ZnWO₄ and CdWO₄ single crystals from melt by the low thermal gradient Czochralski technique, *Crystallogr. Rep.* 54 (2009) 689–691 [transl. from *Kristallografiya* 54 (2009) 733–735].
- [27] A. Watterich, O.R. Gilliam, L.A. Kappers, Colouration, impurities and non-local charge-compensation in ZnWO₄, *Solid State Commun.* 88 (1993) 619–621.
- [28] L.N. Limarenko, Y.V. Zorenko, M.M. Batenchuk, Z.T. Moroz, M.V. Pashkovskii, I. V. Konstankevich, Role of intrinsic defects and impurities in forming the optical characteristics of ZnWO₄ and CdWO₄ crystals, *J. Appl. Spectrosc.* 67 (2000) 287–294.
- [29] A. Volokitina, S.P. David, P. Loiko, K. Subbotin, A. Titov, D. Lis, R.M. Solé, V. Jambunathan, A. Lucianetti, T. Mocek, P. Camy, U. Griebner, V. Petrov, M. Aguiló, F. Díaz, X. Mateos, Monoclinic zinc monotungstate Yb³⁺:Li⁺:ZnWO₄: Part II. Polarized spectroscopy and laser operation, *J. Lumin.* (2020) submitted for publication.
- [30] M.D. Serrano, J.O. Álvarez-Pérez, C. Zaldo, J. Sanz, I. Sobrados, J.A. Alonso, C. Cascales, M.T. Fernández-Díaz, A. Jezowski, Design of Yb³⁺ optical bandwidths by crystallographic modification of disordered calcium niobium gallium laser garnets, *J. Mater. Chem. C* 5 (2017) 11481–11495.
- [31] Z. Pan, J.M. Serres, E. Kifle, P. Loiko, H. Yuan, X. Dai, H. Cai, M. Aguiló, F. Díaz, Y. Wang, Y. Zhao, U. Griebner, V. Petrov, X. Mateos, Comparative study of the spectroscopic and laser properties of Tm³⁺, Na⁺(Li⁺)-codoped Ca₃Nb_{1.5}Ga_{3.5}O₁₂-type disordered garnet crystals for mode-locked lasers, *Opt. Mater. Express* 8 (2018) 2287–2299.
- [32] F. Yang, C. Tu, Growth and spectroscopy of Ni²⁺ in ZnWO₄ crystal, *Mater. Lett.* 61 (2007) 3056–3058.
- [33] A. Watterich, M. Wöhlecke, H. Müller, K. Raksányi, A. Breitkopf, B. Zelei, Fe centers and charge compensation in ZnWO₄ single crystals characterized by ESR and IR spectroscopy, *J. Phys. Chem. Solid.* 53 (1992) 889–895.
- [34] F. Yang, C. Tu, J. Li, G. Jia, H. Wang, Y. Wei, Z. You, Z. Zhu, Y. Wang, X. Lu, Growth and optical property of ZnWO₄:Er³⁺ crystal, *J. Lumin.* 126 (2007) 623–628.
- [35] F. Yang, C. Tu, H. Wang, Y. Wei, Z. You, G. Jia, J. Li, Z. Zhu, X. Lu, Y. Wang, Growth and spectroscopy of Dy³⁺ doped in ZnWO₄ crystal, *Opt. Mater.* 29 (2007) 1861–1865.
- [36] F. Yang, C. Tu, H. Wang, Y. Wei, Z. You, G. Jia, J. Li, Z. Zhu, X. Lu, Y. Wang, Growth and spectroscopy of ZnWO₄:Ho³⁺ crystal, *J. Alloys Compd.* 455 (2008) 269–273.
- [37] R.D. Shannon, Revised effective ionic radii and systematic studies of interatomic distances in halides and chalcogenides, *Acta Crystallogr. A* 32 (1976) 751–767.
- [38] N. Onuma, H. Higuchi, H. Wakita, H. Nagasawa, Trace element partition between two pyroxenes and the host lava, *Earth Planet Sci. Lett.* 5 (1968) 47–51.
- [39] G.M. Kuz'micheva, V.B. Rybakov, K.A. Subbotin, E.V. Zharikov, D.A. Lis, O. Zaharko, D.A. Nikolae, V.G. Senin, Colors of mixed-substituted double molybdate single crystals having scheelite structure, *Russ. J. Inorg. Chem.* 57 (2012) 1128–1133 [transl. from *Zhurnal Neorganicheskoi Khimii* 57 (2012) 1205–1211].
- [40] M. Kuz'micheva, D.A. Lis, K.A. Subbotin, V.B. Rybakov, E.V. Zharikov, Growth and structural X-ray investigations of scheelite-like single crystals Er,Ce:NaLa(MoO₄)₂ and Yb:NaGd(WO₄)₂, *J. Cryst. Growth* 275 (2005) e1835–e1842.
- [41] V. Volkov, M. Rico, A. Méndez-Blas, C. Zaldo, Preparation and properties of disordered NaBi(XO₄)₂, X = W or Mo, crystals doped with rare earths, *J. Phys. Chem. Solid.* 63 (2002) 95–105.
- [42] S.C. Sabharwal, Role of non-stoichiometry in the cracking of oxide crystals, *J. Cryst. Growth* 310 (2008) 2899–2905.
- [43] M.G. Brk, V. Nagirnyi, M. Kirm, Ab-initio studies of the electronic and optical properties of ZnWO₄ and CdWO₄ single crystals, *Mater. Chem. Phys.* 134 (2012) 1113–1120.
- [44] R. Lacomba-Perales, J. Ruiz-Fuertes, D. Errandonea, D. Martínez-García, A. Segura, Optical absorption of divalent metal tungstates: correlation between the band-gap energy and the cation ionic radius, *Europhys. Lett.* 83 (2008) 37002.
- [45] S. O'hara, Zinc tungstate crystal growth, dislocations, and crystallography, *J. Appl. Phys.* 35 (1964) 1312–1316.
- [46] I. Földvári, R. Capelletti, Á. Péter, I. Cravero, A. Watterich, Spectroscopic properties of ZnWO₄:Fe single crystals, *Solid State Commun.* 9 (1986) 855–860.
- [47] L.F. Bencs, K. Raksányi, O. Szakács, L. Kovács, A. Watterich, Á. Péter, Removal of iron, chromium and sodium impurities from zinc tungstate (ZnWO₄), *J. Cryst. Growth* 181 (1997) 455–458.
- [48] A. Kornlyo, A. Jankowska-Frydel, B. Kuklinski, M. Grinberg, N. Krutiak, Z. Moroz, M. Pashkovsky, Spectroscopic properties of ZnWO₄ single crystal doped with Fe and Li impurities, *Radiat. Meas.* 38 (2004) 707–710.
- [49] H. Wang, F.D. Medina, M.S. Antonious, C. Párkányi, J.E. Haky, D.M. Baird, Y. D. Zhou, Spectroscopic studies of ZnWO₄ single crystals, *Chem. Phys. Lett.* 205 (1993) 497–501.
- [50] Z. Kowalski, S.M. Kaczmarek, M. Berkowski, M. Glowacki, Y.A. Zhydachevskii, A. Suchocki, Growth and optical properties of ZnWO₄ single crystals pure and doped with Ca and Eu, *J. Cryst. Growth* 457 (2017) 117–121.
- [51] O.F. Schirmer, O-bound small polarons in oxide materials, *J. Phys. Condens. Matter* 18 (2006) R667.
- [52] P.F. Schofield, K.S. Knight, S.A.T. Redfern, G. Cressey, Distortion characteristics across the structural phase transition in (Cu_{1-x}Zn_x)WO₄, *Acta Cryst. B: Struct. Sci.* 53 (1997) 102–112.
- [53] S.C. Sabharwal, Investigations on cracking in CdWO₄ crystals, *J. Cryst. Growth* 216 (2000) 535–537.
- [54] T.C. Damen, S.P.S. Porto, B. Tell, Raman effect in zinc oxide, *Phys. Rev.* 142 (1966) 570.
- [55] Y. Liu, H. Wang, G. Chen, Y.D. Zhou, B.Y. Gu, B.Q. Hu, Analysis of Raman spectra of ZnWO₄ single crystals, *J. Appl. Phys.* 64 (1988) 4651–4653.
- [56] H. Wang, F.D. Medina, Y.D. Zhou, Q.N. Zhang, Temperature dependence of the polarized Raman spectra of ZnWO₄ single crystals, *Phys. Rev. B* 45 (1992) 10356–10362.
- [57] A.A. Kaminskii, H.J. Eichler, K. Ueda, N.V. Klassen, B.S. Redkin, L.E. Li, J. Findeisen, D. Jaque, J. García-Sole, J. Fernández, R. Balda, Properties of Nd³⁺-doped and undoped tetragonal PbWO₄, NaY(WO₄)₂, CaWO₄, and undoped monoclinic ZnWO₄ and CdWO₄ as laser-active and stimulated Raman scattering-active crystals, *Appl. Optic.* 38 (1999) 4533–4547.

Spectroscopic Study and First Laser Operation of Monoclinic $\text{Yb}^{3+}, \text{Li}^+:\text{ZnWO}_4$ Crystal

A.A.Volokitina^{1,2}, K.A.Subbotin^{3,4,*}, P.A.Loiko², A.I.Titov^{3,4}, D.A.Lis³, S.Slimi¹, R.M.Solé¹, S.P.David⁵, V.Jambunathan⁵, A.Lucianetti⁵, T.Mocek⁵, U.Griebner⁶, V.Petrov⁶, M.Aguiló¹, F.Díaz¹, X.Mateos¹ and E.Zharikov³

¹ FiCMA-FiCNA-EMaS, Universitat Rovira i Virgili (URV), Tarragona, Spain

² ITMO University, Saint-Petersburg, Russia

³ Prokhorov General Physics Institute, Russian Academy of Sciences, Moscow, Russia

⁴ Mendeleev University of Chemical Technology of Russia, Moscow, Russia

⁵ HiLASE Centre, Institute of Physics CAS, Dolní Břežany, Czech Republic

⁶ Max Born Institute for Nonlinear Optics and Short Pulse Spectroscopy, Berlin, Germany

Abstract—Monoclinic $\text{Yb}^{3+}, \text{Li}^+:\text{ZnWO}_4$ crystals were grown by Czochralski and their structure is refined. The spectroscopic properties of Yb^{3+} ions were studied with polarized light and the scheme of Stark splitting of Yb^{3+} manifolds in these crystals was determined. The Raman spectra were measured. A diode-pumped 2.90 W laser action at 1059 nm in the crystals was demonstrated

Keywords—laser materials; spectroscopy; ytterbium ions, tungstates

I. INTRODUCTION

Monoclinic (wolframite-type) tungstate crystals with general formula M^{2+}WO_4 (where $\text{M} = \text{Mg}, \text{Zn}, \text{Mn}, \text{etc.}$) are promising laser hosts for rare-earth laser-active ions, and attracting attention in the last years [1, 2]. Like Scheelite-like and $\text{KGd}(\text{WO}_4)_2$ -type tungstates, they exhibit broad and intense spectral bands owing to a partially disordered their structure and large distortions in the local environment of the dopant ion. However, M^{2+}WO_4 crystals possess better thermal properties [3] and larger ground state Stark splitting of lasing ions. Thus, these crystals are attractive for mode-locked (ML) oscillators [1]. Up to now, the studies were focused mainly on the MgWO_4 host doped by various lanthanides [1, 2], which can be grown by the TSSG method only. Its zinc analogue, ZnWO_4 , can be easily grown by the Czochralski (Cz) technique. Undoped ZnWO_4 crystal is known for a long time as scintillating material [4]. In this work, we report on spectroscopic characterization, and on the first laser action of Yb^{3+} and Li^+ codoped ZnWO_4 crystal.

II. RESULTS

The $\text{Yb}^{3+}, \text{Li}^+:\text{ZnWO}_4$ crystals with different Yb concentrations were grown by the Cz method in Pt/Rh or Pt crucibles in air using [010]-oriented ZnWO_4 seeds. The Li^+ cations were introduced for charge compensation. The actual Yb^{3+} concentration was determined by microprobe analysis, and by spark-source mass-spectrometry, and from the results of these measurements the Yb segregation coefficient in ZnWO_4 crystal was evaluated to be 0.12–0.15.

The structure of $\text{Yb}^{3+}, \text{Li}^+:\text{ZnWO}_4$ (monoclinic, sp. gr. $P2_1/c$) was refined based on X-ray powder diffraction (XRD), Fig. 1(a). The lattice constants are $a = 4.7024(9)$ Å, $b =$

$5.7193(4)$ Å, $c = 4.9313(8)$ Å, $\beta = 90.728(1)^\circ$. It is slightly larger than for the undoped ZnWO_4 , because ionic radius of Yb^{3+} in octahedral environment (0.868 Å) is larger than for Zn^{2+} (0.74 Å). The tensor of thermal expansion coefficients was determined by high-temperature XRD. The polarized Raman spectra were measured indicating the most intense mode at ~ 906 cm^{-1} . Absorption and stimulated-emission (SE) spectra of Yb^{3+} ions were determined, yielding a maximum SE cross-section $\sigma_{\text{SE}} = 2.81 \times 10^{-20}$ cm^2 at 1055.6 nm ($E \parallel Z$), Fig. 1(b). The lifetime of the ${}^2F_{5/2}$ state was measured to be 367 μs . The Stark splitting of Yb^{3+} multiplets was determined, Fig. 1(c) to be 804 cm^{-1} . It is rather high value, that is important for Yb^{3+} lasers operating by quasi-three-level scheme. CW diode-pumped laser action was achieved with maximum power of 2.90 W with a slope efficiency of 41.3%, Fig. 1(d).

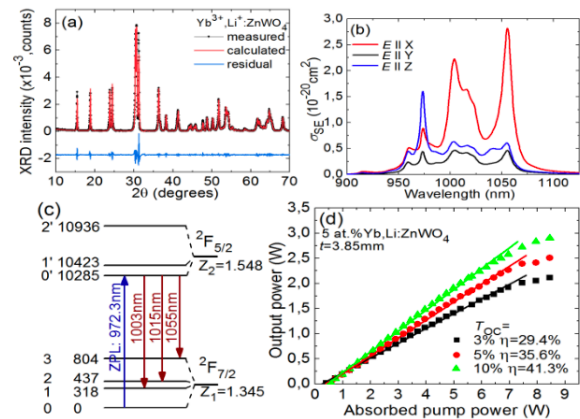


Fig. 1. Characterization of a 5 at.% $\text{Yb}^{3+}, \text{Li}^+:\text{ZnWO}_4$ crystal: (a) XRD pattern (black) showing the result of the Le Bail structure refinement (red); (b) SE cross-section spectra for the ${}^2F_{5/2} \rightarrow {}^2F_{7/2}$ Yb^{3+} transition for polarized light ($E \parallel X, Y, Z$ – optical indicatrix axes); (c) Yb^{3+} Stark splitting in ZnWO_4 ; (d) input-output dependences of a diode-pumped laser at $\text{Yb}^{3+}, \text{Li}^+:\text{ZnWO}_4$ crystal.

REFERENCES

- [1] Y.Wang, *et al.*, Opt. Lett., vol. 42, pp. 3076–3079
- [2] L.Zhang, *et al.*, J. Lumin., 213 (2019) 316–325
- [3] P.A.Popov, *et al.*, Crystallogr. Rep., 63 (2018) 111–116
- [4] E.N.Galashov, *et al.*, Crystallogr. Rep., 54 (2009) 689–691

Novel Molybdate Laser Crystal with a Layered Structure: Orthorhombic $\text{Er}^{3+}:\text{KY}(\text{MoO}_4)_2$

Anna Volokitina^{1,2,*}, Pavel Loiko^{3,**}, Anatoly Pavlyuk⁴, Rosa Maria Solé², Magdalena Aguiló², Francesc Díaz², and Xavier Mateos²

¹ ITMO University, 49 Kronverkskiy Pr., 197101 Saint-Petersburg, Russia

²FiCMA-FiCNA-EMaS, Universitat Rovira i Virgili (URV), Campus Sescelades, E-43007 Tarragona, Spain

³CIMAP, CNRS, Université de Caen Normandie, 6 Boulevard du Maréchal Juin, 14050 Caen Cedex 4, France

⁴A.V. Nikolaev Institute of Inorganic Chemistry, Siberian Branch of RAS, 3 Lavrentyev Ave., Novosibirsk 630090, Russia

*e-mail: anna.itmo@gmail.com, **e-mail: pavel.loiko@ensicaen.fr

Abstract—Potassium yttrium double molybdate crystals, 1.5 at.% $\text{Er}^{3+}:\text{KY}(\text{MoO}_4)_2$, are grown by the Czochralski method. They are orthorhombic and feature a layered structure. The absorption and emission properties of Er^{3+} ions are studied for polarized light. The maximum $\sigma_{\text{SE}} = 0.81 \times 10^{-20} \text{ cm}^2$ at 1617.7 nm for light polarization $E \parallel b$. The $\text{Er}^{3+}:\text{KY}(\text{MoO}_4)_2$ crystals showing a perfect cleavage are promising for eye-safe microchip lasers.

Keywords—molybdate crystals, layered structure, erbium ions, spectroscopy.

I. INTRODUCTION

Potassium rare-earth double tungstate and double molybdate crystals with a general chemical formula $\text{KLn}(\text{XO}_4)_2$, where $\text{Ln} = \text{Y, Gd, Lu}$ and $\text{X} = \text{W / Mo}$, respectively, are attractive hosts for doping with rare-earth ions (RE^{3+}) [1]. They provide high RE^{3+} doping levels with weak luminescence-quenching, strong anisotropy of absorption and SE cross-sections in polarized light and high luminescence quantum yields. The $\text{KY}(\text{MoO}_4)_2$ DMO crystals exhibit a layered structure enhancing such an anisotropy and leading to a perfect cleavage [2]. In the present work, we report on the growth, structure and polarized spectroscopy of Er^{3+} -doped $\text{KY}(\text{MoO}_4)_2$ for applications in eye-safe lasers.

II. RESULTS AND DISCUSSION

The 1.5 at.% $\text{Er}^{3+}:\text{KY}(\text{MoO}_4)_2$ crystal (melting temperature: $\sim 970 \text{ }^\circ\text{C}$) was grown by the Czochralski (Cz) method using a [100]-oriented undoped seed. To stabilize the growth, 5-7 mol% of $\text{K}_2\text{Mo}_3\text{O}_{10}$ were added to the melt. The crystal was transparent and had a slight rose coloration due to the Er^{3+} ions. The phase purity and the crystal structure were confirmed by X-ray powder diffraction: sp. gr. $Pbna - D^{14}_h$. The crystal exhibits a layered structure leading to a perfect natural cleavage along the (100) plane, Fig. 1(a). It is optically biaxial.

The polarized absorption spectra of $\text{Er}^{3+}:\text{KY}(\text{MoO}_4)_2$ (for $E \parallel a, b, c$) measured at room temperature are shown in Fig. 1(b). The strongest absorption corresponds to light polarization $E \parallel b$. For the $^4I_{15/2} \rightarrow ^4I_{11/2}$ pump transition, the maximum $\sigma_{\text{abs}} = 1.22 \times 10^{-21} \text{ cm}^2$ at 981.8 nm. The transition intensities of Er^{3+} ions were analyzed within the Judd-Ofelt (J-O) theory.

The Er^{3+} ions in $\text{KY}(\text{MoO}_4)_2$ exhibit intense emission in the eye-safe spectral range of $\sim 1.5\text{--}1.6 \text{ }\mu\text{m}$ due to the $^4I_{13/2} \rightarrow ^4I_{15/2}$

transition, Fig. 1(c). In the spectral range where laser operation is expected, the maximum $\sigma_{\text{SE}} = 0.81 \times 10^{-20} \text{ cm}^2$ at 1617.7 nm for light polarization $E \parallel b$. The luminescence lifetime for the upper laser level ($^4I_{13/2}$) $\tau_{\text{lum}} = 4.79 \text{ ms}$, Fig. 1(d). According to the radiative lifetime determined from the J-O calculations, the luminescence quantum yield is close to unity.

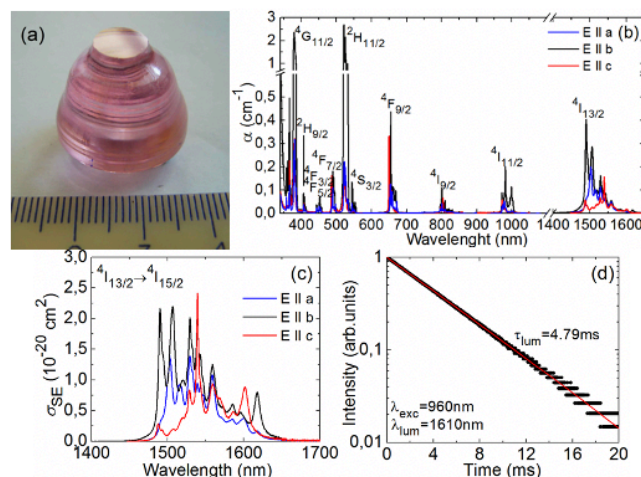


Fig. 1. Orthorhombic $\text{Er}^{3+}:\text{KY}(\text{MoO}_4)_2$ crystal: (a) photograph of the as-grown crystal boule; (b) polarized RT absorption spectra; (c) polarized SE cross-section, σ_{SE} , spectra for the $^4I_{13/2} \rightarrow ^4I_{15/2}$ transition; (d) luminescence decay curve, $\lambda_{\text{exc}} = 960 \text{ nm}$, $\lambda_{\text{lum}} = 1610 \text{ nm}$.

III. CONCLUSIONS

Orthorhombic $\text{Er}^{3+}:\text{KY}(\text{MoO}_4)_2$ DMO crystals are promising for eye-safe microchip lasers emitting at $\sim 1.6 \text{ }\mu\text{m}$. Thin crystal plates ($< 1 \text{ mm}$) are fabricated by mechanical cleavage and the laser experiments are in progress.

The reported study was funded by RFBR, project number 19-32-90199.

REFERENCES

- [1] V. Petrov *et al.*, "Growth and properties of $\text{KLu}(\text{WO}_4)_2$, and novel ytterbium and thulium lasers based on this monoclinic crystalline host," *Laser Photon. Rev.*, vol. 1, pp. 179-212, May 2007.
- [2] A. Volokitina, *et al.*, " $\text{Eu}^{3+}:\text{KY}(\text{MoO}_4)_2$: A novel anisotropic red-emitting material with a layered structure", *J. Alloy Compd.*, vol 762, pp. 786-796, Sept. 2018.

UNIVERSITAT ROVIRA I VIRGILI
SPECTRAL-LUMINESCENT PROPERTIES OF ORTHORHOMBIC AND MONOCLINIC TUNGSTATE AND MOLYBDATE CRYSTALS DOPED
WITH EUROPIUM, TERBIUM, THULIUM, AND YTTERBIUM IONS
Anna Volokitina



UNIVERSITAT
ROVIRA i VIRGILI